

**Forschungsbericht 2022-06**

**System Identification of  
Parameter-Varying Aeroelastic  
Systems using Real-Time  
Operational Modal Analysis**

Goran Jeličić

Deutsches Zentrum für Luft- und Raumfahrt  
Institut für Aeroelastik  
Göttingen



**DLR**

**Deutsches Zentrum  
für Luft- und Raumfahrt**

# **Forschungsbericht 2022-06**

## **System Identification of Parameter-Varying Aeroelastic Systems using Real-Time Operational Modal Analysis**

Goran Jeličić

Deutsches Zentrum für Luft- und Raumfahrt  
Institut für Aeroelastik  
Göttingen

343 Seiten  
174 Bilder  
17 Tabellen  
255 Literaturstellen



Deutsches Zentrum  
DLR für Luft- und Raumfahrt




*Herausgeber:*

Deutsches Zentrum  
für Luft- und Raumfahrt e. V.  
Wissenschaftliche Information  
Linder Höhe  
D-51147 Köln

ISSN 1434-8454  
ISRN DLR-FB-2022-06  
Erscheinungsjahr 2022

<https://doi.org/10.57676/p9qv-ck92>

### **Erklärung des Herausgebers**

Dieses Werk ist unter einer Creative Commons Lizenz vom Typ Namensnennung 3.0 Deutschland zugänglich.  Um eine Kopie dieser Lizenz einzusehen, konsultieren Sie <http://creativecommons.org/licenses/by/3.0/de/> oder wenden Sie sich brieflich an Creative Commons, Postfach 1866, Mountain View, California, 94042, USA.

### **Lizenz**



Creative Commons Lizenz vom Typ Namensnennung 3.0 Deutschland

*Systemidentifikation; Modalanalyse; Aeroelastik; zeitvariante Systeme; parametervariante Systeme; Signalverarbeitung; Simulation; operationelle Modalanalyse*

Goran Jeličić  
DLR, Institut für Aeroelastik, Göttingen

### ***Systemidentifikation parametervarianter aeroelastischer Systeme mit echtzeitfähiger Operationeller Modalanalyse***

#### ***Southern Denmark University (Syddansk Universitet)***

Fliegende Flugzeuge können als lineare parametervariante aeroelastische Systeme modelliert werden. Die Wechselwirkung zwischen aerodynamischen, Trägheits- und elastischen Kräften beeinflusst ihre modalen Parameter in Abhängigkeit von Flughöhe und -geschwindigkeit. Bei kritischen Luftstrombedingungen kann Flattern auftreten, eine dynamische Instabilität der Struktur, die sich als selbstinduzierte Schwingungen manifestiert, wenn der Dämpfungsgrad einer Schwingungsform negativ wird. Die Entwicklung und Erprobung neuer oder modifizierter Flugzeuge erfordert die Bewertung der Flatterstabilität. Flugschwingungsversuche bleiben eine gefährliche Tätigkeit, da eine ausreichende aeroelastische Stabilität innerhalb des gesamten Flugbereichs bis zur maximalen Höhe und Geschwindigkeit im Flug nachgewiesen werden muss.

Um die Sicherheit und die Effizienz von Flugschwingungsversuchen zu erhöhen, kann eine permanente Online-Schwingungsüberwachung durchgeführt werden. Damit kann die Entwicklung der Eigenfrequenz und des Dämpfungsgrades im Laufe der Zeit oder als Funktion von Flugvariablen verfolgt werden, um den Testingenieur über jede plötzliche Reduzierung der Dämpfung informieren zu können.

Die Schwingungsüberwachung erfolgt mittels operationeller Modalanalyse aus der durch Turbulenz erregter Beschleunigungsantwort der Struktur. Weitere Erregungsarten durch Manöver, Kontrollflächen und den Nachlauf anderer Flugzeuge werden auch berücksichtigt.

Die Theorie linear aeroelastischer parametervarianter Systeme und die Methoden zur Spektraldichteschätzung, Systemidentifikation und Modenverfolgung, die zur Analyse solcher Systeme erforderlich sind, werden in dieser Dissertation weiterentwickelt. Die theoretischen Werkzeuge wurden in eine echtzeitfähige Software für Schwingungsüberwachung implementiert und ihr Einsatz in Windkanal- und Flugschwingungsversuche demonstriert.

Zusammenfassend lässt sich sagen, dass modale Parameter von Flugzeugen, die schließlich durch Luftturbulenzen angeregt werden, erfolgreich geschätzt und verfolgt werden können. Die Auswertung erfolgt mithilfe der *Output-Only* Systemidentifikation für verschiedene Arten von Erregungen und Flugbedingungen. Diese Echtzeit-Modalanalyse hat das Potenzial, die Sicherheit der Experimente zu erhöhen, indem sie eine objektive Messung der Flatterstabilität liefert. Die permanente Schätzung der modalen Parameter ermöglicht eine effizientere Führung von Flugschwingungsversuchen.

*System identification; modal analysis; aeroelasticity; time-varying systems; parameter-varying systems, signal processing, simulation, operational modal analysis*

*(Published in English)*

Goran Jeličić

DLR, Institute of Aeroelasticity, Göttingen

***System Identification of Parameter-Varying Aeroelastic Systems using Real-Time Operational Modal Analysis***

***Southern Denmark University (Syddansk Universitet)***

Aircraft in flight can be modeled as linear parameter-varying aeroelastic systems. The interaction between aerodynamic, inertial and elastic forces influences their modal parameters depending on flight altitude and speed. At critical airflow conditions, flutter can occur, a dynamic instability of the airframe that manifests as self-induced oscillations when the damping ratio of a mode of vibration becomes negative. The development and testing of new or modified aircraft require the evaluation of the flutter margin. Flight vibration testing remains a hazardous activity since adequate aeroelastic stability must be demonstrated in flight within the whole flight envelope up to maximum altitude and speed.

In order to enhance the safety and efficiency of flight vibration testing, permanent in-flight online vibration monitoring can be performed by tracking the evolution of the eigenfrequency and damping ratio over time or flight variables such as speed and altitude in order to inform the test engineer about any sudden damping reduction.

Vibration monitoring is performed by means of operational modal analysis from the acceleration response due to air turbulence. Maneuvers, control surface deployment and excitation by the wake of other aircraft are also considered.

The thesis developed further the theory of aeroelastic parameter-varying systems and the spectral estimation, system identification and mode tracking techniques required to analyze such systems. The theoretical tools have been implemented into a real-time vibration monitoring application and demonstrated in wind tunnel tests and during flight vibration testing.

In conclusion, modal parameters of aircraft excited by air turbulence can be estimated and tracked successfully by output-only system identification methods for different types of excitation and flight conditions. Real-time modal analysis has the potential to enhance safety by providing the test engineers with objective measures of the flutter margin. It can improve efficiency by allowing continuous modal parameter estimation while experiments are ongoing.



**Deutsches Zentrum  
für Luft- und Raumfahrt**  
German Aerospace Center

# System Identification of Parameter-Varying Aeroelastic Systems using Real-Time Operational Modal Analysis

Department of Mechanical and Electrical Engineering  
University of Southern Denmark  
Odense

Institute of Aeroelasticity  
German Aerospace Center  
Göttingen

Doctoral Thesis

GORAN JELIČIĆ  
born in Zagreb

February 2022

Supervisor: Anders Brandt  
Co-supervisor: Marc Böswald



To my son Neven





## Preface

After I have worked for some time in the aeronautic industry, the opportunity to conduct research on structural dynamics arose. This field of engineering attracted me because of its beautiful applications of mathematics to real-world problems.

*Carpe diem*, I thought, and joined the Institute of Aeroelasticity at DLR.

The initiation into aeroelastic testing occurred a few months later with my first measurement in the transonic wind tunnel in Göttingen: the prototype program I developed for online vibration monitoring performed successfully its first operational modal analysis in parallel with other concurrent experiments.

Over the years, this software expanded greatly in scope, complexity and capabilities. Crucially, it was deployed during the flight vibration testing on the HALO research aircraft to collect data under variable excitation and flight conditions. These measurements raised the first questions about time-varying system dynamics. A year later, the permanent modal parameter tracking of a wing with nacelle model was performed at the high-speed wind tunnel in Amsterdam while approaching the stability boundary. The experiment required accurate damping estimates of a parameter-varying system using output-only methods.

At this point an interesting research subject began to coalesce: the examination of time-varying dynamics, the role of rate and amplitude of parameter variation and their influence on operational modal analysis of aeroelastic systems. Some time thereafter this topic was formalized and proposed to my academic supervisor.

The thesis attains from the experience acquired by performing modal analysis on several wind tunnel models, rotor blades, ground and flight vibration tests of aircraft. Experimental activities are complemented by equally extensive theoretical developments. The thesis is enriched by exchanges and discussions with members of the modal analysis community and beyond. The topic is vast, but presented with balance between depth and breadth in order to make it both accessible and complete. It has been written during hard times and a lot of heart has been put into each of its formulae, paragraphs and figures.

I hope that You, the reader, will find it informative and interesting.

*Göttingen, December 2021*

*Goran Jeličić*



## Acknowledgement

I would like to express my gratitude to everyone who has contributed in any way to this thesis. For some the support extends over the years to even before the start of the PhD project. Like rain droplets that eventually reach the sea, a myriad little things contributed to shaping and improving this thesis: time, effort, advice, critique, encouragement... Learning and developing benefited greatly from exchanges and discussions with colleagues and the members of the modal analysis community – thank you for your expertise and competence.

If I have not mentioned somebody explicitly – you know full well who you are.

I am very grateful to my supervisor Anders Brandt for promoting this topic and for the many qualities of a good mentor: being interested, communicative, optimistic. His broad knowledge and experience were influential factors in getting things done.

I would like to thank my co-supervisor Marc Böswald for the support, the mentorship and for making this project possible, from the first job training till its completion.

I wish to thank Yves Govers for his patience, advice and support over the years. The successful execution of the projects we conducted together is due to his organizational and leadership skills.

I am thankful to Jan Schwochow, with whom I share the enthusiasm for aeroelasticity and system identification, for tons of fruitful explanations, discussions and suggestions. Sometimes the solution to a problem was just an unrelated topic away.

A big thank you to my colleagues at DLR for the pleasant work environment, the interesting conversations, the teamwork during experiments and the many meals together over the years. You have contributed greatly.

Shout-out to my fellow PhD students and to many others at SDU, who helped me along the way and who all contributed to such a great experience at the university.

To those who know me well, whose friendship I value greatly but was committed elsewhere, thank you for your patience.

To my family – thank you for your support and for having confidence in me.

To my dear Wei, who always stood by my side, thank you for everything.



## Declaration of Authorship

I hereby declare that I have written this thesis without any help from others and without the use of documents and aids other than those stated in this document.

I have mentioned all used sources and I have cited them correctly according to established academic citation rules.

This thesis is submitted as partial fulfillment of the requirement of obtaining the Danish degree of PhD. The present work has been carried out as a collaboration between the Department of Mechanical and Electrical Engineering, University of Southern Denmark (SDU) and the Institute of Aeroelasticity at the German Aerospace Center (DLR) between March 2019 and February 2022. The PhD project has been funded by the Institute of Aeroelasticity at the German Aerospace Center (DLR) in Göttingen.

The PhD project has been supervised by Anders Brandt (SDU) and co-supervised by Marc Böswald (DLR).

Date

Signature



## Abstract

Aircraft in flight can be modeled as linear parameter-varying aeroelastic systems. The interaction between aerodynamic, inertial and elastic forces influences their modal parameters depending on flight altitude and speed. Under critical airflow conditions, flutter can occur, a dynamic instability of the airframe that manifests as self-induced oscillations when the damping ratio of a mode of vibration becomes negative. The development and testing of new or modified aircraft require the evaluation of the flutter margin. Flight vibration testing remains a hazardous activity since adequate aeroelastic stability must be demonstrated in flight within the whole flight envelope up to maximum altitude and speed.

In order to enhance the safety and efficiency of flight vibration testing, permanent in-flight online vibration monitoring can be performed by tracking the evolution of the eigenfrequency and damping ratio over time or flight variables such as speed and altitude in order to inform the test engineer about any sudden damping reduction.

Vibration monitoring is performed by means of operational modal analysis from the acceleration response due to air turbulence. Maneuvers, control surface deployment and excitation by the wake of other aircraft are also considered.

The thesis developed further the theory of aeroelastic parameter-varying systems and the spectral estimation, system identification and mode tracking techniques required to analyze such systems. The theoretical tools have been implemented into a real-time vibration monitoring application and demonstrated in wind tunnel tests and during flight vibration testing.

In conclusion, modal parameters of aircraft excited by air turbulence can be estimated and tracked successfully by output-only system identification methods for different types of excitation and flight conditions. Real-time modal analysis has the potential to enhance safety by providing the test engineers with objective measures of the flutter margin. It can improve efficiency by allowing continuous modal parameter estimation while experiments are ongoing.





## Resumé

Fly under flyvning kan modelleres som lineære parametervarierende aeroelastiske systemer. Samspejlet mellem aerodynamiske, inerti og elastiske kræfter påvirker deres modale parametre afhængigt af flyvehøjde og hastighed. Ved kritiske luftstrømsforhold kan der forekomme *flutter*, som er en dynamisk ustabilitet af flystellet, der viser sig som selv-inducerede svingninger, når dæmpningsforholdet for en svingningsform bliver negativt. Udvikling og afprøvning af nye eller modificerede fly kræver evaluering af flutter grænsen. Vibrationsforsøg af fly forbliver en farlig aktivitet, da tilstrækkelig aeroelastisk stabilitet skal påvises under flyvningen inden for hele *flight envelope* op til maksimal højde og hastighed.

For at øge sikkerheden og effektiviteten af flyvibrationstestning kan permanent onlineovervågning under flyvning udføres ved at spore udviklingen af egenfrekvensen og dæmpningsforholdet over tid eller flyvevariabler såsom hastighed og højde for at informere testingeniøren om enhver pludselig dæmpningsreduktion.

Vibrationsovervågning udføres ved hjælp af operationel modal analyse fra accelerationsresponset forårsaget af luftens turbulens. Manøvrer, indsættelse af kontroloverflader og excitation fra det turbulente flow forårsaget af andre fly tages også betragtning.

Denne afhandling videreudvikler teorien om aeroelastiske parametervarierende systemer og teknikker som spektralestimering, systemidentifikation og sporing af svingningsformer, der er nødvendige for at analysere dem. De teoretiske værktøjer implementeres i en vibrationsovervågningsapplikation i realtid og demonstreres i vindtunneltest og under flyvevibrationstest.

Modale parametre for fly exciteret af luftens turbulens kan estimeres og spores med succes ved hjælp af output-only systemidentifikationsmetoder for forskellige typer excitation og flyveforhold. Modal analyse i realtid har potentialet til at øge sikkerheden ved at give testingeniørerne objektive mål for flutter grænsen. Det kan forbedre effektiviteten ved at tillade kontinuerlig modal parameterestimering imens eksperimenter er i gang.



# Contents

<i>Index</i> . . . . .	I
<i>Nomenclature</i> . . . . .	VII
<i>Notation</i> . . . . .	XI
<i>1. Introduction</i> . . . . .	1
1.1 Context of the present study . . . . .	4
1.1.1 Summary of state-of-the-art . . . . .	6
1.2 Objectives . . . . .	7
1.3 Main contributions . . . . .	8
1.4 Outline . . . . .	9
<i>2. Linear time-varying systems</i> . . . . .	11
2.1 Linear time-varying systems . . . . .	13
2.1.1 Linear parameter-varying systems . . . . .	14
2.1.2 Second-order systems . . . . .	15
2.1.3 State transition matrix . . . . .	16
2.1.4 Impulse response of time-varying systems . . . . .	19
2.1.5 Impulse response in frequency-domain . . . . .	20
2.1.6 Stability of time-varying systems . . . . .	23
2.1.7 On eigenvalues and eigenvectors . . . . .	24
2.2 Linear time-invariant systems . . . . .	29
2.2.1 Second-order time-invariant systems . . . . .	32
2.3 Periodic systems . . . . .	34
2.3.1 Floquet's theorem . . . . .	35
2.3.2 Lyapunov-Floquet transformation . . . . .	36
2.3.3 Impulse response of periodic systems . . . . .	39
2.3.4 Frequency-domain description of periodic systems . . . . .	40
2.3.5 On the influence of period . . . . .	44
2.3.6 Windowed spectra . . . . .	48
2.4 Numerical methods for time-varying systems . . . . .	50
2.4.1 Discretization of the state matrix . . . . .	52
2.4.2 Initial value problem . . . . .	52
2.4.3 Boundary value problem . . . . .	54
2.4.4 Harmonic balance . . . . .	55
2.4.5 System identification applied to periodic systems . . . . .	57
2.4.6 Multiple shooting method . . . . .	58
2.4.7 Comparison of numerical methods . . . . .	58

---

2.5	Analytical solutions for time-varying systems . . . . .	59
2.5.1	Linear parameter variation . . . . .	59
2.5.2	Complex exponential parameter variation . . . . .	62
2.5.3	Examples of analytical solutions . . . . .	64
2.6	Chapter summary . . . . .	67
3.	<i>Aeroelastic systems</i> . . . . .	69
3.1	Aeroelastic modeling . . . . .	71
3.1.1	Aerodynamic forces . . . . .	71
3.1.2	Calculation of the aerodynamic influence coefficients . . . . .	74
3.1.3	Aeroelastic equation of motion . . . . .	76
3.1.4	Rational function approximation of aerodynamic influence coefficients . . . . .	77
3.1.5	Aeroelastic model: state matrix . . . . .	79
3.1.6	State matrix inverse . . . . .	83
3.1.7	Aeroelastic model: full state-space formulation . . . . .	84
3.2	Flutter mechanism . . . . .	85
3.3	Wind turbulence model . . . . .	87
3.4	Time-dependency of system matrices . . . . .	89
3.4.1	Variation of system matrices . . . . .	90
3.4.2	Variation of instantaneous eigenvalues . . . . .	91
3.4.3	Eigenvector rotation . . . . .	95
3.5	Chapter summary . . . . .	96
4.	<i>Spectral estimation</i> . . . . .	97
4.1	Fourier transform . . . . .	99
4.2	Power spectral density . . . . .	101
4.3	Spectral estimation methods . . . . .	105
4.3.1	Welch's modified periodogram . . . . .	107
4.3.2	Multi-taper spectral estimation . . . . .	111
4.3.3	Segmented multi-taper method . . . . .	113
4.4	Spectral estimation of time-varying systems . . . . .	116
4.4.1	On spectral estimation applied to aeroelastic systems . . . . .	121
4.5	Chapter summary . . . . .	124
5.	<i>System identification</i> . . . . .	125
5.1	Modal analysis frameworks . . . . .	126
5.2	Modal analysis of aeroelastic systems . . . . .	127
5.3	System identification methods . . . . .	128
5.3.1	Modeling assumptions . . . . .	128
5.3.2	System formulations . . . . .	129
5.3.3	Stabilization diagram . . . . .	130
5.4	Stochastic Subspace Identification (SSI) . . . . .	133

5.4.1	Subspace matrix construction . . . . .	137
5.4.2	Reconstruction of input spectra . . . . .	138
5.4.3	Efficient construction of the stabilization diagram . . . . .	139
5.4.4	Multi-band processing . . . . .	140
5.4.5	Contribution to system identification with SSI . . . . .	141
5.5	Least-Squares Complex Frequency (LSCF) . . . . .	142
5.5.1	Efficient construction of the stabilization diagram . . . . .	147
5.5.2	Reconstruction of input spectra . . . . .	147
5.5.3	Weighting choice . . . . .	148
5.5.4	Contributions to system identification with LSCF . . . . .	148
5.6	Least-squares frequency-domain method (LSFD) . . . . .	149
5.7	Chapter summary . . . . .	152
6.	<i>Mode tracking</i> . . . . .	153
6.1	Mode tracking problem statement . . . . .	155
6.2	Similarity metrics . . . . .	157
6.2.1	Output sensor selection . . . . .	158
6.2.2	MAC - modal assurance criterion . . . . .	159
6.2.3	MAC- $\lambda$ - modal assurances criterion with eigenvalues . . . . .	159
6.2.4	MACXP - expanded modal assurance criterion . . . . .	159
6.2.5	HDM - hyperbolic distance metric . . . . .	160
6.2.6	Tracking of analytical eigenvalues . . . . .	160
6.2.7	Comparison of mode similarity metrics . . . . .	161
6.3	Mode quality indices . . . . .	162
6.3.1	MIF - mode indicator function . . . . .	162
6.3.2	MPC - mode phase collinearity . . . . .	163
6.3.3	MPD - mean phase deviation . . . . .	163
6.3.4	MOV - mode overcomplexity value . . . . .	163
6.3.5	Comparison of mode quality criteria . . . . .	164
6.4	The tracking algorithm . . . . .	165
6.4.1	Mode matching . . . . .	166
6.4.2	Mode library . . . . .	167
6.4.3	Variance of modal parameters . . . . .	171
6.4.4	Cleaning of the stabilization diagram . . . . .	172
6.5	Parametric representation of tracked data . . . . .	173
6.6	Chapter summary . . . . .	175
7.	<i>Aeroelastic system simulation</i> . . . . .	177
7.1	Numerical analysis of time-varying systems . . . . .	178
7.1.1	Generation of system matrices . . . . .	179
7.1.2	Excitation signals . . . . .	180
7.1.3	Numerical methods . . . . .	181

---

7.1.4	Ad-hoc fixed-step Runge-Kutta solver . . . . .	183
7.1.5	Ad-hoc Adams-Bashforth-Moulton solver . . . . .	184
7.1.6	Higher-order discretization of time-varying systems . . . . .	184
7.1.7	Comparison of numerical methods . . . . .	187
7.2	Aeroelastic model . . . . .	189
7.3	Simulation results . . . . .	193
7.3.1	Simulation parameters . . . . .	194
7.3.2	Spectral estimation . . . . .	194
7.3.3	System identification . . . . .	194
7.3.4	Mode tracking . . . . .	195
7.3.5	Influence of rate of variation . . . . .	197
7.3.6	Influence of number of averages . . . . .	197
7.3.7	Influence of block length . . . . .	201
7.3.8	Flutter boundary extrapolation . . . . .	203
7.4	Chapter summary . . . . .	204
8.	<i>Experimental results</i> . . . . .	205
8.1	Dynamic effects in parameter-varying aeroelastic systems . . . . .	207
8.1.1	Wind tunnel tests . . . . .	209
8.1.2	Flight vibration testing . . . . .	210
8.2	HALO flight vibration test . . . . .	211
8.2.1	Instrumentation . . . . .	213
8.2.2	Modes of vibration . . . . .	216
8.2.3	Flight aerodynamic quantities . . . . .	218
8.2.4	Measurement plan . . . . .	222
8.3	Real-time automated modal analysis . . . . .	223
8.3.1	Design principle . . . . .	225
8.3.2	Data flow . . . . .	225
8.3.3	Performance . . . . .	226
8.4	Results . . . . .	228
8.5	Stationary system identification . . . . .	229
8.5.1	Time-domain data . . . . .	231
8.5.2	Frequency-domain data . . . . .	233
8.5.3	Reference channels . . . . .	238
8.5.4	Harmonic components . . . . .	238
8.5.5	System identification . . . . .	239
8.5.6	Eigensurface reconstruction . . . . .	242
8.6	Continuous system identification . . . . .	244
8.6.1	Chase flight . . . . .	245
8.6.2	Time-domain data . . . . .	247
8.6.3	Frequency-domain data . . . . .	249
8.6.4	System identification . . . . .	250

8.6.5	Mode tracking . . . . .	251
8.6.6	Large parameter variation . . . . .	256
8.6.7	Fuel consumption . . . . .	258
8.6.8	Descent maneuver . . . . .	260
8.6.9	Periodic flow separation . . . . .	262
8.7	Chapter summary . . . . .	263
9.	<i>Conclusions</i> . . . . .	265
9.1	Summary of the conclusions . . . . .	268
9.2	Take-home message . . . . .	268
9.3	Further research . . . . .	269
9.3.1	Parameter-varying aeroelastic systems . . . . .	269
9.3.2	Spectral estimation . . . . .	269
9.3.3	System identification . . . . .	269
9.3.4	Mode tracking . . . . .	270
9.3.5	Flight vibration testing . . . . .	270
9.4	Words of wisdom . . . . .	271
	<i>Appendix</i> . . . . .	295
A.	<i>Appendix</i> . . . . .	297
A.1	Matrix exponential . . . . .	297
A.2	Iterative diagonalization of the state matrix . . . . .	297
A.3	Linear parameter variation . . . . .	298
A.4	Exponential parameter variation . . . . .	301
A.5	Theodorsen's function . . . . .	304
A.6	Wagner's function . . . . .	304
A.7	Measurement time nomogram . . . . .	305
A.8	Automated decimation algorithm . . . . .	306
A.9	Ordinary differential equation solvers . . . . .	307
A.10	G550 DLR-HALO aircraft data . . . . .	310
A.11	Standardized principal moments . . . . .	311
A.12	Continuous wavelet transform . . . . .	312
A.13	Model of the eigenfrequency variation due to fuel consumption . . . . .	313





# Nomenclature

## *Lowercase Latin letters*

$b$	Semi-chord
$c_{ref}$	Airfoil reference chord
$f$	Frequency
$f_\lambda(f_n, \zeta)$	Eigenvalue funtion
$f_n$	Eigenfrequency
$f_s$	Sample rate
$i$	Index or imaginary unit
$j$	Index
$k$	Index or reduced frequency
$n$	Index
$o(\cdot)$	Little-o (asymptotic) notation
$p$	Index or system pole
$\mathbf{p}(t)$	Parameters vector
$\mathbf{q}(t)$	Generalized (modal) coordinates
$q$	Dynamic pressure
$s$	Laplace-domain variable
$t$	Time
$\mathbf{u}(t)$	System input
$\mathbf{x}(t)$	System state
$\mathbf{y}(t)$	System output
$\mathbf{z}(t)$	Aerodynamic lag states

## *Uppercase Latin letters*

$\mathbf{A}$	State matrix
$\mathbf{B}$	Input matrix
$\mathbf{C}$	Output matrix
$\mathbf{D}$	Feed-through matrix or damping matrix
$\mathbf{E}$	Descriptor matrix
$\mathbf{G}(\omega)$	Single-sided power spectral density
$\mathbf{H}(\omega)$	Frequency response function of time-invariant systems
$\mathbf{H}(t, \cdot)$	Impulse response function of time-varying systems
$\mathbf{K}$	Stiffness matrix
$\mathbf{M}$	Mass matrix or generic matrix
$Ma$	Mach number
$N_m$	Number of degrees of freedom
$N_u$	Number of inputs
$N_x$	Number of states or number of CPSD columns

---

$N_y$	Number of outputs or number of CPSD rows
$\mathcal{O}(\cdot)$	Big-O (asymptotic) notation
$\mathbf{P}(t)$	Floquet-Lyapunov transformation matrix
$\mathbf{Q}(k)$	Aerodynamic Influence Coefficients (AIC) matrix
$\mathbf{R}_k$	Residue matrix associated to $k$ -th pole
$\mathbf{S}(\omega)$	Double-sided power spectral density
$\mathbb{S}$	Subset of indices
$\mathcal{S}$	Linear system
$T$	Duration or period or absolute temperature
$\mathbf{U}$	Left-singular vectors
$\mathbf{V}$	Right-singular vectors
$V$	Air speed
$\mathbf{X}(t)$	Fundamental matrix of a time-varying system

### *Lowercase Greek letters*

$\alpha$	Angle of attack
$\gamma$	Aerodynamic lag state
$\delta$	Dirac delta
$\epsilon$	Error or tolerance
$\zeta$	Damping ratio
$\lambda$	Eigenvalue
$\mu$	Mean value
$\rho$	Air density
$\sigma$	Variance
$\tau$	Time-domain integration variable or time constant
$\phi$	Right eigenvector
$\psi$	Left eigenvector or mode shape
$\omega$	Circular frequency
$\omega_0$	Fundamental harmonic
$\omega_n$	Circular eigenfrequency

### *Uppercase Greek letters*

$\Lambda$	Diagonal eigenvalue matrix
$\Sigma$	Singular values (diagonal matrix)
$\Phi(\cdot, \cdot)$	State transition matrix
$\Psi$	Eigenvector matrix
$\Theta(\cdot, \cdot)$	Mode similarity metric

### *Abbreviations*

APSD	Autopower spectral density
CFD	Computational fluid dynamics
CPSD	Cross-power spectral density

DAQ	Data acquisition system
DFT	Discrete Fourier transform
DLM	Doublet lattice method
DLR	Deutsches Zentrum für Luft- und Raumfahrt (German Aerospace Center)
DNW	German-Dutch wind tunnels
DoF	Degrees of freedom
EMA	Experimental modal analysis
FEM	Finite element method
FFT	Fast Fourier transform
FRF	Frequency response function
FVT	Flight vibration test
AIC	Aerodynamic influence coefficients matrix
GAF	Generalized aerodynamic forces
GVT	Ground vibration test
HALO	High altitude and long range research aircraft
LPV	Linear parameter-varying system
LSCF	Least-squares complex frequency
LTI	Linear time-invariant system
LTP	Linear time-periodic system
LTV	Linear time-varying system
MTM	Multi-taper method
ODE	Ordinary differential equation
OLM	OnLine Monitoring software
OMA	Operational modal analysis
PSD	Power spectral density
SMT	Segmented multi-taper method
SSI	Stochastic subspace identification
STM	State transition matrix
TWG	Transonic wind tunnel Göttingen
WMP	Welch's modified periodogram

***Other symbols***

$(\cdot)(t)$	Variable is explicitly time-varying
$\tilde{(\cdot)}(t)$	Transformed variable due to coordinate change
$\tilde{(\cdot)}(f)$	Transformed variable in frequency-domain
$\hat{(\cdot)}$	Estimated variable
$(\cdot)^0$	Total quantity (in the context of thermodynamics)
$(\cdot)_\infty$	Free-stream quantity (in the context of aerodynamics)



## Notation

The conventions adopted for the notation in this thesis are listed here. Consistency is a virtue, but there are well-known equations that use symbols of such wide adoption that the rules listed below will be broken. Nevertheless, the symbol in question will be clearly defined in the text next to the equation.

**Notation.** *Particular notation conventions are highlighted in a box like this. Sometimes an exception is required in order to be consistent with the established notation in literature or for elegance. Notation changes are clearly stated every time.*

### Linear algebra

- Scalars are typeset with normal font weight, e.g.  $\alpha$ ,  $P$ .  
Column vectors are denoted by lowercase bold letters, e.g.  $\mathbf{x}$ ,  $\mathbf{v}$ .  
Row vectors are denoted as transposed column vectors, e.g.  $\boldsymbol{\psi}^T$ ,  $\mathbf{b}^T$ .  
Matrices are denoted by uppercase bold letters, e.g.  $\mathbf{A}$ ,  $\mathbf{H}$ .
- Square brackets denote matrices and the concatenation of scalars, vectors or matrices, for example  $\mathbf{M} \triangleq [\mathbf{v}_1, \mathbf{v}_2, \dots, \mathbf{v}_n]$ . A matrix that is assembled from other matrices can be denoted explicitly by  $[\mathbf{M}]$ , for example  $[\mathbf{M}] = [\mathbf{0} \ \mathbf{I}]$ .
- Curly brackets denote column vectors, e.g.  $\mathbf{a} = \{a_0, a_1 \dots, a_n\}$ .  
Vectorization is denoted by  $\{\mathbf{M}\} \triangleq \text{vec}(\mathbf{M})$ .
- Diagonalization of a vector  $\mathbf{v}$  is denoted by  $\text{diag}(\mathbf{v})$ .  
The diagonal of matrix  $\mathbf{M}$  is denoted by  $\text{diag}(\mathbf{M})$ .  
A block diagonal matrix is constructed by  $\text{diag}(\mathbf{M}_1, \mathbf{M}_2, \dots, \mathbf{M}_3)$ .
- The zero matrix is  $\mathbf{0}$ , the identity matrix is  $\mathbf{I}$ . They have implicitly the correct size.
- The Moore-Penrose pseudoinverse is denoted by a superscripted plus-sign.  
Let  $\mathbf{b} \in \mathbb{C}^N$ ,  $\mathbf{A} \in \mathbb{C}^{N \times M}$  and  $\mathbf{x} \in \mathbb{C}^M$ , then  $\mathbf{b} = \mathbf{A}\mathbf{x} \implies \mathbf{x} = \mathbf{A}^+\mathbf{b}$ .

### Indexing

- The subscripts of scalars designate:
  - an element of a set  $a_k \in \mathbb{S}$ .
  - an entry of a vector or matrix  $a_k \equiv \mathbf{a}[k]$ .
- The subscripts of vectors designate:
  - a particular quantity where the subscript distinguishes it from another related symbol, e.g.  $\mathbf{x}_h$  /  $\mathbf{x}_i$ : homogeneous vs inhomogeneous solutions.
  - the  $k$ -th element  $\mathbf{v}_k$  of a set of vectors  $\mathbb{V} = \{\mathbf{v}_1 \dots \mathbf{v}_{N_k}\}$ .
  - a particular entry of a vector, e.g.  $\mathbf{v}_0$  is  $v_{0,k} \equiv \mathbf{v}_{0,k} \equiv \mathbf{v}_0[k]$

- The subscripts of matrices designate:
  - the scalar entry  $(i, j)$  of a matrix  $\mathbf{M}$ : e.g.  $\mathbf{M}_{ij} \equiv \mathbf{M}[i, j] \equiv M_{ij}$ .
  - the diagonal element of a diagonal matrix. For example, if  $\mathbf{D} = \text{diag}(\mathbf{v})$ , then the  $k$ -th diagonal element is  $\mathbf{D}_k \equiv \mathbf{D}_{kk} \equiv \mathbf{v}[k] \equiv v_k$  (a scalar).
  - a submatrix of an assembled matrix. For example, the submatrix  $(2, 1)$  of  $[\mathbf{M}] = [\mathbf{A}, \mathbf{B}; \mathbf{C}, \mathbf{D}]$  is  $[\mathbf{M}][2, 1] \equiv [\mathbf{M}]_{21} \equiv \mathbf{C}$ .
  - the  $k$ -th element of a set of matrices  $\mathbb{K} = \{\mathbf{M}_1 \cdots \mathbf{M}_{N_k}\}$  is  $\mathbf{M}_k$ .
  - the columns of a matrix when said matrix does not belong to a set:  $\mathbf{M}_i \equiv \mathbf{M}[:, i]$
  - the rows and columns of a matrix:  $\mathbf{M}_{2:3, 1:3} \equiv \mathbf{M}[2 : 3, 1 : 3]$
- Let  $\mathbf{M} \in \mathbb{C}^{N \times M}$  be a matrix and define the selector vectors for the rows and columns  $\mathbf{e}_1 = \{1, \dots, 0\} \in \mathbb{N}^N$ ,  $\mathbf{e}_2 = \{0, 1, \dots, 0\} \in \mathbb{N}^M$  and so forth. The  $i$ -th row of  $\mathbf{M}$  is  $\mathbf{e}_i^T \mathbf{M}$ . The  $j$ -th column  $\mathbf{M}$  is  $\mathbf{M} \mathbf{e}_j$ . Entry  $(i, j)$  of  $\mathbf{M}$  is  $\mathbf{M}_{ij} \equiv \mathbf{e}_i^T \mathbf{M} \mathbf{e}_j$ .

## Sets

- Blackboard bold capital letters denote sets. The symbols  $\mathbb{N}$ ,  $\mathbb{Z}$ ,  $\mathbb{R}$  and  $\mathbb{C}$  denote respectively natural numbers, integers, real and complex numbers. The symbols  $\mathbb{I}$ ,  $\mathbb{J}$  and  $\mathbb{S}$  are sets of indices (integers).

## Summations

- The symbol  $\mathbb{S}$  denotes the indices of sums. For example, let  $\mathbf{a} = \{2, 3, 5, 7, 11\}$ , and define a subset  $\mathbb{S} = \{1, 3, 5\}$ , then  $\sum_{k \in \mathbb{S}} a_k \equiv a_1 + a_3 + a_5 \equiv 2 + 5 + 11$ .
- Summations over all elements of a set are denoted as  $\sum_{n \in \mathbb{Z}} a_n \equiv \sum_{n=-\infty}^{+\infty} a_n$
- Implicit summations are over *all* elements. For example, let  $a_{k,n} \in \mathbf{a}_k$  be the  $n$ -th term of vector  $\mathbf{a}_k \in \mathbb{C}^{N_k}$  (where the subscript  $k$  distinguishes it from a similar quantity, say  $\mathbf{a}_l$ ), then  $\sum \mathbf{a}_k \triangleq a_{k,0} + a_{k,1} + \dots + a_{k,N_k} \equiv \sum_{n=0}^{N_k} a_{k,n}$

## Matrix decompositions

- The eigendecomposition of a matrix is denoted with  $\mathbf{M} \stackrel{\text{eig}}{=} \mathbf{\Psi} \mathbf{\Lambda} \mathbf{\Psi}^{-1}$  where  $\mathbf{\Lambda}$  is the diagonal matrix of *eigenvalues* and  $\mathbf{\Psi}$  are the *eigenvectors*. If clear from context, the operator  $\stackrel{\text{eig}}{=}$  is omitted. The subscript  $k$  denotes the  $k$ -th eigenvalue  $\mathbf{\Lambda}_k$  and the  $k$ -th column of the eigenvector matrix  $\mathbf{\Psi}_k$ . Sometimes the  $k$ -th eigenpair is denoted by  $\psi_k$  and  $\lambda_k$ .
- The singular value decomposition of a matrix  $\mathbf{M} \in \mathbb{C}^{m \times n}$  is denoted by  $\mathbf{M} \stackrel{\text{svd}}{=} \mathbf{U} \mathbf{\Sigma} \mathbf{V}^T$  where  $\mathbf{U} \in \mathbb{C}^{m \times m}$  is a complex unitary matrix of *left singular vectors*,  $\mathbf{\Sigma} \in \mathbb{R}_+^{m \times n}$  is the diagonal matrix of non-negative *singular values* and  $\mathbf{V} \in \mathbb{C}^{n \times n}$  is the unitary matrix of *right singular vectors*. If clear from context, the operator  $\stackrel{\text{svd}}{=}$  is omitted. The subscript  $k$  denotes the  $k$ -th singular value  $\mathbf{\Sigma}_k$ , the  $k$ -th column of the left singular vectors  $\mathbf{U}_k$  and the  $k$ -th row of the right singular vectors  $\mathbf{V}_k^H$ .

## Transforms

- The imaginary unit is denoted by  $i$ . The letter  $j$  does not denote the imaginary unit. When they are typeset as subscripts, they are integer indices  $i, j \in \mathbb{Z}$ .
- The Fourier transform is non-unitary for convenience of notation:

$$\mathcal{F}\{f(t)\} = f(\omega) \triangleq \int_{-\infty}^{+\infty} f(t)e^{-i\omega t} dt$$

$$\mathcal{F}^{-1}\{f(\omega)\} = f(t) \triangleq \frac{1}{2\pi} \int_{-\infty}^{+\infty} f(\omega)e^{i\omega t} d\omega$$

The transformation is unitary when the factor of  $\mathcal{F}$  and  $\mathcal{F}^{-1}$  is  $1/\sqrt{2\pi}$ .

- The Laplace variable is  $s = \sigma + i\omega$  where  $\sigma, \omega \in \mathbb{R}$ . The symbol  $s_k$  denotes a complex frequency from a set  $k \in \mathbb{S}$ .
- The Laplace transform:

$$\mathcal{L}\{f(t)\}(s) \triangleq f(s) \equiv \int_0^{\infty} f(t)e^{-st} dt$$

is denoted by:

$$\begin{aligned} f(s) = \mathcal{L}\{f(t)\}(s) &\iff f(t) \circ \bullet f(s) \\ f(t) = \mathcal{L}^{-1}\{f(s)\}(t) &\iff f(s) \bullet \circ f(t) \end{aligned}$$

## Other

- The colon  $:$  is used for creating vectors with consecutive elements, for example  $3 : 6 = \{3, 4, 5, 6\}$  or  $6 : -1 : 3 = \{6, 5, 4, 3\}$ .
- The matrix exponential is:  $\exp \mathbf{M} \equiv e^{\mathbf{M}} = \sum_{n=0}^{\infty} \frac{1}{n!} \mathbf{M}^n$ . It is stated clearly when  $\exp(\mathbf{M})$  denotes the scalar exponential of the matrix entries  $\exp(M_{ij})$ .
- The eigenvector function  $f_\lambda$  maps the eigenfrequency  $f_n$  [Hz] and damping ratio  $\zeta$  [adim] onto the complex plane  $\lambda$  [rad/s]:

$$f_\lambda(f_n, \zeta) \longrightarrow \lambda : \quad \lambda = 2\pi f_n \left( -\zeta + i\sqrt{1 - \zeta^2} \right) \quad [\text{rad/s}]$$





# 1 Introduction

The influence of aerodynamics on aircraft in flight can be observed in the variation of stability and modal parameters depending on airflow variables such as flight altitude and wind speed. The structure's *modal parameters* – eigenfrequencies, damping ratios and normal modes – describe how it vibrates and responds to external forces. Aeroelasticity researches the interaction between inertial, elastic and aerodynamic forces in structures immersed in a fluid flow. It encompasses the study of phenomena such as divergence, control reversal, flutter, gust response and maneuver loads. While the first two are static, the others are dynamic in nature. The multidisciplinary character of aeroelasticity is illustrated well by Collar's triangle in figure 1.1.

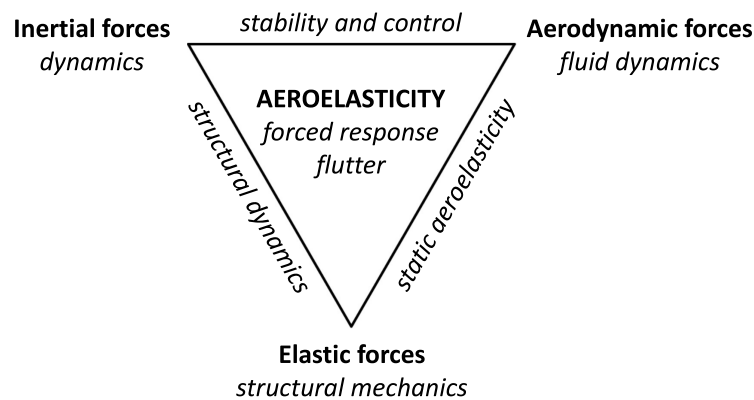


FIGURE 1.1: Collar's aeroelastic triangle showing the major disciplines in aeroelasticity.

Vibrating structures exchange permanently potential and kinetic energy due to the work performed by elastic and inertial forces. Part of the total energy is dissipated as heat by the internal or external influence of damping. In the absence of any outside excitation, the system is eventually brought to rest. Even with ideal non-dissipative materials, the interaction with the airflow modifies this energy exchange mechanism and introduces additional damping. However, aeroelastic systems at critical airflow conditions may instead absorb energy from the stream and become unstable, leading to catastrophic structural failure – the *flutter* phenomenon. Flutter is a dynamic aeroelastic instability that results in a self-excited oscillation; it is not to be confused with resonance, where the system response amplitude increases when the excitation has a frequency component in the vicinity of an eigenfrequency. Aeroelastic stability is an essential design concern in the development of new aircraft or modification of existing ones and must be demonstrated in flight. The analytical and numerical aeroelastic models for the determination of the flutter boundary are complemented by flight vibration tests. In this regard the state-of-the-art consists of estimating the damping ratio of critical modes by control surface excitation during stabilized level flight using system identification techniques. The procedure is repeated for all points of interest within the flight envelope by holding the altitude constant and by carefully increasing the speed in small steps and observing the damping trend.

System identification is the study of statistical methods that analyze the response of an unknown physical process induced by some excitation in order to construct a parametric representation of its behavior. The resulting mathematical models provide a simplified description of complex dynamic systems in the time or frequency domains. System identification is employed in control applications, to predict the response to arbitrary input signals, to validate numerical models, to quantify structural nonlinearities and to gain further physical insight into a dynamic system. It is performed in the input-output or output-only frameworks, depending on whether the excitation signals are available or not. The experimenter selects a mathematical model to represent the physical process, after which the identification method fits the model structure to acquired data by tuning its parameters so that the difference between physical system and mathematical representation is low; the concept is illustrated in figure 1.2.

Operational modal analysis (OMA) is a branch of system identification that focuses on modeling an unknown dynamic process from the examination of its measured response during operation or in the presence of unknown or unmeasurable excitation. Conversely, when the input is known, identification is performed within the experimental modal analysis (EMA) framework. OMA has many applications in engineering, such as permanent non-invasive structural health monitoring and damage detection of bridges, wind turbines and historical buildings, or vibration monitoring of machinery and vehicles during operation, for instance engines and aircraft. The OMA methods estimate the normal modes and the associated eigenfrequency and damping ratio with a confidence that depends on the signal-to-noise ratio, the presence of errors, extraneous signals, deviations from assumptions and so forth. An example of operational modal analysis performed on a wing model is illustrated in figures 1.3 and 1.4.

The continuous estimation of modal parameters from the acceleration response to atmospheric turbulence while the flight vibration test is ongoing can save time and increase safety by providing permanently an objective measure of aeroelastic stability to the flight test engineer or pilot; a similar function is performed during aeroelastic testing in wind tunnels. Real-time system identification applied to parameter-varying aeroelastic systems is therefore a research topic attracting great interest and clear demand from the industry.

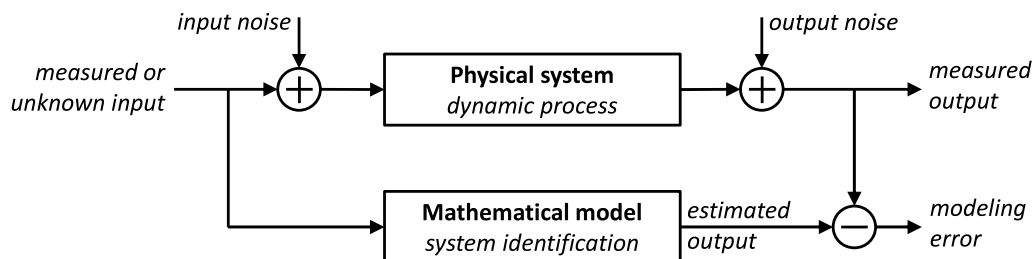


FIGURE 1.2: System identification concept: an unknown dynamic process responds to some excitation signals in the presence of noise. The model's structure is selected based on first principles. The chosen identification technique estimates the values of the model's parameters in the input-output or output-only frameworks. The model is validated by assessing how it describes the physical system in the time or frequency domains.

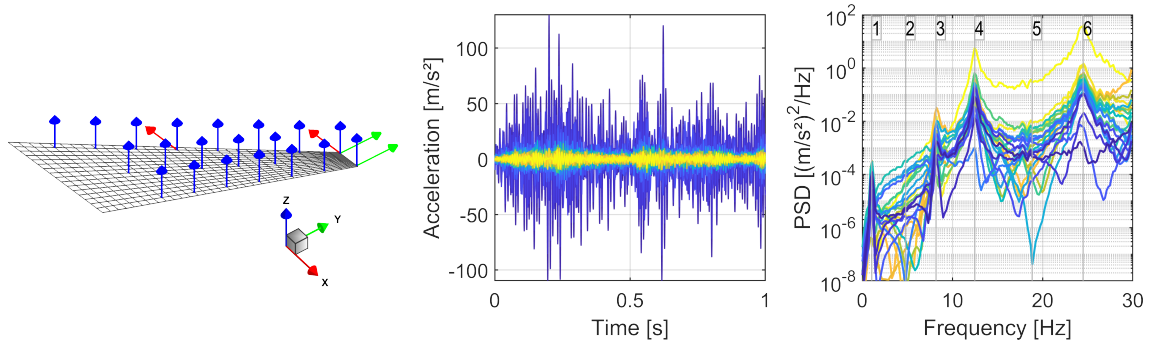


FIGURE 1.3: Operational modal analysis procedure: example with a swept wing modeled by shell elements. Left plot: geometry (wire-frame) and accelerometers (arrows). Middle plot: random response due to unknown turbulent excitation. Right plot: power spectral density of measured responses and six identified eigenfrequencies (denoted by numbers).

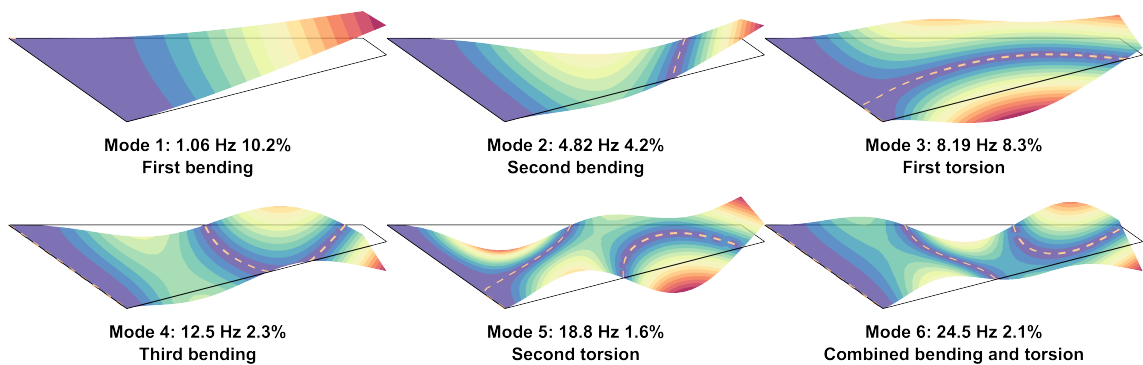


FIGURE 1.4: Operational modal analysis results: the first six eigenmodes (also known as modes of vibration or normal modes) and the associated eigenfrequency (in Hertz) and damping ratio (in percent) as reconstructed only from the measured response. The structural model is undamped, but aeroelastic effects contribute significantly to the system's damping, in particular in the lowest modes. The eigenmodes are labeled according to the predominant vibration type and number of nodes.

The topic of this thesis is the application of operational modal analysis to parameter-varying aeroelastic systems in order to determine their modal parameters as they vary due to the influence of external airflow variables. Physical dynamic processes are in general nonlinear and time-varying, nevertheless important real-world applications and engineering problems can still be described adequately and efficiently by linear time-invariant models. However, a rapid change of flow variables introduces dynamic effects that invalidate some of the hypotheses of spectral estimation and system identification, leading to results that may not seem reasonable. In order to address this issue, a theoretical foundation of time-varying dynamics, followed by spectral estimation, system identification and mode tracking methods, is researched to produce a parametric representation of parameter-varying aeroelastic systems. This knowledge is then applied to modal analysis to determine the evolution of the system's parameters as function of airflow variables. Lastly, the procedure is deployed in aeroelastic experiments to monitor a vibration test in real-time using output-only methods.

## 1.1 Context of the present study

Operational modal analysis has seen important developments and engineering applications over the last two decades.

The methods of subspace identification and least-squares polynomial fraction models [GUILLAUME ET AL., 1999; VAN OVERSCHEE AND DE MOOR, 1996; VERHAEGEN AND DEWILDE, 1992] have evolved and found widespread use in the modal analysis of structures. Modal parameter estimation for online monitoring has been addressed by [VERBOVEN ET AL., 2004] using an input-output iterative frequency-domain rational function estimator that models transient phenomena in the data. The research in [PEETERS ET AL., 2006] and [MEVEL ET AL., 2006] compared the modal results obtained from different estimators using turbulence and artificial sweep excitation; the authors note that in this type of measurements short records and the variance of the estimated damping are challenging, but output-only system identification is still viable and useful. [BASSEVILLE ET AL., 2007] discuss the in-flight vibration monitoring from the point of view of identification versus detection algorithms; the latter have a shorter reaction time compared to the former, but deliver less accurate estimates. [BRENNER ET AL., 1997] review the system identification, excitation devices and flutter prediction techniques applied to flight vibration testing at NASA Dryden. The authors discuss how time-varying and transient dynamics impact negatively the spectral and damping estimates and describe the adopted identification procedure to counter those effects. The paper from [MORELLI AND KLEIN, 2005] presents a historical overview of the research conducted at NASA Langley on system identification applied to aircraft. Information about ground vibration testing of large airplanes conducted at DLR and ONERA in Europe is found respectively in [BÖSWALD ET AL., 2006; GOVERS ET AL., 2014] and in [GICLAIS ET AL., 2016; STÉPHAN ET AL., 2015]; several aspects of the experimental modal analysis procedures described in the aforementioned references can be adapted to flight vibration testing. In [VAN WINGERDEN ET AL., 2010] the parameters of a flutter model are estimated in closed-loop in an input-output framework. [LATAIRE, 2011] developed the identification of slowly-varying systems by means of multi-sine excitation in conjunction with an estimator that models the parameter variation using polynomials. [ERTVELDT ET AL., 2014] applied the time-varying nonlinear least-squares estimator from [LATAIRE AND PINTELON, 2010] to a slowly-varying wind tunnel model with known artificial excitation in order to determine the system's transfer function and predict the onset of flutter. [HOUTZAGER ET AL., 2012] apply a recursive predictor-based subspace identification method on a wind tunnel model to estimate uncertain closed-loop parameters; the technique is applicable to slowly-varying systems for modal parameter tracking and suitable for online flutter detection. Subspace identification is popular in operational modal analysis with applications in flight testing [DE COCK ET AL., 2006; SCHWOCHOW AND ZÖGER, 2013]. Recently, [TANG ET AL., 2017] developed a two-step technique for identifying reduced-order aeroelastic models from test data by combining frequency-domain and subspace identification. Flutter predictions methods are assessed in [IOVNOVICH ET AL., 2018] from the point of view of system identification; the authors conclude that OMA

applied to aircraft excited by atmospheric turbulence is accurate and cost-effective for this purpose. Since continuous monitoring produces large amounts of data, system identification methods are frequently paired with increasingly sophisticated mode tracking algorithms, particularly in structural health and vibration monitoring applications [BEAVERSTOCK ET AL., 2015; LUSPAY ET AL., 2018; MARRONGELLI AND GENTILE, 2019; NEU ET AL., 2017; YAGHOUBI ET AL., 2018].

For time-varying systems, strictly speaking there is no “transfer function” describing a bijective correspondence between inputs and outputs like for time-invariant systems, but there are still attempts to transpose LTI concepts onto the LTV case [WERELEY AND HALL, 1990; ZADEH, 1950]. Likewise, the notion of “eigenvalues” is generally not helpful or not well-defined [RUGH, 1996] and there exist different formulations, for instance in [KAMEN, 1988; LIU, 1999; WU, 1980]. Modal analysis is thus often performed with the assumption of a slowly-varying system, i.e. the parameter variation is such that it does not modify stability or introduce additional dynamic effects. This is a necessary assumption when ensemble identification (repeated system realizations with the same variation) cannot be performed. However, to the best of the author’s knowledge, a measure of “slow variation” is absent. In [GAO ET AL., 2018] and the references therein the authors provide theorems for verifying stability directly from the system’s state matrix and its derivative and authors summarize that time-varying systems may temporarily enter an unstable state, but maintain global stability. An output-only time-domain extension of the maximum-likelihood frequency-domain rational function estimator that fits a bilinear time-frequency distribution is developed in [ZHOU ET AL., 2014]. [EUGENI ET AL., 2018] presented the operational modal analysis of a launch vehicle, where large mass variations over a short time occur and proposed a criterion for the applicability of output-only methods for time-varying systems. Simulations support the concept of performing modal analysis while the aircraft is slowly accelerating [JACQUIER AND AYME, 2018]. Gaussian process models (from the family of auto-regressive methods) have found successful applications in the operational modal analysis and structural health monitoring of time-varying wind turbines [AVENDAÑO-VALENCIA ET AL., 2020]. Other methods that have recently entered system identification are based on the dynamic mode decomposition. [ZHANG ET AL., 2017] discuss its application to online identification of time-varying systems. In [BAI ET AL., 2020] dynamic mode decomposition is coupled with compressed sensing to reconstruct a larger system from limited input-output data. Several powerful time-varying identification techniques for controller design are limited to low-order models, which is inadequate for the intended use on aeroelastic systems. From the point of view of aeroelastic modeling, [HUANG AND QIU, 2013] performed the flutter analysis of a variable-span wing. The extension rate is modeled as a constant parameter and has a considerable effect on the flutter speed, but the analysis is within the time-invariant framework. The aeroelastic modeling in [KIM, 2019] is coupled with the dynamic eigenvalue decomposition to produce reduced-order models. The method produces small parameter-varying aeroelastic models and is applied in the time-invariant framework.

### 1.1.1 Summary of state-of-the-art

Some of the key points from the literature research are summarized below:

- There exists clear demand in the industry for modal analysis for the assessment of the vibration environment, validation and updating of numerical methods, monitoring of operating conditions. In-flight analysis of aeroelastic stability is desirable for reducing testing time and increasing safety.
- Artificial excitation has limited bandwidth and requires fly-by-wire control systems, which are available on military and large civil aircraft, but absent in many light and freight vehicles. Ambient excitation increases the number of application cases and reduces costs because no additional equipment and devices are necessary.
- Since the atmospheric turbulence and acoustic excitation is unknown, the modal parameters must be estimated in the output-only framework. Subspace identification methods in time-domain are robust with respect to non-stationary excitation and are common in flight testing. Frequency-domain rational function estimators perform strongly in the input-output framework, but find applications in operational modal analysis as well.
- The system's modes of vibration must be tracked automatically over time or as function of external variables in the presence of high variance of estimated parameters, noise, errors or quickly-varying conditions.
- Ensemble identification must be employed for general time-varying systems by acquiring several realizations with the same parameter variation, which is not feasible for aircraft in flight. Time-varying systems whose parameters vary slowly can be analyzed using time-invariant techniques.
- In the time-varying case, the definition of modal parameters is more complex than for time-invariant systems. Furthermore, the influence of rate and amplitude of parameter variation on system dynamics should be assessed.
- According to the bibliographic research, the theoretical modeling of the influence of the variation rate and amplitude is lacking, therefore the assumption of "slowly-varying system", despite being necessary and adequate, remains quite vague. The dynamic effects due to fast parameter variation and the limits of the slow variation assumption necessitate more in-depth research.

## 1.2 Objectives

Within the current research context, the thesis objective is formulated in a nutshell as:

*The permanent, real-time modal parameter estimation of aircraft subject to varying flight conditions from the acceleration response due to atmospheric turbulent excitation.*

The thesis shall contribute to increased experimental data exploitation by continuous system identification, to reduced testing time by performing in-flight vibration monitoring and to higher levels of safety by providing permanently modal parameter estimates. This proposition is supported by the research of time-varying system dynamics, the implementation of a modal analysis procedure and the application to aeroelastic experiments.

The thesis' global goal is thus subdivided into three tasks:

1. *Theoretical development*: the linear time-varying systems theory and application to parameter-varying aeroelastic systems are introduced in the first part. This task's objective is to develop a parametric frequency-domain representation of time-varying systems. This will enable us to understand the effects of rate and amplitude of parameter variation, to perform signal processing correctly and to interpret system identification results.
2. *Modal analysis procedure*: development of the spectral estimation, system identification and mode tracking methods for operational modal analysis of time-varying systems for the application on wind tunnel models and aircraft. Spectral estimation and system identification must be performed efficiently in the presence of noise, nonstationary excitation and system parameter variation. A mode tracking algorithm is to be developed for organizing modal data estimated from heterogeneous sources and to determine the evolution of eigenfrequency and damping as functions of airflow variables.
3. *Application to aeroelastic experiments*: real-time online operational modal analysis during measurements. The vibration monitoring application is to be first tested in a controlled simulated environment and then validated on experimental data from wind tunnel models in open-loop conditions. The final objective is the deployment during flight vibration testing to perform system identification of aircraft subject to turbulent excitation.



### 1.3 Main contributions

Several methodologies have been developed, refined or expanded in order to achieve the global objective of the thesis. They will be described in detail in the corresponding chapters. With regard to the three tasks in which this work is subdivided, the following contributions are briefly presented:

1. The thesis develops the analytical frequency-domain representation of linear time-varying systems to provide a quantitative interpretation of their dynamics. Exact solutions are derived for linear and complex exponential parameter variations. The influence of amplitude and rate of parameter variation is investigated providing new insight into their role in the system response. Aeroelastic modeling is extended by including time-dependency to study the influence of flight variables on its entries and eigenvalues. Two criteria for quantifying the importance of parameter variation are proposed to define when the system varies sufficiently slowly to allow a frozen-time formulation. This research furthers the understanding of time-varying aeroelastic systems.
2. The thesis implements an efficient modal analysis procedure performing signal processing, system identification and mode tracking into a software for the monitoring of parameter-varying systems. The new segmented multi-taper method is proposed for estimating the power spectral densities and spectrogram, showing better performance for short records. The thesis contributes to multi-band processing for the stochastic subspace identification (SSI) method and to clearer stabilization diagrams in the least-squares complex frequency (LSCF) algorithm. An automated mode tracking algorithm, capable of organizing heterogeneous modal data to determine the eigenfrequency and damping evolution of tracked modes, is developed and tested. These developments contribute to other modal analysis applications within the research group.
3. The thesis validates the modal analysis procedure using a newly-developed simulation method for time-varying systems based on state-space series expansions. Real-time output-only modal analysis is demonstrated during flight vibration and wind tunnel testing by the fully-featured vibration monitoring application coded within the scope of this thesis. It attains from the experience collected by performing vibration testing at DLR, DNW, ONERA and Airbus facilities. Tracking of aircraft eigenmodes under varying flight and excitation conditions is demonstrated in-flight. Several insights into nonstationary data, response spectra, identified modal parameters and time-varying effects are provided. This experimental infrastructure supports other research activities at the Institute of Aeroelasticity at DLR.

## 1.4 Outline

The main content of the thesis is organized in chapters as follows:

- Ch. 2 *Linear time-varying systems theory*: the chapter lays down the theoretical groundwork by illustrating the time-varying, parameter-varying, periodic and time-invariant linear systems. An important research item here is the frequency-domain representation of the system response in order to characterize how parameter variation affects the system's dynamics. Various numerical methods are researched and compared. A simplified analytical formulation is derived for extreme cases.
- Ch. 3 *Aeroelastic systems modeling*: the chapter describes the linearized theory used to model the interaction between airflow and structure and the occurrence of flutter. The system matrices are augmented to include the influence of aerodynamics. The theoretical development is applied to characterize a time-varying aeroelastic system.
- Ch. 4 *Spectral estimation*: real signals are sampled, of limited duration and noisy. Since the amount of data is finite, the experimenter must compromise between the achievable frequency resolution and spectral variance reduction. The chapter describes estimation techniques for random signals and time-varying systems responses.
- Ch. 5 *System identification*: the measured responses are analyzed to construct a parametric description of the system. Established time-domain and frequency-domain methods are detailed and implemented. The objective is the monitoring of the eigenfrequency, damping ratio and mode shape of several modes of vibration.
- Ch. 6 *Mode tracking*: online monitoring of modal parameters requires automation to organize results. To this end, the identified modes must be tracked over time or as function of external parameters such as flight altitude and Mach speed. The chapter describes the mode tracking strategy applied to continuous system identification.
- Ch. 7 *Aeroelastic system simulation*: simulated data of a parameter-varying aeroelastic system is produced to assess the modal analysis procedure and investigate the effect of speed of parameter variation on spectral estimation and system identification.
- Ch. 8 *Experimental results*: the analytical and numerical developments presented in the previous chapters are applied to flight vibration testing of a research aircraft. Several excitation types and flight conditions are analyzed. The effectiveness of real-time output-only system identification of aircraft excited by air turbulence is proved.

Each chapter begins with an abstract and ends with a short summary. Chapters 2 and 3 research task 1, chapters 4, 5 and 6 support task 2 and chapters 7 and 8 implement task 3. Finally, the conclusions and future research are presented in the final chapter.



## 2 Linear time-varying systems

### *Abstract*

---

The chapter introduces the mathematical tools required in the analysis of linear time-varying (LTV) systems. A subset of this category are linear parameter-varying (LPV) systems, whose characteristics are explicitly dependent on a set of external parameters and model aeroelastic systems such as aircraft. The chapter begins with general concepts of linear systems theory and refines its scope towards two important special cases: linear time-invariant (LTI) and linear periodic (LTP) systems. The former provide the theoretical basis of many signal processing and system identification methods. The latter have interesting properties that can be used to simplify the treatment of general time-varying processes. In the final part numerical methods and simplified general analytical solutions are presented.

---

Physical processes that are governed by differential equations can be described by functions that map input signals onto output signals. This mapping may be expressed by systems of coupled first-order ordinary differential equations  $f(\cdot)$  in the form

$$\dot{\mathbf{x}}(t) = f(t, \mathbf{x}(t), \mathbf{u}(t)) \quad (2.1)$$

where  $t$  is the time variable,  $\mathbf{x}(t)$  the states and  $\mathbf{u}(t)$  the system inputs. Depending on the particular process, this input-output relationship may be linear or nonlinear. In this thesis we focus exclusively on linear systems, i.e. the dynamic process modeled by equation (2.1) has only a linear dependence on the state and input variables:

$$\sum_{k=0}^{N_a} a_k(t) \frac{d^k}{dt^k} x(t) = \sum_{k=0}^{N_b} b_k(t) \frac{d^k}{dt^k} u(t) \quad (2.2)$$

where  $N_a \geq N_b$  so that the system is physically realizable. Under this assumption the superposition principle simplifies considerably the solution of the resulting equations. The most general case, where the coefficients  $a_k(t)$  and  $b_k(t)$  are functions of time, is used to describe *linear time-varying* (LTV) systems. The particular case of constant coefficients  $a_k$  and  $b_k$  models *linear time-invariant* (LTI) systems.

Linear systems have widespread use in the modeling of important engineering and physical processes. Their popularity lies in the extremely broad range of applications where they provide accurate predictions, for instance in structural dynamics, electronics, biological processes, optics and acoustics. The detailed theoretical foundation of linear systems can be found in works such as [OPPENHEIM ET AL., 1996] and [RUGH, 1996]. When the simplifying assumptions in the linear modeling of a physical process are not adequate anymore, more complex models are employed. In this regard, nonlinear systems for engineering applications are treated in [KHALIL, 1996] and [JORDAN AND SMITH, 2007]. Every so often we will be confronted with the limits of linear descriptions and mention more accurate models.

The main objective of this chapter is to introduce the analytical tools for the study of time-varying systems, in particular for the application on modal analysis of aeroelastic systems that are the topic of later parts of the thesis. The linear theory delineated here, while having such generality that it is employed in different engineering fields, will be applied solely to mechanical systems such as aircraft, wind turbines, rotor blades et cetera. Aeroelastic modeling, in particular, will be described in detail in the next chapter.

Most readers with an engineering background know linear time-invariant systems well. This chapter will familiarize them with the more complex time-varying case where many of the usual LTI concepts such as transfer functions and eigenvalues may not be defined. This is necessary in order to interpret correctly signal processing and system identification results in later chapters. For instance, it will become apparent very early that the spectra of the LTV system response present many features that may not be immediately associated to a mode of vibration. A central assumption of many LTV models is that the system be slowly-varying, i.e. that the additional dynamics induced by the variation of the system's characteristics can be neglected. This is often a necessity for signal processing and system identification algorithms. In this regard it will be beneficial to characterize the regimes of a time-varying systems in order to define what "slow" or "fast" really mean. One sub-goal is therefore to explain the effects that parameter variation rate and amplitude have on the system response. To this end, a quantitative description of time-varying effects and to describe the response parametrically in frequency-domain will be provided.

Apart from the aforementioned sources, the linear systems theory is described with contributions from various other reference, such as [DECARLO, 1989], [CHEN, 1999], [ANTSAKLIS AND MICHEL, 2006] and [SHMALIY, 2007]. We shall proceed by expressing the linear system (2.2) in the matrix state-space form because it is a convenient and compact mathematical formulation for treating multi-input-multi-output (MIMO) systems. The state-space form is widely adopted in control theory and system identification [LJUNG, 1999].

The chapter's roadmap is as follows:

1. Linear time-varying theory, general characteristics and properties, mathematical tools, transformations
2. Linear time-invariant systems: main properties and formulations
3. Linear periodic systems: decomposition, frequency-domain representation, influence of rate of variation
4. Numerical methods for the solution and decomposition of LTV systems
5. Analytical solutions for the linear and complex exponential parameter variation

## 2.1 Linear time-varying systems

The explicit state-space representation of continuous linear time-varying systems (LTV) in time-domain (2.2) is given by the differential algebraic equations [SHMALIY, 2007]:

$$\begin{aligned}\dot{\mathbf{x}}(t) &= \mathbf{A}(t)\mathbf{x}(t) + \mathbf{B}(t)\mathbf{u}(t) \\ \mathbf{y}(t) &= \mathbf{C}(t)\mathbf{x}(t) + \mathbf{D}(t)\mathbf{u}(t)\end{aligned}\quad (2.3)$$

where the symbols denote:

$\mathbf{x}(t) \in \mathbb{C}^{N_x}$ state vector	$\mathbf{A}(t) \in \mathbb{C}^{N_x \times N_x}$ state matrix
$\mathbf{u}(t) \in \mathbb{C}^{N_u}$ input vector	$\mathbf{B}(t) \in \mathbb{C}^{N_x \times N_u}$ input matrix
$\mathbf{y}(t) \in \mathbb{C}^{N_y}$ output vector	$\mathbf{C}(t) \in \mathbb{C}^{N_y \times N_x}$ output matrix
	$\mathbf{D}(t) \in \mathbb{C}^{N_y \times N_u}$ feedthrough matrix

A linear system  $\mathcal{S}$  can be conveniently written in a compact form as:

$$\mathcal{S} : \left[ \begin{array}{c|c} \mathbf{A}(t) & \mathbf{B}(t) \\ \hline \mathbf{C}(t) & \mathbf{D}(t) \end{array} \right] = [\mathbf{A}(t), \mathbf{B}(t), \mathbf{C}(t), \mathbf{D}(t)] \quad (2.4)$$

This notation will be useful when applying transformations of the system matrices. Alternatively, equation (2.3) can be rendered with the block diagram in figure 2.1. The state-space model describes a linear dynamic system (2.2) with first-order ordinary differential equations relating the input, output and state variables. Examples include a rocket expending its fuel as it ascends, a bridge with moving traffic, electrical circuits subject to temperature change. The first equation in (2.3) is called *state equation* and constitutes the feedback loop of the dynamic model; it is an inhomogeneous system of first-order ordinary differential equations. The second equation in (2.3) is the *output* or *measurement* equation. The input is also called excitation or driving force, while the output is also called response. The states are the minimal set of variables that is able to express all process dynamics at any given time; they are not necessarily physical quantities. The system matrices are assumed to be continuous  $C^1$  functions of time and therefore bounded. The input vector can be simply a piece-wise continuous  $C^0$  function.

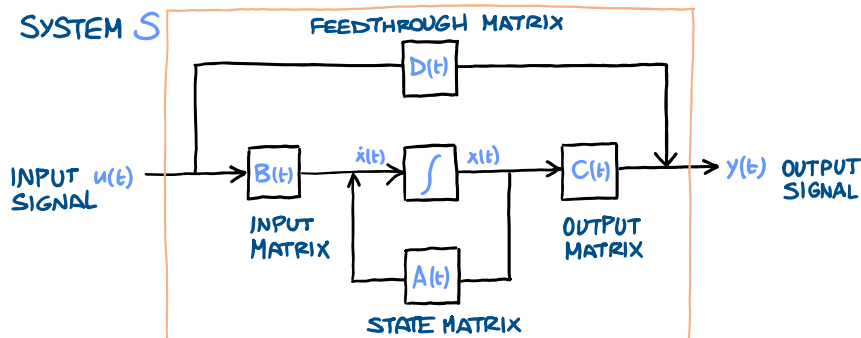


FIGURE 2.1: Block diagram of the state-space representation of a linear time-varying system.

### 2.1.1 Linear parameter-varying systems

In the linear parameter-varying framework, the system matrices (and the coefficient of the corresponding differential equation form (2.2)) are explicitly functions of a parameter vector  $\mathbf{p} \in \mathbb{C}^{N_p}$ :

$$\begin{aligned}\dot{\mathbf{x}}(t) &= \mathbf{A}(\mathbf{p})\mathbf{x}(t) + \mathbf{B}(\mathbf{p})\mathbf{u}(t) \\ \mathbf{y}(t) &= \mathbf{C}(\mathbf{p})\mathbf{x}(t) + \mathbf{D}(\mathbf{p})\mathbf{u}(t)\end{aligned}\tag{2.5}$$

The system's characteristics depend thus solely on the values assumed by  $\mathbf{p}$ , which may be a scheduling parameter that varies arbitrarily or some function of time. Examples: a pendulum with a variable rod length, the tuning of a radio or variable-gain amplifiers, a structure that can change shape such as a robot arm. Relevant to this work are aeroelastic systems, whose dynamic characteristics vary primarily with air speed and air density; they will be introduced fully in the next chapter.

From now on, it is assumed that the parameters are continuous vector functions of time  $\mathbf{p} = \mathbf{f}(t)$ , therefore we can consider such a parameter-varying system (2.5) as a particular kind of the LTV case:

$$\begin{aligned}\dot{\mathbf{x}}(t) &= \mathbf{A}(\mathbf{p}(t))\mathbf{x}(t) + \mathbf{B}(\mathbf{p}(t))\mathbf{u}(t) \\ \mathbf{y}(t) &= \mathbf{C}(\mathbf{p}(t))\mathbf{x}(t) + \mathbf{D}(\mathbf{p}(t))\mathbf{u}(t)\end{aligned}\tag{2.6}$$

In order to fall purely within the LPV framework, the system matrices must depend solely on the parameter path  $\mathcal{S} = f(\mathbf{p})$  and be the same irrespective of a time scaling constant  $c$  in  $\mathbf{p}(ct)$ <sup>1</sup> (however, the response  $\mathbf{y}(t)$  may still depend on  $\dot{\mathbf{p}}(t)$ ). For instance, a variable pendulum's amplitude increases if its length is shortened quickly, whereas it changes little if the length varies slowly.

In computations, the system is either constructed from a continuous function of the parameters  $\mathcal{S} = [\mathbf{A}(\mathbf{p}), \mathbf{B}(\mathbf{p}), \mathbf{C}(\mathbf{p}), \mathbf{D}(\mathbf{p})]$  or is known on a discrete grid  $\mathbf{p}[n]$ , therefore  $\mathcal{S} = [\mathbf{A}[n], \mathbf{B}[n], \mathbf{C}[n], \mathbf{D}[n]]$  (e.g. large linearized aeroelastic models). In the latter case, the system matrices between known grid points are constructed by interpolation. This aspect is important in the simulation of LTV systems and we shall come back to it in chapter 7.

<sup>1</sup> For example, let us consider the simple harmonic oscillator with variable resonant frequency  $\omega_n(t)$ :

$$\mathbf{A}(t) = \begin{bmatrix} 0 & 1 \\ -\omega_n^2(t) & 0 \end{bmatrix} \quad \begin{cases} 1: & \omega_n(t) = \omega_n \cos(\omega_0 t) \\ 2: & \omega_n(t) = \omega_0 \cos(\omega_0 t) \end{cases} \quad t \in [0, 2\pi/\omega_0] \tag{2.7}$$

In case 1 the system is LPV because the values assumed by  $\omega_n(t)$  are always the same. In case 2 the system is LTV because the magnitude of  $\omega_n(t)$  depends on the period  $2\pi/\omega_0$ .

### 2.1.2 Second-order systems

An important class of linear ordinary differential equations (2.2) are second-order models that describe, for example, oscillating electrical or mechanical systems. A broad reference for this topic, albeit limited to the time-invariant case, is [CHOPRA, 2019].

We shall focus on the mass-damping-stiffness models used commonly in mechanics, for instance a mass connected to a spring and damper. The dynamic behavior of a structure is described by Newton's equation of motion:

$$\mathbf{M}(t)\ddot{\mathbf{q}}(t) + \mathbf{D}(t)\dot{\mathbf{q}}(t) + \mathbf{K}(t)\mathbf{q}(t) = \mathbf{u}(t) \quad (2.8)$$

where the symbols denote

$$\begin{array}{ll} \mathbf{q}(t) \in \mathbb{R}^{N_d} & \text{displacement} \\ \mathbf{u}(t) \in \mathbb{R}^{N_d} & \text{excitation} \end{array} \quad \begin{array}{ll} \mathbf{M}(t) \in \mathbb{R}^{N_d \times N_d} & \text{mass matrix} \\ \mathbf{D}(t) \in \mathbb{R}^{N_d \times N_d} & \text{damping matrix} \\ \mathbf{K}(t) \in \mathbb{R}^{N_d \times N_d} & \text{stiffness matrix} \end{array}$$

and where  $N_d$  is the number of degrees of freedom. The corresponding state-space representation is derived by defining the new state variable  $\mathbf{x}(t) = \{\mathbf{q}(t), \dot{\mathbf{q}}(t)\}$  to be able to reduce the equation order to one:

$$\mathcal{S} = \left[ \begin{array}{cc|c} \mathbf{0} & \mathbf{I} & \mathbf{0} \\ -\mathbf{M}^{-1}(t)\mathbf{K}(t) & -\mathbf{M}^{-1}(t)\mathbf{D}(t) & \mathbf{M}^{-1}(t) \\ \hline \mathbf{I} & \mathbf{0} & \mathbf{0} \end{array} \right] \quad \mathbf{x}(t) = \begin{Bmatrix} \mathbf{q}(t) \\ \dot{\mathbf{q}}(t) \end{Bmatrix} \quad (2.9)$$

The vector  $\mathbf{q}(t)$  represents physically the translational and torsional degrees of freedom, while  $\mathbf{u}(t)$  are external forces and moments exciting the system. The entries of  $\mathbf{M}(t)$  are physically masses and moments of inertia,  $\mathbf{D}(t)$  is assumed to model viscous damping acting on the system (proportional to velocity), while the stiffness matrix  $\mathbf{K}(t)$  describes the system's translational and rotational elastic properties. The system matrices are real, square and, for a system at equilibrium, symmetric. Dynamic terms are added to the system matrices depending on the model, for instance gyroscopic or aerodynamics terms<sup>2</sup>. There exist other damping models depending on the type of analyzed dissipative phenomena (viscous, proportional, hysteresis...) [ADHIKARI, 2000]. Structural damping is often conservatively ignored because of the uncertain applicability of numerical models to complex real structures, therefore it is rather determined experimentally and then used to update the numerical models [GOVERS, 2012]. Furthermore, dynamic effects on damping are more important in aeroelastic and rotating systems because they can increase the energy dissipation rate – or even reverse it. One of the goals of later chapters will be the experimental identification of the damping as function of external parameters.

<sup>2</sup> For example, consider a variable point mass connected to a spring. The equation of motion includes a damping term due to the mass variation:  $\frac{d}{dt}(m\dot{x}) = -kx \implies m(t)\ddot{x}(t) + \dot{m}(t)\dot{x}(t) + kx(t) = 0$



### 2.1.3 State transition matrix

The linear system state equation (2.3) can be separated into a homogeneous and inhomogeneous part in order to solve it. The homogeneous term

$$\dot{\mathbf{x}}(t) = \mathbf{A}(t)\mathbf{x}(t) \quad (2.10)$$

implies that for every initial state  $\mathbf{x}(t_0)$  there exists a unique  $\mathbf{x}(t)$  solution.

**Definition** (State Transition Matrix). *The unique function of time  $\Phi(t, t_0)$  that maps the state at one time instant  $\mathbf{x}(t_0)$  onto the state at another time instant  $\mathbf{x}(t)$*

$$\mathbf{x}(t) = \Phi(t, t_0)\mathbf{x}(t_0) \quad t \geq t_0 \quad (2.11)$$

is called the state transition matrix (STM) of the system.

The state transition matrix is the continuously-differentiable solution of the linear state equation (2.10) [RUGH, 1996, Th. 3.3]. The study of time-varying linear systems begins with the examination of its properties because it provides a general and convenient means for describing the system response. The mapping it performs between two system states is illustrated schematically in figure 2.2.

**Definition** (Fundamental matrix). *Let  $\mathbf{X}(t) = [\mathbf{x}_1(t) \dots \mathbf{x}_{N_x}(t)] \in \mathbb{C}^{N_x \times N_x}$  be the matrix of any  $k = 1:N_x$  linearly independent solutions  $\mathbf{x}_k(t)$  of the homogeneous matrix state equation*

$$\dot{\mathbf{X}}(t) = \mathbf{A}(t)\mathbf{X}(t) \quad (2.12)$$

The matrix  $\mathbf{X}(t)$  is called the fundamental matrix.

If  $\mathbf{X}(t_0)$  is nonsingular, then  $\mathbf{X}(t)$  is also invertible for all  $t$ . The fundamental matrix is determined by solving equation (2.12) with any linearly independent set of initial conditions (for example  $\mathbf{X}(t_0) = \mathbf{I}$ ) and is therefore not unique.

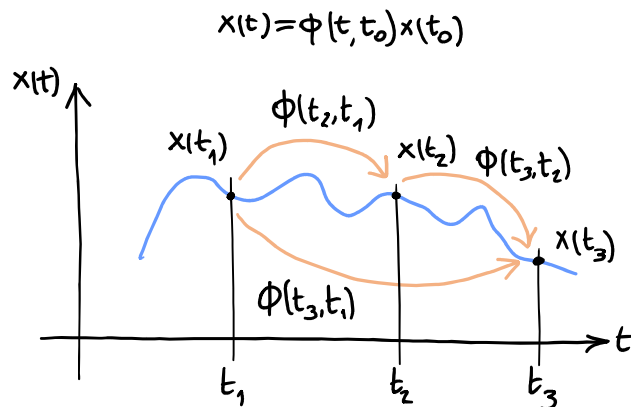


FIGURE 2.2: The state transition matrix  $\Phi(t, t_0)$  maps the state of a linear system at one time instant  $\mathbf{x}(t_0)$  onto the state at another  $\mathbf{x}(t)$  with the linear relation  $\mathbf{x}(t) = \Phi(t, t_0)\mathbf{x}(t_0)$ .

The direct relationship between any fundamental matrix and the unique state transition matrix arises from its definition [CHEN, 1999, Def. 4.2]:

$$\Phi(t, t_0) = \mathbf{X}(t)\mathbf{X}^{-1}(t_0) \quad (2.13)$$

Equations (2.10) to (2.13) can now be used to derive several properties of the state transition matrix of continuous linear systems:

**Property** (State transition matrix properties).

- *differentiation*:  $\frac{\partial}{\partial t}\Phi(t, t_0) = \mathbf{A}(t)\Phi(t, t_0)$
- *duality*:  $\frac{\partial}{\partial t}\Phi^T(t_0, t) = -\mathbf{A}^T(t)\Phi^T(t_0, t)$
- *inversion*:  $\Phi^{-1}(t, t_0) = \Phi(t_0, t)$
- *composition*:  $\Phi(t, t_0) = \Phi(t, t_1)\Phi(t_1, t_0)$
- *identity*:  $\Phi(t, t) = \mathbf{I}$
- *determinant*:  $\det \Phi(t, t_0) = \exp \int_{t_0}^t \text{tr} \mathbf{A}(\tau) d\tau$

The STM's properties are given here to be applied in the coming pages. Detailed proofs can be found in the references cited at the beginning of the chapter, for example in [RUGH, 1996], [ANTSACLIS AND MICHEL, 2006] and [SHMALIY, 2007].

A general method used to determine the state transition matrix is the *Peano-Baker* series:

$$\begin{aligned} \Phi(t, t_0) = \mathbf{I} &+ \int_{t_0}^t \mathbf{A}(\tau_1) d\tau_1 + \int_{t_0}^t \mathbf{A}(\tau_1) \int_{t_0}^{\tau_1} \mathbf{A}(\tau_2) d\tau_2 d\tau_1 + \\ &+ \int_{t_0}^t \mathbf{A}(\tau_1) \int_{t_0}^{\tau_1} \mathbf{A}(\tau_2) \int_{t_0}^{\tau_2} \mathbf{A}(\tau_3) d\tau_3 d\tau_2 d\tau_1 + \dots \end{aligned} \quad (2.14)$$

which converges absolutely and uniformly for any  $t$  and  $t_0$  [BAAKE AND SCHLAEGEL, 2012].

Another way of determining the state transition matrix that has found many applications in physics is the *Magnus expansion* [BLANES ET AL., 2009]. There exist a matrix  $\Omega(t)$  such that the STM is  $\Phi(t, 0) = e^{\Omega(t)}$  where

$$\begin{aligned} \Omega(t) = \int_0^t \mathbf{A}(\tau_0) d\tau_0 &+ \frac{1}{2} \int_0^t \int_0^{\tau_0} [\mathbf{A}(\tau_0), \mathbf{A}(\tau_1)] d\tau_1 d\tau_0 + \\ &+ \frac{1}{6} \int_0^t \int_0^{\tau_0} \int_0^{\tau_1} ([\mathbf{A}(\tau_0), [\mathbf{A}(\tau_1), \mathbf{A}(\tau_2)]] + [[\mathbf{A}(\tau_0), \mathbf{A}(\tau_1)], \mathbf{A}(\tau_2)]) d\tau_2 d\tau_1 d\tau_0 + \dots \end{aligned} \quad (2.15)$$

and where  $[\mathbf{A}, \mathbf{B}] \triangleq \mathbf{AB} - \mathbf{BA}$  is the matrix commutator. The expansion's pattern is not as obvious as it might look like from the first few terms [BUTCHER ET AL., 2009].

The effort of finding the STM is the first step in the analysis of time-varying systems, but meeting the necessary conditions for determining its analytical form is difficult. The Peano-Baker series (2.14) and the Magnus expansion (2.15), while useful theoretically, can

be calculated analytically but in the simplest of cases [RUGH, 1996]. Computer-aided symbolic solutions are theoretically possible but still unfeasible for large systems. In general the STM's structure is too intricate to be expressed in a simple way, but there are important particular cases where it assumes a favorable and elegant form, such as for linear time-invariant and periodic systems. Fortunately, there are also convenient ways of determining  $\Phi(t, t_0)$  according to the following theorem:

**Theorem** (Exponential form of the state transition matrix). [RUGH, 1996, Th. 4.2] *If the state matrix commutes with its antiderivative*

$$\mathbf{A}(t) \left( \int_{t_0}^t \mathbf{A}(\tau) d\tau \right) = \left( \int_{t_0}^t \mathbf{A}(\tau) d\tau \right) \mathbf{A}(t) \quad \forall t, t_0 \quad (2.16)$$

then the state transition matrix has the form:

$$\Phi(t, t_0) = \sum_{k=0}^{\infty} \frac{1}{k!} \left( \int_{t_0}^t \mathbf{A}(\tau) d\tau \right)^k = \exp \int_{t_0}^t \mathbf{A}(\tau) d\tau \quad (2.17)$$

where  $\exp(\cdot)$  is the matrix exponential (see appendix A.1). This condition is satisfied if and only if  $\mathbf{A}(t)\mathbf{A}(t_0) = \mathbf{A}(t_0)\mathbf{A}(t)$  for all  $t, t_0$ .

The hypothesis of the theorem is always satisfied when the state matrix is:

- *constant*  $\mathbf{A}(t) = \mathbf{A}$ : the STM is the well-known result of time-invariant systems theory  $\Phi(t, t_0) = \exp(\mathbf{A}(t - t_0))$
- *scalar*  $\mathbf{A}(t) = a(t)$ : the state transition matrix can be calculated by the variation of constants method for ordinary differential equations:  $\Phi(t, t_0) = \exp \int_{t_0}^t a(\tau) d\tau$
- *diagonal*  $\mathbf{A}_{ij}(t) = 0 \quad \forall i \neq j$ : this is a system of uncoupled ordinary differential equations, therefore:  $\Phi_{ii}(t, t_0) = \exp \int_{t_0}^t \mathbf{A}_{ii}(\tau) d\tau$
- *triangular*  $\mathbf{A}_{ij}(t) = 0 \quad \forall i > j$ :  $\Phi(t, t_0)$  is constructed by successive integration of each state.

Additionally, theorem (2.17) holds when the state matrix is a series of scalar functions  $f_k$  with constant coefficients  $\mathbf{A}_k$

$$\mathbf{A}(t) = \sum_{k=1}^{N_k} \mathbf{A}_k f_k(t) \implies \Phi(t, t_0) = \prod_{k=1}^{N_k} \exp \int_{t_0}^t \mathbf{A}_k f_k(\tau) d\tau \quad (2.18)$$

providing that the series' terms  $\mathbf{A}_i \mathbf{A}_j = \mathbf{A}_j \mathbf{A}_i \quad \forall i, j \in 1:N_k$  commute. This simple form of the STM is elegant, but the strict commutativity requirement of theorem (2.17) for each term  $\mathbf{A}_k$  is difficult to satisfy for dimensions higher than one.

When all analytical options are exhausted, the state transition matrix can be determined using direct numerical integration [CHEN, 1999] by solving the homogeneous system

$$\dot{\mathbf{X}}(t) = \mathbf{A}(t)\mathbf{X}(t) \quad \xrightarrow[\text{with } \mathbf{X}(t_0)=\mathbf{X}_0]{\text{solve for } \mathbf{X}(t)} \quad \Phi(t, t_0) = \mathbf{X}(t)\mathbf{X}^{-1}(t_0) \quad (2.19)$$

where  $\mathbf{X}_0$  is any set of linearly independent initial conditions (usually for convenience  $\mathbf{X}(t_0) = \mathbf{I}$ ). This is a system of  $N_x^2$  first-order ordinary differential equations in the form  $\dot{x}(t) = f(t, x(t))$  that can be integrated with classical ODE-solvers. Numerical methods for the determination of the STM will be expanded in more detail in section 2.4.

#### 2.1.4 Impulse response of time-varying systems

The general solution of the time-varying system can be written by making use of the state transition matrix's properties [ANTSAKLIS AND MICHEL, 2006, Eq. 6.2]:

$$\begin{aligned} \mathbf{x}(t) &= \Phi(t, t_0)\mathbf{x}(t_0) + \int_{t_0}^t \Phi(t, \tau)\mathbf{B}(\tau)\mathbf{u}(\tau) d\tau \\ \mathbf{y}(t) &= \mathbf{C}(t)\mathbf{x}(t) + \mathbf{D}(t)\mathbf{u}(t) \end{aligned} \quad (2.20)$$

This equation is the *complete solution* of the first-order linear differential state equation (2.3) with initial conditions  $\mathbf{x}(t_0)$  and input  $\mathbf{u}(t)$ . It is the sum of the homogeneous (general) and inhomogeneous (particular) solutions, which in linear system theory are called respectively *zero-input* and *zero-state* responses.

$$\begin{aligned} \mathbf{y}_{zi}(t) &\triangleq \mathbf{C}(t)\Phi(t, t_0)\mathbf{x}(t_0) \\ \mathbf{y}_{zs}(t) &\triangleq \mathbf{C}(t) \int_{t_0}^t \Phi(t, \tau)\mathbf{B}(\tau)\mathbf{u}(\tau) d\tau + \mathbf{D}(t)\mathbf{u}(t) \end{aligned} \quad (2.21)$$

The former is the transient response due to an initial state of the system. The latter describes the transient and steady-state responses of the system due to an input. Assuming that the system is initially at rest, the input  $\mathbf{C}(t)$  and feedthrough  $\mathbf{D}(t)$  matrices can be brought into the integral and the input  $\mathbf{u}(t)$  collected:

$$\mathbf{y}(t) = \int_{t_0}^t \mathbf{D}(\tau)\delta(t - \tau) + \mathbf{C}(t)\Phi(t, \tau)\mathbf{B}(\tau)\mathbf{u}(\tau) d\tau \triangleq \int_{t_0}^t \mathbf{H}(t, \tau)\mathbf{u}(\tau) d\tau \quad (2.22)$$

where the  $\mathbf{H}(t, \tau) \in \mathbb{C}^{N_y \times N_u}$  denotes the system's *impulse response*<sup>3</sup> (the integral's kernel). Since in reality a system cannot respond to future inputs, the constraint of causality must be inserted by imposing  $\mathbf{H}(t, \tau) = 0$  for  $t < \tau$ .

$$\mathbf{H}(t, \tau) = \begin{cases} \mathbf{D}(t)\delta(t - \tau) + \mathbf{C}(t)\Phi(t, \tau)\mathbf{B}(\tau) & t \geq \tau \\ 0 & t < \tau \end{cases} \quad (2.23)$$

<sup>3</sup> In structure dynamics the impulse response is conventionally denoted with a lowercase  $h$ , whereas the uppercase  $H$  is used for the frequency response function. In control theory the symbols  $g$  and  $G$  are used instead. In this text the symbol  $\mathbf{H}(\cdot)$  states the function's domain explicitly.

The impulse response is the unique characteristic of the linear system that determines the response as the kernel of the integral in equation (2.22).

Before proceeding further, an example of the state transition matrix and impulse response is given in figure 2.3 for a simple damped harmonic oscillator with variable stiffness. It is immediately apparent that the impulse response depends on the instant at which the impulse occurs. In the limit of the stiffness variation amplitude or variation rate going towards zero, the LTV solution approaches the response of the corresponding time-invariant system.

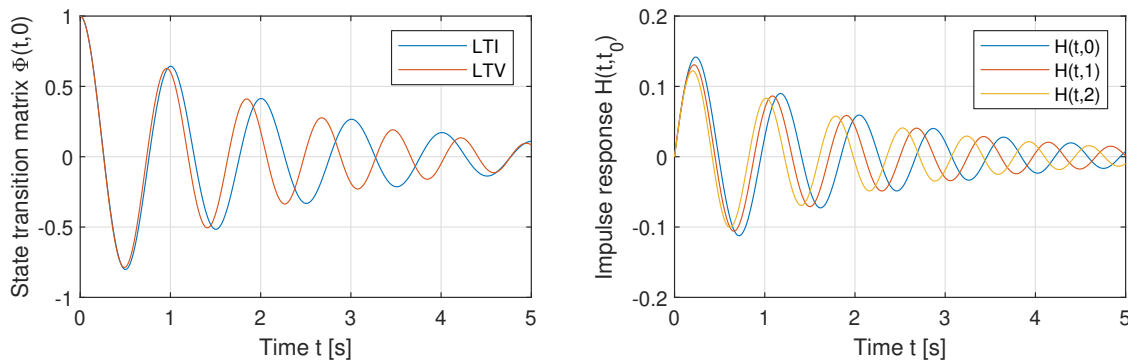


FIGURE 2.3: State transition matrix and impulse response of a damped harmonic oscillator with variable stiffness. The system equation is  $\ddot{x}(t) + 2\zeta\omega_n\dot{x}(t) + \omega_0^2x(t) + p t\omega_n^2x(t) = 0$  where  $\zeta = 0.07$ ,  $\omega_n = 2\pi$  rad/s. The entry (1,1) of  $\Phi(t,0)$  is shown with  $p = 0.2$  s $^{-1}$  and  $p = 0$  s $^{-1}$  (LTV vs LTI cases). The impulse response  $\mathbf{H}(t,\tau)$  depends on the time instant  $\tau$  at which the impulse occurs (displayed here for  $\tau = [0, 1, 2]$  s). In this particular example,  $\mathbf{H}(t,0)$  is equal to the LTI system's impulse response.

### 2.1.5 Impulse response in frequency-domain

In time-invariant systems the impulse response (2.23) is independent from the time  $\tau$  at which the impulse occurs, therefore the integral's kernel in equation (2.22) is  $\mathbf{H}(t,\tau) = \mathbf{H}(t - \tau)$ . The system response can be then written as:

$$\mathbf{y}(t) = \int_{t_0}^t \mathbf{H}(t,\tau)\mathbf{u}(\tau) d\tau = \int_{t_0}^t \mathbf{H}(t - \tau)\mathbf{u}(\tau) d\tau \equiv \mathbf{H}(t) * \mathbf{u}(t) \quad (2.24)$$

The convolution between the input signal and the system's impulse response has an immediate Laplace transform:

$$\mathbf{y}(t) = \int_{t_0}^t \mathbf{H}(t - \tau)\mathbf{u}(\tau) d\tau \quad \circ \bullet \quad \mathbf{y}(s) = \mathbf{H}(s)\mathbf{u}(s) \quad (2.25)$$

**Definition.** The matrix  $\mathbf{H}(s)$  is the transfer function of the time-invariant system with impulse response  $\mathbf{H}(t)$ , i.e. it describes the relationship (2.25) between the input  $\mathbf{u}(s)$  and output  $\mathbf{y}(s)$  in Laplace-domain. When its argument is a purely imaginary frequency,  $\mathbf{H}(i\omega)$  is called the frequency response function.

The zero-state response to an impulse characterizes the zero-state response to all input signals through the convolution integral in time-domain or equivalently through multiplication in frequency-domain. Knowledge of the transfer function is thus sufficient for determining the system response to any input. One important consequence of equation (2.25) is that a time-invariant system modifies the amplitude  $A$  and the phase  $\phi$  of a complex exponential input  $Ae^{i\omega t + \phi}$ , but not its fundamental frequency  $\omega$  [PROAKIS AND MANOLAKIS, 2013]. We shall come back to the LTI system's transfer function in the next section.

In the more general time-varying case, the impulse response  $\mathbf{H}(t, \tau)$  is a function of the time  $\tau$  at which the impulse happens. As a consequence, the steady-state response contains not only the frequency components of the input signal but also additional frequencies due to the coefficient variation. An example is illustrated in figure 2.4. The reader may recognize this as a fundamental difference between time-invariant and time-varying linear systems, since the response to a sinusoidal signal in the latter case is generally neither sinusoidal nor periodic. Based on this observation, the frequency-domain representation of a time-varying system's impulse response  $\mathcal{L}\{\mathbf{H}(t, \tau)\}(s)$  is not functionally analogous to the transfer function of a time-invariant system  $\mathcal{L}\{\mathbf{H}(t)\}(s) = \mathbf{H}(s)$ , i.e. it does not form a bijective correspondence between the frequency content of input and output [RUGH, 1996; SHMALIY, 2007]: in the context of LTV systems, we shall thus say “impulse response in frequency-domain” instead of “transfer function”. Furthermore, equation (2.23) in the time-varying case does not generally lead towards a rational function representation of the impulse response in frequency-domain (2.55). For example, in section (2.5) we will consider a system with a linear variation and show that the response in frequency-domain assumes complicated expressions involving error functions; the impulse response in frequency-domain of such a system undergoing linear variation is displayed in figure 2.5. On the other hand, we shall see in section 2.3 that, at least for periodic systems, a formulation similar to that of the LTI case still holds.

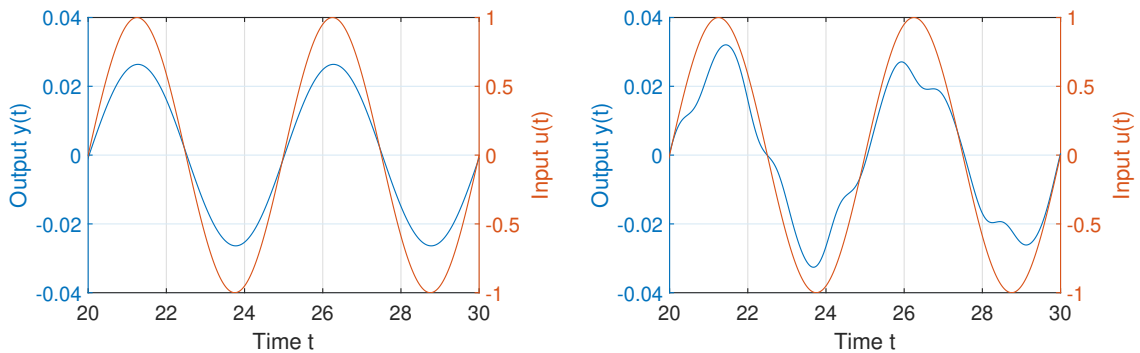


FIGURE 2.4: Steady-state response of a forced damped harmonic oscillator. The system equation is  $\ddot{x}(t) + 2\zeta\omega_n\dot{x}(t) + \omega_n^2(1 + r_f^2 \sin(\pi t))x(t) = \sin(0.4\pi t)$  where  $\zeta = 0.07$ ,  $\omega_n = 2\pi$  rad/s. Left plot:  $r_f = 0$ , time-invariant system. When the system matrices are constant, the steady-state response contains the scaled and phase-shifted input with the same frequency of the input. Right plot:  $r_f = 0.4$ , as soon as the system is time-varying, the response's frequency content is different from the excitation's. As the time variation transitions from slow to fast, from weak to strong, the periodic response becomes pseudo-periodic and then finally aperiodic.

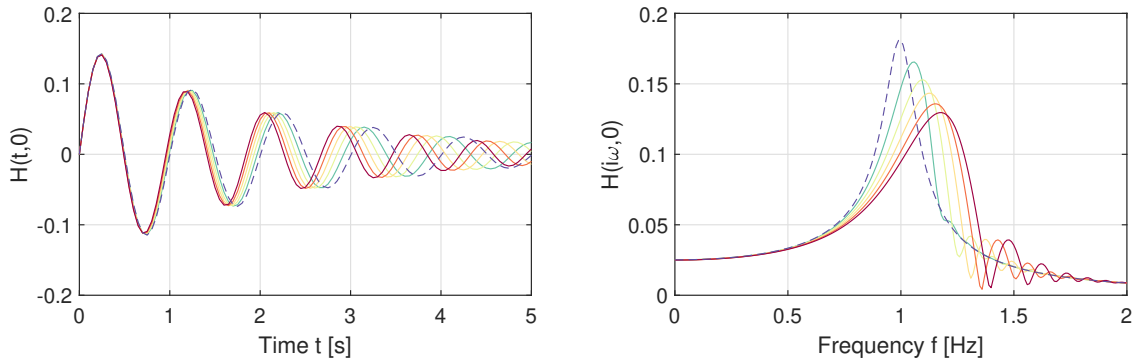


FIGURE 2.5: Impulse response and its frequency-domain representation of a damped harmonic oscillator with variable stiffness. The system is  $\ddot{x}(t) + 2\zeta\omega_n\dot{x}(t) + \omega_n^2(1 + pt/T)x(t) = 0$  where  $\zeta = 0.07$ ,  $\omega_n = 2\pi$  rad/s,  $T = 1$  s. The plot displays various values of the parameter  $p = 0:0.02:0.2$  (blue: low, red: high). The dashed line represents the system with  $p = 0$ , which has a single resonance peak. Due to time-varying dynamics, the impulse response in frequency-domain exhibits a more complicated form: the main resonance peak shifts and additional peaks appear. We shall derive an analytical solution in section 2.5.

The concept of transfer function is extremely helpful in the mathematical treatment of LTI systems, consequently there have been efforts in defining a relation between inputs and outputs for LTV systems as well, but this generalization is not straightforward. In the widely-cited paper by [ZADEH, 1950] the frequency response to a complex exponential is defined as  $\mathbf{H}\{e^{i\omega t}\} = e^{i\omega t} \int_0^\infty \mathbf{H}(t, t - \tau)e^{-i\omega\tau} d\tau$  in which the time-dependence of the result is clearly expressed. The output is not necessarily periodic because the kernel  $\mathbf{H}(t, t_0)$  is time-varying. [WERELEY AND HALL, 1990] define the transfer function for periodic systems as a linear operator that maps inputs and outputs one-to-one and characterizes its gain and phase. A more general formulation is introduced in [BALL ET AL., 1995] via an integral operator to map an input complex exponential to a time-dependent frequency response function. LTV models described by ordinary differential equations (2.2) where the coefficients  $a_k(t)$  and  $b_k(t)$  are polynomials are studied in frequency-domain in [LATAIRE, 2011] with the purpose of identification and applied in [ERTVELDT ET AL., 2014] on an aeroelastic system.

Often the notion of “frozen-time” system is considered, namely an LTV system is described at each time instant by the LTI system corresponding to (constant) parameters at that time instant. This modeling is a valid approach as long as the system variation is slow, i.e. there are no significant dynamics introduced by time variation or changes in stability. Fortunately for many real time-varying mechanical and aeroelastic systems this assumption is satisfied. The coming sections will cover this case in more detail. There are also cases where a time-varying system behaves almost like a time-invariant one, for example rotating machinery such as wind turbines, helicopter blades, compressors. We will give more substance to these statements in the coming pages.

### 2.1.6 Stability of time-varying systems

An intuitive explanation of stability is that any small perturbation of a system does not result in a large response. In most real systems, free oscillations decay with time because the energy loss is larger than its gain. Stability is an important topic in linear systems: elastic structures in a fluid flow such as a bridge can reach a state in which they absorb energy from the wind and undergo self-oscillations resulting in excessive displacements. Rotating machinery like wind turbines have critical rotation speeds at which the system's vibration will increase without bound. In particular, for aeroelastic systems, the interaction with aerodynamic forces can reduce the energy dissipation to zero and further to a negative value, where free oscillations increase without bound. This topic will be elaborated further in chapter 3 where the border of the stable region can be determined for a combination of air density and wind speed. We are thus interested in stability in order to prevent catastrophic structural failure.

The stability of linear systems is treated in more detail in [RUGH, 1996, Ch. 6] and [SHMALIY, 2007, Ch. 2]. More particular results for slowly-varying systems are found in [AMATO ET AL., 1993; ILCHMANN ET AL., 1987; SOLO, 1994]. In [GAO ET AL., 2018] a detailed bibliographic research on this topic is found. The stability analysis aims to provide formal criteria for which the so-called BIBO stability holds:

**Definition** (BIBO stability). *The system is bounded-input-bounded-output stable if for any bounded input  $\|\mathbf{u}(t)\| \leq M < \infty$  there is a bounded output  $\|\mathbf{y}(t)\| \leq M < \infty$ , where  $M$  is a positive constant.*

**Definition** (Stability). *The LTV system described by  $\mathbf{y}(t) = \int_{t_0}^t \mathbf{H}(t, \tau) \mathbf{u}(\tau) d\tau$  (2.22) is stable if and only if there exist a positive constant  $M$  for which:*

$$\int_{t_0}^t \|\mathbf{H}(t, \tau)\| d\tau \leq M < \infty \quad (2.26)$$

Let us assume that the system matrices are bounded. The output equation does not contribute to stability, so we may ignore  $\mathbf{C}(t)$  and  $\mathbf{D}(t)$ . According to the definition of stability, the output may not diverge as long as the input is bounded, therefore we may as well assume  $\mathbf{u}(t) = 0$  and ignore  $\mathbf{B}(t)$ . We are left with the homogeneous state equation  $\dot{\mathbf{x}}(t) = \mathbf{A}(t)\mathbf{x}(t)$ , whose solution is  $\mathbf{x}(t) = \Phi(t, t_0)\mathbf{x}(t_0)$ :

**Theorem** (Uniform exponential stability). *[Th. 6.8][RUGH, 1996] If there is a positive constant such that  $\|\mathbf{A}(t)\| \leq \alpha < \infty$  for all  $t$ , then the linear state equation  $\dot{\mathbf{x}}(t) = \mathbf{A}(t)\mathbf{x}(t)$  is exponentially stable if and only if*

$$\int_t^{t_0} \|\Phi(t, \tau)\| d\tau \leq \beta < \infty \quad \forall t, t_0 : t \leq t_0 \quad (2.27)$$

This theorem assumes a simpler form in the case of time-invariant and periodic systems (sections 2.2 and 2.3).



**Definition** (Exponential stability). *The homogeneous time-varying system  $\dot{\mathbf{x}}(t) = \mathbf{A}(t)\mathbf{x}(t)$  is exponentially stable with rate of convergence  $\alpha > 0$  if there exists  $c_0 > 0$  such that*

$$\|\mathbf{x}(t)\| = c_0 e^{-\alpha(t-t_0)} \|\mathbf{x}(t_0)\| \quad \forall t \in [t_0, \infty[ \quad (2.28)$$

The rate of convergence is useful in quantifying the stability (or instability) of different systems as it provides an upper bound of the system's response. An example is shown in figure 2.22 for a family of time-varying aeroelastic systems. BIBO stability however, does not guarantee that a stable time-varying system's response will not exceed a dangerous level. An example is provided in figure 2.6.

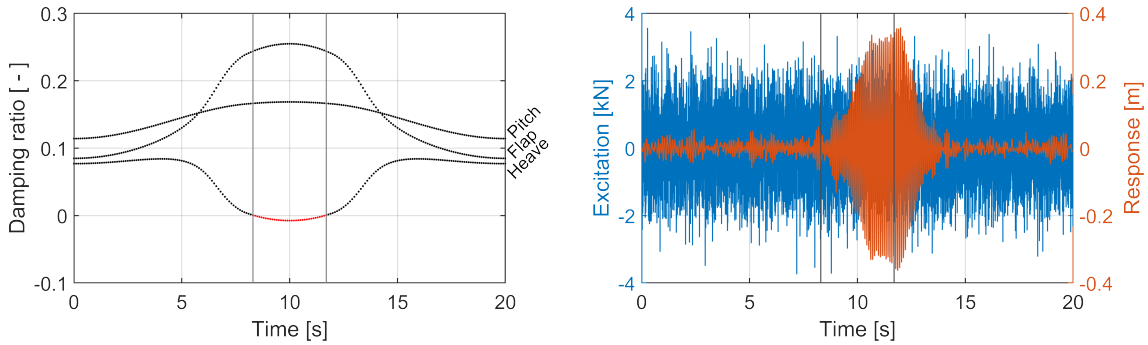


FIGURE 2.6: Response of a time-varying aeroelastic system excited by a random stationary signal. The stability analysis reveals that the system is stable despite the instantaneous eigenvalues crossing the stability boundary (red dots delimited by vertical lines). However, during this time the response amplitude grows significantly because the system temporarily absorbs energy instead of dissipating it.

### 2.1.7 On eigenvalues and eigenvectors

The linearity property of the state-space representation implies that there exists a coordinate change that transforms a linear system into another equivalent linear system. Two systems are equivalent when their input-output behavior is the same.

**Theorem** (Linear system transformation). *Consider a linear time-varying system and let the transformation matrix  $\mathbf{P}(t) \in \mathbb{C}^{N_x \times N_x} \in C^1$  be nonsingular. Define the state variable change (or coordinate transformation):*

$$\mathbf{x}(t) = \mathbf{P}(t)\tilde{\mathbf{x}}(t) \implies \dot{\mathbf{x}}(t) = \dot{\mathbf{P}}(t)\tilde{\mathbf{x}}(t) + \mathbf{P}(t)\dot{\tilde{\mathbf{x}}}(t) \quad (2.29)$$

The original system is thus transformed into an equivalent one [RUGH, 1996, Th. 4.13]:

$$\left[ \begin{array}{c|c} \mathbf{A}(t) & \mathbf{B}(t) \\ \mathbf{C}(t) & \mathbf{D}(t) \end{array} \right] \xrightarrow[\text{transform}]{\mathbf{x}(t)=\mathbf{P}(t)\tilde{\mathbf{x}}(t)} \left[ \begin{array}{c|c} \mathbf{P}^{-1}(t)\mathbf{A}(t)\mathbf{P}(t) - \mathbf{P}^{-1}(t)\dot{\mathbf{P}}(t) & \mathbf{P}^{-1}(t)\mathbf{B}(t) \\ \mathbf{C}(t)\mathbf{P}(t) & \mathbf{D}(t) \end{array} \right] \quad (2.30)$$

where  $\dot{\mathbf{P}}(t)\mathbf{P}^{-1}(t)$  is the dynamic coupling term. The transformed homogeneous state equation is thus:

$$\dot{\tilde{\mathbf{x}}}(t) = \tilde{\mathbf{A}}(t)\tilde{\mathbf{x}}(t) \quad \tilde{\mathbf{x}}(t_0) = \mathbf{P}^{-1}(t_0)\mathbf{x}(t_0) \quad (2.31)$$

The state transition matrix of the transformed system is given by

$$\tilde{\Phi}(t, t_0) = \mathbf{P}^{-1}(t)\Phi(t, t_0)\mathbf{P}(t_0) \quad (2.32)$$

The coordinate change preserves the system's stability.

**Definition** (Lyapunov transformation). *If there exists a constant  $c_0$  such that the coordinate transformation matrix  $\|\mathbf{P}(t)\| \leq c_0$  and its inverse  $\|\mathbf{P}^{-1}(t)\| \leq c_0$  are bounded for all  $t \geq t_0$ , then  $\mathbf{P}(t)$  is a Lyapunov transformation.*

This theorem is used in various ways to simplify the handling of a system, for example in balanced realizations and model reduction schemes [LANG ET AL., 2016; LUSPAY ET AL., 2018; SHOKOOHI ET AL., 1983] or to satisfy the commutativity condition of theorem (2.16) with a coordinate change [ZHU AND JOHNSON, 1989].

Let us consider a time invariant system for a moment. The eigenvalues and eigenvectors of the state matrix satisfy:

$$\mathbf{A}\Psi = \Psi\Lambda \quad (2.33)$$

Assuming that  $\Psi$  is non-singular, the coordinate change  $\mathbf{x}(t) = \Psi\tilde{\mathbf{x}}(t)$  transforms the system in its modal form:

$$\left[ \begin{array}{c|c} \mathbf{A} & \mathbf{B} \\ \hline \mathbf{C} & \mathbf{D} \end{array} \right] \xrightarrow[\text{transform}]{\mathbf{x}(t)=\Psi\tilde{\mathbf{x}}(t)} \left[ \begin{array}{c|c} \Lambda & \Psi^{-1}\mathbf{B} \\ \hline \mathbf{C}\Psi & \mathbf{D} \end{array} \right] \quad (2.34)$$

where the state matrix is diagonal and the states are uncoupled from each other. This is an important result. The reader is certainly aware that an LTI system is stable if and only if the state matrix eigenvalues have all negative real part. However, we shall see that the concept of eigenvalue is not generally meaningful in the time-varying case.

Given the time-varying state matrix  $\mathbf{A}(t)$ , the *instantaneous* (or *frozen-time*) eigenvalues  $\Lambda(t)$  and eigenvectors  $\Psi(t)$  of the system are functions that, at any instant, satisfy

$$\mathbf{A}(t)\Psi(t) = \Psi(t)\Lambda(t) \quad \forall t \quad (2.35)$$

We recall from theorem (2.1.3) that the state transition matrix has an exponential form when the state matrix is diagonal. We are thus tempted to apply the eigendecomposition to diagonalize the LTV system. The coordinate transformation  $\mathbf{x}(t) = \Psi(t)\tilde{\mathbf{x}}(t)$  returns:

$$\left[ \begin{array}{c|c} \mathbf{A}(t) & \mathbf{B}(t) \\ \hline \mathbf{C}(t) & \mathbf{D}(t) \end{array} \right] \xrightarrow[\text{transform}]{\mathbf{x}(t)=\Psi(t)\tilde{\mathbf{x}}(t)} \left[ \begin{array}{c|c} \Lambda(t) - \Psi^{-1}(t)\dot{\Psi}(t) & \Psi^{-1}(t)\mathbf{B}(t) \\ \hline \mathbf{C}(t)\Psi(t) & \mathbf{D}(t) \end{array} \right] \quad (2.36)$$

where the state matrix of the transformed system  $\tilde{\mathbf{A}}(t) = \Lambda(t) - \Psi^{-1}(t)\dot{\Psi}(t)$  is the sum of the instantaneous eigenvalues and the *mode coupling term*. The eigendecomposition of a time-varying state matrix does not generally uncouple the system states and the location of the instantaneous eigenvalues is neither necessary nor sufficient for stability. Early in the development of linear systems theory it was attempted to transpose the LTI

concept of stability onto LTV systems [ZADEH, 1951]. References [RUGH, 1996] and [CHEN, 1999] provide examples of instability with bounded matrices or stability with unstable eigenvalues. Nevertheless, the location of instantaneous eigenvalues can still be meaningful for slowly-varying systems [SOLO, 1994]. In this regard, a sufficient condition for the asymptotic stability is established in [ILCHMANN ET AL., 1987] based on an upper bound of the parameter variation with some a priori knowledge of the state matrix. A similar result is found in [AMATO ET AL., 1993] for the time derivative of the frozen-time system characteristics. Since the frozen-time formulation is essentially a local approximation of the system's behavior, the instantaneous eigenvalues lose their significance in the determination of the stability. Despite this, they often represent closely the locations of the resonance peaks and are thus still useful. Frozen-time eigenvalues can characterize LPV systems under the assumption that the state corresponding to each scheduling parameter  $\mathcal{S}(\mathbf{p})$  is reached so slowly, that any contributions from the dynamic coupling can be neglected. This is a common hypothesis in many signal processing and system identification methods, for it allows a definition of a transfer function for each parameter and consequently the applicability of LTI methods, for instance, in the description of aeroelastic structures (as function of speed and altitude), of robotic arms (as function of joint angles), of bridges (as function of the load position) [ERTVELDT ET AL., 2014; HOUTZAGER ET AL., 2012; MERCERE ET AL., 2011; SPIRIDONAKOS AND FASSOIS, 2009]. We shall come back to the topic in section 3.4.2.

In the LTV framework a different concept of “eigenvalues” is introduced [WU, 1980]: the continuous functions  $\mathbf{\Lambda}_d(t)$  and  $\mathbf{\Psi}_d(t)$  (subscript  $d$ ) satisfying the condition

$$\mathbf{A}(t)\mathbf{\Psi}_d(t) = \mathbf{\Psi}_d(t)\mathbf{\Lambda}_d(t) + \dot{\mathbf{\Psi}}_d(t) \quad \forall t \quad (2.37)$$

are called respectively *dynamic eigenvalues* and *dynamic eigenvectors*. These are not unique and do not possess the same physical meaning as their time-invariant counterpart. In the case of slowly-varying systems, equation (2.37) reduces to the definition of time-invariant eigenvalues because  $\dot{\mathbf{\Psi}}_d(t) \ll \mathbf{\Lambda}_d(t)\mathbf{\Psi}_d(t)$ .

In the time-varying case, if the state matrix is diagonal, the state transition matrix has conveniently an exponential form (2.17). We are looking for a particular transformation matrix  $\mathbf{P}(t)$  that transforms the system's state matrix  $\mathbf{A}(t)$  into a diagonal one  $\tilde{\mathbf{A}}(t) \equiv \tilde{\mathbf{\Lambda}}(t)$ . The (Lyapunov) transformation matrix is thus:

$$\tilde{\mathbf{A}}(t) \equiv \tilde{\mathbf{\Lambda}}(t) \implies \tilde{\mathbf{\Phi}}(t, t_0) = \exp \int_t^{t_0} \tilde{\mathbf{\Lambda}}(\tau) d\tau \implies \mathbf{P}(t) = \mathbf{\Phi}(t, t_0) \exp \int_t^{t_0} \tilde{\mathbf{\Lambda}}(\tau) d\tau \quad (2.38)$$

The system is therefore transformed into:

$$\left[ \begin{array}{c|c} \mathbf{A}(t) & \mathbf{B}(t) \\ \mathbf{C}(t) & \mathbf{D}(t) \end{array} \right] \xrightarrow[\text{transform}]{\mathbf{x}(t)=\mathbf{P}(t)\tilde{\mathbf{x}}(t)} \left[ \begin{array}{c|c} \tilde{\mathbf{\Lambda}}(t) & \mathbf{P}^{-1}(t)\mathbf{B}(t) \\ \mathbf{C}(t)\mathbf{P}(t) & \mathbf{D}(t) \end{array} \right] \quad (2.39)$$

By comparing equations (2.37) and (2.39) we see that  $\tilde{\mathbf{\Lambda}}(t)$  and  $\mathbf{P}(t)$  are indeed the

dynamic eigenvalues and eigenvectors of the system and they are not unique because  $\tilde{\Lambda}(t)$  is *arbitrary* (even constant or zero!). The appropriate choice of dynamic eigenpairs can simplify considerably the system, however it is not always clear which to pick [WU, 1980]. This kind of transformation can be performed after the state transition matrix has been determined (by whatever means). Alternatively, algorithm (5) proposed in [WU, 1984] and refined in [VAN DER KLOET AND NEERHOFF, 2000] can be employed when the state matrix has only distinct instantaneous eigenvalues. When the system transformation does not uncouple completely the states, in [LUSPAY ET AL., 2018] it is shown that it is possible to set to zero the entries of the dynamic coupling term  $\mathbf{P}^{-1}(t)\dot{\mathbf{P}}(t)$  there where  $\mathbf{P}^{-1}(t)\mathbf{A}(t)\mathbf{P}(t)$  is zero and to accept a modeling error in the input-output behavior of the system (that depends on the importance of the neglected entries). An example of the difference between dynamic and instantaneous eigenvalues is shown in figure 2.8.

In [LIU, 1999] the *pseudo modal parameters* (subscript  $p$ ) corresponding to the interval  $[t, t_0]$  are defined by the eigendecomposition of the state transition matrix:

$$\Phi(t, t_0) = \Psi_p(t_0)e^{\Lambda_p(t_0)(t-t_0)}\Psi_p^{-1}(t_0) \quad (2.40)$$

This equation essentially states that the system is considered invariant in the interval  $[t, t_0]$  (compare this expression to the exponential form of the state transition matrix (2.17)). As  $t - t_0 \rightarrow 0$ ,  $\Lambda_p(t)$  tends to the instantaneous eigenvalues  $\Lambda(t)$ .

The concept of time-varying modes is introduced in [KAMEN, 1988] and expanded in [O'BRIEN AND IGLESIAS, 1997] and [MA ET AL., 2017]. Let us impose that the transformed state matrix  $\tilde{\mathbf{A}}(t)$  be upper triangular:

$$\tilde{\mathbf{A}}(t) = \begin{bmatrix} \lambda_1(t) & * & \cdots & * \\ 0 & \lambda_2(t) & \cdots & * \\ \vdots & \vdots & \ddots & \vdots \\ 0 & 0 & \cdots & \lambda_{N_x}(t) \end{bmatrix} \quad (2.41)$$

and that its associated state transition matrix is  $\tilde{\Phi}(t, t_0)$ . We are looking for a Lyapunov transformation matrix  $\mathbf{P}(t)$  which satisfies  $\dot{\mathbf{P}}(t) = \mathbf{A}(t)\mathbf{P}(t) - \mathbf{P}(t)\tilde{\mathbf{A}}(t)$ :

$$\mathbf{P}(t) = \Phi(t, t_0)\mathbf{P}(t_0)\tilde{\Phi}(t, t_0) \quad (2.42)$$

Let us now consider the QR-decomposition of the state transition matrix of the original system. We can write

$$\Phi(t, t_0) \stackrel{\text{QR}}{=} \mathbf{Q}(t)\mathbf{R}(t) \quad (2.43)$$

where  $\mathbf{Q}(t)$  is orthogonal and  $\mathbf{R}(t)$  is an upper triangular matrix<sup>4</sup>. Unlike the eigendecomposition (2.35) (instantaneous eigenvalues), the QR matrices are real because the STM of a physical system is real.  $\mathbf{Q}(t) = \mathbf{P}(t)$  is a Lyapunov transformation since  $\|\mathbf{Q}(t)\| = 1$ .

<sup>4</sup> The QR-decomposition is unique up to a factor of a diagonal matrix with entries  $\pm 1$ . Uniqueness is enforced by imposing that the diagonal of  $\mathbf{R}(t)$  be positive. Let  $\mathbf{D}_{ii}(t) \triangleq \text{sgn}\{\mathbf{R}_{ii}(t)\}$  be a diagonal matrix. Then the QR-decomposition  $\mathbf{R}(t) \leftarrow \mathbf{D}(t)\mathbf{R}(t)$ ,  $\mathbf{Q}(t) \leftarrow \mathbf{Q}(t)\mathbf{D}^T(t)$  is unique.

Furthermore,  $\mathbf{Q}(t_0) = \mathbf{I}$  because  $\Phi(t_0, t_0) = \mathbf{I}$ , therefore  $\tilde{\Phi}(t, t_0) = \mathbf{R}(t)$ . The solution of the homogeneous state equation  $\dot{\mathbf{x}}(t) = \mathbf{A}(t)\mathbf{x}(t)$  can be written as a linear combination of time-varying vectors:

$$\mathbf{x}(t) = \sum_{i=1}^{N_x} c_i \mathbf{v}_i(t) \quad (2.44)$$

where  $c_i \triangleq \mathbf{e}_i^T \mathbf{P}^{-1}(t_0) \mathbf{x}(t_0) = \mathbf{e}_i^T \mathbf{x}(t_0)$  and  $\mathbf{v}_i(t) \triangleq \mathbf{P}(t) \mathbf{e}_i \tilde{\Phi}_{ii}(t, t_0) = \mathbf{Q}(t) \mathbf{e}_i \mathbf{R}_{ii}(t)$ . The  $i$ -th time-varying modes are then given by the diagonal elements of  $\tilde{\Phi}(t, t_0)$ :

$$\psi_i(t, t_0) = \mathbf{R}_{ii}(t) \quad \in \mathbb{R} \quad (2.45)$$

The time-varying poles  $\lambda_i(t)$  in the upper triangular transformed state matrix (2.41) are derived by the differentiation property of the state transition matrix (2.1.3):

$$\frac{\partial}{\partial t} \Phi(t, t_0) = \mathbf{A}(t) \Phi(t, t_0) \implies \lambda_i(t) = \frac{\partial}{\partial t} \psi_i(t, t_0) \psi_i^{-1}(t, t_0) \quad \in \mathbb{R} \quad (2.46)$$

The time-varying modes contain information about the stability of the system [O'BRIEN AND IGLESIAS, 2001]. An example is provided in figure 2.7.

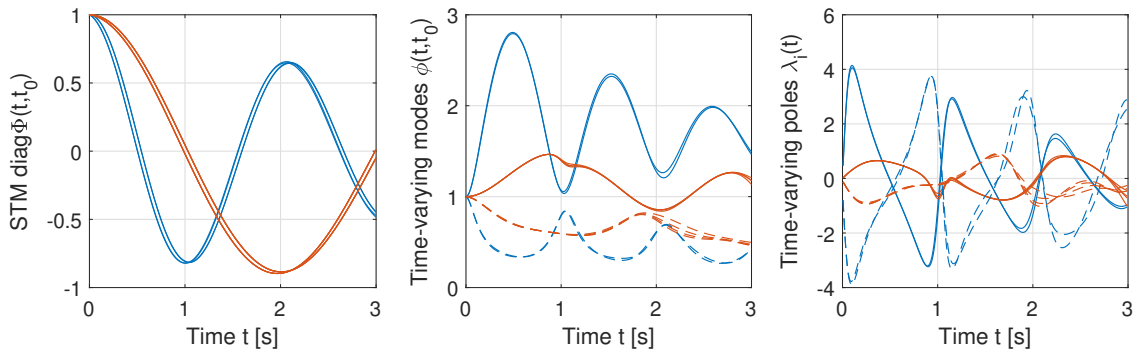


FIGURE 2.7: State transition matrix, time-varying modes and poles of a helicopter model from [JHINAOU ET AL., 2014] (2 landing gear degrees of freedom + 4 blades, one revolution with period  $T = 3$  s). The time-varying modes and poles can be grouped by component (blue: landing gear, red: rotor blades) and by state (solid line: displacement, dashed line: velocity).

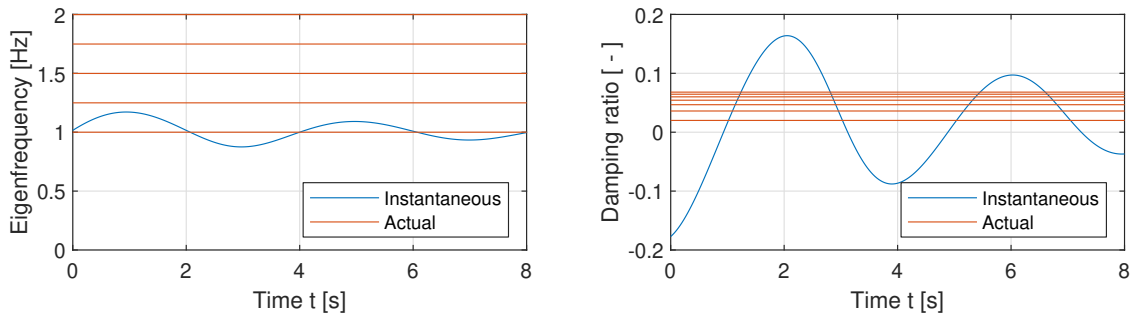


FIGURE 2.8: Instantaneous and actual poles of the STM of  $\dot{x}(t) = a_0(1 + 0.2e^{s_1 t})x(t)$ , where  $a_0 = f_\lambda(1, 0.02)$  and  $s_1 = f_\lambda(0.25, 0.1)$ . The instantaneous poles vary as a complex exponential. The STM in frequency domain can be computed analytically (see section 2.5.2) and it turns out that it has constant poles.

## 2.2 Linear time-invariant systems

The most important special case of linear systems is when the system matrices are constant:

$$\begin{aligned}\dot{\mathbf{x}}(t) &= \mathbf{A}\mathbf{x}(t) + \mathbf{B}\mathbf{u}(t) \\ \mathbf{y}(t) &= \mathbf{C}\mathbf{x}(t) + \mathbf{D}\mathbf{u}(t)\end{aligned}\tag{2.47}$$

The theory of linear time-invariant systems (LTI) is widely used in all sorts of fields because of its elegance, relative simplicity and broad applicability. Two typical examples would be an ideal mass-damper-spring system or an electrical circuit with inductors, capacitors and resistors. LTI systems have an extremely large number of applications in various fields of physics and engineering: simulation of mechanical systems, description of electrical circuits, control theory, signal processing, acoustics, optics; the body of literature on LTI systems is accordingly immense [SHMALIY, 2007]. Under certain conditions or with some acceptable approximations, LTI system theory can provide adequate descriptions of discontinuous or nonlinear systems [KHALIL, 1996]. A comprehensive and detailed reference for an introduction on the subject, is the book [OPPENHEIM ET AL., 1996]. The results in this section are either derived as particular cases from the equations of time-varying systems or are taken from the references.

The focus in this thesis lies generally in linear time-varying systems, but there are many limiting cases in which system parameters vary so slowly that they can be considered constant within a certain time interval or with an acceptable degree of accuracy. In such cases the equations introduced in the previous section undergo considerable simplifications and assume more familiar forms. For example, aircraft in stationary level flight can be considered as time-invariant even though their dynamic properties depend on speed and altitude.

The linearity and invariance of LTI systems lead to a theoretically sound and practically efficient framework. Some of the results in this section have already been anticipated or can be deduced from the previous pages, nevertheless we shall establish here some important equations and concepts that will be necessary further on for system identification in chapter 5. Causality and stability are much simpler to check compared to the LTV case. The fundamental property is that LTI systems can be completely characterized by their impulse response or equivalently by their transfer function. Importantly, input-output relationships are conveniently described by the convolution of the impulse response with the input signal in time-domain or by the multiplication of the transfer function with the input in frequency-domain.

The state transition matrix of a time-invariant system<sup>5</sup> is given by theorem (2.1.3):

$$\Phi(t, t_0) = e^{\mathbf{A}(t-t_0)}\tag{2.48}$$

---

<sup>5</sup> In many texts, the state transition matrix from  $\mathbf{x}(t_0)$  to  $\mathbf{x}(t_0 + \Delta t)$  is denoted by  $\mathbf{A}_d \triangleq \Phi(t_0 + \Delta t, t_0) = e^{\mathbf{A}\Delta t}$  in the context of discretized or sampled time-invariant systems.

The complete solution is then a special case of equation (2.20) with constant matrices:

$$\begin{aligned}\mathbf{x}(t) &= e^{\mathbf{A}(t-t_0)}\mathbf{x}(t_0) + \int_{t_0}^t e^{\mathbf{A}(t-\tau)}\mathbf{B}\mathbf{u}(\tau) d\tau \\ \mathbf{y}(t) &= \mathbf{C}\mathbf{x}(t) + \mathbf{D}\mathbf{u}(t)\end{aligned}\quad (2.49)$$

Equation (2.49) can be solved exactly for inputs that are combinations of polynomial and exponential functions, therefore, in this thesis the methods developed in [JELIČIĆ ET AL., 2021] are the preferred tools for the simulations of LTI systems, rather than direct ordinary differential equations solvers. LTI system benchmarks can be found in [CHAHLAOUI AND VAN DOOREN, 2005].

The general impulse response expression 2.23 for constant state matrices is

$$\mathbf{H}(t, \tau) = \begin{cases} \mathbf{D}\delta(t - \tau) + \mathbf{C}e^{\mathbf{A}(t-\tau)}\mathbf{B} & t \geq \tau \\ 0 & t < \tau \end{cases} \quad (2.50)$$

where it is clear that  $\mathbf{H}(t, \tau) = \mathbf{H}(t - \tau)$  does not depend on the instant at which the impulse happens. This means that a time shift of the input signal will produce the same shift in the output. For time-invariant systems, the impulse response and the transfer function are thus coupled by the Laplace transform:

$$\mathbf{H}(t) = \mathbf{D}\delta(t) + \mathbf{C}e^{\mathbf{A}t}\mathbf{B} \quad \circ\text{---}\bullet \quad \mathbf{H}(s) = \mathbf{D} + \mathbf{C}(s\mathbf{I} - \mathbf{A})^{-1}\mathbf{B} \in \mathbb{C}^{N_y \times N_u} \quad (2.51)$$

Alternatively, it is possible to write the steady-state solution (2.49) in Laplace-domain to obtain the well-known expression relating input and output:

$$\mathbf{y}(s) = \mathbf{H}(s)\mathbf{u}(s) \quad (2.52)$$

which was already introduced in equation (2.52). In contrast to LTV systems, time-invariance defines clearly the relationship between input signals and output responses through the transfer function. We have already mentioned before that LTI systems, upon reaching a steady state, respond to a sinusoid with another sinusoid of the same frequency, but modified amplitude and phase; they cannot produce other frequency components. Said formally, the complex exponential is the eigenfunction of a time-invariant linear system.

We can take the ordinary differential equation form of a linear system (2.2) and set its coefficients constant  $a_k(t) = a_k$ ,  $b_k(t) = b_k$ . The relationship between the  $j$ -th input  $u_j(t)$  and the  $i$ -th output  $y_i(t)$  in Laplace-domain is<sup>6</sup>:

$$\sum_{k=0}^{N_a} a_k \frac{d^k}{dt^k} y_i(t) = \sum_{k=0}^{N_b} b_k \frac{d^k}{dt^k} u_j(t) \quad \circ\text{---}\bullet \quad \sum_{k=0}^{N_a} a_k s^k y_i(s) = \sum_{k=0}^{N_b} b_k s^k u_j(s) \quad (2.53)$$

<sup>6</sup> The coefficients correspond only to entry  $(i, j)$ ; a more precise notation for the multi-input-multi-output case would be  $a_{ij,k}$  and  $b_{ij,k}$ , but we drop the subscript  $ij$  in favor of legibility.

We can write  $y_i(s)/u_j(s)$  to obtain the entry  $(i, j)$  of  $\mathbf{H}(s)$ :

$$H_{ij}(s) = \frac{y_i(s)}{u_j(s)} = \frac{\sum_{k=0}^{N_b} b_k s^k}{\sum_{k=0}^{N_a} a_k s^k} \quad (2.54)$$

The roots of the numerator and denominator polynomials are called respectively zeroes  $z_k$  and poles  $p_k$  of  $H_{ij}(s)$ . The factoring of the two polynomials, followed by a partial fraction decomposition delivers two other forms of the transfer function:

$$H_{ij}(s) = \frac{\sum_{k=0}^{N_b} b_k s^k}{\sum_{k=0}^{N_a} a_k s^k} = g \frac{\prod_{k=1}^{N_b} (s - z_k)}{\prod_{k=1}^{N_a} (s - p_k)} = k(s) + \sum_{n=1}^{N_a} \frac{r_k}{s - p_k} \quad (2.55)$$

where  $g$  is the scalar gain and  $k(s)$  a polynomial in  $s$  of order  $N_b - N_a + 1$  (if  $N_b < N_a$ , then  $k(s) = 0$ ). The transfer function  $H_{ij}(s)$  between the  $j$ -th input and the  $i$ -th output can be thus expressed, from left to right in equation (2.55), in the *rational*, in the *zero-pole-gain* and in the *pole-residue* forms. In particular the latter tells us that in the LTI case the transfer function is the weighted sum of simple poles (plus the direct term  $k(s)$  if the system is not proper). The poles assume significance in determining the system's stability and the amplification of the input at resonance. The zeros on the other hand determine the location of the antiresonances where the oscillation amplitude is significantly reduced. The same results are obtained by transforming the system into modal space (2.34):

$$\mathbf{H}(s) = \mathbf{D} + \mathbf{C}\Psi (s\mathbf{I} - \mathbf{\Lambda})^{-1} \Psi^{-1} \mathbf{B} = \mathbf{D} + \sum_{k=1}^{N_x} \frac{\mathbf{c}_k \mathbf{b}_k^T}{s - \mathbf{\Lambda}_k} \quad (2.56)$$

where  $\mathbf{c}_k \triangleq \mathbf{C}\Psi_k \mathbf{e}_k$  is the  $k$ -th column of the transformed input matrix and  $\mathbf{b}_k^T \triangleq \mathbf{e}_k^T \Psi^{-1} \mathbf{B}$  the  $k$ -th row of the transformed input matrix. The residual matrices  $\mathbf{R}_k = \mathbf{c}_k \mathbf{b}_k^T \in \mathbb{C}^{N_y \times N_u}$  have rank one. In this equation we see that the eigenvalues of the state matrix are the system's poles and that  $\mathbf{c}_k$  are the normal modes. The pole-residue form can be factored to write the rational and zero-pole-gain representation of the transfer function (2.55) in full matrix form. Let us denote the  $k$ -th eigenvalue with  $\lambda_k = \Re\lambda_k + i\Im\lambda_k$  and write the impulse response function:

$$\mathbf{H}(t) = \mathbf{D} + \sum_{k=1}^{N_x} \mathbf{c}_k \mathbf{b}_k^T e^{(\Re\lambda_k + i\Im\lambda_k)t} \quad (2.57)$$

We see immediately that the circular terms  $e^{i\Im\lambda_k t} \in [-1, 1]$  are bounded, while  $e^{\Re\lambda_k t}$  is finite as long as  $\Re\lambda_k \leq 0$ . The imaginary part of  $\lambda_k$  defines the period of one oscillation. The real part of  $\lambda_k$  quantifies the decay rate of free vibration due to the energy loss. The stability of an LTI system can be thus easily checked from its eigenvalues:

**Theorem** (Stability of time-invariant systems). *A linear time-invariant system is stable if and only if the real part of all eigenvalues  $\lambda$  of the state matrix  $\mathbf{A}$  is non-negative  $\Re\lambda < 0$ .*



### 2.2.1 Second-order time-invariant systems

Since the state matrix is real, all eigenvalues with imaginary part different than zero must come in complex-conjugated pairs. As a consequence, mechanical systems can be decomposed into second-order models plus possibly some purely real poles.

Second-order models represent physically systems with one oscillating element (for example a mass attached to a spring), therefore they are also called single degree-of-freedom systems (1-DoF). The study of their dynamic behavior serves as the prototype for understanding more complex cases. A detailed treatment of single degree-of-freedom systems in structural dynamics, with derivations, formulae and plots, is found in [BRANDT, 2011; DEN HARTOG, 1985; OPPENHEIM ET AL., 1996; RAO, 2017]. The notions that will be necessary later are taken from these references. The homogeneous equation of the simple harmonic oscillator is:

$$\ddot{x}(t) + 2\zeta\omega_n\dot{x}(t) + \omega_n^2 x(t) = 0 \quad (2.58)$$

where  $\omega_n$  [rad/s] is the circular eigenfrequency and  $\zeta$  [adim] the damping ratio. The frequency response function is found by transforming into frequency-domain:

$$H(\omega) = \frac{1}{-\omega^2 + i2\zeta\omega_n\omega + \omega_n^2} = \frac{1}{(i\omega - \lambda)(i\omega - \lambda^*)} = \frac{1}{\lambda - \lambda^*} \left( \frac{1}{i\omega - \lambda} - \frac{1}{i\omega - \lambda^*} \right) \quad (2.59)$$

where the roots  $\lambda$  and  $\lambda^*$  of the denominator are:

$$\begin{aligned} \lambda &= -\omega_n\zeta \pm i\omega_n\sqrt{1 - \zeta^2} & \omega_n &= |\lambda| \\ & & \zeta &= -\Re\lambda/|\lambda| \end{aligned} \quad (2.60)$$

The impulse response of the system (2.59) is thus:

$$H(t) = \frac{1}{\lambda - \lambda^*} \left( e^{\lambda t} + e^{\lambda^* t} \right) = \frac{1}{\omega_n\sqrt{1 - \zeta^2}} e^{-\omega_n\zeta t} \sin\left(\omega_n t\sqrt{1 - \zeta^2}\right) \quad (2.61)$$

The dimensionless impulse and frequency response functions  $\omega_n H(t)$  and  $\omega_n^2 H(\omega)$  are plotted in figure 2.9 with the damping ratio as parameter. We see that the amplification factor is  $1/(2\zeta)$  at resonance and that the output of a stable system lags behind the input. In the presence of low damping the system amplifies the input signals whose frequencies  $\omega$  lie in the vicinity of the eigenfrequency  $\omega_n$ . For free oscillations, the decay rate is  $\zeta\omega_n$ , its reciprocal is the time constant of the system  $\tau \triangleq (\zeta\omega_n)^{-1}$ , while the period is  $T = 2\pi/(\omega_n\sqrt{1 - \zeta^2})$ .

Depending on the damping ratio, each eigenvalue can be classified as: *unstable* when  $\zeta < 0$  (the system absorbs energy and vibration amplitudes grow exponentially with time), *undamped* when  $\zeta = 0$  (oscillations persist indefinitely), *underdamped* when  $0 < \zeta < 1$  (oscillations decrease in amplitude with time), *critically damped* when  $\zeta = 1$  (there are no more oscillations and the system reaches the rest position in the minimal time) and *overdamped* when  $\zeta > 1$  (the energy dissipation is so high that it takes even longer to reach the rest position). When  $|\zeta| \geq 1$ , the eigenvalue is purely real. The damping ratio of

a real structure is positive because its mechanical energy is being continually converted into heat and dissipated. For aircraft, structural modes have typically  $\zeta < 3\%$ . Modes of components that are designed to dissipate energy such as the landing gear or shock absorbers have much higher damping. More about damping and its modeling in structural dynamics can found in [CHOPRA, 2019]. A particularity of aeroelastic phenomena is that the interaction between fluid flow and structure can increase the damping ratio of some modes above 20%. In such cases there is a small structural component and a much larger aerodynamic contribution. This topic will be discussed at length in the next chapter.

When  $\zeta = \sqrt{2}/2$ , the frequency response is monotonically decreasing, therefore, for the usage in this thesis, we shall introduce two additional types:

**Definition.** Poles with  $0 < \zeta < \sqrt{2}/2$  are called “lightly-damped”; conversely, the poles with  $\zeta \geq \sqrt{2}/2$  are “highly-damped”.

This definition will be useful in the next chapter when the state matrix of aeroelastic systems will be constructed because structural modes gather in the proximity of the imaginary axis, while aerodynamic modes wander next to the real axis.

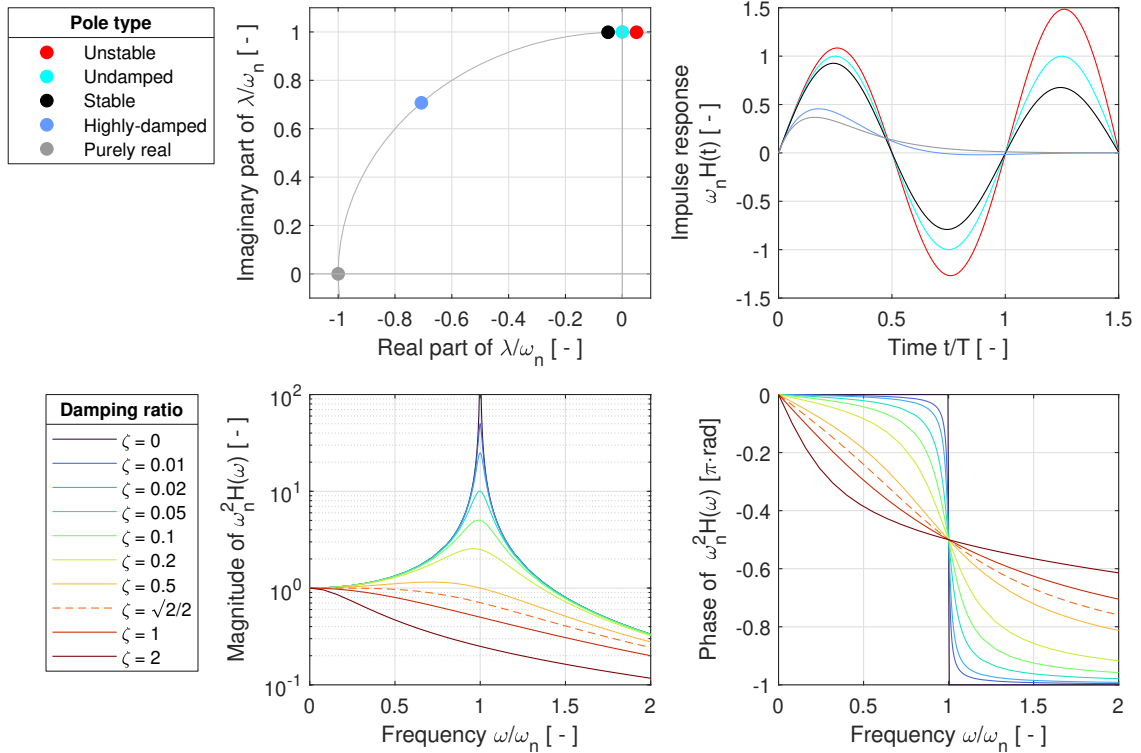


FIGURE 2.9: Simple damped harmonic oscillator  $\ddot{x}(t) + 2\zeta\omega_n\dot{x}(t) + \omega_n^2x(t) = 0$ . Upper row: pole classification and the dimensionless impulse response  $\omega_n H(t)$  corresponding to the poles displayed on the left  $\zeta = [-0.05, 0, 0.05, \sqrt{2}/2, 1]$ . The color-coded poles will be appear in the frozen-time eigenvalue diagrams in the next chapters. Lower row: magnitude and phase of the dimensionless frequency response function  $\omega_n^2 H(\omega)$ . For negative damping the magnitude is the same but the phase changes sign. The maximum  $1/(2\zeta\sqrt{1-\zeta^2})$  is attained at  $\omega/\omega_n = \sqrt{1-\zeta^2}$ , while at resonance  $\omega_n^2 H(\omega_n) = (2\zeta)^{-1}$ . If  $\zeta \geq \sqrt{2}/2$ , then  $H(\omega)$  is monotonically decreasing, otherwise the input is always attenuated when  $\omega/\omega_n > \sqrt{2-4\zeta^2}$ .

### 2.3 Periodic systems

Linear systems whose coefficients vary periodically are called *linear time-varying periodic systems* (LTP) and appear in many fields of science and engineering. Rotating machinery such as wind turbines and helicopter rotors belong to this important special case [ALLEN ET AL., 2011; JHINAOU ET AL., 2014; MAURICE ET AL., 2009; SKJOLDAN AND HANSEN, 2009]. Satellite orbital mechanics and control of elliptic orbits can be treated as linear periodic systems with periodic solutions [SHERRILL ET AL., 2015]. Nonlinear systems that exhibit periodic behavior such as oscillating circuits can be linearized and treated as LTP systems in order to characterize noise or stability [KHALIL, 1996; TRAVERSA AND BONANI, 2011]. The dispersion properties of structures that are periodic in space is computed by the same mathematical framework that is used for LTP systems [COLLET ET AL., 2011]. Other applications are mass spectrometry, dynamic buckling of structures, elliptical waveguides, solid-state physics. A detailed review of linear periodic systems and their applications is found in [RICHARDS, 1983].

The mathematical foundation for the study of LTP systems is *Floquet's theory*. It provides a convenient decomposition of the state transition matrix from which stability can be inferred. The relevant corollaries and consequences of the theorem will be explored in this section.

Before diving deep into the details of Floquet theory, the relevance of periodic systems to the study of time-varying aeroelastic systems should be motivated. The particular interest of this work is the effect of parameter rate or amplitude of change on system response, therefore an analytical description of the response's spectral content may provide a convenient investigation tool. The flexibility of Floquet theory is clearly illustrated in literature, therefore a general method for analyzing time-varying systems is proposed in this chapter. The previous sections have mentioned how the frequency-domain description of LTI systems that is so important for modal analysis is generally not such a clear matter in the time-varying case. One complicating factor is the form of the state transition matrix; section 2.1.3 has given a very general account of its determination. On the other hand, Floquet theory is more particular in its assumptions but offers an attractive analytical tool to determine and decompose the STM of periodic systems. This is the crucial aspect of the theory: if a time-varying system's response is restricted to a finite time interval and the state matrix is continuous, then it has an absolutely convergent Fourier series within said interval. This periodic representation of the system can be used to decompose its STM, respectively to find its system response analytically. It is then possible to determine the spectrum of the response. This approach is similar to the solution of the heat equation, which is described by a parabolic partial differential equation: the solution is represented in terms of trigonometric functions in order to simplify the mathematical treatment and the resulting temperature distribution within the domain is described by Fourier series even though domain, boundary and initial conditions are not periodic. The same principle is used here to render general time-varying systems tractable.

### 2.3.1 Floquet's theorem

Consider the homogeneous linear periodic system

$$\dot{\mathbf{x}}(t) = \mathbf{A}(t)\mathbf{x}(t) \quad (2.62)$$

where  $\mathbf{A}(t) = \mathbf{A}(t + T)$  is a  $T$ -periodic piece-wise continuous state matrix. The state transition matrix evaluated over one period  $\Phi(t_0 + T, t_0)$  (a constant) is called the *monodromy matrix*. The STM of LTP systems is generally not periodic.

**Theorem** (Floquet's theorem). *If the linear time periodic system (2.62) has a non-defective monodromy matrix  $\Phi(T, 0)$ , then its state transition matrix over any  $t, t_0$  can be factored as:*

$$\Phi(t, t_0) = \mathbf{P}(t)e^{\mathbf{Q}(t-t_0)}\mathbf{P}^{-1}(t_0) \quad (2.63)$$

where  $\mathbf{P}(\cdot) \in \mathbb{C}^{N_x \times N_x}$  is the invertible, continuous and bounded Lyapunov-Floquet transformation matrix of period  $T$  and  $\mathbf{Q} \in \mathbb{C}^{N_x \times N_x}$  is a constant matrix [ANTSAKLIS AND MICHEL, 2006, Th. 5.2].

Knowledge of the state transition matrix in the interval  $t \in [0, T]$  is sufficient to characterize the system's behavior in any other interval because of the recurrence relation:

$$\Phi(t + nT, t_0) = \Phi(t, t_0)\Phi(T, t_0)^n \quad (2.64)$$

Under Floquet's theorem's assumptions, the monodromy matrix does have a matrix logarithm from which  $\mathbf{Q}$  can be calculated:

$$\Phi(T, 0) = e^{\mathbf{Q}T} \implies \mathbf{Q} = \frac{1}{T} \ln \Phi(T, 0) \quad (2.65)$$

**Definition.** *The unique eigenvalues  $\mu$  of the monodromy matrix  $\Phi(T, 0)$  are called the "Floquet multipliers" of the system. The "Floquet exponents"  $\lambda$  are the eigenvalues of  $\mathbf{Q}$ . They are complex numbers such that  $\mu = e^{\lambda T}$  and they are not unique because  $e^{\lambda T + i2\pi k} = e^{\lambda T}$ , therefore they are defined modulo  $i2\pi k$ .*

The matrices  $\Phi(T, 0)$  and  $\mathbf{Q}$  share the same eigenvectors:

$$\Phi(T, 0) = e^{\mathbf{Q}T} \stackrel{\text{eig}}{=} e^{\Psi\Lambda\Psi^{-1}T} = \Psi e^{\Lambda T} \Psi^{-1} \quad (2.66)$$

The transformation matrix  $\mathbf{P}(t)$  is then obtained by inverting equation (2.63) and setting  $t_0 = 0$ :

$$\mathbf{P}(t) = \Phi(t, 0)e^{-\mathbf{Q}t} \quad (2.67)$$

from which it can be seen that  $\mathbf{P}(0) = \mathbf{P}(T) = \mathbf{I}$ .

The computation of the inverse of the transformation matrix  $\mathbf{P}^{-1}(t)$  through matrix inversion should be avoided because the calculated transformation matrix  $\mathbf{P}(t)$  may itself be inaccurate. Instead, the duality property of the state transition matrix should be used

(2.1.3). Consider the *dual* (or *adjoint*) system of the homogeneous state equation (2.62):

$$\dot{\mathbf{z}}(t) = -\mathbf{A}^T(t)\mathbf{z}(t) \implies \mathbf{z}(t) = \Phi_d(t, t_0)\mathbf{z}(t_0) \quad (2.68)$$

where  $\Phi_d(t, t_0)$  designates the state transition matrix corresponding to the state matrix  $-\mathbf{A}^T(t)$  of the dual system. It is related to  $\Phi(t, t_0)$  by:

$$\Phi_d^T(t, t_0) = \Phi^{-1}(t, t_0) = \mathbf{P}(t_0)e^{\mathbf{Q}^T(t_0-t)}\mathbf{P}^{-1}(t) \quad (2.69)$$

from which:

$$\mathbf{P}^{-1}(t) = e^{\mathbf{Q}^T t}\Phi_d^T(t, 0) \quad (2.70)$$

This property is particularly helpful when determining the Floquet quantities numerically.

Figure 2.10 displays, as an example, the influence of period on the state transition matrix of a wind turbine model. The practical calculation of the Floquet quantities is discussed section 2.4; for now it is important to focus on their properties.

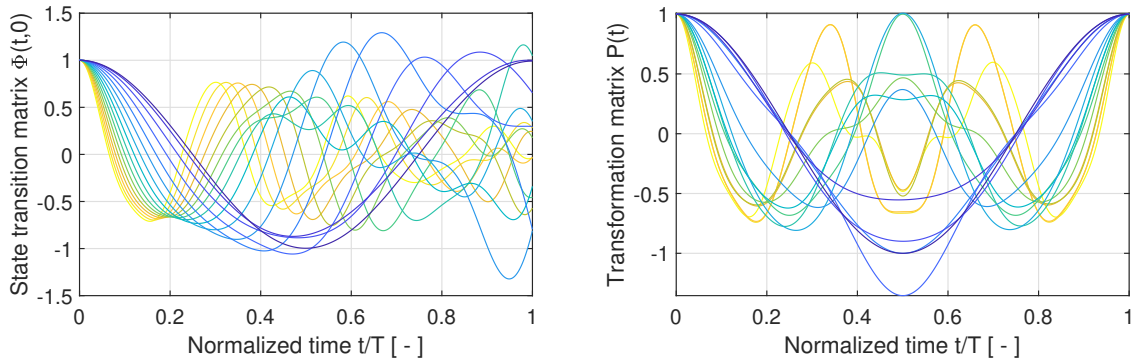


FIGURE 2.10: State transition matrix and transformation matrix for various values of the system's period (blue: low, yellow: high). Generally the STM is not periodic and the transformation matrix is not symmetric. The figure displays entry (1,1) of the 5-DoF system from [SKJOLDAN AND HANSEN, 2009] for  $T = 0.05:5$  s.

### 2.3.2 Lyapunov-Floquet transformation

An important consequence of Floquet's theorem is that a periodic time-varying system can be transformed into an equivalent time-invariant system by a coordinate change (Lyapunov-Floquet transformation). For LTP systems, the derivation property of the state transition matrix implies [CHEN, 1999, Th. 4.3]:

$$\frac{\partial}{\partial t}\Phi(t, 0) = \mathbf{A}(t)\Phi(t, 0) \xrightarrow[\text{substitute}]{\Phi(t,0)=\mathbf{P}(t)e^{\mathbf{Q}t}} \dot{\mathbf{P}}(t) + \mathbf{P}(t)\mathbf{Q} = \mathbf{A}(t)\mathbf{P}(t) \quad (2.71)$$

which, together with theorem (2.30), leads to the state variable change

$$\left[ \begin{array}{c|c} \mathbf{A}(t) & \mathbf{B}(t) \\ \mathbf{C}(t) & \mathbf{D}(t) \end{array} \right] \xrightarrow[\text{transform}]{\mathbf{x}(t)=\mathbf{P}(t)\tilde{\mathbf{x}}(t)} \left[ \begin{array}{c|c} \mathbf{Q} & \mathbf{P}^{-1}(t)\mathbf{B}(t) \\ \mathbf{C}(t)\mathbf{P}(t) & \mathbf{D}(t) \end{array} \right] \quad (2.72)$$

where the matrix  $\mathbf{Q}$  reveals its meaning as the *constant state matrix* of the transformed system. The system states can then be uncoupled (2.34) to obtain:

$$\left[ \begin{array}{c|c} \mathbf{Q} & \mathbf{P}^{-1}(t)\mathbf{B}(t) \\ \hline \mathbf{C}(t)\mathbf{P}(t) & \mathbf{D}(t) \end{array} \right] \xrightarrow[\text{transform}]{\tilde{\mathbf{x}}(t)=\mathbf{\Psi}\mathbf{q}(t)} \left[ \begin{array}{c|c} \mathbf{\Lambda} & \mathbf{\Psi}^{-1}\mathbf{P}^{-1}(t)\mathbf{B}(t) \\ \hline \mathbf{C}(t)\mathbf{P}(t)\mathbf{\Psi} & \mathbf{D}(t) \end{array} \right] \quad (2.73)$$

where  $\mathbf{\Lambda}$  are the eigenvalues of  $\mathbf{Q}$  (Floquet exponents) and  $\mathbf{\Psi}$  the associated eigenvectors. The columns of  $\mathbf{P}(t)\mathbf{\Psi}$  can be interpreted as periodic mode shapes of the system and are therefore often called *Floquet eigenvectors*. Since the state matrix of the transformed systems (2.72) and (2.73) is constant, the stability criterion for LTP and LTI systems is the same:

**Theorem** (Stability of periodic systems). *A linear periodic system is stable if and only if the real part of all eigenvalues  $\lambda$  of the transformed state matrix  $\mathbf{Q}$  (Floquet exponents) is non-negative  $\Re\lambda < 0$ . Equivalently: if and only if the all eigenvalues  $\mu$  of the monodromy matrix  $\mathbf{\Phi}(T, 0)$  (Floquet multipliers) lie within the unit circle  $|\mu| < 1$ .*

The (instantaneous) eigenvalues of the state matrix do not determine system stability (as a matter of fact it is possible for periodic systems to be globally stable while crossing local instability regions and vice versa (see figure 2.11 for such an example). A significant difference from the time-invariant case is the existence of bifurcation points where the system's dynamic behavior varies abruptly as a function of period. These can be observed as sudden changes in the Floquet exponents' path (see for example figure 2.12). The stability analysis of rotating systems is conducted by varying rotation speeds and identifying the regions where the Floquet exponents have positive real parts [ALLEN ET AL., 2011]. More about stability criteria can be found in [RICHARDS, 1983].

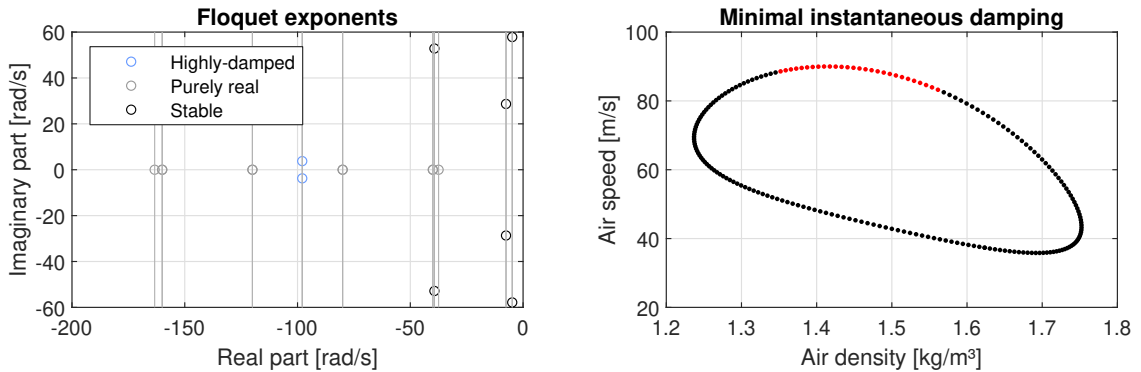


FIGURE 2.11: Floquet exponents of a periodic aeroelastic system (parameters: air density and air speed). The red dots indicate where the minimal damping of the instantaneous eigenvalues becomes negative. Floquet analysis reveals that the system is globally stable because it dissipates more energy than it acquires in one cycle. However, the vibration amplitude in the red region can quickly exceed unacceptable levels.

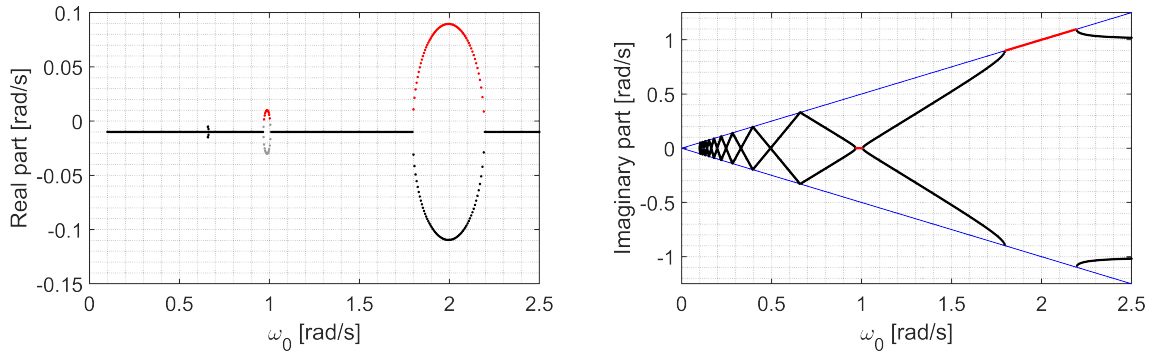


FIGURE 2.12: Floquet exponents of a time-varying harmonic oscillator  $\ddot{x}(t) + 0.02\dot{x}(t) + x(t) + 0.4\cos(\omega_0 t)x(t) = 0$  as a function of  $\omega_0$ . The instantaneous eigenvalues  $\lambda(t) = -0.01 \pm i\sqrt{0.01^2 + 1 + 0.4\cos\omega_0 t}$  have always negative real parts irrespective of  $\omega_0$ . However, Floquet analysis reveals that the system has unstable exponents (red dots) for some intervals of  $\omega_0$  and that there are several bifurcations. The gray dots around  $\omega_0 = 1$  rad/s denote purely real eigenvalues. The blue lines in the right plot are  $\Im\lambda = \pm\omega_0/2$ .

Figure 2.13 shows the state transition matrix and its FFT for various periods  $T$  arranged in three regimes. The qualitative influence of “short” and “long” periods can be observed in both time and frequency domains. What is denoted as “intermediate” period is characterized by abrupt dynamic behavior changes. As is clear from the plot, the STM in time-domain reveals little and the interpretation of the underlying dynamics would benefit from an analytical frequency-domain representation of the state transition matrix. Fortunately, this is possible for periodic systems, as we shall see in the coming sections.

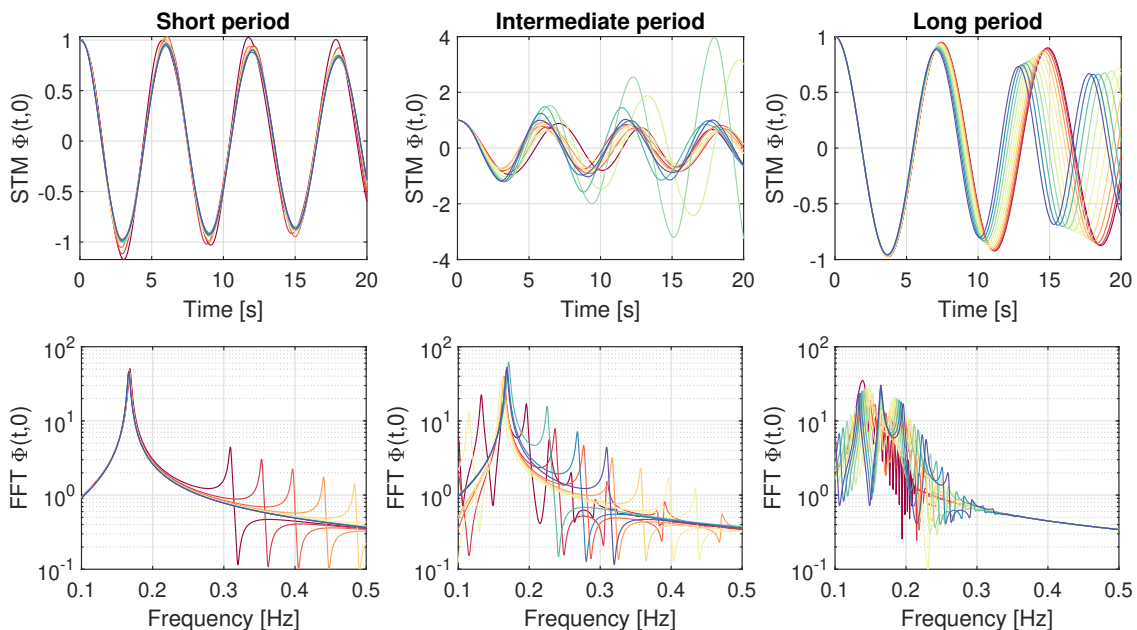


FIGURE 2.13: The system’s period  $T = 2\pi/\omega_0$  has a marked influence on the state transition matrix (in each subplot: red - high, blue - low). The same system as in figure 2.12 is displayed. The frequency-domain representation of the STM can provide some key insight.

### 2.3.3 Impulse response of periodic systems

The solution of periodic systems is obtained easily by applying Floquet's theorem (2.63) to obtain the transformed system with constant state matrix (2.72):

$$\begin{aligned}\mathbf{x}(t) &= e^{\mathbf{Q}(t-t_0)}\mathbf{x}(t_0) + \int_{t_0}^t e^{\mathbf{Q}(t-\tau)}\mathbf{P}^{-1}(\tau)\mathbf{B}(\tau)\mathbf{u}(\tau) d\tau \\ \mathbf{y}(t) &= \mathbf{C}(t)\mathbf{P}(t)\mathbf{x}(t) + \mathbf{D}(t)\mathbf{u}(t)\end{aligned}\quad (2.74)$$

The impulse response is given by equation (2.23):

$$\mathbf{H}(t, \tau) = \begin{cases} \mathbf{D}(t)\delta(t - \tau) + \mathbf{C}(t)\mathbf{P}(t)e^{\mathbf{Q}(t-\tau)}\mathbf{P}^{-1}(\tau)\mathbf{B}(\tau) & t \geq \tau \\ 0 & t < \tau \end{cases} \quad (2.75)$$

The state equation integral above has a form similar to the general solution of LTI systems (2.49). The main difference is that the input is modulated by the transformed input matrix  $\mathbf{P}^{-1}(t)\mathbf{B}(t)$ , where at least  $\mathbf{P}^{-1}(t)$  is periodic (the output equation adds modulation through  $\mathbf{C}(t)\mathbf{P}(t)$ ). It is clear that this modulation adds additional frequency components apart from those present in the input signal<sup>7</sup> (see figure 2.4).

Let  $\mathbf{f}(t) \triangleq \mathbf{P}^{-1}(t)\mathbf{B}(t)\mathbf{u}(t)$  be the forcing function of the system and assume that it can be expressed by a Fourier series with fundamental harmonic  $\omega_0 = 2\pi/T$ :

$$\mathbf{f}(t) \triangleq \mathbf{P}^{-1}(t)\mathbf{B}(t)\mathbf{u}(t) = \sum_{k \in \mathbb{Z}} e^{ik\omega_0 t} \mathbf{f}_k \quad (2.76)$$

so that the convolution integral in the state equation (2.74) can be written as:

$$\int_0^t e^{\mathbf{Q}(t-\tau)}\mathbf{f}(\tau) d\tau = \sum_{k \in \mathbb{Z}} \int_0^t e^{\mathbf{Q}t} e^{(ik\omega_0 \mathbf{I} - \mathbf{Q})\tau} \mathbf{f}_k d\tau = \sum_{k \in \mathbb{Z}} \left[ (ik\omega_0 - \mathbf{Q})^{-1} e^{\mathbf{Q}t} e^{(ik\omega_0 \mathbf{I} - \mathbf{Q})\tau} \mathbf{f}_k \right]_{\tau=0}^{\tau=t} \quad (2.77)$$

The exact solution in the time-domain is then:

$$\mathbf{x}(t) = e^{\mathbf{Q}t}\mathbf{x}(0) - \sum_{k \in \mathbb{Z}} e^{\mathbf{Q}t} \mathbf{x}_k + \sum_{k \in \mathbb{Z}} e^{ik\omega_0 t} \mathbf{x}_k \quad (2.78)$$

where  $\mathbf{x}_k \triangleq (ik\omega_0 \mathbf{I} - \mathbf{Q})^{-1} \mathbf{f}_k$ . The first addend is the homogeneous solution, the second is the transient response due to the excitation and the third is the forced response. The system response  $\mathbf{y}(t)$  is thus the sum of a transient and a steady-state response:

$$\mathbf{y}(t) = \mathbf{C}(t)\mathbf{P}(t)e^{\mathbf{Q}t} \left( \mathbf{x}(0) - \sum_{k \in \mathbb{Z}} \mathbf{x}_k \right) + \mathbf{D}(t)\mathbf{u}(t) + \mathbf{C}(t)\mathbf{P}(t) \sum_{k \in \mathbb{Z}} e^{ik\omega_0 t} \mathbf{x}_k \quad (2.79)$$

The series expansion (2.76) has in general an infinite number of terms, but a subset of just  $N$  harmonics and coefficients  $\{\omega_k, \mathbf{f}_k\}$  can be taken into account. The state equation can

<sup>7</sup> For example, if  $\mathbf{P}^{-1}(t)\mathbf{B}(t) = \sin(t)$  and  $\mathbf{u}(t) = 2 \sin 2t$ , then  $\mathbf{P}^{-1}(t)\mathbf{B}(t)\mathbf{u}(t) = \cos t - \cos 3t$



be then vectorized<sup>8</sup> as [JELIČIĆ ET AL., 2021]:

$$\mathbf{x}(t) = e^{\mathbf{Q}t} \mathbf{x}'_0 + \mathbf{F} e^{i\omega_0 t} \quad (2.81)$$

where  $\mathbf{x}_k \triangleq (i\omega_k \mathbf{I} - \mathbf{Q})^{-1} \mathbf{f}_k$  as before,  $\mathbf{x}'_0 \triangleq \mathbf{x}(0) - \sum \mathbf{x}_k$  are the augmented initial conditions,  $\mathbf{F} \triangleq [\mathbf{x}_1 \ \mathbf{x}_2 \ \cdots \ \mathbf{x}_N]$  and  $\omega_0 \triangleq \{\omega_1, \omega_2, \cdots, \omega_N\}$  are auxiliary variables. The eigendecomposition of the constant state matrix  $\mathbf{Q} = \mathbf{\Psi} \mathbf{\Lambda} \mathbf{\Psi}^{-1}$  leads to a computationally efficient formulation of equation (2.81)

$$\mathbf{x}(t) = e^{\mathbf{\Lambda}t} \mathbf{x}'_0 + \mathbf{F} e^{i\omega_0 t} \quad (2.82)$$

where  $\mathbf{x}_k \triangleq (i\omega_k \mathbf{I} - \mathbf{\Lambda})^{-1} \mathbf{\Psi}^{-1} \mathbf{f}_k$  and  $\mathbf{x}'_0 \triangleq \mathbf{\Psi}^{-1} \mathbf{x}(0) - \sum \mathbf{x}_k$ . This formulation has the advantage of performing scalar divisions and exponentiation of the state matrix instead of the corresponding matrix operations. This is the preferred method for the simulation of LTP systems instead of direct numerical integration.

### 2.3.4 Frequency-domain description of periodic systems

The frequency-domain representation of the impulse response of periodic systems cannot be interpreted as a “transfer function” as it has been defined in the time-invariant case because it does not describe a one-to-one correspondence between the input’s and output’s frequency content. However, the so-called *harmonic transfer function* (HTF) can be defined as the analogous to the transfer function of time-invariant systems using the harmonic balance method. We follow [WERELEY AND HALL, 1990] in the subsequent derivations.

Let us consider the Floquet-Lyapunov coordinated change (2.73) (repeated here)

$$\mathcal{S} = [\mathbf{Q}, \mathbf{P}^{-1}(t)\mathbf{B}(t), \mathbf{C}(t)\mathbf{P}(t), \mathbf{D}(t)] \quad (2.83)$$

and assume that the system’s time-dependent state, input and output vectors and system matrices can be expressed as complex Fourier series:

$$\mathbf{v}(t) = \sum_{k \in \mathbb{Z}} \mathbf{v}_k e^{ik\omega_0 t} \quad \mathbf{M}(t) = \sum_{k \in \mathbb{Z}} \mathbf{M}_k e^{ik\omega_0 t} \quad (2.84)$$

where  $\mathbf{v}(t)$  and  $\mathbf{M}(t)$  are a placeholder vector and matrix respectively.

The infinite harmonics vector is defined as

$$[\mathbf{v}] \triangleq \{\cdots \mathbf{v}_{-2}, \mathbf{v}_{-1}, \mathbf{v}_0, \mathbf{v}_1, \mathbf{v}_2 \cdots\} \quad (2.85)$$

---

<sup>8</sup> The approach employed to find the solution to the state equation can be given even more generality by considering a forcing function that is a combination of polynomial and exponential terms (i.e. poles with multiplicity):

$$\mathbf{f}(t) \triangleq \mathbf{P}^{-1}(t)\mathbf{B}(t)\mathbf{u}(t) = \sum_{k \in \mathbb{S}} t^{p_k} e^{s_k t} \mathbf{f}_k \quad \circ \bullet \quad \mathbf{f}(s) = \sum_{k \in \mathbb{S}} \frac{p_k!}{(s - s_k)^{p_k+1}} \mathbf{f}_k \quad (2.80)$$

where  $p_k$  are polynomial orders and  $s_k$  complex frequencies.

The series terms  $\mathbf{M}_k$  are likewise arranged into a doubly-infinite block-Toeplitz matrix where  $n \in \mathbb{Z}$  and  $m \in \mathbb{Z}$  are respectively the indices of the rows and columns:

$$[\mathbf{M}]_{nm} = \mathbf{M}_{n-m} \implies [\mathbf{M}] \triangleq \begin{bmatrix} \ddots & \vdots & \vdots & \vdots & \ddots \\ \cdots & \mathbf{M}_0 & \mathbf{M}_{-1} & \mathbf{M}_{-2} & \cdots \\ \cdots & \mathbf{M}_1 & \mathbf{M}_0 & \mathbf{M}_{-1} & \cdots \\ \cdots & \mathbf{M}_2 & \mathbf{M}_1 & \mathbf{M}_0 & \cdots \\ \ddots & \vdots & \vdots & \vdots & \ddots \end{bmatrix} \quad (2.86)$$

The state, input and output vectors of system (2.83) are arranged according to equation (2.85). The same is performed with the series terms of the state, input, output and feedthrough matrices as shown in equation (2.86). Furthermore, the diagonal entries of the block-Toeplitz state matrix are defined as  $[\mathbf{A}]_{kk} \triangleq \mathbf{Q} - ik\omega_0\mathbf{I}$  (Hill matrix). The algebra and properties of infinite Toeplitz matrices are explained in [WERELEY, 1991]. In practice, the block-Toeplitz matrices are limited in size by the number of terms of the Fourier series; the truncation can be performed based on the desired fidelity. This leads to a state-space representation of the LTP system [WERELEY AND HALL, 1990]

$$\begin{aligned} s[\mathbf{x}] &= [\mathbf{A}][\mathbf{x}] + [\mathbf{B}][\mathbf{u}] \\ [\mathbf{y}] &= [\mathbf{C}][\mathbf{x}] + [\mathbf{D}][\mathbf{u}] \end{aligned} \quad (2.87)$$

The input-output relationship is thus

$$[\mathbf{y}] = [\mathbf{H}(s)][\mathbf{u}] \quad [\mathbf{H}(s)] \triangleq [\mathbf{D}] + [\mathbf{C}](s[\mathbf{I}] - [\mathbf{A}])^{-1}[\mathbf{B}] \quad (2.88)$$

where  $[\mathbf{H}(s)]$  is the harmonic transfer function in analogy to the transfer function of time-invariant systems (2.51). Among its applications are system identification and controller design [TCHERNIAK AND ALLEN, 2015; UYANIK ET AL., 2015].

It is possible to use another approach to derive the system's response in frequency-domain. From Floquet's theorem:

$$\Phi(t, t_0) = \mathbf{P}(t)e^{\mathbf{Q}(t-t_0)}\mathbf{P}^{-1}(t_0) = \mathbf{P}(t)\Psi e^{\mathbf{A}(t-t_0)}\Psi^{-1}\mathbf{P}^{-1}(t_0) \quad (2.89)$$

the STM can be reformulated as a sum:

$$\Phi(t, t_0) = \sum_{j=1}^{N_x} \mathbf{R}_j(t, t_0)e^{\lambda_j(t-t_0)} \quad \mathbf{R}_j(t, t_0) \triangleq (\mathbf{P}(t)\Psi \mathbf{e}_j)(\mathbf{e}_j^T \Psi^{-1}\mathbf{P}^{-1}(t_0)) \quad (2.90)$$

where the residue  $\mathbf{R}_j(t, t_0) \in \mathbb{C}^{N_x \times N_x}$  associated to the  $j$ -th Floquet exponent  $\lambda_j$  is equal to the outer product of the  $j$ -th column of  $\mathbf{P}(t)\Psi$  and the  $j$ -th row of  $\Psi^{-1}\mathbf{P}^{-1}(t_0)$  (rank-1 matrices). This step is the same as has been done in equation (2.56) to transform the transfer function of an LTI system. The residues  $\mathbf{R}_j(t, t_0)$  are continuous and periodic because the transformation matrix  $\mathbf{P}(t)$  is continuous and periodic, therefore they have an

absolutely convergent Fourier series with terms  $\mathbf{R}_{j,k}$  and fundamental harmonic  $\omega_0 = 2\pi/T$ :

$$\mathbf{R}_j(t, t_0) = \sum_{k \in \mathbb{Z}} \mathbf{R}_{j,k} e^{ik\omega_0(t-t_0)} \quad \forall j = 1: N_x \quad (2.91)$$

We can put this expression into the STM series, set  $t_0 = 0$  and transform immediately into Laplace-domain:

$$\Phi(t, 0) = \sum_{j=1}^{N_x} \sum_{k \in \mathbb{Z}} \mathbf{R}_{j,k} e^{(\lambda_j + ik\omega_0)t} \quad \circ \bullet \quad \Phi(s, 0) = \sum_{j=1}^{N_x} \sum_{k \in \mathbb{Z}} \frac{\mathbf{R}_{j,k}}{s - \lambda_j - ik\omega_0} \quad (2.92)$$

Let  $p_{j,k} \triangleq \lambda_j + ik\omega_0$  be the pole associated to the  $j$ -th Floquet exponent and the  $k$ -th harmonic. For each index  $j$ , the corresponding poles all lie along a vertical line in the complex plane (respectively, on the hyperbolae  $\zeta = -\Re p_{j,k}/\omega_n$  in an eigenfrequency-damping plot), which implies that their real part does not change  $\Re\{p_{j,k}\} = \Re\{\lambda_j + ik\omega_0\} = \Re\{\lambda_j\}$  (respectively, the product  $\zeta\omega_n = -\Re p_{j,k}$  is constant). The eigendecomposition of  $\mathbf{Q}$  places the imaginary part of the Floquet exponents within the strip  $\Im \lambda_j \in [-\omega_0/2, \omega_0/2]$  in the complex plane. Some combinations of  $j$  and  $k$  result in pole-residue pairs  $\{p_{j,k}, \mathbf{R}_{j,k}\}$  that have more physical significance than other (for example correspond to a prominent resonance peak). Indeed only a subset of all eigenpairs  $\mathbb{S} \subset \{p_{j,k}, \mathbf{R}_{j,k}\}$  has a noteworthy contribution in the series expansion of the state transition matrix. Since the STM is real, we may consider only one pole from each complex-conjugated pair. With this in mind we can write the STM elegantly as:

$$\Phi(t, 0) \approx \sum_{n \in \mathbb{S}} \mathbf{R}_n e^{p_n t} \quad \circ \bullet \quad \Phi(s, 0) \approx \sum_{n \in \mathbb{S}} \frac{\mathbf{R}_n}{s - p_n} \quad (2.93)$$

where the index  $n$  now enumerates the elements of  $\mathbb{S} = \{p_n, \mathbf{R}_n\}$ . Assuming that the input  $\mathbf{B}(t)$  and output matrices  $\mathbf{C}(t)$  are periodic, the same reasoning can be applied to the impulse response function to obtain:

$$\mathbf{H}(s, t_0) = \mathbf{D}(t_0) + \sum_{j=1}^{N_x} \sum_{k \in \mathbb{Z}} \frac{\mathbf{c}_{j,k} \mathbf{b}_{j,k}^T}{s - p_{j,k}} \approx \mathbf{D}(t_0) + \sum_{n \in \mathbb{S}} \frac{\mathbf{c}_n \mathbf{b}_n^T}{s - p_n} \quad (2.94)$$

where  $n \in \mathbb{S}$  is again the index of most significant terms of the Fourier series of  $\mathbf{c}_j \triangleq \mathbf{C}(t)\mathbf{P}(t)\Psi\mathbf{e}_j$  and  $\mathbf{b}_j \triangleq \mathbf{e}_j^T \Psi^{-1} \mathbf{P}^{-1}(t_0)\mathbf{B}(t_0)$ . A subset of  $ik\omega_0$  harmonics of a Fourier series can be selected according to some criterion, for example:

- *frequency*: keep a certain number of negative and positive frequency bins around the greatest harmonic plus the DC bin (e.g. the first 10% of harmonics).
- *amplitude*: excluding DC, ignore harmonics whose amplitude is below a certain threshold (e.g. below 1% compared to the largest amplitude).
- *energy*: keep the desired fraction of the system's total energy plus the DC bin (e.g. keep 99% of the energy).

The harmonics selection can be performed independently for each matrix entry. The selection of the most significant terms of the series expansions of the state transition matrix or of the impulse response function amounts to model order reduction. Given the similarity between the pole-residue structures of equation (2.94) for LTP systems and equation (2.56) for LTI systems, some established model order reduction techniques can be adapted, e.g. modal truncation; reference [BENNER ET AL., 2015] provides a survey of this topic. It is normally possible to obtain an accurate approximation of the system by considering just a few harmonics [ALLEN ET AL., 2011; WERELEY, 1991].

Figure 2.14 illustrates the reduced modal decomposition of the state transition according to (2.93) and compares it with the exact solution. Figure 2.15 shows the chosen poles among the possible combinations of Floquet exponents  $\lambda_j$  and harmonics  $ik\omega_0$  and the magnitude of the associated residuals.

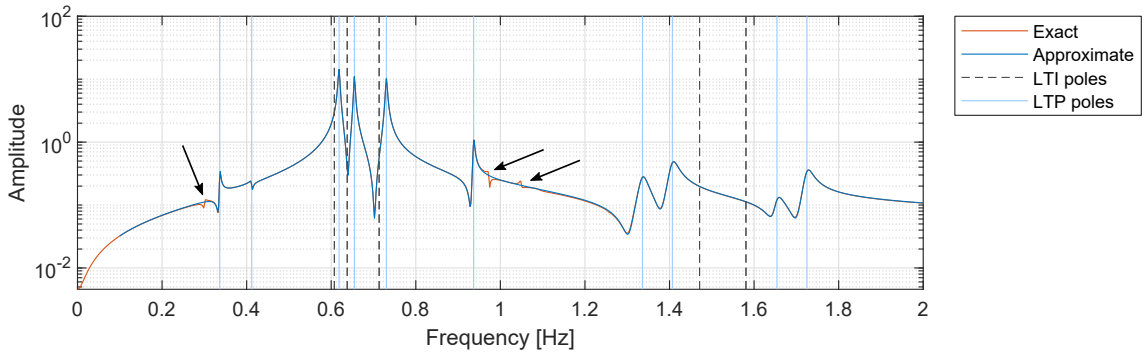


FIGURE 2.14: Exact and approximate frequency-domain representation of the state transition matrix. Only the poles that represent 90% of the energy of each entry  $\Phi_{ij}(t, 0)$  are used in the modal decomposition. The arrows denote some of the ignored poles. This approximation is sufficient to characterize most features of the spectrum. The figure displays entry (1,1) of the 5-DoF wind turbine model from [SKJOLDAN AND HANSEN, 2009] with  $\omega_0 = 1$  rad/s.

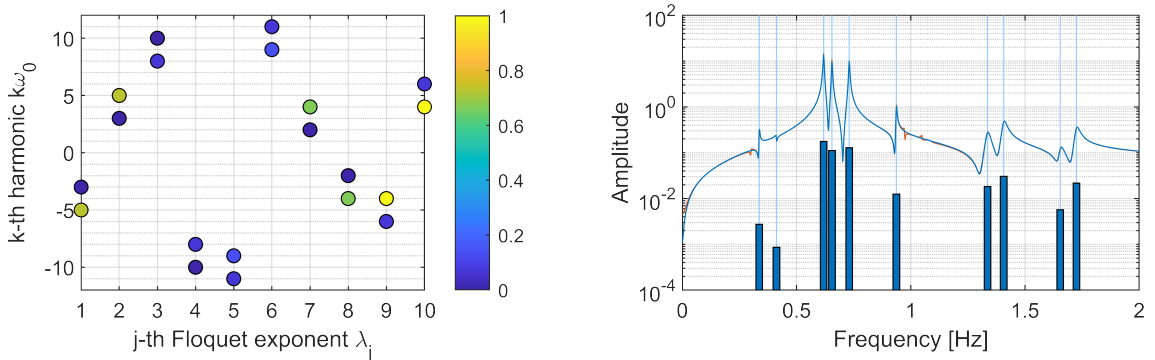


FIGURE 2.15: Same data as in figure 2.14. The grid on left displays the selected poles  $\lambda_j + ik\omega_0$  and the marker color the magnitude of the associated residue. Ten Floquet exponents (five complex-conjugated pairs) are displayed, each with 2 harmonics. One additional harmonic component per Floquet exponent is sufficient for an accurate representation of the system. The bar plot on the right shows the absolute value of the residues corresponding to the displayed poles (vertical lines).

### 2.3.5 On the influence of period

We have noted in section 2.1.7 that one major theoretical difficulty for time-varying systems is the lack of a clearly-defined concept of eigenvalues as for time-invariant and periodic systems. In many applications a time-varying system is assumed to be “slowly-varying”, i.e. the dynamics arising because of parameter variation can be neglected and therefore a frozen-time formulation can be applied to model the system and to understand its behavior. This is often a necessary but completely acceptable simplification in order to render the problem tractable. Many published works in the field utilize this assumption, for example [ERTVELDT ET AL., 2014; HOUTZAGER ET AL., 2012; LATAIRE AND PINTELON, 2010; SPIRIDONAKOS AND FASSOIS, 2009; ZHOU ET AL., 2014]. Period has a marked influence on periodic systems, firstly on their stability, which can be determined by computing Floquet’s exponents. Depending on how fast does the system vary, the state transition matrix assumes different forms (see figures 2.12 and 2.13). As another example, the state transition matrix of a periodic system is illustrated in figure 2.16 for different periods. As  $T$  grows, the spacing  $i\omega_0$  between the dynamic poles diminishes and they cluster beside the location of the LTI poles. Given a Floquet exponent  $\lambda_j$ , the corresponding poles  $\lambda_j + ik\omega_0$  of the STM are each  $i\omega_0$  apart in the complex plane. Depending on the system, the resonance peaks may be heavily deformed by the presence of many close poles with significant residues.

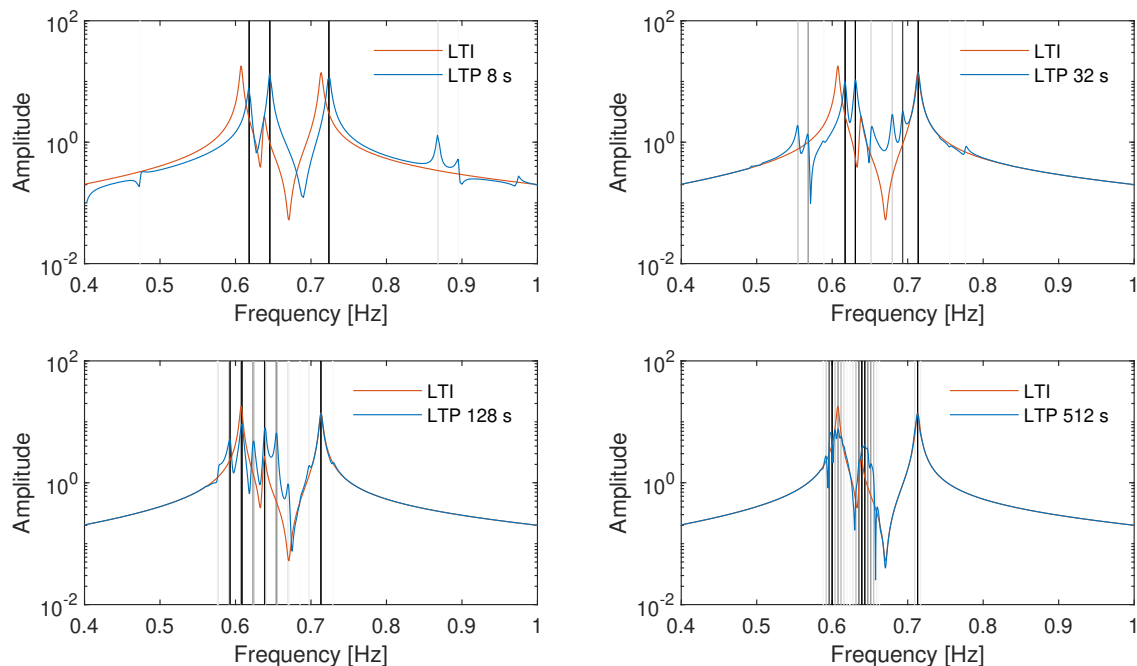


FIGURE 2.16: The state transition matrix in frequency-domain as a function of period compared to the underlying time-invariant system. Each vertical line denotes a pole and its hue the magnitude of the corresponding residue. The figure displays a detail of STM entry (1,1) of a 5-DoF wind turbine model from [SKJOLDAN AND HANSEN, 2009] for  $T = [8, 32, 128, 512]$  s ( $\omega_0 = [0.785, 0.196, 0.0491, 0.0123]$  rad/s). In this frequency range, the system has three very lightly-damped LTI poles with  $\zeta\omega_n = [0.0109, 0.0106, 0.0125]$  rad/s. The third pole is quite insensitive to time variation.

Let us consider the damped harmonic oscillator undergoing a periodic variation:

$$\ddot{x}(t) + 2\zeta\omega_n\dot{x}(t) + \omega_n^2(1 + r_a^2 \sin(r_f\omega_n t))x(t) = 0 \quad (2.95)$$

where  $\zeta$  and  $\omega_n$  are respectively the damping ratio<sup>9</sup> and eigenfrequency of the underlying LTI system and the dimensionless quantities  $r_a$  and  $r_f$  are respectively the amplitude and frequency ratios of the parameter variation ( $\omega_0 = r_f\omega_n$ ). When  $r_a = 0$  or  $r_f = 0$  the system is time-invariant and has eigenfrequency  $\omega_n$ . We can use the system's eigenfrequencies to define a scale for what is “slow” or “fast”. Essentially three regimes appear:

- *slowly-varying system*  $\omega_0 \ll \zeta\omega_n$ : a frozen-time representation is an accurate description of the system's dynamics. This may be valid even for large variations of a parameter, depending on the system's sensitivity.
- *intermediate variation rate*  $\omega_0 \approx \zeta\omega_n$ : dynamic poles slowly emerge in close proximity to the “main” resonance peak and deform severely its shape.
- *fast system variation*  $\omega_0 \gg \omega_n$ : dynamic poles move away from the main peak and become clearly separated.

As  $\omega_0$  increases further, the system varies so quickly that it appears to be insensitive to parameter variation and the main peak is approximately at the location of the corresponding time-invariant case. The system's impulse response is displayed in a time-frequency plot for different  $r_f$  frequency ratios in figure 2.17. Each subplot is built by calculating  $\mathbf{H}(i\omega, t)$  at multiple instants within one period  $t \in [0, T]$ . The frequency axis is normalized by the eigenfrequency  $\omega/\omega_n$ ; likewise the time axis is normalized by the period  $t/T$ . When the system is slowly-varying, the location of the main resonance peak is described well by the instantaneous value of the eigenfrequency. When the rate of variation is intermediate, side lobes appear and grow in magnitude until they become overwhelming. Their prominence increases if the damping ratio  $\zeta$  decreases. Eventually the system varies so quickly, that

<sup>9</sup> Equation (2.95) is similar to the Mathieu equation  $\ddot{x}(t) + (a - 2q \cos(2t))x(t) = 0$  [RICHARDS, 1983]. This expression is widely studied in literature, particularly with regard to the stability region as a function of the parameters  $a$  and  $q$ .

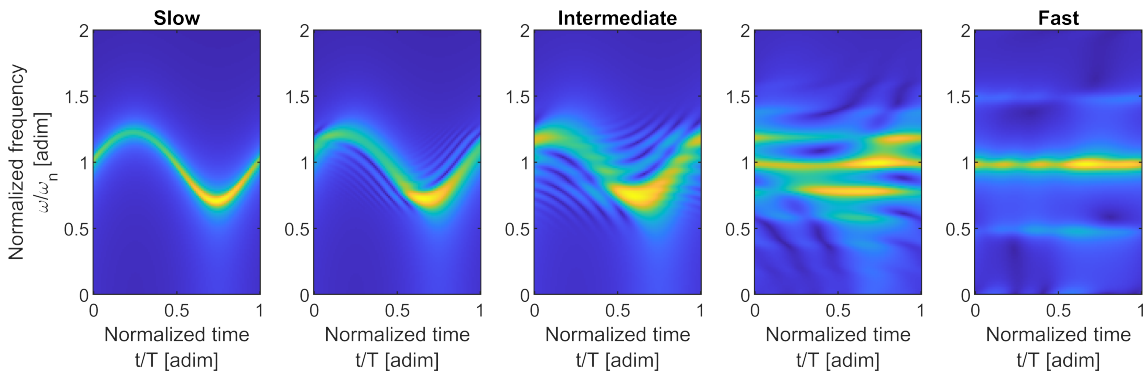


FIGURE 2.17: Magnitude of the time-varying impulse response of system (2.95), where  $\omega_n = 1$  rad/s,  $\zeta = 0.04$ ,  $r_f = [0.002, 0.02, 0.05, 0.2, 0.5]$  and  $r_a = 1/\sqrt{2}$ . The system varies slowly on the left and varies quickly on the right. See text for discussion.

the main resonance peak appears fixed at its time-invariant location, accompanied by dynamic poles at approximately  $\omega/\omega_n = 1 \pm r_f$ . Different regimes can be observed for the combinations of low, middle and high variation amplitudes  $r_a$  and for slow, intermediate and fast variation rates  $r_f$ . Figure 2.19 displays again the time-varying impulse response of system (2.95) in a grid of three different variation amplitude and frequency ratios  $r_a$  and  $r_f$ . When the system is slowly-varying, the frozen-time description is accurate even with large  $r_a$ , whereby the frozen-time eigenfrequency is  $\omega_n(t) = \omega_n \sqrt{1 + r_a^2 \sin(r_f \omega_n t)}$ . In this case the instantaneous eigenvalues still have significance. When the system varies quickly, the main resonance peak is at the mean location of the instantaneous eigenfrequency  $\frac{1}{T} \int_0^T \omega_n \sqrt{1 + r_a^2 \sin(r_f \omega_n t)} dt$  (even for high  $r_a$ ). The most dynamically complex case arises when the side lobes become significant, typically with moderate variation rates, even for low amplitude ratios  $r_a$ . In this regime it is not possible to predict the system's dynamics in a simple way.

The information contained in the last two figures can be condensed by evaluating the amplitude of the impulse response in frequency-domain  $\mathbf{H}(i\omega_n, 0)$  at the time-invariant eigenfrequency  $\omega_n$  in order to compare it with the corresponding time-invariant values  $\mathbf{H}(i\omega_n)$ . The result is pictured in figure 2.18. We can see that there is a large region where the system is insensitive to parameter variation  $\mathbf{H}(i\omega_n, 0)/\mathbf{H}(i\omega_n) > 0.9$  (the LTV spectrum at  $\omega_n$  and the LTI resonance peak have the same height). Time-varying effects due to large amplitude ratios  $r_a$  can be mitigated by increasing the frequency ratio  $r_f$ . The same happens when  $r_f$  is very low (less noticeable in the plot because the resonance peak shifts while maintaining essentially the same magnitude).

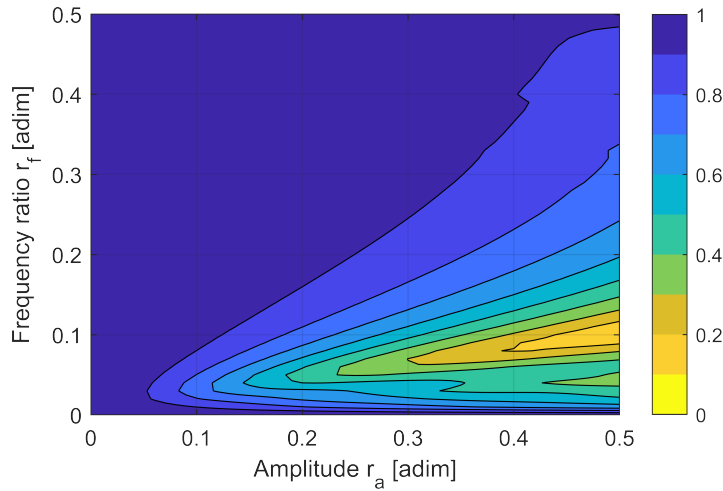


FIGURE 2.18: Amplitude ratio between the LTV and LTI impulse responses  $\mathbf{H}(i\omega_n, 0)/\mathbf{H}(i\omega_n)$  of a time-varying damped harmonic oscillator (2.95) evaluated at the location of the frozen-time eigenfrequency  $\omega_n$ .

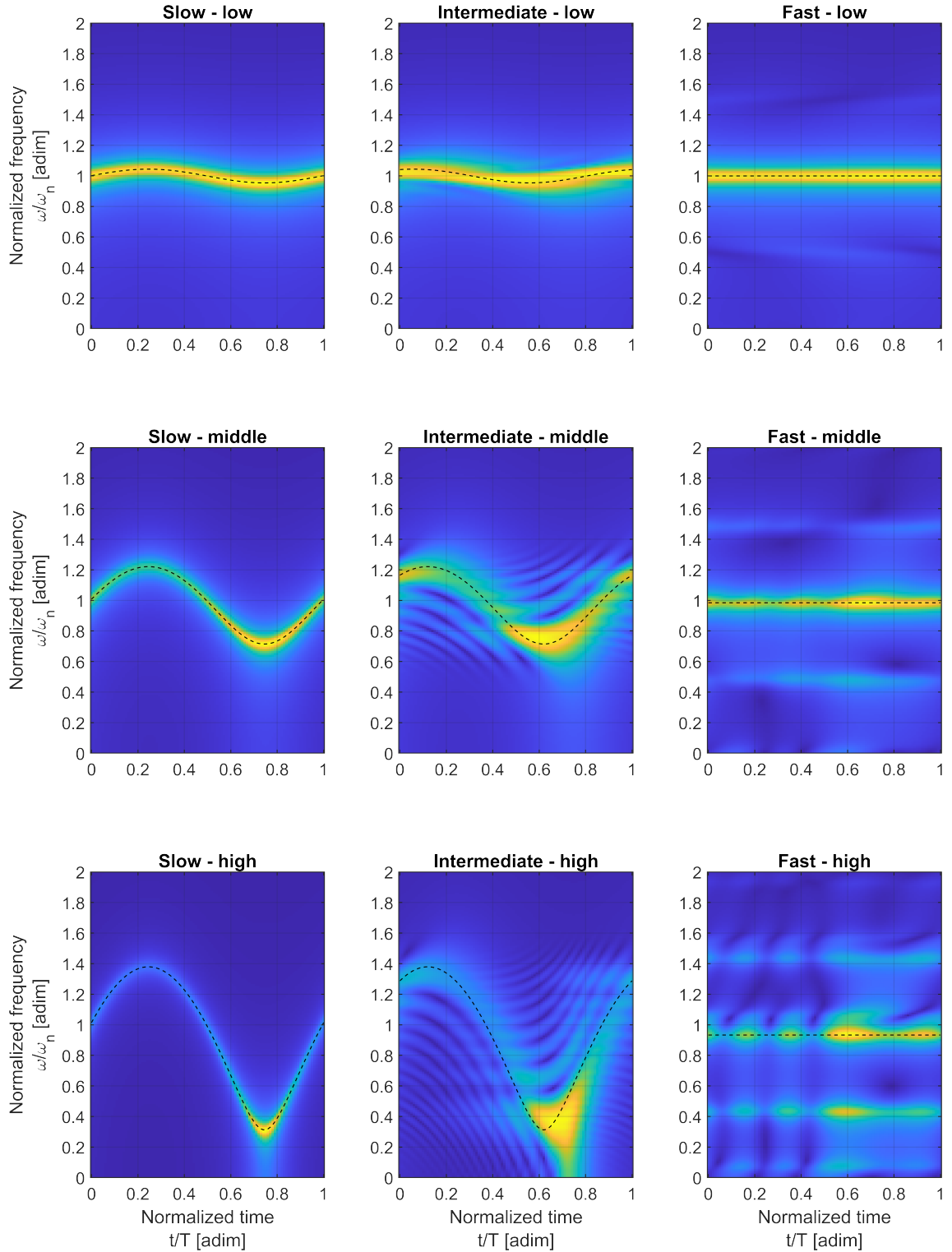


FIGURE 2.19: Magnitude of the time-varying impulse response of a damped harmonic oscillator undergoing a sinusoidal stiffness variation (2.95), where  $\zeta = 0.04$ ,  $\omega_n = 1$  rad/s,  $r_a = [0.3, 0.7, 0.95]$  (low-middle-high) and  $r_f = [0.001, 0.05, 0.5]$  (slow-intermediate-fast). The dashed line is the predicted location of the main peak. The eigenfrequency variation is constant in each row, the period is constant in each column. See text for discussion.



### 2.3.6 Windowed spectra

The state transition matrix in frequency-domain has been expressed as a weighted sum of poles in equation (2.93), therefore it is fairly simple to calculate its windowed spectra. This idea can be developed further into an analytical (parametric) formulation that is able to determine the frequency content of time-varying systems that are not necessarily periodic, but have a periodic representation in a limited domain. Consider the rectangular window  $\Pi(t/T - 1/2)$ . The Fourier transform of a pole  $e^{p_n t}$  in the interval  $[0, T]$  is:

$$\begin{aligned} \mathcal{F} \left\{ \Pi \left( \frac{t}{T} - \frac{1}{2} \right) e^{p_n t} \right\} &= \int_0^T e^{p_n t} e^{-i\omega t} dt \\ &= \frac{1 - e^{-(i\omega - p_n)T}}{i\omega - p_n} \\ &= T \exp \left( -\frac{i\omega - p_n}{2/T} \right) \operatorname{sinc} \left( -i \frac{i\omega - p_n}{2/T} \right) \end{aligned} \quad (2.96)$$

where “sinc” is the unnormalized sinc function  $\frac{\sin x}{x}$ . With this result in mind, the Fourier transform of the state transition matrix (2.93) limited to  $[0, T]$  is:

$$\mathcal{F} \left\{ \Pi \left( \frac{t}{T} - \frac{1}{2} \right) \Phi(t, 0) \right\} = \int_0^T \Phi(t, 0) e^{-i\omega t} dt = \sum_{n \in \mathbb{S}} \frac{\mathbf{R}_n}{i\omega - p_n} \left( 1 - e^{-(i\omega - p_n)T} \right) \quad (2.97)$$

The exponential term  $e^{-(i\omega - p_n)T}$  introduces an amplitude variation in the spectrum of each pole  $p_n$  with peak-to-peak height<sup>10</sup>  $\Delta = \exp(\Re\{p_n\}T)$  and wavelength (in the frequency axis)  $1/T$ . It is then clear that  $\lim_{T \rightarrow \infty} \Delta = 0$  for stable poles. Figure 2.20 compares the FFT of the state transition matrix over a limited time interval with the analytical frequency-domain representation over the same interval calculated with equation (2.97).

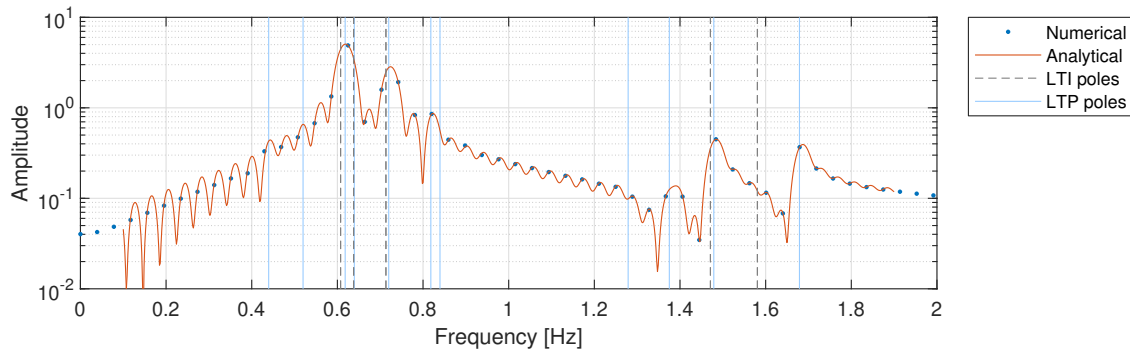
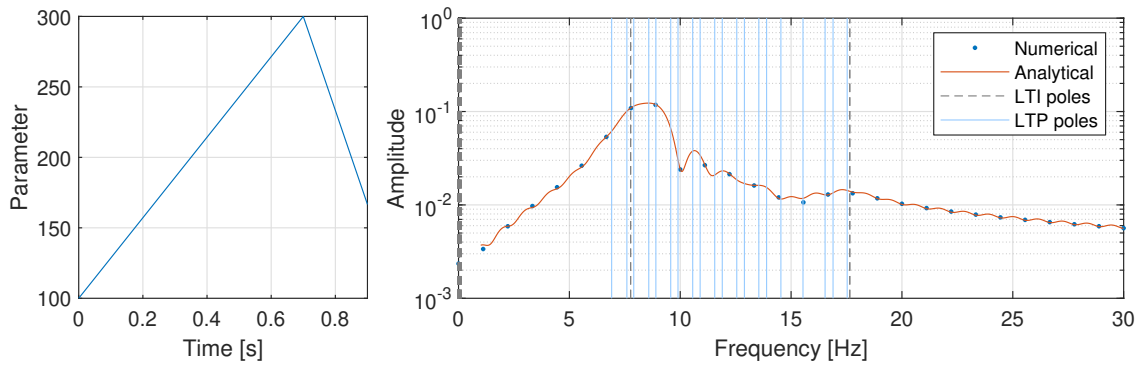


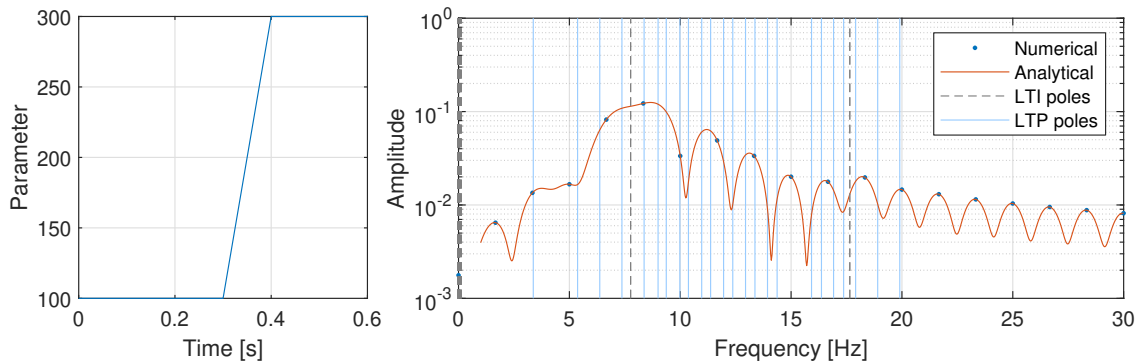
FIGURE 2.20: Spectrum of the state transition matrix varying from 0 to  $2.56T$ . The numerical result is the FFT of the STM with zero-padding. The analytical solution is the windowed modal decomposition of the STM. Only the poles representing 90% of the energy are used in the modal decomposition. The figure displays the STM entry (1,1) of the 5-DoF wind turbine model from [SKJOLDAN AND HANSEN, 2009] with  $T = 10$  s.

<sup>10</sup> For example, if we wish to reduce the effect of the finite window length to below  $\Delta = 5\%$ , the duration should be  $T > \ln \Delta / \Re\{p_k\}$ . For a pole with 2% damping this corresponds to  $\ln(0.05) / (-0.02 \cdot 2\pi) = 23.84$  periods.

The spectrum of a time-varying system with at least a piece-wise periodic parameter representation can be computed by windowing and shifting in time-domain (respectively by convolving with the sinc function and multiplying by the complex exponential in frequency-domain). Figure 2.21 illustrates a rapidly linearly-varying system for which only a tiny amount of time data can be acquired before the variation ends and compares the numerical (nonparametric) and analytical (parametric) solutions. The former is obtained by solving the differential equation of motion directly and calculating its FFT from the available data. The latter is calculated analytically with the pole-residue form of the state transition matrix (2.97). The continuous curve that represents the analytical spectrum could be obtained by zero-padding the FFT, however this produces no information about poles. We can see that many dynamic poles arise from the time variation, however only few are important.



(A) Piece-wise linear parameter variation



(B) Step parameter variation

FIGURE 2.21: Frequency-domain solution of a parameter-varying aeroelastic system that undergoes piece-wise linear parameter variations over a very short time (see chapter 7). The system is decomposed using a periodic representation of the actual parameter variation. Two time-invariant poles lie in the range [5, 20] Hz. The nonparametric solution is obtained by direct numerical integration and FFT interpolation (zero-padding), the parametric solution is given by a periodic representation and Floquet decomposition. The shorter the duration, the further apart are the FFT bins on the frequency axis (the lower the resolution). Numerous additional poles arise due to the parameter variation, but only few have large associated residues.

## 2.4 Numerical methods for time-varying systems

When the state matrix commutes, the state transition matrix has an exponential form according to theorem (2.1.3) and can be often computed analytically. An analytical formulation is possible in simple cases with the Peano-Baker series (2.14) or Magnus expansion (2.15) formulae. However, in the majority of practical cases, there is no other choice but to resort to numerical techniques. Following the argumentation from the previous section, we can decompose a periodic representation of a time-varying system. If we are interested in stability, it is sufficient to compute the Floquet exponents from the monodromy matrix. If we need the pole-residue form of the state transition matrix, then the Floquet eigenvectors must be computed as well. Floquet analysis is commonly applied to rotating machinery or electrical circuits. Several numerical techniques are available in literature, but their application to time-varying aeroelastic systems appears to be novel or at least not mature as those used in other fields. Specifically, aeroelastic systems such as wings are characterized by the large aerodynamic damping acting on the lowest eigenmodes and by the long time scale of parameter variation in comparison to the system's eigenfrequencies. This leads to some demanding aspects that need to be addressed: in the quest for the optimal numerical recipe, the following techniques have been explored:

1. Time-discretization of the system
2. Direct numerical integration of an initial value problem
3. Solution of a boundary value problem
4. Harmonic balance method
5. System identification applied to LTP systems

Although mathematically equivalent, in practice there is usually a preferred approach for a given system size, stability and parameter variation. Methods 1 and 2 and 5 can be applied directly to any LTV systems, while methods 3 and 4 are specific to the LTP case. The computation time and numerical conditioning of each are important concerns.

Since the state matrix is by assumption periodic and continuous, it has an absolutely convergent Fourier series that can be truncated to the desired accuracy: this Fourier series is the “reference” state matrix for all numerical calculations.

$$\mathbf{A}(t) = \sum_{k=-\infty}^{+\infty} \mathbf{A}_k e^{ik\omega_0 t} \approx \sum_{k=-N_k}^{+N_k} \mathbf{A}_k e^{ik\omega_0 t} \triangleq \mathbf{A}_{ref}(t) \quad (2.98)$$

The Fourier series representation is used in order to relate the amplitude and rate of change of the state matrix with the system response. Furthermore, it is easy to represent and manipulate without a symbolic computing environment. The *Jacobi-Liouville equation* relates directly the characteristic exponents with the trace of the state matrix :

$$\int_0^T \text{tr} \mathbf{A}(\tau) d\tau = \ln \det \mathbf{\Phi}(T, 0) = \ln \prod_{j=1}^{N_x} \mu_j = T \sum_{j=1}^{N_x} \lambda_j \quad (2.99)$$

This identity is derived by pairing Floquet’s theorem with the state transition matrix’s determinant property 2.1.3. The integral above is known exactly because the reference state matrix is a Fourier series. The other terms (monodromy matrix, Floquet multipliers and exponents) are determined numerically. The discrepancy from the integral of the state matrix’s trace provides a means to quantify the accuracy of the calculated Floquet quantities. Computation time is an ever-present worry, but the most considerable concern is finite precision arithmetic, therefore some particular techniques are employed for the precise calculation of Floquet quantities [LUST, 2001; NUREKI AND MURASHIGE, 2009].

Why are numerical precision and accuracy important? Because Floquet multipliers may have vastly different magnitudes and the columns of the monodromy matrix must be linearly independent. In this regard an airfoil or wing model pose a formidable challenge because the addition of aerodynamic lag terms increases the number of states and adds critically-damped poles to the system. More damping implies larger time constants and therefore longer periods correspond to events far in the future where errors have had the time to propagate enough to render the solution inaccurate. Because of this, a lot of effort is condensed in this short section to implement several numerical techniques. Figure 2.22 shows the envelope of the STM of an aeroelastic system undergoing the same parameter variation but with different rates.

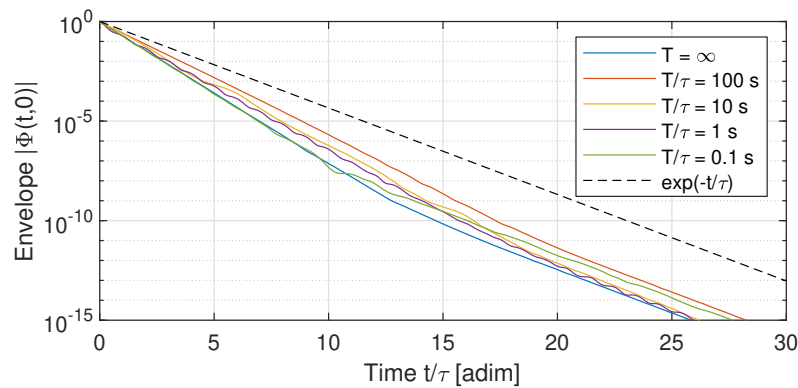


FIGURE 2.22: Envelope of the state transition matrix of the aeroelastic system described in section 7.2. The period and the time axis are scaled by the time constant  $\tau \triangleq -1/\max \Re\{\lambda\}$ , where  $\lambda$  are the eigenvalues of the mean time-invariant system. The decay of a single degree-of-freedom system  $\exp(-t/\tau)$  provides an upper bound (the rate of convergence is  $1/\tau$ ). The value of  $\Phi(t,0)$  decays to machine precision over long periods and its column stop being linearly independent.

### 2.4.1 Discretization of the state matrix

The simplest approach for the calculation of the state transition matrix is the division of the period into very small intervals  $[n\Delta t, (n+1)\Delta t]$  where the state matrix is effectively constant:

$$\mathbf{A}_n \triangleq \frac{1}{\Delta t} \int_{n\Delta t}^{(n+1)\Delta t} \mathbf{A}(\tau) d\tau \approx \frac{\mathbf{A}(n\Delta t) + \mathbf{A}((n+1)\Delta t)}{2\Delta t} \quad (2.100)$$

The state transition matrix for  $t \in [n\Delta t, (n+1)\Delta t]$  is then:

$$e^{\mathbf{A}_n \Delta t} = \Phi((n+1)\Delta t, 0) = \Phi(\Delta t, 0)\Phi(n\Delta t, 0) \quad (2.101)$$

This is the so-called Hsu's method for time-varying systems [HSU, 1974]. A higher-order discretization formula is developed in chapter (7). For a periodic system, in the limit of the time interval's duration becoming vanishingly small, the monodromy matrix is given by the composition property (2.1.3):

$$\Phi(T, 0) = \lim_{\Delta t \rightarrow 0} \prod_{n=1}^N e^{\mathbf{A}_n \Delta t} \quad (2.102)$$

The computation of the matrix exponential is expensive, therefore several variants with different accuracy exist. This work employs the accurate squaring-and-scaling algorithm with Padé approximation [AL-MOHY AND HIGHAM, 2010] as implemented in MATLAB.

### 2.4.2 Initial value problem

The initial value problem approach (IVP, also called *direct numerical integration*) is conceptually simple and of widespread use (it can be applied to any time-varying system). It consists of integrating the homogeneous state equation numerically

$$\dot{\mathbf{X}}(t) = \mathbf{A}(t)\mathbf{X}(t) \xrightarrow[\text{from } 0 \text{ to } T]{\text{solve}} \mathbf{X}(t) \implies \Phi(t, 0) = \mathbf{X}(t)\mathbf{X}^{-1}(0) \quad (2.103)$$

for any set of linearly independent initial conditions (for convenience usually  $\mathbf{X}(0) = \mathbf{I}$ ). Equation (2.103) is a system of  $N_x^2$  homogeneous first-order ordinary differential equations in the form  $\dot{x}(t) = f(t, x(t))$ , that can be solved with common single-step and multi-step algorithms [HAIRER ET AL., 2008; QUARTERONI ET AL., 2006; SHAMPINE ET AL., 2003]. The method is implemented more generally in chapter 7 with the inhomogeneous term to compute the forced response of any LTV system.

In the case of periodic systems, the fundamental solution is calculated up to  $t = T$  in order to determine the monodromy matrix. The Floquet quantities are determined from the eigendecomposition of the monodromy matrix, therefore the calculation of  $\mathbf{X}(T)$  must attain the best possible accuracy (ideally machine precision). This seems extreme compared to many other applications, but it is necessary because eigenvalues (Floquet multipliers) are sensitive to changes in matrix entries (monodromy matrix). However, despite all precautions, there is no guarantee that the columns of the solution  $\mathbf{X}(t)$  (respectively

of  $\Phi(t, 0)$ ) will be linearly independent within the domain  $[0, T]$ . Especially when the system's period is very long, errors propagate and become significant enough to affect the calculation of subsequent steps.

This thesis employs efficient ad-hoc implementations of the Runge-Kutta (single-step) and Adams-Bashforth-Moulton (multi-step) algorithms (see algorithms 7 and 8):

- *Runge-Kutta* (RK) method of order  $N_p$  is

$$\begin{cases} \mathbf{K}_i & \leftarrow \Delta t \mathbf{A}(t_n + c_i \Delta t) \left( \mathbf{X}_n + \sum_{j=1}^{i-1} a_{ij} \mathbf{K}_{j-1} \right) \\ \mathbf{X}_{n+1} & \leftarrow \mathbf{X}_n + \sum_{i=1}^{N_p} b_i \mathbf{K}_i \\ t_{n+1} & \leftarrow t_n + \Delta t \end{cases} \quad (2.104)$$

where the coefficients  $a_{ij}$ ,  $b_i$  and  $c_i$  for stages  $i = 1 : N_p$  are tabulated for each order or variant (Butcher's array). RK performs as many evaluations of  $\mathbf{A}(t)$  as there are stages for each grid point  $t_n$ .

- *Adams-Bashforth-Moulton* (ABM) predictor-corrector method of order  $N_p$  is:

$$\begin{cases} \mathbf{X}_{n+1} & \leftarrow \mathbf{X}_n + \Delta t \sum_{j=0}^{N_p} b_{p,j} \mathbf{A}(t_{n-j}) \mathbf{X}_{n-j} \\ \mathbf{X}_{n+1} & \leftarrow \mathbf{X}_n + \Delta t \sum_{j=0}^{N_p} b_{c,j} \mathbf{A}(t_{n-j+1}) \mathbf{X}_{n-j+1} \\ t_{n+1} & \leftarrow t_n + \Delta t \end{cases} \quad (2.105)$$

The first equation (Adams-Bashforth method with predictor coefficients  $b_p$ ) uses the last  $N_p$  calculated points to predict the next one, then the second equation (Adams-Moulton method with corrector coefficients  $b_c$ ) refines the solution. The algorithm is started by providing the first  $N_p$  points with RK.

A single-step method performs several function evaluations  $\mathbf{A}(t)$  per step, which may be expensive for large systems or long duration. This computational cost is not present in multi-step methods because  $\mathbf{A}(t)$  is only evaluated at the grid points  $t_n$  once per step. Multi-step methods are efficient because previous steps are utilized to obtain a more accurate solution, however they necessitate a smaller step size  $\Delta t$  to attain the same precision of a single-step method of the same order. When rounding errors limit accuracy, then higher order or single-step methods are preferable because they require fewer steps. The classical fourth-order Runge-Kutta solver is sufficient for some rotorcraft applications [MAURICE ET AL., 2009]. MATLAB's `ode45.m` solver (ODE45) utilizes an adaptive 7-stages RK method with the Dormand-Prince coefficients [SHAMPINE ET AL., 2003].

In order to better control code execution and function evaluations, this work utilizes custom RK10 and ABM16 algorithms with constant step size (see algorithms 7 and 8).

### 2.4.3 Boundary value problem

Floquet's theorem and the derivation property of the STM (2.1.3) lead to equation (2.71) (repeated here):

$$\frac{\partial}{\partial t} \Phi(t, 0) = \mathbf{A}(t) \Phi(t, 0) \xrightarrow[\text{substitute}]{\Phi(t,0) = \mathbf{P}(t)e^{\mathbf{Q}t}} \dot{\mathbf{P}}(t) + \mathbf{P}(t)\mathbf{Q} = \mathbf{A}(t)\mathbf{P}(t) \quad (2.106)$$

The calculation of the monodromy matrix can be then reformulated as a boundary value problem (BVP) where the unknowns are  $\mathbf{P}(t)$  and  $\mathbf{Q}$ :

$$\begin{cases} \dot{\mathbf{P}}(t) = \mathbf{A}(t)\mathbf{P}(t) - \mathbf{P}(t)\mathbf{Q} \\ \dot{\mathbf{Q}} = \mathbf{0} \end{cases} \quad \mathbf{P}(0) = \mathbf{P}(T) = \mathbf{I} \quad (2.107)$$

This system of first-order differential equations has the desirable property of having bounded unknowns and very simple boundary conditions that can be enforced exactly. The BVP can be better conditioned than the initial value problem [MONTAGNIER ET AL., 2004], but it requires the solution of a nonlinear problem, therefore an initial guess must be provided by the discretization or the state matrix (2.102) or by direct numerical integration (2.104) (2.105). Equation (2.107) can be solved using a collocation method for boundary value problems of ordinary differential equations, for example MATLAB's `bvp4c.m` / `bvp5c.m` [KIERZENKA AND SHAMPINE, 2001] and TU Wien's `BVPSUITE2.0` [KITZHOFFER ET AL., 2010]. While certainly an elegant theoretical approach, the practical solution of the boundary value problem can easily overflow the computer memory because the number of necessary grid points increases with the system's period and because  $2N_x^2$  equations must be solved simultaneously. The available solvers are not optimized for heavy-duty computations required for large dynamic systems. Long computation times must be taken into account since the BVP is solved iteratively until a certain tolerance is met. An example is presented in figure 2.23.

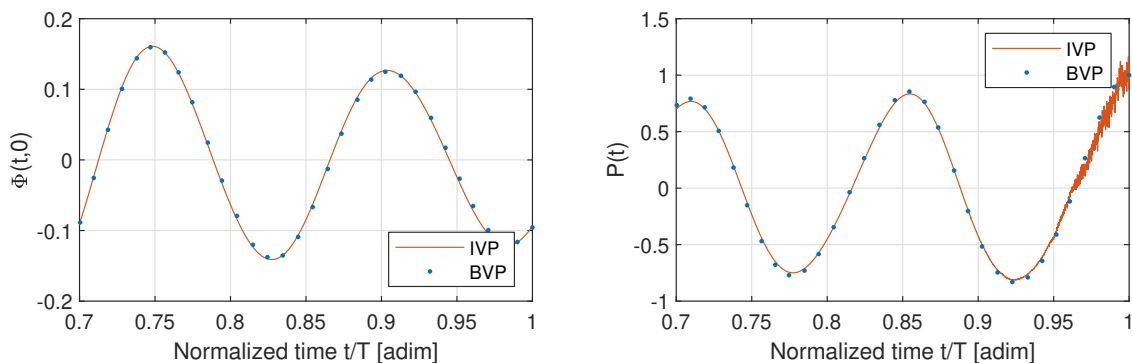


FIGURE 2.23: Comparison of IVP and BVP solutions (state transition matrix and Lyapunov-Floquet transformation matrix). Aeroelastic system from section 7.2 with  $T = 1.53\tau$  s, where  $\tau$  is the largest time constant of the mean time-invariant system. Compared to the system's characteristics, the period is long, therefore both the IVP and BVP methods struggle to meet tolerances. Nevertheless, the latter is able to compute accurately the transformation matrix, while the former succumbs to numerical noise towards the end of the period.

### 2.4.4 Harmonic balance

The boundary value problem can be reformulated to determine the Floquet exponents and eigenvectors directly. Let  $\Psi(t) \triangleq \mathbf{P}(t)\Psi$  be the Floquet eigenvectors:

$$\frac{\partial}{\partial t} \Phi(t, 0) = \mathbf{A}(t)\Phi(t, 0) \xrightarrow[\text{substitute}]{\Phi(t,0)=\Psi(t)e^{\Lambda t}} \dot{\Psi}(t) + \Lambda\Psi(t) = \mathbf{A}(t)\Psi(t) \quad (2.108)$$

The periodic functions  $\mathbf{A}(t) = \sum \mathbf{A}_h e^{ih\omega_0 t}$  and  $\Psi(t) = \sum \Psi_k e^{ik\omega_0 t}$  can be expressed as absolutely convergent Fourier series and inserted into the previous equation to obtain:

$$\sum_{k=-\infty}^{+\infty} (ik\omega_0 + \Lambda) \Psi_k e^{ik\omega_0 t} = \sum_{h=-\infty}^{+\infty} \mathbf{A}_h e^{ih\omega_0 t} \cdot \sum_{k=-\infty}^{+\infty} \Psi_k e^{ik\omega_0 t} \quad (2.109)$$

After applying the Cauchy product:

$$\sum_{h=-\infty}^{+\infty} \mathbf{A}_h e^{ih\omega_0 t} \cdot \sum_{k=-\infty}^{+\infty} \Psi_k e^{ik\omega_0 t} = \sum_{k=-\infty}^{\infty} \left( \sum_{h=0}^k \mathbf{A}_{k-h} \Psi_h \right) e^{ik\omega_0 t} \quad (2.110)$$

we arrive at

$$\sum_{k=-\infty}^{+\infty} \left( (ik\omega_0 + \Lambda) \Psi_k - \sum_{h=0}^k \mathbf{A}_{k-h} \Psi_h \right) e^{ik\omega_0 t} = \mathbf{0} \quad (2.111)$$

The *harmonic balance* (HB) method consists of equating each  $k$ -th harmonic to zero. Its use is widespread in the analysis of nonlinear systems with periodic solutions and a large body of literature exists [BONNIN ET AL., 2018; KHALIL, 1996; LAZARUS AND THOMAS, 2010; TRAVERSA AND BONANI, 2011]. This equation can be formulated as an infinite-dimensional eigenproblem akin to what we have seen in the definition of the harmonic transfer function (2.88):

$$(i[\Omega] + [\mathbf{A}_k]) [\Psi] = [\Psi][\Lambda] \quad (2.112)$$

where  $[\Lambda]$ ,  $[\Psi]$  are the block-Toeplitz matrices (2.86) of eigenvalues and eigenvectors respectively and  $i[\Omega] + [\mathbf{A}_k]$  is the Hill matrix:

$$i[\Omega] + [\mathbf{A}_k] \triangleq \begin{bmatrix} \ddots & \vdots & \vdots & \vdots & \ddots \\ \cdots & \mathbf{A}_0 + i\omega_0 \mathbf{I} & \mathbf{A}_{-1} & \mathbf{A}_{-2} & \cdots \\ \cdots & \mathbf{A}_1 & \mathbf{A}_0 & \mathbf{A}_{-1} & \cdots \\ \cdots & \mathbf{A}_2 & \mathbf{A}_1 & \mathbf{A}_0 - i\omega_0 \mathbf{I} & \cdots \\ \ddots & \vdots & \vdots & \vdots & \ddots \end{bmatrix} \quad (2.113)$$

The harmonic balance can be implemented as a generalized eigenvalue problem in frequency-domain. In practice only a finite number  $N_h$  of harmonics is considered in the series expansion (2.111). The corresponding time and harmonics vectors are:

$$\mathbf{t} \triangleq \{t_1 \cdots t_{2N_h+1}\} \quad \boldsymbol{\omega} \triangleq \omega_0 \{-N_h : N_h\} \quad (2.114)$$



from which the Vandermonde block matrix (DFT operator) is assembled:

$$\mathbf{V} \triangleq \exp(it\boldsymbol{\omega}^T) \implies [\mathbf{V}] \triangleq \text{diag}(\mathbf{V}, \dots, \mathbf{V}) \quad (2.115)$$

where “exp” indicates the *scalar* exponential. In order for  $\mathbf{V}$  to be well-conditioned, the time vector  $\mathbf{t}$  should be irregularly-spaced. The differentiation operator  $[\boldsymbol{\Omega}]$  is a block diagonal matrix built with  $N_x$  copies of  $\boldsymbol{\omega}$ :

$$[\boldsymbol{\Omega}] \triangleq \text{diag}(\boldsymbol{\omega}, \dots, \boldsymbol{\omega}) \in \mathbb{R}^{N_x(2N_h+1) \times N_x(2N_h+1)} \quad (2.116)$$

Finally, the state matrix is composed as follows:

$$[\mathbf{A}] \triangleq \begin{bmatrix} \hat{\mathbf{A}}_{1,1} & \cdots & \hat{\mathbf{A}}_{1,N_x} \\ \vdots & \ddots & \vdots \\ \hat{\mathbf{A}}_{N_x,1} & \cdots & \hat{\mathbf{A}}_{N_x,N_x} \end{bmatrix} \in \mathbb{R}^{N_x(2N_h+1) \times N_x(2N_h+1)} \quad (2.117)$$

where the entries  $\hat{\mathbf{A}}_{i,j} = \text{diag}(\mathbf{A}_{i,j}(t_1), \mathbf{A}_{i,j}(t_2), \dots, \mathbf{A}_{i,j}(t_{2N_h+1}))$  are formed from the values of  $\mathbf{A}_{ij}(t)$  arranged in a diagonal matrix. The resulting eigenvalue problem

$$(i[\boldsymbol{\Omega}] + [\mathbf{V}]^{-1}[\mathbf{A}][\mathbf{V}]) \boldsymbol{\Psi} = \boldsymbol{\Psi} \boldsymbol{\Lambda} \quad (2.118)$$

returns the required Floquet exponents  $\boldsymbol{\Lambda}$  and the Floquet eigenvectors  $\boldsymbol{\Psi}$ . The best estimation of the latter is obtained from the associated Floquet exponents found within the strip  $\Im\lambda \in [-\omega_0/2, +\omega_0/2]$ . Figure 2.24 displays the typical result of the HB method applied to a periodic system. Compared to the IVP and BVP formulations, the HB approach is simpler to implement because it only requires the Fourier series of the state matrix. However, a careful assembly of its matrices is necessary for good numerical conditioning. Its main drawback is the dimension of the eigenproblem (2.118).

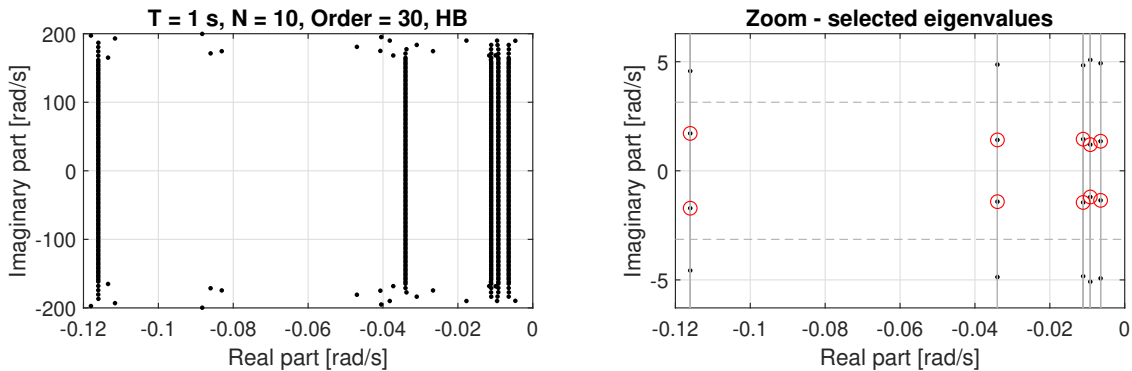


FIGURE 2.24: Harmonic balance applied to the 5-DoF system from [SKJOLDAN AND HANSEN, 2009] ( $T = 1$  s). The black points display the eigenvalues of equation (2.111), the red circles the selected eigenvalues, i.e. the Floquet exponents. The dashed lines delimit the  $-\omega_0/2 \leq \Im\lambda \leq \omega_0/2$  strip, the vertical lines the real part of the poles within this strip. Ideally each Floquet exponent appears multiple times with the same real part and imaginary parts modulo  $i\omega_0$ , in practice there is always some scatter away from the real axis.

### 2.4.5 System identification applied to periodic systems

We have shown previously in equation (2.92) that the state transition matrix of periodic systems has a pole-residue form:

$$\Phi(s, t) = \sum_{j=1}^{N_x} \sum_{k \in \mathbb{Z}} \frac{\mathbf{R}_{j,k}}{s - \lambda_j - ik\omega_0} \quad \begin{aligned} p_{j,k} &= \lambda_j + ik\omega_0 \\ \mathbf{R}_{j,k} &= (\mathbf{P}_k \Psi \mathbf{e}_j)(\mathbf{e}_j^T \Psi^{-1} \mathbf{P}_k) \end{aligned} \quad (2.119)$$

The following approach is proposed for finding the Floquet parameters:

1. Compute the state transition matrix in time-domain by direct numerical integration
2. Extract the poles and residues with a system identification procedure

The residues are rank-1 matrices, therefore we can recover the harmonics of the Floquet eigenvectors by taking the left and right singular vectors associated with the first singular value:

$$\mathbf{R}_{j,k} \stackrel{\text{svd}}{=} \mathbf{U} \Sigma \mathbf{V}^H \implies \begin{cases} \mathbf{P}_k \Psi \mathbf{e}_j = \mathbf{U}_1 \sqrt{\Sigma_1} \\ \mathbf{e}_j^T \Psi^{-1} \mathbf{P}_k = \mathbf{V}_1^H \sqrt{\Sigma_1} \end{cases} \quad (2.120)$$

We shall call this method SID (System IDentification). The advantage of this approach is that existing time-domain or frequency-domain identification methods may be employed [ALLEN ET AL., 2011; JHINAOU ET AL., 2014]. The Stochastic Subspace Identification (SSI) and Least-Squares Complex Frequency (LSCF) are the methods of choice in this thesis (see chapter 5). In some cases the identification technique may fail to resolve very close poles (i.e. when the system varies extremely slowly), nevertheless, the identified Floquet parameters minimize the error in the least-squares sense. A pole selection procedure may be applied afterwards (for example, to reduce the model order). A slowly-varying system that is beyond the capabilities of the other methods presented in this section is decomposed successfully in figure 2.25 using system identification.

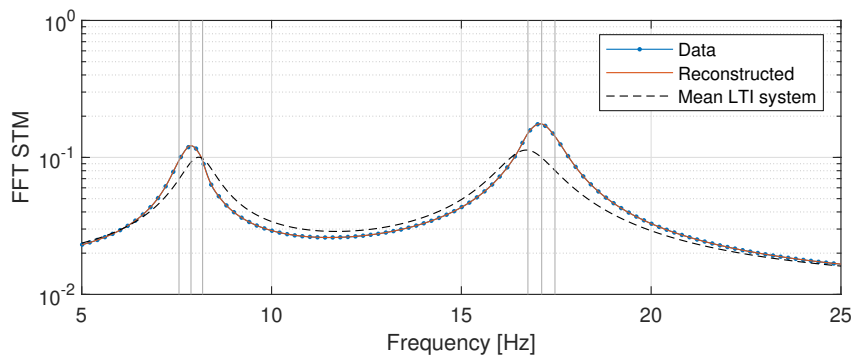


FIGURE 2.25: Floquet decomposition of the system from figure 2.23 using system identification. The plot displays a detail of the STM and its least-squares fit with the identified Floquet parameters (vertical lines). The period is  $T = 10\tau$  s, where  $\tau$  is the largest time constant of the mean time-invariant system (dashed line). Given the long period, other methods fail to decompose this system.

### 2.4.6 Multiple shooting method

The multiple shooting method (MS) for periodic solutions is often encountered in literature because it attains extreme precision [LUST, 2001]. An LTP system has periodic solutions for nonzero initial states if and only if at least one eigenvalue of  $\Phi(T, 0)$  is unity [RUGH, 1996, Th. 5.13]. The method exploits this property by dividing the period into  $M$  sub-intervals such that  $t_0 < t_1 < \dots < t_{M+1} = t_0 + T$ . The  $k$ -th state transition matrix with initial conditions  $\mathbf{x}(t_k)$  is computed for the  $k$ -th sub-interval:  $\mathbf{x}(t_{k+1}) = \Phi(t_{k+1}, t_k)\mathbf{x}(t_k) \forall k = 0: M$ . An iterative Newton method is used to simultaneously enforce the continuity condition  $\mathbf{x}(t_k) = \mathbf{x}(t_{k-1})$  and the periodicity conditions  $\mathbf{x}(t_{M+1}) = \mathbf{x}(t_0)$  across all sub-intervals [NUREKI AND MURASHIGE, 2009]. Since the sub-intervals are short, the errors of a numeric solutions have less time to propagate. However, in the case of aeroelastic non-rotating systems, the system response is periodic only at the flutter condition. The multiple shooting method is thus not considered for this thesis.

### 2.4.7 Comparison of numerical methods

Informally: all presented method work fine but for extreme cases. This problem is acknowledged by some authors [MAURICE ET AL., 2009; MONTAGNIER ET AL., 2004]. In fact, the longer the period, the more difficult it is to obtain an accurate solution using any technique. The number of significant frequency components of the transformation matrix is usually high in the “intermediate” period range (see section 2.3.5). Short periods correspond to a high parameter rate of change, but are usually not difficult to treat because the harmonics are far apart. The accuracy of the presented methods is quantified by the Jacobi-Liouville equation (2.99).

TABLE 2.1: Comparison of numerical methods for LTP systems

Method	Advantages	Disadvantages
Hsu 2.4.1	<ul style="list-style-type: none"> <li>• Simple</li> <li>• Applicable to any LTV system</li> </ul>	<ul style="list-style-type: none"> <li>• Approximate</li> <li>• Computes matrix exponentials</li> </ul>
IVP 2.4.2	<ul style="list-style-type: none"> <li>• Standard/established method</li> <li>• Applicable to any LTV system</li> </ul>	<ul style="list-style-type: none"> <li>• Solution depends on time step</li> <li>• Can be badly conditioned</li> </ul>
BVP 2.4.3	<ul style="list-style-type: none"> <li>• Well-conditioned</li> <li>• Enforces boundary conditions</li> </ul>	<ul style="list-style-type: none"> <li>• Extreme computational cost</li> <li>• Requires initial guess</li> </ul>
HB 2.4.4	<ul style="list-style-type: none"> <li>• Simple</li> <li>• Standard/established</li> </ul>	<ul style="list-style-type: none"> <li>• Can be badly-conditioned</li> <li>• Solves large eigenproblem</li> </ul>
SID 2.4.5	<ul style="list-style-type: none"> <li>• Uses “off-the-shelf” algorithms</li> <li>• Well-documented theory</li> </ul>	<ul style="list-style-type: none"> <li>• Least-squares solution</li> </ul>
MS 2.4.6	<ul style="list-style-type: none"> <li>• Extreme precision</li> </ul>	<ul style="list-style-type: none"> <li>• Only for periodic solutions</li> </ul>

## 2.5 Analytical solutions for time-varying systems

The previous section has highlighted the practical difficulty of computing systems with long periods. Section 2.3.5 has shown that the dynamic mode coupling term becomes irrelevant if the rate of parameter variation is very low or when the modes are spaced widely apart. When this happens, the system can be diagonalized and the state transition matrix has an exponential form according to theorem (2.1.3):

$$\Phi(t, t_0) = \exp \int_{t_0}^t \tilde{\mathbf{A}}(\tau) d\tau \quad (2.121)$$

This leads to significant simplifications because the system can be treated as a collection of uncoupled ordinary differential equations.

Let us then develop a simplified framework for the analysis of such systems. This section's objective is to provide more insight into the dynamics of time-varying systems by deriving analytical solutions. The simplified approach presented here can be utilized to compute extreme cases and to understand the relationships between parameter variation and system response.

We shall consider the  $i$ -th state and the  $j$ -th input to define the parameter  $a(t) \triangleq \tilde{\mathbf{A}}_{ii}(t)$  and the inhomogeneous term  $q(t) \triangleq \tilde{\mathbf{B}}_{ij}(t)\mathbf{u}_j(t)$ . The state equation (2.20) in this scalar case is then in the form

$$\dot{x}(t) = a(t)x(t) + q(t) \quad (2.122)$$

and its solution can be found with the method of variation of parameters:

$$x(t) = e^{A(t)}x(t_0) + e^{A(t)} \int_{t_0}^t e^{-A(\tau)}q(\tau) d\tau \quad A(t) \triangleq \int_{t_0}^t a(\tau) d\tau \quad (2.123)$$

It is apparent that a general closed-form solution of equation (2.123) does not exist unless some restrictions are imposed on  $a(t)$  and  $q(t)$ . To this end, the parameter variation shall be narrowed to linear and complex exponential functions to determine an analytical solution in the time and frequency domains.

### 2.5.1 Linear parameter variation

Let the parameter  $a(t)$  be a linear function of time:

$$\dot{x}(t) = a(t)x(t) + q(t) \quad a(t) = a_0 + a_1t \quad (2.124)$$

We shall derive an analytical solution to this linear equation. The full derivations are found in appendix A.3. The effect of linear parameter variation on the instantaneous eigenfrequency and damping ratio is displayed in figure 2.26. The integral of  $a(t)$  is

$$A(t) = \int a(\tau) d\tau = a_0t + \frac{1}{2}a_1t^2 + c \quad (2.125)$$

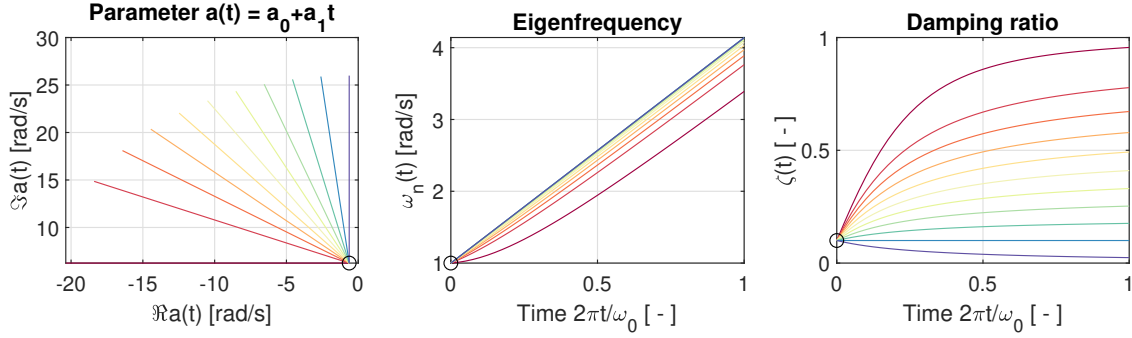


FIGURE 2.26: Linear parameter variation  $a(t) = a_0 + a_1 t$ , where  $a_0 = f_\lambda(1, 0.1)$  rad/s and  $a_1 = f_\lambda(0.5, p)$  rad/s<sup>2</sup> for  $p = 0:0.1:1$  (blue: zero, red: one).  $f_\lambda(\cdot, \cdot)$  is the eigenvalue function. The instantaneous eigenfrequency varies linearly, while the instantaneous damping ratio approaches  $p = -\Re\{a_1\}/|a_1|$  hyperbolically. If  $\Re\{a_1\} = 0$ , then the instantaneous damping ratio approaches 0, if  $\Im\{a_1\} = 0$ , then the instantaneous damping ratio approaches 1.

The homogeneous solution in time-domain is thus simply:

$$x_h(t) = x(0)e^{A(t)} = x(0)e^{a_0 t + \frac{1}{2}a_1 t^2} \quad (2.126)$$

The Fourier transform of the homogeneous solution is a shifted Gaussian function:

$$x_h(\omega) = \int_{-\infty}^{+\infty} x_h(t)e^{-i\omega t} dt = x(0) \frac{\sqrt{\pi}}{\alpha} \exp\left(\frac{i\omega - a_0}{2\alpha}\right)^2 \quad (2.127)$$

where  $\alpha \triangleq \sqrt{-a_1/2}$ . A comparison of the LTV and LTI solutions in the time and frequency domains is presented in figure 2.27. In the time-varying case, the instantaneous eigenfrequency increases continuously, therefore the response decays faster. The spectrum exhibits multiple bumps whose spacing varies geometrically. Figure 2.28 illustrates the influence the parameter's eigenfrequency and damping ratio  $a_1 = f_\lambda(\omega_1, \zeta_1)$  on the spectrum of the homogeneous solution. The peak amplitudes decay with increasing frequency with a rate that depends on the damping ratio. The LTV solution approaches the time-invariant case when the rate of change is low ( $\sqrt{|a_1|}/|a_0| \rightarrow 0$ ). When the rate of change is high,

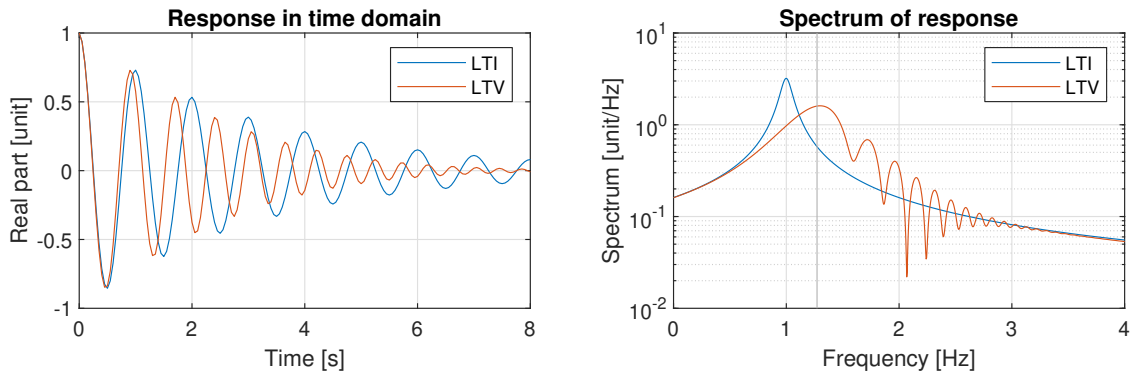


FIGURE 2.27: Analytical solutions of  $\dot{x}(t) = (a_0 + a_1 t)x(t)$ . The initial condition is  $x(0) = 1$ , the parameters are  $a_0 = f_\lambda(1, 0.05)$  rad/s and  $a_1 = f_\lambda(0.2, 0.05)$  rad/s<sup>2</sup> (the damping ratio does not vary). The main LTV peak is at  $|a_0 + 2\sqrt{a_1}|$  rad/s for small damping values.

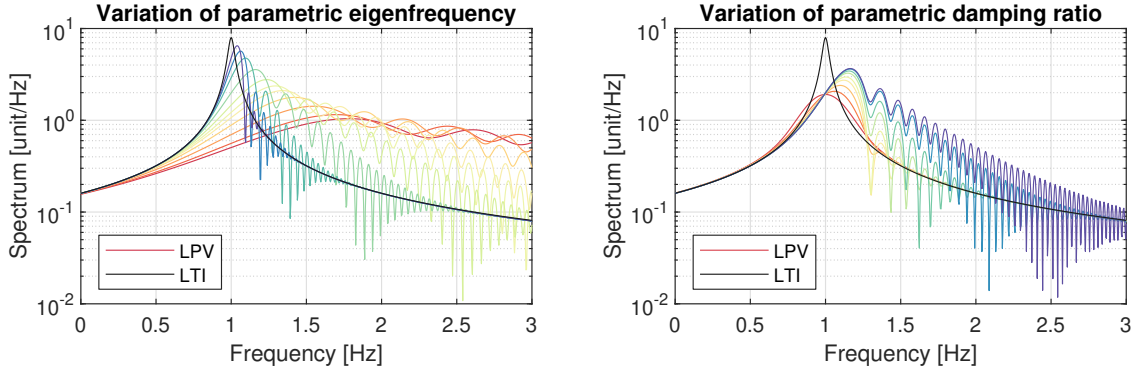


FIGURE 2.28: Spectrum of  $\dot{x}(t) = a(t)x(t)$ , with  $x(0) = 1$ ,  $a_0 = f_\lambda(1, 0.02)$  rad/s and  $a(t) = a_0 + a_1 t$ . Let  $p \in [0, 1]$  (blue: low, red: high). In the left plot  $a_1 = f_\lambda(p, 0.02)$  (eigenfrequency change). As  $p \rightarrow 0$ , the LTV solution converges towards the LTI case. In the right plot  $a_1 = f_\lambda(0.05, p)$  (damping ratio change).

the energy content in higher frequency increases compared to the time-invariant case. The higher the damping ratio of  $a_1$ , the more the LTV peaks are suppressed and the closer the main peak is to  $|a_0|$ . Let the forcing term be a series

$$q(t) = \sum_{q=1}^{N_q} c_q e^{s_q t} \quad c_q, s_q \in \mathbb{C} \quad (2.128)$$

where both the coefficients and frequencies are complex. This assumption includes the broad category of  $L^2$  (square-integrable) functions. The inhomogeneous term is thus

$$x_i(t) = e^{A(t)} \int_{t_0}^t e^{-A(\tau)} q(\tau) d\tau = \frac{\sqrt{\pi}}{2i\alpha} e^{-\alpha^2 t^2 + a_0 t} \sum_{q=1}^{N_q} c_q e^{\mu_q^2} (\operatorname{erf}(i\alpha t + \mu_q) - \operatorname{erf}(\mu_q)) \quad (2.129)$$

where the constants are  $\alpha \triangleq \sqrt{-a_1/2}$ ,  $\mu_q \triangleq (a_0 - s_q)/(2i\alpha)$  and  $\operatorname{erf}(z) \triangleq \frac{2}{\sqrt{\pi}} \int_0^z e^{-u^2} du$  is the complex error function. The transformation of  $x_i(t)$  into frequency-domain is convoluted because it requires a difficult kind of integral involving error functions. Details about the derivations are found in appendix A.3. The final result is:

$$x_i(\omega) = \int_{-\infty}^{+\infty} x_i(t) e^{-i\omega t} dt = \frac{\pi}{2\alpha^2} e^{\left(\frac{i\omega - a_0}{2\alpha}\right)^2} \sum_{q=1}^{N_q} c_q e^{\mu_q^2} (\operatorname{sgn}(i\omega - s_q) - 1 - \operatorname{erf}(\mu_q)) \quad (2.130)$$

where the auxiliary variables are as before and “sgn” is the signum function. An example is shown later in section 2.5.3. We conclude that the frequency-domain representation of the response of a linearly-varying system involves complicated functions of the frequency, in contrast to the much simpler rational form of time-invariant systems. This result has been anticipated in section 2.1.4 (see figure 2.5).

### 2.5.2 Complex exponential parameter variation

Let the parameter  $a(t)$  be a series of exponential functions:

$$\dot{x}(t) = a(t)x(t) + q(t) \quad a(t) = a_0 + \sum_{p=1}^{N_p} c_p e^{s_p t} \quad (2.131)$$

where  $c_p, s_p \in \mathbb{C}$ . The complex frequencies  $s_p$  are not necessarily purely imaginary or multiples of a fundamental frequency (equation (2.131) satisfies the hypothesis of Floquet theory when  $\Re s_p = 0$ ). This assumption gives more generality than what was shown with periodic systems in section 2.3. Figure 2.29 shows an example of such an instantaneous eigenfrequency and damping ratio variations. The integral of the parameter  $a(t)$  is

$$A(t) = \int a(\tau) d\tau = a_0 t + \sum_{p=1}^{N_p} \frac{c_p}{s_p} \exp(s_p t) \quad (2.132)$$

The homogeneous solution is found by the method of variation of parameters (2.123):

$$x_h(t) = x_0 e^{A(t)} = c_0 \exp\left(a_0 t + \sum_{p=1}^{N_p} \frac{c_p}{s_p} e^{s_p t}\right) = c_0 \sum_{k=1}^{\infty} c_k e^{(a_0 + s_k)t} \quad (2.133)$$

where the constant  $c_0 \triangleq x(0) \exp\left(-\sum_{p=1}^{N_p} \frac{c_p}{s_p}\right)$  depends on the initial conditions and where  $c_k$  are the coefficients of the Fourier series of the double exponentials  $\exp\left(\frac{c_p}{s_p} e^{s_p t}\right)$  (they can be computed exactly and their derivation is found in appendix A.4). We observe that  $x_h(t)$  is an infinite series of simple poles, therefore it has an immediate transform into Laplace-domain:

$$x_h(s) = \sum_{\mathbb{S}_h} \frac{r_h}{s - p_h} \quad (2.134)$$

where  $\mathbb{S}_h$  is the set of pole-residue pairs  $\{p_h, r_h\} \triangleq \{c_0 c_k, a_0 + s_k\}$  (the subscript  $h$  denotes the homogeneous solution). The system is stable if  $\Re\{a_0 + s_k\} \leq 0 \quad \forall k$ . The example in figure 2.30 illustrates qualitatively the influence of the parameter  $a(t) = a_0 + c_1 e^{s_1 t}$  on the spectrum of the homogeneous solution, in particular the appearance of additional

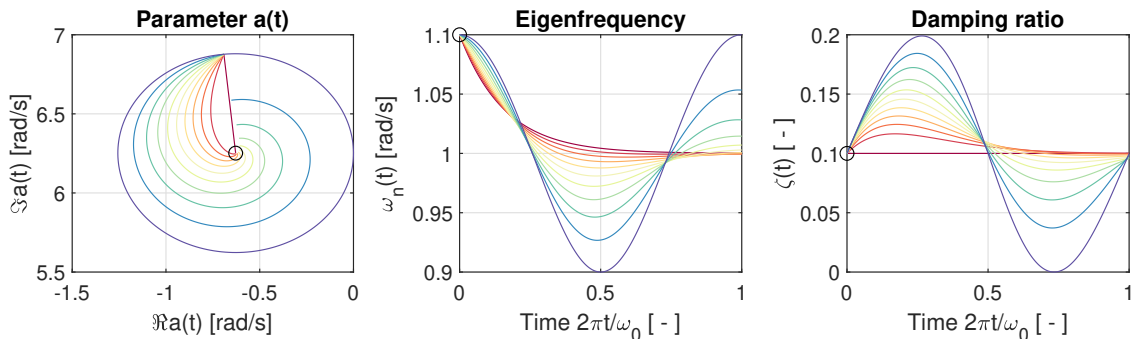


FIGURE 2.29: Exponential parameter variation  $a(t) = a_0 + c_1 \exp(s_1 t)$ , where  $a_0 = f_\lambda(1, 0.1)$  rad/s and  $c_1 = 0.1a_0$  and  $s_1 = f_\lambda(1, p)$  rad/s (so  $\omega_0 = 1$  rad/s), where  $p = 0:0.1:1$  (blue: zero, red: one).  $f_\lambda(\cdot, \cdot)$  is the eigenvalue function (see notation in the preamble). When  $s_1$  is purely imaginary, the parameter variation is periodic. The  $c_1$  coefficient determines the amplitude and phase of the  $c_1 e^{s_1 t}$  term.

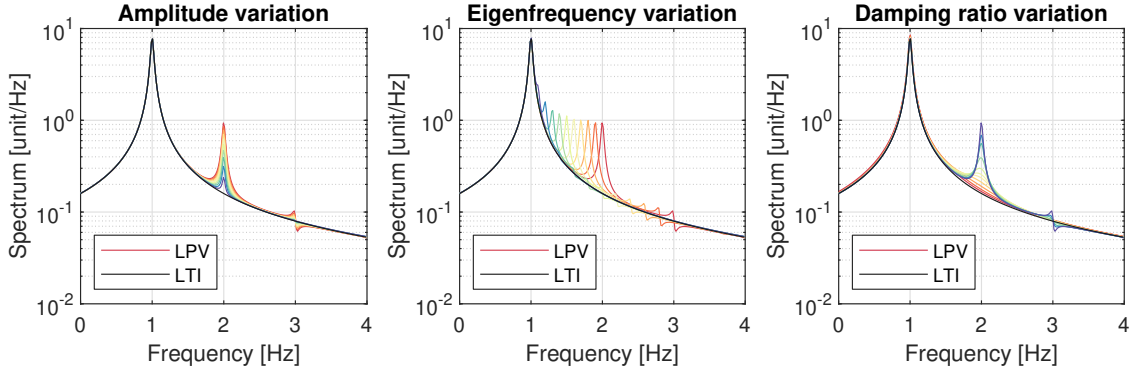


FIGURE 2.30: Spectrum of  $\dot{x}(t) = (a_0 + c_1 \exp(s_1 t)) x(t)$ , with  $x(0) = 1$ ,  $a_0 = f_\lambda(1, 0.02)$  rad/s. Let  $p \in [0, 1]$  (blue: low, red: high). In the left subplot  $a(t) = a_0 + p|a_0| \cdot \exp(f_\lambda(1, 0)t)$  (amplitude change). In the middle subplot  $a(t) = a_0 + p|a_0| \cdot \exp(f_\lambda(p, 0)t)$  (eigenfrequency change). In the right  $a(t) = a_0 + 0.1|a_0| \cdot \exp(f_\lambda(1, p)t)$  (damping ratio change).

poles. Relative to the time-invariant pole  $a_0$ , LTV dynamics are not significant when the amplitude is low  $|c_1|/|a_0| \rightarrow 0$ , the frequency is either much smaller  $|s_1|/|a_0| \ll 1$  or much bigger  $|s_1|/|a_0| \gg 1$  or when the damping ratio is high  $-\Re\{s_1\}/|s_1| > 1/\sqrt{2}$ . The shapes of the LTV peaks vary if  $c_1$  and  $s_1$  are real, complex or purely imaginary.

Let the forcing function be again a sum of complex exponentials:

$$q(t) = \sum_{q=1}^{N_q} c_q e^{s_q t} \quad c_q, s_q \in \mathbb{C} \quad (2.135)$$

After many algebraic manipulations that we are leaving for appendix A.4, the inhomogeneous response turns out to be in the form:

$$x_i(t) = e^{A(t)} \int_0^t e^{-A(\tau)} q(\tau) d\tau = \sum_{\mathbb{S}_t} r_t e^{p_t t} + \sum_{\mathbb{S}_f} r_f e^{p_f t} \quad (2.136)$$

where the subscripts  $t$  and  $f$  refer respectively to the transient and forced response and  $\mathbb{S}_t$ ,  $\mathbb{S}_f$  are the corresponding sets of pole-residue pairs  $\{p, r\}$ . The inhomogeneous response in Laplace-domain is simply:

$$x_i(s) = \sum_{\mathbb{S}_t} \frac{r_t}{s - p_t} + \sum_{\mathbb{S}_f} \frac{r_f}{s - p_f} \quad (2.137)$$

The complete solution is then finally:

$$x(\omega) = \sum_{\mathbb{S}_h} \frac{r_h}{s - p_h} + \sum_{\mathbb{S}_t} \frac{r_t}{s - p_t} + \sum_{\mathbb{S}_f} \frac{r_f}{s - p_f} \quad (2.138)$$

This equation is the sum of the homogeneous response (2.134) and the transient and forced (steady-state) responses due to the inhomogeneous term (2.137). This result is in line with Floquet's theory (2.78) (2.93) but it does not assume a periodic system. The pole-residue pairs  $\{p, r\}$  can be computed exactly for any parameter variation and forcing function that can be expressed by complex Fourier series. As usual, it is then a matter of manipulating



a finite set of most significant pole-residue pairs. The number of terms can be reduced considerably if all the complex frequencies of parameter and forcing function are multiples of a fundamental  $i\omega_0$  (because the Dirac deltas with the same abscissa are summed). The techniques used to derive the complete solution in frequency domain (2.138) can be applied to a parameter variation that is combinations of polynomial and exponential functions such as  $a(t) = a_0 + t^p e^{st}$ . The resulting response contains poles with multiplicity  $p + 1$ .

### 2.5.3 Examples of analytical solutions

Figure 2.31 illustrates the response of three systems subject to the same forcing function, but with different parameter variations. The examples are designed to illustrate the variety of the spectral content depending on the type of parameter variation. In each case the peaks and valleys of the spectrum may be altered greatly by modifying the parameter's phase. The most obvious difference compared to the underlying time-invariant case is that the steady-state response contains additional frequency components. Save for extreme case, few poles are sufficient to describe the response. The examples where the system variation is truly periodic give the same results of Floquet theory.

The simplified single degree-of-freedom approach is used to decompose a time-varying harmonic oscillator in figure 2.32.

In the case of an observation window limited to  $t \in [0, T]$ , the response in frequency-domain can be computed by windowing as shown in section 2.3.6 using a periodic representation of the LTV system. The example of a parameter increasing and then decreasing linearly<sup>11</sup> is illustrated in figure 2.33. Assuming that some error can be accepted, the periodic formulation is simpler to implement and easier to manipulate than the linear one. We can therefore approximate the parameter variation with a series of complex exponentials and then compute its response in the time and frequency domains. The results are shown in figure 2.33. The solution computed from the linear formulation is matched well by the periodic representation of the system. Essentially the same technique has been applied in figure 2.21 for a full aeroelastic system.

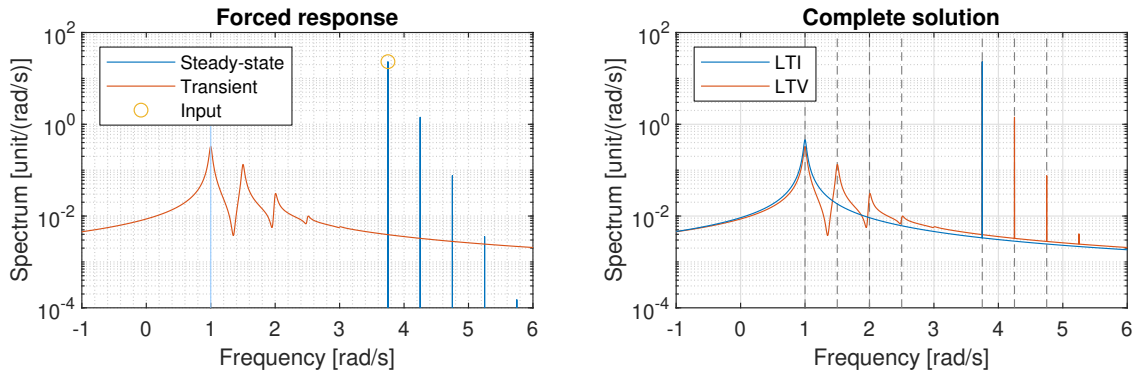
<sup>11</sup> Consider a parameter  $a(t)$  that increases and then decreases linearly:

$$a(t) = \begin{cases} a_0 + a_1 t & 0 \leq t < rT \\ a_0 - a_1 \frac{r}{1-r}(t - rT) & rT \leq t < T \\ a_0 & t \geq T \end{cases} \quad r \in [0, 1] \quad (2.139)$$

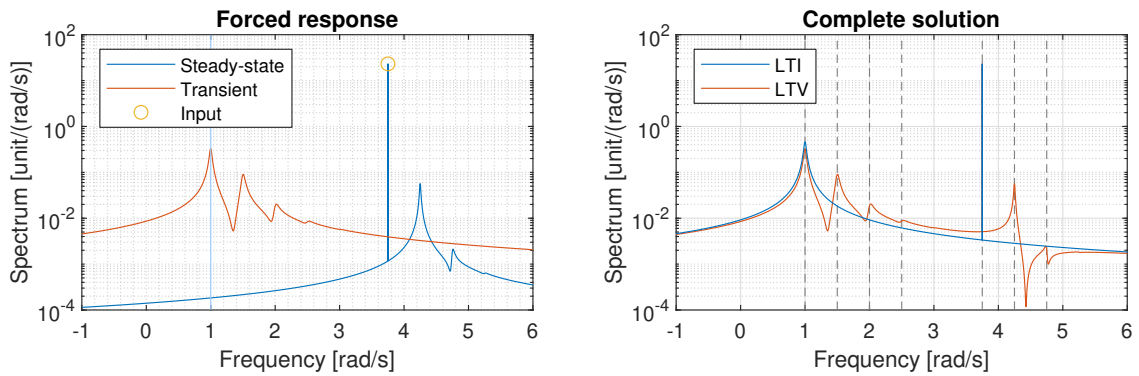
This is a triangle wave of height  $A = a_1 rT$  and period  $2T$  with the first cusp located at  $t = rT$ . The solution of  $\dot{x}(t) = a(t)x(t) + q(t)$  is calculated using the linear and periodic formulations.

$$a(t) = a_0 + \frac{2A}{\pi^2 r(1-r)} \sum_{k=1}^{\infty} \frac{(-1)^k}{k^2} \sin(k\pi(r-1)) \sin\left(2\pi k \frac{t}{2T}\right) \quad (2.140)$$

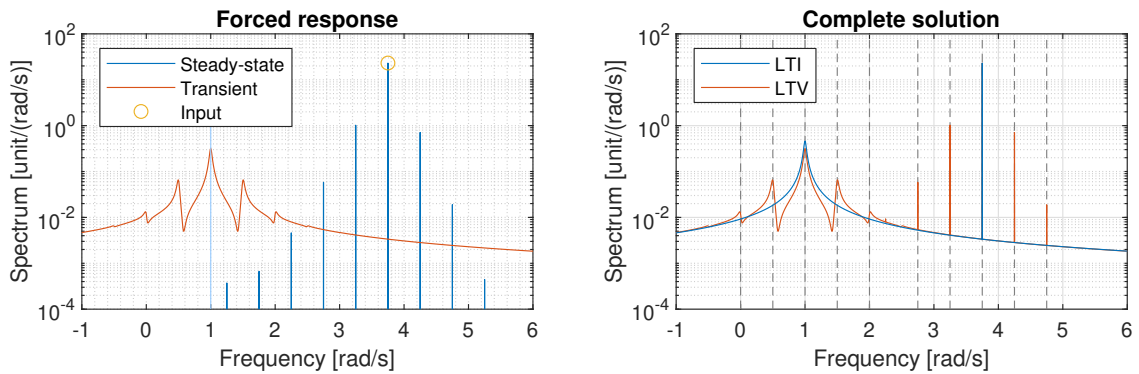
Since  $a(t) \in L^2$ , then its Fourier series converges absolutely.



(A) Complex parameter variation  $a(t) = a_0 + 0.2i \cdot \exp(i0.5t)$



(B) Decaying parameter variation  $a(t) = a_0 + 0.2i \cdot \exp(-0.01t + i0.5t)$



(C) Periodic parameter variation  $a(t) = a_0 - 0.2 \cdot \sin(0.5t)$

FIGURE 2.31: Each subfigure displays the time-varying system  $\dot{x}(t) = a(t)x(t) + q(t)$  in frequency-domain for different  $a(t)$ . In all examples the initial conditions are zero, the constant term is  $a_0 = f_\lambda(2\pi, 0.02)$  and the forcing term is  $q(t) = \exp(3.75t)$ . The corresponding LTI system is  $\dot{x}(t) = a_0x(t) + q(t)$ . The left subplots show the transient response due to the forcing function and the steady-state solution from equation (2.137). The vertical light blue line is the location of the LTI system's eigenfrequency, while the circle represents the forcing term in frequency-domain  $q(\omega) = \delta(\omega - 3.75)$ . The strictly periodic terms in the steady-state response appear as a Dirac delta in the spectrum. The right subplots compare the LTV and LTI cases. The dashed lines denote the locations of significant dynamic poles.

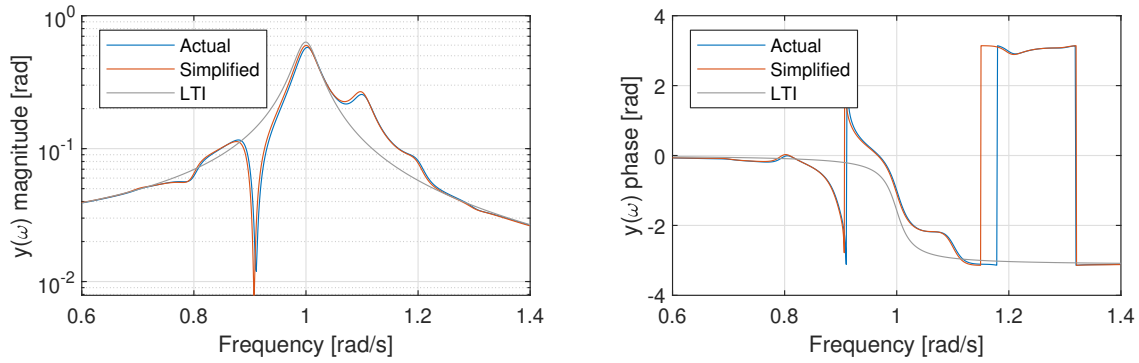
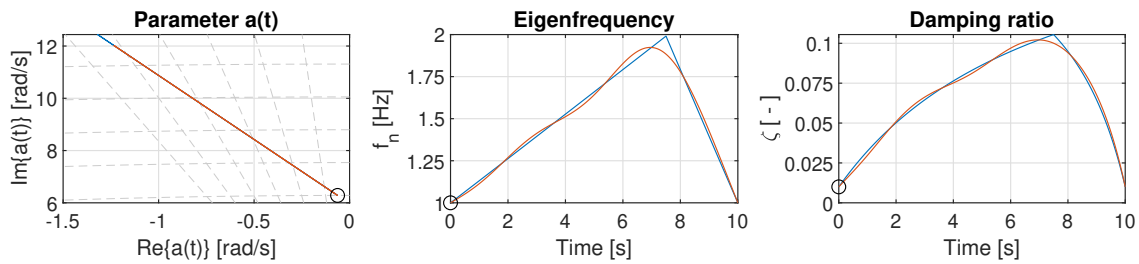
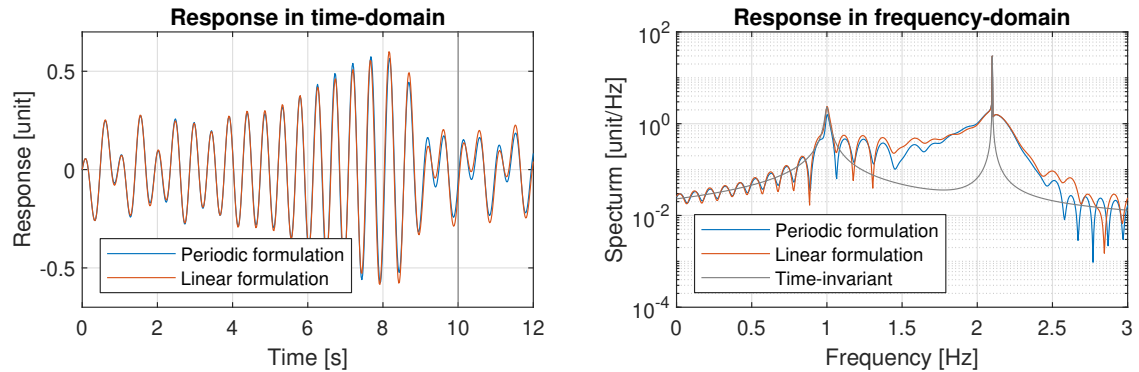


FIGURE 2.32: Harmonic oscillator  $m(t)\ddot{x}(t) + c\dot{x}(t) + kx(t) = 0$ , where the mass varies as  $m(t)/m_0 = 1 - 0.1 \sin(0.1\omega_n t)$ ,  $m_0 = 1$  kg,  $d = 2 \cdot 0.02 \cdot 2\pi$  Nm/s and  $k = (2\pi)^2$  N/m. The response is computed in frequency-domain by the simplified analytical approach using two time-varying poles. The parametric solution compares well to the nonparametric one.



(A) Linear parameter variation and periodic approximation with five terms



(B) Comparison between linear and periodic formulations

FIGURE 2.33: Linear parameter variation: comparison of linear and periodic solutions. The parameter  $a(t)$  increases and decreases linearly according to equation (2.139) where  $a_0 = f_\lambda(1, 0.01)$ ,  $a_1 = f_\lambda(1/r/T, 0.2)$ ,  $T = 10$  s and  $r = 3/4$ . The linear function (red) is approximated with a five-term Fourier series (blue). The eigenfrequency of the system varies from 1 to 2 Hz and the damping ratio from 0.01 to 0.1 circa. The inhomogeneous term is  $q(t) = \exp(2.1 \cdot 2\pi i t)$ . The periodic formulation is set to use only five terms to represent  $a(t)$ , therefore some discrepancy in the results is expected, but the main features of the spectra are the same. The spectrum's waviness is due to the limited duration.

## 2.6 Chapter summary

The chapter introduced the theory of linear time-varying systems and provided some of the mathematical tools necessary for their analysis.

The objective is to study parameter-varying aeroelastic structures and the effect of parameter variation on the system's dynamics. In order to achieve this goal, the chapter put much emphasis in deriving parametric representations of the response of time-varying systems in frequency-domain. This will be required in later chapters for the correct interpretation of modal analysis results. Two important special cases have been elaborated: linear time-invariant (LTI) and linear time-varying periodic (LTP) systems.

The chapter's focus is on parametric representations of time-varying processes. In the LTI case, the system can be conveniently fully characterized by its transfer function and by the eigenvalues and eigenvectors of the state matrix, therefore many spectral estimation and system identification techniques operate within this framework. On the other hand, LTP systems can be decomposed using Floquet's theorem into equivalent time-invariant ones with inputs and outputs modulated by periodic functions. The Floquet exponents and Floquet-Lyapunov transformation matrix assume the role of modal parameters. In the case of slowly-varying systems, the "frozen-time" (instantaneous) eigenvalues are still useful. This is a common, necessary and adequate assumption in the treatment of many time-varying systems to obtain a parametric representation of the response spectra or modal parameters. In the general time-varying case, the concept of eigenvalues is not unique and so-called "pseudo modal parameters", "dynamic eigenvalues" and "time-varying modes" can be defined.

The chapter showed that it is possible to use a periodic representation of a general time-varying system to render it tractable. The influence of amplitude and rate of variation is recognized and studied to define three regimes. If the system varies slowly, the dynamic coupling terms are not significant and a frozen-time representation may be used. Conversely, a system may appear insensible to very fast parameter variations; when this occurs, the main resonance peaks are approximately at the location of the mean frozen-time values. Intermediate regimes are difficult to categorize and must be analyzed case-by-case.

Numerical techniques for the solution of time-varying and periodic systems have been researched and applied. The main practical difficulty arises when the variation is very slow. This issue is addressed by developing a simplified single degree-of-freedom approach with exact solutions for linear and exponential parameter variation. The method is applicable when a system is slowly-varying or where resonance peaks are distant from each other.



### 3 Aeroelastic systems

*Abstract*

---

Aeroelastic modeling couples the structure with the fluid flow surrounding it. The underlying mechanical state-space model is augmented with terms describing the influence of aerodynamics. The resulting system is parameter-varying with air density and air speed as independent variables. An important characteristic of aeroelastic models is the ability to predict flutter – a dynamic instability arising as self-excited oscillations due to the interaction with aerodynamic forces. The theory laid down in the previous chapter is applied here specifically to aeroelastic systems to study the influence of the airflow variables.

---

Aeroelasticity is the study of the interaction between aerodynamic, elastic and inertial forces. The fluid flow around an object generates forces that induce deformations and rigid body motions. In turn, the changes in the object's shape influence the fluid flow around and consequently the forces it induces. Broader definitions or more specialized applications include thermodynamic phenomena (aerothermoelasticity) and the presence of a control system (aeroservoelasticity).

The scope of this chapter is classical linearized aeroelastic modeling. This approach consists of reformulating the equations of motion of a body immersed in a fluid to account for aerodynamic forces. This leads to a state-space representation whose matrices are functions of airflow variables such as wind speed and air density. Depending on the structure's geometry, it is possible for the eigenvalues to cross into the right complex half-plane for certain critical flow conditions and render the system unstable. In fact, a crucial aspect of aeroelastic modeling is the prediction of flutter, a dynamic instability whereby the system absorbs energy from the airflow, leading to unbounded oscillations. Flutter can be modeled by linearization around an equilibrium state even in nonlinear aeroelastic systems, excluding dynamically-stable states such as limit cycle oscillations.

A general and broad introduction into aeroelasticity, loads, control, aeroservoelasticity, maneuvers and industrial practice is found in [WRIGHT AND COOPER, 2007]. The topic is treated rigorously in the book from [BISPLINGHOFF ET AL., 1996], which is a great reference point for mathematical derivations. An advanced text for engineers where aeroelasticity is covered in depth for fixed-wing aircraft, also concerning historical developments, is [RODDEN, 2011]. In the classic approach, the unsteady aerodynamic forces are formulated in the frequency-domain according to [THEODORSEN, 1935] and [KÜSSNER, 1941]. The transformation into time-domain for the state-space model application requires a rational function approximation to introduce the time delay between motion and motion-induced aerodynamic forces, for which a simple and robust approach was formulated by [ROGER, 1977]. A discussion on arbitrary time-dependent equations of motion in fluid dynamics, serving as a starting point for treatable, simplified solution procedures of unsteady aerodynamics is found in [GEISSLER, 1980].

Our objective is the construction of linear parameter-varying state-space models that can predict flutter. To this end, well-established procedures will be employed [GUPTA ET AL., 1991]. In particular, the work of [SCHWOCHOW, 2013] contains a valuable comparison of different flutter analyses. The aeroelastic theory outlined in this section is not evaluated on its degree of accordance with reality – this is the purpose of other works, such as [RITTER, 2019] and [VOSS, 2020a].

The theory introduced in the previous chapter has set up the tools needed to solve time-varying systems. In this chapter we shall apply it specifically in the analysis of parameter-varying aeroelastic systems. We aim to investigate the dynamic effects due to the rapid change of airflow variables, therefore explicit time-dependency will be introduced after aeroelastic modeling has been established for the time-invariant case. These relatively simple mathematical models are the basis for the numerical simulation techniques that will be employed in chapter 7 for fully time-varying systems.

The chapter’s roadmap is the following:

1. Introduction to aeroelastic theory, in particular the modeling of unsteady aerodynamic effects on structures and the characteristics of aeroelastic models
2. Introduction to the flutter phenomenon and its importance for aeroelastic design
3. Continuous turbulence modeling and gusts
4. Study of time-dependency and its effect on parameter variation on system matrices or eigenvalues.

### 3.1 Aeroelastic modeling

Aeroelastic system modeling couples the inertial and elastic properties of a structure with the aerodynamic forces generated by the airflow around it. In essence, this is accomplished by augmenting the state-space of the underlying mechanical system to include aerodynamic terms. In this section we shall introduce the aeroelastic equation of motion to be able to model continuous turbulence excitation.

#### 3.1.1 Aerodynamic forces

We proceed by establishing the linear potential theory in order to derive the aerodynamic loads and delineate their characteristics in the unsteady case. To this end, we consider a thin airfoil in incompressible inviscid flow and small incidence angles. The results of this simplified analysis can be adapted to handle more complex cases; in this regard, the techniques applied in aircraft aeroelastic design will be presented in the next section. [BISPLINGHOFF ET AL., 1996] and [RODDEN, 2011] treat the topic exhaustively. The airflow is characterized by the following free-stream parameters (subscript “ $\infty$ ”):

$$\begin{array}{lll} \rho_\infty & [\text{mass/length}^3] & \text{air density} \\ V_\infty & [\text{length/time}] & \text{air speed} \\ q_\infty = \frac{1}{2}\rho_\infty V_\infty^2 & [\text{force/length}^2] & \text{dynamic pressure} \end{array} \quad (3.1)$$

The airflow induces a lift force and pitching moment upon the airfoil. Let us consider the lift force per unit span  $L$  and determine the change due to a small angle of attack  $\alpha$  variation:

$$L = \frac{1}{2}\rho_\infty V_\infty^2 c_{ref} C_L(\alpha) \implies dL = \frac{1}{2}\rho_\infty V_\infty^2 c_{ref} \frac{dC_L}{d\alpha} d\alpha \quad [\text{force/length}] \quad (3.2)$$

where  $c_{ref}$  is the airfoil reference chord and  $C_L(\alpha)$  the lift coefficient as a function of the angle of attack  $\alpha$  (see figure 3.1). The lift acts perpendicularly to the free-stream speed at the quarter-chord point. The induced pitching moment  $M$  has a similar expression.

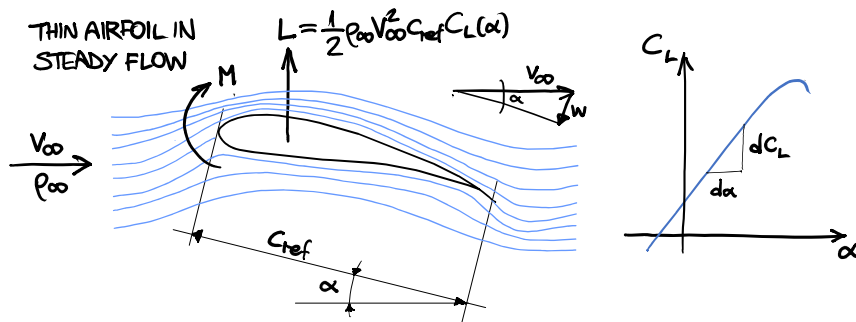


FIGURE 3.1: Thin airfoil in steady incompressible inviscid flow and typical lift curve. The lift force per unit span  $L$  is a function of dynamic pressure  $q_\infty$ , reference chord  $c_{ref}$ , and angle of attack through the lift coefficient  $C_L(\alpha)$ . For small  $\alpha$  the downwash acting on the airfoil is  $w = V_\infty \sin \alpha \approx V_\infty \alpha$ . The lift center is at the quarter-chord point from the leading edge.



In accordance with the assumption of thin airfoil and small angle of attacks, the lift slope is constant  $a_0 \triangleq dC_L/d\alpha$  and the *downwash* is  $w = V_\infty \sin \alpha \approx V_\infty \alpha$ :

$$dL = \frac{1}{2} \rho_\infty V_\infty c_{ref} a_0 dw \quad (3.3)$$

Up to this point, no assumption has been made concerning the time-dependency of the motion. However, in the unsteady case it takes time for the lift to build up after a sudden change of angle of attack because the disturbance propagates at a finite speed. This gradual lift increase is modeled in time-domain by Wagner's function  $\Phi(\cdot)$  (see figure 3.2 or equation (A.38) in the appendix). The lift over time due to a change of downwash is thus:

$$\frac{dL}{dt} = \frac{1}{2} \rho_\infty V_\infty c_{ref} a_0 \Phi(tV/b) \frac{dw}{dt} \quad (3.4)$$

where  $b \triangleq c_{ref}/2$  is the *semi-chord*<sup>1</sup>. This last equation can be used to determine the lift to an arbitrary excitation by a superposition of steps through Duhamel's method:

$$L(t) = \frac{1}{2} \rho_\infty V_\infty c_{ref} a_0 \left( w_0 + \int_{t_0}^t \Phi((\tau - t_0)V_\infty/b) \frac{dw}{d\tau} d\tau \right) \quad (3.5)$$

where  $w_0$  is the steady-state contribution, while the convolution integral models the unsteady change in lift with Wagner's function acting as its kernel. The quantity  $b/V_\infty$  is the time needed by the unperturbed airflow to travel over a distance equal to one semi-chord, therefore  $tV_\infty/b$  is a dimensionless time abscissa. Likewise, in the frequency-domain the dimensionless *reduced frequency* is defined as:

$$k \triangleq \frac{\omega b}{V_\infty} \quad [\text{adim}] \quad (3.6)$$

<sup>1</sup> The semi-chord  $b$  appears in the derivation of the unsteady lift using thin-airfoil theory [SEARS, 1941] and is convenient for writing concisely the aeroelastic equations later on. It should be noted that some authors and software packages use the reference chord length  $c_{ref}$  instead and denote the wingspan with  $b$ .

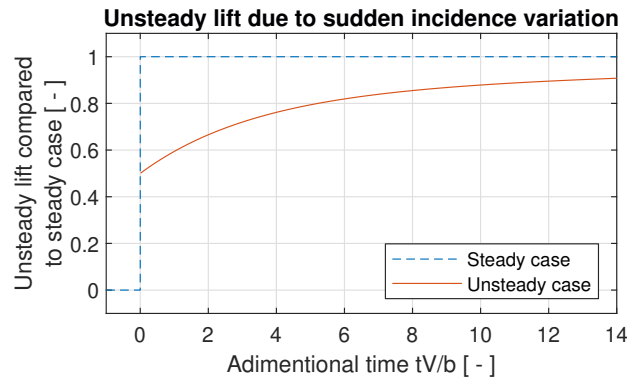


FIGURE 3.2: Lift due to sudden incidence variation compared to the steady case as a function of dimensionless time (or distance traveled in semi-chords). The red curve is Wagner's function. Compared to the steady case, it takes time for the lift to build up. After  $tV/b > 16$ , the unsteady lift is 90% of the steady case.

Aeroelastic equations are more conveniently expressed in frequency-domain as functions of  $k$ . The reduced frequency is zero  $k = 0$  for steady-state aerodynamics and static aeroelastic phenomena such as divergence. Roughly speaking, it is possible to ignore non-stationary effects for quasi-steady flows when  $0 < k \leq 0.05$ . Unsteady aerodynamic effects must be accounted for when  $k > 0.05$ , which is the case for gust response and flutter problems. Based on experience, for a full-size airplane flutter occurs up to  $k \approx 1$ . Figure 3.3 illustrates the physical meaning of the reduced frequency for a harmonically-oscillating freestream (or, equivalently, for an oscillating airfoil in uniform freestream). Equation (3.5) provided the means for computing the unsteady lift for arbitrary downwash in time-domain. Other linear potential theory solutions have been developed in frequency-domain for harmonic motion because aerodynamic loads can be described easily by a superposition of sines. Theodorsen's function (A.37) models the frequency-dependent amplitude reduction and phase lag of a harmonically-oscillating airfoil relative to the steady case [THEODORSEN, 1935] (see figure 3.4). Its role in the unsteady aerodynamics of thin airfoils and frequency-domain is developed fully in [BISPLINGHOFF ET AL., 1996] and [RODDEN, 2011].

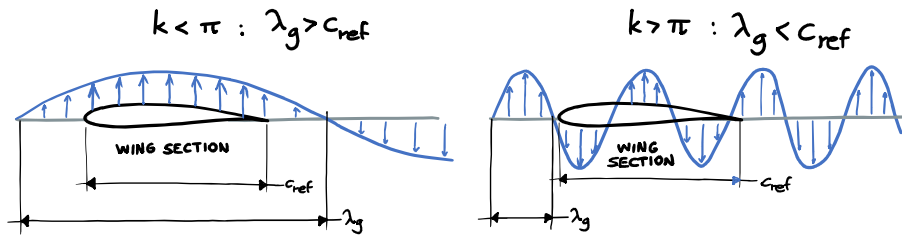


FIGURE 3.3: Incoming continuous gust with wavelength  $\lambda_g$  compared to an airfoil with chord  $c_{ref}$ . The reduced frequency  $k$  compares the time scales of the unsteadiness and the time needed by the airflow to travel by a semi-chord. When the reduced frequency is very low, the downwash induced by the gust is almost constant along the profile.

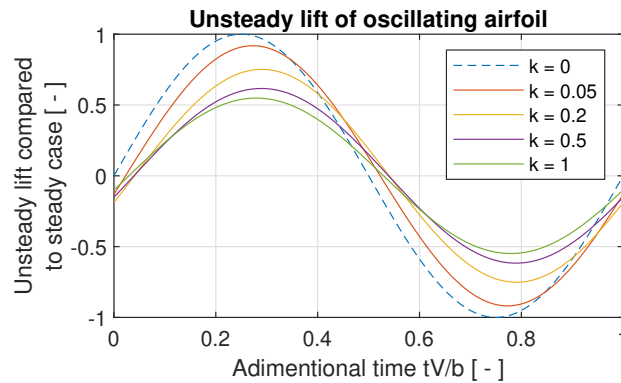


FIGURE 3.4: Lift amplitude reduction and phase lag according to Theodorsen's function (A.37) for an oscillating airfoil compared to steady values (dashed line). For  $k \rightarrow 0$  both amplitude reduction and phase lag tend to zero. For  $k \rightarrow \infty$ , the amplitude tends to 0.5 and phase lag to 0 compared to the steady case.

### 3.1.2 Calculation of the aerodynamic influence coefficients

Ultimately, the goal of the unsteady aerodynamics theory is to describe the aerodynamic forces  $\mathbf{f}_a(\omega)$  induced by the the generalized (modal) coordinates  $\mathbf{q}(\omega)$  by determining the *aerodynamic influence coefficients* (AIC) matrix<sup>2</sup>  $\mathbf{Q}(k)$  [WRIGHT AND COOPER, 2007]:

$$\mathbf{f}_a(\omega) = q_\infty \mathbf{Q}(k) \mathbf{q}(\omega) \quad (3.7)$$

The term  $\mathbf{Q}_{ij}(k)$  relates the  $j$ -th modal displacement  $\mathbf{q}_j$  and velocity  $\dot{\mathbf{q}}_j$  with the  $i$ -th aerodynamic force  $\mathbf{f}_{a,i}$ :

$$\mathbf{Q}_{ij}(k) = \frac{\partial \mathbf{c}_i(k)}{\partial \mathbf{q}_j} + ik \frac{\partial \mathbf{c}_i(k)}{\partial \dot{\mathbf{q}}_j} \quad (3.8)$$

where  $\frac{\partial \mathbf{c}_i(k)}{\partial \mathbf{q}_j}$  and  $\frac{\partial \mathbf{c}_i(k)}{\partial \dot{\mathbf{q}}_j}$  are the Jacobians of the aerodynamic coefficients  $\mathbf{c}_i(k)$  with respect to  $\mathbf{q}_j(t)$  and its derivative  $\dot{\mathbf{q}}_j(t)$ . The units of  $\mathbf{Q}(k)$  depend on the method used to calculate it because  $\mathbf{f}_a(t)$  and  $\mathbf{q}(t)$  are often dimensionless. In the steady case, the term  $ik \frac{\partial \mathbf{c}_i(k)}{\partial \dot{\mathbf{q}}_j}$  is zero and aerodynamic forces only depend on displacements (static aeroelasticity and maneuvers). Within the assumptions of the theory thus far, equation (3.7) linearizes the forces induced by the motion of the structure's fluid boundary according to the amplitude but retains the frequency dependency. The AIC matrix is square but complex and asymmetric and introduces additional coupling terms; section 3.1.4 will illustrate how it is used to solve the aeroelastic equation of motion. For realistic, complex aeroelastic models, the AIC matrix is computed numerically for a given Mach number and discrete set of reduced frequencies using coupled computational fluid dynamics (CFD) or panel methods. Depending on the application, three-dimensional, compressibility, transient or nonlinear effects are modeled for several points in the flight envelope and for different aircraft configurations:

- *CFD techniques* solve numerically the partial differential equations governing the flow by discretizing the fluid domain into small cells. In the framework of aeroelasticity, the fluid dynamics core is coupled with the structural dynamics equations. CFD can simulate the onset of turbulence, flow separation and shockwaves and has thus great predictive power in the transonic regime where nonlinearities appear. However, its high computational cost prevents it from covering the whole flight envelope of an aircraft. An overview of CFD approaches is found in [RAVEH, 2005].
- *Panel methods* represent the lift distribution using aerodynamic potential flow theory, whereby the flow velocity field around the aircraft is expressed by a superposition of flow singularities. The lifting surface of the aircraft and the wake are subdivided into a mesh of panels, each with a *vortex* or *doublet* element and a control point. Each panel generates a velocity field that induces a force on any other. A comprehensive introduction to panel methods is found in [KATZ AND PLOTKIN, 2001]. Figures 3.5 and 3.6 provide an elementary illustration of the concept.

<sup>2</sup> In aeroelastic software packages (see [VOSS, 2020b] and references therein), the AIC matrix is defined as  $\Delta \mathbf{c}_p = \mathbf{AIC} \cdot \mathbf{w}$  where  $\Delta \mathbf{c}_p \triangleq (p - p_\infty)/q_\infty$  is the pressure difference induced on each panel by the adimensional downwash  $\mathbf{w}$  of any other. Despite the same name used for different matrices, both express the same concept.

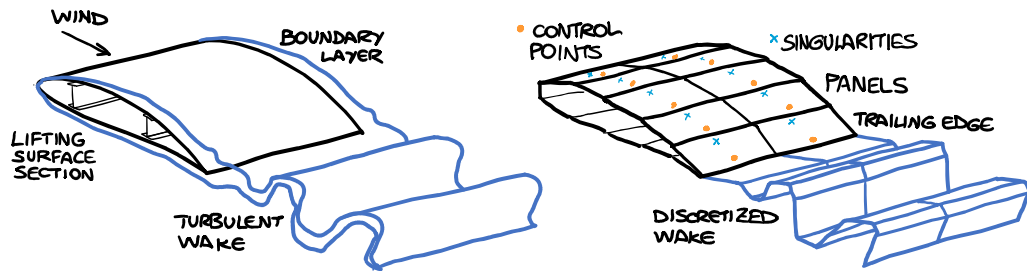


FIGURE 3.5: Simplified illustration of the panel method. The lifting surface and the wake are discretized into panels. Each panel’s vortex or doublet element induces a potential/velocity field describing the airflow around the object sampled at the control points.

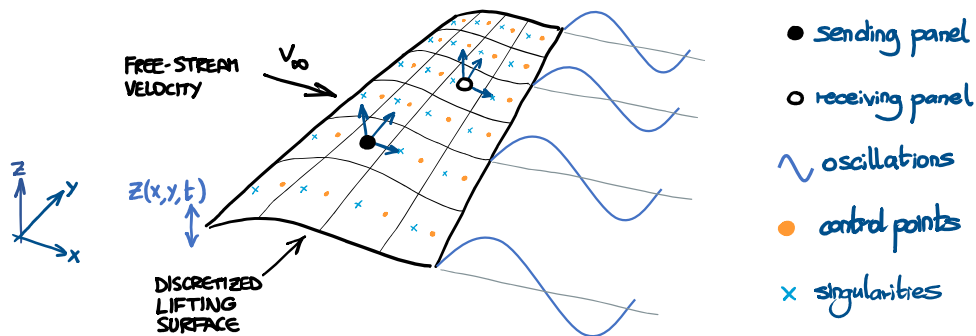


FIGURE 3.6: Schematic representation of panel method applied to a lifting surface undergoing harmonic oscillations. The downwash produced by each “sending” panel on any “receiving” panel is accounted to compute the pressure acting on the latter (that is, to determine the whole velocity field around the lifting surface). The physically consistent solution is found by imposing zero normal velocity at the surface of the panel and that a streamline detaches from the trailing edge. The forces acting on the lifting surface can be calculated from the geometry and velocity at the control points.

In unsteady aerodynamics the effect of a pressure disturbance of each point on the structure due to the downwash on any other is described by Küssner’s integral for the general wing theory [KÜSSNER, 1941]. This integral is evaluated numerically in the doublet lattice method (DLM) or the unsteady vortex lattice method (UVLM) in order to construct the AIC. DLM requires no wake modeling due to the evaluation of the acceleration potential, which is zero in the free wake. On the other hand, the wake must be modeled with UVLM because it evaluates the velocity potential and thus requires much more computational effort. DLM applied to unsteady aerodynamics has been introduced in [ALBANO AND RODDEN, 1969]. For a short introduction on DLM theory, see [NAM ET AL., 2001]. A detailed description and complete application of DLM to aeroelastic problems is found in [SCHWOCHOW, 2013]. A UVLM approach for highly-flexible aircraft structures is described in [RITTER, 2019]. An implementation and validation of both methods with respect to commercial packages is presented in [VOSS, 2020b]; the references therein offer additional information about historical developments and current applications. For the certification of new aircraft types, regulation CS 25.629 [EASA, 2007; FAA, 2014] requires the analysis of aeroelastic response by three-dimensional unsteady panel methods because they generally lead to better modeling of the aerodynamic interference between lifting surfaces. The main advantage of panel methods over CFD is that the AIC can be calculated

in advance without knowing the mode shapes because it only dependent on geometry, reduced frequency and Mach number. Panel methods assume that the flow is inviscid and incompressible and require corrections to include compressibility and nonlinear effects arising in the transonic regime [CROUSE AND LEISHMAN, 1992; FRIEDEWALD ET AL., 2018; GUPTA, 1997]. Nevertheless they provide an analytical relationship between mechanical and aerodynamic forces that is rich in predictive capability. Given their simplicity and speed compared to CFD, panel methods in the subsonic and supersonic regimes are still considered acceptable means for compliance for aeroelastic modeling in the industry [WRIGHT AND COOPER, 2007]. Within the scope of this thesis it is not necessary to completely elucidate the process for calculating the AIC matrix, but rather how it is employed, which will become clearer in the next section.

### 3.1.3 Aeroelastic equation of motion

The development of the aeroelastic equation of motion in the present subsection follows [GUPTA ET AL., 1991] and [NAM ET AL., 2001].

**Notation.** *In aerodynamics, free-stream quantities have subscript “ $\infty$ ” while local quantities have no subscript. In this chapter we only ever consider the free-stream quantities (3.1), therefore the subscript is omitted for readability.*

Let us consider a time-invariant second-order mechanical system (2.8) with  $N_m$  degrees of freedom that is subject to aerodynamic forces modeled by equation (3.7):

$$\tilde{\mathbf{M}}\ddot{\tilde{\mathbf{q}}}(t) + \tilde{\mathbf{D}}\dot{\tilde{\mathbf{q}}}(t) + \tilde{\mathbf{K}}\tilde{\mathbf{q}}(t) + q\tilde{\mathbf{Q}}(k)\tilde{\mathbf{q}}(t) = \tilde{\mathbf{f}}(t) \quad (3.9)$$

where the symbols denote (in physical coordinates):

$\tilde{\mathbf{M}} \in \mathbb{R}^{N_m \times N_m}$	mass matrix
$\tilde{\mathbf{D}} \in \mathbb{R}^{N_m \times N_m}$	damping matrix
$\tilde{\mathbf{K}} \in \mathbb{R}^{N_m \times N_m}$	stiffness matrix
$\tilde{\mathbf{Q}}(k) \in \mathbb{C}^{N_m \times N_m}$	aerodynamic influence coefficients matrix (AIC)
$\tilde{\mathbf{q}}(t) \in \mathbb{R}^{N_m}$	displacement vector
$\tilde{\mathbf{f}}(t) \in \mathbb{R}^{N_m}$	external forces

Equation (3.9) in the time-domain requires a convolution integral for the aerodynamic term. Here time and frequency domain terms appear at the same time, which may confuse the reader; using the approximation introduced by [ROGER, 1977], the integral can be replaced by the aerodynamic model in time-domain with the introduction of lag states. We shall provide more details in the next two sections.

The coordinate  $\tilde{\mathbf{q}}(t)$  describes rigid body, elastic and control surface degrees of freedom. However, the equation of motion of aeroelastic systems is usually written in modal space (generalized displacements), therefore we shall apply a coordinate transformation that is valid for the rest of the chapter. The mode shapes  $\Psi$  of the underlying undamped

mechanical system are

$$\mathbf{M}\ddot{\tilde{\mathbf{q}}}(t) + \mathbf{K}\tilde{\mathbf{q}}(t) = \mathbf{0} \quad \xrightarrow{eig} \quad \Lambda, \Psi \quad (3.10)$$

The coordinate transformation  $\tilde{\mathbf{q}}(t) = \Psi\mathbf{q}(t)$  of equation (3.9) yields:

$$\mathbf{M}\ddot{\mathbf{q}}(t) + \mathbf{D}\dot{\mathbf{q}}(t) + \mathbf{K}\mathbf{q}(t) + q\mathbf{Q}(k)\mathbf{q}(t) = \mathbf{f}(t) \quad (3.11)$$

where  $\mathbf{q}(t)$  are now the generalized coordinates in modal space and

$$\begin{aligned} \mathbf{M} &\triangleq \Psi^{-1}\tilde{\mathbf{M}}\Psi & \mathbf{Q}(k) &\triangleq \Psi^{-1}\tilde{\mathbf{Q}}(k)\Psi \\ \mathbf{D} &\triangleq \Psi^{-1}\tilde{\mathbf{D}}\Psi & \mathbf{f}(t) &\triangleq \Psi^{-1}\tilde{\mathbf{f}}(t) \\ \mathbf{K} &\triangleq \Psi^{-1}\tilde{\mathbf{K}}\Psi \end{aligned} \quad (3.12)$$

The generalized mass, damping and stiffness matrices describe the underlying mechanical system subject only to inertial and elastic forces. The AIC matrix expresses the combined effects of lifting surface airloads, pressure coefficients, gusts, control surfaces, structure motion and deformation.

### 3.1.4 Rational function approximation of aerodynamic influence coefficients

The aerodynamic influence coefficients matrix (3.7) is generally computed for a *discrete* set of  $N$  reduced frequencies  $k$  as  $\mathbf{Q}[k]$ , but we need a *continuous* function of the reduced frequency  $\mathbf{Q}(k)$  to be able to solve the equation of motion. We proceed according to the established aeroelastic modeling introduced in [ROGER, 1977] and [ABEL, 1979] by applying a rational function approximation of the type:

$$\mathbf{Q}[k] \approx \mathbf{Q}(k) = \mathbf{Q}_0 + ik\mathbf{Q}_1 + (ik)^2\mathbf{Q}_2 + \sum_{j=1}^{N_l} \frac{ik}{ik + \gamma_j} \mathbf{Q}_{j+2} \quad \begin{array}{l} \mathbf{Q}_j \in \mathbb{R}^{N_m \times N_m} \\ \gamma_j \in \mathbb{R} \end{array} \quad (3.13)$$

where  $\mathbf{Q}_j$  are called *aerodynamic matrices* and  $\gamma_j$  are the *aerodynamic lag terms*. The former are the unknowns, while the latter are chosen to have a low least-squares error of the approximant. The choice of the approximant's form will become apparent in the next section. The rational terms in the last equation can be written as:

$$\frac{ik}{ik + \gamma_j} = \frac{k^2}{k^2 + \gamma_j^2} + i \frac{k\gamma_j}{k^2 + \gamma_j^2} \quad (3.14)$$

in order to separate the real and imaginary parts of the known discrete AIC matrix:

$$\begin{bmatrix} \Re\mathbf{Q}[k] \\ \Im\mathbf{Q}[k] \end{bmatrix} = \begin{bmatrix} \mathbf{I} & \mathbf{0} & -k^2\mathbf{I} & \frac{k^2}{k^2 + \gamma_1^2}\mathbf{I} & \cdots & \frac{k^2}{k^2 + \gamma_{N_l}^2}\mathbf{I} \\ \mathbf{0} & \mathbf{I} & \mathbf{0} & \frac{k\gamma_1}{k^2 + \gamma_1^2}\mathbf{I} & \cdots & \frac{k\gamma_{N_l}}{k^2 + \gamma_{N_l}^2}\mathbf{I} \end{bmatrix} \begin{bmatrix} \mathbf{Q}_0 \\ \vdots \\ \mathbf{Q}_{N_l} \end{bmatrix} \quad (3.15)$$

This is performed in order to force the unknowns  $\mathbf{Q}_0, \dots, \mathbf{Q}_{N_l}$  to be real. Likewise, the lag terms are assumed to be real to make sure that only damping is introduced into the system, otherwise additional poles might appear and render the system unstable. The last equation can be written for all  $N$  known reduced frequencies  $k$  simultaneously:

$$\begin{bmatrix} \Re \mathbf{Q}[k_1] \\ \Im \mathbf{Q}[k_1] \\ \vdots \\ \Re \mathbf{Q}[k_N] \\ \Im \mathbf{Q}[k_N] \end{bmatrix} = \left( \begin{bmatrix} 1 & 0 & -k_1^2 & \frac{k_1^2}{k_1^2 + \gamma_1^2} & \cdots & \frac{k_1^2}{k_1^2 + \gamma_{N_l}^2} \\ 0 & 1 & 0 & \frac{k_1 \gamma_1}{k_1^2 + \gamma_1^2} & \cdots & \frac{k_1 \gamma_{N_l}}{k_1^2 + \gamma_{N_l}^2} \\ \vdots & \vdots & \vdots & \vdots & \vdots & \vdots \\ 1 & 0 & -k_N^2 & \frac{k_N^2}{k_N^2 + \gamma_1^2} & \cdots & \frac{k_N^2}{k_N^2 + \gamma_{N_l}^2} \\ 0 & 1 & 0 & \frac{k_N \gamma_1}{k_N^2 + \gamma_1^2} & \cdots & \frac{k_N \gamma_{N_l}}{k_N^2 + \gamma_{N_l}^2} \end{bmatrix} \otimes \mathbf{I} \right) \begin{bmatrix} \mathbf{Q}_0 \\ \vdots \\ \mathbf{Q}_{N_l} \end{bmatrix} \quad (3.16)$$

$$\xrightarrow{\text{def}} [\mathbf{Q}] = [\mathbf{P}][\mathbf{X}]$$

where  $[\mathbf{Q}] \in \mathbb{R}^{2NN_x \times N_x}$  are the real and imaginary parts of the discrete AIC matrix  $\mathbf{Q}[k]$ ,  $[\mathbf{P}] \in \mathbb{R}^{2NN_x \times (N_l+3)N_x}$  the known lag and reduced frequency terms and  $[\mathbf{X}]$  the unknowns  $\mathbf{Q}_0, \dots, \mathbf{Q}_{N_l}$  in the rational function approximation (3.13). The solution is computed by pseudoinverse:

$$[\mathbf{X}] = [\mathbf{P}]^+[\mathbf{Q}] \implies [\mathbf{X}] = \left( \sum_{j=1}^N \mathbf{P}_j^T \mathbf{P}_j \right)^+ \left( \sum_{j=1}^N \mathbf{P}_j^T \mathbf{Q}_j \right) \quad (3.17)$$

Various optimization and iterative methods can be applied to obtain a good fit with the minimal number of lag terms [KARPEL, 1982; TIFFANY AND ADAMS, 1988]. An example of the rational functional approximation of the AIC is shown in figure 3.7. A method based on tangential interpolation applied to aeroelastic modeling is proposed in [QUERO ET AL., 2021], together with a detailed comparison between established techniques.

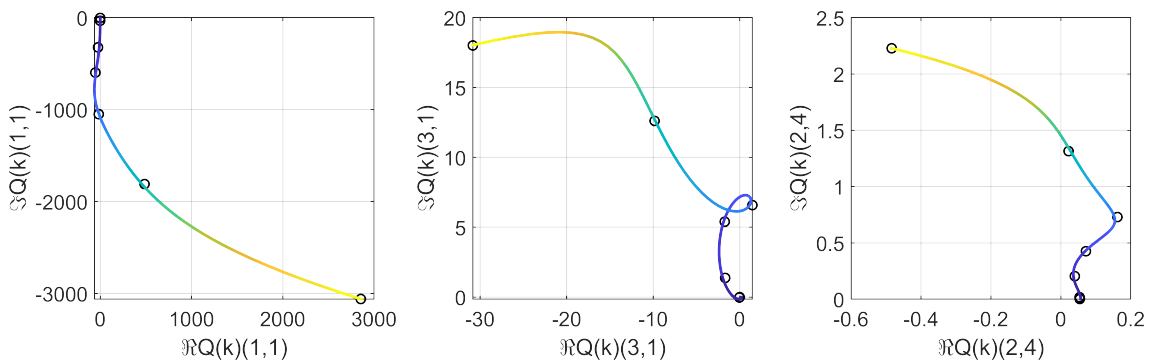


FIGURE 3.7: The plots display three entries of the complex-valued AIC matrix of a sailplane model [SCHWOCHOW, 2013] ( $N_m = 23$ ). The black circles represent the known  $\mathbf{Q}[k]$  at the reduced frequencies  $k = [0.001, 0.01, 0.1, 0.2, 0.4, 0.8, 1.6]$ . The chosen lag states are  $\gamma = [0.2, 0.4, 0.6, 0.8]$ . The resulting rational function approximation  $\mathbf{Q}(k)$  is represented by lines (blue: low  $k$ , yellow: high  $k$ ) and provides a good continuous representation of the AIC matrix. It can be seen that as  $k \rightarrow 0$ , then  $\Im \mathbf{Q}(k) \rightarrow 0$  (steady aeroelastic case).

### 3.1.5 Aeroelastic model: state matrix

Now that a continuous representation of the aerodynamic influence coefficients is available, the assembly of the aeroelastic state matrix can be elucidated. We shall consider for now only the free vibration case; external forces can be added by superposition. The homogeneous equation of motion in modal coordinates (3.11) can be combined with the continuous representation of the AIC matrix (3.13) to yield [GUPTA ET AL., 1991]:

$$\begin{aligned} \left(\mathbf{M} + q(b/V)^2 \mathbf{Q}_2\right) \ddot{\mathbf{q}}(t) + \left(\mathbf{D} + q(b/V) \mathbf{Q}_1\right) \dot{\mathbf{q}}(t) + \left(\mathbf{K} + q \mathbf{Q}_0\right) \mathbf{q}(t) + \dots \\ + q \sum_{j=1}^{N_l} \mathbf{Q}_{j+2} \mathbf{z}_j(t) = \mathbf{0} \end{aligned} \quad (3.18)$$

where the aerodynamic lag states  $\mathbf{z}_j(t)$  follow from equation (3.13):

$$\mathbf{z}_j(s) \triangleq \frac{s}{s + \gamma_j V/b} \mathbf{q}(s) \quad \bullet \text{---} \circ \quad \dot{\mathbf{z}}_j(t) = \dot{\mathbf{q}}(t) - \gamma_j V/b \mathbf{z}_j(t) \quad \in \mathbb{R}_x^N \quad (3.19)$$

The mass, damping and stiffness matrices are thus augmented by aerodynamic terms:

$$\begin{aligned} \hat{\mathbf{M}} &\triangleq \mathbf{M} + q(b/V)^2 \mathbf{Q}_2 &\equiv \mathbf{M} + \frac{1}{2} \rho b^2 \mathbf{Q}_2 &\quad \text{dynamic mass} \\ \hat{\mathbf{D}} &\triangleq \mathbf{D} + q(b/V) \mathbf{Q}_1 &\equiv \mathbf{D} + \frac{1}{2} \rho b V \mathbf{Q}_1 &\quad \text{dynamic damping} \\ \hat{\mathbf{K}} &\triangleq \mathbf{K} + q \mathbf{Q}_0 &\equiv \mathbf{K} + \frac{1}{2} \rho V^2 \mathbf{Q}_0 &\quad \text{dynamic stiffness} \end{aligned} \quad (3.20)$$

The structural matrices  $\mathbf{M}$ ,  $\mathbf{D}$  and  $\mathbf{K}$  from equation (3.12) are symmetric, while the associated AIC terms  $\mathbf{Q}_2$ ,  $\mathbf{Q}_1$  and  $\mathbf{Q}_0$  are not. The dynamic matrices (3.20) are functions of air density and air speed. A better impression of the system's dynamics is obtained by arranging equation (3.18) into a state-space model<sup>3</sup> according to equation (2.9):

$$\begin{bmatrix} \mathbf{I} & & & & \\ & \hat{\mathbf{M}} & & & \\ & & \mathbf{I} & & \\ & & & \ddots & \\ & & & & \mathbf{I} \end{bmatrix} \frac{d}{dt} \begin{Bmatrix} \mathbf{q} \\ \dot{\mathbf{q}} \\ \mathbf{z}_1 \\ \vdots \\ \mathbf{z}_{N_l} \end{Bmatrix} = \begin{bmatrix} \mathbf{0} & \mathbf{I} & \mathbf{0} & \dots & \mathbf{0} \\ -\hat{\mathbf{K}} & -\hat{\mathbf{D}} & -q \mathbf{Q}_3 & \dots & -q \mathbf{Q}_{N_l+2} \\ \mathbf{0} & \mathbf{I} & -\gamma_1 V/b \mathbf{I} & \dots & \mathbf{0} \\ \vdots & \vdots & \vdots & \ddots & \vdots \\ \mathbf{0} & \mathbf{I} & \mathbf{0} & \dots & -\gamma_{N_l} V/b \mathbf{I} \end{bmatrix} \begin{Bmatrix} \mathbf{q} \\ \dot{\mathbf{q}} \\ \mathbf{z}_1 \\ \vdots \\ \mathbf{z}_{N_l} \end{Bmatrix} \quad (3.21)$$

or, compactly:

$$\mathbf{E} \dot{\mathbf{x}}(t) = \mathbf{A} \mathbf{x}(t) \quad (3.22)$$

where  $\mathbf{E}$ ,  $\mathbf{A} \in \mathbb{R}^{N_x \times N_x}$  are respectively the descriptor matrix and augmented state matrix, while  $N_x = N_m(2 + N_l)$  is their size. The state vector  $\mathbf{x}(t) = \{\mathbf{q}(t), \dot{\mathbf{q}}(t), \mathbf{z}(t)\}$  includes the underlying mechanical system's generalized displacements  $\mathbf{q}(t)$  and the lag states  $\mathbf{z}(t)$  modeling the unsteady aerodynamics. The state matrix is solely a function of  $\{\rho, V\}$ , therefore the system is parameter-varying since there is no explicit time-dependency. It

<sup>3</sup> Some authors place the term  $q \mathbf{Q}(k)$  on the right hand side of equation (3.9), therefore, in the state matrix, the aerodynamic terms  $q \mathbf{Q}_j$  and the lower diagonal terms  $\gamma_j V/b$  have positive sign.



is recognizable that, the lower the dynamic pressure, the weaker the coupling between mechanical degrees of freedom and lag states. The system's stability can be analyzed by solving the generalized eigenvalue problem:

$$\mathbf{E}\Psi\Lambda = \mathbf{A}\Psi \quad (3.23)$$

If the descriptor matrix is nonsingular, it is possible to use the explicit form of the system:

$$\mathbf{E}^{-1}\mathbf{A} = \begin{bmatrix} \mathbf{0} & \mathbf{I} & \mathbf{0} & \cdots & \mathbf{0} \\ -\hat{\mathbf{M}}^{-1}\hat{\mathbf{K}} & -\hat{\mathbf{M}}^{-1}\hat{\mathbf{D}} & -q\hat{\mathbf{M}}^{-1}\mathbf{Q}_3 & \cdots & -q\hat{\mathbf{M}}^{-1}\mathbf{Q}_{N_l+2} \\ \mathbf{0} & \mathbf{I} & -\gamma_1 V/b\mathbf{I} & \cdots & \mathbf{0} \\ \vdots & \vdots & \vdots & \ddots & \vdots \\ \mathbf{0} & \mathbf{I} & \mathbf{0} & \cdots & -\gamma_{N_l} V/b\mathbf{I} \end{bmatrix} \quad (3.24)$$

The state matrix has  $2N_m$  complex-conjugate pairs of lightly-damped eigenvalues representing the physical poles and additional  $N_m N_l$  purely real or highly-damped aerodynamic poles. The characteristic sparsity pattern assumed by models based on Roger's formulation [KARPEL, 1981; NAM ET AL., 2001] is shown in figure 3.8.

Figure 3.9 displays a typical frozen-time pole evolution diagram for an aeroelastic system undergoing a parameter change and crossing the instability boundary. Time is normalized by duration because, given a set of parameters  $\{\rho, V\}$ , the state matrix  $\mathbf{A}(\rho(t), V(t))$  is always the same. The poles are displayed on an eigenfrequency-damping ratio plot and in the complex plane. A look at the eigenvalues of the state matrix reveals the contribution of the aerodynamic forces. The magnitude of aerodynamic poles correlates strongly with speed according to equation (3.19), therefore they often wander into the frequency range of

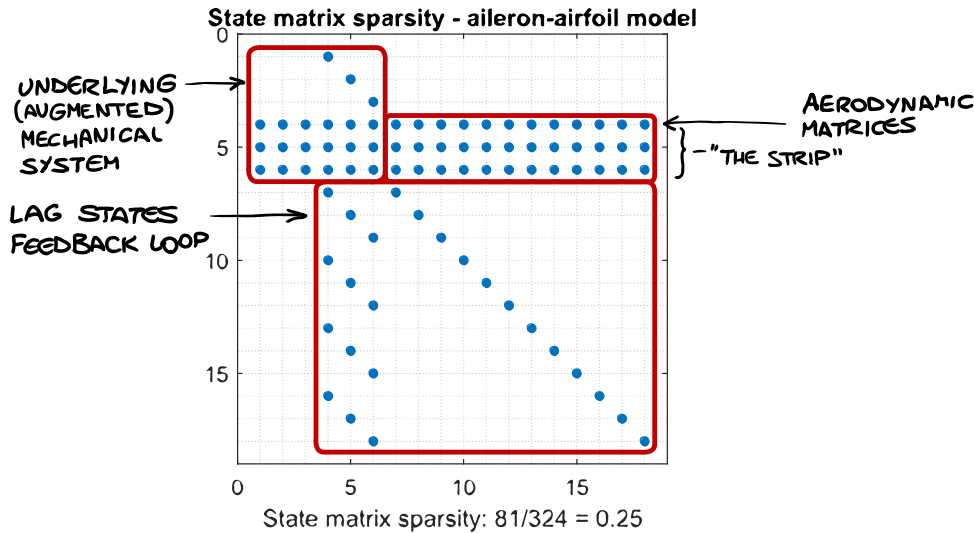
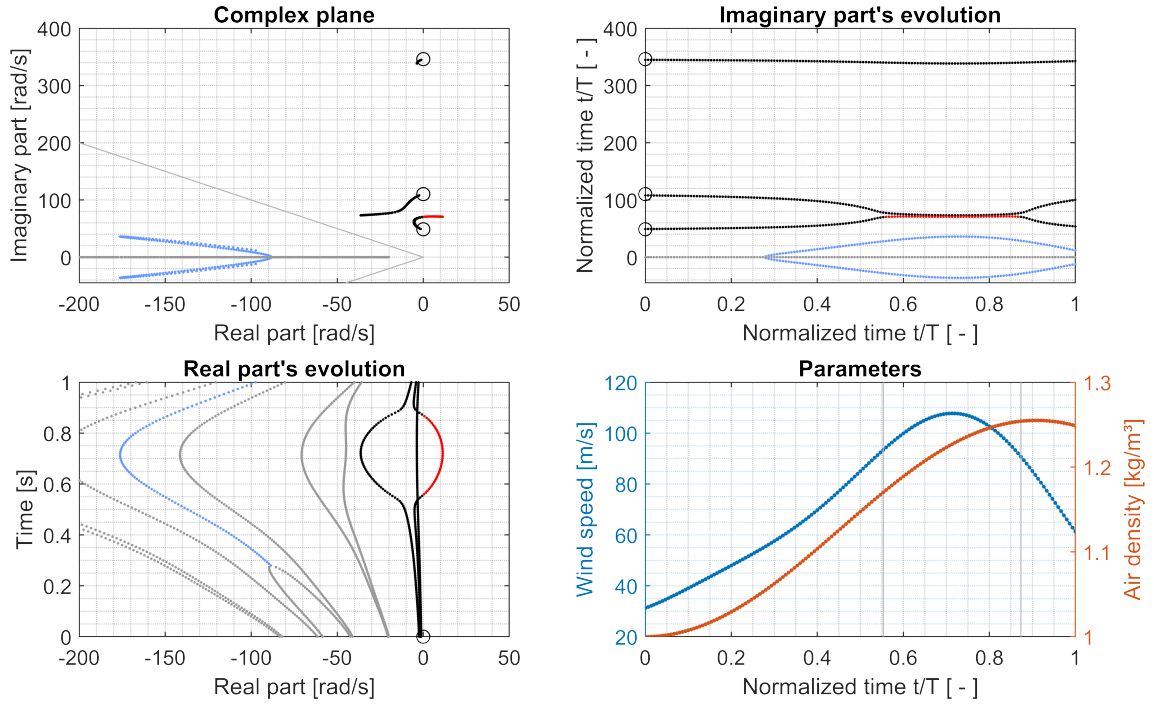
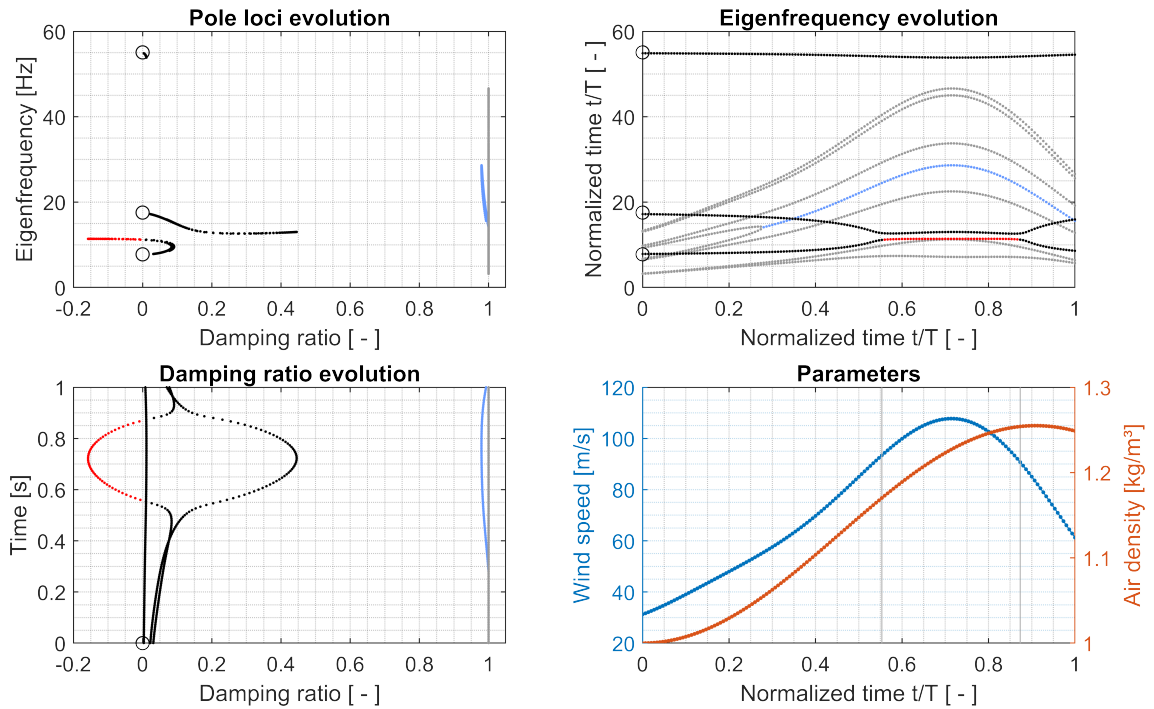


FIGURE 3.8: Typical sparsity plot of the system matrices of an aeroelastic model. The upper left corner describes the underlying mass-damping-stiffness mechanical system. The upper right part contains the rational part of the AIC matrix. The lower part is the feedback loop of the lag states. In this example there are 3 physical degrees-of-freedom and 4 lag states for a total of  $3 \cdot (2 + 4) = 18$  states.



(A) Frozen-time pole loci in the complex plane



(B) Frozen-time pole loci in the eigenfrequency-damping ratio plane

FIGURE 3.9: Example frozen-time poles of the aeroelastic model 7.2 as a function of time. The parameter variation has been chosen so that this example is as rich as possible. The circles are the underlying mechanical system’s poles. The dots represent the system eigenvalues (see figure 2.9): red – unstable, black – lightly-damped, gray – purely real, light blue – highly-damped. Vertical lines in the lower right plots: unstable region boundaries. The diagonal straight lines are where  $\zeta = \pm\sqrt{2}/2$ , or  $|\Re\lambda| = \Im\lambda$ . See text for discussion.

physical poles, but maintain a distinctively high damping ratio. The physical eigenvalues gather next to the imaginary axis, whereas the aerodynamic eigenvalues cluster next to the real axis as shown in figure 3.9. This phenomenon was already observed in [ROGER, 1977]. Two purely real poles are seen splitting into one complex-conjugate pair with high damping. Despite the system being linear, such sudden bifurcation behavior is commonly observed in the dynamics of time-varying or parameter-varying systems (see for example figure 2.12). The locus of  $\{\rho, V\}$  pairs where the system's minimal damping is zero defines the boundary of its stability region. When the damping ratio of an eigenmode becomes negative, the system starts absorbing energy from the stream and its response amplitude grows without bound.

Aeroelastic modeling can generate very large sparse state matrices, therefore techniques for achieving the minimal number of lag states have been developed by modeling their feedback loop with full matrices. The aerodynamic influence coefficient matrix can be represented by a non-proper rational function [KARPEL, 1982; RIPEPI AND MANTEGAZZA, 2013]:

$$\mathbf{Q}(k) = \mathbf{Q}_0 + ik\mathbf{Q}_1 + (ik)^2\mathbf{Q}_2 + \mathbf{C}_a(ik\mathbf{E}_a - \mathbf{A}_a)^{-1}\mathbf{B}_a \quad (3.25)$$

The matrices  $\mathbf{A}_a$ ,  $\mathbf{B}_a$ ,  $\mathbf{C}_a$  and  $\mathbf{E}_a$  can be determined with standard system identification methods [LIND, 1998]. Recently, [GOSEA ET AL., 2020] applied the Loewner framework to this type of problem. The rational function form of the AIC matrix (3.25) is used to construct a state-space model with generalized displacements  $\mathbf{q}(t)$  in input and aerodynamic forces  $\mathbf{f}_a(t)$  in output [PASINETTI AND MANTEGAZZA, 1999]:

$$\begin{aligned} \mathbf{E}_a\dot{\mathbf{z}}(t) &= V/b\mathbf{A}_a\mathbf{z}(t) + V/b\mathbf{B}_a\mathbf{q}(t) \\ \mathbf{f}_a(t) &= q\mathbf{C}_a\mathbf{z}(t) + q\mathbf{Q}_0\mathbf{q}(t) + qb/V\mathbf{Q}_1\dot{\mathbf{q}}(t) + q(b/V)^2\mathbf{Q}_2\ddot{\mathbf{q}}(t) \end{aligned} \quad (3.26)$$

where  $\mathbf{z}(t)$  are the lag states. Following this same principle used to derive the state matrix of the aeroelastic model in section 3.1.5, we can write:

$$\begin{bmatrix} \mathbf{I} & & \\ & \hat{\mathbf{M}} & \\ & & \mathbf{E}_a \end{bmatrix} \frac{d}{dt} \begin{Bmatrix} \mathbf{q} \\ \dot{\mathbf{q}} \\ \mathbf{z} \end{Bmatrix} = \begin{bmatrix} \mathbf{0} & \mathbf{I} & \mathbf{0} \\ -\hat{\mathbf{K}} & -\hat{\mathbf{D}} & -q\mathbf{C}_a \\ -V/b\mathbf{B}_a & \mathbf{0} & -V/b\mathbf{A}_a \end{bmatrix} \begin{Bmatrix} \mathbf{q} \\ \dot{\mathbf{q}} \\ \mathbf{z} \end{Bmatrix} \quad (3.27)$$

where the dynamic mass damping and stiffness matrices are defined as before. Compared to equation (3.21), here  $\mathbf{A}_a$  and  $\mathbf{B}_a$  are full, resulting in possibly less states. The modeling approach in [KIM, 2019] and related publications produces aeroelastic matrices where the number of lag states is only  $N_l = 2N_m$ .

### 3.1.6 State matrix inverse

The state matrix of aeroelastic systems (3.24) has a noteworthy block structure that can be exploited by a divide-and-conquer algorithm to compute its inverse efficiently, for instance in the simulation of time-varying aeroelastic systems. This will be helpful in section 7.1 where numerical methods are presented. The aeroelastic model's state matrix (3.24) can be subdivided into blocks

$$\mathbf{E}^{-1} \mathbf{A} \triangleq \begin{bmatrix} \mathbf{A}_{11} & \mathbf{A}_{12} \\ \mathbf{A}_{21} & \mathbf{A}_{22} \end{bmatrix}$$

where the four sub-matrices are:

$$\begin{aligned} \mathbf{A}_{11} &\triangleq \begin{bmatrix} \mathbf{0} & \mathbf{I} \\ -\hat{\mathbf{M}}^{-1} \hat{\mathbf{K}} & -\hat{\mathbf{M}}^{-1} \hat{\mathbf{D}} \end{bmatrix} & \mathbf{A}_{21} &\triangleq \begin{bmatrix} \mathbf{0} & \mathbf{I} \\ \vdots & \vdots \\ \mathbf{0} & \mathbf{I} \end{bmatrix} \\ \mathbf{A}_{12} &\triangleq -q \hat{\mathbf{M}}^{-1} \begin{bmatrix} \mathbf{0} & \cdots & \mathbf{0} \\ \mathbf{Q}_3 & \cdots & \mathbf{Q}_{N_l} \end{bmatrix} & \mathbf{A}_{22} &\triangleq -\frac{V}{b} \text{diag}\{\gamma\} \otimes \mathbf{I} \end{aligned} \quad (3.28)$$

The block matrix inversion formula [BERNSTEIN, 2009, Eq. 2.8.17] with the lower-right block  $\mathbf{A}_{22}$  as pivot is:

$$\begin{bmatrix} \mathbf{A}_{11} & \mathbf{A}_{12} \\ \mathbf{A}_{21} & \mathbf{A}_{22} \end{bmatrix}^{-1} = \begin{bmatrix} \mathbf{P}^{-1} & -\mathbf{P}^{-1} \mathbf{A}_{12} \mathbf{A}_{22}^{-1} \\ -\mathbf{A}_{22}^{-1} \mathbf{A}_{21} \mathbf{P}^{-1} & \mathbf{A}_{22}^{-1} + \mathbf{A}_{22}^{-1} \mathbf{A}_{21} \mathbf{P}^{-1} \mathbf{A}_{12} \mathbf{A}_{22}^{-1} \end{bmatrix} \quad (3.29)$$

where  $\mathbf{A}_{22}$  and  $\mathbf{P} \triangleq \mathbf{A}_{11} - \mathbf{A}_{12} \mathbf{A}_{22}^{-1} \mathbf{A}_{21}$  must be non-singular. After some simplifications the state matrix inverse turns out to be:

$$\mathbf{A}^{-1} \mathbf{E} = \begin{bmatrix} -\hat{\mathbf{K}}^{-1} (\hat{\mathbf{D}} + \mathbf{D}_a) & -\hat{\mathbf{K}}^{-1} \hat{\mathbf{M}} & -qb/V \gamma_1^{-1} \hat{\mathbf{K}}^{-1} \mathbf{Q}_3 & \cdots & -qb/V \gamma_{N_l}^{-1} \hat{\mathbf{K}}^{-1} \mathbf{Q}_{N_l} \\ \mathbf{I} & \mathbf{0} & \mathbf{0} & \cdots & \mathbf{0} \\ b/V \gamma_1^{-1} \mathbf{I} & \mathbf{0} & b/V \gamma_1^{-1} \mathbf{I} & \cdots & \mathbf{0} \\ \vdots & \vdots & \vdots & \ddots & \vdots \\ b/V \gamma_{N_l}^{-1} \mathbf{I} & \mathbf{0} & \mathbf{0} & \cdots & b/V \gamma_{N_l}^{-1} \mathbf{I} \end{bmatrix} \quad (3.30)$$

where  $\mathbf{D}_a \triangleq q \frac{b}{V} \sum_{j=1}^{N_l} \gamma_j^{-1} \mathbf{Q}_{j+2}$  is the damping induced by aerodynamic coupling terms. This strategy's strength lies in the fact that  $\mathbf{A}_{22}$  is diagonal<sup>4</sup> and  $\mathbf{A}_{11}$  is smaller than the whole state matrix by a factor  $2/(2 + N_l)$  (e.g. with four lag states,  $2/(2 + 4) = 0.33$ ). It is reminded that matrix inversion has the same time complexity  $\mathcal{O}(N_x^3)$  as matrix multiplication. Both the construction of the state matrix (3.24) and its inverse (3.30) requires the calculation of  $\hat{\mathbf{M}}^{-1}$  and  $\hat{\mathbf{K}}^{-1}$  respectively, therefore computational complexity is the same. Equation (3.30) provides a means for the fast calculation of  $\mathbf{A}^{-1} \mathbf{E}$  when the number of states and lag terms is large. This is particularly desirable in the parameter-varying case.

<sup>4</sup> If aerodynamic forces are modeled as in equation (3.25), the  $\mathbf{A}_{22} = -V/b \mathbf{A}_a$  term can be diagonalized by solving a generalized eigenvalue problem.

### 3.1.7 Aeroelastic model: full state-space formulation

Now that the plant dynamics have been described, it is conceptually simple to include the inhomogeneous terms and the output equation. The aeroelastic system can be thus portrayed by the implicit state-space formulation:

$$\begin{aligned} \mathbf{E}\dot{\mathbf{x}}(t) &= \mathbf{A}\mathbf{x}(t) + \mathbf{B}\mathbf{u}(t) \\ \mathbf{y}(t) &= \mathbf{C}\mathbf{x}(t) + \mathbf{D}\mathbf{u}(t) \end{aligned} \quad (3.31)$$

When  $\mathbf{E} = \mathbf{I}$  the system is said to be in explicit form. Depending on the application at hand,  $\mathbf{B}$ ,  $\mathbf{C}$  and  $\mathbf{D}$  assume different forms [GUPTA ET AL., 1991; RIPEPI AND MANTEGAZZA, 2013] (they must be consistent with the modeling employed to augment the state matrix). The input matrix models the forced response, the influence of control surfaces or gusts (see section (3.3)). The output matrix relates the generalized coordinates with the structural displacements or velocities and includes often matrices that transform the states into sensor outputs. The feed-through matrix can be used to describe control surface motions or the influence of gusts. Here we shall consider the basic formulation for  $\mathbf{B}$ ,  $\mathbf{C}$  and  $\mathbf{D}$  that results from the second-order mass-damping-stiffness model (2.9) (3.11) (it is assumed that the state-space model is implicit, therefore the descriptor matrix  $\mathbf{E}$  is not necessarily an identity matrix). The input matrix in this case is:

$$\mathbf{B} = \begin{bmatrix} \mathbf{0} \\ \mathbf{I} \\ \vdots \\ \mathbf{0} \end{bmatrix} \in \mathbb{R}^{N_m(2+N_l) \times N_m} \quad (3.32)$$

Section 3.3 will show how the input matrix is modified to include the influence of gusts. For displacements or velocities, the output matrix is respectively:

$$\mathbf{C} = \begin{bmatrix} \mathbf{I} & \mathbf{0} & \cdots & \mathbf{0} \end{bmatrix} \quad \text{or} \quad \mathbf{C} = \begin{bmatrix} \mathbf{0} & \mathbf{I} & \cdots & \mathbf{0} \end{bmatrix} \in \mathbb{R}^{N_y \times N_m(2+N_l)} \quad (3.33)$$

Finally the feed-through matrix is zero:

$$\mathbf{D} = \mathbf{0} \in \mathbb{R}^{N_y \times N_u} \quad (3.34)$$

It is reminded once more that in order to obtain a solution in the physical domain, the modal responses must be converted back into physical coordinates. Likewise, the physical forces entering the system must be transformed into modal space.

## 3.2 Flutter mechanism

Flutter is a kind of self-exciting linear dynamic instability of aeroelastic structures. It manifests when the system extracts energy from the stream and the resulting positive feedback increases the vibration amplitude until structural failure is reached. It can have such violence that a wing is ripped apart in seconds. Flutter must not be confused with resonance, where, in the absence of damping, an excitation with a frequency component equal to an eigenfrequency leads to a linearly-increasing response amplitude, whereas it grows exponentially irrespective of the excitation's character in an unstable system. Buffeting, another dynamic instability, occurs from airflow separations or shock wave oscillations, but it is not modeled by the linear potential theory employed here.

The avoidance of flutter is a critical task in aircraft design and in the definition of the flight envelope [EASA, 2007; FAA, 2014]. For a fixed altitude, the flutter speed is the minimal air speed at which one eigenmode becomes unstable. A historical, but detailed and widely-cited study of aircraft flutter is [SCANLAN AND ROSENBAUM, 1952]. Classical flutter usually involves the coupling of two or more degrees of freedom. Non-classical flutter is associated to flow separation phenomena [RODDEN, 2011]. The presence of any structural, aerodynamic or control nonlinearities in the system can give rise to limit cycle oscillations, a type of stationary and bounded flutter. The special case of limit cycle oscillations with nonlinear aerodynamics is treated in detail in [ROOIJ, 2017]. In real-world problems, nonlinear characteristics of actuators and control surfaces may effectively reduce the dynamic stiffness of the system. In such cases, small oscillations may be unstable, while large ones maintain a limited amplitude. The most frequently encountered and dangerous situation is instability with small oscillations – flutter is thus analyzed by linear techniques [BISPLINGHOFF ET AL., 1996; RODDEN, 2011].

In the aeroelastic equation of motion (3.18) we see that aerodynamic damping is added to the structural one. The latter is often ignored because of uncertainties in its modeling, unless determined from measurements. In a real aircraft, structural damping provides an additional mechanism for energy dissipation, therefore it is always beneficial in terms of flutter. Likewise, nonlinear effects that provide some margin to flutter onset such as cubic stiffening or geometric nonlinearities are conservatively neglected, but may be favorable in flutter assessments [IOVNOVICH ET AL., 2018]. Active control techniques greatly improve flutter suppression [KARPEL, 1982]; an extensive overview of this topic is found in [LIVNE, 2018]. Under stationary conditions, due to the influence of aerodynamics, the damping ratio of some eigenmodes increases steadily with speed, reaches a maximum that is appreciably higher than what the structure alone has in wind-off conditions and then starts to decrease. The introduction of aerodynamic damping of heave/bending oscillations increases the damping ratio of wing modes substantially: for example, aircraft wings have low structural damping (under 3%), but aerodynamic effects can increase it to more than 20% and even to 100% for pure heave motion in aperiodic condition. At the flutter boundary where the net damping is zero, the system undergoes harmonic motion. Any further reduction leads to instability of critical eigenmodes.

Depending on the gradient of the damping reduction, flutter can be classified into:

- *Hard flutter*: the damping ratio decrease is sudden and pronounced.
- *Soft flutter*: the damping decrease is gentle and the system may eventually recover from instability for higher speeds.

Figure 3.10 illustrates the two types of flutter with two configurations of an airfoil-rudder model (see section 7.2). The flutter boundary is determined using a frozen-time formulation that, strictly speaking, is valid only in the time-invariant case. Time-varying dynamics can excite or dampen the system, i.e. to stabilize (destabilize) a previously unstable (stable) condition, as we have seen in chapter 2. In the LPV case it is necessary to study the path traversed by the parameters and their rate of change, e.g. the instantaneous eigenvalues may cross into the positive Laplace half-plane without impacting stability (see figure 2.6). For slowly-varying systems it is possible to apply the LTI stability criteria or at least to assert that the proximity to the flutter boundary can lead to a large response RMS and must be avoided.

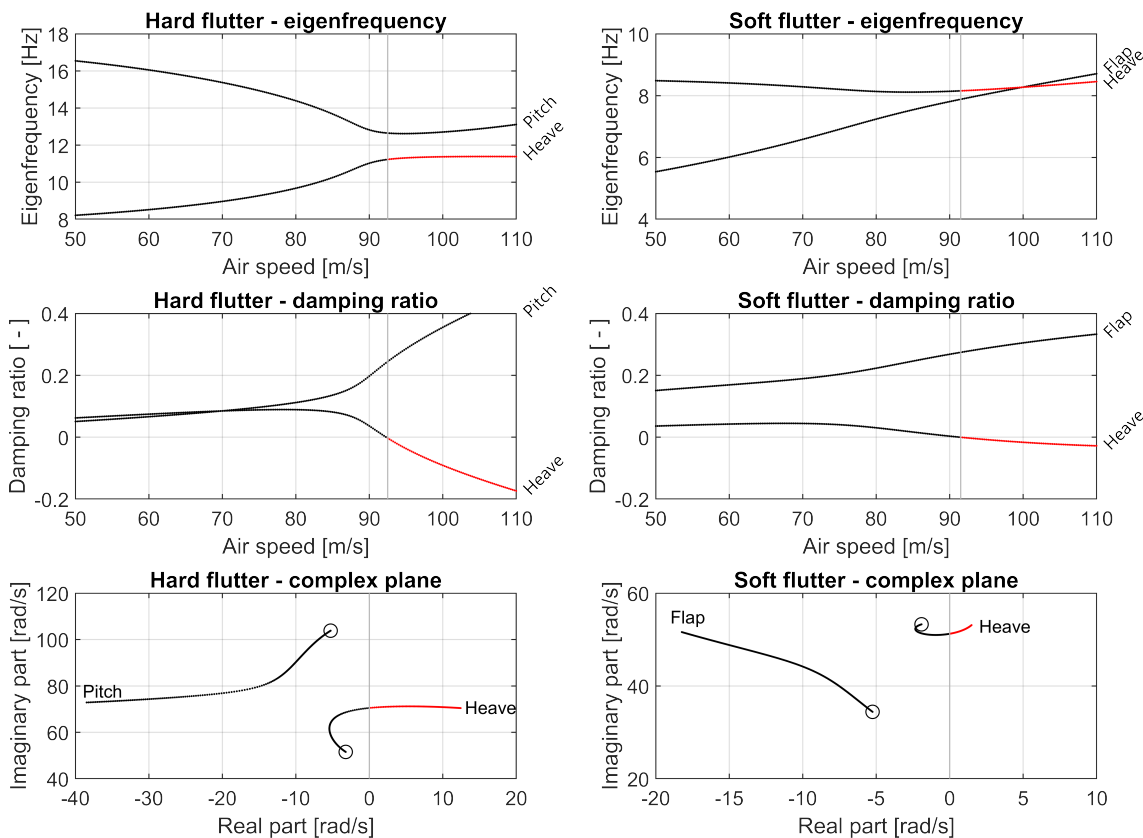


FIGURE 3.10: Example of typical flutter curves, in this case two configurations of an airfoil with rudder for constant air density 7.2. The degrees of freedom are the heave and pitch of the airfoil and the flapping of the rudder. The red dots are unstable eigenvalues. Hard flutter can be observed on the left side: the heave and the pitch modes come closer and then the damping of the former plummets. Soft flutter is illustrated on the right side: the damping decrease is much slower and the system eventually recovers from instability for higher speeds (not pictured). The flutter speeds are 92.2 m/s and 91.3 m/s for  $\rho = 1.225 \text{ kg/m}^3$ .

### 3.3 Wind turbulence model

Aircraft are subject to atmospheric turbulence resulting in gust loads that vary in space and time. The observed turbulent flow encountered by aircraft is described by the von Kármán and the Dryden wind models. The book from [HOBLIT, 1988] is a prime reference on this topic. The von Kármán wind turbulence model is usually adopted because it matches experimental data better than the Dryden model, but in the present research the choice is inconsequential since both have a low-pass characteristic with slightly different roll-off. The Dryden model is analytically simpler because it has integer frequency powers in its transfer function. Nevertheless, we proceed with the Von Kármán model because its use is more common in aircraft design. The gust power spectral densities  $\Phi(\omega)$  for the longitudinal, lateral and vertical directions are given in [HOBLIT, 1988, Eq. 4.16-4.17] as a function of angular frequency  $\omega$ :

$$\begin{aligned}\Phi_u(\omega) &= \sigma_u^2 \frac{2L_g/V}{\pi} \frac{1}{(1 + \nu^2)^{\frac{5}{6}}} \\ \Phi_v(\omega) &= \sigma_v^2 \frac{L_g/V}{\pi} \frac{1 + \frac{8}{3}\nu^2}{(1 + \nu^2)^{\frac{11}{6}}} \\ \Phi_w(\omega) &= \sigma_w^2 \frac{L_g/V}{\pi} \frac{1 + \frac{8}{3}\nu^2}{(1 + \nu^2)^{\frac{11}{6}}}\end{aligned}\quad \nu \triangleq 1.339 \frac{L_g}{V} \omega \quad [\text{adim}] \quad (3.35)$$

where  $\sigma$  is the gust velocity component's variance,  $L_g = 2500 \text{ ft} = 762 \text{ m}$  is the characteristic turbulence scale used in design and  $V$  is the wind speed. The variable  $\nu$  is essentially a scaled reduced frequency. The gusts have zero mean (e.g., there is no preferred lateral direction), therefore  $\Phi(0) = 0$  must be set. The lateral and vertical PSDs are equal, while the longitudinal (fore-aft) gust is seldom needed. Wind turbulence spectra for angular rates contribute less to the aircraft gust response than the turbulence velocity spectra and are thus ignored here. Figure 3.11 displays, for several wind speeds, a vertical gust computed by transforming a frequency-domain signal with random uniformly-distributed phase and amplitude shaped as the von Kármán spectrum (3.35). Analytical gust spectra lose physical significance at very low frequencies as motivated in [HOBLIT, 1988, Ch. 4.5],

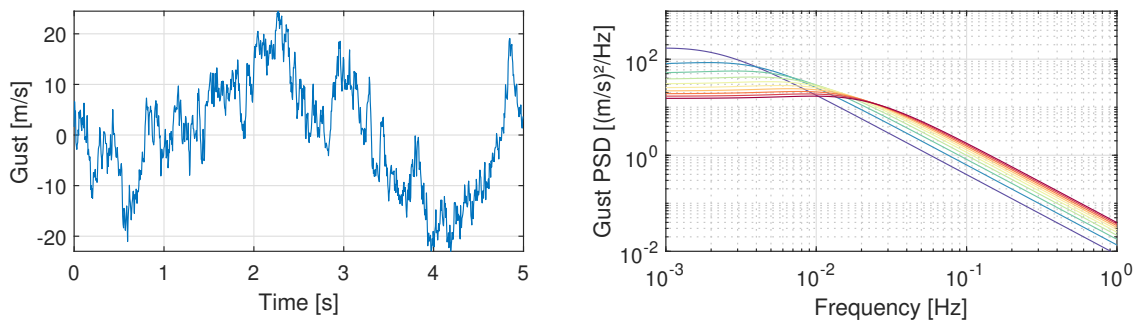


FIGURE 3.11: Vertical Von Kármán gust. The gust's low-pass characteristic is visible in the time-domain data, where high-frequency components are visibly attenuated. The analytical spectra (3.35) are displayed on the right for different wind speeds (blue – low, red – high).



but this is not a concern for design or for our modeling. The von Kármán model's power spectral density does not have integer frequency powers in its numerator, therefore some very accurate rational filter approximations are available for forming white noise into a colored spectrum [U.S. DEPARTMENT OF DEFENSE, 1997]:

$$\begin{aligned}
H_u(s) &= \sigma_u \sqrt{\frac{2\tau}{\pi}} \cdot \frac{1 + 0.25\tau s}{1 + 1.357\tau s + 0.1987\tau^2 s^2} \\
H_v(s) &= \sigma_v \sqrt{\frac{\tau}{\pi}} \cdot \frac{1 + 2.7478\tau s + 0.3398\tau^2 s^2}{1 + 2.9958\tau s + 1.9754\tau^2 s^2 + 0.1539\tau^3 s^3} \\
H_w(s) &= \sigma_w \sqrt{\frac{\tau}{\pi}} \cdot \frac{1 + 2.7478\tau s + 0.3398\tau^2 s^2}{1 + 2.9958\tau s + 1.9754\tau^2 s^2 + 0.1539\tau^3 s^3}
\end{aligned} \tag{3.36}$$

where  $s = i\omega$ ,  $\tau \triangleq L_g/V$  and the range of validity is  $\tau\omega < 50$  rad. These filters are required for the calculation of gusts whose spectrum varies with speed.

The input matrix for gust excitation is assembled depending on the aeroelastic modeling technique employed to construct the state matrix (3.21) [RIPEPI AND MANTEGAZZA, 2013]. The full state space model in our case is:

$$\begin{aligned}
\dot{\mathbf{x}}(t) &= \mathbf{A}\mathbf{x}(t) + \mathbf{B}_0^g \mathbf{u}(t) + \mathbf{B}_1^g \dot{\mathbf{u}}(t) \\
\mathbf{y}(t) &= \mathbf{C}\mathbf{x}(t) + \mathbf{D}\mathbf{u}(t)
\end{aligned} \tag{3.37}$$

where the input matrix models the effect of the gust velocity  $\mathbf{u}(t)$  and its derivative onto the system's mechanical degrees of freedom and lag states:

$$\mathbf{B}_0^g = \frac{q}{V} \begin{bmatrix} \mathbf{0} \\ -\mathbf{Q}_0^g \\ \mathbf{0} \\ \vdots \\ \mathbf{0} \end{bmatrix} \quad \mathbf{B}_1^g = \frac{q}{V} \begin{bmatrix} \mathbf{0} \\ -(b/V)\mathbf{Q}_1^g \\ \mathbf{Q}_3^g \\ \vdots \\ \mathbf{Q}_{N_l}^g \end{bmatrix} \tag{3.38}$$

where the  $\mathbf{Q}^g$  matrices are gust-related terms. The derivative  $\dot{\mathbf{u}}(t)$  can be calculated by applying a differentiator filter (see, for example [BRANDT, 2011]) or by analytical differentiation when the input signal is formed from random-phase multi-sines. A better option is to reformulate the state-space model. Let us define the new state variable  $\mathbf{x}'(t) \triangleq \mathbf{x}(t) - \mathbf{B}_1^g \mathbf{u}(t)$  and put it into the previous equation to get a state-space model without the input derivative<sup>5</sup>  $\dot{\mathbf{u}}(t)$ :

$$\begin{aligned}
\dot{\mathbf{x}}'(t) &= \mathbf{A}\mathbf{x}'(t) + (\mathbf{A}\mathbf{B}_1^g + \mathbf{B}_0^g) \mathbf{u}(t) \\
\mathbf{y}(t) &= \mathbf{C}\mathbf{x}'(t) + (\mathbf{C}\mathbf{B}_1^g + \mathbf{D}) \mathbf{u}(t)
\end{aligned} \tag{3.39}$$

<sup>5</sup> Alternatively, the convolution property  $\mathbf{H}(t) * \frac{d}{dt} \mathbf{u}(t) = \frac{d}{dt} \mathbf{H}(t) * \mathbf{u}(t)$  can be used.

### 3.4 Time-dependency of system matrices

The aeroelastic model has been derived for stationary parameters  $\{\rho, V\}$  following the established state-space model found in literature [ABEL, 1979; ROGER, 1977]. In this section we include the time-dependency in the parameters  $\{\rho(t), V(t)\}$  to study the frequency content of the system matrices and of the instantaneous eigenvalues. Let us rewrite the expressions for dynamic mass, damping and stiffness (3.20) with explicit time-dependency<sup>6</sup>:

$$\begin{aligned}\hat{\mathbf{M}}(t) &= \mathbf{M} + \frac{1}{2}\rho(t)b^2\mathbf{Q}_2 \\ \hat{\mathbf{D}}(t) &= \mathbf{D} + \frac{1}{2}\rho(t)V(t)b\mathbf{Q}_1 \\ \hat{\mathbf{K}}(t) &= \mathbf{K} + \frac{1}{2}\rho(t)V^2(t)\mathbf{Q}_0\end{aligned}\quad (3.41)$$

We are interested in the relationship between parameter variation and system matrices. Instead of studying the effect of air density and speed in terms of influence coefficients, we want to know how their frequency content is reflected in the system's eigenvalues. To this end, we develop the air density and air speed into Fourier series:

$$\rho(t) = \sum_{k \in \mathbb{S}} \rho_k e^{ik\omega_0 t} \quad V(t) = \sum_{k \in \mathbb{S}} V_k e^{ik\omega_0 t} \quad (3.42)$$

where  $\mathbb{S}$  is the set of harmonics<sup>7</sup>. This should provide some insight concerning “slow” and “fast” system variation in the perspective of modal parameter estimation.

Let us consider a generic time-dependent matrix  $\mathbf{P}(t)$  that can be expressed as a Fourier series:

$$\mathbf{P}(t) = \sum_{k=-\infty}^{+\infty} \mathbf{P}_k e^{ik\omega_0 t} \quad (3.43)$$

We start by providing some general results. The positive powers  $\mathbf{P}^n(t)$  can be determined by applying the Cauchy product repeatedly. Squaring the matrix provides the prototype for all other powers:

$$\left( \sum_{k=-\infty}^{+\infty} \mathbf{P}_k e^{ik\omega_0 t} \right) \cdot \left( \sum_{k=-\infty}^{+\infty} \mathbf{P}_k e^{ik\omega_0 t} \right) = \sum_{k=-\infty}^{\infty} \left( \sum_{h=0}^k \mathbf{P}_{k-h} \mathbf{P}_h \right) e^{ik\omega_0 t} = \sum_{k \in \mathbb{Z}} \mathbf{P}'_k e^{ik\omega_0 t} \quad (3.44)$$

<sup>6</sup> In principle it is possible to include the derivatives of the dynamic mass, damping and stiffness matrices. The equation of motion of the underlying mechanical system could then look like:

$$\mathbf{M}(t)\ddot{\mathbf{x}}(t) + \left( \mathbf{D}(t) + \dot{\mathbf{M}}(t) \right) \dot{\mathbf{x}}(t) + \left( \mathbf{K}(t) + \dot{\mathbf{D}}(t) \right) \mathbf{x}(t) + \dot{\mathbf{K}}(t) \int_{t_0}^t \mathbf{x}(\tau) d\tau = \mathbf{0} \quad (3.40)$$

The dynamic terms depend on the specific problem and type of modeling that is carried out. For instance, in [HUANG AND QIU, 2013] the flutter analysis of a morphing vehicle is performed with constant first and second derivatives in order to solve the time-varying problem with a time-invariant model.

<sup>7</sup> The parameters and the system matrices are real and positive. The series is written using exponentials instead of trigonometric functions for compactness, therefore all harmonics are complex conjugates  $\pm k\omega_0$

where  $\mathbf{P}'_k$  are the new terms of  $\mathbf{P}(t)$  and where the fundamental frequency  $\omega_0$  is preserved. If  $\mathbf{P}(t)$  is described by a finite set  $\mathbb{S}$  of frequency components  $e^{i\omega_k t}$ , then

$$\mathbf{P}(t)^2 = \left( \sum_{k \in \mathbb{S}} \mathbf{P}_k e^{ik\omega t} \right)^2 = \sum_{k \in \mathbb{S} \times \mathbb{S}} \mathbf{P}'_k e^{ik\omega t} \quad (3.45)$$

It has been thus established, that positive powers  $\mathbf{P}^n(t)$  have frequency components  $k\omega_0$ , where the index  $k$  belongs to a discrete set that is finite if  $\mathbf{P}(t)$  has a finite number of harmonics. Finally, we recall that the inverse of  $(n\mathbf{I} - \mathbf{P})$  can be expressed as a Neumann series whenever the absolute value of  $\mathbf{P}$ 's eigenvalues is lower than 1:

$$(n\mathbf{I} - \mathbf{P})^{-1} = \sum_{k=0}^{\infty} (-1)^k n^{-k-1} \mathbf{P}^k \quad (3.46)$$

In light of the previous results we now see that the matrix inversion always produces an infinite set of discrete harmonics  $\pm k\omega_0$ .

### 3.4.1 Variation of system matrices

The physical degrees of freedom of an aeroelastic system are influenced by aerodynamic terms  $\mathbf{Q}_k$ , the dynamic pressure  $q(t)$  and dynamic mass  $\hat{\mathbf{M}}(t)$ :

$$\forall k = 3: N_l \quad \hat{\mathbf{M}}^{-1}(t) \cdot q(t) \mathbf{Q}_k \quad (3.47)$$

The inverse of the dynamic mass matrix can be written as:

$$\hat{\mathbf{M}}^{-1}(t) = \left( \mathbf{M} + \frac{1}{2} \rho(t) b^2 \mathbf{Q}_2 \right)^{-1} = \left( \mathbf{I} + \frac{1}{2} \rho(t) b^2 \mathbf{M}^{-1} \mathbf{Q}_2 \right)^{-1} \mathbf{M}^{-1} \quad (3.48)$$

After some simplifications we obtain  $\hat{\mathbf{M}}^{-1}(t)$  as a complex Fourier series:

$$\begin{aligned} \hat{\mathbf{M}}^{-1}(t) &= \sum_{n=0}^{\infty} \left( -\frac{1}{2} \rho(t) b^2 \mathbf{M}^{-1} \mathbf{Q}_2 \right)^n \mathbf{M}^{-1} \\ &= \sum_{n=0}^{\infty} (-1)^n \left( \frac{1}{2} b^2 \mathbf{M}^{-1} \mathbf{Q}_2 \right)^n \mathbf{M}^{-1} \left( \sum_{k \in \mathbb{S}} \rho_k e^{ik\omega_0 t} \right)^n \\ &= \sum_{k \in \mathbb{Z}} \mathbf{M}'_k e^{ik\omega_0 t} \end{aligned} \quad (3.49)$$

where  $\mathbf{M}'_n$  are the series terms that result from the Cauchy product. Similar results can be obtained for the dynamic damping and dynamic stiffness where air speed appears too. Speed plays generally a more prominent role because it appears in the lag states (3.19) and in practice it is more likely to vary considerably. We shall indeed see in chapter 8 that during flight vibration testing speed variation is more prominent than the altitude (air density) variation.

As an example, we consider independent variations of speed and density in the airfoil-rudder system 7.2. Figure 3.12 displays the frequency content of the state matrix when one parameter varies as  $p(t) = p_0 + p_1 \sin(\omega t)$  while the other is held constant.

- *Only air speed variation*  $\rho(t) = \rho_0$ ,  $V(t) = V_0 + V_1 \sin(\omega_0 t)$ : the mean value and fundamental harmonic of  $\mathbf{A}(t)$  are found respectively at  $\omega/\omega_0 = 0$  and  $\omega/\omega_0 = 1$ , but the speed squared in  $\hat{\mathbf{K}}(t) = \mathbf{K} + \frac{1}{2}\rho(t)V^2(t)\mathbf{Q}_0$  and  $q(t)\mathbf{Q}$  injects energy into  $\omega/\omega_0 = 2$  as well.
- *Only air density variation*  $\rho(t) = \rho_0 + \rho_1 \sin(\omega_0 t)$ ,  $V(t) = V_0$ : the term  $\hat{\mathbf{M}}^{-1}(t) = (\mathbf{M} + \frac{1}{2}\rho(t)b^2\mathbf{Q}_2)^{-1}$  spreads the energy over all multiples of the fundamental harmonic  $\omega_0$ , regardless of the number of harmonics in  $\rho(t)$ .

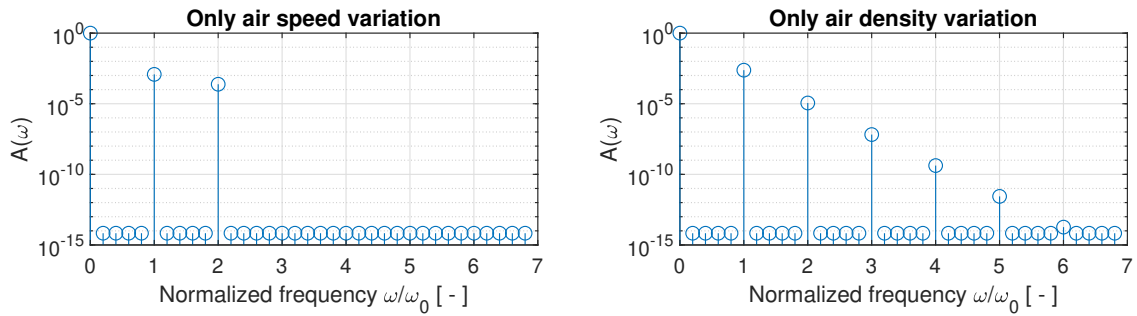


FIGURE 3.12: Frequency components of the state matrix for air speed and air density variations. The plot displays one entry of the time-varying state matrix  $\mathbf{A}(t)$  in frequency-domain. The key fact is that the harmonics are discrete and decaying. Left plot: only air speed variation  $\rho(t) = 1.225 \text{ kg/m}^3$ ,  $V(t) = 70 + 20 \sin(\omega_0 t) \text{ m/s}$ , two harmonics plus DC are correctly predicted. Right plot: only air density variation  $\rho(t) = 1.2 + 0.3 \sin(\omega_0 t) \text{ kg/m}^3$ ,  $V(t) = 80 \text{ m/s}$ , infinite number of decaying harmonics.

### 3.4.2 Variation of instantaneous eigenvalues

Time-dependency assumes a more complex role when dealing with the instantaneous eigenvalues of the system. In light of the linear transformation theorem (2.17), the eigendecomposition of the state matrix  $\mathbf{A}(t) = \Psi(t)\Lambda(t)\Psi^{-1}(t)$  transforms the system into:

$$\left[ \begin{array}{c|c} \mathbf{A}(t) & \mathbf{B}(t) \\ \hline \mathbf{C}(t) & \mathbf{D}(t) \end{array} \right] \xrightarrow[\text{transform}]{\mathbf{x}(t)=\Psi(t)\tilde{\mathbf{x}}(t)} \left[ \begin{array}{c|c} \mathbf{\Lambda}(t) - \Psi^{-1}(t)\dot{\Psi}(t) & \Psi^{-1}(t)\mathbf{B}(t) \\ \hline \mathbf{C}(t)\Psi(t) & \mathbf{D}(t) \end{array} \right] \quad (3.50)$$

where the transformed state matrix is not diagonal<sup>8</sup> because of the *mode coupling term*  $\Psi^{-1}(t)\dot{\Psi}(t)$ . It is reminded that the state matrix is a function of air density and speed

<sup>8</sup> From section 2.1.7: the system can be diagonalized using the Lyapunov matrix (2.32):

$$\mathbf{L}(t) \triangleq \Phi(t, t_0) \exp \left\{ - \int_{t_0}^t \tilde{\Lambda}(\tau) d\tau \right\} \implies \mathbf{x}(t) = \mathbf{L}(t)\tilde{\mathbf{x}}(t) \quad (3.51)$$

where  $\tilde{\Lambda}(t)$  is an *arbitrary* diagonal matrix, therefore the matrix exponential above is equal to a scalar exponential. However, the state transition matrix  $\Phi(t, t_0)$  must be known to apply this transformation, which may prove impractical and in general requires a numerical solution.

alone, therefore its entries and consequently its eigenvalues depend only on the parameter path regardless of their rate of variation. Assuming the instantaneous eigenvectors  $\Psi(t)$  and eigenvalues  $\Lambda(t)$  are  $\mathbb{C}^1$  continuous, they can be expressed as Fourier series:

$$\Lambda(t) = \sum_{k=0}^{\infty} \Lambda_k e^{ik\omega_0 t} \quad \Psi(t) = \sum_{k=0}^{\infty} \Psi_k e^{ik\omega_0 t} \quad \Psi^{-1}(t) = \sum_{k=0}^{\infty} \Psi'_k e^{ik\omega_0 t} \quad (3.52)$$

where the series terms  $\Psi'_k = f(\rho, v)$  are also only a function of parameters and not of time or period. This implies that the derivative is simply  $\dot{\Psi}(t) = \sum_{k \in \mathbb{S}} ik\omega_0 \Psi_k e^{ik\omega_0 t}$ . The terms  $\Psi'_k$  are decaying, so the series (3.52) can be approximated by few terms. The Fourier series of the transformed state matrix is then:

$$\begin{aligned} \tilde{\mathbf{A}}(t) &= \sum_{k=0}^{\infty} \Lambda_k e^{ik\omega_0 t} + \left( \sum_{k=0}^{\infty} \Psi'_h e^{ih\omega_0 t} \right) \left( \sum_{k=0}^{\infty} ik\omega_0 \Psi_k e^{ik\omega_0 t} \right) \\ &= \sum_{k=0}^{\infty} \left( \Lambda_k + ik\omega_0 \tilde{\Psi}_k \right) e^{ik\omega_0 t} \end{aligned} \quad (3.53)$$

where  $\tilde{\Psi}_k \triangleq \sum_{h=0}^k \Psi'_{k-h} \Psi_h$  are the dimensionless Fourier coefficients of the mode coupling term<sup>9</sup>. We can split it into a diagonal and off-diagonal part  $\tilde{\Psi}_k = \tilde{\Psi}_k^{di} + \tilde{\Psi}_k^{nd}$ :

$$\tilde{\mathbf{A}}(t) = \sum_{k=0}^{\infty} \left( \Lambda_k + ik\omega_0 \tilde{\Psi}_k^{di} \right) e^{ik\omega_0 t} + \sum_{k=0}^{\infty} ik\omega_0 \tilde{\Psi}_k^{nd} e^{ik\omega_0 t} \quad (3.54)$$

Equation (3.54) provides the means to quantify the magnitude of the dynamic coupling. When the system varies slowly or when the off-diagonal terms  $ik\omega_0 \tilde{\Psi}_k^{nd}$  can be neglected, the system's time-varying poles can be described by the  $\Lambda_k + ik\omega_0 \tilde{\Psi}_k^{di}$  terms. This observation can be used to justify a single-degree-of-freedom formulation for slowly-varying systems. The  $\Psi^{-1}(t)\dot{\Psi}(t)$  term is inversely proportional to the period  $\omega_0 = 2\pi/T$  and tends to vanish when  $\omega_0$  is small:

$$\lim_{\omega_0 \rightarrow 0} \tilde{\mathbf{A}}(t) = \lim_{\omega_0 \rightarrow 0} \sum_{k=0}^{\infty} \left( \Lambda_k + ik\omega_0 \tilde{\Psi}_k \right) e^{ik\omega_0 t} = \lim_{\omega_0 \rightarrow 0} \sum_{k=0}^{\infty} \Lambda_k e^{ik\omega_0 t} \quad (3.55)$$

The numerical approach used to determine the mode coupling term is to represent the time-varying eigenvectors as a Fourier series using the FFT. In practice this requires a preprocessing step where eigenvectors are scaled, rotated and sorted so that their entries are differentiable. The frozen-time eigenpairs must be tracked in order to have consistent sorting (see chapter 6). A smooth interpolation between the entries of consecutive eigenvectors that preserves the eigenspace can be obtained by solving the Procrustes problem (3.60) as detailed in section 3.4.3. Another problem that is difficult to address is the occurrence of bifurcations because they are singular points that have different right and left derivatives (see figure 3.9). As an example, the mode coupling term of an aeroelastic system is illustrated in figure 3.13.

<sup>9</sup> The mode coupling term may be easier to compute using the identity:  $\Psi^{-1}(t) \cdot \frac{d}{dt} \Psi(t) = \frac{d}{dt} \Psi^{-1}(t) \cdot \Psi(t)$

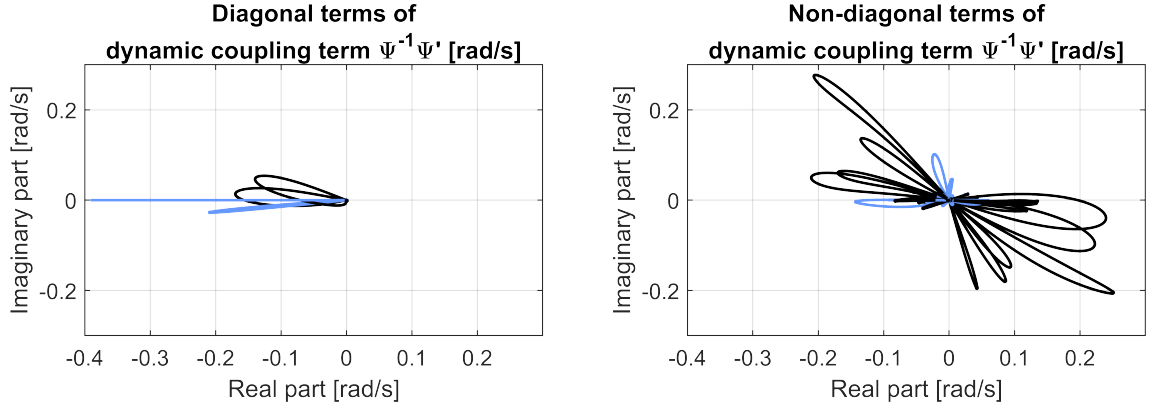


FIGURE 3.13: Dynamic coupling term of an aeroelastic system undergoing a sinusoidal parameter variation with  $\omega_0 = 1$  rad/s. The plots display the diagonal and non-diagonal elements of  $\Psi^{-1}(t)\dot{\Psi}(t)$ . The black lines are mode coupling terms corresponding to stable, physical poles; the blue lines those corresponding to aerodynamic lag states. Complex-conjugated pairs are excluded in the figure.

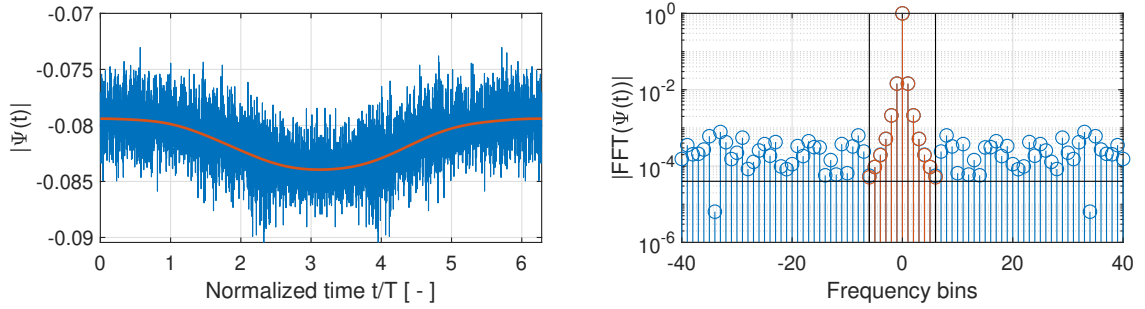


FIGURE 3.14: Numerical noise in the estimation of eigenvectors can be observed even when the parameter variation is smooth (in this case sinusoidal). The color blue refers to one entry of  $\Phi(t)$  as per eigendecomposition of  $\mathbf{A}(t)$ , the color red to the same entry after high-frequency noise components have been removed. The black lines are the thresholds.

The calculation of  $\Psi^{-1}(t)\dot{\Psi}(t)$  is hindered by the numerical high-frequency noise that is inevitably present in some entries of the eigenvector matrix. This noise can create disproportionate effects by the matrix inverse or the calculation of the first derivative. This issue can be addressed by carefully removing high-frequency and low-amplitude components. Figure 3.14 provides an example. The calculation of  $\dot{\Psi}(t)$  can be performed analytically from a regression function or by FFT differentiation if the parameter variation is periodic.

We can collect  $\Lambda(t)$  in the transformed state matrix and insert equation (3.52) to obtain

$$\Lambda(t) - \Psi^{-1}(t)\dot{\Psi}(t) = \Lambda(t) \left( \mathbf{I} - \frac{i\omega_0}{\Lambda(t)} \sum_{k \in \mathbb{Z}} \Psi'_k e^{ik\omega_0 t} \right) \quad (3.56)$$

The ratio  $i\omega_0/\Lambda(t)$  determines the importance of the mode coupling for a given parameter path  $\{\rho(t), V(t)\}$  (which in turn sets the terms  $\Psi'_k$ ) with respect to the instantaneous eigenvalues of the system.

The dimensionless frequency of parameter variation is thus defined as:

$$k_{\omega_0}(t) \triangleq \frac{\omega_0}{\min |\boldsymbol{\Lambda}(t)|} \quad [\text{adim}] \quad (3.57)$$

The higher  $k_{\omega_0}$  is, the more important is the dynamic effect of parameter variation. This criterion is easy to apply.

Alternatively it is possible consider the ratio between element  $(i, j)$  of the mode coupling term and the corresponding  $i$ -th eigenvalue:

$$k_{\Lambda,ij}(t) \triangleq \left| \frac{\mathbf{e}_i^T \boldsymbol{\Psi}^{-1}(t) \dot{\boldsymbol{\Psi}}(t) \mathbf{e}_j}{\boldsymbol{\Lambda}_i(t)} \right| \quad [\text{adim}] \quad (3.58)$$

This dimensionless parameter quantifies the importance of diagonal and off-diagonal terms of  $\boldsymbol{\Psi}^{-1}(t) \dot{\boldsymbol{\Psi}}(t)$ . If the latter are negligible compared to the former, the system is weakly coupled. The model reduction technique presented in [LUSPAY ET AL., 2018] performs a transformation of the time-varying system where the structure of the mode coupling is matched to the structure of the state matrix. The mode coupling's elements corresponding to the state matrix's zero entries are then ignored under the assumption that they do not contribute much the system's input-output behavior. Figure 3.15 displays the parameter  $k_{\Lambda}$  of an aeroelastic system undergoing a half-sinusoidal speed variation. Notice that there is no mode coupling where speed has a minimum or maximum (in this case respectively at  $t/T = 0$  and  $t/T = 1$ ). When the system is weakly dynamically coupled (approximately diagonal) its state transition matrix can be calculated analytically (see section 2.1.3). All things considered, the calculation of  $k_{\Lambda}$  is quite cumbersome even for medium-sized analytical systems, while the adimensional frequency  $k_{\omega_0}$  maintains its usefulness for relating parameter variation speed and system eigenvalues.

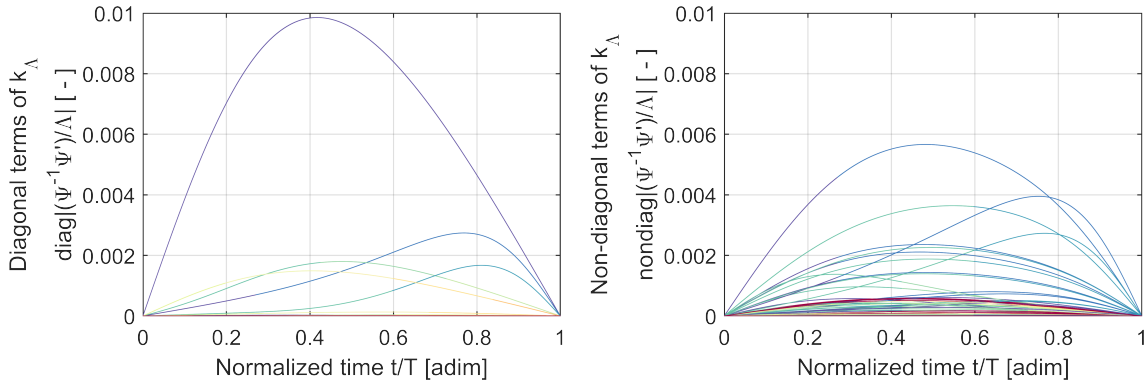


FIGURE 3.15: Scaled mode coupling  $k_{\Lambda}$  for diagonal elements for  $\omega_0 = 1$  rad/s (respectively for diagonal and non-diagonal elements). For example, reading from the right plot, if  $\omega_0 = 1$  rad/s ( $k_{\omega_0} = 0.02$ ) dynamic mode coupling contributes to less than 0.6% of the system's states. If the system varies faster  $\omega_0 = 10$  rad/s, then the coupling term's contribution increases to 6%. Reading from the left plot, the diagonal elements have a similar contribution, but they can be added to the instantaneous eigenvalues. The color represents the associated eigenvalues (blue: low, red: high). Judging by this criterion, the system is weakly coupled. This will be confirmed by simulations in chapter 7.

### 3.4.3 Eigenvector rotation

The eigenvectors may be rotated by an orthogonal matrix without altering their eigenspace. A smooth matrix interpolation between the entries of two consecutive eigenvectors  $\Psi_n$  and  $\Psi_{n+1}$  can be determined by solving an unconstrained Procrustes problem [GEUSS ET AL., 2013]. The goal is to determine the orthogonal matrix  $\mathbf{R}$  that maps the eigenvector as close as possible to the the preceding one

$$\Psi_{n+1} \approx \mathbf{R}\Psi_n \quad (3.59)$$

This can be stated as a minimization problem where  $\mathbf{R}$  is a rotation matrix:

$$\mathbf{Q} = \arg \min_{\mathbf{R}^H \mathbf{R} = \mathbf{I}} \|\mathbf{R}\Psi_n - \Psi_{n+1}\|_F \quad (3.60)$$

The matrix  $\mathbf{Q}$  preserves the eigenspace and norms of  $\Psi_{n+1}$  (i.e. the transformation is a rotation). Its solution is found by the singular value decomposition

$$\Psi_{n+1}^H \Psi_n \stackrel{\text{svd}}{=} \mathbf{U}\Sigma\mathbf{V}^H \implies \mathbf{Q} = \mathbf{U}\mathbf{V}^H \quad (3.61)$$

This procedure is repeated between all eigenvector pairs  $n : n + 1$

$$\Psi_{n+1} \leftarrow \Psi_{n+1} \mathbf{Q} \quad \forall n = 1 : N - 1 \quad (3.62)$$

The eigenvector rotation is put to use in section 3.4 to determine the dynamic coupling term  $\Psi^{-1}(t)\dot{\Psi}(t)$ . This technique will be applied again when comparing the mode shapes estimated from noisy output-only data to minimize the phase difference between each group of sensors. It is applied in the animated plots of two experimentally-determined mode shapes to assist the user in comparing and recognizing the modes of vibration.

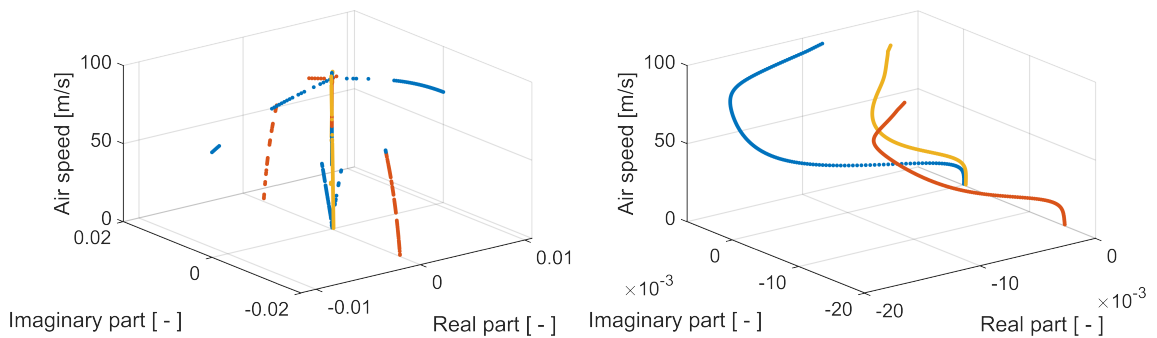


FIGURE 3.16: Eigenvectors of aeroelastic system C2 (refer to table 7.2) undergoing a linear air speed variation. The plots show the first row of  $\Psi(t)$  and the columns corresponding to the heave, pitch and flap modes (only one of the complex-conjugated pairs). Left plot: eigenvectors as computed by the eigendecomposition of the state matrix. Right plot: the solution to the Procrustes problem rotates the eigenvectors while preserving the eigenspace and creating smooth paths.



### 3.5 Chapter summary

The chapter introduced the linearized modeling of aeroelastic systems used to represent the interaction of inertial, elastic and aerodynamic forces.

The air stream around a structure exerts forces that deform its shape, which in turn affects the flow. The unsteady aerodynamic forces are linearly dependent on dynamic pressure and generalized displacement of the structure. This dependence is described by the aerodynamic influence coefficients matrix (AIC). This matrix is computed for a discrete set of reduced frequencies, therefore a continuous representation must be interpolated in order to construct the aeroelastic model. Various techniques exist for this purpose. Once this is done, the equation of motion of the underlying structure can be augmented to include aerodynamic terms. The eigenvalues of the resulting state matrix are a function of air density and air speed. In particular, it is possible to model the occurrence of flutter as an instability arising when damping becomes negative for certain combinations of airflow variables. The input, output and feedthrough matrices are constructed depending on the intended aeroelastic application, for example gust excitation. Wind turbulence is modeled by empirical equations that specify the spectrum magnitude, while the phase is random uniformly distributed.

Making use of the information gathered in the previous chapter, the aeroelastic matrices are studied as explicit functions of time. In particular, it is shown under which conditions the time-varying matrix can be diagonalized, i.e. when the system may be considered slowly-varying. In this regard, two fairly simple criteria are proposed.

## 4 Spectral estimation

### *Abstract*

---

The response of an aeroelastic system to atmospheric turbulence is random and is thus best analyzed in the frequency-domain. Numerous spectral estimation techniques have been developed for a variety of applications on sampled, noisy and finite signals. Our goal is the estimation of the power spectral density in order to monitor the acquired signals and to provide data to frequency-domain identification methods. The chapter focuses on nonparametric estimators, in particular the periodogram approach and multi-taper method. Their limits in terms of achievable frequency resolution and variance reduction are discussed. A mixed spectral estimation method is also proposed. Finally, spectral estimation of time-varying systems is discussed to examine the limits of stationarity assumptions.

---

Spectral estimation is the process of determining a frequency-domain representation of a signal from a limited number of samples. In modal analysis, it is employed in vibration monitoring and system identification. Spectral estimation provides the analyst with vital and easy-to-interpret information about acquired signals and is an important component for the quality control of measurements. For instance, it reveals the location of resonances, the presence of harmonic components and noise, the effect of filters, the excitation bandwidth, the coherence between inputs and outputs, the variance of estimated spectra and so forth.

This chapter focuses on establishing the spectral estimation methods necessary to support the real-time online-monitoring of aeroelastic systems during vibration testing. To reach this goal it is necessary to understand the limitations imposed by finite sample size, noise and the assumptions of spectral estimation. Two expert references on digital signal processing can be found in [OPPENHEIM AND SCHAFER, 2010] and in [PROAKIS AND MANOLAKIS, 2013]. Spectral estimation is the main focus of [STOICA AND MOSES, 2005], who examine numerous techniques that have been developed for various purposes. Ample space is devoted in literature to spectral estimation applied to modal analysis, for example in [PINTELOU AND SCHOUKENS, 2004] and [BRANDT, 2011]. Ambient excitation on aircraft produces stochastic response signals and the classic book from [BENDAT AND PIERSOL, 2010] provides theoretical tools for the analysis of random data in the time and frequency domains. [HOBLIT, 1988] offers an extensive treatment of gust loads on aircraft and covers some spectral estimation topics. [COHEN, 1995] treats extensively the time-frequency description of signals, which can be employed in the analysis of the response of time-varying systems.

In real-world applications, obtaining long records may be excessively costly or impractical. For instance, records in the order of seconds suffice to estimate the spectra of particularly stiff systems [HANNEMANN ET AL., 2015]; on the other hand, a light-weight structure with extremely low eigenfrequencies requires considerable measurement times [BÖSWALD ET AL., 2010]. The nature of the signal may limit the acquisition time or

invalidate some assumptions, e.g. it is second-order stationary only over short observation intervals. In the case of flight vibration testing, the main constraint is the ability to maintain stationarity over a sufficiently long duration [JELIČIĆ ET AL., 2017]. Vibration testing is often confronted with such limitations.

The spectral estimation process must be fast in order to satisfy the real-time monitoring requirement, which restricts somewhat the number of candidate algorithms. We have shown in chapter 2 how to compute parametrically the spectra of periodic or slowly-varying systems, i.e. the analytical frequency-domain representation of the system's response. This theoretical development is necessary to understand the applicability and to correctly interpret the results of a spectral estimator. In chapter 3 we have seen that the interaction between structure and aerodynamic forces modifies the system's modal parameters with wind speed and flight altitude, particularly the damping. We shall discuss here how system variation influences spectral estimation and have a look at experimental data from aeroelastic experiments. The methods presented in this chapter shall be put to use for frequency-domain system identification in chapter 5 and for the analysis of simulated and experimental data in chapters 7 and 8.

The chapter's roadmap is as follows:

1. Introduction of spectral estimation concepts
2. Nonparametric methods for power spectral density estimation
3. Spectral estimation of time-varying systems

## 4.1 Fourier transform

Spectral estimation begins with the study of continuous signals and their representation in the frequency-domain via Fourier transform. This is motivated by the fact that the most widespread analytical, digital signal processing and spectral estimation methods in structural dynamics feature the Fourier transform. Before proceeding, without delving too deep into the topic, this brief section introduces some notation or conventions and reviews some of the properties that will be of use later in the text. Detailed information about the transformation into frequency-domain, various theorems, its applications and many examples can be found in [OPPENHEIM ET AL., 1996; PROAKIS AND MANOLAKIS, 2013; SHMALIY, 2007].

The continuous Fourier transform (CFT) of a real signal  $\mathbf{x}(t)$  is:

$$\tilde{\mathbf{x}}(f) = \mathcal{F}\{\mathbf{x}(t)\} \triangleq \int_{-\infty}^{+\infty} \mathbf{x}(\tau) e^{-i2\pi f\tau} d\tau \quad [\text{signal/Hz}] \quad (4.1)$$

where the frequency variable is  $f$  [Hz]. This definition of CFT is unitary, i.e. its inverse has the same factor in front of the integral (namely, 1). Another common CFT definition utilizes the angular frequency  $\omega$  [rad/s]) as its variable:

$$\tilde{\mathbf{x}}(\omega) = \mathcal{F}\{\mathbf{x}(t)\} \triangleq \int_{-\infty}^{+\infty} \mathbf{x}(\tau) e^{-i\omega\tau} d\tau \quad [\text{signal}/(\text{rad/s})] \quad (4.2)$$

This definition is unitary if the integral's factor is  $1/\sqrt{2\pi}$ .

For a sampled signal  $\mathbf{x}[n]$  of length  $N$ , the discrete Fourier transform (DFT) has a similar definition:

$$\tilde{\mathbf{x}}[k] = \text{DFT}\{\mathbf{x}[n]\} \triangleq \sum_{n=0}^{N-1} \mathbf{y}[n] e^{-i2\pi kn/N} \quad [\text{signal}] \quad (4.3)$$

Notice that the DFT has the same units of the input signal. The correct scaling needed to approximate the CFT using the DFT is obtained by dividing by the sample rate<sup>1</sup>  $f_s$  [Hz]. A factor  $1/\sqrt{N}$  in equation (4.3) makes the DFT unitary. The Fourier series of various analytical signals in chapters 2 and 3 have been computed using the DFT.

**Notation.** *The tilde indicates signals in frequency-domain. For continuous signals the frequency variable is denoted by round brackets “(f)” or “(ω)”. For discrete signals, the frequency bins are denoted by the square brackets “[k]”.*

The sampling theorem establishes a sufficient condition for the perfect (continuous)  $\mathbf{x}(t)$  reconstruction of a band-limited sampled signal  $\mathbf{x}[n]$ : the discrete signal's bandwidth  $f_{max} - f_{min}$  must be less than half the sampling frequency  $f_{max} - f_{min} < f_s/2$ . The theorem, its corollaries and the consequences on digital signal processing are discussed

<sup>1</sup> For example, if  $n = 0 : N - 1$  and  $x[n] = A_0 + A_1 \sin(2\pi k_0/Nn)$ , then  $\frac{2}{N} \text{DFT}\{x[n]\}$  has two peaks of amplitude  $A_1$  located at  $k = k_0$  and  $k = N - k_0$  and one peak of amplitude  $2A_0$  at  $k = 0$ .

at length in the aforementioned references. The theorem sets conditions on the minimal sample rate (or, equivalently, the time step  $\Delta t = 1/f_s$ ) in measurements and simulations. The frequency vector associated to the transformed signal in frequency-domain  $\tilde{\mathbf{x}}[k]$  is:

$$\mathbf{f} = (0 : 1/N : 1/2)f_s \in \mathbb{R}^L \quad (4.4)$$

where  $f_s/N = 1/T = \Delta f$  is the frequency resolution. The  $\text{DFT}\{\cdot\}$  operator outputs the DFT coefficients with the zero frequency bin at the beginning of the array. The zero frequency is often called *DC bin* (constant term). Depending on the DFT's length, the bin with the highest frequency is:

$$\begin{cases} \text{if } \text{mod}(N, 2) = 0 & : L = N/2 + 1 & \mathbf{f}[L] = f_s/2 \\ \text{if } \text{mod}(N, 2) = 1 & : L = (N + 1)/2 & \mathbf{f}[L] = (1 - 1/N)f_s/2 \end{cases} \quad (4.5)$$

If the signal  $\mathbf{x}[n]$  is real, then its DFT is complex-conjugated, hence only its first  $L$  (positive) frequency bins are sufficient. In such case, if  $N$  is even, then  $\tilde{\mathbf{x}}[L]$  is real; if  $N$  is odd, then  $\tilde{\mathbf{x}}[L]$  is complex and  $\tilde{\mathbf{x}}[L] = \tilde{\mathbf{x}}^*[L + 1]$ .

Lastly, it can be shown how the DFT is related to the first two moments of the signal:

$$\begin{cases} \sum_{n=0}^{N-1} \mathbf{x}[n] & = \tilde{\mathbf{x}}[0] \\ \sum_{n=0}^{N-1} \mathbf{x}^2[n] & = \frac{1}{N} \sum_{k=0}^{N-1} |\tilde{\mathbf{x}}[k]|^2 \end{cases} \implies \begin{cases} \mu\{\mathbf{x}[n]\} & = \frac{1}{N} \tilde{\mathbf{x}}[0] \\ \sigma^2\{\mathbf{x}[n]\} & = \frac{1}{N^2} \sum_{k=1}^{N-1} |\tilde{\mathbf{x}}[k]|^2 \end{cases} \quad (4.6)$$

The top equations tell us that  $\tilde{\mathbf{x}}[0]/N$  is equal to the signal's mean and that the DC bin is always real for a real signal. The bottom equations are Parseval's theorem for the DFT (notice that the index on the right excludes the DC bin!). Leakage in signals of period  $N$  is avoided by computing the DFT as  $\text{DFT}\{\mathbf{x}[0 : N - 2]\}$  (the last point is discarded). DFT interpolation is performed by zero-padding, i.e. appending zeros to a signal to increase its frequency resolution (this operation does not add new information, however it is helpful in the interpretation of some spectra).  $N$  periods of a signal are computed by inserting  $N - 1$  zeros between each frequency bin of its DFT and transforming back into time-domain. The discrete Fourier transform is computed using the Fast Fourier Transform (FFT)<sup>2</sup>. Given the FFT's importance in digital signal processing, an entire chapter is dedicated to it in [PROAKIS AND MANOLAKIS, 2013]. Additional information about its properties, computation and applications can be found in this book. Useful examples about the FFT and several of its applications such as convolution can be found in [BRANDT, 2011].

<sup>2</sup> MATLAB employs the FFTW algorithm (Fastest Fourier Transform of the West) [FRIGO AND JOHNSON, 1998]. It is fastest when the sample length has small prime factors, therefore  $N$  is very often selected to be a power of two (but not necessarily!). This algorithm is notable for having a linearithmic  $\mathcal{O}(N \ln N)$  time complexity, therefore the computation time of many operations in time-domain can be significantly improved by switching to the corresponding frequency-domain operation (for example the convolution and cross-correlation).

## 4.2 Power spectral density

The *cross-power spectral density* (CPSD) of two signals  $\mathbf{x}(t) \in \mathbb{R}^{N_x}$  and  $\mathbf{y}(t) \in \mathbb{R}^{N_y}$  is:

$$\mathbf{S}_{yx}(f) \triangleq \lim_{T \rightarrow \infty} \frac{1}{T} \tilde{\mathbf{y}}(f) \tilde{\mathbf{x}}^H(f) \quad \in \mathbb{C}^{N_y \times N_x} \quad (4.7)$$

The cross-correlation of the signals

$$\mathbf{R}_{yx}(t) \triangleq \int_{-\infty}^{\infty} \mathbf{y}(\tau) \mathbf{x}^H(\tau + t) d\tau \quad \in \mathbb{R}^{N_y \times N_x} \quad (4.8)$$

is related to the cross-power spectral density by the Wiener–Khinchin theorem:

$$\mathbf{S}_{yx}(f) = \int_{-\infty}^{+\infty} \mathbf{R}_{yx}(\tau) e^{-i2\pi f\tau} d\tau \quad (4.9)$$

For convenience we shall call  $\mathbf{y}(t)$  the *responses* and  $\mathbf{x}(t)$  the *references* because they are respectively related to the rows and columns of the frequency response function matrix. From equation (4.7) it can be seen that the CPSD<sup>3</sup> has dimensions  $[\text{unit}\{\mathbf{y}\} \cdot \text{unit}\{\mathbf{x}^T\} / \text{Hz}]$  and that it is Hermitian  $\mathbf{S}_{yx}(f) = \mathbf{S}_{xy}^H(f)$ . The physical meaning of the power spectral density is discussed at length in [BENDAT AND PIERSOL, 2010].

The *autopower spectral density* (APSD) of a vector  $\mathbf{x}(t)$  is the real function

$$\mathbf{S}_x(f) \triangleq \lim_{T \rightarrow \infty} \frac{1}{T} |\tilde{\mathbf{x}}(f)|^2 \quad \in \mathbb{R}^{N_x} \quad (4.11)$$

According to equation (4.7), the matrix  $\mathbf{S}_{xx}(f) \in \mathbb{C}^{N_x \times N_x}$  is the *cross-power spectral density* of vector  $\mathbf{x}(t)$  with itself, consequently only its diagonal is real.

**Notation.** The *autopower spectral density* of the vector function  $\mathbf{x}(t)$  is denoted by a single subscript  $\mathbf{S}_x(f) \in \mathbb{R}^{N_x}$  and is the diagonal of the corresponding cross-power spectral density matrix  $\mathbf{S}_{xx}(f) \in \mathbb{C}^{N_x \times N_x}$ . The CPSDs are generally complex. This distinction is necessary because all equations are written for the multi-input-multi-output case. There is usually no such distinction in literature, which can be confusing.

The Fourier transform of a real signal has a complex-conjugated spectrum, therefore in signal processing the *single-sided* PSD  $\mathbf{G}(f)$  is used instead of the *double-sided* PSD  $\mathbf{S}(f)$ . The two are related as:

$$\mathbf{G}(f) = \begin{cases} 2\mathbf{S}(f) & f > 0 \\ \mathbf{S}(0) & f = 0 \end{cases} \quad (4.12)$$

This definition ensures that the signal's energy is conserved  $\int_{-\infty}^{+\infty} \mathbf{S}(f) df = \int_0^{\infty} \mathbf{G}(f) df$ .

<sup>3</sup> Some authors, for example [BENDAT AND PIERSOL, 2010] and [BRINCKER ET AL., 2000], define the CPSD (and correspondingly the cross-correlation) as:

$$\mathbf{S}'_{yx}(f) \triangleq \lim_{T \rightarrow \infty} \frac{1}{T} \tilde{\mathbf{y}}^*(f) \tilde{\mathbf{x}}^T(f) = \mathbf{S}_{yx}^*(f) \quad (4.10)$$

which is the complex conjugate of equation (4.7). The convention in this thesis follows [BRANDT, 2011; OPPENHEIM AND SCHAFER, 2010; PINTELOU AND SCHOUKENS, 2004].

If the frequency is expressed in rad/s, then  $\mathbf{S}(\omega) = \frac{1}{2\pi}\mathbf{S}(f)$ . The scaling of the PSD must be such that the square root of its integral is equal to the signal's RMS value:

$$\int_0^\infty \mathbf{G}_x(f) df = \mu^2\{\mathbf{x}(t)\} + \sigma^2\{\mathbf{x}(t)\} = \text{RMS}^2\{\mathbf{x}(t)\} \quad (4.13)$$

Let us consider the input-output mapping of an LTI system (2.52) and post-multiply it by its Hermitian transpose:

$$\mathbf{y}(s) = \mathbf{H}(s)\mathbf{u}(s) \implies \mathbf{y}(s) \cdot \mathbf{y}^H(s) = \mathbf{H}(s)\mathbf{u}(s) \cdot \mathbf{u}^H(s)\mathbf{H}^H(s) \quad (4.14)$$

If we take the limit for  $T \rightarrow \infty$

$$\lim_{T \rightarrow \infty} \frac{1}{T} \mathbf{y}(s)\mathbf{y}^H(s) = \mathbf{G}_{yy}(s) \quad \lim_{T \rightarrow \infty} \frac{1}{T} \mathbf{u}(s)\mathbf{u}^H(s) = \mathbf{G}_{uu}(s) \quad (4.15)$$

we obtain the well-known formula:

$$\mathbf{G}_{yy}(s) = \mathbf{H}(s)\mathbf{G}_{uu}(s)\mathbf{H}^H(s) \quad (4.16)$$

This is the relationship between input and output PSDs for linear time-invariant systems, but under some circumstances it is valid or at least approximately correct for time-varying systems as well. This equation also tells us that the response PSD contains the system's but also the excitation's poles and zeros.

It is reasonable to assume that the input spectrum's amplitude is constant, at least within a limited frequency range. When  $\mathbf{G}_{uu}(s) = \mathbf{G}_{uu}$ , equation (4.16) can be represented by a sum of simple poles, which will be useful in the next chapter in the framework of operational modal analysis. We start by inserting the frequency response function's pole-residue form (2.56) into equation (4.16):

$$\begin{aligned} \mathbf{G}_{yy}(\omega) &= \mathbf{H}(\omega)\mathbf{G}_{uu}\mathbf{H}^H(\omega) \\ &= \left( \sum_{i=1}^{N_x} \frac{\mathbf{R}_i}{i\omega - \lambda_i} \right) \mathbf{G}_{uu} \left( \sum_{j=1}^{N_x} \frac{\mathbf{R}_j^H}{-i\omega - \lambda_j^*} \right) \\ &= \sum_{i=1}^{N_x} \sum_{j=1}^{N_x} \frac{\mathbf{R}_i \mathbf{G}_{uu} \mathbf{R}_j^H}{\lambda_i + \lambda_j^*} \left( \frac{1}{i\omega - \lambda_i} + \frac{1}{-i\omega - \lambda_j^*} \right) \end{aligned} \quad (4.17)$$

where  $\mathbf{R}_i \triangleq \mathbf{c}_i \mathbf{b}_i^T$ ,  $\mathbf{c}_i \triangleq \mathbf{C} \Psi \mathbf{e}_i$  and  $\mathbf{b}_i \triangleq \mathbf{e}_i^T \Psi^{-1} \mathbf{B}$  (and analogously for index  $j$ ). The indices  $i$  and  $j$  refer to the positive and negative frequencies respectively. The last step was obtained by partial fraction decomposition:

$$\frac{1}{i\omega - \lambda_i} \cdot \frac{1}{-i\omega - \lambda_j^*} = \frac{-1}{\lambda_i + \lambda_j^*} \left( \frac{1}{i\omega - \lambda_i} + \frac{1}{-i\omega - \lambda_j^*} \right) \quad (4.18)$$

Since the input PSD is constant by hypothesis, it is possible to sum the constants  $\frac{\mathbf{R}_i \mathbf{G}_{uu} \mathbf{R}_j^H}{\lambda_i + \lambda_j^*}$

once over the index  $j$  (for the residuals corresponding to positive frequencies) and once over the index  $i$  (for negative frequencies) in order to define:

$$\mathbf{R}_k \mathbf{G}_{uu} \mathbf{L}_k^H \triangleq - \sum_{j=1}^{N_x} \frac{\mathbf{R}_k \mathbf{G}_{uu} \mathbf{R}_j^H}{\lambda_k + \lambda_j^*} \quad \mathbf{L}_k \mathbf{G}_{uu} \mathbf{R}_k^H \triangleq - \sum_{i=1}^{N_x} \frac{\mathbf{R}_i \mathbf{G}_{uu} \mathbf{R}_k^H}{\lambda_i + \lambda_k^*} \quad (4.19)$$

The output CPSD can now be written in a pole-residue form<sup>4</sup>:

$$\mathbf{G}_{yy}(\omega) = \sum_{k=1}^{N_x} \left( \frac{\mathbf{R}_k \mathbf{G}_{uu} \mathbf{L}_k^H}{i\omega - \lambda_k} + \frac{\mathbf{L}_k \mathbf{G}_{uu} \mathbf{R}_k^H}{-i\omega - \lambda_k^*} \right) = \sum_{k=1}^{N_x} \left( \frac{\psi_k \phi_k^H}{i\omega - \lambda_k} + \frac{\phi_k \psi_k^H}{-i\omega - \lambda_k^*} \right) \quad (4.21)$$

where the mode shapes  $\psi_k$  and operational reference vectors  $\phi_k$  are:

$$\mathbf{R}_k \mathbf{G}_{uu} \mathbf{L}_k^H \stackrel{\text{svd}}{=} \mathbf{U} \Sigma \mathbf{V}^H \implies \begin{aligned} \psi_k &= \mathbf{U}_1 \sqrt{\Sigma_1} \\ \phi_k &= \mathbf{V}_1 \sqrt{\Sigma_1} \end{aligned} \quad (4.22)$$

where the subscript 1 denotes the left and right singular vectors corresponding to the largest singular value. The residues in equation (4.19) depend on the system's modal parameters as well as on the excited degrees of freedom. We can see that, in contrast to the frequency response function (2.56), each pole appears also on the negative semi-plane: the PSDs have thus a so-called “4-quadrant symmetry” illustrated in figure 4.1 (complex-conjugated pairs, positive-negative frequencies  $\{-\lambda_k, -\lambda_k^*, \lambda_k, \lambda_k^*\}$ ). The poles are the roots of the denominator, therefore each complex-conjugated eigenvalue pair is represented by a polynomial of order four (whereas the frequency response function requires a polynomial of order two). This observation sets a lower limit to the model order based on the number of poles within a certain frequency band.

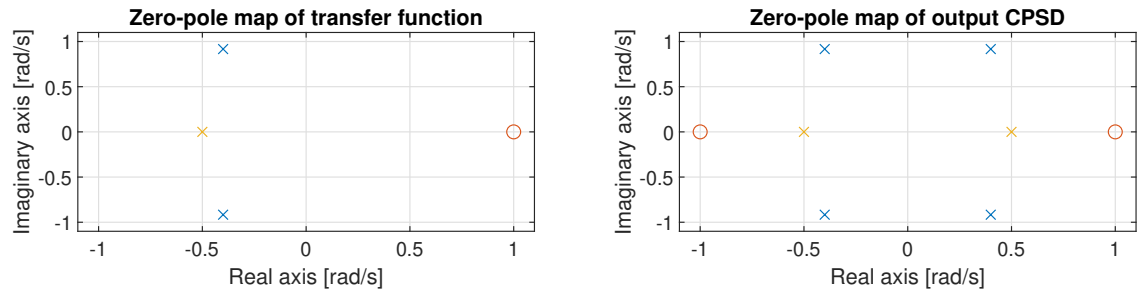


FIGURE 4.1: Pole-zero map of  $H(s) = \frac{s-1}{(s-p_1)(s-p_1^*)(s-p_2)}$  and  $G_{yy}(s) = H(s)G_{xx}H^H(s)$  with  $G_{xx} = 1$ . The system's three eigenvalues are the complex-conjugated pair  $p_1 = f_\lambda(1, 0.4)$ , (blue crosses) and the purely real  $p_2 = f_\lambda(0.5, 1)$  (orange cross). The red circles represent the zero  $z_1 = 1$ .

<sup>4</sup> The output power spectral density for white noise inputs is developed in [BRINCKER AND VENTURA, 2015] and [RAINIERI AND FABBROCINO, 2014] for mass-damping-stiffness systems and is often found in literature as a sum of four residues for each of the complex eigenvalue pairs (“unique” mode shapes):

$$\mathbf{G}_{yy}(\omega) = \sum_{k=1}^{N_m} \left( \frac{\mathbf{L}_k \mathbf{G}_{uu} \mathbf{R}_k^H}{-i\omega - \lambda_k^*} + \frac{\mathbf{L}_k^* \mathbf{G}_{uu} \mathbf{R}_k^T}{-i\omega - \lambda_k} + \frac{\mathbf{R}_k \mathbf{G}_{uu} \mathbf{L}_k^H}{i\omega - \lambda_k} + \frac{\mathbf{R}_k^* \mathbf{G}_{uu} \mathbf{L}_k^T}{i\omega - \lambda_k^*} \right) \quad (4.20)$$

Equation (4.21) is a more general form for any observable combination of states, inputs and outputs.



The modal form of the output cross-power spectral density (4.21) can be related to cross-correlation function through the Wiener-Khinchin theorem (4.9) to obtain:

$$\mathbf{R}_{yy}(\tau) = \int_{-\infty}^{+\infty} \mathbf{S}_{yy}(f) e^{i2\pi f\tau} dt = \begin{cases} \sum_{k=1}^{N_x} \boldsymbol{\psi}_k \boldsymbol{\phi}_k^T e^{\lambda_k \tau} & \tau \geq 0 \\ \sum_{k=1}^{N_x} \boldsymbol{\phi}_k \boldsymbol{\psi}_k^T e^{-\lambda_k |\tau|} & \tau < 0 \end{cases} \quad (4.23)$$

This expression is very similar to the pole-residue form of the impulse response function (2.57) (“2-quadrant symmetry”). The system’s modal parameters can be extracted from the causal part<sup>5</sup> of the correlation function (positive lags  $\tau \geq 0$ ), thus requiring only  $N_x$  instead of  $2N_x$  poles. A similar approach can be applied to frequency-domain identification by estimating the so-called *positive power spectral density* (also known as *half-power PSD*) from the correlation function at positive time lags only:

$$\mathbf{G}_{yy}^+(\omega) = \int_0^{\infty} \mathbf{R}_{yy}(t) e^{-i\omega t} dt = \sum_{k=1}^{N_x} \frac{\boldsymbol{\psi}_k \boldsymbol{\phi}_k^T}{i\omega - \lambda_k} \quad (4.24)$$

The positive power spectra have sometimes preferential applications in operational modal analysis because they have less poles and because of better numerical conditioning [BRINCKER AND VENTURA, 2015; RAINIERI AND FABBROCINO, 2014], however they demand more computation<sup>6</sup>. The contribution of noise, leakage and variance of the tail of the correlation function (higher lags) can be reduced by an exponential window, in which case the estimated damping must be corrected [VERBOVEN, 2002]. An example of positive PSD is provided in figure 4.2.

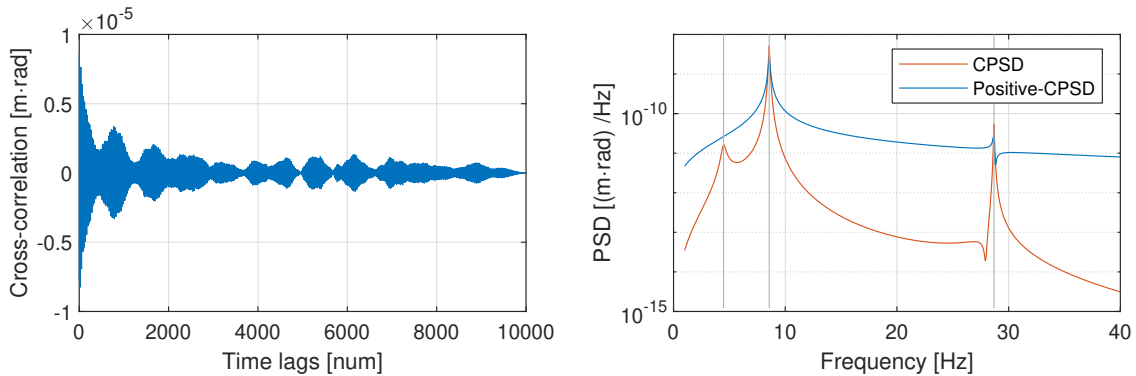


FIGURE 4.2: Cross-correlation  $\mathbf{R}_{yy}(t)$ , cross-power spectral density  $\mathbf{G}_{yy}(\omega)$  and positive cross-power spectral density  $\mathbf{G}_{yy}^+(\omega)$  between the heave and flap degrees of freedom of aeroelastic system 7.2, configuration C2, with unit heave excitation. The positive-CPSD has usually few dominant peaks.

<sup>5</sup> The positive lags contain poles with negative real parts  $\Re\lambda < 0$ , while the negative lags the corresponding poles with positive real parts  $\Re\lambda > 0$ .

<sup>6</sup> Positive power spectra require the estimation of the cross-correlation function, which is performed efficiently using an FFT instead of a convolution. However, it is necessary to calculate of the outer product between responses and references over the whole bandwidth (from DC to the Nyquist frequency). Depending on the number of samples and channels, this operation may be exceedingly expensive.

### 4.3 Spectral estimation methods

The expressions presented so far state that perfect knowledge of a signal's spectrum requires an infinite measurement time. It is clear that this is not achievable in practice, consequently the power spectral density is said to be *estimated* from a limited, but still useful amount of data. This can be stated formally as:

$$\begin{aligned}\hat{\mathbf{S}}_{yx}(f) &\triangleq \lim_{T \rightarrow \infty} \mathbb{E} \left\{ \frac{1}{T} \tilde{\mathbf{y}}(f) \tilde{\mathbf{x}}^H(f) \right\} \\ \hat{\mathbf{S}}_{yx}[k] &\triangleq \lim_{T \rightarrow \infty} \mathbb{E} \left\{ \frac{\Delta t^2}{T} \tilde{\mathbf{y}}[k] \tilde{\mathbf{x}}^H[k] \right\}\end{aligned}\tag{4.25}$$

where  $\mathbb{E}\{\cdot\}$  is the expectation operator and  $\tilde{\mathbf{y}}$ ,  $\tilde{\mathbf{x}}$  are the Fourier transforms of the signals. In digital signal processing the objective is to find the best possible estimate  $\hat{\mathbf{S}}$ .

**Notation.** *In control theory and statistics, a circumflex underlines that the true spectrum  $\mathbf{S}$  has been estimated  $\hat{\mathbf{S}}$  by whatever means; the same convention is applied here.*

The finite length of signals coupled with noise gives rise to some specific challenges such as leakage and variance that distort the estimated spectrum and that must be addressed. Depending on the analysis that is to be performed, for instance transfer function estimation, various experimental procedures exist for obtaining optimal spectra [BRANDT, 2011; PINTELOON AND SCHOUKENS, 2004]. Given our overarching goal of performing output-only system identification, we focus on the determination of the frequency content of stochastic signals, in particular in the PSD estimation. The time data record's duration determines the amount of information that has been collected. Stated in DFT terms, the inverse of the signal's duration  $T$  sets the frequency resolution of the signal:

$$\Delta f = \frac{1}{T} = \frac{f_s}{N}\tag{4.26}$$

Spectral features can be resolved better when  $\Delta f$  is low. Since this is desirable, a “frequency resolution increase” actually means that  $\Delta f$  decreases. The magnitude of  $\Delta f$  is meaningful in relation to the signal's time-scale or its frequency components. For instance, the half-power width of a resonance peak is  $\Delta\omega_n \approx \zeta\omega_n$  for low damping (see section 2.2.1), therefore the peak is well-resolved if  $2\pi\Delta f/\Delta\omega_n \ll 1$ . The quantity  $2\pi\Delta f/\Delta\omega_n$  is thus related to the *frequency bias* of spectral estimation as we shall see in the next section. Wind tunnel models tend to be very stiff ( $f_n > 50$  Hz) due to their small size and strong construction, whereas aircraft have low eigenfrequencies ( $f_n < 50$  Hz) due to larger dimensions and light-weight hollow structure [KEHOE, 1995, Tab. 1]. Compared to the time scale of a typical measurement in vibration testing (in the order of minutes), a signal with very high frequency components requires only a “short” record and vice versa. Extreme cases like the *Solar Impulse* aircraft [BÖSWALD ET AL., 2010] or a hypersonic scramjet model [HANNEMANN ET AL., 2015] require respectively very long and very short measurements for accurate spectral estimates.

In modal analysis the frequency band of interest starts typically at zero to pick up any rigid body motions (in practice: at the minimal frequency that the sensors can pick up) and ends with the highest eigenfrequency that is to be identified. The frequency band of interest  $\Delta f_B$  sets a lower bound for the sample rate according to the sampling theorem<sup>7</sup>:

$$f_s > 2\Delta f_B$$

The sample rate (or bandwidth) is “high” when there is a large number of resonance peaks within the current frequency band. A common misconception is that a high  $f_s$  increases the information content of a measured signal, but in reality it merely extends the spectrum’s frequency abscissa to the right. A slight oversampling is necessary to account for the transition band of the anti-aliasing filters in the data acquisition system, however in experimental setups the sample rate is often *much* higher than strictly necessary due to technical limitations or other concurrent measurements. Decimation or resampling should be carried out to reduce the amount of processed data and subsequent workload.

It can be shown that a finite random sequence has also a random spectrum [BENDAT AND PIERSOL, 2010]. Several realizations of the same stochastic process must be averaged in order to reduce this variance. The estimation of the spectral content from a limited sample of random data has thus two main concerns:

- frequency resolution must be increased by increasing the measurement time; the lower the frequency resolution, the lower the frequency bias error
- spectrum variance must be reduced by averaging several realizations of the system; the lower the variance, the lower the random error

These requirements are conflicting: the spectral estimation theorems mandate that, for a given record length, spectrum variance and frequency resolution cannot be reduced arbitrarily<sup>8</sup>. As already stated, it is the record duration that determines the frequency resolution, the amount of useful information and goodness of spectral estimation. Where possible, the experiment is designed to acquire the necessary data amount plus some margin. Records cannot thus be too short because the noise and variance would be intolerable, nor can they be excessively long because of cost and data management. Furthermore, in the case of LTV systems, multiple realizations must be acquired in order to capture time-varying dynamics [MAJJI ET AL., 2010].

<sup>7</sup> The sampling theorem is often misinterpreted as meaning that the *maximal* frequency (and not the bandwidth) that can be acquired is half the sample rate. This is true if the signal has frequency components near 0 Hz, which is almost always the case in modal analysis. For a structure with free-free boundary conditions, the lowest system poles correspond to the six rigid-body modes and are important for the verification of the measurement setup during ground vibration testing.

<sup>8</sup> This is a consequence of the *uncertainty principle* applied to harmonic analysis: the product of duration and bandwidth has a lower bound that cannot be exceeded. In digital signal processing it is expressed as the product of the second central moment of the signal’s energy distribution in the time and frequency domains:

$$\left( \int_{-\infty}^{+\infty} t^2 |x(t)|^2 dt \right) \left( \frac{1}{2\pi} \int_{-\infty}^{+\infty} \omega^2 |x(\omega)|^2 d\omega \right) \geq \frac{1}{4} \quad (4.27)$$

There are many equivalent variations of this equation in literature [STOICA AND MOSES, 2005].

Several parametric and non-parametric spectral estimators have been devised for a very wide variety of applications. They can be grouped into two large categories:

- *non-parametric methods* estimate the spectrum without assuming any particular structure in the data (for example, FFT-based methods).
- *parametric methods* try to model the underlying stationary stochastic process that generated the time data by describing it with a small number of parameters (for example, auto-regressive or moving-average methods)

The method or algorithm of choice depends on the use case. The monograph from [STOICA AND MOSES, 2005] provides an exhaustive treatment of this topic. An overview of non-parametric time-frequency analysis methods for non-stationary signals is found in [HAMMOND AND WHITE, 1996]. In the next chapter we will see that one of the possible results of system identification is the reconstruction of the output signal's PSD, which is closely related to parametric methods of spectral estimation. In this chapter we shall focus on non-parametric techniques because they require little a priori knowledge, less computational capacity and their results are readily available. Non-parametric spectral estimators are used to analyze the acquired signals before they are passed to more sophisticated procedures that require more processing power. For our intended use, Welch's modified periodogram and the multi-taper method are two candidates.

#### 4.3.1 Welch's modified periodogram

In experimental structural dynamics, spectral estimation of vibration data is commonly carried out using Welch's modified periodogram (WMP), an FFT-based well-known non-parametric method [BRANDT, 2011]. It is commonly used to estimate the cross-power spectral density of vibration data in order to compute the transfer function, coherence, output noise variance et cetera.

The pseudo-code in algorithm 1 provides a simple implementation. Welch's periodogram subdivides the whole record of  $N$  samples into  $N_w$  overlapping segments of length  $L_w < N$  and estimates the cross-power spectral density by averaging them in order to reduce measurement noise. Frequency resolution is thus traded with noise reduction since  $f_s/L_w > f_s/N$ . The fractional overlap  $O_w$  is equivalent to shifting each segment by  $N - [O_w L_w]$  samples. Each data segment is tapered by a smooth bell-shaped window function in order to reduce leakage due to transients at the start of each segment. A quantification of error sources and approaches for reducing said error for WOSA procedures (weighted overlapped segment averaging) such as Welch's modified periodogram, is published in [ANTONI AND SCHOUKENS, 2007]. Many window functions have been developed for specific applications or desired energy concentration characteristics. The window function is selected based on its main lobe width and sidelobe attenuation, with some preference depending on application (spectral analysis, filter design, beamforming etc.). The choice of optimal window type and length for a given finite sequence with unknown signal-to-noise ratio remains an open question that requires some trial-and-error.

**Algorithm 1:** Welch's modified periodogram

**Data:** Discrete signals  $\mathbf{x}[n]$ ,  $\mathbf{y}[n]$  of length  $N$  and sample rate  $f_s$

**Result:** Cross-power spectral density estimate  $\hat{\mathbf{G}}_{yx}[k]$

**Run:**

Select window function  $\mathbf{w}$ , its length  $L_w$  and a fractional overlap  $O_w$

Initialize indices of first segment:  $\mathbb{I}_w \leftarrow \{1 : L_w\}$

Compute number of non-overlapping samples:  $N_o = \lfloor L_w(1 - O_w) \rfloor$

Compute number of windows:  $N_w = \lfloor (N - L_w)/N_o \rfloor + 1$

**for**  $i = 1 : N_w$  **do**

    Compute the DFT of  $i$ -th segment ( $\circ$  is the Hadamard product):

$$\tilde{\mathbf{y}} \leftarrow \text{DFT}(\mathbf{y}[\mathbb{I}_w] \circ \mathbf{w}) \quad \tilde{\mathbf{x}} \leftarrow \text{DFT}(\mathbf{x}[\mathbb{I}_w] \circ \mathbf{w})$$

    Compute outer product of the transformed signals:

$$\hat{\mathbf{G}}_i[k] \leftarrow \tilde{\mathbf{y}}[k] \tilde{\mathbf{x}}^H[k]$$

    Slide data segment forwards:

$$\mathbb{I}_w \leftarrow N_o + \mathbb{I}_w$$

**end**

Calculate the average and scale:

$$\hat{\mathbf{G}}_{yx} \leftarrow \frac{2}{f_s \|\mathbf{w}\|^2} \cdot \frac{1}{N_w} \sum_{i=1}^{N_w} \hat{\mathbf{G}}_i$$

Halve the power at DC:  $\hat{\mathbf{G}}_{yx}[0] \leftarrow \hat{\mathbf{G}}_{yx}[0]/2$

The following window functions are considered for the task at hand:

- *Rectangular*: for periodic signals when no leakage is expected, for impulses/transients or signals where the time-energy distribution is uneven. Provides the highest frequency resolution but poor side-lobe attenuation.
- *Kaiser*: all-purpose window, the main lobe and sidelobes can be tailored to specific needs by changing the window's parameter. For example, when a low  $N_w$  is a serious concern, windows with a high equivalent averaging factor can be designed.
- *Hann*: good compromise between resolution and leakage, safe choice when no other window has a clear advantage and most commonly used in modal analysis. Often called improperly "Hanning".
- *Chebyshev*: the side-lobes have all equal height (equiripple) and can be tuned to the desired attenuation by enlarging the main lobe.
- *Flat-top*: used when the exact amplitude of a frequency component is more important than frequency resolution, for example with engine harmonic components.

Welch's method is not a consistent estimator of the true power spectral density of a broadband signal. This can be observed as frequency bias error on the PSD estimate. The normalized frequency bias error for a single-DoF system is a function of the resonance bandwidth  $B \triangleq 2\zeta f_n$  and the duration of the window  $L_w/f_s$ :

$$\varepsilon_f = \frac{|\hat{G}_y - G_y|}{G_y} = f(BL_w/f_s) \quad (4.28)$$

The causes and appearance of this phenomenon are discussed [BENDAT AND PIERSOL, 2010], while [SCHMIDT, 1985] provides better estimates of  $\varepsilon_f$ . Figure 4.3 shows the frequency bias error as a function of the product  $BL_w/f_s$ . The frequency bias error is low when the resonance bandwidth is high (highly-damped or high-frequency poles) or when the frequency resolution is high ( $f_s/L_w$  is small). Practical limitations on the maximal measurement duration (lower bound on the frequency resolution  $1/T = f_s/N < f_s/L_w$ ) force the experimenter to accept some frequency bias error.

We will be dealing with systems excited randomly by air turbulence and ambient noise. Even the PSD of a noiseless system response due to stochastic excitation has a variance greater than zero that must be reduced by averaging. The normalized random error of a Welch estimate is

$$\varepsilon_r = \frac{1}{\sqrt{k_{ew}N/L_w}} \quad (4.29)$$

where  $N/L_w$  is the ratio between the number of samples and window length and  $k_{ew} \geq 1$  is the *equivalent averaging factor*. The latter is a function of window type and overlap. This inverse square law shows that there are diminishing returns when  $N/L_w$  is large. A more detailed discussion about the spectrum variance error is found in [BRANDT, 2011, Ch. 10.3.5]. Figure 4.4 displays the equivalent averaging factor as a function of overlap. There exists an optimal value for each window type after which  $k_{ew}$  reaches a plateau. Beyond the optimal overlap, adjacent data segments are so correlated with each other

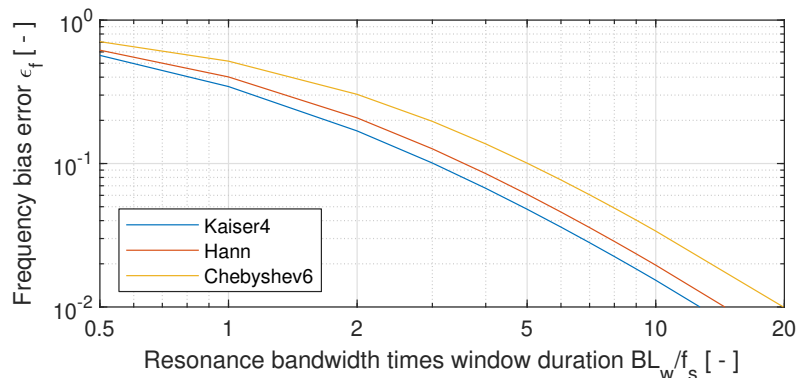


FIGURE 4.3: Frequency bias error in Welch's modified periodogram as a function of  $BL_w/f_s$  for three different window functions. For example, if we accept  $\varepsilon_f = 0.01$ , a mode with  $B = 2 \cdot 1 \cdot 0.01$  would require a record length of about 200 s. For a very stiff wind tunnel model  $f_n > 100$  Hz, the measurement time could be as low as 2 s (without accounting for any spectral averaging).

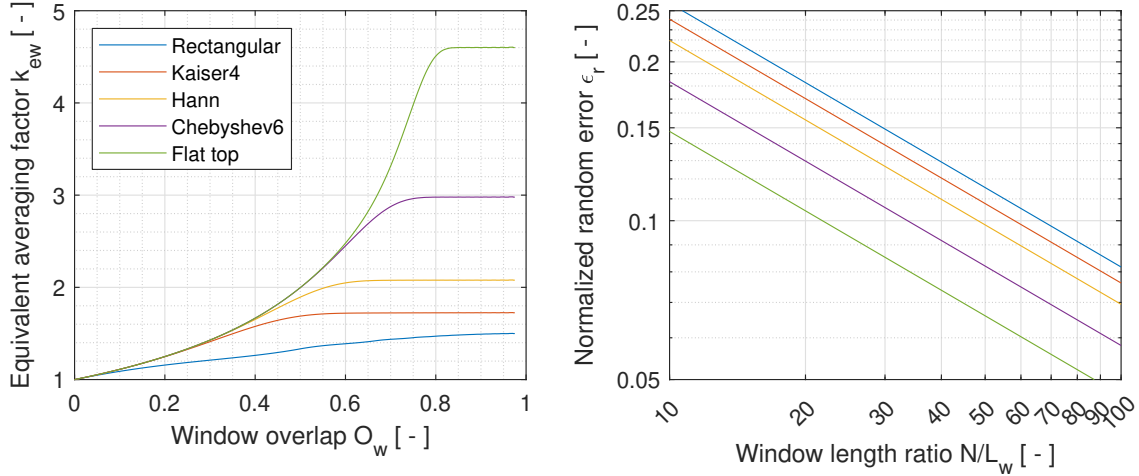


FIGURE 4.4: Left: equivalent averaging factor  $k_{ew}$  as function of window overlap  $O_w$ . Right: normalized random error  $\epsilon_r$  as a function of the ratio between number of samples and window length  $N/L_w$  for optimal overlap (4.29). See text for discussion.

TABLE 4.1: The main lobe width in normalized frequency bins and the sidelobe height in decibel of some window functions.

Window	Main lobe width $[\cdot\pi/N]$	Sidelobe height [dB]	Optimal overlap [adim]	Equivalent averaging factor [adim]
Rectangular	4.0	-13.32	-	-
Kaiser 4	6.5	-30.14	0.64	1.72
Hann	8.0	-31.55	0.66	2.07
Chebyshev 6	18.9	-120.00	0.76	2.97
Flat top	20.0	-69.01	0.82	4.58

that not only there is no improvement of the equivalent number of averages, but it is also detrimental for computation because  $N_w$  grows hyperbolically. Table 4.1 reports the main lobe width, sidelobe height, optimal overlap and equivalent averaging factor for of some window functions. Windows that have better spectrum variance reduction have worse frequency resolution capabilities, or equivalently, windows with a narrow main lobe have a lower sidelobe attenuation. We see from figure 4.4 that a low normalized random error requires a high  $N/L_w$  ratio, which means that the frequency resolution of the estimated spectra is higher than  $1/T$  because  $N/L_w/T > 1/T$  (equivalently:  $f_s/L_w > f_s/N$ ). As already mentioned, the lower bound for the sample rate is set by the maximal eigenfrequency of interest  $f_s > 2\Delta f_B$ . The minimal frequency resolution is determined by the acceptable frequency bias error (or known capabilities of system identification method of choice): this sets a lower bound  $f_s/\Delta f_{min} \leq L_w$  for the window length. The nomogram A.2 in the appendix condenses all this information. Given a certain minimal resonance bandwidth, the maximal frequency of interest, this nomogram can be used to estimate the number of samples and measurement time that lead to acceptable bias and random errors.

### 4.3.2 Multi-taper spectral estimation

The *multi-taper method* (MTM) reduces variance by averaging estimates obtained from a family of mutually orthogonal taper functions. It uses the same principle of Welch's modified periodogram but instead of tapering several data segments with one window function, it uses multiple taper functions with the whole record. The pseudo-code in algorithm 2 shows an implementation of MTM where its similarity with WMP may be apparent. The multi-taper method is well-established in geophysics [PRIETO ET AL., 2007] and bioengineering [BABADI AND BROWN, 2014], but it remains relatively unknown in the modal analysis community. Multiple tapers have favorable characteristics with regard to variance and leakage [BRONEZ, 1992]. The original paper that proposed this technique [THOMSON, 1982] used Slepian tapers (also known as DPSS – discrete prolate spheroidal sequences) because they have optimal energy concentration characteristics. The Slepian tapers are solutions to an eigenvalue problem that determines a family of mutually orthogonal time sequences of length  $N$  samples that maximize their DFT energy in a given frequency interval  $[-2\pi W, 2\pi W]$  [rad/samples]. Alternatively a sequence of orthogonal sine functions may be used (see figure 4.5). The analyst sets the dimensionless time-bandwidth product  $NW$  and computes the tapers of orders  $0 : \lfloor 2NW \rfloor - 1$ . The random error is  $\varepsilon_r = 1/\sqrt{\lfloor 2NW \rfloor - 1}$  because the tapers are uncorrelated. The higher  $NW$  is with respect to  $N$ , the wider the main lobe of a peak becomes and the benefit of variance reduction through tapers is offset by damping bias on the peaks (see figure 4.6). Since the proportion of the energy that is concentrated in the bandwidth diminishes with the order of each

---

#### Algorithm 2: Multi-taper method

---

**Data:** Discrete signals  $\mathbf{x}[n]$ ,  $\mathbf{y}[n]$  of length  $N$  and sample rate  $f_s$

**Result:** Cross-power spectral density estimate  $\hat{\mathbf{G}}_{yx}[k]$

**Run:**

Calculate  $\lfloor 2NW \rfloor$  tapers of length  $N$   $\mathbf{T} \in \mathbb{R}^{\lfloor 2NW \rfloor \times N}$  (sine or Slepian sequences)

Select weighting of each taper  $w_i$  (e.g.: unity or eigenvalues of Slepian windows)

**for**  $i = 1 : \lfloor 2NW \rfloor$  **do**

    Compute the DFT of  $k$ -th taper:

$$\tilde{\mathbf{y}} \leftarrow \text{DFT}(\mathbf{y} \circ \mathbf{T}[i, :]) \quad \tilde{\mathbf{x}} \leftarrow \text{DFT}(\mathbf{x} \circ \mathbf{T}[i, :])$$

    Compute outer product:

$$\hat{\mathbf{G}}_i[k] \leftarrow \tilde{\mathbf{y}}[k] \tilde{\mathbf{x}}^H[k]$$

**end**

Calculate weighted average and scale ( $\circ$  is the Hadamard product):

$$\hat{\mathbf{G}}_{yx} \leftarrow \frac{2}{f_s} \cdot \frac{1}{N_t} \sum_{i=1}^{\lfloor 2NW \rfloor} g_i \hat{\mathbf{G}}_i$$

Halve the power at DC:  $\hat{\mathbf{G}}_{yx}[0] \leftarrow \hat{\mathbf{G}}_{yx}[0]/2$

---



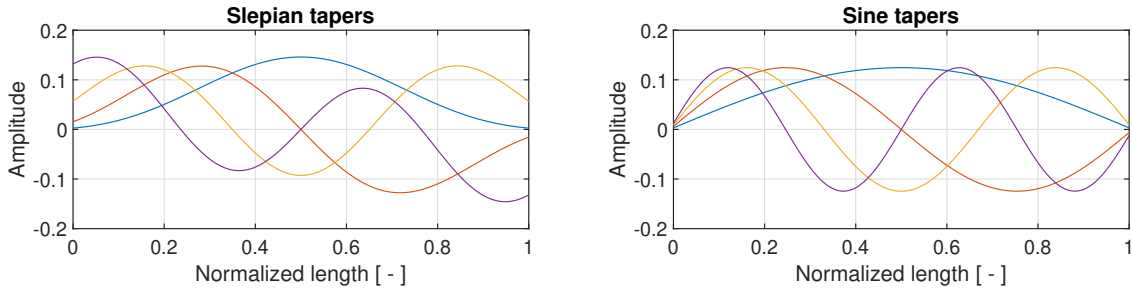


FIGURE 4.5: The first five Slepian and sine tapers (in time-domain). The tapers must be mutually orthogonal functions in order to obtain multiple independent estimates from the same sample. The Slepian (or DPSS) window maximizes the energy in the main lobe. The tapers are often weighted because energy loss increases with order.

Slepian sequence, an adaptive weighting technique has been developed in [PERCIVAL AND WALDEN, 1993]. Typical choices for the time-bandwidth product are [2, 2.5, 3, 3.5, 4], but can be higher when the record length  $N$  is large (for example when the frequency range of interest is small compared to the sample rate). [HALEY AND ANITESCU, 2017] describe the optimal selection of the time-bandwidth product. [PRIETO ET AL., 2007] elaborate a bias reduction technique for MTM based on the estimation of spectral derivatives. [BABADI AND BROWN, 2014] provide a review of multi-taper spectral analysis. The MTM implementation developed for this thesis makes use of the aforementioned techniques to obtain good spectral estimates in difficult situations. The MTM has attractive properties for the analysis of time-varying systems due to the concern about the stationarity of long system responses. The spectrograms in this text are estimated by MTM because a better time resolution can be achieved. Since MTM estimates cross-power spectral densities, it can be exchanged with WMP to determine the frequency response function and coherence in the experimental modal analysis framework. Figure 4.6 compares the PSDs estimated from experimental data using WPM and MTM with different tapers.

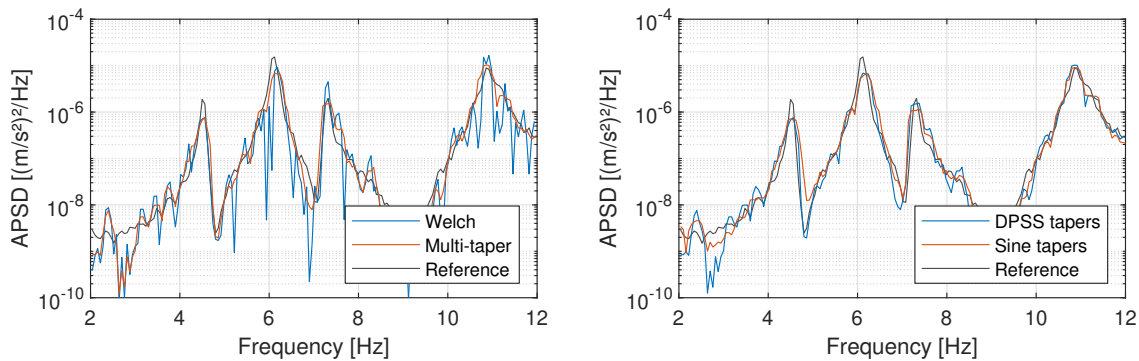


FIGURE 4.6: Left plot: comparison between WPM and MTM. Right plot: comparison between DPSS and sine tapers. The signal is the response of an aircraft model at DLR-Göttingen ( $N = 50000$  samples,  $f_s = 3000$  Hz). The first few modes are displayed (the one with the lowest damping). All spectra have the same frequency precision. The reference spectrum is constructed from 850000 samples using WPM. The half-bandwidth product is  $NW = 3$  (5 tapers). In the left plot, the MTM has smaller spectral variance for a fixed signal duration.

### 4.3.3 Segmented multi-taper method

Welch's modified periodogram tapers each data segment with a window function, while the multi-taper method uses the whole data and multiple tapers. We will show in this section how the two can be combined into a single general estimator, which we shall call *segmented multi-taper method* (SMT). The pseudo-code in algorithm 3 describes the vectorized implementation of the SMT that has been deployed for operational modal analysis during flight vibration testing; the same algorithm estimates the spectrogram. The frequency bias of the SMT method is shown in figure 4.7.  $\varepsilon_f$  tends to be higher compared to WMP because the main lobe width increases with taper order. However, this can be compensated by a greater  $L_w$  since the tapers provide averaging. The WMP and SMT methods are compared in figure 4.8 in terms of the dimensionless quantity<sup>9</sup>  $\varepsilon_f \varepsilon_r \sqrt{BN/f_s}$ .

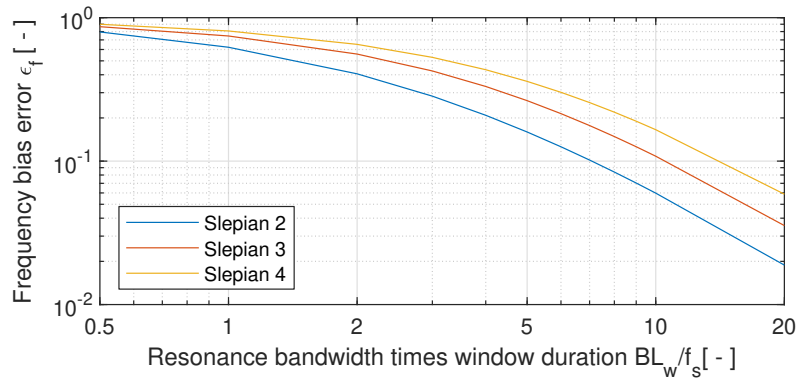


FIGURE 4.7: Frequency bias error of the segmented multi-taper method as a function of  $BL_w/f_s$  for the time-half bandwidth product  $NW = [2, 3, 4]$  using Slepian (DPSS) tapers.

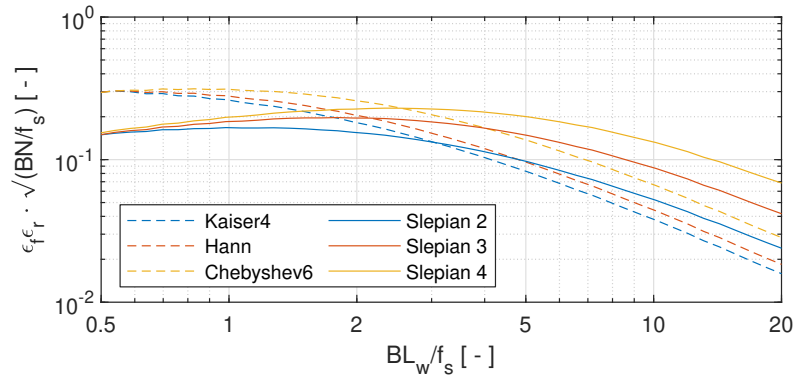


FIGURE 4.8: Comparison between Welch's modified periodogram and the segmented multi-taper method. The quantity  $\varepsilon_f \varepsilon_r \sqrt{BN/f_s}$  combines the frequency bias error and random error as functions of the product of resonance bandwidth and window duration  $BL_w/f_s$ .

<sup>9</sup> If we multiply the random error  $\varepsilon_r$  by  $\sqrt{BN/f_s}$ , we obtain:

$$\varepsilon_r \cdot \sqrt{BN/f_s} = \frac{1}{\sqrt{k_{ew}N/L_w}} \sqrt{BN/f_s} = \sqrt{\frac{BL_w/f_s}{k_{ew}}} \quad (4.30)$$

The frequency bias error  $\varepsilon_f = f(BL_w/f_s)$  and  $\varepsilon_r \sqrt{BN/f_s}$  are both functions of the same abscissa  $BL_w/f_s$ .

The segmented multi-taper method performs better with short records. The bias of multi-taper estimates could be further reduced by applying the technique described in [PRIETO ET AL., 2007]. A comparison of the modal parameters identified using a frequency-domain technique from the response CPSD estimated using WMP and SMT is shown in figure 4.9.

The algorithm 3 is one of the key components of the real-time modal analysis procedure. By tuning its parameters it functions as both WMP and MTM<sup>10</sup>. In the experimental implementation, the most recent data block is appended at the end of the data buffer, therefore the segments slide backwards to be able to observe transients as soon as possible. The most resource-intensive steps in the algorithm are the FFT and the computation of the outer product of response and reference channels. This is addressed by computing the CPSD matrix only for the frequency bins within the current frequency band and from unique channels among the selected responses and references<sup>11</sup>. In principle it is possible to parallelize the loops for additional speed, but this is convenient only when the overhead (setup) time is small compared to the computation time<sup>12</sup>. In [JELIČIĆ ET AL., 2017] operational modal analysis has been performed using a frequency-domain method whose data source is the output cross-power spectral density. Typically only a subset of all sensors can be used as reference because of limits on computational capabilities. In the cited experiment, a CPSD matrix with 51 responses, 21 references and 630 frequency bins had to be computed efficiently in less than two seconds.

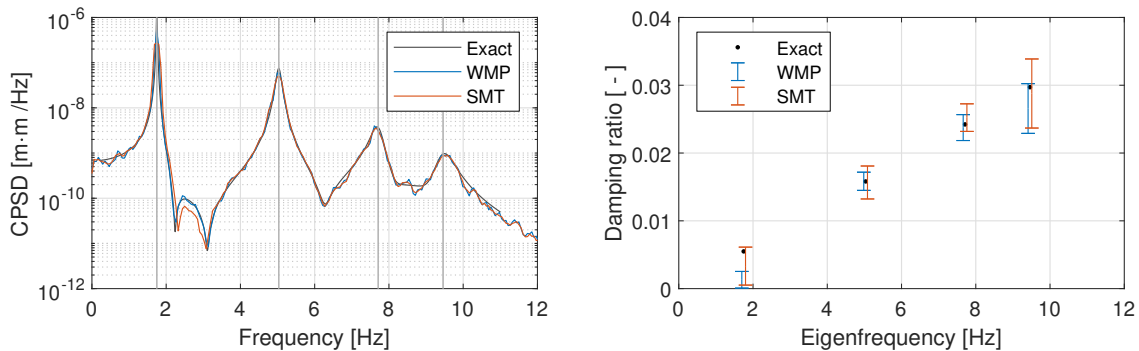


FIGURE 4.9: Comparison between WMP and SMT. The model of a 5-story building with four lateral degrees of freedom is randomly excited at the ground floor in a Monte Carlo simulation with 1000 runs. 10000 samples are acquired to estimate a full  $4 \times 4$  CPSD matrix with a window of length 512 and overlap 2/3 (WMP: Hann window, SMT: DPSS tapers with time-half bandwidth product 2). The modal parameters are then identified with a frequency-domain method. When the number of samples is low, SMT performs better.

<sup>10</sup> If the taper matrix input is a vector and  $L_w < N$ , then SMT is equivalent to WMP (algorithm 1). If the taper matrix input is a matrix and  $L_w = N$ , then SMT is equivalent to MTM (algorithm 2).

<sup>11</sup> The autopower spectral density of all acquired channels is always estimated because it is a very important source of information and diagnostic tool during experiments.

<sup>12</sup> In practice parallelization may not be feasible because the setup time and the portion of the code that cannot be parallelized are large fractions of the total available time, hence Amdahl's law predicts a meager performance improvement.

**Algorithm 3:** Segmented multi-taper method

**Data:** Sampled time data  $\mathbf{v}[n]$  of length  $N$  and sample rate  $f_s$   
**Settings:** response  $\mathbb{Y}$  and reference  $\mathbb{X}$  channels, taper matrix  $\mathbf{T} \in \mathbb{R}^{N_t \times L_w}$ , taper weights  $\mathbf{w} \in \mathbb{R}^{N_t}$ , overlap  $O_w$ , frequency range  $[f_{min}, f_{max}]$   
**Result:** CPSD  $\hat{\mathbf{G}}_{yx}[k]$ , APSD of all channels  $\hat{\mathbf{G}}_c[k]$ , frequency vector  $\mathbf{f}$

**Initialization:**

Construct frequency vector:  $\mathbf{f} \leftarrow \{0 : 1/N : 1/2\} f_s$   
 Compute number of non-overlapping samples:  $N_o = \lfloor L_w(1 - O_w) \rfloor$   
 Compute number of windows:  $N_w = \lfloor (N - L_w)/N_o \rfloor + 1$

Get indices of first segment starting from the back:  $\mathbb{I}_w \leftarrow \{N - L_w + 1 : N\}$   
 Get indices of unique channels:  $\mathbb{I}_u = \mathbb{Y} \cup \mathbb{X}$   
 Get logical indices of unique channels that are responses:  $\mathbb{I}_y \leftarrow \mathbb{I}_u \in \mathbb{Y}$ ?  
 Get logical indices of unique channels that are references:  $\mathbb{I}_x \leftarrow \mathbb{I}_u \in \mathbb{X}$ ?  
 Get logical indices of frequency bins in range  $\mathbb{I}_f \leftarrow \mathbf{f} \geq f_{min} \cap \mathbf{f} \leq f_{max}$   
 Get frequency vector within range  $\mathbf{f} \leftarrow \mathbf{f}(\mathbb{I}_f)$

**Run:**

Initialize PSD matrices  $\hat{\mathbf{G}}_{yx} = \mathbf{0}$  and  $\hat{\mathbf{G}}_c = \mathbf{0}$

**for**  $i = 1 : N_w$  **do**

Scale  $j$ -th taper by its norm-2 and weight:

$$\mathbf{t} \leftarrow \frac{\mathbf{w}[j]}{\|\mathbf{T}[j, :]\|} \mathbf{T}[j, :]$$

**for**  $j = 1 : N_t$  **do**

Compute the DFT of  $i$ -th tapered segment with  $j$ -th taper:

$$\tilde{\mathbf{v}} \leftarrow \text{DFT}(\mathbf{v}[\mathbb{I}_u, \mathbb{I}_w] \circ \mathbf{t})$$

Get DFT of response and reference channels in current frequency range:

$$\tilde{\mathbf{y}} \leftarrow \tilde{\mathbf{v}}[\mathbb{I}_y, \mathbb{I}_f] \quad \tilde{\mathbf{x}} \leftarrow \tilde{\mathbf{v}}[\mathbb{I}_x, \mathbb{I}_f]$$

Compute outer product and square of each DFT:

$$\hat{\mathbf{G}}_{yx}[k] \leftarrow \hat{\mathbf{G}}_{yx}[k] + \tilde{\mathbf{y}}[k] \tilde{\mathbf{x}}^H[k] \quad \hat{\mathbf{G}}_c[k] \leftarrow \hat{\mathbf{G}}_c[k] + |\tilde{\mathbf{v}}[:, \mathbb{I}_f[k]]|^2$$

**end**

Slide data segment backwards:  $\mathbb{I}_w \leftarrow \mathbb{I}_w - N_o$

**end**

**if**  $f_{min} = 0$  **then**

Halve the PSD at DC:  $\hat{\mathbf{G}}_{yx}[0] \leftarrow \hat{\mathbf{G}}_{yx}[0]/2$  and  $\hat{\mathbf{G}}_a[0] \leftarrow \hat{\mathbf{G}}_a[0]/2$

**end**

Calculate average and apply correct scaling:

$$\hat{\mathbf{G}}_{yx} \leftarrow \frac{2}{f_s N_w N_t} \hat{\mathbf{G}}_{yx} \quad \hat{\mathbf{G}}_a \leftarrow \frac{2}{f_s N_w N_t} \hat{\mathbf{G}}_a$$

#### 4.4 Spectral estimation of time-varying systems

The aim of spectral analysis of LTV systems is to obtain a useful time-frequency representation of the response that can provide (immediately or in additional steps) information in terms of eigenfrequency (resonance), damping ratio (decay) and eigenmodes (mode shapes). [COHEN, 1989] reviews at length several time-frequency distributions and concludes that there is no one method that outperforms others in all metrics. Time-frequency analysis is covered exhaustively in the monograph [COHEN, 1995]. Recent and equally detailed surveys of the topic [FENG ET AL., 2013; SHAFI ET AL., 2009] reach similar conclusions: the method of time-frequency analysis should be tailored for its intended purpose and selected for the class of signals it is applied to. The simplest and most intuitive technique is the short-time Fourier transform (STFT) to observe changes in the frequency component of the signal. It is physically meaningful, fast, but has a limited  $\Delta t \Delta f$  resolution because it uses a fixed-size window and its basis functions have infinite support. Wavelets tackle this issues by adopting multiple time-scales and kernels with limited support in both the time and frequency domains [MALLAT, 2008; WALNUT, 2002] (see also appendix A.12). They are a popular and effective choice in detecting transients and low frequency components, but require the selection of the right basis and have bad resolution for high frequencies. Wavelets find applications in both spectral estimation and system identification problems [AVENDAÑO-VALENCIA ET AL., 2020]. Other non-parametric methods utilize bilinear time-frequency distributions [ZHOU ET AL., 2014] and the Hilbert-Huang transform [BAO ET AL., 2009]. Figure 4.10 presents a comparison between the short-time Fourier transform, the continuous wavelet transform and a bilinear time-frequency distribution.

In this research we aim to analyze signals that are broadband random, contain many lightly-damped poles and are affected by noise. The system variation is expected to be sufficiently slow and spectral estimation must be performed efficiently for dozens of channels. The chosen approach is thus to employ the short-time Fourier transform because it is economical, easy to interpret, does not require foreknowledge about the signals and can be paired with existing frequency-domain identification techniques.

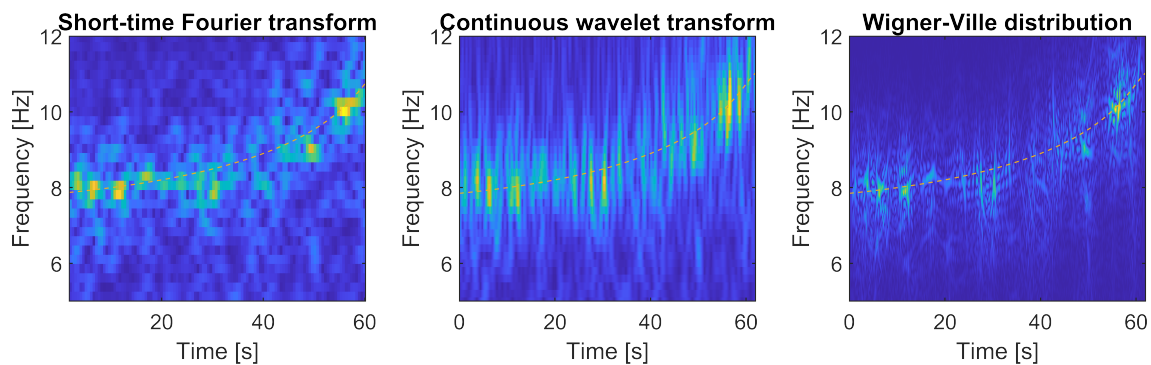


FIGURE 4.10: Comparison of short-time Fourier transform, wavelet transform and a bilinear time-frequency distribution (in this case, the smoothed pseudo Wigner-Ville distribution). Data from the airfoil-rudder system 7.2 with linear speed profile from rest to flutter. Only 4000 samples are available for spectral estimation.

In [EUGENI ET AL., 2018] it is argued that a system is slowly-varying as long as the maximal eigenfrequency variation  $\Delta f_n = T_b \max \left\{ \frac{\partial f_n}{\partial t} \right\}$  over the observation interval  $T_b$  is lower than the corresponding frequency resolution  $\Delta f = 1/T_b$ . The maximal allowed rate of variation is thus:

$$\sqrt{\max \left\{ \frac{\partial f_n}{\partial t} \right\}} \leq \frac{1}{T_b} \quad (4.31)$$

The faster the system variation, the smaller the possible observation interval. However, this simplified criterion is excessively conservative and does not account for the type of parameter variation. For example, for periodic systems the instantaneous eigenvalues may change rapidly, yet the actual eigenvalues (Floquet's exponents) are constant. In this regard we have seen in chapter 2 that time-invariant and periodic systems have a similar pole-residue form in frequency-domain representation. Consequently, spectral estimation works the same way for periodic systems.

When parameter variation is arbitrary, then the working hypothesis is that the system is slowly-varying within the observation interval:

**Hypothesis.** *The system  $\mathcal{S}$  does not vary significantly within the interval  $[t_n, t_n + T_b]$ , where  $T_b = L_w/f_s > 0$  is an appropriately short block used for spectral estimation.*

Depending on the system, the observation time  $T_b$  can be determined based on the criteria delineated in chapters 2 and 3. For instance, the maximal variation of the mode dynamic coupling can be limited to 0.05 (see for example figure 3.15). Without numerical models,  $T_b$  must be determined experimentally. In practice the observation window is as small as necessary for *reasonably* stationary conditions<sup>13</sup>. Equivalently, it may be stated that the system is slowly-varying. This assumption is used, among others, in [ERTVELDT ET AL., 2014; LATAIRE AND PINTELO, 2010; SPIRIDONAKOS AND FASSOIS, 2009].

Let  $\mathbf{G}_{xx}(\omega, t_0)$  be the CPSD of the input signal in the interval  $[t_0, t_0 + T_b]$ . The corresponding output CPSD  $\mathbf{G}_{yy}(\omega, t_0)$  can be determined by equation (4.16):

$$\mathbf{G}_{yy}(\omega, t_0) \approx \mathbf{H}(\omega, t_0)\mathbf{G}_{xx}(\omega, t_0)\mathbf{H}^H(\omega, t_0) \quad (4.32)$$

The transfer function  $\mathbf{H}(\omega, t_0)$  corresponds to the system at the mean time  $\mathcal{S}(\bar{t})$  or mean parameters<sup>14</sup>  $\mathcal{S}(\bar{\mathbf{p}})$ . Equation (4.32) is a frozen-time approximation of the system: the analytical output spectra  $\mathbf{G}_{yy}(\omega, t_0)$  differ from the estimated output spectra estimated  $\hat{\mathbf{G}}_{yy}(\omega, t_0)$  due to time-varying dynamics, but under the current assumptions these are higher-order terms that are less important than estimation bias. Averaging is necessary to reduce variance, but in the time-varying case, each data segment contains the response of a system with different parameters and therefore a “snapshot” of the system at that

<sup>13</sup> Normally  $T_b$  is much larger than the sampling interval  $T_b \gg 1/f_s$ . For an aeroelastic system with a realistic parameter variation this can be as large as a hundred times the lowest time constant. The duration  $T_b$  is determined by the lowest resonance bandwidth of interest.

<sup>14</sup> Taking the mean is one of the possible choices. Poles with low damping have high peaks that tend to dominate the spectrum. This effect is particularly prominent in a hard flutter case because the real part of the critical mode plunges rapidly and the corresponding peak grows (see figure 4.13).

time. Consequently, during the whole data buffer the variation may be significant even when within a single segment it is not. This limitation can be circumvented by acquiring several realizations of the system and by averaging the time data blocks corresponding to the same point along the parameter path.

Two approaches are thus considered for time-varying system spectral estimation:

- *Sequential averaging* (subscript “ $w$ ”) is the average of spectra estimated by from overlapping data blocks (windows) within a long time data buffer (see Welch’s modified periodogram in section 4.3.1).
- *Ensemble averaging* (subscript “ $e$ ”) consists in acquiring several uncorrelated system realizations with the same parameter variation. The spectrum is estimated by averaging all data blocks corresponding to the same starting time within one realization.

Figure 4.11 illustrates the two approaches schematically. Let  $L$  be the data block (window) length and  $f_s$  the sample rate. The data block length is a trade-off between acceptable frequency resolution and system variation during the time  $L/f_s$ . In sequential averaging the window advances by an interval  $\Delta t_w = \lfloor L(1 - O_w) \rfloor / f_s$ , where the optimal overlap  $O_w$  is specific to each window type. For a given frequency resolution, let  $N/f_s$  be the buffer duration needed to reduce the variance below the desired level using  $N_w$  averages. The spectral estimates  $\hat{G}_{yy}(\omega, t_0 + n\Delta t_w)$  are then obtained from the time intervals  $t_0 + n\Delta t_w + [0, N/f_s]$  for  $n = 0, 1, \dots$  by averaging within the buffer and then sliding

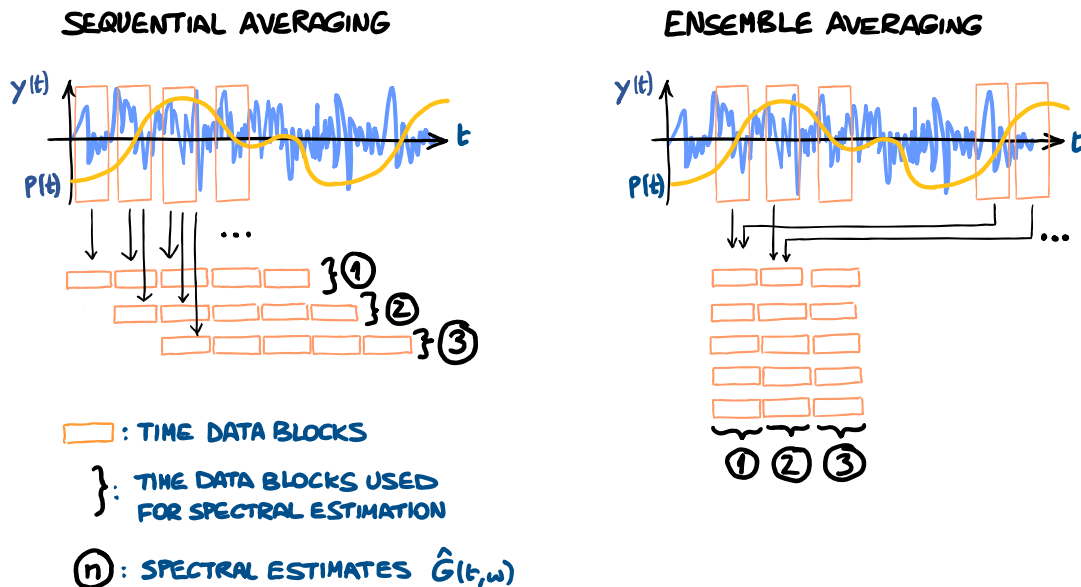


FIGURE 4.11: Sequential and ensemble averaging in the spectral estimation of time-varying systems. For the sake of clarity, the data blocks are not overlapping in this figure. In the sequential approach averaging is performed from  $N_w$  contiguous segments. The buffer is then shifted by  $L$  samples to produce a new spectral estimate. In the ensemble approach the spectrum is estimated from  $N_e$  block from different experiments but with the same phase along the parameter path. The buffer is then shifted by  $L$  samples to produce a new estimate valid for different parameter. Both approaches process the same amount of data and result in a temporal resolution of  $L/f_s$ . See text for discussion.

it forward. On the other hand, in ensemble averaging the fractional overlap  $O_e$  can be chosen freely (in some cases even 0.99) based on the desired temporal resolution  $\Delta t_e = \lfloor L(1 - O_e) \rfloor / f_s$  of the spectra. The spectral estimates  $\hat{\mathbf{G}}_{yy}(\omega, t_0 + n\Delta t_e)$  are now obtained from the time intervals  $t_0 + n\Delta t_e + [0, L/f_s]$  for  $n = 0, 1, \dots$  by averaging  $N_e$  realizations and then sliding the buffer forward. The system must now be slowly-varying only within the duration of a data segment  $L/f_s$  instead of  $N/f_s$ , a condition that is easier to satisfy in the normal operating range of aircraft and wind tunnels.

Figure 4.12 provides an example of sequential averaging from a buffer of duration  $N/f_s$ . In this case one estimate  $\hat{\mathbf{G}}_{yy}(\omega, 0)$  is obtained. Figure 4.13 displays the comparison between the analytical prediction and the spectra estimated using ensemble averaging. For a given overlap  $O_e$ , the spectral estimates are  $\hat{\mathbf{G}}_{yy}(\omega, n\Delta t_e)$  where  $n = 0 : \lfloor (N - L)/\Delta t_e / f_s \rfloor$ . There is good agreement between the experimental and predicted spectra and sufficient temporal resolution to observe the eigenvalue evolution.

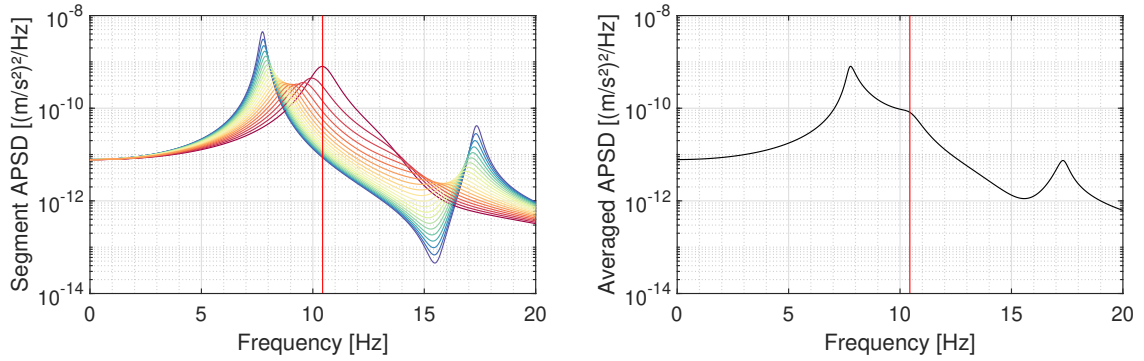


FIGURE 4.12: Short-time spectral estimation of airfoil-rudder system response with linear speed profile from rest to flutter (blue: low, red: high) in  $T = 20$  s. The line color represents the parameter (blue: low, red: high). Left column: instantaneous spectra corresponding to 20 windows, right column: resulting average. A large parameter variation results in three peaks appearing where there are only two eigenmodes. Conversely a smaller parameter variation would enlarged one peak due to superposition; the estimated damping is consequently higher.

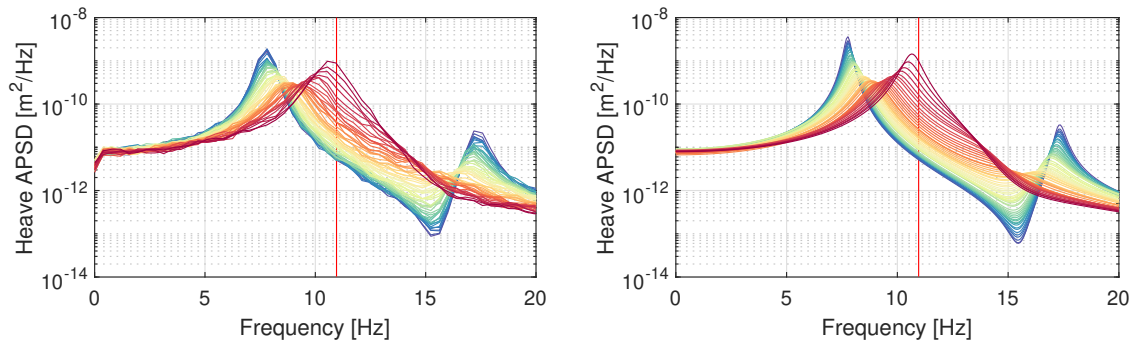


FIGURE 4.13: Same system as in figure 4.12. Short-time spectral estimation of airfoil-rudder system response with linear speed profile from rest to flutter (blue: low, red: high) in  $T = 20$  s. The red line marks the location of the unstable mode. The left plot displays APSDs estimated using very short time intervals (as long as a single periodogram segment). The right plot shows, in very good agreement, the analytical output spectra calculated from the mean system within this short interval. The temporal resolution of the spectra is very high.



Let us set the number  $N_t$  of time instants (or parameter points) at which the system must be identified and impose that the two methods have the same number of spectral averages  $N_a$  and frequency resolution  $\Delta f = f_s/L$ , i.e. equal frequency bias and random error. The total number of samples  $N_w^{tot}$  and  $N_e^{tot}$  that must be acquired is<sup>15</sup>:

$$\begin{aligned} N_w^{tot} &= N_t \cdot L((N_a - 1)(1 - O_w) + 1) \\ N_e^{tot} &= N_a \cdot L((N_t - 1)(1 - O_e) + 1) \end{aligned} \quad (4.34)$$

The two equations look very similar, but data is employed differently. Sequential averaging overlaps its data blocks, but it requires a contiguous and long data buffer. Ensemble averaging does not overlap its data blocks, but it compensates with a lower parameter variation within the buffer it uses to estimate spectra. This means that in sequential averaging the system evolves longer than with ensemble averaging by a factor:

$$\frac{N/f_s}{L/f_s} = (N_w - 1)(1 - O_w) + 1 \quad (4.35)$$

Let us take a look at the random error  $\varepsilon_r$ . In the usual sequential approach we have  $\varepsilon_r = 1/\sqrt{N_w k_{eq}}$ , where  $k_{eq}$  is the equivalent number of averages factor based on the chosen window function and overlap<sup>16</sup> (see figure 4.4). In contrast, in ensemble approach the spectral averages do not overlap, therefore the normalized random error is  $\varepsilon_r = 1/\sqrt{N_e}$ , which implies  $N_w < N_e$ .

In conclusion:

- *Sequential averaging* is suitable for invariant or, at most, very slowly-varying systems because it uses a contiguous data buffer for each parameter point / time instant. If the experiment's purpose is measuring time-varying dynamics, then this point-by-point frozen-time estimation arguably does not fulfill the requirement. This approach can estimate spectra continually "online" as new data comes in.
- *Ensemble averaging* is to be used where the experiment must take a faster system variation into account. It requires several equal system realizations, which might be difficult to execute experimentally (this has to be verified case by case). If the system is periodic, this approach can refine "online" its estimate with each new parameter cycle (period). The important advantage of this technique is the less stringent requirement on parameter variation.

<sup>15</sup> The number of samples for a *single* parameter is (for convenience we drop the floor function):

$$\begin{aligned} N_w &= (N_a - 1) \cdot L(1 - O_w) + L \\ N_e &= N_a L \end{aligned} \quad \implies N_w \leq N_e \quad (4.33)$$

<sup>16</sup> For example, assuming an optimal Hann window overlap  $O_w = 2/3$ , which corresponds to an equivalent number of averages factor  $k_{eq} = 2.04$ , a normalized random error of  $\varepsilon_r = 0.1$  is achieved when:

$$\frac{N}{L} = (0.1^{-2}/2.04 - 1)(1 - 2/3) + 1 \approx 17$$

therefore, for a certain block length  $L$ , the system must evolve approximately 17 times longer when employing the sequential averaging.

Ensemble averaging may be applied in an experimental setting when fast parameter variation warrants a closer inspection of its dynamics and when obtaining the necessary number of realizations is not a concern. For arbitrary LTV systems, multiple experiments must be carried out to collect enough data for system identification. This is well attested in literature, see for example [LIU, 1997; MA ET AL., 2017; MAJJI ET AL., 2010; SPIRIDONAKOS AND FASSOIS, 2009; ZHOU ET AL., 2014] and references therein. Ensemble averaging will be applied in chapter 7 to study time-varying systems whose variation is too fast for a single contiguous data buffer.

#### 4.4.1 On spectral estimation applied to aeroelastic systems

In ground vibration testing of aircraft, the frequency response function estimation is performed by a carefully-designed experiment, with methodical sensor selection and placement to increase the signal-to-noise ratio, optimal excitation, location, level and direction, controlled boundary conditions, noise characterization and long acquisition times over several runs [GOVERS ET AL., 2014; STÉPHAN ET AL., 2015]. In this regard, the book from [PINTELON AND SCHOUKENS, 2004] is a recommended reference on the topic.

Spectral estimation applied to aeroelastic systems in operating conditions has unfortunately few such amenities. Duration is always constrained by schedule and cost (e.g. flight hours, wind tunnel operation, testing of different configurations, hiccups). Sensor selection may be severely limited in number, location, type and operating temperatures. The experimenter may have little control over excitation types or levels and weather conditions. Additionally, there may be unavoidable contributions from feedback loops (for example an aircraft's flight control system and the pilot) or interactions with neighboring systems (for instance the brakes, balance and pumps in a wind tunnel).

An important consequence of the system's linearity is that a random input produces a random output with the same distribution and a different amplitude and phase. Since turbulent excitation is normally-distributed, the responses must be as well. Channels that deviate from the Gaussian distribution can indicate that data is non-stationary, that nonlinearities are at play, that a flutter condition is being approached, that a sensor is faulty or that there is another component exciting the system such as rotating machinery. As an example, figure 4.14 displays the measured acceleration distributions of a wind tunnel test near the flutter conditions.

Aircraft are subject to gust excitation, aerodynamic forces and maneuver loads under different flight conditions, therefore the response signals have in general a non-stationary character. Implicitly it is assumed that the time data record provided to spectral estimation is stationary and ergodic (i.e. its principal moments do not vary). This assumption is not easy to satisfy during flight vibration testing as excitation levels may change due to transient turbulence, maneuvers, flight speed or altitude variations. As an example, figure 4.15 displays the principal moments of the measured responses at constant altitude during flight vibration testing in order to highlight their non-stationary character.

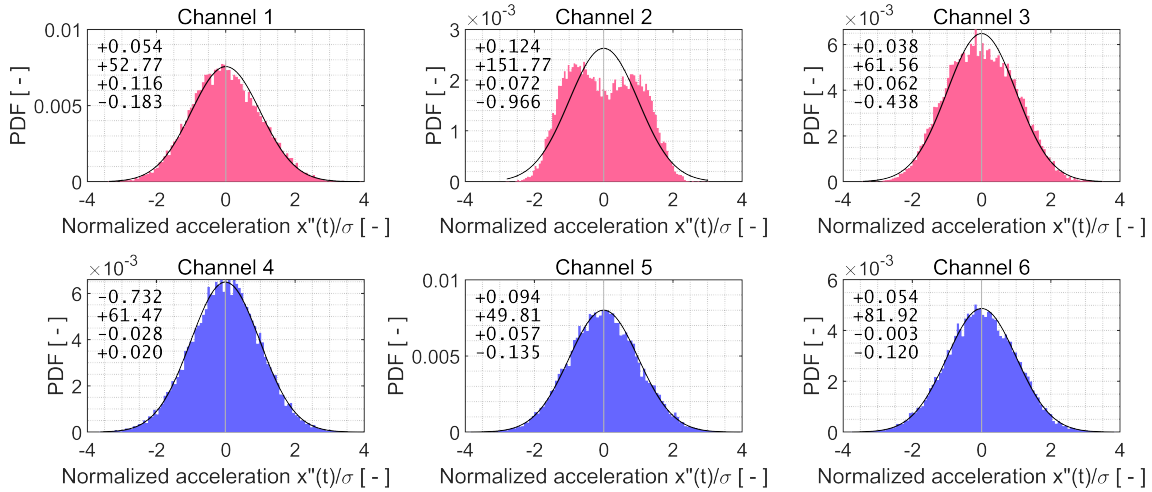


FIGURE 4.14: Probability density distribution of the measured accelerations during a wind tunnel test displayed as histograms. The mean, variance, skewness and excess kurtosis of each channel (see appendix A.11) are displayed in the upper left corner. The top channels deviate considerably from the Gaussian function distribution computed from the sample's mean and variance (black line). In channel 2 the onset of flutter is seen as a sine overlaid with a normal distribution. Data from the transonic wind tunnel DNW-TWG [JELIČIĆ ET AL., 2014].

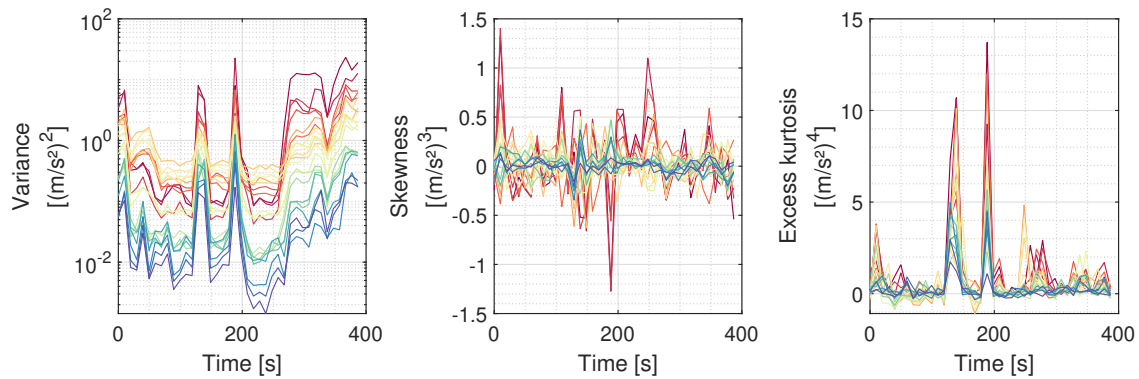


FIGURE 4.15: Three principal moments of vertical accelerations recorded on an airplane while entering turbulence. The time blocks where skewness and excess kurtosis deviate suddenly from zero denote non-stationary conditions because the response is not normally-distributed. Flight test data from [JELIČIĆ ET AL., 2017] (see chapter 8).

Figure 4.16 displays the spectrogram of a channel acquired while flying in the wake of another aircraft. The local characteristics of the signal are resolved by short overlapping buffers (short-time Fourier transform). The spectrogram reveals immediately that the excitation level is not constant and a closer inspection reveals that resonance peaks shift due to flight speed variation. The spectral estimation parameters are chosen carefully in order to maintain simultaneously adequate time and frequency resolutions. The MTM is set up to have the same spectrum variance of Welch's modified periodogram, but with a higher frequency resolution, which is beneficial to frequency-domain system identification methods. In the construction of the spectrogram, the faithful estimation of the resonance peak (reducing the frequency bias error) may be relaxed for more flexibility in the choice of  $\Delta t \Delta f$ .

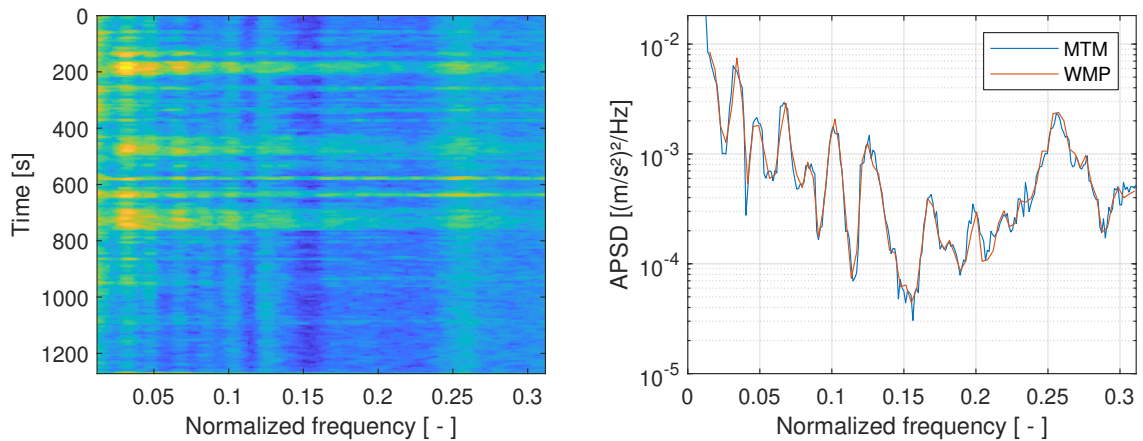


FIGURE 4.16: The spectrogram on the left displays the uneven turbulence encountered by an aircraft flying into the wake of another. The plot on the right is a section of the same spectrogram. The WMP and MTM methods have approximately the same variance, but the latter has a threefold frequency resolution increase. Flight test data from [JELIČIĆ ET AL., 2017] (see chapter 8).

In [BRENNER ET AL., 1997], in the context of aeroservoelastic investigations with nonstationary and time-varying dynamics, the authors note the limits of FFT-based spectral estimates and supplement them with time-frequency techniques to assist the detection of nonlinearities and to improve modal analysis. The frequency-domain representation of non-stationary signals of LTV systems may be difficult to interpret, that is, it may not clearly reveal the locations of the system’s poles or the input’s frequency components. However, there are circumstances under which time-varying systems can be considered stationary or quasi-stationary enough for spectral estimation methods to deliver sensible results. Wind tunnel experiments are essentially stationary and spectra can be estimated by “classical” methods [JELIČIĆ ET AL., 2014]. Flight vibration testing is more challenging due to the non-stationary character of excitation but also because the signal-to-noise ratio may be inadequate for some sensors [JELIČIĆ ET AL., 2017]. Experimental results will be discussed in chapter 8 where this topic will be expanded further.

## 4.5 Chapter summary

Spectral estimation is introduced for the purpose of vibration monitoring and modal analysis of experimental data. Two non-parametric approaches are considered: Welch's modified periodogram and the multi-taper method. Based on existing theory, we have combined them into the segment multi-taper method, which shows better performance for very short signals.

Two issues arise with real measurements of random data: limited frequency resolution and variance of spectral estimates. To address the first problem, the signal's duration (amount of collected information) must be greater than a certain threshold. On the other hand, in order to reduce variance, several spectral estimates must be averaged. It is not possible to reduce both at will lest more data is collected, consequently the experimenter must find a compromise between frequency bias and random errors. To this end, the chapter has detailed the parameters of spectral estimation.

Sequential averaging can be employed when the system undergoes a limited variation. Ensemble averaging employs several realizations with the same parameter variation to attain better time-frequency resolution. There exist numerous time-frequency analysis methods for the general time-varying case. However, when the system is slowly-varying with respect to the estimation buffer or window, it is possible to obtain useful spectral estimates with adequate time resolution. The non-parametric spectral estimation based on the Fourier transform is therefore the preferred approach for the application at hand because it is easy to compute and interpret.

## 5 System identification

### *Abstract*

---

The system identification methods estimate the modal parameters from time-domain or frequency-domain data. The objective is to determine the eigenfrequency, damping ratio and mode shapes solely from the measured system responses and to track their evolution over time or external variables. For this purpose, the Stochastic Subspace Identification and Least-Squares Complex Frequency algorithms are employed within the operational modal analysis framework.

---

System identification is the analysis of the measured response of a dynamic system subject to some excitation in order to construct a simplified mathematical representation of it. The system's complex behavior is thus modeled by a limited set of variables whose purpose is to provide an adequate characterization of its dynamics. This task incorporates experiment design, model structure selection, parameter estimation and validation. Several different techniques have been developed to estimate the system parameters under various experimental conditions. The identified model enhances the physical understanding of the system and forms a basis for simulation, control, prediction and filtering. System identification is therefore a multidisciplinary science that attains from control theory, signal processing, optimization and statistics. It has found a very broad range of applications in structural dynamics, robotics, electronics, bioengineering, chemical processes and astrophysics. The reader is referred, among many others, to [LJUNG, 1999], [PINTELOON AND SCHOUKENS, 2004] and [VERHAEGEN AND VERDULT, 2007] for a complete overview and treatment of the topic.

In the context of modal analysis applied to aircraft, modal parameter estimation is performed to determine the eigenfrequency, damping ratio and modes of vibration, to study the sensitivity to structural modification, to update finite element models with experimental data, to tune flight control laws, to understand the vibroacoustic coupling between structure and radiated noise. The identification of time-varying systems is still an open issue whose theoretical background is being constantly expanded. Our goal is the real-time system identification of parameter-varying aeroelastic systems excited by turbulence and acoustic noise. We are interested in the in-flight monitoring of the structure's modal parameters as a function of wind speed and air density. This can be accomplished by modal parameter estimation techniques that process the measured system outputs.

The chapter's roadmap is thus:

1. Introduction of system identification and modal analysis frameworks.
2. Description of the adopted output-only system identification methods.

This chapter is dedicated to the methodology, while the application on simulations and experimental data will be presented in chapter 8.

## 5.1 Modal analysis frameworks

The measured outputs are the primary data source of system identification. Three scenarios appear depending on whether the input can be acquired as well:

- When the excitation is known, system identification is performed within the framework of *input-output* or *experimental modal analysis* (EMA). In this scenario optimal experimental conditions are designed to estimate the system's transfer function.
- When the excitation is unknown, unmeasurable or the structure's modal parameters must be determined during operation, the methods of *output-only* or *operational modal analysis* (OMA) are invoked. In this case only the structure's response signals (typically accelerations, velocities or strains) can be used to extract modal parameters.
- When the system is subject to both known and unknown inputs, then the *operational modal analysis with exogenous inputs* (OMAX) approach provides maximal data exploitation by utilizing the ambient excitation to extract information about the system as well.

In the EMA framework, the measurement of the frequency response function provides the full description of a linear time-invariant system. The experimenter strives to realize almost ideal and controlled laboratory conditions. Furthermore, it is possible to characterize the input and output noise spectra in order to improve the estimated transfer function in the errors-in-the-variable framework. This is a field of great engineering interest because it can provide very accurate information about dynamic systems [PINTELOON AND SCHOUKENS, 2004; VERHAEGEN AND VERDULT, 2007].

When conditions for EMA are not possible or feasible, the modal parameters must be extracted using output-only techniques. This happens when the available system model is not representative of actual operating conditions or when ambient excitation cannot be isolated or measured. This is typically the case for buildings, ships, wind turbines, aircraft in flight and any other very large structure. A specific application of OMA is structural health monitoring: modal analysis is performed to identify the structure's real behavior under operating conditions, to monitor its integrity over a very long period and to reduce inspection costs due to its remoteness. The OMA framework is challenging because the quality or quantity of available information is inferior compared to EMA. The analyst is confronted with non-ideal experimental conditions, higher susceptibility to errors and unaccounted dynamical effects. A key assumption is that the input is stationary and normally distributed white noise, which is almost never the case. Nevertheless, it remains a topic of active research and of great interest for engineers because OMA delivers useful data. The books from [VAN OVERSCHEE AND DE MOOR, 1996], [BRINCKER AND VENTURA, 2015] and [RAINIERI AND FABBROCINO, 2014] offer an overview of several aspects of operational modal analysis.

## 5.2 Modal analysis of aeroelastic systems

Within the context of aeronautic testing there are three modal analysis approaches:

- The *ground vibration test* (GVT) of an aircraft is carried out by applying known forces and measuring the response of the structure, hence it is conducted within the EMA framework. The airplane is suspended to realize a free-free condition while sweep or random signals are applied by electrodynamic shakers. The measurement campaign is designed to achieve optimal sensor distribution, excitation locations and directions, signal duration, signal-to-noise ratio, and so forth. During GVT several load levels, driving point locations and geometric configurations are investigated to construct a complete modal model of the aircraft [GOVERS ET AL., 2014; STÉPHAN ET AL., 2015]. The experimental results are typically used to validate the structural dynamics modeling and for the design of the electronic flight control system.
- The *taxi vibration test* (TVT) is performed by taxiing or towing the aircraft on the taxiway. Excitation is provided either by the uneven pavement, path roughness or low-lying obstacles such as wood planks. The TVT assists in checking the flight test instrumentation before actual testing. This is of great importance for assessing the data acquisition setup when large numbers of different sensors are employed [GOVERS ET AL., 2017; SINSKE ET AL., 2018].
- The *flight vibration test* (FVT) of an aircraft is conducted by analyzing the structure's dynamics under a variety of flight conditions. The real operating environment can differ significantly from the ideal laboratory conditions of a GVT. The simulation of new aircraft's flutter behavior is conducted with considerable effort, but adequate aeroelastic stability must be demonstrated in flight for the whole flight envelope up to maximum speed and maximum altitude. Often artificial excitation with control surface impulses is employed to inject energy into the system. The identified modal parameters are used to analyze the system stability within the flight envelope or to update numerical models [CORDA ET AL., 2002; IOVNOVICH ET AL., 2018; SCHWOCHOW AND ZÖGER, 2013].

Parameter-varying aeroelastic systems such as aircraft in flight or wind tunnel models during operation are subject to air turbulence and acoustic noise, therefore identification is carried out in the output-only framework. If available, information from a GVT is utilized to locate and label the main modes, to construct a reference modal model, to gain further insight about the system. An overview of aircraft vibration testing can be found in [BÖSWALD ET AL., 2017; KÖNIG, 1995]. The system identification methodology applied in this thesis has been developed and gradually improved and refined during ground vibration testing [GOVERS ET AL., 2014], wind tunnel testing [BÖSWALD ET AL., 2019; JELIČIĆ ET AL., 2014] and flight vibration testing [JELIČIĆ ET AL., 2017]. We shall focus on the practical aspects of FVT in chapter 8



### 5.3 System identification methods

In the endless quest of finding the most efficient, unbiased and robust modal parameter estimator, a great number of system identification methods in the time and frequency domains have been developed over the years. The ability to estimate modal parameters reliably under various experimental circumstances is important to many engineering applications. As one should always “expect the unexpected” when performing experiments, the chosen method must be able to deal with faulty sensors, interruptions, bad data, noise and errors. Importantly, the system identification procedure must be fast and responsive because the user is allowed to constantly adjust settings during data acquisition. Such requirements restrict the algorithm choice. [REYNDERS, 2012] describes in much mathematical detail several system identification methods for modal analysis and provides a review and comparison.

In the present work we need to perform vibration monitoring and modal analysis in real-time. In order to accomplish this goal, two methods have been taken into consideration:

- *SSI*: Stochastic Subspace Identification
- *LSCF*: Least-Squares Complex Frequency

Both are popular in the modal analysis community as experimental tools and as research topics and are implemented in various vibration analysis software packages. SSI features predominantly in time-domain data-driven applications, whereas LSCF is a frequency-domain technique particularly suited for EMA. The two methods have advantages and disadvantages that may clearly favor one over the other in certain circumstances, but they are generally complementary. In the author’s experience it is difficult to state a preference. For flexibility and redundancy, both methods have been researched and implemented as fail-safe when performing online vibration monitoring (see chapter 8). Their algorithms have been adapted to the task at hand particularly with regard to efficiency and clear stabilization diagrams. We shall provide more details and references in the corresponding sections 5.4 and 5.5.

#### 5.3.1 Modeling assumptions

Let us consider a time-varying system in the operational modal analysis framework:

$$\begin{aligned}\dot{\mathbf{x}}(t) &= \mathbf{A}(t)\mathbf{x}(t) + \mathbf{v}(t) \\ \mathbf{y}(t) &= \mathbf{C}(t)\mathbf{x}(t) + \mathbf{w}(t)\end{aligned}\tag{5.1}$$

where  $\mathbf{v}(t)$  are the unknown/unmeasured inputs and  $\mathbf{w}(t)$  is the output measurement noise. It is assumed that the system is observable and controllable, i.e. that the observability and controllability Gramians are nonsingular [RUGH, 1996]. In operational modal analysis the inputs are unmeasurable, but random. It is also assumed that the excitation satisfies wide-sense stationarity (the covariance between two samples depends only on time difference and not on the time at which they have been sampled) and quadratic mean ergodicity

(ensemble averaging can be replaced by time averaging) [DOUGHERTY, 1998]. The variance of the identified modal parameters increases when the last two assumptions are not fully met. [BENVENISTE AND MEVEL, 2007] show that subspace algorithms can converge to the “true” eigenstructure (only the system poles, not the zeroes) despite nonstationary excitation. In real-life situations, the unobserved input is mostly: random, harmonic or a combination of the two. Within operational modal analysis it is assumed that the excitation is white noise, i.e. a stochastic process with constant-amplitude power spectral density within a finite interval and with uniformly-distributed random phase [BENDAT AND PIERSOL, 2010]. In reality, the input is more likely to be colored (see, for example, the von Kármán gust spectra in section 3.3), therefore highly-damped and complex modes may be fitting the colored input spectrum [NEU ET AL., 2016]. Furthermore, there might be harmonic components due to the presence of rotating machinery and electronic devices (see figure 5.2 for a real example). The characterization or modeling of input and output noise leads to better spectral estimates and system identification results, however this is not always feasible or possible [PINTELOON AND SCHOUKENS, 2004].

### 5.3.2 System formulations

Depending on the system identification method, the system is described in one formulation or the other. We shall at first consider the time-invariant case and describe the application of “classic” techniques to time-varying systems in later sections. We shall review concisely the forms of the transfer function introduced in section 2.2 and, for simplicity, ignore the feed-through matrix because it can be simply added back later:

- *State-space form*: the transfer function of an LTI system is:

$$\mathbf{H}(s) = \mathbf{C}(s\mathbf{I} - \mathbf{A})^{-1}\mathbf{B} \quad (5.2)$$

where  $\mathbf{A} \in \mathbb{R}^{N_x \times N_x}$ ,  $\mathbf{B} \in \mathbb{R}^{N_x \times N_u}$  and  $\mathbf{C} \in \mathbb{R}^{N_y \times N_x}$ . Subspace methods determine the system in this form [VAN OVERSCHEE AND DE MOOR, 1996].

- *Pole-residue form*: the system can be diagonalized by the eigendecomposition of the state matrix and written as a sum of simple poles:

$$\mathbf{H}(s) = \mathbf{C}\Psi(s\mathbf{I} - \mathbf{\Lambda})^{-1}\Psi^{-1}\mathbf{B} = \sum_{k=1}^{N_x} \frac{\mathbf{c}_k \mathbf{b}_k^T}{s - \lambda_k} = \sum_{k=1}^{N_x} \frac{\mathbf{R}_k}{s - \lambda_k} \quad (5.3)$$

where  $\lambda_k$  are eigenvalues,  $\mathbf{R} = \mathbf{c}_k \mathbf{b}_k^T$  the residues and  $\mathbf{c}_k \triangleq \mathbf{C}\Psi \mathbf{e}_k \in \mathbb{C}^{N_y}$  and  $\mathbf{b}_k^T \triangleq \mathbf{e}_k^T \Psi^{-1} \mathbf{B} \in \mathbb{C}^{1 \times N_u}$  the columns and rows of the transformed output and input matrices respectively. In modal analysis applied to mechanical or aeroelastic structures, identification results are usually presented in the modal form because the interest lies in the resonances and modes of vibration [BÖSWALD ET AL., 2010; GOVERS ET AL., 2014].

- *Polynomial form*: by factoring the previous equation we obtain

$$\mathbf{H}(s) = \frac{\sum_{k=0}^{N_b} \mathbf{B}_k s^k}{\sum_{k=1}^{N_a} a_k s^k} \quad (5.4)$$

where  $\mathbf{B}_k \in \mathbb{R}^{N_y \times N_u} \in \mathbb{R}$  and  $a_k$  are respectively the  $k$ -order numerator and denominator polynomial's coefficients. This equation is a *common-denominator model* because the denominator is a scalar function. Other formulations are the left- and right-polynomial fraction models where the denominator is a matrix:  $\mathbf{H}(s) = \mathbf{A}^{-1}(s)\mathbf{B}(s)$  and  $\mathbf{H}(s) = \mathbf{B}(s)\mathbf{A}^{-1}(s)$  [RUGH, 1996, Ch. 16]. LSCF methods fit a polynomial model [CAUBERGHE, 2004].

- *Zero-pole-gain form*: by writing the roots of the numerator and denominator polynomials the transfer function can be expressed in the zero-pole-gain formulation for each pair of outputs and inputs:

$$\mathbf{H}_{ij}(s) = \mathbf{G}_{ij} \frac{\prod_{k=1}^{N_z} (s - \mathbf{Z}_{k,ij})}{\prod_{k=1}^{N_p} (s - p_k)} \quad (5.5)$$

where  $p_k$  are the poles (denominator's roots),  $\mathbf{Z}_{k,ij} \in \mathbb{C}^{N_y \times N_u}$  are the zeros (numerator's roots) and  $\mathbf{G}_{ij} \in \mathbb{R}^{N_y \times N_u}$  the gain between the  $i$ -th output and  $j$ -th input.

In theory all formulations are equivalent, but in practice some transformations are numerically badly conditioned. For instance, a rational polynomial's partial fraction decomposition is an ill-posed numerical problem because slight changes in the data can cause disproportionate change in the poles and residues. It is thus advisable to use the state-space or zero-pole-gain representations as much as possible [PROAKIS AND MANOLAKIS, 2013]. Mechanical systems are mostly described by the pole-residue form<sup>1</sup>.

### 5.3.3 Stabilization diagram

The primary result of a system identification method is a set of eigenvalue and eigenvector pairs that have been estimated for various model orders. The row of each eigenvector describes a mode shape's amplitude and phase at the corresponding response channel on

<sup>1</sup> Mechanical systems are second-order and the mass, damping and stiffness matrices are real and symmetric (2.8), which leads to a pole-residue (or modal) form of the frequency response function (5.6) that is omnipresent in structural dynamics [BRANDT, 2011; RAINIERI AND FABBROCINO, 2014]:

$$\mathbf{H}(\omega) = \sum_{k=1}^{N_m} \left( \frac{\mathbf{R}_k}{i\omega - \lambda_k} + \frac{\mathbf{R}_k^*}{i\omega - \lambda_k^*} \right) \quad (5.6)$$

where  $\mathbf{R}_k \triangleq \boldsymbol{\psi}_k \boldsymbol{\psi}_k^T / a_k \in \mathbb{C}^{N_m \times N_m}$  are the residues corresponding to each eigenpair  $\{\boldsymbol{\psi}_k, \lambda_k\}$  and  $a_k$  are the so-called "modal-a" scaling constants. They can be computed by

$$\begin{bmatrix} \mathbf{0} & \mathbf{I} \\ -\mathbf{M}^{-1}\mathbf{K} & -\mathbf{M}^{-1}\mathbf{D} \end{bmatrix} = \boldsymbol{\Psi}\boldsymbol{\Lambda}\boldsymbol{\Psi}^{-1} \implies a_k = \hat{\boldsymbol{\psi}}_k^T (\mathbf{D} + 2\lambda_k\mathbf{M}) \hat{\boldsymbol{\psi}}_k \quad (5.7)$$

where  $\hat{\boldsymbol{\psi}}_k$  denotes the upper half of each eigenvector  $\boldsymbol{\psi}_k$  [REYNDERS, 2012, Eq. 172].

the structure. Model order, band, variance and other metadata are associated to each identified mode. The *modal model* is the collection of those modes that have been selected to represent the system, i.e. the terms in its pole-residue form.

The *stabilization diagram* is an effective system identification results supervision tool. It is the plot of each identified pole's eigenfrequency over its model order overlaid above a frequency-domain representation of the acquired data (transfer function for EMA or power spectral density for OMA). Reconstructed spectra are also displayed to validate the identification procedure. If available, coherence, spectrum variance, (complex) mode indicator function and so forth can be plotted. The stabilization diagram is often accompanied by a geometry plot to display the animated mode shapes and an eigenvector orthogonality plot to check if there are missing or double modes (see section 6.2). If available, the variance of each identified pole can be displayed as a horizontal bar to indicate visually the accuracy of fitted poles, as shown in [DÖHLER ET AL., 2013b]. Figure 5.1 displays an example constructed from real data and figure 5.2 comments some of its features. The stabilization diagram shows graphically which system poles have been estimated consistently over several model orders. Poles that are identified with little variation in terms of absolute value, damping ratio or associated eigenvector are termed “stable” and give a strong indication that they are indeed physical poles of the system. Conversely, “unstable” poles that wander around are fitting artifacts (in this context “unstable” modes do not assess the system's stability!). We refer to the classification of poles introduced in section 2.2.1. In the case of mechanical structures, lightly-damped  $0 \leq \zeta \leq 1/\sqrt{2}$  eigenvalues are very likely to represent the physical poles of the system, therefore any unstable  $\zeta < 0$  or highly-damped  $\zeta > 1/\sqrt{2}$  modes are usually automatically ignored. Aeroelastic systems, however, have several purely real or highly-damped eigenvalues corresponding to the lag states or the colored input (see chapter 3.1). Purely imaginary or very slightly unstable estimated eigenvalues may appear near the flutter boundary. Undamped periodic vibration corresponds to the flutter condition, a limit cycle oscillation or the harmonics of rotating machinery. Since the system is real, the identified eigenvalues must come in complex-conjugated pairs, possibly with some single purely real poles: we shall therefore display only poles with  $\Im\lambda \geq 0$ . For identification methods that represent the system with a rational polynomial (5.4), *poles at infinity* are obtained when the order of the numerator is higher than the order of the denominator (for example for acceleration spectra). Given a frequency range in which we want to identify the system, we shall thus apply the constraint  $f_{min} + 0.005\Delta f_B \leq f_n \leq f_{max} - 0.005\Delta f_B$  where  $\Delta f_B \triangleq f_{max} - f_{min}$ . Mathematical (spurious) poles arise as the system identification method tries to fit disturbances in the data. They may appear due to the presence of errors, nonlinearities, or because of poor signal-to-noise ratio on some sensors. They appear as lone poles with unrealistic damping, where there is no resonance peak, do not have a stable eigenfrequency over several model orders or have highly complex associated mode shapes.

A clean stabilization diagram is obtained – first and foremost – by good estimators, careful numerical implementation and proper signal processing. No sorting or cleaning of estimated modal parameters is performed on the stabilization diagrams in this thesis.

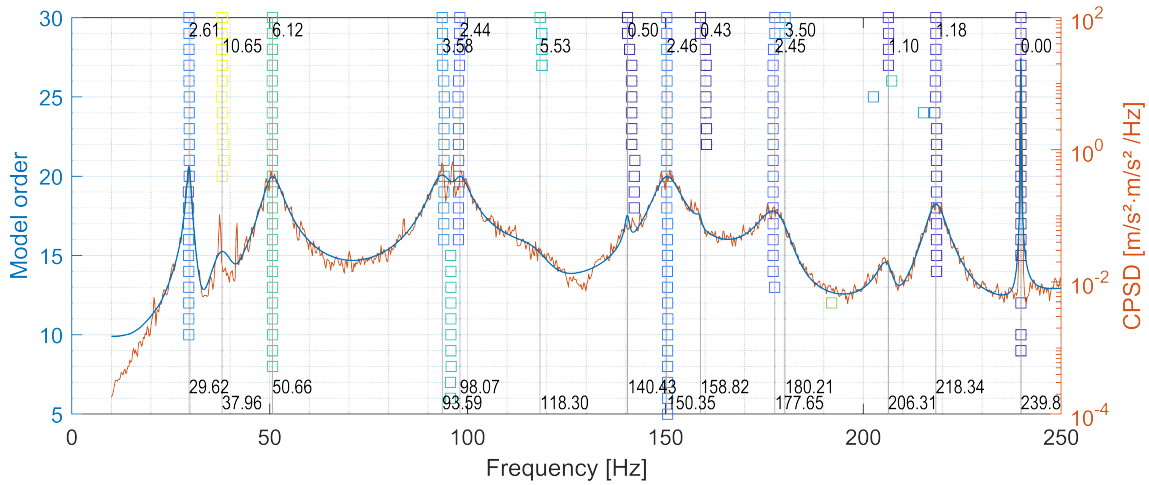


FIGURE 5.1: Stabilization diagram example. The square markers represent the identified poles over several model orders and their color encodes the damping ratio (blue: low, yellow: high) (color highlights unrealistic variations between model orders). The text reports the modal model’s eigenfrequency in Hz (bottom) and damping ratio in % (top). The vertical gray lines are located at the modal model’s eigenfrequencies. The red line (or dots) is the frequency-domain representation of the input data (OMA: CPSD, EMA: FRF). The blue line is the mean of the reconstructed (synthesized) spectrum according to the current modal model. No sorting or cleaning of the eigenvalues has been applied. Data from the transonic wind tunnel DNW-TWG [JELIČIĆ ET AL., 2014].

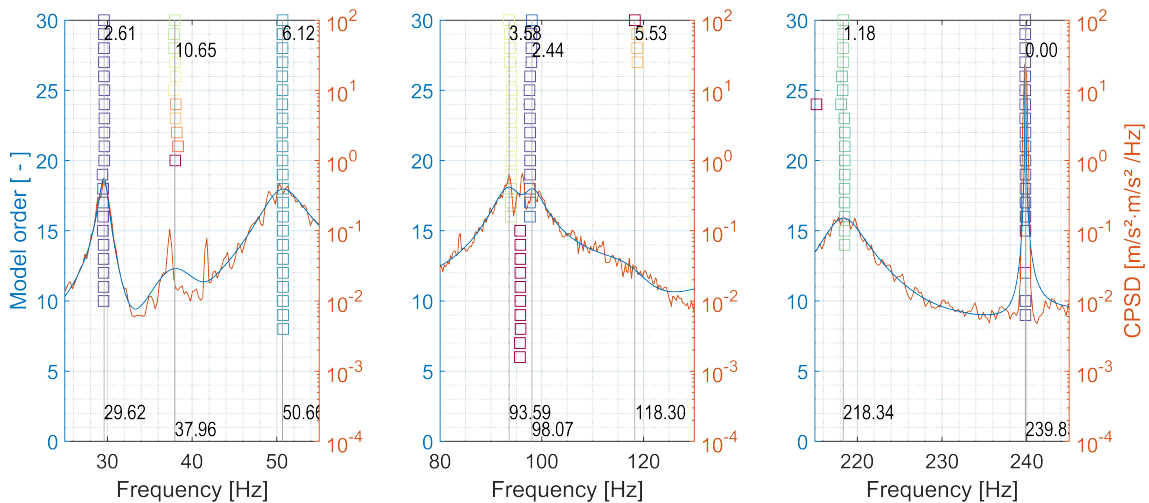


FIGURE 5.2: Details from figure 5.1. Left plot: the second mode did not stabilize completely and its estimated damping is too high (the model order may be too low). Middle plot: when the model order is sufficiently high the main peak is fitted by two modes and the damping ratio stabilizes. A closer look at the data reveals that all three modes are indeed physical. Right plot: the pole with vanishingly small damping is the vibration induced by a pump in the wind tunnel. Periodic disturbances such as power line frequency and rotating machinery are discussed in [BRANDT, 2015].

## 5.4 Stochastic Subspace Identification (SSI)

Stochastic Subspace Identification (SSI) is a family of widely-adopted system identification methods that are especially suitable for data-driven applications. Mathematically it is based on geometric projections extended to multidimensional spaces and makes use of various factorization techniques to improve numerical robustness and noise tolerance. It incorporates directly a model order reduction technique that is helpful in dealing with noise found in experimental data. SSI is particularly well-represented in the structural health monitoring community. There also exist variants for experimental modal analysis, but we shall focus only on output-only applications.

The core concept behind subspace identification has been developed into at least four variants:

- *data-driven* (SSI-dd): output-only method, utilizes time-domain data directly.
- *covariance-based* (SSI-cov): performs modal parameter estimation from the covariance of time data.
- *reference-based* (SSI-ref): only reference sensors are considered in the identification phase, but all sensors are used to determine mode shapes.
- *frequency-domain-based* (SSI-f): uses frequency response functions or power spectral densities as input data.

Subspace identification can be applied to time-invariant, slowly-varying, periodic and arbitrarily-varying systems, however the identification of LTI systems enjoys the broadest development and applications. A review of SSI methods applied to mechanical engineering is found in [DE COCK ET AL., 2002; VERHAEGEN, 2013]. The mathematical details of the aforementioned SSI variants are found in [MCKELVEY, 2004; PEETERS AND DE ROECK, 1999; VAN OVERSCHEE AND DE MOOR, 1996], while [TRNKA AND HAVLENA, 2007] describe their unifying features and the geometrical interpretation of their operation. The basic SSI algorithm can be expanded to estimate the eigenvalue and mode shape variance to provide additional information when constructing the modal model of the system [DÖHLER ET AL., 2013a; REYNDERS ET AL., 2008]. The SSI stabilization diagram can be cleaned up by eliminating poles whose eigenfrequency, damping ratio or mode shape vary excessively from one model order to the next [GOURSAT ET AL., 2011].

When it is reasonable to assume that a system is slowly-varying within the time frame used to extract the modal parameters, a sliding-window approach can be applied. In this regard, an application of SSI to in-flight modal analysis of aircraft is presented in [DE COCK ET AL., 2006; JELIČIĆ ET AL., 2017; SCHWOCHOW AND JELIČIĆ, 2015].

Floquet analysis in chapter 2.3 revealed that an LTP system can be thought as time-invariant with periodically-modulated inputs and outputs and that its state transition matrix has a pole-residue form (2.92) with multiple harmonics of its Floquet exponents [ALLEN, 2009]. It is possible to analyze periodic systems with LTI techniques by increasing the model order to compensate for the additional harmonics (a procedure called “lifting”).

This is computationally not a sound choice, therefore specialized SSI variants have been developed that have proven popular in the output-only modal analysis of periodic systems such as wind turbines, helicopters rotors and turbomachinery [JHINAOU ET AL., 2014] [UYANIK ET AL., 2019].

In the case of arbitrarily-varying systems it is possible to identify the state transition matrix between two time instants by performing multiple independent experiments with the same system variation (“ensemble identification”, analogous to ensemble averaging in spectral estimation 4.4) [LIU, 1997; MA ET AL., 2017; MAJJI ET AL., 2010; VERHAEGEN AND YU, 1995; ZHOU ET AL., 2018]. The eigenvalues and eigenvectors of the state transition matrix can be then interpreted a “pseudo” modal parameters (2.40).

The time-invariant and slowly-varying formulations will be adopted in the flight vibration testing application that will be described in chapter 8. This choice is adequate given the parameter variation in relation to the aircraft’s dynamic characteristics. Ensemble identification is not practically feasible for testing aircraft in flight. Likewise, the assumptions required by specialized variants for periodic systems are not satisfied or impose stiff conditions. These two methodologies can be still applied to aeroelastic testing in controlled environments such as wind tunnels and simulations. The current section will provide a general explanation of SSI’s functioning in the time-varying case; the same principle can be transferred to periodic and time-invariant systems. The mathematical details attain from the aforementioned references. Subsection 5.4.1 will be more specific concerning the data-driven, reference-based and covariance-based versions of the algorithm.

**Notation.** Let  $\Delta t$  be the sampling time. Sampled time-dependent vectors and matrices are denoted by  $\mathbf{x}(n) \triangleq \mathbf{x}(n\Delta t)$ . Likewise, for the STM:  $\mathbf{x}(k) = \Phi(k, n)\mathbf{x}(n)$ .

The time-varying state-space formulation with unknown inputs (5.1) can be combined with the definition of the state transition matrix (2.1.3) to write:

$$\begin{aligned}\mathbf{x}(n+1) &= \Phi(n+1, n)\mathbf{x}(n) + \mathbf{v}(n) \\ \mathbf{y}(n) &= \mathbf{C}(n)\mathbf{x}(n) + \mathbf{w}(n)\end{aligned}\tag{5.8}$$

From this equation it holds that the output after  $k$  steps is:

$$\begin{aligned}\mathbf{y}(n+k) &= \mathbf{C}(n+k)\Phi(n+k, n+1)\mathbf{x}(n+1) + \mathbf{w}(n+k) + \\ &+ \mathbf{C}(n+k) \sum_{j=1}^k \Phi(n+k, n+j)\mathbf{v}(n+j)\end{aligned}\tag{5.9}$$

We can post-multiply this expression by  $\mathbf{y}^T(n)$  and compute the expectation to obtain:

$$\mathbb{E}\{\mathbf{y}(n+k)\mathbf{y}^T(n)\} = \mathbf{C}(n+k)\Phi(n+k, n+1)\mathbf{G}(n)\tag{5.10}$$

where  $\mathbf{G}(n) \triangleq \mathbb{E}\{\mathbf{x}(n+1)\mathbf{y}^T(n)\}$  is the next state-output covariance matrix. The unmeasured inputs and output noise are uncorrelated with the states, therefore  $\mathbb{E}\{\mathbf{w}(n)\mathbf{x}^T(n)\} = \mathbf{0}$

and  $\mathbb{E}\{\mathbf{v}(n)\mathbf{x}^T(n)\} = \mathbf{0}$ . Subspace methods store acquired data into a structured block-Hankel matrix of order  $p$ . In the case of a general time-varying system, let us assume that  $j = 1 : N_E$  independent experiments have been acquired where the system undergoes the same parameter variation. The measured outputs  $\mathbf{y}_j$  of the  $j$ -th realization are arranged in a block-Hankel matrix as:

$$\mathcal{H}(n) = \begin{bmatrix} \mathbf{y}_1(n) & \mathbf{y}_2(n) & \cdots & \mathbf{y}_j(n) \\ \mathbf{y}_1(n+1) & \mathbf{y}_2(n+1) & \cdots & \mathbf{y}_j(n+1) \\ \vdots & \vdots & \ddots & \vdots \\ \mathbf{y}_1(n+p-1) & \mathbf{y}_2(n+p-1) & \cdots & \mathbf{y}_j(n+p-1) \end{bmatrix} \quad (5.11)$$

For periodic systems with period  $T = P\Delta t$ , the state transition matrix satisfies  $\Phi(n+1+P, n+T) = \Phi(n+1, n)$ . The Hankel matrix can be then assembled as:

$$\mathcal{H}(n) = \begin{bmatrix} \mathbf{y}(n) & \mathbf{y}(n+P) & \cdots & \mathbf{y}(n+NP-P) \\ \mathbf{y}(n+1) & \mathbf{y}(n+1+P) & \cdots & \mathbf{y}(n+1+NP-N) \\ \vdots & \vdots & \ddots & \vdots \\ \mathbf{y}(n+p-1) & \mathbf{y}(n+P+p-1) & \cdots & \mathbf{y}(n+NP+P+p-1) \end{bmatrix} \quad (5.12)$$

In the case of time-invariant or slowly-varying systems, the classical SSI formulation arranges the recorded output data samples into the so-called “past” and “future” block-Hankel matrices  $\mathbf{Y}_- \in \mathbb{R}^{qN_r \times N}$  and  $\mathbf{Y}_+ \in \mathbb{R}^{pN_y \times N}$ :

$$\mathcal{H} = \begin{bmatrix} \mathbf{Y}_- \\ \mathbf{Y}_+ \end{bmatrix} \triangleq \frac{1}{\sqrt{N}} \begin{bmatrix} \mathbf{y}^r(q) & \mathbf{y}^r(q+1) & \cdots & \mathbf{y}^r(q+N-2p) \\ \mathbf{y}^r(q+1) & \mathbf{y}^r(q+2) & \cdots & \mathbf{y}^r(q+N-2p+1) \\ \vdots & \vdots & \ddots & \vdots \\ \mathbf{y}^r(q+p) & \mathbf{y}^r(q+p+1) & \cdots & \mathbf{y}^r(q+N-p) \\ \mathbf{y}(q+p+1) & \mathbf{y}(q+p+2) & \cdots & \mathbf{y}(q+N-p+1) \\ \mathbf{y}(q+p+2) & \mathbf{y}(q+p+3) & \cdots & \mathbf{y}(q+N-p+2) \\ \vdots & \vdots & \ddots & \vdots \\ \mathbf{y}(q+2p) & \mathbf{y}(q+2p+1) & \cdots & \mathbf{y}(q+N) \end{bmatrix} \quad (5.13)$$

where a subset of the outputs can be selected as reference sensors  $\mathbf{y}^r \in \mathbb{R}^{N_r}$  for identifying the system while all outputs  $\mathbf{y} \in \mathbb{R}^{N_y}$  are still used for estimating the mode shapes. The number  $p$  is the maximal model order of the system, while  $q$  is the number of rows ( $p \geq q+1$ ). For numerical and statistical reasons,  $N \gg p+q$ .

The SSI algorithm constructs the so-called *subspace matrix* from the block-Hankel matrix (5.11) (5.12) (5.13). More details are provided later in subsection 5.4.1 because its construction depends on the method variant. This subspace matrix has the factorization:

$$\mathcal{H}(n) = \mathcal{O}(n)\mathcal{C}(n) \in \mathbb{R}^{(p+1)N_y \times (p+1)N_r} \quad (5.14)$$

where  $\mathcal{O}(n) \in \mathbb{C}^{(p+1)N_y \times N_x}$  and  $\mathcal{C}(n) \in \mathbb{C}^{N_x \times (p+1)N_r}$  denote respectively the observability



and controllability matrices:

$$\mathcal{O}(n) \triangleq \begin{bmatrix} \mathbf{C}(n) \\ \mathbf{C}(n+1)\Phi(n+1,n) \\ \mathbf{C}(n+2)\Phi(n+2,n) \\ \vdots \\ \mathbf{C}(n+p+1)\Phi(n+p-1,n) \end{bmatrix} \quad (5.15)$$

$$\mathcal{C}(n) \triangleq \begin{bmatrix} \mathbf{G}(n) & \Phi(n+1,n)\mathbf{G}(n+1) & \cdots & \Phi(n+p-1,n)\mathbf{G}(n+p-1) \end{bmatrix} \mathbf{W}(n)$$

and where the matrix  $\mathbf{W}(n)$  depends on SSI variant [TRNKA AND HAVLENA, 2007]. The observability and controllability matrices are computed by the singular value decomposition of the subspace matrix (5.14). It is possible to consider only the significant singular values  $\Sigma_1$  and ignore the others  $\Sigma_2$  (low-rank approximation):

$$\mathcal{H}(n) \stackrel{\text{SVD}}{=} \begin{bmatrix} \mathbf{U}_1 & \mathbf{U}_2 \end{bmatrix} \begin{bmatrix} \Sigma_1 & \mathbf{0} \\ \mathbf{0} & \Sigma_2 \end{bmatrix} \begin{bmatrix} \mathbf{V}_1 & \mathbf{V}_2 \end{bmatrix}^T \implies \mathcal{H}(n) \approx \mathbf{U}_1 \Sigma_1 \mathbf{V}_1^T \quad (5.16)$$

The subspace matrix is thus truncated at the desired model order (that is, the assumed number of states  $N_x \leq (p+1)N_y$ ):

$$\mathcal{O}(n) = \mathbf{U}_1 \Sigma_1^{1/2} \quad \mathcal{C}(n) = \Sigma_1^{1/2} \mathbf{V}_1^H \quad (5.17)$$

The observability matrix has rank equal to the system order in the purely noiseless analytical case. Experimental data have typically a high number of degrees of freedom plus contributions from colored noise and possibly nonlinearities, therefore the model order determination is not as clear. Figure 5.3 provides an example.

**Notation.** From now on, the “ $p$ -th row block” refers to rows with indices  $pN_y + (1 : N_y)$ , where  $p$  starts from 0. A negative subscript such as “ $-p$ ” refers to all but the  $p$ -th block.

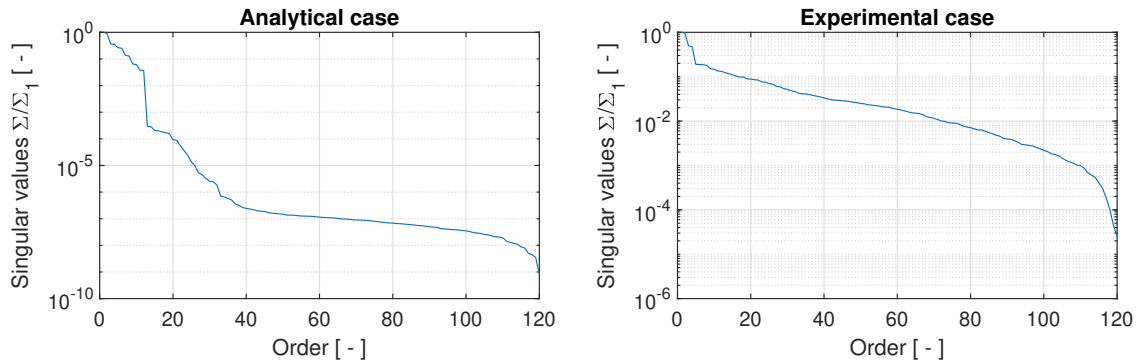


FIGURE 5.3: Subspace matrix singular values from an analytical 7-DoF model [CAUBERGHE, 2004] and from experimental data (wind tunnel test from DNW-TWG [JELIČIĆ ET AL., 2014]). The former has a sharp drop when the model order (14) is exceeded, the latter has typically a relatively irregular drop followed by a steady decrease and then a final sharp drop.

The system's state and output matrices can be extracted from the observability matrix  $\mathcal{O}(n)$  by exploiting its structure (5.15). For an LTV system we need to compute also  $\mathcal{O}(n+1)$  from  $\mathcal{H}(n+1)$ . The state transition matrix  $\Phi(n+1, n)$  is estimated by the least-squares solution:

$$\Phi(n+1, n) = \mathcal{O}_{-p}^+(n+1)\mathcal{O}_{-0}(n) \in \mathbb{C}^{N_x \times N_x} \quad (5.18)$$

where  $\mathcal{O}_{-p}$  are all but the last row block of the observability matrix and  $\mathcal{O}_{-0}$  are all but the first row block (often denoted  $\mathcal{O}^\uparrow$  and  $\mathcal{O}^\downarrow$  in literature). We have seen in chapter 2 that the STM of LTI systems is  $\Phi(n+1, n) = \Phi(\Delta t, 0) = e^{\mathbf{A}\Delta t}$  (often denoted by  $\mathbf{A}_d$ ) and that its eigenvalues  $\Lambda'$  are related to the system's poles  $\Lambda$  by:

$$\Phi(\Delta t, 0) = e^{\mathbf{A}\Delta t} = \Psi\Lambda'\Psi^{-1} = \Psi e^{\Lambda\Delta t}\Psi^{-1} \implies \Lambda = \frac{\ln \Lambda'}{\Delta t} \quad (5.19)$$

In the time-varying case this expression becomes [LIU, 1997]:

$$\begin{aligned} \Phi(n+1, n) &\stackrel{\text{eig}}{=} \Psi(n+1, n)\Lambda'(n+1, n)\Psi^{-1}(n+1, n) \\ &\implies \Lambda(n+1, n) = \frac{\ln \Lambda'(n+1, n)}{\Delta t} \end{aligned} \quad (5.20)$$

where  $\Lambda(n+1, n)$  are now the pseudo eigenvalues. Since the state transition matrix is real, they come in complex-conjugated pairs. In analogy to time-invariant systems, it is possible to define a pseudo eigenfrequency and pseudo damping ratio:

$$\omega_{n,k}(n+1, n) = |\lambda_k(n+1, n)| \quad \zeta_k(n+1, n) = -\frac{\Re\lambda_k(n+1, n)}{|\lambda_k(n+1, n)|} \quad (5.21)$$

The properties of LTV systems can now be discussed in terms of pseudo modal parameters. Temporary stability can be checked by the sign of the pseudo damping ratio. If the system is slowly-varying, the pseudo eigenvalues approach the frozen-time eigenvalues of the system.

The output matrix  $\mathbf{C}(n)$  is given by the first block (first  $N_y$  rows) of  $\mathcal{O}$  (5.15)

$$\mathbf{C}(n) = \mathcal{O}_0(n) \quad (5.22)$$

The modal parameters computed up to this point correspond to the highest model order  $p$ . The stabilization diagram is built by estimating the eigenvalues over several model orders: section 5.4.3 details a method for efficient computation.

#### 5.4.1 Subspace matrix construction

There are several ways of constructing the subspace matrix, depending on SSI variant. More details are found, for example, in [PEETERS AND DE ROECK, 1999]. In [TRNKA AND HAVLENA, 2007] it is proved that the concept of orthogonal projection extended to subspaces unites the subspace identification algorithms N4SID [VAN OVERSCHEE AND DE MOOR, 1996], MOESP [VERHAEGEN AND DEWILDE, 1992] and CVA [LARIMORE, 1990]

into one general formulation. The subspace matrix estimation is where the SSI algorithms differ and spend most computational resources:

- *Data-driven SSI*: the subspace matrix is formed from the projection of the future data horizon onto the past data horizon:

$$\mathcal{H}^{dd} = \mathbf{Y}_+ / \mathbf{Y}_- \equiv \mathbf{Y}_+ \mathbf{Y}_-^T (\mathbf{Y}_- \mathbf{Y}_-^T)^{-1} \mathbf{Y}_- \quad (5.23)$$

Alternatively, this operation can be performed by an LQ-decomposition of the stacked past and future matrices:

$$\begin{bmatrix} \mathbf{Y}_- \\ \mathbf{Y}_+ \end{bmatrix} \stackrel{\text{LQ}}{\equiv} \begin{bmatrix} \mathbf{R}_{1,1} & \mathbf{0} \\ \mathbf{R}_{2,1} & \mathbf{R}_{2,2} \end{bmatrix} \begin{bmatrix} \mathbf{Q}_1 \\ \mathbf{Q}_2 \end{bmatrix} \implies \mathcal{H}^{dd} = \mathbf{R}_{2,1} \quad (5.24)$$

The canonical variate analysis algorithm performs one step more to provide a better separation between noise and the physical poles of the signal:

$$\begin{bmatrix} \mathbf{R}_{2,1} & \mathbf{R}_{2,2} \end{bmatrix} \begin{bmatrix} \mathbf{R}_{2,1} & \mathbf{R}_{2,2} \end{bmatrix}^H \stackrel{\text{Chol}}{\equiv} \mathbf{L} \mathbf{L}^H \implies \mathcal{H}^{cva} = \mathbf{L}^{-1} \mathbf{R}_{2,1} \quad (5.25)$$

where  $\stackrel{\text{Chol}}{\equiv}$  is the Cholesky decomposition.

- *Covariance-driven SSI*: it can be shown that output covariances can be considered as impulse responses of a time-invariant system, therefore algorithms that employ the latter can also utilize the former for system identification. The covariance-based SSI constructs the subspace matrix from the past and future block matrices:

$$\mathcal{H}^{cov} = \mathbf{Y}_+ \mathbf{Y}_-^T \quad (5.26)$$

or by assembling a block Hankel matrix of the covariances:

$$\mathcal{H}^{cov} = \begin{bmatrix} \hat{\mathbf{R}}_1 & \hat{\mathbf{R}}_2 & \cdots & \hat{\mathbf{R}}_q \\ \hat{\mathbf{R}}_2 & \hat{\mathbf{R}}_3 & \cdots & \hat{\mathbf{R}}_{q+1} \\ \vdots & \vdots & \ddots & \vdots \\ \hat{\mathbf{R}}_{p+1} & \hat{\mathbf{R}}_{p+2} & \cdots & \hat{\mathbf{R}}_{p+q} \end{bmatrix} \quad \hat{\mathbf{R}}_k \triangleq \frac{1}{N-k} \sum_{n=k+1}^N \mathbf{y}_n \mathbf{y}_{n-k}^{r,T} \quad (5.27)$$

The correlation function and the power spectral density are Fourier transform pairs (Wiener-Khinchin theorem), therefore the former can be computed efficiently as the product of two DFTs instead of calculating the convolutions in time-domain.

#### 5.4.2 Reconstruction of input spectra

The output cross-power spectral density  $\mathbf{G}_{yy}(z)$  can be synthesized from the identified modal parameters by [REYNDERS ET AL., 2012]:

$$\mathbf{G}_{yy}^{syn}(z) = \mathbf{R}_0 + \mathbf{C}(z\mathbf{I} - \mathbf{A}_d)^{-1} \mathbf{G} + \mathbf{G}^H (z^{-1}\mathbf{I} - \mathbf{A}_d^H)^{-1} \mathbf{C}^H \quad (5.28)$$

The zero-lag output covariance matrix  $\mathbf{R}_0 \in \mathbb{R}^{N_y \times N_y}$  is estimated by:

$$\mathbf{R}_0 = \mathbb{E}\{\mathbf{y}, \mathbf{y}^T\} \approx \frac{1}{N} \sum_{n=1}^N \mathbf{y}_n \mathbf{y}_n^T \approx \mathcal{H}_0 \mathcal{H}_0^H \quad (5.29)$$

where  $\mathcal{H}_0$  denotes first  $N_y$  rows of the subspace matrix. The next state-reference output matrix  $\mathbf{G}$  in the data-driven or the covariance-based variants is estimated respectively by:

$$\mathbf{G}_{dd} = \Sigma_1^{1/2} \mathbf{V}_1^H \mathbf{e}_0 \quad \mathbf{G}_{cov} = \mathcal{O}^+ \mathcal{H} \mathbf{R}_{1,1}^H \mathbf{e}_p \quad (5.30)$$

where  $\mathbf{e}_0$  denotes the first  $N_y$  columns (0-th block) and  $\mathbf{e}_p$  denotes the last  $N_y$  columns ( $p$ -th block). The first equation is derived from (5.17); matrix  $\mathbf{R}_{1,1}$  is taken from (5.24). Equation (5.28) can be vectorized by computing the eigendecomposition of  $\Phi(n+1, n) \equiv \mathbf{A}_d = \Psi \Lambda' \Psi^{-1}$  in order to obtain its pole-residue form:

$$\mathbf{G}_{yy}^{syn}(z) = \mathbf{R}_0 + \sum_{k=1}^{N_x} \left( \frac{\tilde{\mathbf{c}}_k \tilde{\mathbf{g}}_k^T}{z - \Lambda'_k} + \frac{\tilde{\mathbf{g}}_k^* \tilde{\mathbf{c}}_k^H}{z^* - \Lambda_k'^*} \right) \quad (5.31)$$

where  $\tilde{\mathbf{c}}_k \triangleq \mathbf{C} \Psi \mathbf{e}_k$  and  $\tilde{\mathbf{g}}_k^T \triangleq \mathbf{e}_k^T \Psi^{-1} \mathbf{G}$  as usual. Equation (5.31) involves only scalar divisions. The pole-residue form can be used to validate identification results assembled by peak-picking or obtained from different data sets. Positive power spectra can be reconstructed from in a similar way:

$$\mathbf{S}_{yy}^{+,syn}(z) = \frac{\mathbf{R}_{0,k}}{2} + \sum_{k=1}^{N_x} \frac{\tilde{\mathbf{c}}_k \tilde{\mathbf{g}}_k^T}{z - \Lambda'_k} \quad (5.32)$$

where  $\mathbf{R}_0 = \sum_{k=1}^{N_x} \tilde{\mathbf{c}}_k \tilde{\mathbf{g}}_k^T / \Lambda'_k$  is the zero-lag output covariance matrix.

### 5.4.3 Efficient construction of the stabilization diagram

The modal parameters computed up to this point correspond to the highest model order  $p$ . The stabilization diagram is built by calculating the system eigenvalues over several model orders: this corresponds to solving equation (5.18) for all desired orders in a set  $q \in \mathbb{S}$  up to  $p$ :

$$\forall q \in \mathbb{S}: \quad \Phi_q(n+1, n) = \mathcal{O}_{0:(q-1)}^+ \mathcal{O}_{1:q} \quad (5.33)$$

where the subscripts indicate the row blocks of  $\mathcal{O}$ . In our implementation of SSI we adapt the procedure detailed in [DÖHLER AND MEVEL, 2010] to compute the stabilization diagram faster. This approach factorizes only the observability matrix (5.17) corresponding to the highest-order  $p$ :

$$\begin{cases} \mathcal{O}_{-p} & \stackrel{\text{QR}}{=} \mathbf{Q} \mathbf{R} \\ \mathbf{T} & \triangleq \mathbf{R}^{-1} \\ \mathbf{S} & \triangleq \mathbf{Q}^T \mathcal{O}_{-0} \end{cases} \implies \forall n \in \mathbb{S}: \begin{cases} \Phi_q(n+1, n) & = \mathbf{T}_{1:q, 1:q} \mathbf{S}_{1:q, 1:q} \\ \mathbf{C}_q & = \mathcal{O}_{0, 1:q} \end{cases} \quad (5.34)$$

where the subscripts  $1 : q$  refer to rows or columns. The size of the observability matrix  $\mathcal{O} \in \mathbb{C}^{(p+1)N_y \times N_x}$  depends on the product of model order and number of inputs, therefore it is not uncommon to work with over two thousand rows. The SSI implementation is efficient when most of the time is spent constructing the subspace matrix; thanks to equation (5.34) the estimation of the observability matrix is sped-up appreciably.

#### 5.4.4 Multi-band processing

In aeroelastic testing it is common to work with sample rates that are much higher than the frequency band of interest, consequently decimation or resampling of the signal should be carried out to reduce the amount of processed data and the sample rate. The model order determines how many modes can be identified within a given frequency band. The algorithm may miss some eigenmodes when their density is high with respect to the model order. SSI performs several matrix decompositions, multiplications and divisions that have computational complexity of about  $\mathcal{O}(n^3)$ . If the acquired data stream is downsampled by a factor  $q$ , the workload of subsequent operations is reduced by a factor  $q^2$  at least. A narrower frequency band necessitates therefore a lower model order and consequently much less computation. Figure 5.4 compares identification results obtained from a single large band and multiple ones.

Let us suppose that the frequency range of interest is  $[f_{min}, f_{max}]$ . The automated multi-band procedure for SSI is as follows:

1. Perform data reduction using the method of choice:
  - *resampling*: perform frequency shift  $-f_{min}$ . Resample data by  $p/q$  where  $p$  and  $q$  are given by a rational fraction approximation of  $2(f_{max} - f_{min})/f_s$ .
  - *decimation*: given the actual rational downsampling factor  $q \triangleq f_s/2/(f_{max} - f_{min})$ , determine the integer decimation stages  $q_i$  where  $q \approx \prod q_i$ . The maximal recommended decimation factor per stage is 13 therefore algorithm 6 (see appendix) has been developed to determine the number of stages. Design a FIR low-pass filter and decimate data  $\mathbf{y}(t)$  by integer factor  $q_i$ . Repeat for every stage. The filter order must be a multiple of the decimation factor<sup>2</sup>.
  - *brick-wall*: Set DFT bins corresponding to positive and negative frequencies outside the band  $|f| < f_{min} \vee |f| > f_{max}$  to zero. Remove bins corresponding to  $f_s/2 \pm f_{min}$  and transform back into time-domain.
2. Compute the effective sample rate and frequency ranges after data reduction:
 
$$f_s^r \leftarrow p/q \cdot f_s \text{ and } [f_{min}^r, f_{max}^r] \leftarrow p/q \cdot [f_{min}, f_{max}]$$
3. Perform system identification on decimated and shifted data. The identified eigenvalues must be corrected by  $\lambda \leftarrow (2\pi f_{min}^r + |\lambda|) \exp(i\angle\lambda)$ .

<sup>2</sup> Example: Let the actual decimation factor be  $q_0 = 26.5$ , for which  $q = 26 = 2 \cdot 13$ . The algorithm would try the effective decimation factors  $q = 25 = 5 \cdot 5$  ( $R = 26^{1/2} = 5.0990$ ) or  $q = 27 = 3 \cdot 3 \cdot 3$  ( $R = 26^{1/3} = 2.962$ ). The effective decimation factors lead to a slightly different bandwidth of the decimated data, respectively by factors  $26.5/25 = 1.060$  and  $26.5/27 = 0.9815$ .

The frequency shift is performed as follows:

1. Compute DFT of data  $\hat{\mathbf{y}}[k] = \text{DFT}\{\mathbf{y}[n]\}$
2. Get frequency shift in samples  $d \triangleq \lfloor f_{min}/\Delta f \rfloor$
3. Perform circular shift of FFT bins:  $\mathbf{y}[k] \leftarrow [\hat{\mathbf{y}}[d + (1 : L)], \hat{\mathbf{y}}^*[d + (N - L : -1 : 2)]]$  where  $L$  is the DFT's length from DC to Nyquist frequency.
4. Convert back into time-domain  $\text{DFT}^{-1}\{\mathbf{y}[k]\}$  to obtain real data.

#### 5.4.5 Contribution to system identification with SSI

The SSI data-driven, reference-based and covariance-driven variants have been implemented to perform output-only modal parameter estimation using the cited sources as references. The base algorithms have been then improved to achieve the best performance possible. The main contribution to this identification pipeline is in the form of careful digital signal processing to allow automated data reduction and multi-band identification. Furthermore, the output cross-power spectral densities are reconstructed efficiently to validate the identification's quality as detailed in section (5.4.2). In this regard, some results are illustrated in figure 5.4. When multiple bands must be identified, the SSI algorithm can be paired with the mode shape estimation procedure described in section 5.6.

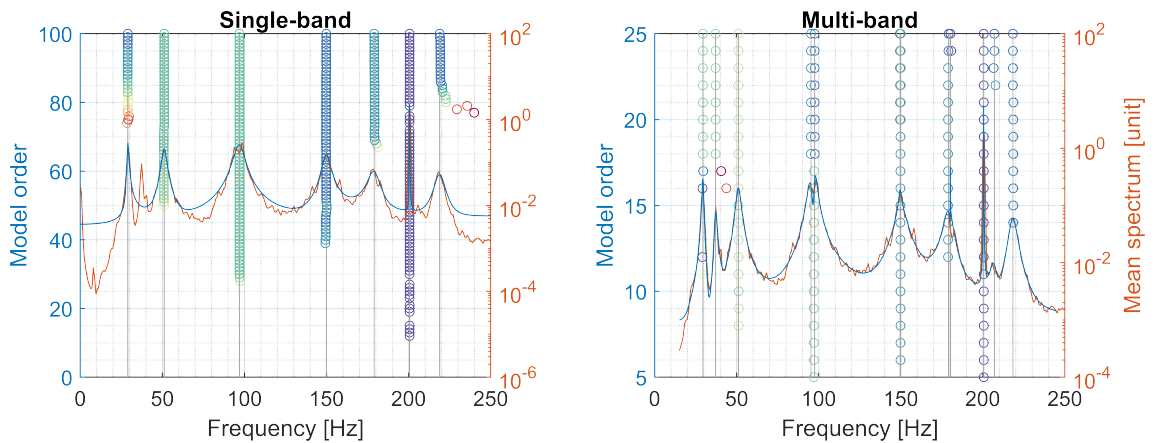


FIGURE 5.4: Wind tunnel measurements: the raw data stream is sampled at  $4 \text{ kHz}$ . The two stabilization diagrams display the lower frequency range, where the flutter-critical modes are. A very high model order is necessary for the single band, however not all peaks are fitted. The multi-band approach in  $[15, 250] \text{ Hz}$  is much faster and delivers better results. Data from the transonic wind tunnel DNW-TWG [JELIĆIĆ ET AL., 2014]

## 5.5 Least-Squares Complex Frequency (LSCF)

The LSCF family fits a polynomial model (5.4), which, depending on the algorithm variant, is a common-denominator, right or left polynomial fraction. [ALLEMANG AND BROWN, 1998] compare several modal parameter estimation algorithms that utilize this matrix polynomial approach. Detailed descriptions of LSCF, some of its variants, applications and drawbacks are found in [VERBOVEN, 2002] and [CAUBERGHE, 2004]. The simplest LSCF version represents the input spectra with a common-denominator model (rational function). The poly-reference pLSCF algorithm (commercially known as *PolyMax* [PEETERS AND VAN DER AUWERAER, 2005]) models the input spectra as a right matrix fraction polynomial model. Concerning the modal analysis of flight data, [MEVEL ET AL., 2006] comment that pLSCF provides clear stabilization diagrams. The literature reports variants that compute the confidence intervals of identified modal parameters [TROYER ET AL., 2009] or employ an iterative maximum-likelihood scheme [AMADOR ET AL., 2019; EL-KAFAY ET AL., 2013; GUILLAUME ET AL., 1999]. [VERBOVEN ET AL., 2004] describes a flutter monitoring application with mode tracking using an iterative weighted LSCF. The rational polynomial description of the system can be adjusted to include the contribution of time-varying coefficients for the prediction of aeroelastic flutter [ERTVELDT ET AL., 2014]. In [TANG ET AL., 2017], LSCF is employed to generate reduced-order LTI modes from flutter test data. This procedure is enhanced by an iterative maximum-likelihood step and validated with nonparametric frequency response function estimates.

LSCF can be adapted to fit bivariate time-frequency functions maintaining essentially the same formulation employed for the LTI case [ZHOU ET AL., 2014]. Following the same argumentation exposed for SSI, we shall focus on slowly-varying systems. Periodic systems can be still identified by lifting the model. The identification of general time-varying systems can be performed by computing the spectra using ensemble averaging (see section 4.4), which will be demonstrated in chapter 7.

In the coming pages we attain from the aforementioned references. We shall consider the poly-reference pLSCF algorithm because the simpler LSCF method can be seen as a special case. Iterative (maximum-likelihood) versions can refine the initial modal parameters estimate, but are not considered here because they require additional computation cycles that we cannot afford. Data is provided as frequency response functions for EMA or full/positive cross-power spectral densities for OMA. We focus on the output-only case where the data source is a CPSD matrix  $\hat{\mathbf{F}}(\omega) = \hat{\mathbf{G}}_{yx}(\omega) \in \mathbb{C}^{N_y \times N_x}$ . Its rows shall be referred to as *responses* and its columns as *references*. The rows correspond to the selected  $N_y$  output channels on the structure, while the columns to a subset of  $N_x$  sensor channels used to construct the CPSD matrix.

**Notation.** *Given the focus on the output-only case, we use  $N_y$  for the number of rows and  $N_x$  for the number of columns of the input spectra. Some authors use  $N_o$  and  $N_i$  instead.  $N_m$  denotes the number of poles.*

The poly-reference pLSCF algorithm fits a right matrix fraction representation of the estimated spectra:

$$\hat{\mathbf{F}}(\omega) = \mathbf{B}(z)\mathbf{A}^{-1}(z) \in \mathbb{C}^{N_y \times N_x} \quad \mathbf{B}(z) \triangleq \sum_{p=0}^{N_b} \mathbf{B}_p z^p \quad \mathbf{A}(z) \triangleq \sum_{p=0}^{N_a} \mathbf{A}_p z^p \quad (5.35)$$

where  $\mathbf{B}(z) \in \mathbb{C}^{N_y \times N_x}$  and  $\mathbf{A}(z) \in \mathbb{C}^{N_x \times N_x}$  are respectively the numerator and denominator matrices expressed as polynomials,  $z \triangleq e^{i\omega/\omega_N}$  is the discrete frequency and  $\omega_N$  is the highest frequency bin of the input spectrum  $\hat{\mathbf{F}}(\omega)$ . The parameters that must be identified are the numerator and denominator coefficients in the rational polynomial model (5.35). We seek to minimize the linear-in-the-parameters error model in the least-squares sense:

$$\forall i: \quad \mathbf{E}_i(\omega_n) \triangleq \mathbf{w}_i(\omega) \left( \mathbf{B}_i(z) - \hat{\mathbf{F}}_i(\omega)\mathbf{A}(z) \right) \implies \text{minimize} \sum_{n=1}^N \sum_{i=1}^{N_i} |\mathbf{E}_i(\omega_n)|^2 \quad (5.36)$$

where  $\mathbf{w}(\omega) \in \mathbb{C}^{N_y}$  is a frequency-dependent weight function for each output. The choice of weighting is discussed in section 5.5.3.

**Notation.** The index “ $i$ ” denotes one of the  $N_y$  rows of  $\hat{\mathbf{F}}(\omega)$ ,  $\mathbf{B}(z)$ ,  $\mathbf{A}(z)$ ,  $\mathbf{E}(z)$  or  $\mathbf{w}(z)$ . The index “ $p$ ” refers to the  $p = 0 : N_p - 1$  polynomial orders of the coefficient matrices  $\mathbf{B}_p$  and  $\mathbf{A}_p$ , where  $N_p \triangleq \max\{N_a, N_b\} + 1$ . The index “ $n$ ” refers to the frequency  $\omega$  or  $z$  (the symbol “ $\omega_n$ ” does not denote the eigenfrequency as in previous chapters).

Minimizing the error in the least-squares sense (5.36) is equivalent to solving the normal equation

$$\mathbf{J}\boldsymbol{\theta} = \mathbf{0} \quad (5.37)$$

where  $\mathbf{J}$  is the Jacobian of the error function  $\frac{\partial}{\partial \boldsymbol{\theta}} \mathbf{E}(\omega)$  and  $\boldsymbol{\theta}$  are the parameters that must be identified:

$$\boldsymbol{\beta}_i \triangleq \begin{bmatrix} \mathbf{B}_{i,0} \\ \vdots \\ \mathbf{B}_{i,N_p} \end{bmatrix} \in \mathbb{C}^{N_p \times N_x} \quad \boldsymbol{\alpha} \triangleq \begin{bmatrix} \mathbf{A}_0 \\ \vdots \\ \mathbf{A}_{N_p} \end{bmatrix} \in \mathbb{C}^{N_p N_x \times N_x} \quad \boldsymbol{\theta} = \begin{bmatrix} \boldsymbol{\beta}_1 \\ \vdots \\ \boldsymbol{\beta}_{N_y} \\ \boldsymbol{\alpha} \end{bmatrix} \quad (5.38)$$

where  $\boldsymbol{\beta}_i$  and  $\boldsymbol{\alpha}$  are respectively the numerator and denominator coefficients (5.35) each arranged into matrices in ascending polynomial order

**Notation.** The block matrices  $\boldsymbol{\beta}_i$ ,  $\boldsymbol{\alpha}$  and  $\boldsymbol{\theta}$  are denoted with lowercase Greek letters in order to be consistent with existing literature.

The Jacobian of the error function (5.36) is:

$$\mathbf{J} = \begin{bmatrix} \mathbf{E}_i \\ \vdots \\ \mathbf{E}_{N_y} \end{bmatrix} \begin{bmatrix} \frac{\partial}{\partial \boldsymbol{\beta}_1} & \cdots & \frac{\partial}{\partial \boldsymbol{\beta}_{N_y}} & \frac{\partial}{\partial \boldsymbol{\alpha}} \end{bmatrix} = \begin{bmatrix} \mathbf{X}_1 & \cdots & \mathbf{0} & \mathbf{Y}_1 \\ \vdots & \ddots & \vdots & \vdots \\ \mathbf{0} & \cdots & \mathbf{X}_{N_y} & \mathbf{Y}_{N_y} \end{bmatrix} \in \mathbb{C}^{NN_y \times N_p N_x (N_y + 1)} \quad (5.39)$$



where  $\mathbf{X}_i$  and  $\mathbf{Y}_i$  are weighted Vandermonde sub-matrices:

$$\begin{aligned}\mathbf{X}_i &\triangleq \frac{\partial \mathbf{E}_i}{\partial \boldsymbol{\beta}_i} = \begin{bmatrix} \mathbf{w}_i(\omega_1)[1 & z_1 & \cdots & z_1^n] \\ \vdots \\ \mathbf{w}_i(\omega_N)[1 & z_N & \cdots & z_N^n] \end{bmatrix} \in \mathbb{C}^{N \times N_p} \\ \mathbf{Y}_i &\triangleq \frac{\partial \mathbf{E}_i}{\partial \boldsymbol{\alpha}} = \begin{bmatrix} -\mathbf{w}_i(\omega_1)[1 & z_1 & \cdots & z_1^n] \otimes \hat{\mathbf{F}}_i(\omega_1) \\ \vdots \\ -\mathbf{w}_i(\omega_N)[1 & z_N & \cdots & z_N^n] \otimes \hat{\mathbf{F}}_i(\omega_N) \end{bmatrix} \in \mathbb{C}^{N \times N_x N_p}\end{aligned}\quad (5.40)$$

The Jacobian is a very large matrix, however the dimension of the normal equation (5.37) can be significantly reduced by premultiplying it by its Hermitian transpose to obtain:

$$\mathbf{J}^H \mathbf{J} \boldsymbol{\theta} = \begin{bmatrix} \mathbf{R}_1 & \cdots & \mathbf{0} & \mathbf{S}_1 \\ \vdots & \ddots & \vdots & \vdots \\ \mathbf{0} & \cdots & \mathbf{R}_{N_y} & \mathbf{S}_{N_y} \\ \mathbf{S}_1^H & \cdots & \mathbf{S}_{N_y}^H & \sum_{i=1}^{N_y} \mathbf{T}_i \end{bmatrix} \begin{bmatrix} \boldsymbol{\beta}_1 \\ \vdots \\ \boldsymbol{\beta}_{N_y} \\ \boldsymbol{\alpha} \end{bmatrix} = \mathbf{0} \quad (5.41)$$

where  $\mathbf{R}_i$ ,  $\mathbf{S}_i$  and  $\mathbf{T}_i$  are sub-matrices corresponding to the  $i = 1 : N_y$  outputs:

$$\begin{aligned}\mathbf{R}_i &\triangleq \mathbf{X}_i^H \mathbf{X}_i \in \mathbb{C}^{N_p \times N_p} \\ \mathbf{S}_i &\triangleq \mathbf{X}_i^H \mathbf{Y}_i \in \mathbb{C}^{N_p \times N_y N_p} \\ \mathbf{T}_i &\triangleq \mathbf{Y}_i^H \mathbf{Y}_i \in \mathbb{C}^{N_y N_p \times N_y N_p}\end{aligned}\quad (5.42)$$

Equation (5.41) has now as many columns as there are parameters  $N_p N_x (N_y + 1)$ . The entries of  $\mathbf{R}_i$ ,  $\mathbf{S}_i$  and  $\mathbf{T}_i$  are equal to:

$$\begin{aligned}\mathbf{R}_i[k, l] &= \sum_{n=1}^N |\mathbf{w}_i(\omega_n)|^2 z_n^{l-k} \\ \mathbf{S}_i[k, \mathbb{K}] &= \sum_{n=1}^N |\mathbf{w}_i(\omega_n)|^2 \hat{\mathbf{F}}_i(\omega_n) z_n^{l-k} \\ \mathbf{T}_i[\mathbb{K}, \mathbb{L}] &= \sum_{n=1}^N |\mathbf{w}_i(\omega_n)|^2 \hat{\mathbf{F}}_i^H(\omega_n) \hat{\mathbf{F}}_i(\omega_n) z_n^{l-k}\end{aligned}\quad (5.43)$$

where  $\mathbb{K} \triangleq (k-1)N_x + (1:N_x)$  and  $\mathbb{L} \triangleq (l-1)N_x + (1:N_x)$  are blocks of consecutive rows or columns for  $k, l = 1 : N_p$ . Equations (5.43) show that the sub-matrices  $\mathbf{R}_i$ ,  $\mathbf{S}_i$  and  $\mathbf{T}_i$  have a Toeplitz structure because their entries depend on  $l - k$ . Only one row of  $\mathbf{R}_i$  and  $\mathbf{T}_i$  and only one row and column of  $\mathbf{S}_i$  need to be computed to construct the whole sub-matrix. This means that they can be constructed efficiently using the FFT [VERBOVEN, 2002]. We have shown in [JELIČIĆ ET AL., 2015] how this efficiency is important to real-time system identification applications. When the common-denominator LSCF algorithm is employed an even larger gain in computation time is achieved.

The rows pertaining to the numerator coefficients  $\beta_i$  can be substituted into the lower row of equation (5.41) to obtain a system of equations where only the denominator coefficients  $\alpha$  are unknowns:

$$\begin{cases} \mathbf{R}_i \beta_i + \mathbf{S}_i \alpha = \mathbf{0} \\ \sum_{i=1}^{N_y} (\mathbf{S}_i^H \beta_i + \mathbf{T}_i \alpha) = \mathbf{0} \end{cases} \implies \begin{cases} \beta_i = -\mathbf{R}_i^{-1} \mathbf{S}_i \alpha \\ \sum_{i=1}^{N_y} (\mathbf{T}_i - \mathbf{S}_i^H \mathbf{R}_i^{-1} \mathbf{S}_i) \alpha = \mathbf{0} \end{cases} \quad (5.44)$$

Taking the bottom equation we can finally write:

$$\sum_{i=1}^{N_y} (\mathbf{T}_i - \mathbf{S}_i^H \mathbf{R}_i^{-1} \mathbf{S}_i) \triangleq \mathbf{M} \implies \mathbf{M} \alpha = \mathbf{0} \quad (5.45)$$

The square matrix  $\mathbf{M}$  has only  $N_x N_p$  rows.

The least-squares solution of the equation (5.45) is obtained by adding one constraint, for example by fixing one denominator coefficient to 1 (usually the zero or highest orders). For instance, by fixing the denominator's highest order coefficient  $\mathbf{A}_{N_p} = \mathbf{I}$  we obtain:

$$\forall p \in \mathbb{S} \quad \alpha_p \equiv \begin{bmatrix} \mathbf{A}_0 \\ \vdots \\ \mathbf{A}_{p-1} \\ \mathbf{I} \end{bmatrix} = \begin{bmatrix} -\mathbf{M}_{+p}^{-1} \mathbf{M}_{-p} \\ \mathbf{I} \end{bmatrix} \in \mathbb{C}^{(p+1)N_y \times N_y} \quad (5.46)$$

where  $\mathbf{M}_{+p}$  denotes the square submatrix  $\mathbf{M}_{1:pN_x, 1:pN_x}$ , while  $\mathbf{M}_{-p}$  is a rectangular submatrix  $\mathbf{M}_{1:pN_x, p+(1:N_x)}$ . The same logic applies if the order zero coefficient is fixed  $\mathbf{A}_0 = \mathbf{I}$ . This equation is solved multiple times to calculate the denominator coefficients  $\alpha_p$  corresponding to the desired model orders  $p \in \mathbb{S}$  (for example  $p = 0 : N_p - 1$ ). [CAUBERGHE, 2004] provides a helpful analysis of the coefficient choice that allows a simple separation of physical (stable) and mathematical (unstable) poles to obtain clear stabilization diagrams; figure 5.5 provides an example.

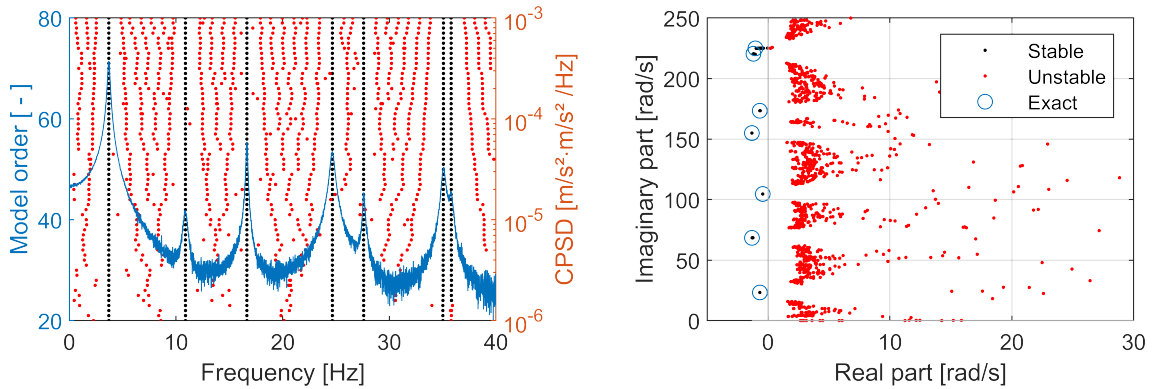


FIGURE 5.5: OMA system identification of a 7-DoF model from [VERBOVEN, 2002]. Left plot: stabilization diagram with all the stable (physical) and unstable (spurious) poles. Right plot: in the complex plane, the unstable poles lie on the right semi-plane (outside the unit circle). This clear separation depends on the choice of coefficients in equation (5.46).

The system eigenvalues and participation factors for order  $p$  can be extracted by the eigendecomposition of the companion matrix:

$$\begin{bmatrix} \mathbf{A}_{p-1} & \cdots & \mathbf{A}_1 & \mathbf{A}_0 \\ \mathbf{I} & \cdots & \mathbf{0} & \mathbf{0} \\ \vdots & \ddots & \vdots & \vdots \\ \mathbf{0} & \cdots & \mathbf{I} & \mathbf{0} \end{bmatrix} \stackrel{\text{eig}}{=} \mathbf{\Psi}_p \mathbf{\Lambda}'_p \mathbf{\Psi}_p^{-1} \in \mathbb{C}^{pN_y \times pN_y} \quad (5.47)$$

where  $\mathbf{A}_p$  is the  $p$ -th block of matrix  $\boldsymbol{\alpha}$  in equation (5.46) (denominator coefficient matrix of order  $p$ ). For each order  $p$ , the system eigenvalues  $\mathbf{\Lambda}$  and the modal participation factors  $\phi_j$  related to the  $j$ -th mode are computed by:

$$\forall p : \quad \mathbf{\Lambda} = \frac{1}{\Delta t} \ln \mathbf{\Lambda}' \quad \mathbf{\Psi}_j = \left\{ \mathbf{\Lambda}'_j^{p-1} \phi_j, \dots, \mathbf{\Lambda}'_j \phi_j, \phi_j \right\} \quad (5.48)$$

where  $1/\Delta t$  is the sample rate. Assuming the inputs  $\hat{\mathbf{F}}(\omega)$  are CPSDs, the mode shapes are extracted in a second step (covered in section 5.6) by fitting:

$$\begin{bmatrix} \hat{\mathbf{F}}_i(\omega) \\ \vdots \\ \hat{\mathbf{F}}_{N_y}(\omega) \end{bmatrix} = \sum_{k=1}^{N_m} \left( \frac{\psi_k \phi_k^H}{i\omega - \lambda_k} + \frac{\phi_k \psi_k^H}{-i\omega - \lambda_k^*} \right) - \frac{\mathbf{R}_L}{\omega^4} + \mathbf{R}_u \quad (5.49)$$

The companion matrix is assembled for each model order  $p = 0 : N_p - 1$  in order to construct the stabilization diagram. The eigendecomposition of the companion matrix (5.47) is an unavoidable bottleneck of the identification procedure. When the model order  $p$  or the number of response channels  $N_y$  is high, this matrix can easily grow to a thousand rows. In a common-denominator model estimator (for example LSCF) the coefficients  $\boldsymbol{\alpha}_p$  are simply a vector and the system poles are the denominator polynomial's roots. The model order can be reduced by performing the analysis over different frequency bands or by utilizing positive power spectra (4.24) instead of cross-power spectral densities.

In a real structure the energy transfer to certain modes of vibration is in many cases suboptimal because the excitation is perpendicular to the dominant direction of a mode, e.g. to identify the wing in-plane bending mode by applying a vertical excitation. The quality of the mode shapes estimates can be increased by applying the appropriate weighting. Common-denominator models appear to produce lesser fits for highly-damped modes and to have a lower resolution capability for closely-spaced modes. The first drawback leads to a more conservative damping estimate, the second can be solved by increasing the model order. Right matrix fraction polynomial models tend to be more sensitive to data inconsistencies and the model order increments are the number of columns of the data matrix. They require significantly more computation because of a cubic complexity dependency on the number of columns of the input spectra. This observation is also found in [CAUBERGHE, 2004; VERBOVEN, 2002].

### 5.5.1 Efficient construction of the stabilization diagram

The stabilization diagram is constructed in a fast way by computing the pseudo-inverse in equation (5.46) for all model orders of interest  $\mathbb{S}$  :

$$\forall p \in \mathbb{S} : \quad \boldsymbol{\alpha}_p = \begin{bmatrix} -\mathbf{M}_{+p}^{-1} \mathbf{M}_{-p} \\ \mathbf{I} \end{bmatrix} \quad (5.50)$$

where  $\mathbf{M}_{+p} \in \mathbb{C}^{pN_y \times pN_y}$  and  $\mathbf{M}_{-p} \in \mathbb{C}^{pN_y \times N_y}$  are sub-matrices of  $\mathbf{M}$  from equation (5.45). We can improve the computation of  $\boldsymbol{\alpha}_p$  by adapting the QR decomposition technique introduced in section 5.4.3 for SSI:

$$\forall p \in \mathbb{S} : \quad \begin{cases} \mathbf{M}_{+p} & \stackrel{\text{QR}}{=} \mathbf{Q}\mathbf{R} \\ \mathbf{T} & \triangleq \mathbf{R}^{-1} \\ \mathbf{S} & \triangleq \mathbf{Q}^T \mathbf{M}_{1:pN_y, :} \end{cases} \quad \Longrightarrow \quad \boldsymbol{\alpha}_p = \begin{bmatrix} -\mathbf{T}_{1:pN_y, 1:pN_y} \mathbf{S}_{1:pN_y, pN_y+(1:N_y)} \\ \mathbf{I} \end{bmatrix} \quad (5.51)$$

### 5.5.2 Reconstruction of input spectra

The numerator coefficients referring to each response-reference pair are calculated by substituting the denominator coefficients  $\boldsymbol{\alpha}$  back into the normal equation (5.41):

$$\boldsymbol{\beta}_i = -\mathbf{R}_i^{-1} \mathbf{S}_i \boldsymbol{\alpha} \quad (5.52)$$

from which  $\mathbf{B}_p$  can be reassembled according to equation (5.38). Instead of the naive sum (5.35), we calculate the synthesized spectrum utilizing a Vandermonde matrix:

$$\mathbf{V} = \mathbf{z}^{-(0:p)T} \quad \Longrightarrow \quad \begin{aligned} \mathbf{B}(z) &= \mathbf{V}[\boldsymbol{\beta}_1 \cdots \boldsymbol{\beta}_{N_y}] \\ \mathbf{A}(z) &= \mathbf{V}\boldsymbol{\alpha} \end{aligned} \quad (5.53)$$

where  $\mathbf{z} = \exp\{i\pi(0 : N - 1)/N\}$  is the discrete frequency vector. The pole-residue form of the transfer function (5.3) is:

$$\mathbf{F}^{syn}(z) = \mathbf{P}(z) + \sum_{k=1}^{N_m} \frac{\mathbf{R}'_k}{z - z_k} \quad (5.54)$$

where the residues matrices  $\mathbf{R}'_k$  are:

$$\mathbf{R}'_k = \lim_{z \rightarrow z_k} (z - z_k) \mathbf{H}(z) = \frac{z_k \sum_{p=0}^{N_p} \mathbf{B}_p z_k^{-p}}{\prod_{m \neq k}^{N_p} (1 - z_m z_k^{-1})} \quad (5.55)$$

Once the pole-residue form has been determined, it is possible to compose the modal model by mode selection. However, in [CAUBERGHE, 2004; RAINIERI AND FABBROCINO, 2014] it is noted that the computation of residuals from the coefficients  $\boldsymbol{\beta}_i$  (respectively  $\mathbf{B}_p$ ) should be avoided. A better approach is explained in section 5.6.

### 5.5.3 Weighting choice

In the EMA framework the optimal weighting is the frequency response covariance matrix, which can be estimated when some information about output noise is available [PINTELO AND SCHOUKENS, 2004]. In the OMA framework this information is not obtainable.

- If white additive noise on the estimated spectra is expected, then the weight is simply  $\mathbf{W}_i(\omega_n) = 1$ . Good results can be obtained even if no weighting is used.
- If relative noise is assumed, then the weight function is  $\mathbf{W}_i(\omega_n) = 1/|\hat{\mathbf{G}}_i(\omega_n)|$ . This gives the same importance to the resonances and antiresonances in the error function (5.36). Since the latter contain information about mode shapes, better results can be achieved in mode tracking. In OMA the assumption of relative noise is often in good agreement with the actual noise conditions [CAUBERGHE, 2004].

### 5.5.4 Contributions to system identification with LSCF

The LSCF algorithm outlined has been improved for real-time identification. Figure 5.6 illustrates some of the differences between the “canonical” and “modified” versions.

- The one-sided input spectrum  $\hat{\mathbf{F}}(\omega)$  is mirrored to provide better separation of stable and unstable poles.
- The strategy outlined in section 5.5.1 is implemented for better numerical conditioning when computing the system eigenvalues.
- The algorithm fits complex instead of real denominator coefficients in order to have more liberty. The system eigenvalues are then  $\Lambda_p = i\omega_1 - \frac{1}{\pi}(\omega_N - \omega_1) \ln\{\Lambda'_p\}$  where  $\omega_1, \omega_N$  are the first and last circular frequencies of the input spectrum  $\hat{\mathbf{F}}(\omega)$  (compare to equation (5.48)).

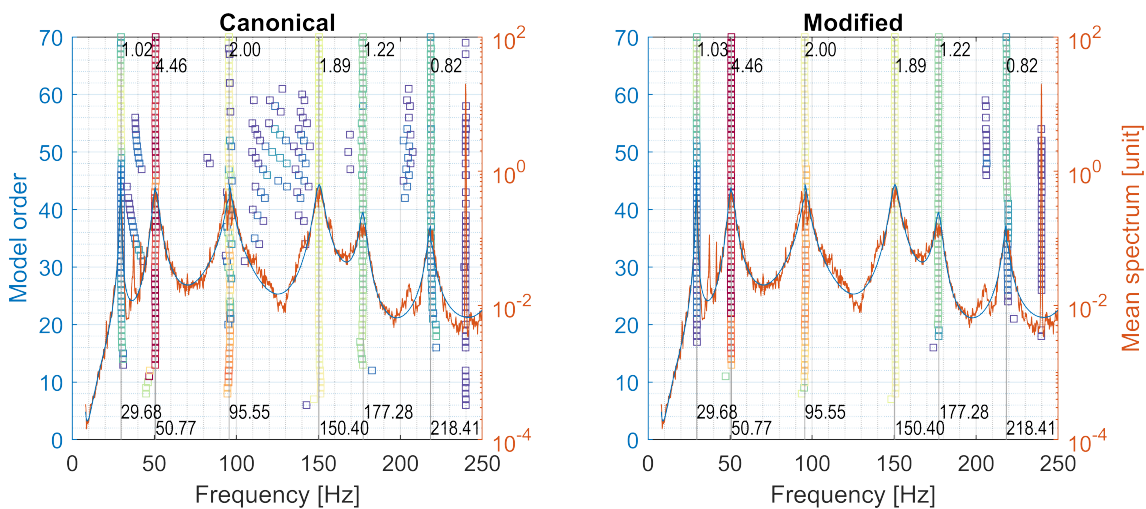


FIGURE 5.6: Comparison between the canonical LSCF and the modified version implemented in the current research. Raw algorithm output, no sorting or cleaning of the eigenvalues has been applied. Data from the transonic wind tunnel DNW-TWG [JELIČIĆ ET AL., 2014].

## 5.6 Least-squares frequency-domain method (LSFD)

There are circumstances in modal analysis where eigenvalues have been estimated from heterogeneous sources, for instance different runs, excitation type or bands. When the system's eigenvalues are known from a previous identification step, it is possible to fit a pole-residue model using the whole band of estimated spectra. Historically this approach has been used to obtain consistent mode shape estimates when eigenvalues have been determined using different methods or even different experiments [VAN DER AUWERAER ET AL., 2000]. Systems that have a high density of poles are identified in limited frequency bands, lest a very high model order be used, especially in the OMA case and even more so when the system is time-varying. Excessive model orders are detrimental due to numerical inaccuracies, longer computation times, spurious mathematical modes or fitting of noise artifacts. The identification of separate frequency bands is straightforward for eigenvalues but more involved for eigenvectors. Multi-band identification is a common practice because it delivers better results and can find local or badly-excited modes [GOVERS ET AL., 2014].

The least-squares frequency-domain (LSFD) algorithm fits the residues using a least-squares approach. We shall describe the method in the OMA framework when CPSDs are the data source, but the same principle can be applied to EMA or positive power spectral densities as well. Assuming the input spectrum  $\mathbf{G}_{uu}(\omega)$  has constant amplitude at least within a certain range (see modeling assumptions in section 5.3.1) and recalling equation (4.21), the pole-residue form of the output cross-power spectral density  $\mathbf{G}_{yx}$  is:

$$\mathbf{G}_{yx}(\omega) = \sum_{k=1}^{N_m} \left( \frac{\psi_k \phi_k^H}{i\omega - \lambda_k} + \frac{\phi_k \psi_k^H}{-i\omega - \lambda_k^*} \right) \quad (5.56)$$

This equation can be written in matrix form as:

$$\begin{bmatrix} \{\mathbf{G}_{yx}(\omega_1)\}^T \\ \{\mathbf{G}_{yx}(\omega_2)\}^T \\ \vdots \\ \{\mathbf{G}_{yx}(\omega_N)\}^T \end{bmatrix} = \begin{bmatrix} \mathbf{p}_{1,1} & \mathbf{p}_{1,2} & \cdots & \mathbf{p}_{1,N_m} & f_L(\omega_1) & f_U(\omega_1) \\ \mathbf{p}_{2,1} & \mathbf{p}_{2,2} & \cdots & \mathbf{p}_{2,N_m} & f_L(\omega_2) & f_U(\omega_2) \\ \vdots & \vdots & \ddots & \vdots & \vdots & \vdots \\ \mathbf{p}_{N,1} & \mathbf{p}_{N,2} & \cdots & \mathbf{p}_{N,N_m} & f_L(\omega_N) & f_U(\omega_N) \end{bmatrix} \begin{bmatrix} \mathbf{R}_1 \\ \mathbf{R}_2 \\ \vdots \\ \mathbf{R}_N \\ \mathbf{R}_L \\ \mathbf{R}_U \end{bmatrix} \quad (5.57)$$

where  $\mathbf{p}_{nk}$  are the known  $N_m$  poles for positive and negative frequencies:

$$\mathbf{p}_{n,k} \triangleq \begin{bmatrix} 1 & 1 \\ i\omega_n - \lambda_k & -i\omega_n - \lambda_k \end{bmatrix} \in \mathbb{C}^{1 \times 2} \quad (5.58)$$

where  $\mathbf{R}_k$  are the unknown  $N_m$  CPSD residues corresponding to the  $k$ -th eigenvalue:

$$\mathbf{R}_k = \begin{bmatrix} \{\psi_k \phi_k^H\}^T \\ \{\phi_k \psi_k^H\}^T \end{bmatrix} \in \mathbb{C}^{2 \times N_y^2} \quad (5.59)$$

TABLE 5.1: Factors  $f_L(\omega)$  and  $f_U(\omega)$  of the lower and upper residuals  $\mathbf{R}_L$   $\mathbf{R}_U$  when the input spectra are frequency response functions, full or positive cross-power spectral densities of displacements, velocity and accelerations (or their dynamic equivalents).

Input spectra	FRF		CPSD		P-CPSD	
	$f_L(\omega)$	$f_U(\omega)$	$f_L(\omega)$	$f_U(\omega)$	$f_L(\omega)$	$f_U(\omega)$
Displacement	$\frac{1}{(i\omega)^2}$	1	$\frac{1}{(i\omega)^4}$	1	$\frac{1}{i\omega}$	$i\omega$
Velocity	$\frac{1}{i\omega}$	$i\omega$	$\frac{1}{(i\omega)^2}$	$(i\omega)^2$	$\frac{1}{i\omega}$	$i\omega$
Acceleration	1	$(i\omega)^2$	1	$(i\omega)^4$	$\frac{1}{i\omega}$	$i\omega$

and where  $\mathbf{R}_L$  and  $\mathbf{R}_U$  are respectively the lower and upper residues added to model out-of-band terms and  $f_L(\omega)$  and  $f_U(\omega)$  their factors<sup>3</sup> according to table 5.1. The order in which the terms in  $\mathbf{p}_{n,k}$  and  $\mathbf{R}_n$  are written must match according to equation (5.57). Some authors define  $\mathbf{p}_{n,k}$  so that the real and imaginary parts of each residual are estimated separately [AMADOR ET AL., 2019]. Equation (5.57) is assembled from the matrix of known output cross-power spectral densities  $[\mathbf{G}] \in \mathbb{C}^{N \times N_y^2}$ , the known eigenvalues with lower and upper residuals  $[\mathbf{P}] \in \mathbb{C}^{N \times (2N_m + N_r)}$  and the matrix of the unknown residues  $[\mathbf{R}] \in \mathbb{C}^{(2N_m + N_r) \times N_y^2}$ . It is solved in least-squares terms by the pseudoinverse:

$$[\mathbf{G}] = [\mathbf{P}][\mathbf{R}] \implies [\mathbf{R}] = [\mathbf{P}]^+[\mathbf{G}] \quad (5.61)$$

The rows corresponding to the lower and upper residuals in  $[\mathbf{R}]$  can be removed and the matrix reshaped to obtain the  $2N_m$  residue matrices corresponding to the  $N_x$  known eigenvalues. In the final step, each estimated residue  $\mathbf{R}_k$  is decomposed into a mode shape vector  $\boldsymbol{\psi}_k$  and an operational reference vector  $\boldsymbol{\phi}_k$  corresponding to the  $k$ -th eigenvalue [RAINIERI AND FABBROCINO, 2014]:

$$\mathbf{R}_k \stackrel{\text{SVD}}{=} \mathbf{U}_1 \boldsymbol{\Sigma}_1 \mathbf{V}_1^H = \boldsymbol{\psi}_k \boldsymbol{\phi}_k^H \quad \begin{array}{l} \boldsymbol{\psi}_k = \mathbf{U}_1 \sqrt{\boldsymbol{\Sigma}_1} \in \mathbb{C}^{N_y} \\ \boldsymbol{\phi}_k = \mathbf{V}_1^* \sqrt{\boldsymbol{\Sigma}_1} \in \mathbb{C}^{N_x} \end{array} \quad (5.62)$$

where the subscript 1 denotes the columns of left-singular  $\mathbf{U}_k$  and right-singular  $\mathbf{V}_k$  vectors associated to the largest singular value  $\boldsymbol{\Sigma}_1$ . The left-singular vectors correspond to the operational mode shapes. The estimated output and input matrices in modal space are thus:

$$\begin{aligned} \mathbf{C}\boldsymbol{\Psi} &= [\boldsymbol{\psi}_1 \cdots \boldsymbol{\psi}_{N_m}] \\ \boldsymbol{\Psi}^{-1}\mathbf{B} &= [\boldsymbol{\phi}_1 \cdots \boldsymbol{\phi}_{N_m}] \end{aligned} \quad (5.63)$$

<sup>3</sup> For example, in EMA, for displacements, the LSFD model is usually written as:

$$\mathbf{H}(\omega) = \sum_{k=1}^{N_m} \left( \frac{\mathbf{R}_k}{i\omega - \lambda_k} + \frac{\mathbf{R}_k^*}{i\omega - \lambda_k^*} \right) - \frac{\mathbf{R}_L}{\omega^2} + \mathbf{R}_U \quad (5.60)$$

This equation is common in literature, see for example [RAINIERI AND FABBROCINO, 2014].

Since  $\hat{\mathbf{G}}_{yx}(\omega)$  is in general not square, the vectors  $\boldsymbol{\psi}_k$  and  $\boldsymbol{\phi}_k$  are not equal to each other<sup>4</sup>. Furthermore, they are similar to  $\mathbf{C}\boldsymbol{\Psi}\mathbf{e}_k$  and  $\mathbf{e}_k^T\boldsymbol{\Psi}^{-1}\mathbf{B}$  up to a scaling and rotation. In aeroelastic systems, when the influence of aerodynamics is low, the linearity between  $\boldsymbol{\psi}_k$  and  $\boldsymbol{\phi}_k$  is high for the eigenvectors associated to physical poles and low for those corresponding to lag states. Conversely, when the aerodynamic influence is high (for instance close to the flutter boundary), the modes shape  $\boldsymbol{\psi}_k$  and the operational reference vectors  $\boldsymbol{\phi}_k$  become dissimilar.

Let us assume that we are interested in  $N_m$  lightly-damped modes (i.e. complex-conjugated eigenvalue pairs) within a certain frequency band. If CPSDs are being used for frequency-domain system identification, we can guess that a denominator polynomial order of at least  $N_a > 4N_m$  is necessary to account for noise and out-of-band modes. On the other hand, if we were to identify a system using estimated positive power spectra, equation (4.24) shows that the necessary model order is just  $N_a > 2N_m$ . These relationships imply that the model order is high when the number of modes within a frequency band is substantial. Doubling the model order (or number of poles within the band) has an  $\mathcal{O}(n^3)$  effect in the estimator's complexity<sup>5</sup>, whereas doubling the bands has only an  $\mathcal{O}(n)$  effect. In part due to this constraint, system identification with LSCF is often performed in multiple bands.

Figure 5.7 displays an inconsistency in the synthesized spectra because the modal parameters (including eigenvectors) have been estimated from two different bands. This can be corrected by estimating the residues using LSFD.

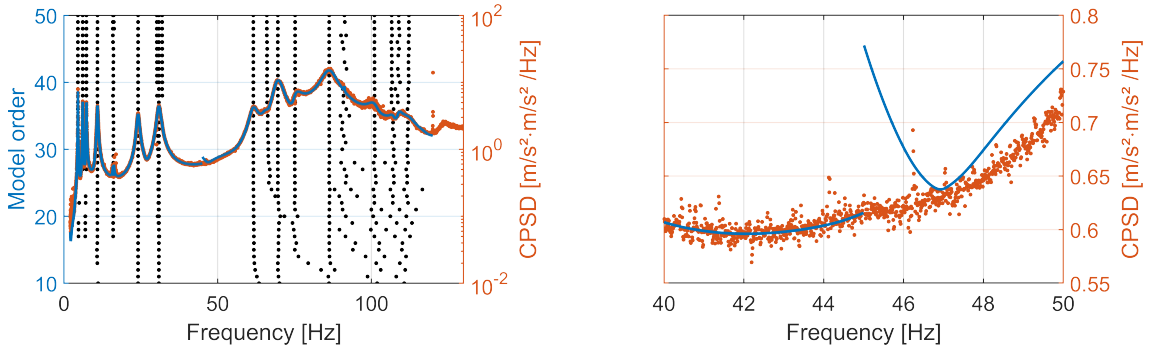


FIGURE 5.7: Frequency-domain parameter estimation using output-only data from an aircraft model at DLR-Göttingen. The spectra tell that there are two clusters of poles in the bands [2, 45] Hz and [45, 120] Hz. Better results are achieved by identifying two bands. If the spectrum is reconstructed separately for each band, inconsistencies are visible in the detail on the right.

<sup>4</sup> For mass-damping-stiffness systems the residual is the outer product of a mode shape by itself:

$$\boldsymbol{\psi}_k = \boldsymbol{\phi}_k = -\mathbf{U}_1 \sqrt{\boldsymbol{\Sigma}_1 \mathbf{V}_{1,1} / \mathbf{U}_{1,1}} \implies \mathbf{R}_k = \boldsymbol{\psi}_k \boldsymbol{\psi}_k^T$$

<sup>5</sup> All system identification methods perform some kind of matrix decomposition (EIG, QR, LU, SVD) and matrix multiplications or divisions. For a  $n \times m$  matrix, these operations have at least  $\mathcal{O}(\min\{n, m\}^3)$  complexity.



## 5.7 Chapter summary

The methods of system identification construct a parametric model of a dynamic system by analyzing its response to known or unknown excitation signals. Within the scope of the current research, modal parameter estimation of aircraft in flight excited by air turbulence and acoustic noise is performed in the operational modal analysis framework. In such applications, the experimenter is confronted with the presence of noise and with the high variance of the estimated modal parameters. A central assumption here is that the excitation spectrum, at least within a certain frequency range, has a flat magnitude, otherwise poles representing colored noise could be fitted. Such white noise input is almost never the case, but fortunately the coloring filter's poles are highly-damped and can be thus easily separated from the physical ones.

The model structures selected for our intended experimental case represent the system in the state-space or rational function forms. The mathematical details of two widely-adopted approaches and some of their variants have been delineated: the Stochastic Subspace Identification (SSI) and the Least-Squares Complex Frequency (LSCF) algorithms. Both have been developed for maximal computational efficiency with regard to real-time applications. SSI estimates the modal parameters from time-domain or frequency-domain data to construct a state-space model of the system. A preprocessing step has been developed in this work to allow multi-band identification and therefore reduce the model order and improve the stabilization diagram. The LSCF algorithm in the OMA framework utilizes full or positive power spectral densities to identify the system. In this thesis it has been upgraded to obtain clearer stabilization diagrams.

The identification frameworks for general time-varying, periodic, slowly-varying and time-invariant systems have been considered for each estimator. In the general time-varying case it is necessary to perform ensemble identification with repeated realizations undergoing the same system variation, which may not be feasible experimentally. For periodic systems it is possible to use specialized algorithms to reduce the model order, however LTI variants are still viable. In the slowly-varying case, identification algorithms for time-invariant systems can be applied to determine the modal parameter variation over time. The intended use case – monitoring during flight vibration testing – falls within the latter category.

## 6 Mode tracking

### *Abstract*

---

Continuous system identification estimates mode sets that must be tracked to be able to follow the evolution of the eigenmodes as a function of time or external parameters. However, given the presence of noise and errors in the measurements and the limited amount of data, the eigenmode variation is characterized by high variance, spurious poles and interruptions. Furthermore, permanent vibration monitoring generates huge amounts of data that must be organized. It is consequently necessary to resort to automation. The chapter describes the automated mode tracking process applied to permanent operational modal analysis.

---

Automated mode tracking is a fundamental component in the modal analysis of time-varying or parameter-varying systems. Its purpose is to organize the system identification algorithm's output so that modal data can be correlated with other parameters such as air speed and air density. Tracking is an absolute necessity for large systems, unfavorable experimental conditions and real-time applications. The topic has attracted attention from several fronts and much effort has been expended in devising strategies for pairing modes.

Output-only system identification of time-varying systems can be classified into *parametric* and *nonparametric* techniques. The former are based on time-dependent autoregressive moving average methods (TARMA), while the latter utilize a nonparametric time-frequency representation such as short-time Fourier transforms or wavelets (see section 4.4). Parametric methods estimate a modal model that is also a function of time or external parameters; nonparametric methods identify each mode set independently and must perform mode tracking in a separate step.

One of the first researches to apply an automated procedure on experimental data has been presented in [PAPPA ET AL., 1997] where system identification is complemented with mode quality indices and autonomous mode selection. Tracking of the time-varying damping ratio can be implemented into recursive subspace identification and applied to flight vibration test data [DE COCK ET AL., 2006]. An exhaustive survey of TARMA methods is conducted in [POULIMENOS AND FASSOIS, 2006] and a recent example is found in [AVENDAÑO-VALENCIA ET AL., 2020]. Some approaches aim to simplify the interpretation of the stabilization diagram and to select the best representative of each stabilization column (multiple instances of the same eigenmode identified over several model orders), for example [REYNDERS ET AL., 2012]. Mode tracking is useful in the numerical investigations of time-varying systems as well: for example, the finite element analysis of rotating machinery requires the plots of eigenfrequency over rotation speed, but since the eigenvalue traces intersect or present sharp turns, the correct paths must be reconstructed by tracking [MOGENIER ET AL., 2012]. In [BEAVERSTOCK ET AL., 2015] a minimum spanning tree algorithm is employed in the tracking of an aircraft model capable of morphing its wingspan. Recently, a general multi-stage clustering technique that does not require user-defined

thresholds has been coupled with data-driven SSI in [NEU ET AL., 2017] to monitor a plate in a wind tunnel in closed loop. In [SOAL, 2018] a modal tracking procedure is applied to the operational modal analysis of a ship under nonstationary excitation and time-varying conditions. The management of continually-estimated modal parameters in structural health monitoring applications is performed by grouping several instances of the same mode to perform statistical analyses or to observe variations over time. Automated procedures are deployed for example in [CABBOI ET AL., 2017] and [MARRONGELLI AND GENTILE, 2019]. A novel application of mode tracking is the model reduction of parameter-varying systems by clustering smaller subsystems of similar dynamic properties [LUSPAY ET AL., 2018]. Recently, [YAGHOUBI ET AL., 2018] have applied bootstrap sampling to forgo the need of high-dimensional optimization to obtain statistical information about identified modes.

Given the selected identification framework, in order to analyze parameter-varying systems, we need to develop a mode tracking technique that allows us to observe the variation of estimated eigenvalues over time, external parameters or model order. In order to do so, we need to define a methodology to quantify how “similar” or “distant” two modes are in order to pair them together or sort them into different groups. Furthermore, it is necessary to assess the “quality” of the identified data to be able to recognize spurious modes.

The chapter roadmap is therefore as follows:

1. Problem statement
2. Definition of mode similarity metrics
3. Definition of mode quality indices
4. Description of the tracking algorithm
5. Fitting of tracking data

## 6.1 Mode tracking problem statement

The overarching goal of mode tracking is the automation of modal analysis. Specifically, it is applied to the following tasks:

- Mode matching in stabilization diagrams over model order. This is often performed in the EMA framework in order to assist the user in the pole-picking procedure.
- Real-time sorting of identified modes during aeroelastic testing, for instance, for different flight conditions or wind tunnel parameters.
- Comparison between several identification algorithms, for example time-domain and frequency-domain methods.
- Mode pairing of system identification results with analytical or numerical models of the physical system. This is commonly performed in the context of model updating.

A nonparametric time-varying system identification approach has been selected for speed and simplicity. Measurements are stored into a first-in-first-out buffer and analyzed as soon as a new data block arrives. Since the tracking algorithm is uncoupled from the system identification procedure, it can be applied to any of the tasks above. This chapter focuses on the procedure used to organize the modal parameters determined experimentally during real-time monitoring of time-varying aeroelastic systems.

Some clarification about terminology is given first:

- *Mode set*: group of eigenvector-eigenvalue pairs (shorthand: *modes*) identified from a single data source. Each mode set is assigned an identification number (set ID) and linked to system parameters and other metadata.
- *Mode matching* (or pairing): the association of a mode from a *reference* set to a mode of a *comparison* set. Paired modes are assigned the same identification number (mode ID); modes that cannot be paired are assigned a new ID. The matching is performed by evaluating the “distance”/“similarity” between each pair of modes.
- *Mode family*: collection of matching modes from several sets with the same mode ID. When possible, mode families are named, for instance “first wing torsion”, “pylon pitch”, “winglet bending”.
- *Mode tracking*: matching of several mode sets, each with an associated parameter (time, speed, order, etc...). The final result is an organized collection of mode families plus spurious modes. The latter are identification artifacts arising from noise, errors or nonlinearities that do not display a realistic or consistent eigenfrequency trail.
- *Mode paths*: the continuous track in a graph left by an evolving eigenvalue.
- *Mode traces*: the single eigenvalues represented by dots in a graph, signifying that they have not been matched.

Matching is one step in the *clustering* process – a general procedure that groups data points with similar characteristics. This can be performed by histogram analysis, partitioning methods, hierarchical clustering and more recently by neural networks and deep learning techniques. An overview is found in [SAXENA ET AL., 2017]. *In this chapter we focus on solving this problem as fast as possible by collecting all similar modes in the same mode family.* The result of non-parametric identification of a time-varying system is a collection of mode sets whose members are not related to each other. The matching algorithm’s task is to “connect the dots”, something simple for a human, but not so for a machine. The matching algorithm does not alter modal data, but merely assigns the correct mode ID to each eigenpair. The user may name each mode family afterwards.

Figure 6.1 illustrates the process of building mode families by matching different mode sets. The mode matching procedure is explained in more detail later in the text. Figure 6.2 illustrates the raw system identification output on the left and the processed (tracked) data on the right. The expected results from a mode tracking procedure are plausible or smooth eigenfrequency paths, the removal of spurious modes and that mode families are labeled or numbered.

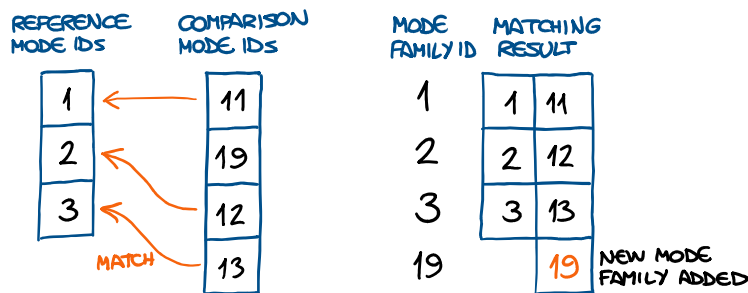


FIGURE 6.1: Mode matching example. Three modes from the *comparison set* are matched to the *reference set* modes. One unpaired mode becomes the ancestor of a new mode family.

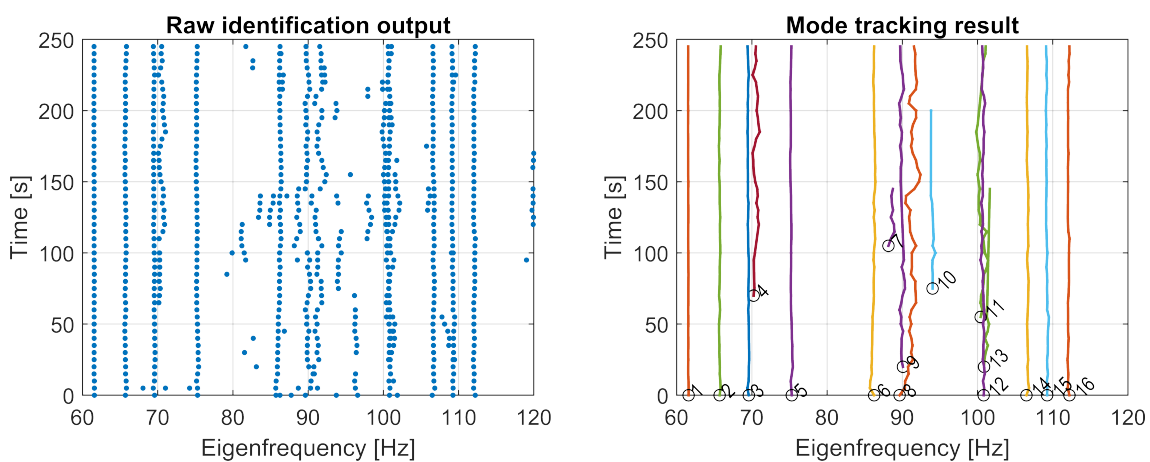


FIGURE 6.2: Completed mode matching example. The left plot displays the eigenfrequency trace over time as raw identification output. The right plot shows the corresponding eigenfrequency paths in the completed tracking diagram: the members of the same mode family are connected neatly by a line and lonely poles are erased. The ancestor of each mode family is denoted by a circle. Output-only data from an aircraft model at DLR-Göttingen.

## 6.2 Similarity metrics

Two scalars  $z_i$  and  $z_j$  can be compared by defining a “distance” between them, for example the norm-2:

$$d(z_i, z_j) = \|z_i - z_j\| \quad (6.1)$$

In this case a distance equal to zero indicates perfect congruence. Comparably, two vectors  $\mathbf{v}_i$  and  $\mathbf{v}_j$  are “similar” when their inner product is almost equal to the product of their norms (Cauchy-Schwarz inequality):

$$\mathbf{v}_i^H \mathbf{v}_j \leq \|\mathbf{v}_i\| \|\mathbf{v}_j\| \quad (6.2)$$

The two sides are equal only if the two vectors are equal.

Distance and similarity are complementary. In modal analysis these concepts are extended to eigenvalue-eigenvector pairs. Tracking relies on quantifying the distance or similarity between identified modes of vibration in order to assign each to its corresponding mode family. We shall settle on concept of “similarity” because historically, in the structural dynamics community, mode shapes have been compared in terms of orthogonality. Several measures have been devised and we shall call them *similarity metrics*. This formalism introduces some generality that is helpful later in this section.

**Definition.** *The similarity metric is an operator  $\Theta(\cdot, \cdot)$  that takes two sets of eigenvectors and/or eigenvalues  $\{\Psi, \Lambda\}^{ref}$   $\{\Psi, \Lambda\}^{cmp}$  (respectively the reference and comparison sets) and computes a similarity matrix  $\Theta \in \mathbb{R}^{N_i \times N_j}$  whose entry  $(i, j)$  quantifies the similarity between the  $i$ -th eigenmode of  $\{\Psi, \Lambda\}^{ref}$  and the  $j$ -th eigenmode of  $\{\Psi, \Lambda\}^{cmp}$ :*

$$\Theta_{ij} = \Theta\left(\{\Psi, \Lambda\}_i^{ref}, \{\Psi, \Lambda\}_j^{cmp}\right) \quad \begin{array}{ll} \Psi^{ref} \in \mathbb{C}^{N_y \times N_i} & \Psi^{cmp} \in \mathbb{C}^{N_y \times N_j} \\ \Lambda^{ref} \in \mathbb{C}^{N_i} & \Lambda^{cmp} \in \mathbb{C}^{N_j} \end{array} \quad (6.3)$$

The similarity is a real number between zero and one  $0 \leq \Theta_{ij} \leq 1$ . It is defined so that  $\Theta = 1$  indicates perfect congruence and  $\Theta = 0$  that the modes are completely dissimilar. The rows of  $\Psi^{ref}$  and  $\Psi^{cmp}$  refer implicitly to the same outputs.

**Notation.** *The reference modes have subscript “i” because they relate to the rows of the similarity matrix  $\Theta$ . Conversely, the comparison modes has subscript “j” and appear on the columns.*

**Notation.** *For ease of notation, instead of writing the similarity metric’s full argument as  $\{\Psi, \Lambda\}$  we shall sometimes simply write  $\Psi$  and refer to the eigenpair as “mode”. The symbol  $\Psi$  denotes all modes of a set, while  $\psi_k$  denotes the  $k$ -th mode of a set.*

In order to perform mode tracking, we need to define when two modes can belong to the same family. We say that  $\psi_i$  and  $\psi_j$  are “similar” when their similarity is higher than a threshold (this value may have to be adjusted depending on the chosen metric):

$$\Theta(\psi_i, \psi_j) \geq \Theta_{min} \implies \psi_i \text{ and } \psi_j \text{ are similar} \quad (6.4)$$

A similarity metric must satisfy the following properties:

**Property. Similarity metric** *The operator  $\Theta(\cdot, \cdot)$  is reflexive, commutative and insensitive to scaling and phase rotation of eigenvectors:*

$$\begin{aligned}\Theta(\boldsymbol{\psi}_i, \boldsymbol{\psi}_i) &= 1 \\ \Theta(\boldsymbol{\psi}_i, \boldsymbol{\psi}_j) &= \Theta(\boldsymbol{\psi}_j, \boldsymbol{\psi}_i)^T \\ \Theta(\boldsymbol{\psi}_i, \boldsymbol{\psi}_j) &= \Theta(z\boldsymbol{\psi}_i, \boldsymbol{\psi}_j) \quad \forall z \in \mathbb{C}\end{aligned}\tag{6.5}$$

Our intended application of mode tracking needs selectivity and speed. We shall consider the following metrics:

- *MAC*: modal assurance criterion
- *MAC- $\lambda$* : modal assurance criterion with eigenvalues
- *MACXP*: expanded modal assurance criterion
- *HDM*: hyperbolic distance metric

Several other metrics can be defined; reference [REYNDERS ET AL., 2012] provides more. In [YAGHOUBI AND ABRAHAMSSON, 2014] the modal observability correlation (MOC) criterion is introduced. It is based on the orthogonality between the columns of the observability matrix of a balanced system realization, therefore it can be easily combined with subspace identification. Regarding our application however, it is not suitable for comparing modal data from heterogeneous sources.

### 6.2.1 Output sensor selection

When two eigenvectors are compared, their rows must refer to the same output sensors on the structure for consistency. This is often overlooked, but during measurements it is common to modify the channel setup when preparing different system configurations. In the OMA framework it may be convenient to use different sets of responses to identify the modal parameters, for example, to exclude faulty sensors or badly excited directions or structure components. This means that there are usually several slightly different channel tables over the course of one experimental campaign.

Let us suppose that the eigenvectors  $\boldsymbol{\psi}_i$  and  $\boldsymbol{\psi}_j$  have been identified using different sets of outputs with global indices  $\mathbb{Y}_i$  and  $\mathbb{Y}_j$ . The similarity is computed considering only the common sensors (rows of the eigenvector matrix)<sup>1</sup>:

$$\mathbb{Y}_u = \mathbb{Y}_i \cap \mathbb{Y}_j \implies \Theta_{ij} = \Theta(\boldsymbol{\psi}_i[\mathbb{Y}_u], \boldsymbol{\psi}_j[\mathbb{Y}_u])\tag{6.6}$$

Output channels that do not appear in both eigenvectors are ignored. We shall tacitly assume that the rows of two eigenvectors are consistent when computing their similarity.

---

<sup>1</sup> The output channels must be intersected and sorted consistently. This requires additional computation but it is first and foremost a considerable challenge from the point of view of algorithmic implementation because the rows (outputs) of any combination of reference and comparison modes must be checked.

### 6.2.2 MAC - modal assurance criterion

This is by far the most known and widespread similarity metric. A detailed treatise about the modal assurance criterion, its historical development and applications is found in [ALLEMANG, 2003]. The MAC-value quantifies the degree of eigenvector linearity:

$$\text{MAC}(\boldsymbol{\psi}_i, \boldsymbol{\psi}_j) \triangleq \left( \frac{\boldsymbol{\psi}_i^H \boldsymbol{\psi}_j}{\|\boldsymbol{\psi}_i\| \cdot \|\boldsymbol{\psi}_j\|} \right)^2 \quad (6.7)$$

The MAC is used extensively for validating numerical mode shapes on the basis of experimental data, comparing eigenvectors calculated from different sources or checking if the neighboring poles in the stabilization diagram have the same associated mode shape [GOVERS ET AL., 2014]. MAC-based tracking is applied in [JELIČIĆ ET AL., 2014] to a wind tunnel model to determine the flutter boundary.

### 6.2.3 MAC- $\lambda$ - modal assurances criterion with eigenvalues

The modal assurance criterion (6.7) does not include any information about the associated eigenvalues. In [REYNDERS ET AL., 2012] a criterion that incorporates eigenvector orthogonality and eigenvalue distance is proposed. The equivalent definition as similarity metric is presented here and, lacking an established name, it is called MAC- $\lambda$ :

$$\text{MAC-}\lambda(\boldsymbol{\psi}_i, \lambda_i, \boldsymbol{\psi}_j, \lambda_j) \triangleq \frac{1}{2} \left( 1 - \frac{|\lambda_i - \lambda_j|}{\max(|\lambda_i|, |\lambda_j|)} + \left( \frac{\boldsymbol{\psi}_i^H \boldsymbol{\psi}_j}{\|\boldsymbol{\psi}_i\| \cdot \|\boldsymbol{\psi}_j\|} \right)^2 \right) \quad (6.8)$$

This criterion has been applied to mode tracking of civil structures, for example in [CABBOI ET AL., 2017; MARRONGELLI AND GENTILE, 2019].

### 6.2.4 MACXP - expanded modal assurance criterion

The expanded modal assurance criterion has been proposed in [VACHER ET AL., 2010] to improve some of the shortcomings of the MAC (6.7). This metric utilizes both eigenvalues and eigenvectors to determine similarity:

$$\text{MACXP}(\boldsymbol{\psi}_i, \lambda_i, \boldsymbol{\psi}_j, \lambda_j) \triangleq \frac{\left( \left| \frac{\boldsymbol{\psi}_i^H \boldsymbol{\psi}_j}{\lambda_i^* + \lambda_j} \right| + \left| \frac{\boldsymbol{\psi}_i^T \boldsymbol{\psi}_j}{\lambda_i + \lambda_j} \right| \right)^2}{\left( \frac{|\boldsymbol{\psi}_i^H \boldsymbol{\psi}_i|}{2|\Re \lambda_i|} + \frac{|\boldsymbol{\psi}_i^T \boldsymbol{\psi}_i|}{2|\lambda_i|} \right) \left( \frac{|\boldsymbol{\psi}_j^H \boldsymbol{\psi}_j|}{2|\Re \lambda_j|} + \frac{|\boldsymbol{\psi}_j^T \boldsymbol{\psi}_j|}{2|\lambda_j|} \right)} \quad (6.9)$$

Its derivation is based on maximizing the correlation between two complex vectors and extending this concept to the free-decay response corresponding to each eigenpair. The mathematical details are found in the aforementioned reference. MACXP has much better selectivity than MAC, a helpful property when the amount of sensors is limited, when experimental data is scarce or when the estimated modal parameters contain many spurious poles. The price is a higher computational burden that can become considerable for larger



data sets. We have applied MACXP in the tracking of flight vibration testing data in [JELIČIĆ ET AL., 2017; SCHWOCHOW AND JELIČIĆ, 2015].

### 6.2.5 HDM - hyperbolic distance metric

The distance between eigenvalues can be measured using the so-called pseudo-hyperbolic metric:

$$d(z_i, z_j) = \left| \frac{z_i - z_j}{1 - z_i^* z_j} \right| \quad (6.10)$$

where  $z \triangleq e^{\lambda/f_s}$  is a “discretized” version of the eigenvalue  $\lambda$  (in the continuous case the sample rate can be set as  $f_s = 2.1 \max\{f_n\}$ ). Unstable eigenvalues are mapped inside the unit circle by  $z \leftarrow 1/z$ . According to this definition,  $d = 0$  indicates no distance between eigenvalues and thus perfect correspondence. This equation can be combined with the modal assurance criterion to include eigenvectors for the calculation of the hyperbolic distance metric (HDM):

$$\text{HDM}(\boldsymbol{\psi}_i, \lambda_i, \boldsymbol{\psi}_j, \lambda_j) \triangleq \left( 1 - \left| \frac{z_i - z_j}{1 - z_i^* z_j} \right| \right) \frac{\boldsymbol{\psi}_i^H \boldsymbol{\psi}_j}{\|\boldsymbol{\psi}_i\| \cdot \|\boldsymbol{\psi}_j\|} \quad (6.11)$$

The HDM has a very good selectivity that is comparable with the MACXP, but can be calculated much faster. Because of this, it is the preferred similarity metric applied to experimental data in chapter 8. The research by [LUSPAY ET AL., 2018] documents its use in the sorting of instantaneous eigenvalues of a parameter-varying system.

### 6.2.6 Tracking of analytical eigenvalues

Tracking of instantaneous eigenvalues of time-varying matrices is necessary to construct flutter plots, but this is not easily performed even with analytical or numerical data. For example, [MOGENIER ET AL., 2012] describe the mode tracking technique applied to finite-element models of rotating systems in order to construct clean Campbell diagrams. A simpler and effective approach in our case is pairing modes with the help of the *interpoint distance* (IPD). This a metric devised for a linear assignment problem to track eigenvalues of analytically-determined state matrices. The IPD is calculated by evaluating two full sets of eigenvalues and eigenvectors:

$$\text{IPD}(\boldsymbol{\Psi}_i, \boldsymbol{\Lambda}_i, \boldsymbol{\Psi}_j, \boldsymbol{\Lambda}_j) \triangleq \left( 1 - \left| \tilde{\boldsymbol{\Psi}}_i^H \tilde{\boldsymbol{\Psi}}_j \right| \right) \circ \|\boldsymbol{\Lambda}_i - \boldsymbol{\Lambda}_j^T\| \quad (6.12)$$

where  $\circ$  is the Hadamard (element-wise) product and  $\tilde{\boldsymbol{\Psi}} \triangleq \boldsymbol{\Psi}/\|\boldsymbol{\Psi}\|$  is the norm-2 scaled eigenvector (so that that  $\mathbf{A} \stackrel{\text{eig}}{=} \tilde{\boldsymbol{\Psi}} \boldsymbol{\Lambda} \tilde{\boldsymbol{\Psi}}^{-1}$ ). A consistent eigenvalue sorting algorithm for analytical data that employs the IPD is provided in [D’ERRICO, 2020]. The IPD score is robust enough to handle bifurcations, crossing eigenvalue paths and modes changing stability. Naturally, a big advantage for the analytical case is the constant number of eigenvalues and the absence of spurious modes. In this thesis most plots of analytical time-varying modal parameters have been produced with the help of this algorithm.

### 6.2.7 Comparison of mode similarity metrics

Figure 6.3 displays the similarity between two mode sets using the MAC, MAC- $\lambda$ , MACXP and HDM metrics (IPD is meant only for analytical data). This type of plot is universally known as “MAC-plot” in the structural dynamics community. As already mentioned, criteria that incorporate information about eigenvalues have better selectivity. The ability to filter out two adjacent modes is particularly important for effective mode tracking.

One of the first checks to be performed on identified mode shapes is the auto-MAC matrix  $\text{MAC}(\boldsymbol{\psi}_i, \boldsymbol{\psi}_i)$ . The eigenvectors are orthogonal when weighted by the mass matrix ( $\boldsymbol{\psi}_i^T \mathbf{M} \boldsymbol{\psi}_j = 0$  for  $i \neq j$ ), but in the OMA framework this information is not available, therefore even in the ideal case the auto-MAC matrix is not perfectly diagonal (unless the system mass is lumped). Nevertheless, if the MAC value between two adjacent modes is high, it can hint at a mode of vibration that has been identified twice<sup>2</sup>. This can happen when a pole has moved within the system identification buffer. In periodic systems several harmonics associated to the same Floquet exponents can cluster together – in this case the MAC value between neighboring modes is supposed to be very high (for example the identified eigenvalues in figure 2.25 have almost identical associated residuals). Very often, however, based on the stabilization diagram, it is just a spurious mode next to a physical one and can thus be ignored.

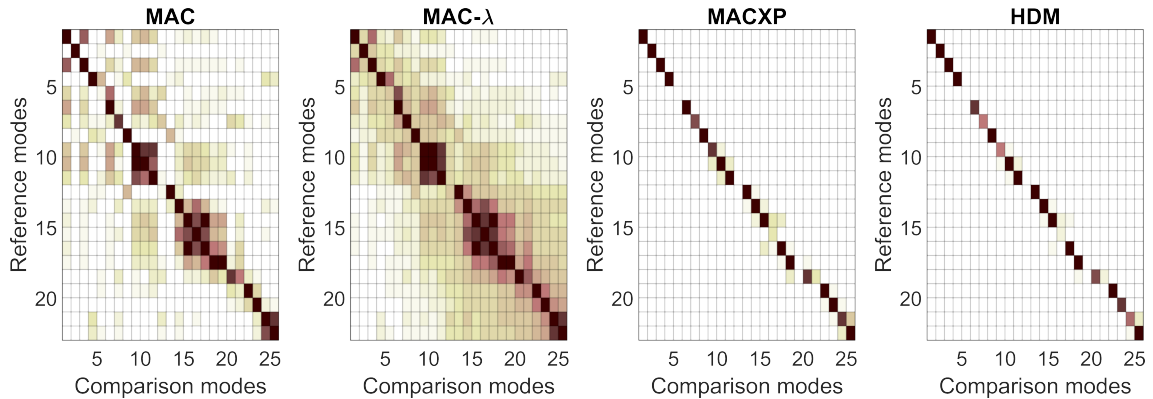


FIGURE 6.3: Comparison of two mode sets estimated from two uncorrelated realizations of the same system (output-only data from an aircraft model at DLR-Göttingen). The similarity metric is visualized as a matrix and the color of cell  $(i, j)$  encodes the similarity between mode  $i$  from the reference set and mode  $j$  from the comparison set (white:  $\Theta_{ij} = 0$ , dark brown:  $\Theta_{ij} = 1$ ). The MACXP and HDM criteria are useful in filtering out cross-similarities. MACXP and HDM are very similar, however the latter can be calculated much faster.

<sup>2</sup> Let us suppose that the system identification procedure has found two very close eigenvalues  $\lambda_1 \approx \lambda_2$  where only one physical pole  $\lambda_0$  should be. The corresponding term in the pole-residue form (5.3) is then:

$$\lambda_0 \approx \lambda_1 \approx \lambda_2 : \quad \frac{\boldsymbol{\psi}_0 \boldsymbol{\phi}_0^T}{i\omega - \lambda_0} \approx \left( \frac{1}{i\omega - \lambda_1} + \frac{1}{i\omega - \lambda_2} \right) \frac{\boldsymbol{\psi}_0 \boldsymbol{\phi}_0^T}{2} \approx \frac{\boldsymbol{\psi}_1 \boldsymbol{\phi}_1^T}{i\omega - \lambda_1} + \frac{\boldsymbol{\psi}_2 \boldsymbol{\phi}_2^T}{i\omega - \lambda_2} \implies \text{MAC}(\boldsymbol{\psi}_1, \boldsymbol{\psi}_2) \approx 1 \quad (6.13)$$

The MAC-matrix reveals that same mode shape appears twice (with different scaling), therefore one of the two eigenvalues can be picked and the other ignored.

### 6.3 Mode quality indices

The tracking algorithm must be able to assess the “quality” of identified modes in order to perform a choice in case of a double match or to remove modes that are likely spurious.

Several indices can be found in literature. We shall focus on the following:

- *MIF*: mode indicator function
- *MPC*: mode phase collinearity
- *MPD*: mean phase deviation
- *MOV*: mode overcomplexity value

A mode quality index associates a dimensionless number between zero and one to each eigenvalue-eigenvector pair. The next pages describe briefly some mode quality indices, while more detailed descriptions, such as a geometrical interpretation of how they work and how they have been derived, are provided in the cited literature.

The combination of several quality indices into a weighted sum provides the means to assign a “score” to each identified mode and hopefully to recognize spurious poles. Nevertheless, a manual inspection of the representative of each mode family is always recommended. For instance, a mode shape with irregular phase difference between eigenvector components / neighboring sensors (high complexity) is unlikely to represent a physical mode of vibration. However, a critical mode near the flutter boundary exhibits high complexity because of high aerodynamic damping and the interaction with another nearby mode. Since mode quality indices do not incorporate any geometric information, such a mode could be erroneously labeled as spurious, therefore an animated plot can reveal if the identified mode shape is physical.

Lastly, quality can be assessed effectively by the estimated variance of eigenvalues, if available. SSI and maximum-likelihood LSCF can compute the variance of the estimated modal parameters and include this information in the stabilization diagram [DÖHLER ET AL., 2013b; EL-KAFAFY ET AL., 2013].

#### 6.3.1 MIF - mode indicator function

The MIF<sup>3</sup> is defined as [BREITBACH, 1973]:

$$\begin{cases} \text{MIF}(\boldsymbol{\psi}) \triangleq 1 - |\Re\tilde{\boldsymbol{\psi}}|^T|\tilde{\boldsymbol{\psi}}|/\|\tilde{\boldsymbol{\psi}}\|^2 & \text{when } \sum_k |\Re\tilde{\boldsymbol{\psi}}_i| \leq \sum_k |\Im\tilde{\boldsymbol{\psi}}_i| \\ \text{MIF}(\boldsymbol{\psi}) \triangleq 1 - |\Im\tilde{\boldsymbol{\psi}}|^T|\tilde{\boldsymbol{\psi}}|/\|\tilde{\boldsymbol{\psi}}\|^2 & \text{when } \sum_k |\Re\tilde{\boldsymbol{\psi}}_i| > \sum_k |\Im\tilde{\boldsymbol{\psi}}_i| \end{cases} \quad (6.14)$$

where  $\tilde{\boldsymbol{\psi}} = \boldsymbol{\psi} / \max\{\boldsymbol{\psi}\}$  are scaled eigenvectors and  $i$  is the index of their rows. Purely real modes have  $\text{MIF}(\boldsymbol{\psi}) = 1$ , while for badly-identified modes  $\text{MIF}(\boldsymbol{\psi}) \approx 0$ .

<sup>3</sup> There exist at least another function with the same name (MIF) that is used to find the location of poles with frequency response functions as input [BRANDT, 2011; RADEŞ, 2010]. The OMA equivalent is the complex mode indicator function (CMIF).

### 6.3.2 MPC - mode phase collinearity

The mode phase collinearity quantifies the spatial consistency of identified mode shapes<sup>4</sup> [PAPPA ET AL., 1993]:

$$\text{MPC}(\boldsymbol{\psi}) \triangleq \frac{(\sigma_{yy} - \sigma_{xx})^2 + 4\sigma_{xy}^2}{(\sigma_{xx} + \sigma_{yy})^2} \quad (6.17)$$

where

$$\sigma_{xx} \triangleq \Re \boldsymbol{\psi}^T \Re \boldsymbol{\psi} \quad \sigma_{yy} \triangleq \Im \boldsymbol{\psi}^T \Im \boldsymbol{\psi} \quad \sigma_{xy} \triangleq \Re \boldsymbol{\psi}^T \Im \boldsymbol{\psi} \quad (6.18)$$

The eigenvector entries lie on a straight line in the complex plane in the presence of proportional damping. When  $\text{MPC}(\boldsymbol{\psi}) = 1$  the mode is perfectly collinear.

### 6.3.3 MPD - mean phase deviation

The MPD quantifies the discordance of the eigenvector from the mean phase in the complex plane [REYNDERS ET AL., 2012]:

$$\text{MPD}(\boldsymbol{\psi}) \triangleq \frac{\mathbf{w}^T \arccos |\cos(\angle \boldsymbol{\psi} - \bar{\phi})|}{\sum_{j=1}^{N_y} \mathbf{w}_j} \quad (6.19)$$

where the mean phase  $\bar{\phi}$  is computed by:

$$[\Re \boldsymbol{\psi}, \Im \boldsymbol{\psi}] \stackrel{\text{SVD}}{=} \mathbf{U} \boldsymbol{\Sigma} \mathbf{V}^H \implies \bar{\phi} \triangleq \arctan(-\mathbf{V}[1, 2]/\mathbf{V}[2, 2]) \quad (6.20)$$

The positive weights  $\mathbf{w}$  can be assigned to give more importance to some sensors over others (by default  $\mathbf{w} = |\boldsymbol{\psi}|$ ). When  $\text{MPD}(\boldsymbol{\psi}) = 1$ , the mode's mean phase difference from the linear fit of its entries is zero.

### 6.3.4 MOV - mode overcomplexity value

The mode overcomplexity value is defined as the (weighted) percentage of the response stations, for which a mass addition decreases the natural frequency for a specific mode [HEYLEN ET AL., 1998]:

$$\text{MOV}(\boldsymbol{\psi}) \triangleq \frac{\sum_{j=1}^{N_y} \mathbf{w}_j \mathbf{a}_j}{\sum_{j=1}^{N_y} \mathbf{w}_j} \quad \begin{cases} \mathbf{a}_j = 1 & \boldsymbol{\psi}_j^2 / \|\boldsymbol{\psi}_j\| > 0 \\ \mathbf{a}_j = 0 & \boldsymbol{\psi}_j^2 / \|\boldsymbol{\psi}_j\| = 0 \end{cases} \quad (6.21)$$

where  $j$  is the index of the rows of  $\boldsymbol{\psi}$  and  $\mathbf{w}$  is their weights.

<sup>4</sup> [REYNDERS ET AL., 2012] define the MPC equivalently as:

$$\text{MPC}(\boldsymbol{\psi}) = \frac{\|\Re \boldsymbol{\psi}'\|^2 + \epsilon^{-1} \Re \boldsymbol{\psi}'^T \Im \boldsymbol{\psi}' (2(\epsilon^2 + 1) \sin^2 \theta - 1)}{\|\Re \boldsymbol{\psi}'\|^2 + \|\Im \boldsymbol{\psi}'\|^2} \quad (6.15)$$

where the auxiliary variables  $\boldsymbol{\psi}'$ ,  $\epsilon$  and  $\theta$  are:

$$\boldsymbol{\psi}' \triangleq \boldsymbol{\psi} - \text{mean}\{\boldsymbol{\psi}\} \quad \epsilon \triangleq \frac{\|\Im \boldsymbol{\psi}\|^2 - \|\Re \boldsymbol{\psi}\|^2}{2\Re \boldsymbol{\psi}^T \Im \boldsymbol{\psi}} \quad \theta \triangleq \arctan \left( |\epsilon| + \text{sgn} \epsilon \cdot \sqrt{1 + \epsilon^2} \right) \quad (6.16)$$

### 6.3.5 Comparison of mode quality criteria

Figure 6.4 presents a comparison of quality indices evaluated on the modes of an aeroelastic system in order to illustrate their behavior.

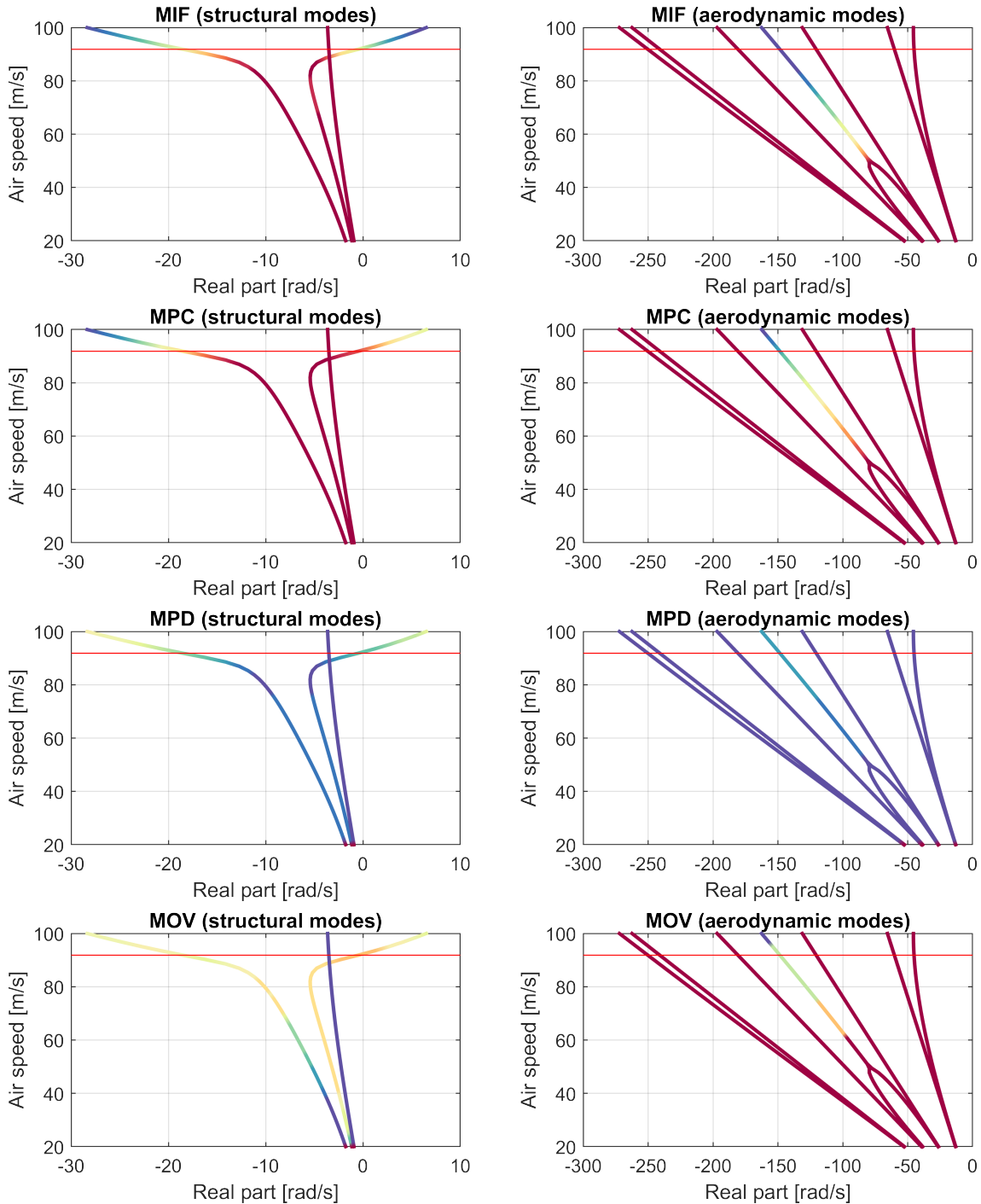


FIGURE 6.4: Comparison of the mode quality indices MPC, MIF, MOV and MPD using data from the C1 aeroelastic model 7.2. The marker color indicates the value of each mode quality index (blue: 0, red: 1). The horizontal red line denotes the flutter speed.

## 6.4 The tracking algorithm

We have seen in chapter 3.1 that the eigenvalues and eigenvectors of an aeroelastic system can vary significantly, especially for flutter-critical modes. We know from experience that a large number of spurious modes appear when performing operational modal analysis. There are cases where identified eigenvalues can be clustered by defining frequency intervals, but this approach is unable to resolve bifurcations or crossings and is vulnerable to the presence of spurious poles. Tracking methods recognize identified poles by their associated eigenvector because, at least in the ideal case, mode shapes are generally approximately orthogonal to each other even for closely-spaced poles.

Let us assume that a mode  $\Psi(x)$  varies continuously within the time or parameter interval  $x \in [x_0, x_f]$  to such extent that the similarity between the extremes is very low  $\Theta(\Psi(x_0), \Psi(x_f)) \approx 0$ . We assume that a sufficient number of intermediate steps is available so that the following condition can be satisfied:

**Hypothesis.** *The modes  $\Psi(x)$  are identified  $\Delta x$  units apart, where  $\Delta x$  is such that consecutive eigenpairs are similar  $\Theta(\Psi(x), \Psi(x + \Delta x)) \geq \Theta_{min}$ .*

Figure 6.5 displays an aeroelastic system undergoing a linear variation from low speed to a little over the flutter speed. As the flutter condition is approached, the eigenvectors become increasingly more complex and change shape. Aerodynamic poles display dramatic changes as speed increases. Nevertheless, the system can be tracked if the modes vary negligibly between mode sets. We conclude that, for successful tracking, an adequate temporal/parameter resolution is required.

In an online monitoring application for aeroelastic systems this assumption is verified when the modal analysis is completed fast enough relative to the system's rate of variation. This observation forms the basis for the tracking algorithm described in the coming pages. We have seen in section 4.2 that the cross-power spectral density's residuals contain information about the mode shapes but also the poles of the excitation spectrum. In

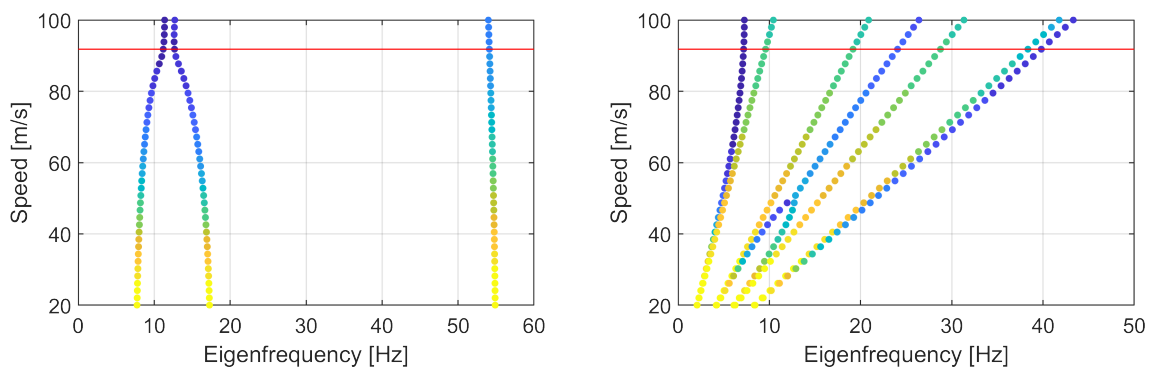


FIGURE 6.5: Aeroelastic system undergoing linear speed variation ( $v_f = 91.8 \text{ m/s}$ ). The plots display the physical modes on the left and the aerodynamic ones on the right. The marker color denotes the MACXP value of each mode shape with respect to the system at rest (blue: 0, yellow: 1). The parameter's variation  $\Delta v = 2 \text{ m/s}$  is such that adjacent mode sets are so similar that no difference is visible.

output-only applications, it may be difficult to maintain stationary conditions. Due to varying excitation levels or external parameters, some modes may be identified poorly or not at all, thus severing the chain of a mode family. This must be dealt with by devising a robust mode matching strategy. Several approaches can be found in literature. [REYNDERS ET AL., 2012] present a fully-automated modal analysis procedure that makes use of hierarchical clustering. A method using self-adjusting thresholds is presented in [CABBOI ET AL., 2017] and [MARRONGELLI AND GENTILE, 2019]. In [YAGHOUBI ET AL., 2018] a combination of correlation-based clustering and bootstrapping is proposed. The paper of [LUSPAY ET AL., 2018] presents a multi-step technique for the purpose of LPV system model reduction of aeroelastic systems.

In our approach, the mode tracking algorithm's purpose is the consistent pairing of all the mode sets that have been identified during an experiment or data run. Its inputs are estimated mode sets with corresponding parameters and metadata, the chosen similarity metric, threshold and settings. Its output is simply a table containing the mode IDs associated with each set ID. Through the set ID there is a one-to-one correspondence between all identified eigenvector-eigenvalue pairs and metadata. The tracking diagram is then built by plotting the eigenfrequencies of all modes with the same ID over the corresponding abscissa as a simple polygonal chain (see for example figure 6.9).

#### 6.4.1 Mode matching

We begin by illustrating the mode matching process. The pairing is performed by assigning each comparison mode to a reference mode – when possible. This can be carried out in at least two ways:

- For each column of  $\Theta$ , get the index of the row where the maximum similarity is found. This index corresponds to the matched reference mode. This is a very simple and fast approach that delivers good results.
- Solve an assignment problem with the Hungarian (Munkres) algorithm where  $\Theta$  is the cost matrix. The similarity matrix is generally rectangular, therefore some “dummy” columns/rows with the minimal cost (0) must be added. The algorithm solves a combinatorial optimization problem in polynomial time [BURKARD ET AL., 2009].

A multiple match happens when two comparison modes are assigned to the same reference mode (mode family). When a multiple match is detected, the algorithm must perform a choice, for example by assigning a score to each mode and picking the one with the highest one. A possible score is:

$$\text{SCORE}(\psi_j) = 1 - \text{MPC}(\psi_j) + \text{MPD}(\psi_j) + \text{MAC}(\psi_i, \psi_j) \quad (6.22)$$

The comparison mode  $\psi_j$  with the highest score is matched, the others unpaired. Unmatched modes become the ancestors of new mode families. Figure 6.6 illustrates the matching process schematically.

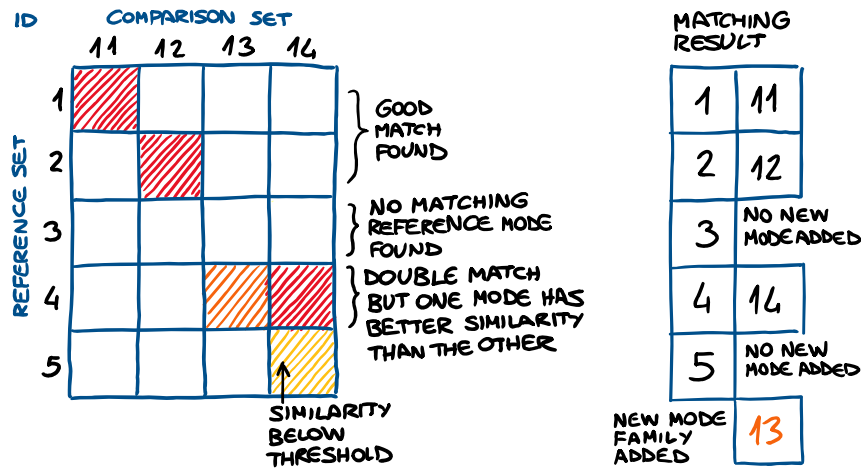


FIGURE 6.6: Mode matching procedure example. The reference set is  $0x$  and the comparison set is  $1x$ . In the figure the colors symbolize the level of similarity between each pair of modes (red: high, white: low). Two modes are paired when their similarity exceeds a threshold. It is possible that no matches are found for some reference modes (in this case 03 and 05). Multiple matches are resolved by assigning a score to each mode (modes 13 and 14). Unmatched modes are not discarded but become the ancestor of a new mode family (mode 13). Mode families with large variance and sparse members are marked as spurious.

### 6.4.2 Mode library

The core strategy of the tracking algorithm developed in this thesis consists in storing the identified mode sets in a large *mode library* and maintain a dynamically-updated index of reference modes within it. Multiple slightly different estimations (instances) of the same modes are thus stored to provide a larger reference base for any newly-estimated modes. Spurious eigenpairs will not be matched consistently and will form mode families whose members are few and sparse, thus being much easier to recognize and eliminate. This approach is necessary for OMA because the estimated mode shapes have a large variance even in the nominally stationary conditions and more so when the system is time-varying. Figure 6.7 presents three mode matching steps to illustrate the concept of mode library.

[DE COCK ET AL., 2006] presented a recursive EMA method that utilizes a forgetting factor for tracking abrupt changes in modal parameters. In [JACQUIER AND AYME, 2018] a tracking tool that utilizes a similar “mode library” concept has been recently presented. The pseudo-code of the algorithm that has been developed for flight vibration testing in [JELIČIĆ ET AL., 2017] is described in algorithm 4 at the end of this subsection. The library is a reference base that contains significantly more elements than the comparison set (typically thousands of modes versus less than a hundred). Fast computation of the similarity criterion and efficient solution of the assignment problem are required for a real-time application (it may be necessary to employ the HDM metric (6.11) instead of the MACXP (6.9) or to forgo the Hungarian algorithm when available CPU resources are scarce).



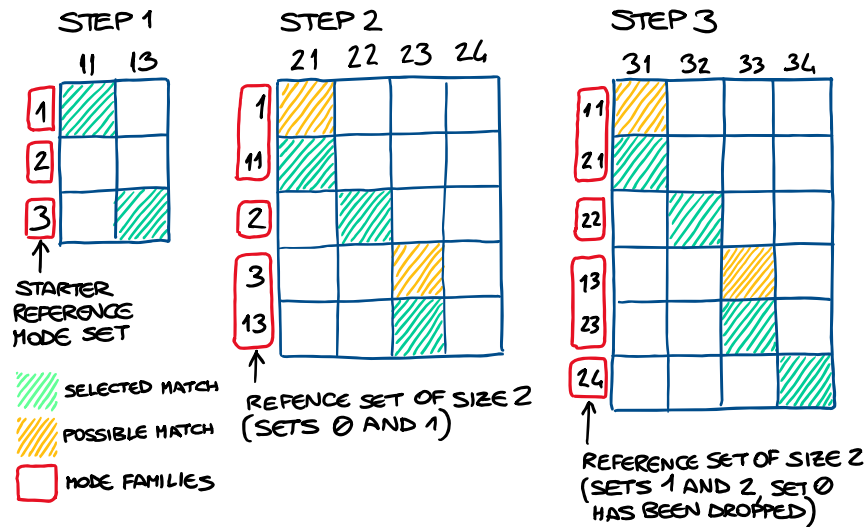


FIGURE 6.7: In this example the reference library is set to use only the last two mode sets. Step 1: the first set  $1x$  is matched with the starter reference set  $0x$ . Reference mode  $02$  finds no corresponding comparison mode. Step 2: the reference contains sets  $0x$  and  $1x$  and is used to match  $2x$ . There is no match for mode  $24$ , so it becomes the ancestor of a new mode family. Step 3: since the library is to use only the last two sets, set  $0x$  is removed from the reference set. All comparison modes are matched in this step.

In order to limit the unbound growth of the mode library, the user defines the maximal number of mode sets that are stored within and how they are replaced as new data is acquired. There are various ways of selecting the reference mode sets:

- A simple approach is to consider just to the last few sets that have been identified (first-in-first-out buffer). The tracking algorithm has thus a “fading memory” and forgets the older mode sets with a hard cut-off.
- In the time-varying case a weight function that depends on the “distance” from the current external parameters can be applied. This strategy is sound, but it requires potentially a large reference base.
- Scoring the modes to use only the “best” ones as reference, for example the least complex ones or by performing a search on the stabilization diagram. This is a topic of ongoing research, see for example [VOLKMAR ET AL., 2019].

The first approach requires the least amount of computation and has proven quite effective.

Two phases of our tracking procedure are illustrated in figure 6.8 using real data. As tracking progresses, there can be thousands of modes in the library. Figure 6.9 displays an intentionally “bad” tracking diagram. The goal is to highlight what happens when the similarity threshold is too low or when the library’s length is too short. In this example the threshold is so low that some modes are clearly mismatched. Similarly, a threshold close to 1 may be too restrictive for OMA data. Transient phenomena that impede the identification of some modes should not have longer time scales than the library’s length, lest a mode family chain be broken (see example in figure). This can be corrected by increasing the library’s length.

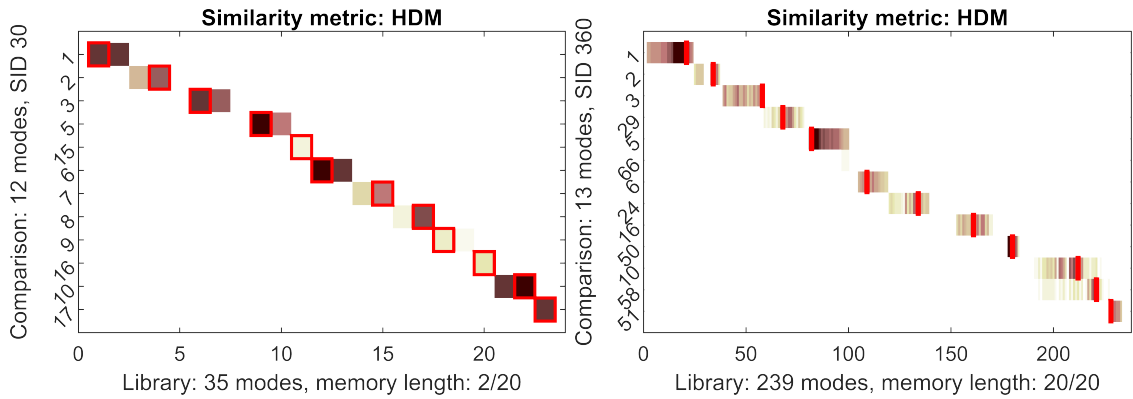


FIGURE 6.8: Two snapshots of the tracking process. The comparison modes are shown along the rows for clarity. Left plot: similarity between a comparison set (12 modes) and a reference library containing 2 sets with 35 modes in total. Each row in the matrix (comparison mode) has up to two matches because there are this many instances of the same mode in the library. The library grows up to the specified length by inserting these newly-matched modes and this procedure is repeated for all identified sets. Right plot: the last step of the tracking process. At this stage the library contains the last 20 sets containing 239 modes in total. The red outline indicates which reference mode has been matched.

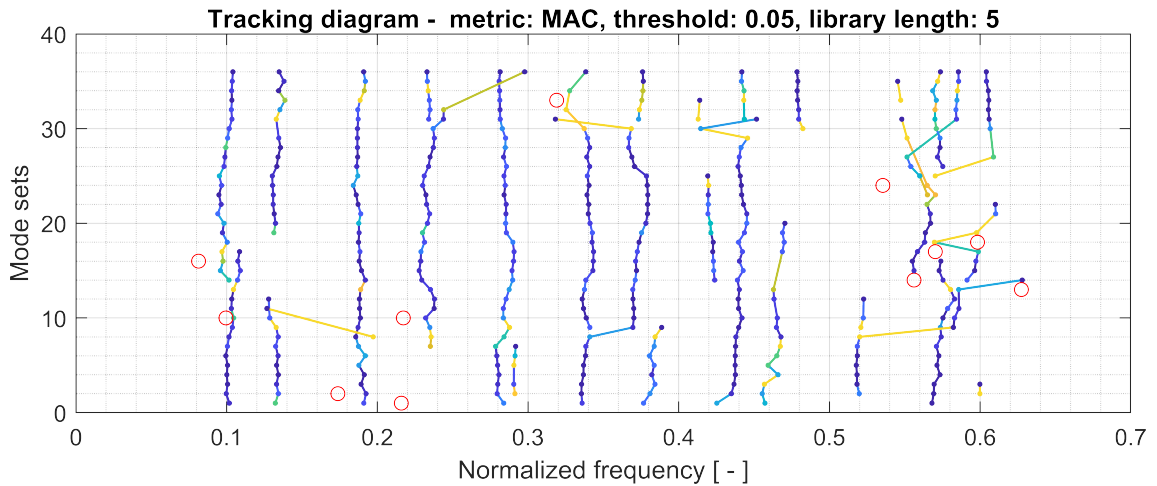


FIGURE 6.9: Tracking diagram with very low threshold and short library length. The red circles are lone spurious poles. The line color represents the MAC value between consecutive modes within the same family (blue: high, yellow: low). The oblique yellow lines denote thus clearly mismatched modes. The library's length determines the algorithm's capability to track disappearing modes. For example, the mode family at  $f = 0.14$  is disrupted because the library contains only the last 5 sets (a length 10 would have "bridged" this jump where the mode has not been identified). Flight test data from [JELIČIĆ ET AL., 2017].

**Algorithm 4:** Tracking algorithm

**Data:**  $N$  sets of identified modes  $[\Psi^1, \Psi^2, \dots, \Psi^N]$  (with consistent rows)  
**Result:** Global mode IDs  $\mathbb{I}[n]$ , where the  $n$ -th array element contains the mode IDs of the  $n$ -th mode set.

**Initialization:**

Get starter reference set  $\Psi^{ref} \leftarrow \Psi^0$  (from FEM, GVT or first identified set)

Assign mode IDs  $\mathbb{I}_{ref} \leftarrow 1 : N_0$  ( $N_0$ : number of modes in  $\Psi^0$ )

Initialize global mode IDs:  $\mathbb{I}[1] \leftarrow \mathbb{I}_{ref}$

**Run:**

**for** every identified mode set after the first  $n = 1 : N$  **do**

Get reference set  $\Psi^{ref}$  and corresponding mode IDs  $\mathbb{I}_{ref}$

Get comparison set  $\Psi^{cmp} \leftarrow \Psi^n$

Consider only common sensors for the computation of the similarity; get correct row sorting for the reference and comparison sets:

$$\mathbb{Y}_u \triangleq \mathbb{Y}^{ref} \cap \mathbb{Y}^{cmp} \quad \implies \quad \mathbb{Y}_u^{ref} = \mathbb{Y}^{ref} \in \mathbb{Y}_u \quad \mathbb{Y}_u^{cmp} = \mathbb{Y}^{cmp} \in \mathbb{Y}_u$$

Compute similarity between reference and comparison mode sets:

$$\Theta_{ij} = \Theta(\Psi^{ref}[\mathbb{Y}_u^{ref}, i], \Psi^{cmp}[\mathbb{Y}_u^{cmp}, j])$$

Solve assignment problem  $f(\cdot)$  with  $\Theta$  as cost matrix to obtain local indices  $\mathbb{J}$ :

$$\mathbb{J} = f(\Theta)$$

where  $\mathbb{J}[j] = i$  indicates that  $\Psi_j^{cmp}$  is matched to  $\Psi_i^{ref}$

Assign referenced IDs to matched comparison modes:  $\mathbb{I}_{cmp} \leftarrow \mathbb{I}_{ref}[\mathbb{J}]$

**for** every reference mode  $i = 1 : N_i$  **do**

    Calculate score (mode quality index)  $\mathbf{s}$  of each mode matched with  $i$ -th reference mode

    Unmatch multiple matches  $\mathbb{I}_{cmp}[\mathbf{s} < \max(\mathbf{s})] \leftarrow 0$

**end**

**for** every comparison mode  $j = 1 : N_j$  **do**

**if** the similarity is below the threshold  $\Theta[\mathbb{J}[j], j] < \Theta_{min}$  **then**

        Unmatch comparison mode:  $\mathbb{I}_{cmp}[j] \leftarrow 0$

**end**

**if** the comparison mode has been unmatched  $\mathbb{I}_{cmp}[j] == 0$  **then**

        Assign new ID to unmatched comparison mode:  $\mathbb{I}_{cmp}[j] \leftarrow \max(\mathbb{I}_{ref}) + j$

**end**

**end**

Update global mode IDs  $\mathbb{I}[n] \leftarrow \mathbb{I}_{cmp}$

Select which mode sets  $\mathbb{I}_{sel}$  can remain in the reference set according to the mode library management strategy:  $\mathbb{I}_{ref} \leftarrow \mathbb{I}_{ref}[\mathbb{I}_{sel}]$

Build new reference indices by appending comparison indices:

$$\mathbb{I}_{ref} \leftarrow \{\mathbb{I}_{ref}, \mathbb{I}_{cmp}\}$$

The new reference modes are  $\Psi^{ref} \leftarrow \Psi[\mathbb{I}_{ref}]$

**end**

### 6.4.3 Variance of modal parameters

The SSI and maximum-likelihood LSCF methods that estimate the population variance of modal parameters (see chapter 7) are the focus of several publications, for example [DÖHLER ET AL., 2013b; EL-KAFIFY ET AL., 2013; GUILLAUME ET AL., 1999; PINTELON ET AL., 2007; REYNDERS ET AL., 2008]. The estimated modal parameters are assumed to have Gaussian distribution and their variance quantifies the confidence with which they have been identified.

SSI can perform a sensitivity analysis of the identified system matrices starting from perturbations of the observability matrix (5.15). This leads ultimately to an estimate of the covariances of the system eigenvalues, which can be extended to mode shapes. The maximum-likelihood LSCF estimator performs an iterative minimization of the error between the estimated and synthesized spectra. The inverse of the reduced Jacobian matrix (5.41) computed this way is an estimate of the modal parameters covariance matrix. The eigenvalue variance is usually represented as error bars on the stabilization diagram in order to assist the test engineer in the composition of the modal model. Spurious poles have commonly a standard deviation that is at least one order of magnitude greater than that of physical poles.

Due to tight limitations on computation time, the tracking strategy described in this chapter does not have access to the estimated *population variance*, but can calculate the *sample variance* from one or several stabilization diagrams. When a statistically significant number of model orders has been computed, the eigenvalues can be tracked to estimate their variance. In [YAGHOUBI ET AL., 2018] bootstrap sampling is used to provide information for clustering and noisy modes removal. Figure 6.10 provides an example with real data. Another approach is to identify the system during nominally stationary conditions using short data blocks, track the mode sets and then calculate the variance. Figure 8.39 will provide an example using flight vibration testing data.

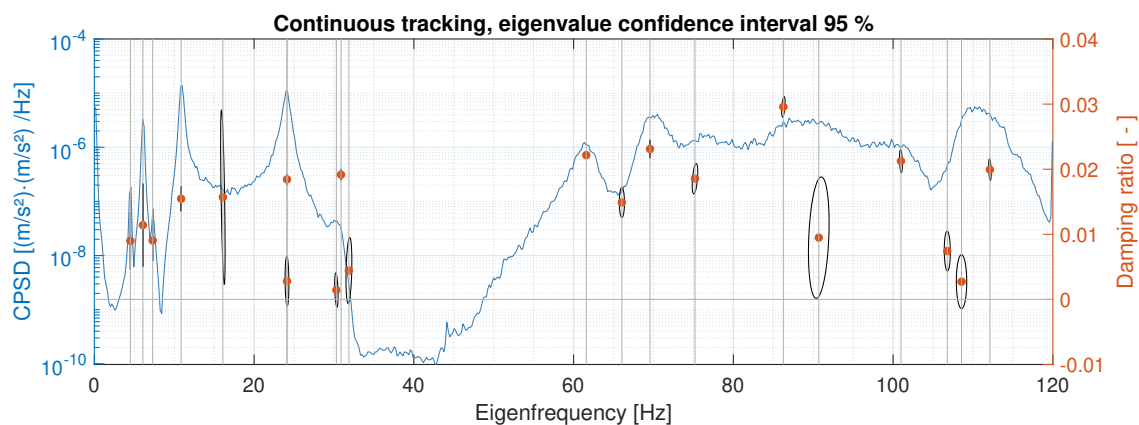


FIGURE 6.10: The eigenvalue and their variance are estimated using the covariance-driven SSI. The mean value is denoted by a dot, the ellipses represent the covariance of eigenfrequency and damping ratio. The variance of the former is typically larger than that of the latter. Two clearly spurious poles are visible at about 15 and 90 Hz. Output-only data from an aircraft model at DLR-Göttingen.

#### 6.4.4 Cleaning of the stabilization diagram

The tracking algorithm can be used to clean up the stabilization by scooping identified poles with large variance, lone poles or the ones whose modal parameters vary excessively between two consecutive model orders  $p$  and  $p - 1$  (starting from the top) [GOURSAT ET AL., 2011]. A common and effective strategy is to define the maximal relative variation for eigenfrequency  $\varepsilon_f$  and damping  $\varepsilon_\zeta$ :

$$\left| 1 - \frac{f_{p-1}}{f_p} \right| \leq \varepsilon_f \quad \left| 1 - \frac{\zeta_{p-1}}{\zeta_p} \right| \leq \varepsilon_\zeta \quad (6.23)$$

Based on such stability criteria, many authors and modal analysis packages label the poles with letters (**s**: stable, **f**: stable frequency, **d**: stable damping, **m**: stable mode, **o**: origin mode). The poles can be selected automatically or manually, depending on the situation. In [LANSLOTS ET AL., 2004] a validation methodology for automated pole selection is presented. During ground vibration testing, as more knowledge about the structure becomes available through the analysis of many data runs, the modal model is constructed by selecting the best from a pool of identified modes [GOVERS ET AL., 2014]. Recently neural networks have been applied to modal model selection in the post-processing phase [VOLKMAR ET AL., 2019]. In this regard real-time system identification is challenging because there is very little available time to perform any selection. The approach followed in this thesis and that has been deployed during flight testing constructs the full stabilization diagram, but the eigenmodes and reconstructed input spectra are only estimated for the highest four model orders. These four model orders are compared by computing a mode quality index. The order with the best overall score is used to form the modal model. Tracking over model order is fortunately easier to perform than tracking over time, but it requires the additional identification over many model orders to produce statistically relevant results. This may not be feasible because additional computation may be necessary to estimate the eigenvectors. Figure 6.11 provides an example of our technique applied to the full stabilization diagram.

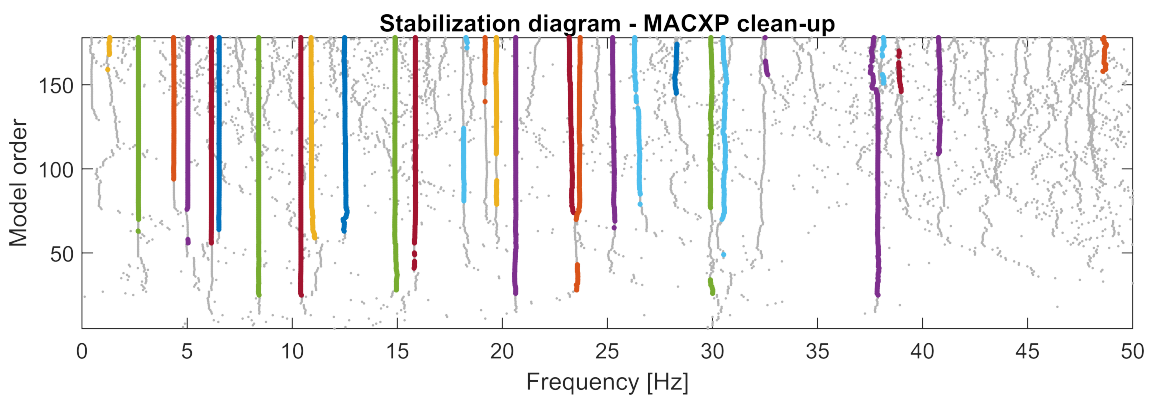


FIGURE 6.11: Automatic clean-up of stabilization diagram using tracking along mode orders. This is normally not performed in an online application due to time constraints. Plot adapted from [SCHWOCHOW AND JELIČIĆ, 2015].

## 6.5 Parametric representation of tracked data

After the identification data has been tracked or organized, the eigenvalue traces can be interpolated or regression can be applied to construct a parametric representation of each mode family with respect to time or external parameters. Fitting can be helpful in compensating insufficient data acquisition time, sub-optimal signal processing or system identification parameters, errors, outliers and bad tracking. When the system is time-varying some running average technique must be employed. In the case of flutter diagrams, polynomials of order 2 can be used for fitting [VERBOVEN ET AL., 2004]. The extrapolation of flutter data from quasi-stationary input-output measurements is discussed in [DE TROYER ET AL., 2008]. A model-based technique is applied in [ERTVELDT ET AL., 2014] to predict the onset of flutter. In our approach we employ two main methods:

- The locally-weighted polynomial (LOWESS) approach can be applied with different combinations of kernels and polynomial orders. Since it computes the so-called smoothing matrix, various validation techniques (such as Akaike's information criterion) can be employed. A local regression toolbox is found in [JEKABSONS, 2016].
- The Savitzky-Golay filter is a finite impulse response filter that can be designed in advance for a certain order and frame length and then deployed to provide moving average smoothing. It is a very efficient solution that can be easily implemented. It is applied to flight vibration testing results in chapter 8.

The Gaussian kernel up to order 3 has been found to deliver good results for constructing flutter diagrams, while a moving average method is preferred in real-time monitoring applications.

Figure 6.12 presents the experimental flutter diagram constructed while conducting a measurements in a transonic wind tunnel and the fit used to extrapolate the critical speed.

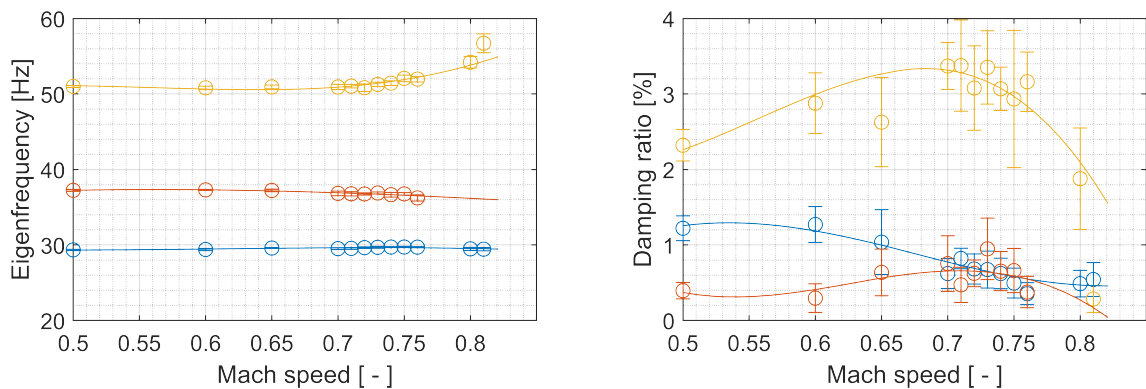


FIGURE 6.12: Wind tunnel results for constant pressure and variable Mach number. The circles are mean values, the bars represent three standard deviations, the lines a Gaussian smoothing kernel fit of order 3. The system is held under stationary free-stream conditions at each Mach number and a pitching moment impulse is applied to the model. Several uncorrelated system identifications are performed to assess the modal parameter variance. The variability that can be observed in the identified damping is due to artificial excitation (atop turbulence). Data from the transonic wind tunnel DNW-TWG [JELIČIĆ ET AL., 2014].

In figure 6.13 the modal parameters are estimated in real-time and regression is performed as new data is acquired. Spurious modes appear when the system undergoes an abrupt variation, when linearity assumptions are violated, when few data points are available or when the excitation varies. Information about damping is displayed more effectively in the complex plane as the real part of the eigenvalue because each mode is then well-separated vertically. The damping fit is computed with time as the independent variable. The eigenvalue variance is due to nonstationary flight conditions and short data blocks.

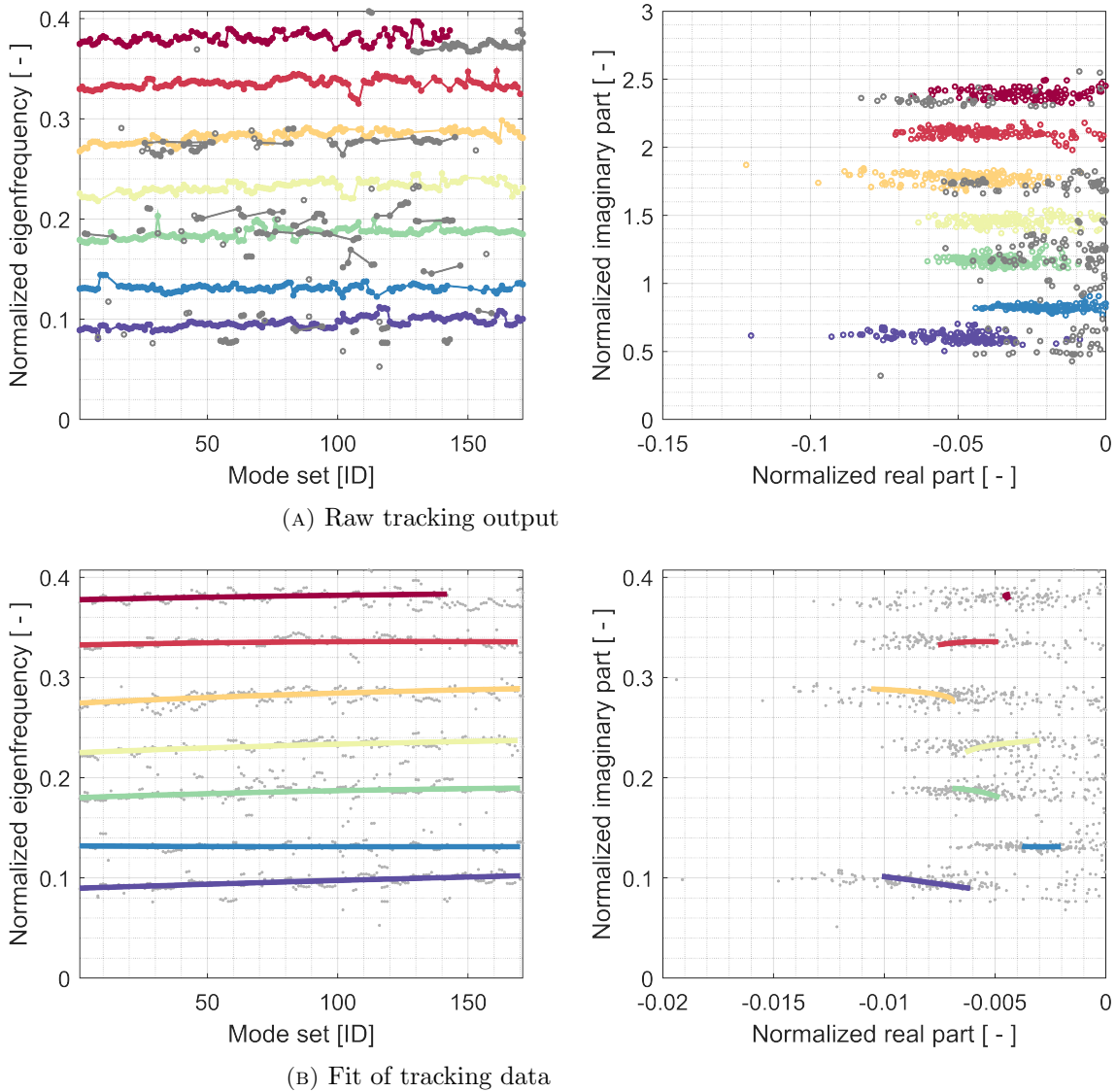


FIGURE 6.13: Top: tracked modal parameters from a flight vibration test from [JELIČIĆ ET AL., 2017]. The gray markers are spurious modes, the colored markers denote tracked mode families, a line connects two adjacent modes belonging to the same family. This tracking diagram is a completely automatic output. Bottom: tracked modes fitted using a Gaussian smoothing kernel of order 1.

## 6.6 Chapter summary

The results of continuous system identification during vibration testing must be organized in relation to time or external parameters in order to monitor the evolution of eigenfrequency and damping ratio.

The chapter described the mode tracking strategy that has been developed within this research for the automation of real-time modal analysis. The tracking algorithm is based on a library of many instances of the same eigenmodes that is constructed as measurements progress in order to successfully match newly-identified eigenmodes. These are paired by similarity criteria based on some concept of distance between different eigenpairs, such as the modal assurance criterion (MAC). The goodness of estimated and matched modes is evaluated by mode quality criteria such as the mean phase deviation (MPD). Modes that are matched with each other belong to the same mode family and trace smooth lines on a time-eigenfrequency plot. It is then possible to observe the damping ratio variation over flight parameters to construct flutter curves.

The end result is a nonparametric representation of time-varying modal parameters. Once the identified modes have been organized into families, it is possible to apply regression techniques to construct a parametric representation.





## 7 Aeroelastic system simulation

### *Abstract*

---

The theoretical development and modal analysis tools described in the previous chapters are put to the test on simulated data. The chapter elaborates the solvers used to compute the numerical solution of time-varying systems. A three degrees-of-freedom aeroelastic system with two configurations that display hard and soft flutter is employed. The system response to stochastic excitation is simulated under various parameter variation profiles and the system's modal parameters are identified. The influence of duration, block length and number of averages is investigated.

---

The previous chapters have set up the theoretical tools required to model parameter-varying aeroelastic systems and to perform spectral estimation, system identification and mode tracking. The present chapter demonstrates the applicability of those methods on simulated data. The results of operational modal analysis can be compared with an analytical model or instantaneous modal parameters if the system is slowly-varying. To this end, records with sufficiently long duration and ensemble identification are necessary to produce good estimations, but lengthy simulations of large dynamic systems have many demanding aspects. Numerical solutions must have the correct frequency-domain characteristics, lest the identified system present some kind of bias, unaccounted poles and zeroes, numerical damping added by the integrator et cetera. In order to control the quality of simulated data, ad-hoc numerical methods are implemented with particular attention to accuracy and computation time.

To recapitulate, our objectives are:

- Simulations of large time-varying systems
- Datasets of adequate length for the verification of system identification techniques
- Investigation of the effect of amplitude and rate of parameter change

The requirements for the simulation methods are: precisely known assumptions and approximations, controllable distortions and artifacts of the simulated data, computationally efficient handling of large systems for long duration.

The chapter's roadmap is thus:

1. Simulation of parameter-varying systems: system matrix generation, excitation signals and numerical implementation.
2. Presentation of a simple benchmark aeroelastic system with two flutter configurations.
3. Modal analysis: spectral estimation, system identification and mode tracking.
4. Discussion of results

## 7.1 Numerical analysis of time-varying systems

The bounded-input-bounded-output stability assessment does not exclude a localized response amplification (see for example figure 2.6). For real-world mechanical systems, structural integrity must be guaranteed by limiting the maximal vibration amplitude below a certain level. For this purpose, a direct numerical solution is necessary.

In the case of periodic systems, section 2.3.4 explained that the stability and a parametric frequency-domain description of the response can be computed via Floquet decomposition. Furthermore, an aperiodic system can be approximated by an arbitrarily accurate periodic representation. A number of practical methods have been implemented for this purpose in section 2.4 with various degrees of accuracy. Unfortunately, even for variation rates in the order of the lowest eigenfrequency, it may not be possible to decompose the system due to numerical limitations, preventing us from constructing the parametric frequency-domain representation of the system's response. The simplified approach described in section 2.5 may help with such extreme cases.

As an example applied to a periodic aeroelastic system, figure 7.1 plots the rank decay of the monodromy matrix  $\Phi(T, 0)$  as a function of the adimensional frequency  $k_{\omega_0} = \omega_0/\omega_{min}$ , where  $\omega_{min} = \min |\lambda|$  is the lowest eigenfrequency of interest for the system at rest (see section 3.4.2). The critically-damped aeroelastic poles decay much faster than those associated with structural modes, therefore the computation of the state transition matrix for a large period displays a rank drop. This sets a limit for the slowest systems that we can analyze with this technique. This illustrates the same phenomenon discussed in section 2.4. Fortunately, for slowly-varying systems the frozen-time eigenvalues are easy to compute.

In aeroelastic systems such as aircraft and wind tunnel models the rate and amplitude of parameter variation over the typical operating range is low, therefore the dynamic effects they induce are expected to be small or negligible.

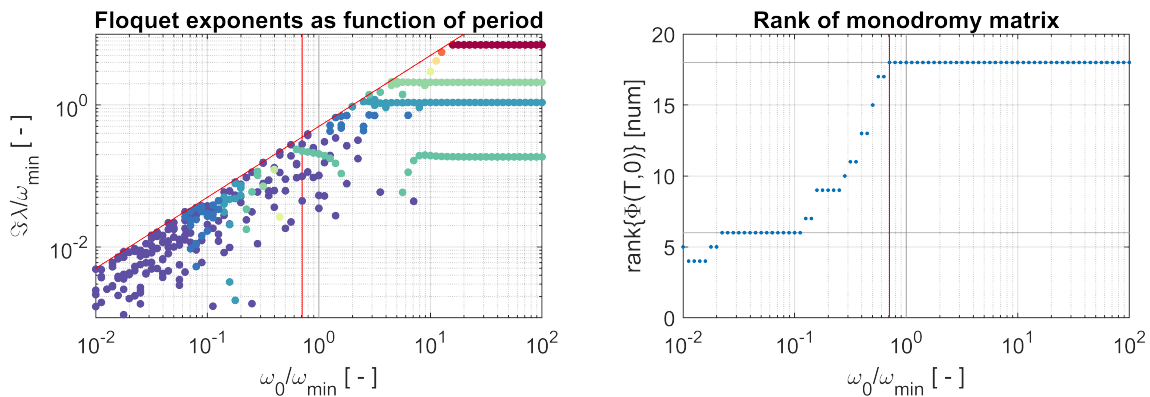


FIGURE 7.1: Floquet exponents over the normalized fundamental frequency for the C1 system 7.2 with a sine velocity profile. The vertical gray line indicates the lowest eigenfrequency of the system at rest, the vertical red line indicates the start of the rank decay. The horizontal gray lines on the right plot show where the rank is full (18) and where the aerodynamic states lose importance (6). The rank decay for this system appears at  $\omega_0/\omega_{min} = 0.7$ .

### 7.1.1 Generation of system matrices

Aeroelastic modeling has been elucidated in chapter 3. The main concern lies in the system's feedback loop where  $\mathbf{A}(t)$  and  $\mathbf{B}(t)$  must be known/constructed at each time instant  $t$  as functions of air density and air speed  $\{\rho(t), V(t)\}$ . Two scenarios appear:

- *State-space model arrays* (system matrix interpolation): the system matrices are known at discrete time instants or for some parameters on a grid. Intermediate values are interpolated from neighboring known grid points.
- *Procedural generation* (parameter interpolation): the system matrices are constructed numerically or calculated analytically at the desired time instant or parameters.

State-space model arrays are common for parameter-varying systems that are described by interpolated LTI arrays. The latter are obtained from large finite-element models or by linearization around an operating point of nonlinear systems for a grid (discrete set) of parameters. Figure 7.2 illustrates the concept. A continuous representation of the whole system is obtained by applying some kind of interpolation within the grid of known parameters, e.g. standard  $n$ -dimensional polynomial interpolation (nearest-neighbor, linear, Akima, spline,...) either for gridded (uniform or nonuniform) or scattered data. An interpolation technique for LTV systems is proposed in [DE CAIGNY ET AL., 2014] to produce numerically well-conditioned coherent state-space representations with some limitations on parameter variation. Memory or data management requirements penalize this formulation for large parameter spaces. On the other hand, procedural generation is more favorable because no interpolation or complicated data storage are needed, but, in return, memory is traded for computation. For the analysis at hand the system matrices will be generated as functions of  $\{\rho(t), V(t)\}$  as detailed in section 3.1. The eigendecomposition is generally sensitive to the modification of matrix entries and frozen-time eigenvalues of time-varying systems can display sudden jumps due to bifurcations even when the parameters vary smoothly (see figure 3.9). Consequently, in order to remove at least one source of uncertainty, procedural generation is preferred. If the parameters are known only at discrete points, then one-dimensional interpolation techniques such as splines are employed.

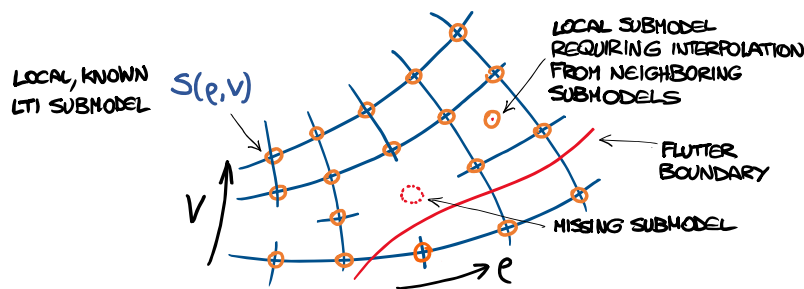


FIGURE 7.2: Example of an aircraft's aerodynamic behavior scheduled over a grid parameters. The available grid points are known LTI submodels  $\mathcal{S}(\rho, V)$ . The system matrices between grid points are either interpolated from the LTI submodels or procedurally generated from interpolated system parameters. The latter option is not possible with very complex models.

### 7.1.2 Excitation signals

The excitation signals are designed in frequency-domain with the magnitude being either constant or a von Kármán gust spectrum, with a random uniformly-distributed phase (random-phase multi-sine RPMS signal). The inter-sample behavior of the discrete random sequence is modeled piece-wise by splines with some light oversampling (see section 7.1.6 for more details). Von Kármán spectra are defined by equation (3.35) for constant speed (only vertical gusts are considered here as motivated in section 3.3). Time-dependent speed is handled using two approaches:

1. Speed is segmented using zero-order hold (assumed constant within an interval) and the gust is computed by  $\mathcal{F}^{-1}\{\Phi_g(\omega)\}$ . The phase of adjacent segments is adjusted to match the starting sample of the next segment with the end sample of the previous one. This approximation is fast.
2. The Von Kármán gust can be defined as a rational function whose coefficients vary with air speed (3.36). This  $s$ -domain model can be converted into  $z$ -domain filter coefficients to color input white noise in order to provide a time response with the desired gust spectrum. This approach is slower and delicate because of the continuous-to-discrete filter coefficient conversion, but more accurate.

The excitation signal is band-limited, therefore it can be upsampled without modifying its spectrum by padding its FFT with zeroes and transforming back into time-domain. Some oversampling must be allowed to achieve the appropriate simulation accuracy, but since high frequencies excite the decaying part of the system's spectrum, the excitation signal's band can be limited to, say,  $1.1 \max\{f_n\} < f_s/2$ . A time-varying gust excitation computed this way is shown in figure 7.3.

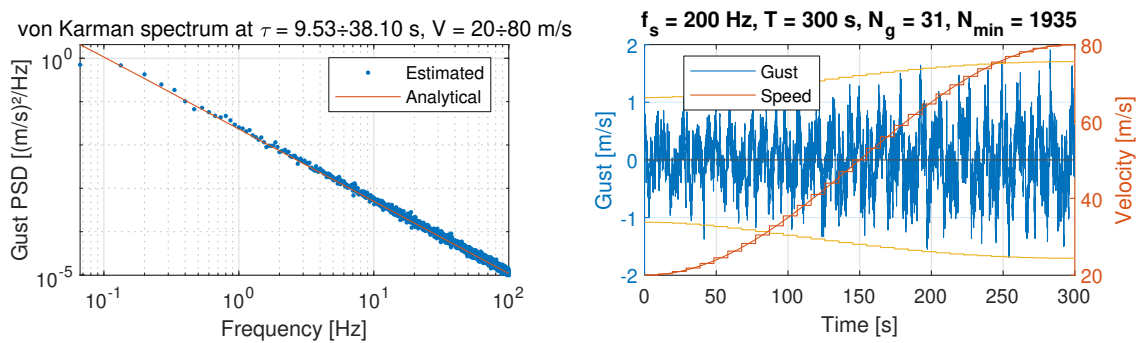


FIGURE 7.3: Example of a time-varying von Kármán gust in the frequency and time domains. Right plot: the air speed varies like a sine and is discretized using zero-order hold. Within each such interval, the gust is computed as an RPMS signal. In each interval, a boundary condition is enforced to match the first sample with the last point of the preceding interval. Left plot: the resulting signal's PSD matches the analytical prediction obtained by summing the delayed theoretical gust spectrum corresponding to each speed interval.

### 7.1.3 Numerical methods

LTV systems in general do not have a well-defined frequency-domain representation as LTI systems do, therefore we need to resort to time-domain numerical integration schemes. We shall consider the explicit form of the time-varying system in the coming discussion:

$$\begin{aligned}\dot{\mathbf{x}}(t) &= \mathbf{A}(t)\mathbf{x}(t) + \mathbf{B}(t)\mathbf{u}(t) \\ \mathbf{y}(t) &= \mathbf{C}(t)\mathbf{x}(t) + \mathbf{D}(t)\mathbf{u}(t)\end{aligned}\tag{7.1}$$

Equation (7.1) can be solved with various well-known single-step and multi-step algorithms. To meet our requirements, three methods are considered:

- Runge-Kutta (RK) single-step family
- Adams-Bashforth-Moulton (ABM) multi-step predictor-corrector methods
- Discretization of the state transition matrix (LSIM)

Numerical techniques are certainly attractive but they are not a panacea:

- Systematic error may be introduced by integration or signal processing
- The interpolation of system matrices and input signals influences results
- Very long computation times are necessary
- Loss of information compared to an analytical formulation

An excellent reference for scientific computing that treats exhaustively various topics in numerical mathematics (and provides the related code) is the book from [QUARTERONI ET AL., 2006], where the Runge-Kutta and Adams-Bashforth-Moulton families are explained in detail. RK and ABM have been already mentioned in chapter 2 to compute the homogeneous solution of equation (7.1). The LSIM method calculates the response of a linear system in state-space form [DECARLO, 1989; JELIČIĆ ET AL., 2021].

Aeroelastic models of aircraft have states describing the free-body motion and several extremely low-frequency or lightly-damped poles. These are often challenging to address because their response may be unrealistic due to numerical artifacts. An “off-the-shelf” solver meant for some other application may introduce some numerical damping if not checked appropriately. The implementation of dedicated fast algorithms is therefore a sensible choice. For this thesis, efficient ad-hoc implementations of the RK, ABM and LSIM for time-varying systems excited by random signals have been implemented in order to provide controllable results. They are validated with code provided by other authors. Why is computation time important? Chiefly because the amount of information that must be collected about time-varying systems is inevitably higher than for time-invariant ones, particularly for large parameter spaces and even more so when system identification must be performed where long time histories are required. The faster the simulation throughput, the better the exploration of the parameter space.

**Notation.** For ease of notation, the state equation (7.1) is rewritten as

$$\dot{\mathbf{x}}(t) = \mathbf{f}(t, \mathbf{x}) \quad (7.2)$$

where the vector-valued forcing function is:

$$\mathbf{f}(t, \mathbf{x}) \triangleq \mathbf{A}(\rho(t), V(t))\mathbf{x}(t) + \mathbf{B}(\rho(t), V(t))\mathbf{u}(t) \quad (7.3)$$

Equation (7.2) is solved by the chosen ODE solver.

We divide the simulation process into two phases:

- *Set-up*: settings check, collection of all metadata required by the run-time, estimation of space and time requirements. We need to precompute the aerodynamic influence coefficients matrix and its rational function approximation 3.1.1 (provide all the necessary information for the procedural generation of the aeroelastic system). Since integrator time may be different from the grid points at which the excitation and the parameter are known, an interpolating function may have to be computed beforehand.
- *Run-time*: numerical integrator execution. The evaluation of  $\mathbf{f}(t, \mathbf{x})$  at integrator time  $t$  requires the input  $\mathbf{u}(t)$ , the parameters  $\{\rho(t), V(t)\}$  and the corresponding matrices  $\mathbf{A}(t)$  and  $\mathbf{B}(t)$ . These evaluations may require significant resources given that they are performed at least once per time step. The input  $\mathbf{u}(t)$  or parameters  $\{\rho(t), V(t)\}$  are thus calculated from precomputed interpolation functions. The state matrices are assembled on-the-fly using procedural generation. This step exploits the sparse<sup>1</sup> array implementation and the known structure of the state matrix. The run-time phase executes only strictly necessary operations. The number of  $\mathbf{f}(t, \mathbf{x})$  evaluations can be reduced with a tolerance on parameter variation, for example by requiring that a certain threshold be exceeded, say  $|p_n - p_{n+1}| > 10^{-9}|p_n|$ .

The coming pages provide more details about the run-time of the ad-hoc RK, ABM and LSIM algorithms.

**Notation.**  $\Delta t$  is the time step of the numerical solution. The subscript “ $n$ ” denotes the matrices and vectors referring to the time instant  $t = n\Delta t$ . The state matrix at the time instant  $t = n\Delta t$  is denoted by  $\mathbf{A}_n \equiv \mathbf{A}(n\Delta t)$ ; the same notation applies to other time-dependent matrices and vectors. Left curly braces encompassing several equations denote for-loops.

---

<sup>1</sup> The unit cost of assembling the system matrices grows linearly with the number of evaluations in the time integration scheme. It is negligible at first but can be crippling in long simulations. For this reason, a practical implementation *must* employ the sparse matrix formulation [GILBERT ET AL., 1992]. For example, in MATLAB the state matrix can be assembled fairly easily in one line using `sparse(i, j, A)` where  $\{i, j\}$  are the indices of the nonzero elements of  $\mathbf{A}$ .

### 7.1.4 Ad-hoc fixed-step Runge-Kutta solver

The Runge-Kutta solvers are explained in great detail in [QUARTERONI ET AL., 2006, Ch. 11]. The present implementation of the fixed-step  $N_p$ -stage RK method for the integration of the state equation is

$$\begin{cases} t_i &= t_n + c_i \Delta t \\ \mathbf{x}_i &= \mathbf{x}_n + \Delta t \sum_{j=1}^{i-1} a_{ij} \mathbf{k}_{j-1} \\ \mathbf{k}_i &= \mathbf{f}(t_i, \mathbf{x}_i) \\ \mathbf{x}_{n+1} &= \mathbf{x}_n + \Delta t \sum_{i=1}^{N_p} b_i \mathbf{k}_i \\ t_{n+1} &= t_n + \Delta t \end{cases} \quad (7.4)$$

where the *Butcher's tableau* coefficients  $a_{ij}$ ,  $b_i$  and  $c_i$  are tabulated for each order or variant<sup>2</sup>. The pseudo-code can be found in algorithm 7 in the appendix. The algorithm integrates the states  $\mathbf{x}_n$  one step at a time by calculating and storing the slopes  $\mathbf{k}_i$  at the intermediate instants  $t_i \in [t_n, t_n + \Delta t]$ . The next step  $\mathbf{x}_{n+1}$  is a weighted average of the slopes times the time increment  $\Delta t$ . The order of the method is not always related to the number of stages. The evaluation of  $\mathbf{f}(t_i, \mathbf{x}_i)$  at each stage for every step is very expensive for large systems or long duration. This entails interpolating  $\rho(t_i)$ ,  $V(t_i)$  and  $\mathbf{u}(t_i)$  and constructing  $\mathbf{A}(t_i)$  and  $\mathbf{B}(t_i)$  for each intermediate  $t_i$ , therefore the algorithmic implementation must be correspondingly efficient<sup>3</sup>.

The popular MATLAB `ode45.m` solver (ODE45) implements an adaptive 7-stages RK method with the Dormand-Prince coefficients [SHAMPINE ET AL., 2003], but its very general implementation is not fast. Since the step size is modified in order to keep errors within a tolerance, the results must be interpolated to a regular grid. It is advisable to use a fixed-step method because the simulated data will be scrutinized in frequency-domain and interpolation artifacts may affect the peaks of the spectra. In this thesis the simulations are computed with fixed-step RK 8-7 and RK 10 [HAIRER ET AL., 2008].

<sup>2</sup> Example: the Butcher's tableau of the well-known RK4 is

$$\begin{array}{c|ccc} 0 & & & \\ 1/2 & 1/2 & & \\ 1/2 & 0 & 1/2 & \\ 1 & 0 & 0 & 1 \\ \hline & 1/6 & 1/3 & 1/3 & 1/6 \end{array} \quad (7.5)$$

where the  $b_i$  and  $c_i$  coefficients are respectively the row and the column and  $a_{ij}$  the remaining ones.

<sup>3</sup> An efficient RK implementation makes use of the FSAL (*first same as last*) property to reduce the number of evaluations by at least one. There is always  $c_1 = 0$  and at least one  $c_i$  coefficient is equal to 1, therefore

$$c_i = 1 \implies t_i = t_n + 1 \cdot \Delta t = t_{n+1} + 0 \cdot \Delta t \quad (7.6)$$

This means that  $\mathbf{f}(t_{n+1}, \mathbf{x}_{n+1})$  is calculated already at step  $n$  and then stored for the first stage of step  $n + 1$ . For example, the 8<sup>th</sup>-order Runge-Kutta has 13 stages and two  $c_i = 1$  coefficients. Making use of the FSAL property requires 11 evaluations of  $\mathbf{f}(t, \mathbf{x})$  per time step.



### 7.1.5 Ad-hoc Adams-Bashforth-Moulton solver

Multi-step methods are discussed in [QUARTERONI ET AL., 2006, Ch. 11]. The present implementation of the Adams-Bashforth-Moulton of order  $N_p$  is:

$$\begin{cases} \mathbf{x}_{n+1} &= \mathbf{x}_n + \Delta t/k_p \sum_{j=0}^{N_p} b_{p,j} \mathbf{f}(t_{n-j}, \mathbf{x}_{n-j}) \\ \mathbf{x}_{n+1} &= \mathbf{x}_n + \Delta t/k_c \sum_{j=0}^{N_p} b_{c,j} \mathbf{f}(t_{n-j+1}, \mathbf{x}_{n-j+1}) \\ t_{n+1} &= t_n + \Delta t \end{cases} \quad (7.7)$$

where  $b_{p,j}$  and  $b_{c,j}$  are respectively the predictor and corrector weights (integers) and  $k_p$  and  $k_c$  the respective denominators<sup>4</sup> [HAIRER ET AL., 2008]. The pseudo-code can be found in algorithm 8 in the appendix. The first equation (Adams-Bashforth predictor) predicts the next step using the last  $N_p$  computed steps, then the second equation (Adams-Moulton corrector) refines the solution. ABM stores the last  $N_p$  values of the system matrices and states and evaluates the input  $\mathbf{u}(n\Delta t)$  only at the grid points, therefore only *one* new evaluation  $\mathbf{f}(t, \mathbf{x})$  per step is performed and no input interpolation is necessary. RK provides the first  $N_p$  steps to start ABM. Multi-step methods like ABM have great efficiency because they employ information from previous steps in order to obtain a higher-order approximation of the solution. In return they need a smaller step size to attain the same precision of a single-step method of the same order. This lower accuracy of ABM is compensated by upsampling the input signal and then downsampling the response, typically by a factor 4 or more. This work uses an efficient ABM formulation of orders 8, 10 and 12, depending on the case at hand.

### 7.1.6 Higher-order discretization of time-varying systems

There is no general closed-form solution of the state equation if the system is continuous and time-varying (see chapter 2). Nevertheless, it is plausible to assume that the system matrices barely change within  $[n\Delta t, (n+1)\Delta t]$ , where  $\Delta t$  is an appropriately short time step. This observation is equivalent to treating a time-continuous system as discrete, therefore its state transition matrix is  $\Phi(t, t_0) \approx e^{\mathbf{A}(t-t_0)}$ . The state-space representation of a discrete system is:

$$\begin{cases} \mathbf{x}_{n+1} &= \mathbf{A}_n \mathbf{x}_n + \mathbf{B}_n \mathbf{u}_n \\ \mathbf{y}_n &= \mathbf{C}_n \mathbf{x}_n + \mathbf{D}_n \mathbf{u}_n \end{cases} \quad (7.9)$$

<sup>4</sup> Example: the predictor and corrector coefficients for the fifth-order ABM method are:

$$\begin{aligned} \frac{\mathbf{b}_p}{k_p} &= \frac{1}{720} \{+1091 \quad -2774 \quad +2616 \quad -1274 \quad +251\} \\ \frac{\mathbf{b}_c}{k_c} &= \frac{1}{720} \{+251 \quad +646 \quad -264 \quad +106 \quad -19\} \end{aligned} \quad (7.8)$$

In literature the coefficients are usually provided in reversed order: the first coefficient  $b$  corresponds to the newest sample  $\{t_n, \mathbf{x}_n\}$  and the last one to the oldest  $\{t_{n-N_p}, \mathbf{x}_{n-N_p}\}$ .

The discretization, assuming constant input between two time steps, is explained in texts on linear systems such as [DECARLO, 1989] and [RUGH, 1996]. It is possible to discretize the system in such a way to return exact solutions for a large class of inputs. The LSIM algorithm implements this procedure. We follow the development presented in [JELIČIĆ ET AL., 2021], with some key differences to adapt it to time-varying systems.

Let the input be modeled by a polynomial

$$\mathbf{u}(t) = \sum_{p=0}^{N_p} \mathbf{u}_{n,p} t^p \quad (7.10)$$

where  $p$  is the polynomial order. The states in the interval  $[n\Delta t, (n+1)\Delta t]$  can be then computed by:

$$\dot{\mathbf{x}}(t) = \mathbf{A}_n \mathbf{x}(t) + \mathbf{B}_n \mathbf{u}(t) \quad \circ \bullet \quad \mathbf{x}(s) = (s\mathbf{I} - \mathbf{A}_n)^{-1} \left( \mathbf{x}_0 + \mathbf{B}_n \sum_{p=0}^{N_p} \frac{p!}{s^{p+1}} \mathbf{u}_{n,p} \right) \quad (7.11)$$

In order to transform the expression above back into time-domain, we must integrate the impulse response  $(s\mathbf{I} - \mathbf{A}_n)^{-1}$  for each hold order  $p$ :

$$\frac{1}{s^{p+1}} (s\mathbf{I} - \mathbf{A}_n)^{-1} \bullet \circ \quad \mathbf{H}_{n,p} \triangleq \mathbf{A}_n^{-p-1} \left( e^{\mathbf{A}_n t} - \sum_{q=0}^p \frac{t^q}{q!} \mathbf{A}_n^q \right) \quad \forall p \geq 0 \quad (7.12)$$

The equation above can be separated into the transient and steady-state contributions of the forced response  $\mathbf{H}_{n,p} = \mathbf{H}_{n,p}^{tr} e^{\mathbf{A}_n \Delta t} + \mathbf{H}_{n,p}^{fr}$  (respectively superscripts “tr” and “fr”) and calculated recursively:

$$\begin{cases} \mathbf{H}_{n,-1}^{tr} & \triangleq \mathbf{I} \\ \mathbf{H}_{n,p}^{tr} & \triangleq \mathbf{A}_n^{-1} \mathbf{H}_{n,p-1}^{tr} \end{cases} \quad \begin{cases} \mathbf{H}_{n,-1}^{fr} & \triangleq \mathbf{0} \\ \mathbf{H}_{n,p}^{fr} & \triangleq \mathbf{A}_n^{-1} \left( \mathbf{H}_{n,p-1}^{fr} - \frac{\Delta t^p}{p!} \mathbf{I} \right) \end{cases} \quad (7.13)$$

Given the structure of the state matrix of an aeroelastic system, its inverse  $\mathbf{A}_n^{-1}$  can be constructed block-wise directly from equation (3.30). We can then write the zero-state response at the  $n$ -th time step as the sum of transient and forced responses and add them to the zero-input response:

$$\begin{cases} \mathbf{x}_{n,tr} & = \sum_{p=0}^{N_p} p! \mathbf{H}_{n,p}^{tr} \mathbf{B}_n \mathbf{u}_{n,p} \\ \mathbf{x}_{n,fr} & = \sum_{p=0}^{N_p} p! \mathbf{H}_{n,p}^{fr} \mathbf{B}_n \mathbf{u}_{n,p} \\ \mathbf{x}_{n+1} & = e^{\mathbf{A}_n \Delta t} (\mathbf{x}_n + \mathbf{x}_{n,tr}) + \mathbf{x}_{n,fr} \end{cases} \quad (7.14)$$

There are specialized numerical techniques that compute the product  $e^{\mathbf{M}} \mathbf{v}$  without calculating the matrix exponential  $e^{\mathbf{M}}$ , for example based on Krylov subspaces [AL-MOHY AND HIGHAM, 2011]. Let “expf” denote a function performing this kind of operation

$$\text{expf} \{ \mathbf{A}_n \Delta t, \mathbf{x}_n + \mathbf{x}_{n,tr} \} \triangleq e^{\mathbf{A}_n \Delta t} (\mathbf{x}_n + \mathbf{x}_{n,tr}) \quad (7.15)$$

The final algorithm is thus:

$$\begin{cases} \mathbf{x}_{n,tr} &= \sum_{p=0}^{N_p} p! \mathbf{H}_{n,p}^{tr} \mathbf{B}_n \mathbf{u}_{n,p} \\ \mathbf{x}_{n,fr} &= \sum_{p=0}^{N_p} p! \mathbf{H}_{n,p}^{fr} \mathbf{B}_n \mathbf{u}_{n,p} \\ \mathbf{x}_{n+1} &= \text{expf} \{ \mathbf{A}_n \Delta t, \mathbf{x}_n + \mathbf{x}_{n,tr} \} + \mathbf{x}_{n,fr} \end{cases} \quad (7.16)$$

where  $\mathbf{u}_{n,p}$  are the coefficients of the piece-wise polynomial that interpolates the input  $\mathbf{u}(t)$  and where the matrices  $\mathbf{H}_{n,p}^{tr}$  and  $\mathbf{H}_{n,p}^{fr}$  are computed from (7.13). For LTI systems, order three  $p = 3$  is preferable to zero-order hold or first-order hold because it can work with a higher  $\Delta t$  and therefore reduce computation time [JELIČIĆ ET AL., 2021]. In the LTV case, the almost cubic effect of hold order on time complexity dominates, therefore it is better to increase the computation time linearly by decreasing the time step. Aeroelastic modeling with a minimal number of lag states can be applied to reduce the overall size of the state matrix and thus improve performance [KARPEL, 1982; QUERO ET AL., 2021].

The state transition matrix can be discretized to take into account the system variation. Let us write the homogeneous solution as a MacLaurin series:

$$\mathbf{x}(t) = \sum_{p=0}^{\infty} \frac{t^p}{p!} \frac{d^p}{dt^p} \mathbf{x}(t_0) \quad (7.17)$$

The state derivatives  $\frac{d^p}{dt^p} \mathbf{x}(t_0)$  can be found recursively from  $\dot{\mathbf{x}}(t_0) = \mathbf{A}(t_0) \mathbf{x}(t_0)$ :

$$\frac{d^p}{dt^p} \mathbf{x}(t_0) = \mathbf{A}_p(t_0) \mathbf{x}(t_0) \quad \text{where} \quad \begin{cases} \mathbf{A}_0(t) &= \mathbf{I} \\ \mathbf{A}_p(t) &= \mathbf{A}_{p-1}(t) \mathbf{A}(t) - \frac{d}{dt} \mathbf{A}_{p-1}(t) \end{cases} \quad (7.18)$$

which allows us to express  $\mathbf{x}(t)$  without evaluating  $\frac{d^p}{dt^p} \mathbf{x}(t_0)$  explicitly. The desired MacLaurin series of the state transition matrix follows by combining  $\mathbf{x}(t) = \Phi(t, t_0) \mathbf{x}(t_0)$  (2.1.3) and equation (7.18):

$$\mathbf{x}(t) = \left( \sum_{p=0}^{\infty} \frac{t^p}{p!} \mathbf{A}_p(t_0) \right) \mathbf{x}(t_0) \implies \Phi(t, t_0) = \sum_{p=0}^{\infty} \frac{t^p}{p!} \mathbf{A}_p(t_0) \quad (7.19)$$

whose first few terms<sup>5</sup> are:

$$\begin{aligned} \Phi(t, t_0) &= \mathbf{I} + t \mathbf{A}(t_0) + \\ &+ \frac{t^2}{2!} \left( \mathbf{A}^2(t_0) + \dot{\mathbf{A}}(t_0) \right) + \\ &+ \frac{t^3}{3!} \left( \mathbf{A}^3(t_0) + \ddot{\mathbf{A}}(t_0) + \mathbf{A}(t_0) \dot{\mathbf{A}}(t_0) + 2 \dot{\mathbf{A}}(t_0) \mathbf{A}(t_0) \right) + o(\mathbf{A}^4(t_0)) \end{aligned} \quad (7.21)$$

<sup>5</sup> Generally  $\mathbf{A}(t)$  and  $\dot{\mathbf{A}}(t)$  do not commute, therefore the derivative of the square of a matrix is

$$\frac{d}{dt} \mathbf{A}^2(t) = \frac{d}{dt} (\mathbf{A}(t) \cdot \mathbf{A}(t)) = \mathbf{A}(t) \dot{\mathbf{A}}(t) + \dot{\mathbf{A}}(t) \mathbf{A}(t) \neq 2 \mathbf{A}(t) \dot{\mathbf{A}}(t) \neq 2 \dot{\mathbf{A}}(t) \mathbf{A}(t) \quad (7.20)$$

In the previous expression it is possible to collect the matrix exponential to write:

$$\Phi(t, t_0) = e^{\mathbf{A}(t_0)t} + \frac{t^2}{2!} \dot{\mathbf{A}}(t_0) + \frac{t^3}{3!} \left( \ddot{\mathbf{A}}(t_0) + \mathbf{A}(t_0) \dot{\mathbf{A}}(t_0) + 2\dot{\mathbf{A}}(t_0) \mathbf{A}(t_0) \right) + o(\mathbf{A}^4(t_0)) \quad (7.22)$$

The terms with the powers of  $t$  represent a correction of the LTI state transition matrix due to the system variation. For each power  $p$ , when the terms with derivatives of  $\mathbf{A}(t)$  are small compared to  $\mathbf{A}^p(t)$ , the system is slowly-varying. The series (7.22) can be reformulated using a Padé approximant for faster convergence because we know its Taylor series terms  $\mathbf{A}_p(t)$  from equation (7.18). The STM can be computed in steps  $\Delta t$ :

$$\Phi((n+1)\Delta t, t_0) = \Phi((n+1)\Delta t, n\Delta t) \Phi(n\Delta t, t_0) \implies \mathbf{x}_{n+1} = \Phi_n \mathbf{x}_n \quad (7.23)$$

Once the state transition matrix is known, the inhomogeneous solution can be formulated. If  $\mathbf{A}(t)$  can be represented by a Fourier series, then so do the coefficients  $\mathbf{A}_r(t)$  of the powers of  $t$  in equation (7.22):  $\mathbf{A}_r(t) = \sum_{k \in \mathbb{S}} \mathbf{A}_{r,k} e^{ik\omega_0 t}$ . It is then possible to write:

$$\Phi(t, t_0) = e^{\mathbf{A}(t_0)t} + \sum_{r=2}^{N_r} \left( \frac{t^r}{r!} \sum_{k \in \mathbb{S}} \mathbf{A}_{r,k} e^{ik\omega_0 t_0} \right) + o(\mathbf{A}^{N_r}(t_0)) \quad (7.24)$$

where the index  $r$  refers to the powers of  $t$ , the index  $k$  to the harmonics of  $\mathbf{A}_r(t)$ . The coefficients  $[\mathbf{A}_{r,1}, \mathbf{A}_{r,1}, \dots, \mathbf{A}_{r,N_k}]$  can be computed exactly before entering run-time. This expression can be inserted into equation (7.16) to obtain the full solution.

### 7.1.7 Comparison of numerical methods

The three solvers all have advantages and disadvantages when applied to time-varying systems. The standard MATLAB solver for ordinary differential equations `ode45.m` is added for reference. Table 7.1 summarizes their merits and flaws.

TABLE 7.1: Simulation method comparison

Method	Advantages	Disadvantages
ODE45	<ul style="list-style-type: none"> <li>• High accuracy</li> <li>• Standard/established method</li> </ul>	<ul style="list-style-type: none"> <li>• Computationally very expensive</li> <li>• Unoptimized solver</li> </ul>
RK	<ul style="list-style-type: none"> <li>• High accuracy</li> <li>• Flexible order selection</li> </ul>	<ul style="list-style-type: none"> <li>• Multiple <math>\mathbf{f}(t, \mathbf{x})</math> evaluations per step</li> <li>• Input interpolation <math>\mathbf{u}(t)</math></li> </ul>
ABM	<ul style="list-style-type: none"> <li>• One <math>\mathbf{f}(t, \mathbf{x})</math> evaluation per step</li> <li>• No input interpolation</li> <li>• Flexible order selection</li> </ul>	<ul style="list-style-type: none"> <li>• Higher oversampling required</li> <li>• Resampling of input and response</li> </ul>
LSIM	<ul style="list-style-type: none"> <li>• High accuracy</li> <li>• Large <math>\Delta t</math> acceptable</li> <li>• Uses interpolation coefficients</li> </ul>	<ul style="list-style-type: none"> <li>• Computationally expensive</li> <li>• Places assumptions on the input</li> </ul>

The effort of writing dedicated ordinary differential equations solvers is rewarded by the flexibility necessary when balancing computation time, memory requirements and results accuracy. The three methods do not exclude each other and disparate simulations require different approaches. When rounding errors limit accuracy, then higher order or single-step methods are preferable because they require fewer steps. Depending on the system's characteristics, this effect can manifest itself for either fast or slow parameter variations.

In ascending order of importance, the total computation time is most sensible to:

- Number of steps: linear increase of the number of total operations
- Order: depending on the method, it can have a marked effect on performance (from least to most affected: ABM, RK, LSIM)
- System size: strong effect on operations with matrices (quadratic or more)

Depending on the combinations of these three factors, a slow algorithm can be faster than an asymptotically fast one due to the constants of the time complexity powers. Because of this, when a new simulation case is being set up, the solvers are ranked in terms of accuracy and computation time, after which one of the three is used to gather the necessary results. The procedure is as follows:

1. The sample rate is selected for each input interpolation order by the appropriate oversampling factor [JELIČIĆ ET AL., 2021, Eq. 51] and maximal frozen time eigenfrequency

$$f_s = 2k_f \max\{f_n\} \quad (7.25)$$

2. The input is a band-limited RPMS signal with the desired PSD.
3. The input is upsampled and an accurate solution is computed with low step size. The response is then decimated to the original sample rate. This data set constitutes the “reference” solution.
4. The solvers are ranked based on milliseconds per time step and the error with respect to the reference:

$$\varepsilon_y = \frac{\|y - y_{ref}\|}{\|y_{ref}\|} \quad [\text{adim}] \quad (7.26)$$

## 7.2 Aeroelastic model

The airfoil with rudder (trailing edge flap) is an instructive model because, by tuning its geometrical properties, it can display different aeroelastic behaviors. The airfoil is suspended by a spring, and torque is applied by two torsion springs: one at the airfoil's shear center and one on the rudder's hinge. There is no element introducing structural damping. The system has three mechanical degrees of freedom: heave, pitch and rudder pitch (flap). The model is illustrated in figure 7.4 and its geometry data are listed in table 7.2. The corresponding eigenfrequencies of the mass-damping-stiffness model are reported in table 7.3. Two model configurations are set up to display different kinds of instabilities: in C1 the airfoil pitch and heave modes are critical, while in C2 they are the rudder pitch and airfoil heave modes.

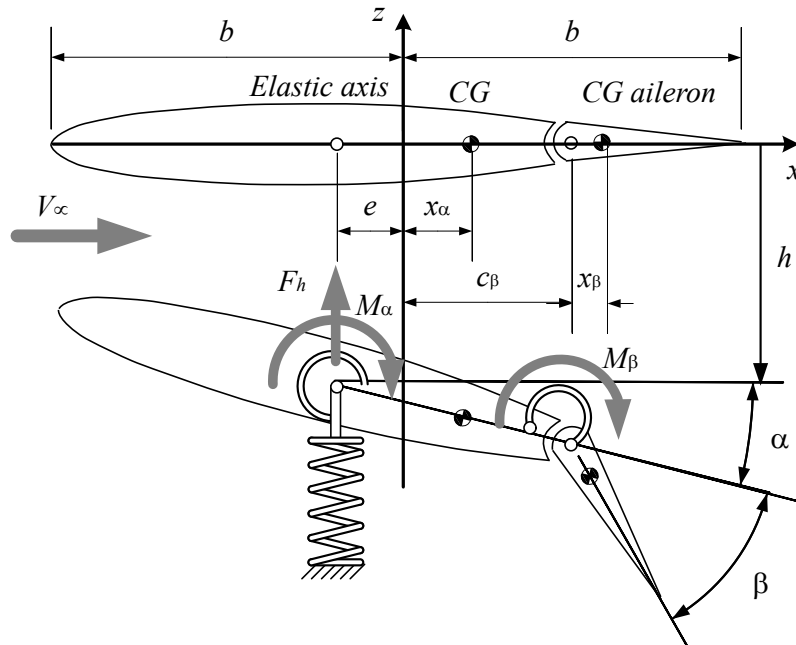


FIGURE 7.4: Aeroelastic model: airfoil with rudder [SCHULZE, 1999].

TABLE 7.2: Airfoil-rudder aeroelastic model. Configuration C1 from [NAM ET AL., 2001], configuration C2 from [SCHULZE, 1999]

Quantity	Symbol	Unit	C1	C2
Semi-chord	$b$	m	0.3048	1
Elastic axis location	$e$	m	-0.4	-0.2
Aileron hinge location.	$c_\beta$	m	0.6	0.5
Center of gravity location	$x_\alpha$	m	0.2	0.1
Aileron center of gravity location	$x_\beta$	m	0.0125	0.005
Spring stiffness	$k_h$	N/m	35770	38373
Torsional spring stiffness	$k_\alpha$	N · m	3323.1	86339
Aileron torsional spring stiffness	$k_\beta$	N · m	747.7	195.7
Total mass	$m$	kg	14.3	12.0
Airfoil moment of inertia	$I_\alpha$	kg · m <sup>2</sup>	0.332	3
Aileron moment of inertia	$I_\beta$	kg · m <sup>2</sup>	0.0083	0.2448

TABLE 7.3: Structural eigenfrequencies of the base mechanical C1 and C2 configurations. Structural damping is zero. C1 has a stiffer rudder pitch mode than C2.

Structural mode	Eigenfrequency C1 model [Hz]	Eigenfrequency C2 model [Hz]	Approximation [rad/s]
Heave	7.7615	8.9887	$\omega_h \approx \sqrt{k_h/m}$
Pitch	17.546	29.351	$\omega_\alpha \approx \sqrt{k_\alpha/I_\alpha}$
Rudder pitch	55.077	4.4918	$\omega_\beta \approx \sqrt{k_\beta/I_\beta}$

The analytical construction of the aerodynamic influence coefficients matrix from the geometrical characteristics of the model is detailed (with code) in [NAM ET AL., 2001]. Its AIC matrix can be derived analytically from the theory of [KÜSSNER, 1941] and [THEODORSEN, 1935]. The mathematical details are collected in [SCANLAN AND ROSENBAUM, 1952]. Figure 7.5 displays the rational function approximation of the system's aerodynamic forces. The system has  $3 \cdot 2 = 6$  states from the underlying 3-DoF mechanical structure plus  $3 \cdot 4 = 12$  lag states, for a total of 18 states.

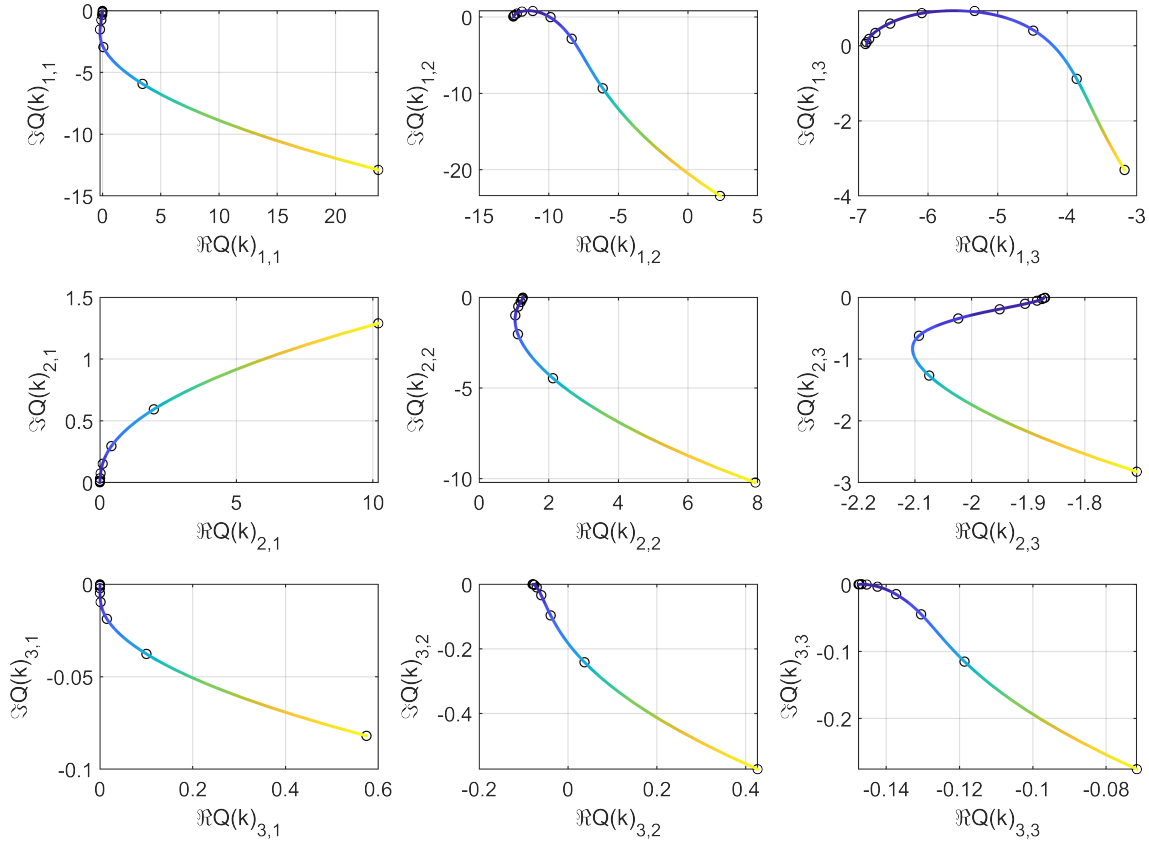


FIGURE 7.5: Rational function approximation (3.13) of the aerodynamic influence coefficients (AIC) matrix of model C1 (the entries for model C2 are qualitatively the same). The AIC matrix has been computed at 10 logarithmically-spaced reduced frequencies  $k = 0.01 : 2$  with 4 lag states  $\gamma = [0.02, 0.0737, 0.2714, 1]$ . The color of the line denotes the reduced frequency (blue:  $k = 0.01$ , yellow:  $k = 2$ ). The error of the rational function approximation is  $< 1\%$ .

The frozen-time flutter diagrams in figure 7.6 highlight two different types of flutter:

- *Hard flutter* in C1: the damping ratio reduction is sudden and pronounced, the heave and pitch modes get closer until the former becomes unstable.
- *Soft flutter* in C2: damping decreases slowly and eventually recovers for higher speed (not displayed in the figure), the heave and the critical rudder pitch modes cross eigenfrequencies, the critical damping reduction is softer.

The flutter diagrams can be extended into a third dimension by plotting the eigenvalues on a grid of density and speed. The eigenvalue locus draws an “eigensurface” that is only a function of  $\{\rho, V\}$  (see figure 7.7). The eigensurface of the critical eigenmode is displayed as contour in figure 7.8 with overlaid gradient. The gradient quantifies the sensitivity of a certain eigenmode to density and speed variations. Far away from the flutter boundary the parameter variation has limited effect on the frozen-time eigenvalues of the system (aerodynamic effects are weak for low speed or density). There can still be regions near the flutter boundary where a parameter change does not influence the eigenmode (see C2 eigenfrequency subplot in figure 7.8: dynamic effects due to parameter variation have little importance there). It is reminded once again that the flutter boundary is determined using a frozen-time formulation. The flutter behavior of each system must be investigated individually; it is not possible to generalize all results. For strongly time-varying systems stability must be investigated for each parameter path  $\{\rho, V\}$ .

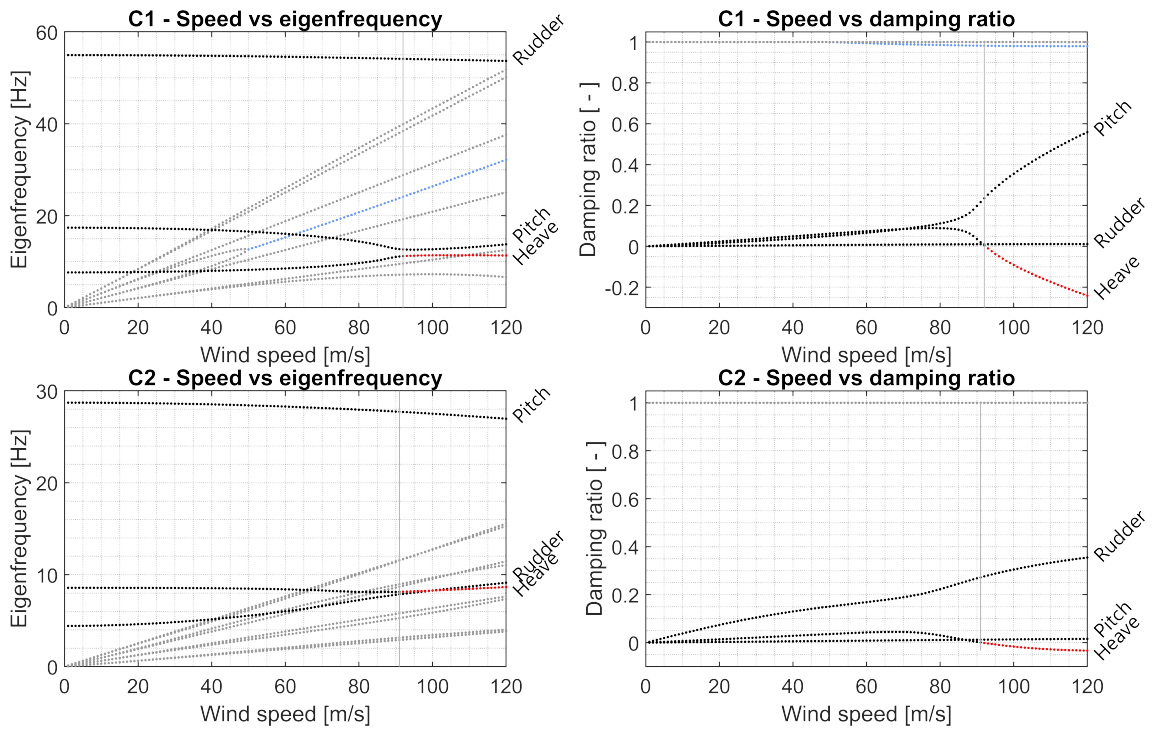


FIGURE 7.6: Flutter curves of (C1: top, C2: bottom) for constant air density and linearly-varying speed (frozen-time description). The black dots are the heave, pitch and rudder pitch modes. The red dots indicate critical eigenvalues. The flutter speeds are 92.2 m/s and 91.3 m/s ( $\rho = 1.225 \text{ kg/m}^3$ ). See text for discussion.



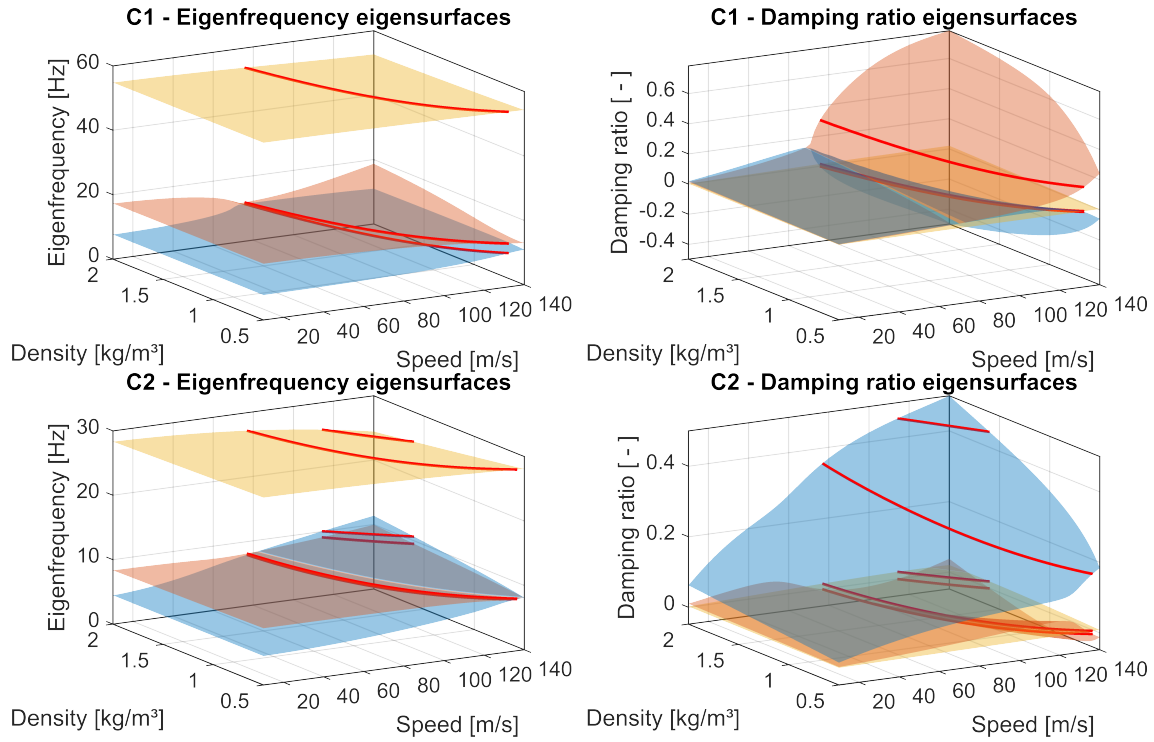


FIGURE 7.7: Heave, pitch and rudder pitch eigensurfaces (C1: top, C2: bottom). The red line is the flutter boundary. The instantaneous damping ratio is sensitive to parameter variation.

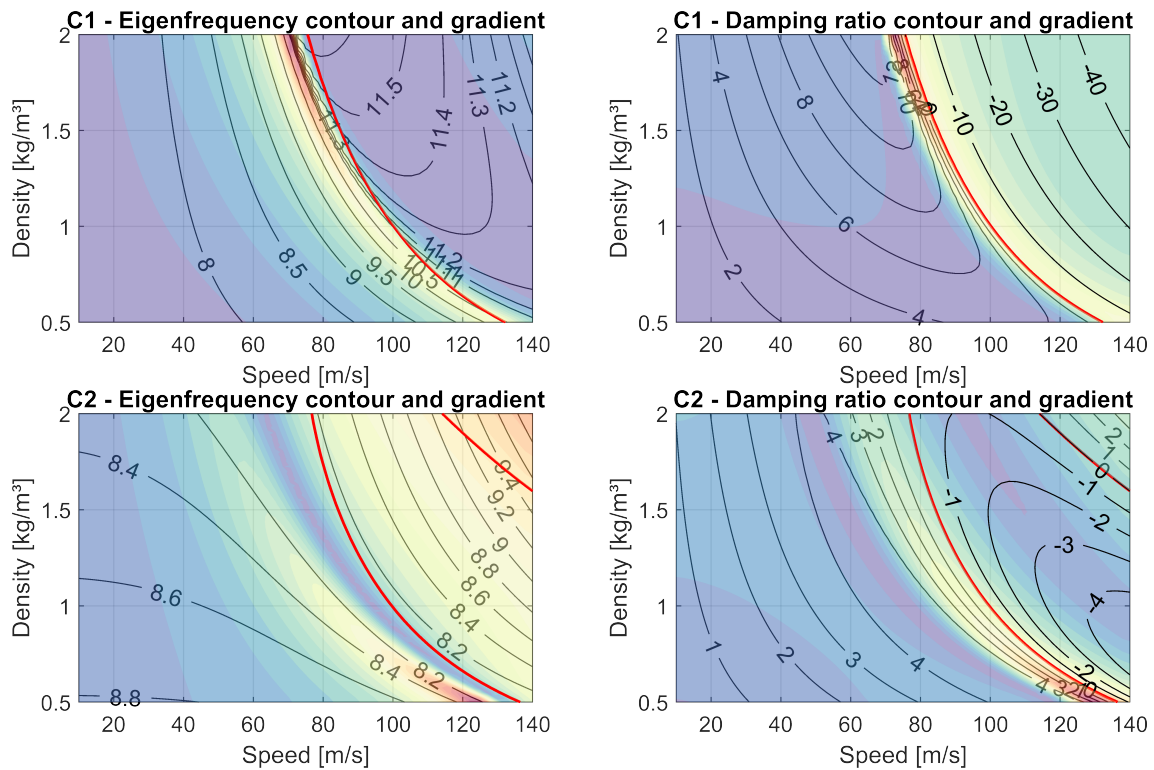


FIGURE 7.8: Critical mode of C1 (top row) and C2 (bottom row). The contour lines are the eigenfrequency in Hz (left column) and damping ratio in percent (right column), the surface is their gradient's magnitude, the red line is the flutter boundary. The damping of C1's critical mode increases, then drops abruptly just before the flutter boundary (hard flutter). C2 has a circumscribed unstable region and a softer damping decrease (soft flutter).

### 7.3 Simulation results

The modal analysis procedure consists of the methods detailed in chapters 4, 5 and 6. Spectral estimation and system identification are performed on the simulated data and the modal parameters are tracked to assess the damping estimate. The results of the C1 configuration of the airfoil-rudder model are presented because it displays the occurrence of hard flutter. Compared to configuration C2 (soft flutter), the damping ratio decline within a narrow region induces stronger dynamic effects.

The system undergoes a linear and a sinusoidal speed change at constant air density. Five runs with different duration are simulated for each type of parameter variation. The rate of change is halved (respectively: the duration is doubled) between each run. The information pertaining to each simulation run is reported in tables 7.4 and 7.5.

TABLE 7.4: Simulation L1: effect of speed rate of change with constant air density  $\rho = 1.0$  kg/m<sup>3</sup> and linear speed profile  $V_0 = 10$  m/s,  $\Delta V = 80$  m/s. The flutter speed is  $v_f = 99.8$  m/s

Quantity	L1R1	L1R2	L1R3	L1R4	L1R5
Air density [kg/m <sup>3</sup> ]	1.0				
Sample rate [Hz]	180				
Air speed [m/s]	$20 + 80 \cdot t/T$ (linear profile)				
Excitation [N/m]	RPMS at pitch DoF, $\sigma^2(u) = 1$				
Duration [s]	10	20	40	80	160
Fundamental harmonic [rad/s]	0.6283	0.3142	0.1571	0.07854	0.03927
Adimensional period [adim · 10 <sup>-3</sup> ]	6.442	3.221	1.611	0.8053	0.4026
Maximal speed variation [m/s/s]	8	4	2	1	0.5

TABLE 7.5: Simulation S1: effect of speed rate of change with constant air density  $\rho = 1.0$  kg/m<sup>3</sup> and sine speed profile  $V_0 = 10$  m/s,  $\Delta V = 80$  m/s. The flutter speed is  $v_f = 99.8$  m/s.

Quantity	S1R1	S1R2	S1R3	S1R4	S1R5
Air density [kg/m <sup>3</sup> ]	1.0				
Sample rate [Hz]	180				
Air speed [m/s]	$20 + 80 \sin(\pi t/T)^2$ (sinusoidal profile)				
Excitation [N/m]	RPMS at pitch DoF, $\sigma^2(u) = 1$				
Duration [s]	20	40	80	160	320
Fundamental harmonic [rad/s]	0.3142	0.1571	0.07854	0.03927	0.01963
Adimensional period [adim · 10 <sup>-3</sup> ]	6.442	3.221	1.611	0.8053	0.4026
Maximal speed variation [m/s/s]	12.57	6.283	3.142	1.579	0.7854

### 7.3.1 Simulation parameters

The Runge-Kutta order 8 solver is selected following the criterion described in section 7.1.7. Hold order 3 for the input discretization is chosen to reduce the sample rate and number of time steps as much as possible, resulting in an oversampling factor  $k_f = 1.64$  ( $f_s = 2 \cdot 1.64 \cdot 55.08 = 180$  Hz). The airfoil-rudder aeroelastic system has 18 states, but only three degrees of freedom (heave, pitch and rudder flap). The response vector's physical units are one displacement and two angles. The excitation is broadband random applied at one physical degree-of-freedom. The output noise is set as 2% of the response RMS.

For a given parameter path, the duration may be still constrained by the rate of parameter change, therefore ensemble averaging is performed by computing one hundred system realizations. The computation time for the longest run is about 45 seconds, therefore 75 minutes are needed for just one full data set with all necessary realizations.

### 7.3.2 Spectral estimation

Spectral estimation is performed by a nonparametric approach and compared with analytical results to validate the assumption of slow system variation. The speed of parameter change affects the number of available data samples: a higher variation rate, respectively a shorter duration, imposes stronger limitations on the signal processing procedure and on the temporal resolution of the identified modal parameters, which therefore set a lower bound. The system's lowest eigenfrequency at wind-off conditions is  $\omega_{min} = 7.76$  Hz (heave mode, refer to table 7.3), therefore the variation rate is  $k_{\omega_0} = \omega_0/\omega_{min} < 6.4 \cdot 10^{-3}$ . The mode coupling term  $\Psi^{-1}(t)\dot{\Psi}(t)$  can be computed as described in section 3.4. Its non-diagonal terms relative to the instantaneous eigenvalues contribute to less than 0.4 % of the system's dynamics. The system can be considered slowly-varying and a frozen-time approach for spectral estimation and system identification is justified. Block length and number of averages determine the spectral estimation bias (see section 4.3). The results in this chapter are produced with an ensemble overlap  $O_e$  of either 0.75 or 0.80. The real-time output-only modal analysis application we have presented in [JELIČIĆ ET AL., 2017] sets  $1 - 1/20 = 0.95$  (set by the desired refresh rate of the monitoring software). Some authors use as much as  $1 - 1/128 = 0.992$  [AVENDAÑO-VALENCIA ET AL., 2020]. Figure 7.9 displays the estimated PSD with adequate time-frequency resolution, in good agreement with the analytical prediction. This echoes the results from figure 4.13.

### 7.3.3 System identification

Time-domain techniques utilize data collected from several experiments to perform ensemble identification, while frequency-domain algorithms can process spectra estimated by ensemble averaging. In this chapter system identification is performed in the OMA framework using the Least-Squares Complex Frequency (LSCF) algorithm. Its data source is the  $3 \times 3$  response cross-power spectral density matrix estimated in the range [0 70] Hz using the segmented multi-taper method 4.3.3. CPSDs have 4-quadrant symmetry (see section 4.2)

for 3 physical degrees of freedom. In order to compensate for any out-of-range poles and noise, 4 poles are added for residuals. The model order is at least  $3 \times 4 + 4 = 16$  with a single-band evaluation. The aerodynamic eigenmodes have high damping  $\zeta \geq 1/\sqrt{2}$ , therefore they can be easily separated from the physical ones. The eigenvalues are obtained from the roots of the denominator polynomial, while the eigenvectors are calculate in a second step by the LSFD algorithm (see section 5.6). The modes identified at each step are then passed to the tracking algorithm for sorting. A typical stabilization diagram is illustrated in figure 7.10.

#### 7.3.4 Mode tracking

The chosen system identification methods are nonparametric with respect to time variation, therefore the estimated modal parameters are obtained as independent data sets whose interrelation is unknown at first. Mode tracking is performed as the last step of the analysis chain. Details about the mode tracking algorithm and similarity metrics have been provided in chapter 6. The tracking algorithm's purpose is connecting the estimated modes so that they can be related to aeroelastic parameters through regression analysis, moving averages or interpolation. For smooth variations we expect the physical eigenmodes to follow similarly smooth paths since their eigensurfaces do not present any crease or jump (refer to figure 7.7).

As an example, figure 7.11 illustrates the system undergoing a complex parameter variation and the estimated and instantaneous modal parameters. The modes are matched to the three reference modes at wind-off conditions using the hyperbolic distance metric (HDM) (6.11) with threshold 0.5. The tracking algorithm's reference memory is set to 5% of the run duration. Some general observations can be made. The eigenfrequency of physical modes leaves a smooth trace that normally has little variance. Spurious, purely mathematical poles may gather between or next to physical poles, but do not form an orderly set with similar eigenvectors or eigenvalues and can thus be recognized and discarded (this is performed automatically by the tracking algorithm). The damping variance is higher and its estimate tends to be biased for  $\zeta > 0.2$

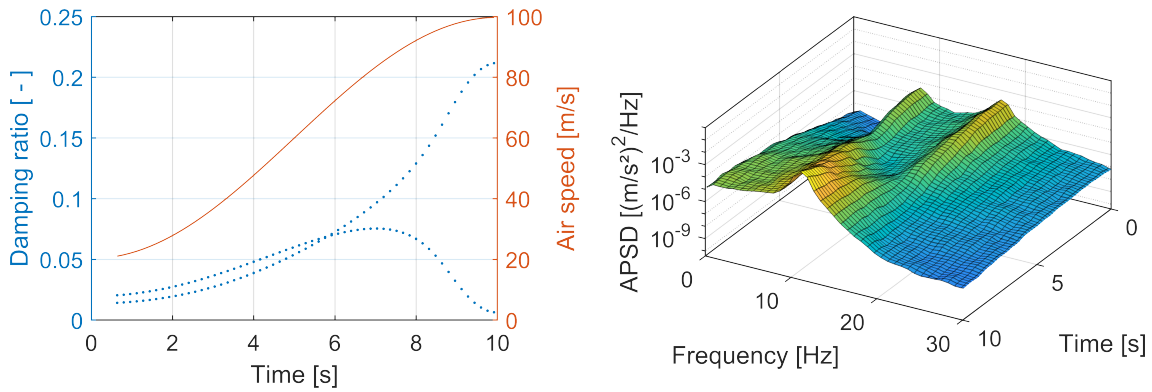


FIGURE 7.9: C1 system with varying speed from rest to flutter for  $T = 10$  s. Left plot: the frozen-time heave and pitch damping ratios are displayed on the left. Right plot: PSD estimated from ensemble averaging in the neighborhood of the heave and pitch modes. The estimated spectrum is in accordance with the analytical result.

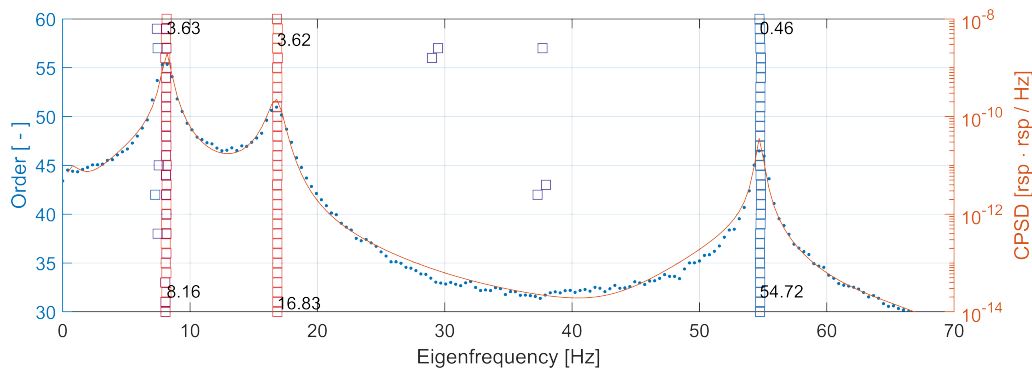


FIGURE 7.10: Typical stabilization diagram of output-only data. There are always spurious poles due to noise. Those that appear next to a physical pole are insidious because they have a very similar associated eigenvector that can mislead the tracking algorithm.

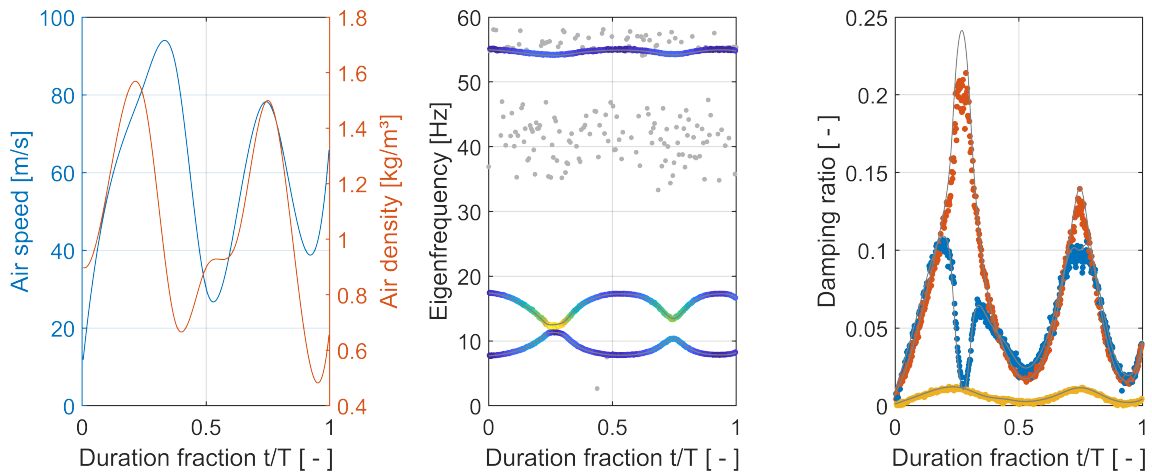


FIGURE 7.11: Example of mode tracking results. Round markers or dots represent the identified poles. Gray dots are spurious mathematical poles. The gray lines are the instantaneous (frozen-time) eigenvalues of the physical degrees of freedom. The colors in the middle plot denote the damping ratio (blue: low – yellow: high). In the right plot each eigenmode is assigned one color (blue – heave, red – pitch, yellow – rudder flap). Other figures follow this prototype.

### 7.3.5 Influence of rate of variation

Figure 7.12 illustrates the influence of speed of variation on modal parameter estimation (set S1R, half-sine speed change). The spectral estimation settings are the same for all runs, i.e. LSCF works with the same data quality for every parameter point and for each run. The number of averages  $N_b = 100$  is high in order to rule out at least the uncertainty due to the random error. The window length  $L_b = 512$  is a compromise between frequency resolution and parameter variation during one block. The block overlap is only  $O_b = 0.75$  to reduce the load for the tracking algorithm. The shortest run lasts 20 seconds (S1R1) and has the coarsest temporal and frequency resolution ( $\Delta f = 0.352$  Hz), but the damping estimate is still acceptable. Although it may not appear so in the plot, the density of spurious poles (number per unit time) is constant. The numerical nonparametric results confirm what was predicted parametrically, i.e. that the time-varying dynamics are not observable because the system varies too slowly. That being said, the parameter variation is still fast compared to the amount of data that is necessary for sequential spectral estimation or system identification, thus motivating the use of ensemble averaging.

### 7.3.6 Influence of number of averages

The tracking diagram 7.13 displays the effect of number of averages on estimated modal parameters on set S1R3 (half-sine speed variation, middle duration). Few averages increase the spectral variance, which in turn affects the smoothness of the eigenfrequency and produces bias on the identified damping ratio. This result mirrors what happens for time-invariant systems. The eigenfrequency estimation is usually not problematic even in adverse conditions, therefore we focus on damping estimation because it is a more critical aspect of aeroelastic system identification.

The tracking diagram 7.14 illustrates the effect of number of averages size on the identified damping ratio for constant air density and linearly-varying speed. The more system realizations (experiments) are performed, the lower are bias and scatter in the identified damping. The same can be observed for all rates of change. The available data suggests that about twenty averages appear enough to track the damping of the critical heave mode. The two modes participating in the flutter (experiencing a significant variation) are more affected by time variation than the rudder flap. The same behavior could be observed in chapter 2 for other systems.

The same data are plotted again in the complex plane in figure 7.15. Similar observations about averaging and bias can be deduced from these plots, namely that the eigenvalue's real part can be estimated better with more averages. As the system approaches the flutter boundary, the critical (heave) and interacting (pitch) modes become increasingly complex and dissimilar with respect to the reference at wind-off conditions. This phenomenon motivates the first-in-first-out buffer in the tracking algorithm's reference memory (see section 6.4.2). Additionally, while the modal indicator function MIF (6.14) can be used as an effective quality criterion for selecting the "best" eigenvalues in the EMA framework (that is, with the highest phase purity), it is less useful for aeroelastic modes.

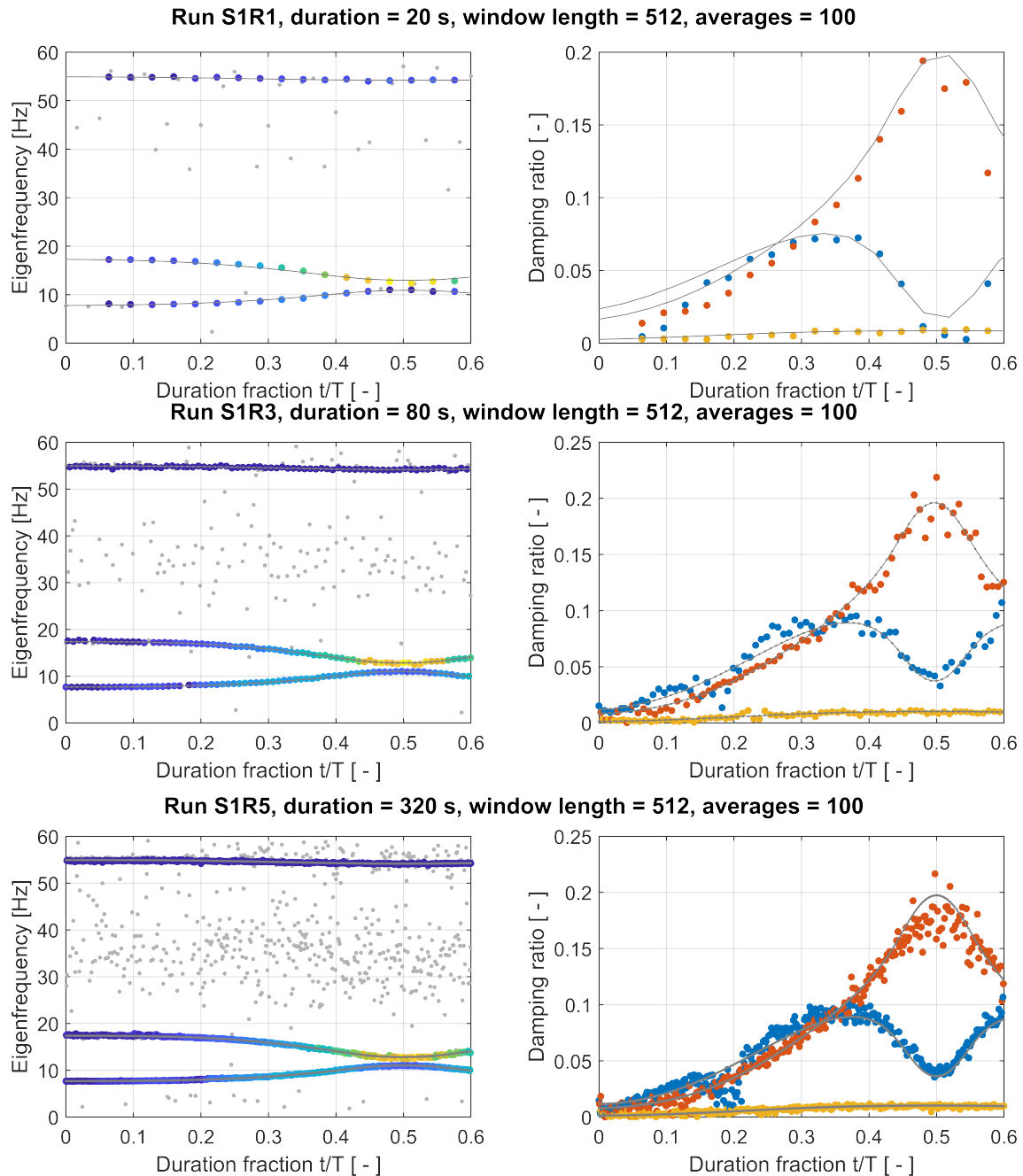


FIGURE 7.12: Mode tracking of set S1R. Refer also to figure 7.11. The three runs provide the same amount of information to the spectral estimation and system identification algorithms, the only difference being the duration and thus the corresponding temporal resolution.

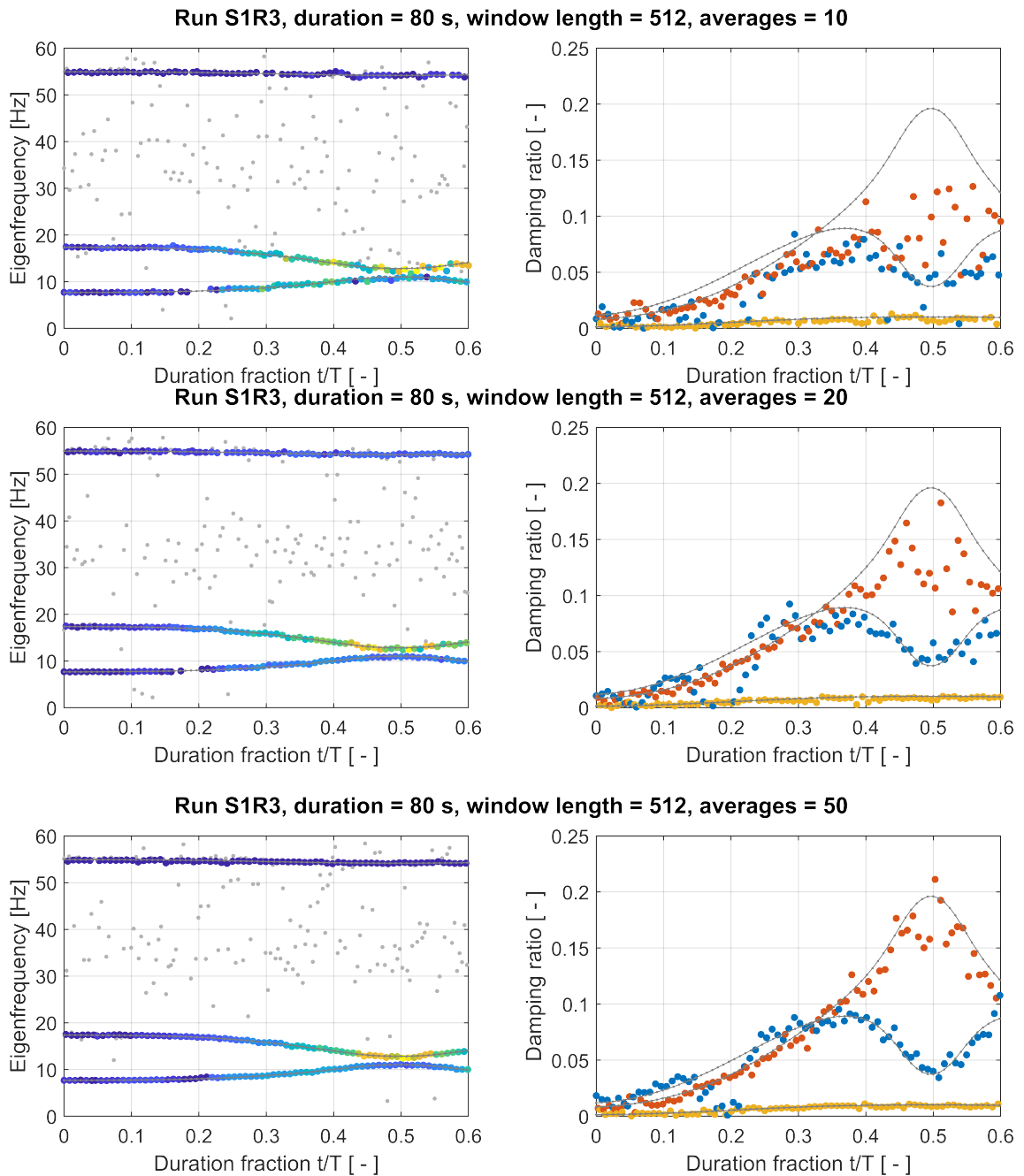


FIGURE 7.13: Effect of number of spectral averages on damping estimation. Same data as in figure 7.12. Refer also to figure 7.11. Right plot: blue – heave, red – pitch, yellow – rudder flap.



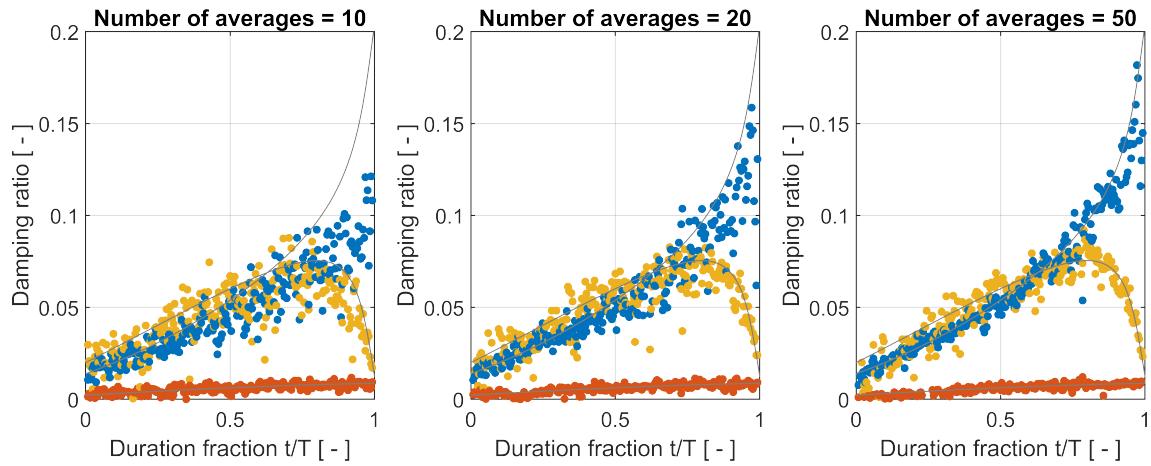


FIGURE 7.14: Effect of number of spectral averages on damping estimation (data from set L1R5, block length: 512). Twenty averages appear sufficient for adequate tracking with this block length. See text for discussion.

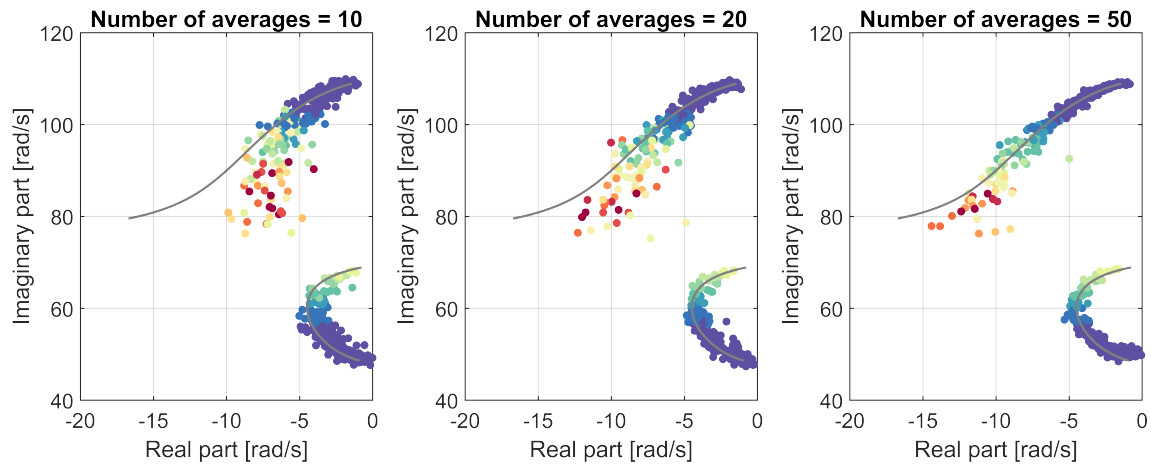


FIGURE 7.15: The heave and pitch modes are displayed in the complex plane (same data as in figure 7.14). The colors indicate the MAC value with respect to the base eigenmodes (blue: high, red: low). As the flutter boundary is approached, the mode shapes should become increasingly complex.

### 7.3.7 Influence of block length

The power spectral density of a long record (where poles may wander substantially, but slowly) is equal to the sum of many short-time PSDs (whose poles are approximately invariant, refer to section 4.4). The block length is a compromise between good frequency resolution and sufficiently low parameter variation within the block's duration. Too short a data block does not contain enough information about the system. On the other hand, too long a data sample will contain multiple instances of the same mode of vibration. The system identification algorithm will catch the most dominant poles and try to reduce the fit's least-squares error by placing additional spurious poles. Table 7.6 reports the spectral estimation parameters for different block lengths for a data set where speed varies linearly.

Figure 7.16 displays the effect of block size on identified damping ratio for a fast parameter variation ( $T_b = 20$  s). Set S1R1 (sine variation) is chosen in order to reduce the border effects that would be preponderant for such a short duration. In principle, a more sophisticated method could set the block length dynamically depending on the rate of change the aeroelastic parameters. In this case it can be long in the interval  $t/T < 0.75$ ), but must be short next to the flutter point for modes whose eigenfrequency or damping changes rapidly. It is possible to use different block lengths for each frequency band of the analysis. For instance, modes that are not coupled aeroelastically can be identified using longer block lengths (in this case the rudder flap).

Figure 7.17 shows the heave and pitch modes in the complex plane. The effect of exceedingly coarse or fine frequency resolution is clearly visible in the scatter of the eigenvalues. The same eigenvalues are compared to the corresponding analytical eigenvectors in figure 7.18. The marker color displays the MAC value between the estimated eigenvector and the nominal one. It can be deduced that too long a block length affects the quality of the estimated mode shapes as well. The further the system strays from the time-invariant case and the less data is collected, the lower the quality of identified modal parameters. Typically the damping ratio is the most affected, followed by mode shapes, while eigenfrequency is normally quite accurate.

TABLE 7.6: Parameter variation as function of data block length. The sample rate is 180 Hz, the frequency range is [0 60] Hz, the maximal speed variation is 8 m/s/s. The block speed increase is specific to case S1R1 (run with fastest sinusoidal variation).

Block length $L_b$ [num]	256	512	1024
Block overlap $O_b$ [adim]	0.75	0.75	0.75
Spectrum length $\lfloor L_b/f_s \cdot f_{max} \rfloor$ [num]	85	171	341
Block duration $T_b = L_b/f_s$ [s]	1.422	2.844	5.689
Block frequency resolution $\Delta f = 1/T_b$ [Hz]	0.7031	0.3516	0.1758
Block angular frequency $\omega_b = 2\pi/T_b$ [rad/s]	4.418	2.209	1.104
Block adim. frequency $\omega_b/\omega_{min}$ [adim]	0.09059	0.04529	0.02265

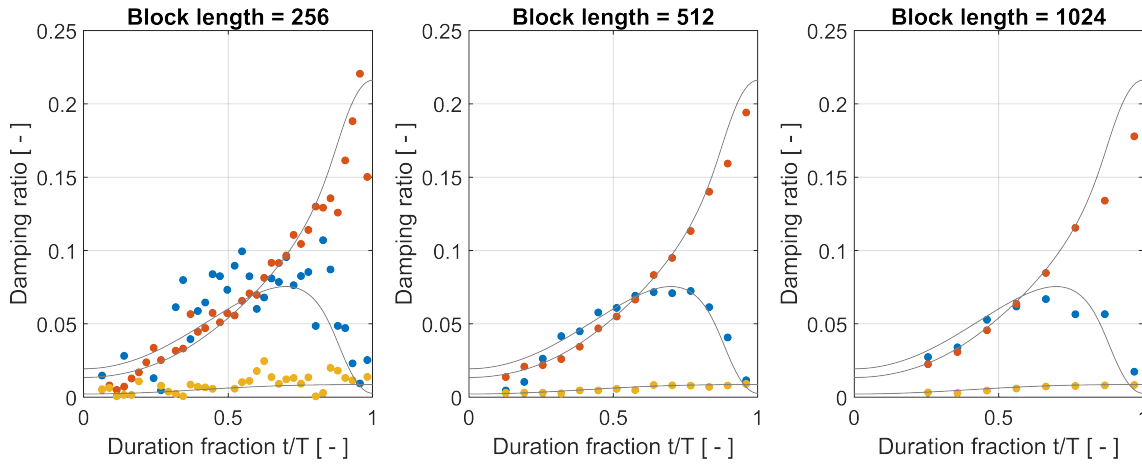


FIGURE 7.16: Effect of block length on damping estimation (data from set S1R1). This short data set exemplifies a difficult estimation case. The shorter the block, the bigger the variance and the number of spurious poles (not pictured here).

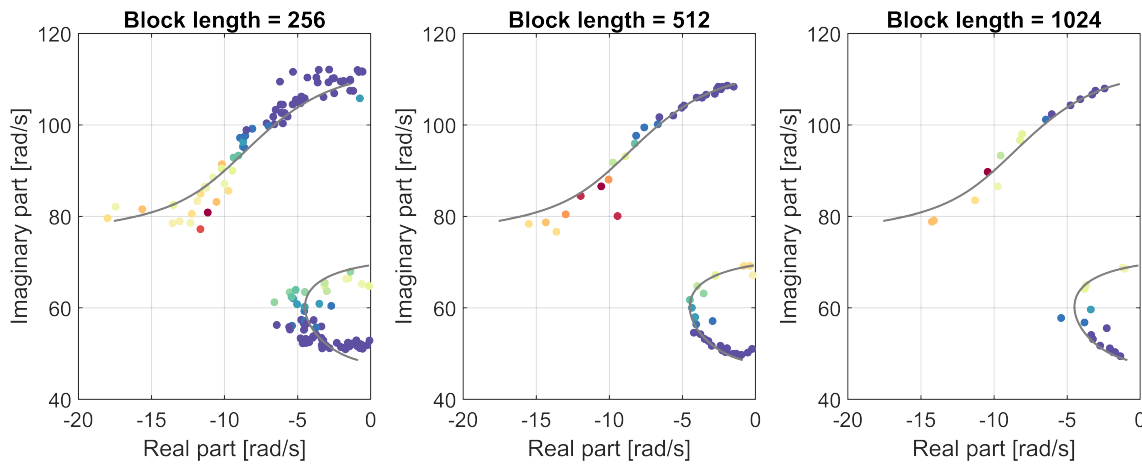


FIGURE 7.17: The heave and pitch modes in the complex plane (same data as in figure 7.16). The colors indicate the MAC value with respect to the base eigenmodes (blue: high, red: low). As the flutter boundary is approached, the mode shapes become increasingly complex.

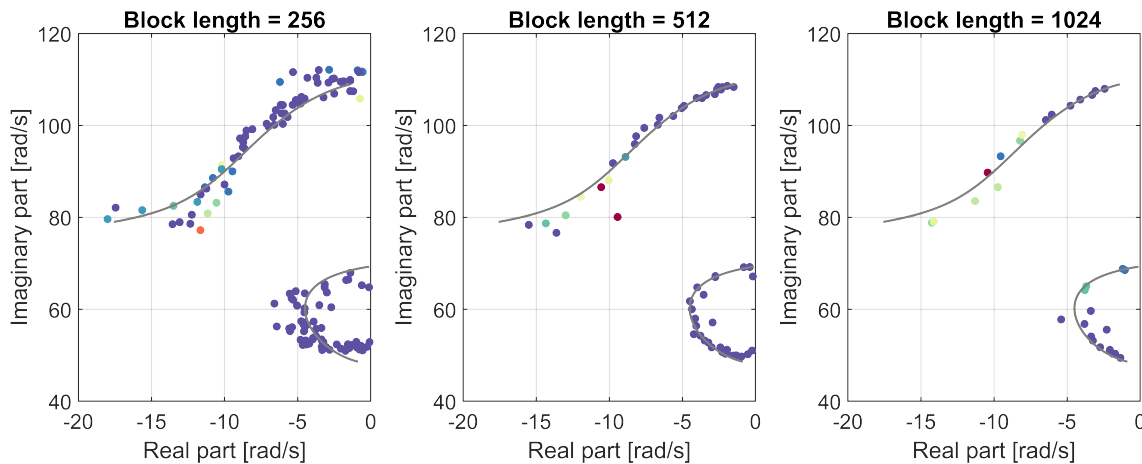


FIGURE 7.18: Same data as in figure 7.16, but the estimated mode shapes are compared with the corresponding analytical ones. The MAC value in the figure varies from 0.85 (red) to 0.99 (blue). Excessive block length correlates with slightly worse mode shape estimates when the system varies excessively within one estimation window.

### 7.3.8 Flutter boundary extrapolation

The flutter boundary and eigensurfaces are reconstructed from estimated modal parameter using a multivariate regression method for empirical modeling. Part of the task's difficulty comes from the quality of experimental data (missing points, scattered data, variance of damping estimates, etc...), but also from the eigensurface's shape. With some modeling effort and by reducing the parameter range, data can be fitted using low model orders to extrapolate the flutter boundary. A classic and comprehensive reference for regression analysis is [KUTNER ET AL., 2008]. We shall use the following methods:

- *Locally estimated scatterplot smoothing (LOESS)*: provides simplicity and flexibility that make it ideal when no theoretical models exist. However, since it relies on the local data structure, it requires a fairly dense grid to provide accurate results.
- *Polynomial fitting*: easy to use and well-understood, but it may notoriously behave poorly between sample points and when extrapolating.
- *Rational functions*: simple nonlinear models that fit a large array of shapes and require less coefficients than equivalent polynomial models. Asymptotes may appear over the range of data and the method is generally less understood than others.

Figure 7.19 displays the fitted eigensurfaces for the heave and pitch modes. The modal parameters are identified from a linear speed sweep with constant density (the speed variation  $dV/dt$  stays the same). Data acquisition is arrested just before the flutter boundary is reached. Once the estimated eigenvalues have been tracked, the fit is performed one eigenmode at a time. When the overall fit is satisfactory, the damping ratio of the critical mode can be extrapolated to determine the flutter boundary.

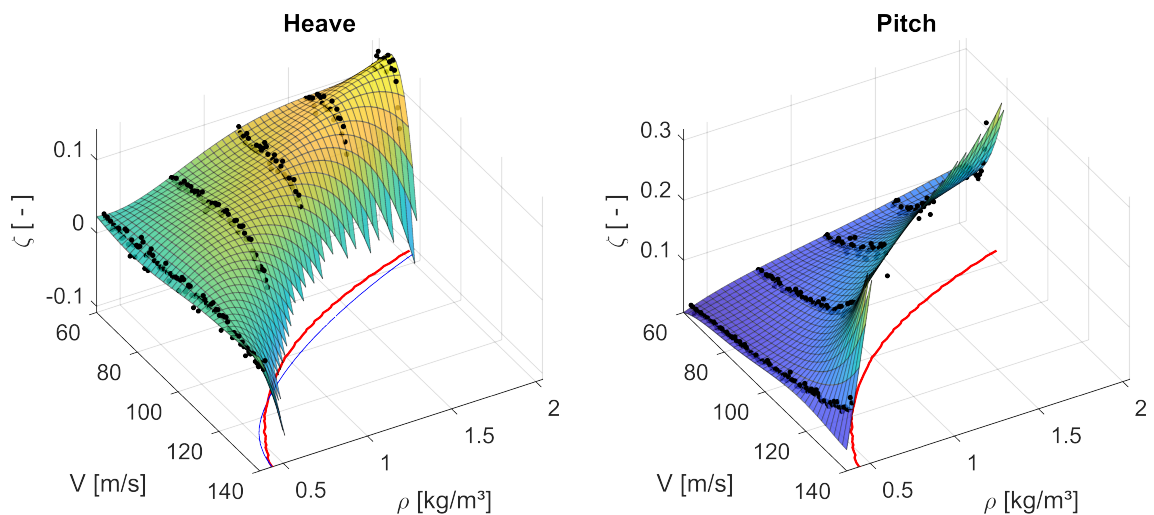


FIGURE 7.19: Eigensurface fit of the estimated damping ratio for the heave and pitch modes. The blue line is the predicted flutter boundary, the red line is the analytical one. The fitted surface is a polynomial function of order 5 for speed and order 4 for air density with least absolute residual robust fitting and normalization of data points. The fit struggles where damping plummets, particularly for higher values of  $\rho$ .

## 7.4 Chapter summary

The modal analysis tools presented in the previous chapters have been demonstrated here with a simple analytical aeroelastic model. Two configurations of the aeroelastic model of an airfoil with rudder are set up to display hard and soft flutter.

The chapter elaborates the numerical procedures for the simulations of time-varying systems. The well-known fixed-step Runge-Kutta and Adams-Bashforth-Moulton solvers are implemented for maximal efficiency. Additionally, in this research an analytical method based on the discretization and series expansion of the state transition matrix has been derived for the simulation of time-varying systems. The technique allows the characterization of the rate of parameter variation using the state matrix and its derivatives.

The simulations focus on the verification of the slow system variation assumption and the influence of duration, number of averages and block length on the estimated damping ratio. Dynamic effects due to parameter variation are not important for the system under consideration. An upper bound for the rate of variation is imposed by the spectral estimation and system identification methods in this case. The block length must be moderate - neither too short (impacts identification performance), nor too long (modes wander significantly within the block's duration). By conducting several experiments with the same parameter variation, it is possible to reduce the variance of estimated modal parameters by ensemble averaging. At least twenty averages appear to be necessary for good damping ratio tracking.

## 8 Experimental results

### *Abstract*

---

The methods and tools described in the previous chapters are finally applied in experiments. The real-time system identification of parameter-varying systems is performed during the flight vibration testing of a research aircraft. Different excitation and flight conditions are reviewed and the acquired data is analyzed to estimate the modal parameters of the aircraft.

---

The aeroelastic stability of new aircraft or modifications of existing ones is investigated with numerical models that combine structural dynamics and unsteady aeroelastic loads. Their validity must be proven by a comparison with experimental results obtained from a ground vibration test (GVT) and a flight vibration test (FVT). The modal parameters are determined experimentally with GVT and are used for refining the aircraft finite element model and for updating the control laws of the electronic flight control system. The evaluation of aeroelastic stability, however, must be performed in-flight and demonstrated for the whole flight envelope. FVT remains a hazardous activity, since stability must be investigated point-wise for several altitude/Mach number combinations and flight conditions to cover the full flight envelope.

Conventional flight vibration testing is performed by introducing additional forces into the aircraft structure through the control surfaces by means of pulses or swept sines or sometimes by external oscillating vanes or unbalanced masses. This approach requires a fly-by-wire or electronic control system and the installation of external wing exciters can be expensive and demanding. The AGARD report [VAN NUNEN ET AL., 1979] provides an overview of the classical testing approach in terms of flight test instrumentation, excitation types and analysis procedures. [KÖNIG, 1995] reviews flutter-relevant tests and discusses the contrast between desired and obtained reliability of acquired data, pointing out that flutter tests would benefit from continuous updating of estimated parameters. A historical survey of flutter testing has been compiled by [KEHOE, 1995]. The report from [BRENNER ET AL., 1997] reviews the developments in flutter testing at NASA Dryden, particularly excitation mechanisms. [MORELLI AND KLEIN, 2005] discuss the research conducted at NASA Langley on system identification applied to aircraft, in particular with regard to real-time parameter estimation and low-order equivalent model identification. [SCHWOCHOW AND ZÖGER, 2013] describe the flutter test activities performed at DLR and present a comparison of experimental data and aeroelastic analysis.

In some circumstances, the purpose of FVT may be to assess the vibration environment encountered by aircraft in steady flight or while performing maneuvers [CORDA ET AL., 2002]; in this case the analysis is conducted in terms of frequency content and magnitude levels of the aircraft response. The comparison between sweep excitation and ambient turbulence in terms of estimated modal parameters in [PEETERS ET AL., 2006] suggested that OMA can be performed without artificial system inputs. [MEVEL ET AL., 2006] analyze

the same topic and conclude that, while it is of course preferable to operate with known inputs, output-only techniques still provide satisfactory results. Recently, [IOVNOVICH ET AL., 2018] published an assessment of flutter prediction methods; the authors confirm that atmospheric turbulence provides adequate stochastic excitation for the identification of lightly-damped modes and conclude that operational modal analysis is an accurate and cost-effective flutter testing methodology.

Aircraft have typically sufficiently low eigenfrequencies that atmospheric turbulence encountered during normal flight provides a useful amount of natural broadband excitation. The resulting acceleration response can be acquired by a compact data acquisition system and combined with the methods of operational modal analysis to perform system identification in-flight. The whole process can be set up to run autonomously in order to estimate almost in real-time the instantaneous damping ratio and eigenfrequency of the aircraft's modes of vibration. This information is provided to the flight test engineer to monitor flutter-critical conditions by comparing experimentally-determined modal parameters with available computational flutter analysis results. The extrapolation of the damping ratio trend of critical modes towards higher flight speed, i.e. the rapid decrease after reaching a maximum, can signal the approach of an unstable state (combination of altitude and speed). This information can inform the pilot about the available flutter margin and thus enhance the test safety. Such a real-time online monitoring of the aircraft response is a novel application that can contribute towards cost and flight time reductions.

The previous chapters of this thesis offered an overview of the theoretical and numerical tools that are at our disposal for investigating the dynamics of time-varying systems. The current chapter will describe in detail the cooperation of said tools – from data acquisition to modal parameter tracking – in an automated modal analysis application deployed during output-only vibration testing. In order to achieve practical real-time capabilities, considerations about the application's architecture and its software implementation will be briefly provided here. The rest of the chapter shall focus on the results.

The chapter is organized as follows:

1. Review of dynamic effects in time-varying systems. Of specific importance to this research are flight parameter variation during FVT.
2. Description of the flight vibration test whose data will be analyzed in this chapter. This section details the experimental setup, the instrumentation and the test matrix.
3. Short review of the aerodynamic quantities relevant for FVT. This is necessary to describe the flight conditions and understand their effect on modal parameters.
4. Brief presentation of the real-time automatic modal analysis application that has been deployed during FVT.
5. Flight vibration test results and detailed analysis of experimental data.

## 8.1 Dynamic effects in parameter-varying aeroelastic systems

The analytical and numerical investigation of LTV systems in chapter 2 showed that the parameter variation's magnitude and frequency contribute together to the system's dynamics. Starting from periodic systems, whose spectra can be computed analytically for a large class of input functions, it has been shown how to extend this formulation to aperiodic variations as well, to obtain a frequency-domain representation of the system's output. Here we restrict the treatment to aeroelastic systems such as aircraft and wind tunnel models, therefore dynamic effects are not expected to be as prominent as in rotating systems like propellers, helicopters and wind turbines.

If either the magnitude or frequency are very small, the system will not deviate significantly from the time-invariant case. The sensibility to the amplitude of parameter variations must be investigated case-by-case, as generalization is not possible. For instance, we have seen in chapter 3 that the effect of air density or speed change is large in the flutter boundary's proximity, whereas it is not significant otherwise.

On the other hand, the parameter variation's frequency defines, broadly speaking, three regimes. These are related to the frequency of parameter variation  $1/T$  and pole bandwidth of the frozen-time system  $\zeta f_n$ , or, equivalently, to the variation's time scale  $T$  and frozen-time time constant  $1/(\zeta f_n)$ :

- *Fast parameter variation*: the frequency is comparable to or larger than the system's time constant  $1/T \gg \zeta f_n$ . Time-varying effects manifest as dynamic poles appearing at equally-space intervals  $f_n + k/T$ , where  $k$  are small integers (in practice,  $|k| \leq 3$ ). The shorter the time scale, the larger the peak separation in the response spectra. The parameter variation's magnitude determines the amplitude of the dynamic peaks and the number of visible ones, but unless parameters change substantially, only few peaks are significant.
- *Intermediate parameter variation rate*: dynamic effects appear when  $1/T \approx \zeta f_n$  and generate complex patterns around the location of the frozen-time eigenvalues.
- *Slow parameter variation*: the variation's time scale is much larger than the system's time constants  $1/T \ll \zeta f_n$ . In practice, under such conditions, the system will behave like its frozen-time representation.

As an example, we consider the simulation of a large sailplane model from [SCHWOCHOW, 2013] undergoing the same air density and air speed variation but with different rates. Figure 8.1 presents the response spectra and system identification results undergoing a fast variation where dynamic effects are clearly visible. Figure 8.2 shows the same parameter variation with an intermediate rate of change. Figure 8.3 displays a system undergoing a slow variation.

A parameter change does not translate uniformly over all eigenmodes, as some are clearly more affected than others and some not at all. The dynamic poles are visible already in the estimated spectra if the frozen-time eigenvalue variation is large enough or damping is low (the dynamic peaks are pronounced). However, under nominal operating



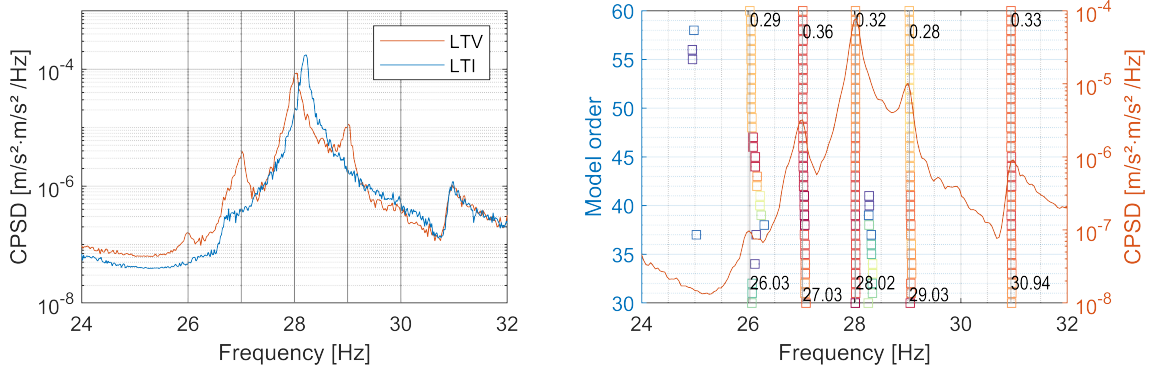


FIGURE 8.1: Fast parameter variation: simulated sailplane model with speed variation with frequency  $1/T = 1$  Hz. Two modes are in this frequency range at about 28 and 31 Hz (time constants  $\zeta f_0 \approx 0.1$  Hz). In the left plot, one output APSD is displayed for the LTV and the “mean” LTI systems. The vertical lines denote the mode at 28 Hz and its dynamic poles induced by the parameter variation. System identification confirms that the first four poles are associated to the same mode shapes and the fifth belongs to another mode (verified by the MAC values between eigenvectors).

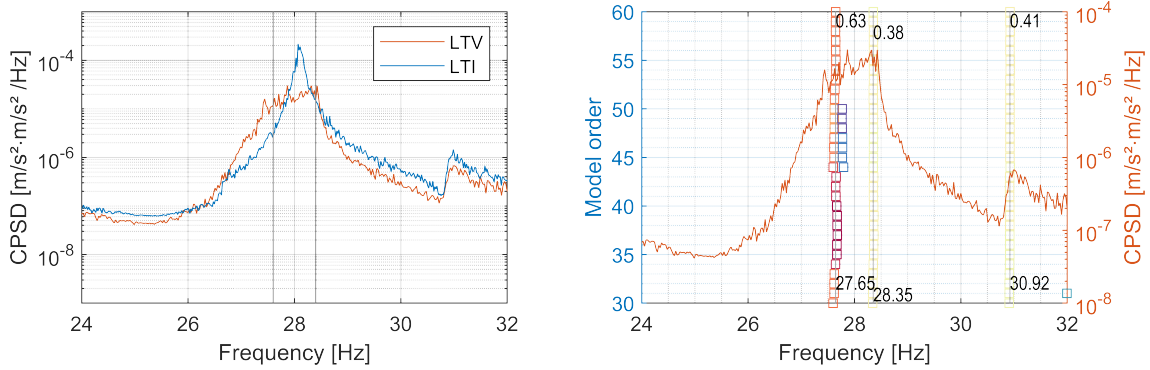


FIGURE 8.2: Intermediate parameter variation rate  $1/T = 0.01 < \zeta f_0 = 0.1$  Hz. The first mode’s frozen-time eigenfrequencies vary approximately between 27.6 and 28.4 Hz (denoted by the gray vertical lines in the left plot). The APSDs estimated from the whole data set display a “plateau” because of the continuous summation of slowly-varying spectral estimation windows (see section 4.4). In the stabilization diagram the extreme eigenvalues are identified with matching damping ratio. The second mode at 31 Hz does not vary.

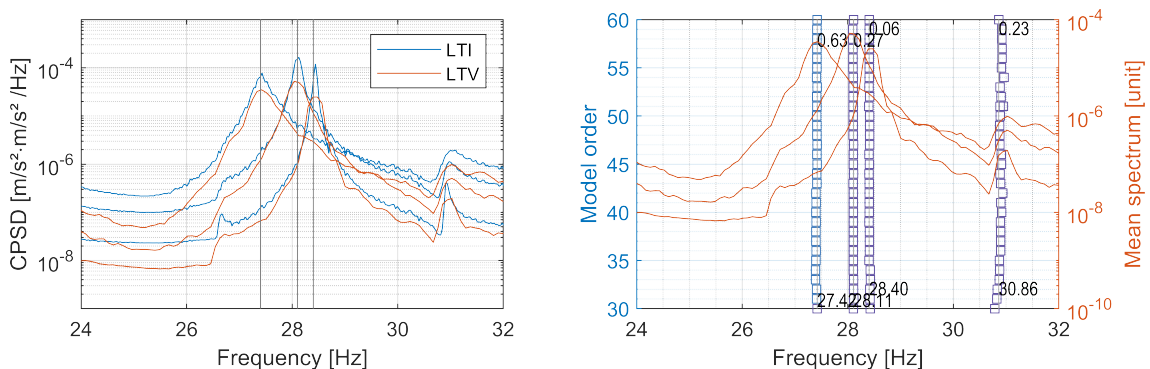


FIGURE 8.3: Slow parameter variation rate  $1/T = 0.0001 < \zeta f_0 = 0.1$  Hz. The stabilization diagram displays, from right to left, the eigenvalues identified at the beginning, middle and end of parameter variation. Time data is analyzed in several overlapping blocks.

conditions far from the flutter boundary, the first elastic modes tend to be highly damped, therefore it is unlikely that a dynamic pole has a significant residual associated to it. Furthermore, safety concerns and operational guidelines for wind tunnels and aircraft may prevent or prohibit large and sudden parameter variations. Lastly, the investigation of dynamic effects of real time-varying systems is often limited by the available control on external and operational parameters.

Numerical analyses have been carried out in chapter 7 to investigate the effect of parameter variation on system identification and mode tracking. Noise and limited frequency resolution render the dynamic poles invisible to spectral estimation or system identification methods. We concluded that, lest unrealistic operating conditions are forced, the appearance of dynamic poles can be ruled out and that a frozen-time formulation can be employed. This assumption shall be used in this chapter.

### 8.1.1 Wind tunnel tests

Wind tunnel tests are usually organized in a measurement matrix, i.e. various combinations of total pressure, Mach number, angle of attack and so forth. The wind tunnel operators control the flow parameters until the desired conditions are met and stationary, after which a static measurement is performed, for instance lift and drag or pressure distribution. The system's behavior while undergoing an angle of attack variation or the appearance of limit-cycle oscillations are often of interest during aeroelastic experiments in the wind tunnel. System identification is carried out by holding the measurement point until enough data has been collected. The wind tunnel parameters are then set to the next measurement point and, by repeating this process, a flutter diagram can be slowly filled out. Strictly speaking, such an experiment estimates the frozen-time eigenvalues of the parameter-varying aeroelastic system. This test procedure is illustrated in figure 8.4.

Wind tunnel models have typically higher eigenfrequencies than aircraft because they are smaller, not hollow and often made of stronger materials than aluminum, thus being stiffer (typical frequency ranges are  $\gtrsim 50$  Hz, although some special models reach  $\gtrsim 500$  Hz). Based on the author's own experience in the DNW-TWG, DNW-KKK and DNW-HST facilities [DNW, 2021], measurement times in the order of one minute are therefore normally sufficient to estimate the system's eigenvalues with confidence<sup>1</sup> [BÖSWALD ET AL., 2019; JELIČIĆ ET AL., 2014, 2015]. The wind tunnel's design makes it impossible to change the flow variables in a way that induces dynamic effects. Under normal conditions, within the duration of a spectral estimation window, the modal parameters present only the secular variation of slowly-varying systems.

---

<sup>1</sup> The measurement's duration, i.e. the amount of data that can be collected about a system, affects the variance of the spectral and modal parameter estimates (see section 4.3). Given a certain allowed error, the duration is related to the frequency band of interest for spectral estimation or system identification: the higher the eigenfrequencies of interest, the lower the measurement time.

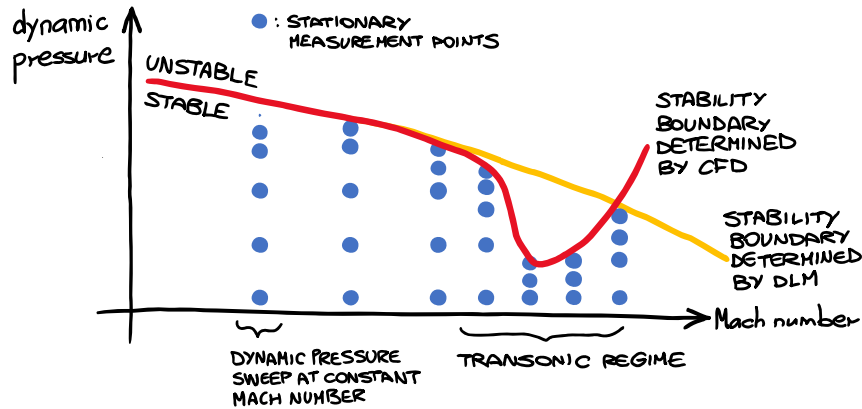


FIGURE 8.4: Aeroelastic testing procedure. The stability boundary is carefully approached by slowly increasing the dynamic pressure while keeping the Mach number constant. In the transonic regime the “transonic dip” occurs due to nonlinear flow conditions.

### 8.1.2 Flight vibration testing

Airworthiness requirements mandate that new or modified aircraft perform a full flutter test at speeds up to maximum speed and monitor the response amplitude, frequency and damping changes [EASA, 2007; FAA, 2014]. The purpose of FVT is to prove that flutter does not occur within the flight envelope up to maximal airspeed and altitude.

Flight vibration testing is traditionally carried out by stabilizing the aircraft at the specified altitude and airspeed and then by exciting the airframe through control surfaces or other devices [IOVNOVICH ET AL., 2018; KÖNIG, 1995; MEVEL ET AL., 2006]. The resulting response is analyzed to estimate the damping ratio of the aeroelastic modes and to reconstruct its trend over several test points. Once a test point has been cleared and the trend is deemed safe, airspeed is carefully increased until the next test point is reached (see figure 8.4). The flutter diagram is thus slowly constructed by testing several airspeed-altitude combinations within the flight envelope. In principle it would be possible to construct the flutter diagrams by accelerating the aircraft slowly, a claim that numerical investigations seem to support [JACQUIER AND AYME, 2018]. Continuous system identification of FVT is discussed in this chapter.

The eigenfrequencies of most aircraft are low because of their lightweight construction (usually in the range  $1 \div 50$  Hz) [KEHOE, 1995, Tab. 1]. This implies that, in order to collect a sufficient amount of data for system identification, longer records are necessary compared to wind tunnel models. The low eigenfrequency may be offset by large aerodynamic damping for some modes. Longer measurement times increase the probability of including transients, course corrections, maneuvers or gusts within one nominally stationary condition. Due to safety concerns, flight vibration testing has serious constraints on what can and cannot be done, therefore sudden and simultaneously large airspeed and altitude variations are off the table. Consequently, we can expect the aircraft to behave mostly as a slowly-varying system, while still experiencing significant parameter variation in the course of one flight test. Under some circumstances it is still possible to observe time-varying effects due to aerodynamic phenomena.

## 8.2 HALO flight vibration test

Flight vibration testing was conducted aboard DLR's *High Altitude and Long Range Research Aircraft* (HALO). The HALO is based on a Gulfstream Aerospace G550 business jet modified to be easily configurable for a wide array of research projects. Apart from the extended flight envelope and improved range, its most prominent features are various hardpoints for outfitting equipment for atmospheric experiments, for example a ventral pod, a dorsal sensor array and instrument carriers on the wings. The HALO provides an important platform for the execution of aeroelastic experiments thanks to its flexible mission capabilities. Part of HALO's technical data is reported in the appendix in table A.1 and its flight envelope is reproduced in figure 8.14.

Aeroelasticity is a big issue for external installations on the aircraft fuselage or wings, therefore stability must be demonstrated experimentally for any modifications up to maximum altitude and airspeed. The airworthiness requirements for new aircraft configurations, with particular focus on the HALO, are outlined in [SCHWOCHOW AND ZÖGER, 2013] and the references therein. For the mission at hand, we are mainly interested in its operating ceiling: pressure altitude 51000 ft and Mach number 0.885.



FIGURE 8.5: Front view of the G550 DLR-HALO before a test flight. Photo credit: DLR.



FIGURE 8.6: Aft view of the HALO aircraft during roll-out. Author's photograph.



FIGURE 8.7: HALO performing a banked turn. The under-wing stores (PMS carriers) are visible under both wings. Photo credit: DLR.

Within the framework of the *iLOADS* project [KRÜGER AND KLIMMEK, 2016], the HALO has been equipped with under-wing stores for atmospheric research called *Particle Measurement Sensors* (PMS) carrier (see figure 8.7). The dynamic loads and aeroelastic stability of the PMS carriers had to be evaluated in-flight and compared with numerical analyses [SINSKE ET AL., 2018]. The project provided the opportunity to conduct an extensive measurement campaign, to acquire aeroelastic system responses in flight and to assess the real-time capabilities of the modal analysis procedure that has been developed within the scope of this thesis. This application provides autonomously information that can be used to monitor flutter-critical conditions by comparing the instantaneous estimated modal parameters with available numerical results. This has the potential to inform the flight test engineer or test pilot about the remaining flutter stability margin and to enhance safety and efficiency. There is no regulation requirement for specific excitation to be performed within the flight envelope, since no reference to system inputs is evaluated, therefore, the monitoring application can contribute to reduce the test's duration and consequently its cost. During the course of the *iLOADS* experimental campaign, the ground, taxi and flight vibration tests have been performed (see chapter 5.2). Considering the scope of this research, we shall focus only on the latter. Data have been acquired over the course of five days for a total of 14 hours of flight. At the maximal pressure altitude of 48000 ft (14.6 km) the HALO was flying in the stratosphere at maximal Mach number 0.88 (936 km/h).

We proceed with the description of the FVT instrumentation, the modes of vibration of the aircraft and the automated modal analysis application. Section 8.2.3 describes how the flight parameters are calculated. More information about the flights is provided in section 8.2.4.

### 8.2.1 Instrumentation

Data acquisition during FVT has been carried out by a distributed network configuration that combines three NI-cDAQ chassis, the aircraft on-board measurement system BAHAMAS (BAsic HALO Measurement And Sensor system), a DAQ computer and four analysis PCs. Flight parameters such as Mach number, positioning, pressure data and so forth are recorded by BAHAMAS. The rugged flight test instrumentation (FTI) developed for this experimental campaign and the requirements imposed by the mission are detailed in [BURWITZ ET AL., 2017] and [SINSKE ET AL., 2018]. Prior to the test flights, the taxi vibration test provided an adequate test-bed for the vibration monitoring application by proofing the sensor setup by means of OMA [GOVERS ET AL., 2017]. To sum up, the analysis computers have accelerometer and flight data at their disposal for modal analysis. The more response channels are acquired during modal analysis, the better the estimate of the structure's modal parameters. However, *in a flight vibration test the number of sensors and their location must account for cable management and accessibility within the airframe, therefore it is unlikely to be optimal.* The HALO aircraft was instrumented with 51 piezoelectric accelerometers for vibration monitoring. Figure 8.8 displays the sensor layout, while figure 8.9 shows the unique locations of all sensors and the names of each sensor group (component).

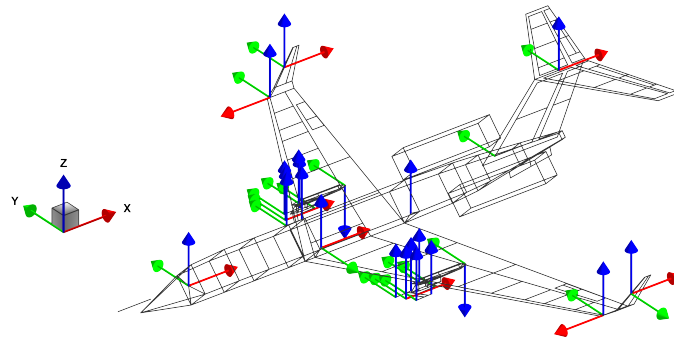


FIGURE 8.8: HALO flight vibration test sensor layout. There are 51 accelerometers in total (9 longitudinal, 20 lateral and 22 vertical). Sensor number and location must account for accessibility within the airframe.

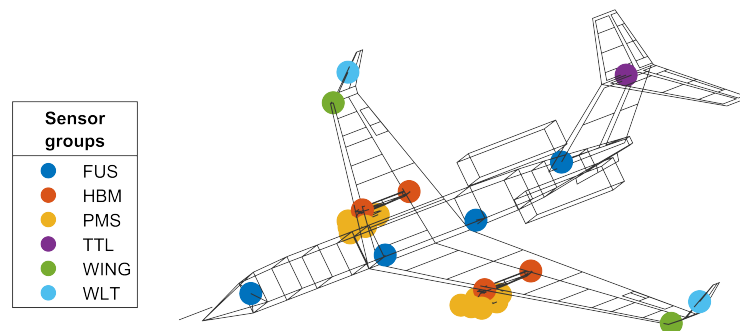


FIGURE 8.9: HALO flight vibration test sensor groups. Throughout the text and in the plots the sensors are denoted by abbreviations (sensor number in parentheses). FUS: fuselage (8), HBM: hanger beam (8), PMS: particle measurement system (20), TTL: T-tail (3), WING: wings (6), WLT: winglets (6).

The HALO carried the PMS component in its under-wing stores (see figure 8.7), therefore most wing sensors were installed on it in order to resolve the local dynamic behavior. The wing should be instrumented along its span with vertical sensors on the leading and trailing edges in order to distinguish bending and torsion modes, but this was not possible for FVT. No accelerometers could be attached to the engines or to their pylons, therefore the engine modes known from GVT are likely to blend with other global modes. Regarding wing torsion and engine modes, foreknowledge from the GVT about their location is applied to OMA results when the similarity of neighboring mode shapes is high. The hanger beam component (wing hardpoint) was instrumented with 16 strain gauges for load monitoring, but also provided convenient locations for accelerometers.

The sensor location and direction are of great importance for both the system identification algorithms and for the test engineer analyzing the identified eigenmodes [COVIOLI AND COPPOTELLI, 2019]. The mode tracking procedure described in chapter 6 uses eigenvectors to distinguish one eigenvalue trace from another, consequently a good sensor setup is necessary. Figure 8.10 provides a simple example.

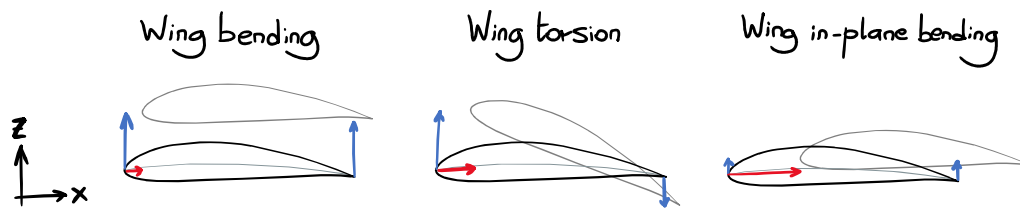


FIGURE 8.10: Identification of mode shapes of wing profile using three sensors. The leading edge is instrumented with  $x$  and  $z$  sensors, the trailing edge only with a  $z$  sensor. This configuration can distinguish between the (first) wing bending, the torsion and the in-plane bending modes. Additional sensors along the wingspan are necessary to resolve eigenmodes with more nodes (e.g. the higher wing bending and torsion modes).

The instrumentation must account for spread, sparsity and locality of the sensors:

- *Spread*: ability to visually recognize a global mode shape because of sensor location, orientation and number. For example, wing torsion (especially for swept wings) is difficult to distinguish from wing bending if the leading and trailing edges are not both instrumented.
- *Sparsity*: important substructures may not be instrumented, e.g. the stabilizer or the engines. Two global modes may appear very similar if the substructure vibrates in one but not in the other. Control surfaces must be instrumented if their flap modes are important to aeroelastic stability.
- *Locality*: local modes are over-represented when sensors are clustered on a substructure, which can be a disadvantage for system identification as well as for mode tracking. This should be avoided if there is a significant non-linearity on the connection with the rest of structure.

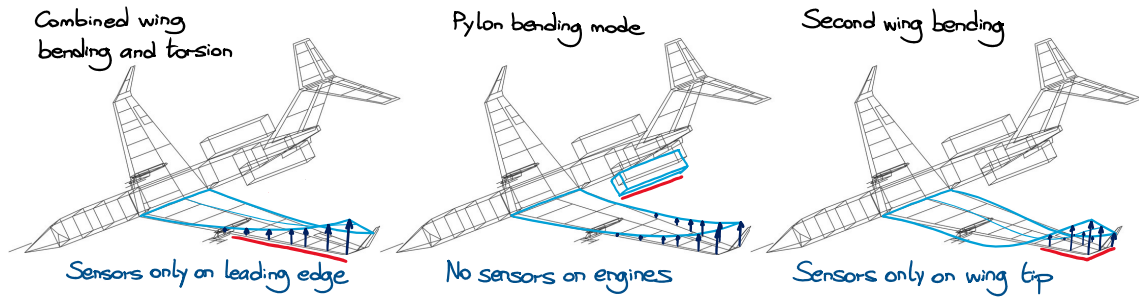


FIGURE 8.11: Examples of sensor setup issues. Left: poor sensor spread – the sensors are located only on leading edge, therefore the wing torsion appears as a wing bending. Middle: bad sparsity – the pylon bending mode appears similar to a wing bending mode (not instrumented substructure). Right: excessive locality – the wing tip has many sensors, but the first and second wing bending modes are difficult to distinguish.

Figure 8.11 provides an example of bad sensor spread, sparsity and locality. Let us consider the problem from the test engineer’s point of view: the sensor distribution along the structure should aid visual identification of the eigenmodes in order to name and to recognize them. This is desirable in order to compare different data runs, to eliminate spurious modes from the stabilization diagram or to assist the automated mode tracking procedure. System identification or mode tracking methods do not have any geometrical information, therefore eigenvectors are analyzed only in terms of similarity or mode quality criteria. The visualization and animation of mode shapes are powerful tools delivering precious insight about measurement setup errors, identification quality and, in the case of aeroelasticity, about the interaction between different modes. During FVT it is to be expected that some flying conditions or excitation types can be inadequate for the identification of some eigenmodes. In the case of HALO, some modes are indeed difficult to identify depending on the kind of excitation acting on the aircraft. For example, when the phase difference between neighboring output sensors is high, an animated mode can be immediately recognized as spurious and eliminated.

Visual inspection of the mode shapes brings the following improvements:

- *Channel table correction*: errors in the channel table setup can be correct by reconstructing the “ideal” shape of the first few elastic modes and correcting the channel table entries with the wrong location, orientation or calibration factor (for instance, the first wing bending eigenvectors must point all in the same direction and display an approximately parabolic trend).
- *Modal model selection*: the visual inspection of identified mode shapes resolves bifurcations in the stabilization diagram (such as those arising when a pole shifts within the time data buffer).
- *Mode tracking enhancement*: mode tracking is of course automated, but it can be greatly assisted by occasional human intervention, for example, by selecting the “best identified instance” of an important mode as the ancestor of its mode family or by discarding badly-identified, complex and irregular mode families.



Theoretically, the response measured at any location on a linear system contains all its poles, but in practice the signal-to-noise ratio might be inadequate for part of the frequency range of interest. In the modal analysis of real structures there is a connection between the excitation vector and dominant direction of a particular eigenmode: for example, wing modes are best identified by applying a vertical force during ground vibration testing [GOVERS ET AL., 2014]. The number of linearly independent eigenvectors that can be identified is at most equal to the number of system outputs. This can be a limiting factor in experimental setups with few sensors. For instance, in the wind tunnel data from [JELIČIĆ ET AL., 2014] at least a dozen clearly-defined resonance peaks are observable, yet only six response channels are available.

### 8.2.2 Modes of vibration

The mode shapes of an aircraft are first estimated during GVT and constitute later the reference data for the flight vibration test. From now on we shall often refer to HALO's modes of vibration, either in terms of eigenfrequency or mode shapes. In order to help commit them to memory, we anticipate some of the results that will be presented later in this chapter. The mode shapes do not vary much and are recognizable during almost any flight condition, therefore it is convenient to visualize and name them.

Figure 8.12 displays the first eight HALO mode shapes identified during stationary flight conditions. Their eigenfrequency and damping ratio are, strictly speaking, valid only for the flight condition at which they have been identified, but are nevertheless reported for the reader's convenience. The modes with large participation of the wings are expected to be well-excited during normal stationary flight and to feature prominently as well-defined resonance peaks in the spectra. The first symmetrical wing bending has a high damping ratio (typically  $\geq 10\%$ ) because of aerodynamic damping. There are modes that are known from GVT (where a more comprehensive sensor setup is used) but that are difficult to observe in-flight, for example aft fuselage torsion with wing in-plane bending.

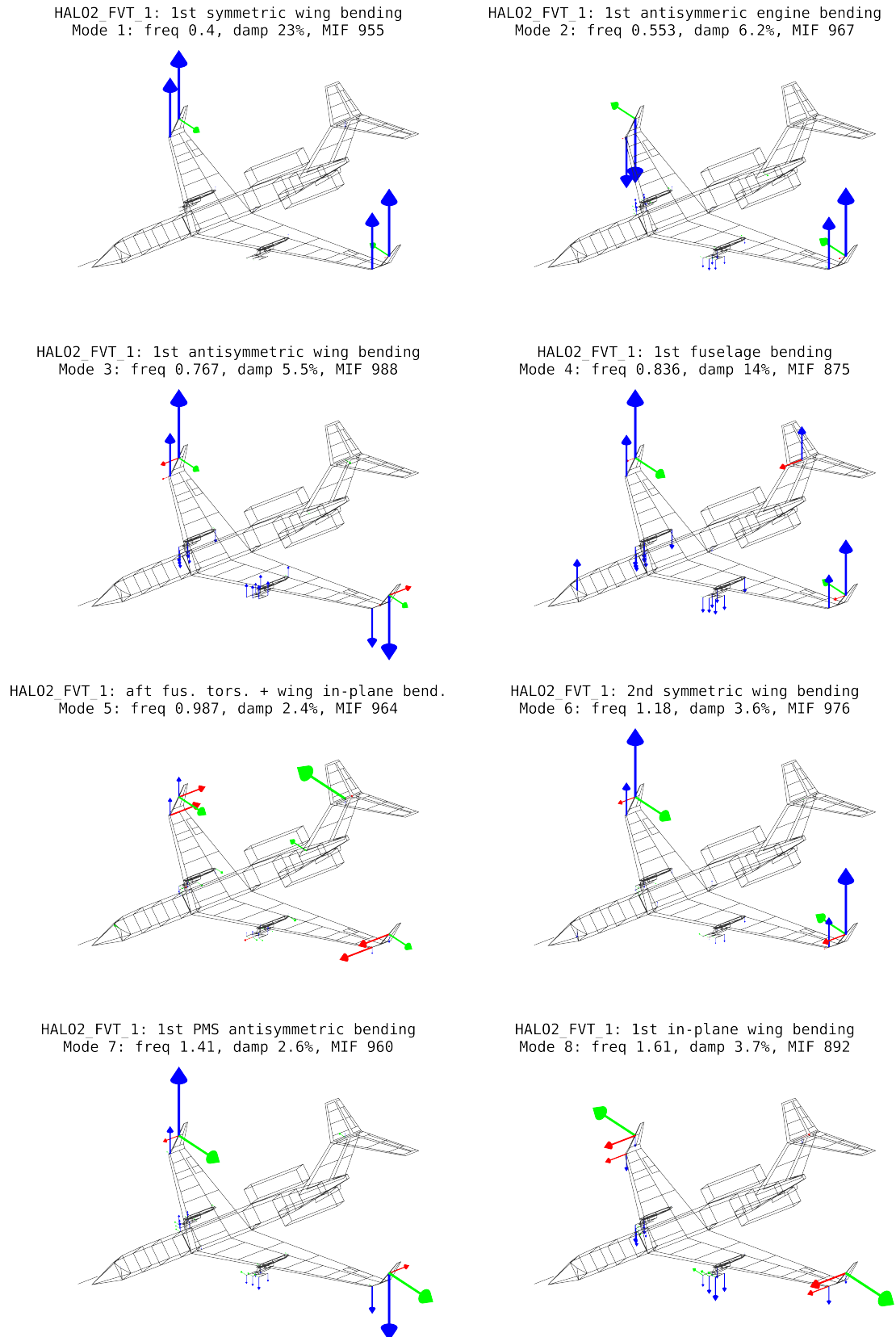


FIGURE 8.12: First eight elastic HALO modes (normalized mode shape amplitude): 1 - first symmetric wing bending, 2 - first antisymmetric engine bending, 3 - first antisymmetric wing bending, 4 - first fuselage bending, 5 - aft fuselage torsion with wing in-plane bending, 6 - second symmetric wing bending, 7 - first antisymmetric PMS bending, 8 - first in-plane wing bending. The displayed modal parameters have been identified from the stationary measurement point MP12 (steady level flight at 27000 ft, Mach number 0.65, see table 8.1).

### 8.2.3 Flight aerodynamic quantities

The linearized aeroelastic theory based on potential flow introduced in chapter 3 has described the influence on the structure of the unperturbed freestream's speed  $V_\infty$  and density  $\rho_\infty$ . This section elaborates further on the experimental determination of flow parameters during flight using [GRACEY, 1981] as reference. Strictly speaking, the following treatment is valid for an ideal gas but it is nevertheless still accurate for air.

**Notation.** *In aerodynamics, freestream variables are subscripted by “ $\infty$ ”, whereas local ones have no subscript. Total variables (also known as impact or stagnation variables) have superscript “0”.*

The potential flow theory describes the forces acting on an object as function of the surrounding velocity field. The flow is considered incompressible and there is no account of thermodynamics. The modeling of an aircraft flying at high speed must include temperature in order to describe air compressibility effects.

#### *Mach number*

The Mach number is the dimensionless parameter describing point-wise the flow regime and the phenomena arising from compressibility. It is the ratio between the local flow speed and the local speed of sound:

$$Ma \triangleq \frac{V}{\sqrt{\gamma R_* T}} \quad [\text{adim}] \quad (8.1)$$

where  $V$  is the speed,  $\gamma$  the ratio of specific heat<sup>2</sup> ( $\gamma = 1.4$  for air),  $R_* = 286.94$  J/(kg·K) the specific ideal gas constant for dry<sup>3</sup> air and  $T$  the local static temperature.

Fluids with the same Mach number behave in a similar way and many flight characteristics depend on the local  $Ma$  and not on the actual local flow speed. For example, since air temperature in the troposphere decreases with altitude, so does the speed of sound and the Mach number consequently increases even if the aircraft's speed relative to the air were to stay the same. Where the local wind speed is equal to the speed of sound ( $Ma = 1$ , the sonic condition), a shock wave forms, i.e. an instantaneous and abrupt variation of the flow's variables. The formation of shock waves is important in aerodynamics because they alter the flow around the aircraft, increase the drag coefficient and affect the propulsive efficiency, but also for aeroelastic stability because of buffeting (high-frequency flow separation or shock oscillation) and the transonic dip phenomenon (sudden decrease of the flutter margin, see figure 8.4).

<sup>2</sup> The ratio of specific heat at constant pressure to heat at constant volume is denoted by the letter  $\gamma$  in aerospace engineering, while in thermodynamics the symbols  $k$  or  $\kappa$  are much more common.

<sup>3</sup> The effect of humidity is negligible below -10 degrees Celsius (at altitudes  $12400 \leq h \leq 131000$  ft). For the current flight test we can ignore it. This value of the ideal gas constant is taken from HALO's air data computer.

We shall consider the following regimes:

- *Incompressible subsonic*  $0 < Ma_\infty \leq 0.3$ : air density varies very little with speed. Classic aerodynamic potential theory can be applied for quasi-steady and isothermal flows (for the purpose of aeroelastic design, this regime is  $0 < Ma \leq 0.5$ ).
- *Compressible subsonic*  $0.3 < Ma_\infty \leq 0.8$ : the aerodynamic potential theory must account for compressibility effects by applying corrections. Most time during the experimental campaign was spent in this regime.
- *Transonic*  $0.8 < Ma_\infty \leq 1.2$ : since the stream moving next to the aircraft is accelerated, local supersonic patches develop (typically around the wings). The flow is highly nonlinear and a modified aeroelastic formulation must be applied.

The supersonic  $Ma_\infty \geq 1.2$  and higher regimes are outside the scope of this work. The incompressible subsonic regime is of importance for sailplanes and other light aircraft. Modern airplanes are engineered to fly in the transonic regime at higher flight altitudes because of optimal propulsive efficiency and lift-to-drag ratio [HILL AND PETERSON, 1992]. Compressibility and nonlinear effects must be incorporated in the calculation of the aerodynamic influence coefficients. The AIC matrix can be computed directly using computational fluid dynamics or by applying corrections to the potential flow theory [FRIEDEWALD ET AL., 2018], but the construction of the state-space model still follows the steps outlined in chapter 3.

At cruise altitude the flight speed is given as Mach number because it is more representative of aerodynamic phenomena. The freestream Mach number can be calculated using the isentropic flow relations [HILL AND PETERSON, 1992]:

$$Ma^2 = \frac{2}{\gamma - 1} \left( \frac{T^0}{T} - 1 \right) = \frac{2}{\gamma - 1} \left( \left( \frac{p^0}{p} \right)^{\frac{\gamma-1}{\gamma}} - 1 \right) \quad (8.2)$$

where  $T^0$  and  $T$  are the total and static temperatures<sup>4</sup> and  $p^0$  and  $p$  the total and static pressures<sup>5</sup>. Aircraft have a Pitot tube to measure stagnation and static pressures in the subsonic regime. Coupled with a measurement of stagnation and static temperature of the airflow, the Mach number, air speed, air density and pressure altitude can be calculated. The static quantities are measured where freestream conditions are met (in the case of HALO, on the aft sensor boom). Equation (8.2) is used to calculate  $Ma_\infty$  and from there the other freestream flow variables.

<sup>4</sup> The total temperature is the stagnation temperature of a flow line whose the kinetic energy has been converted entirely into internal energy:

$$T^0 = T + \frac{v^2}{2c_p} \quad (8.3)$$

where  $T$  is the static temperature,  $v$  the flow speed and  $c_p$  the specific isobaric heat capacity.

<sup>5</sup> The total pressure is calculated from Bernoulli's principle as

$$p^0 = p + \frac{1}{2}\rho v^2 + \rho g z \quad (8.4)$$

where  $p$  is the static pressure,  $\frac{1}{2}\rho v^2$  the dynamic pressure and  $\rho g z$  the gravitational head. For air traveling on a horizontal path the latter term is so small that it is ignored.

### Air speed

In aeronautics several types of “airspeed” are defined: *calibrated* (CAS), *equivalent* (EAS), *indicated* (IAS) and *true* (TAS) airspeed. Their purpose and measurement are detailed in every flight manual. These conventions serve different needs in navigation or testing and the instruments of an airplane usually display or record all four. We only need the true airspeed (TAS), i.e. the relative velocity between aircraft and the air mass. This is equivalent to what in aerodynamics is classically called freestream/wind speed  $V_\infty$  and what has been known simply as “air speed” in previous chapters. True airspeed is *not* equivalent to ground speed because compressibility effects or winds are not taken into account [GRACEY, 1981].

When the Mach number and static temperature are known, the true airspeed can be computed from reference quantities at sea level:

$$V = Ma \cdot a_0 \sqrt{\frac{T}{T_0}} \quad [\text{m/s}] \quad (8.5)$$

where  $a_0 = 340.29$  m/s and  $T_0 = 288.15$  K are respectively the speed of sound and the reference temperature at sea level. The accurate measurements of Mach number and true airspeed are provided by the HALO flight data computer.

### Air density

The ideal gas law relates the state quantities  $p$ ,  $\rho$  and  $T$  of an ideal gas with each other:

$$\frac{p}{\rho} = R_* T \implies \rho = \frac{p}{R_* T} \quad (8.6)$$

Air density is not directly measured by the flight data computer, but it can be calculated either from the dynamic pressure and true airspeed or from the static pressure and static temperature. In equation (8.6) humidity must be accounted for in order to compute the air density accurately. Fortunately, the correction factor is in the range of the measurement’s error already at 4000 m above sea level, therefore it can be ignored since the lowest HALO flight level of interest to us is at 15000 ft (4500 m).

The HALO has a nose boom housing the five-hole-probe to determine the air velocity vector in conjunction with pressure sensors to measure the static pressure accurately. The technical report from [GIEZ ET AL., 2020] details the calibration of the nose boom sensors and provides rich information about static pressure measurements on aircraft. The flight data computer (air data system) applies some corrections and calibration factors to provide accurate static pressure and static temperature values to the DAQ computer. According to the available technical expertise, the most accurate way to compute air density is thus equation (8.6) through the measured static pressure and static temperature.

### Flight altitude

The variation of air temperature, pressure and density as a function of altitude is described by the *International Standard Atmosphere* model [ISO, 1975]. The measured atmospheric data from the HALO campaign are reproduced in figure 8.13 as a function of altitude. The lower part of the atmosphere down to sea level is the troposphere, where most of the air turbulence and almost all weather phenomena take place. The thin layer starting at circa 39000 ft (11900 m) where the temperature is constant is the tropopause. Above 40000 ft (12100 m) (with seasonal and latitude variations) the temperature gradient changes sign and thus signals the beginning of the stratosphere. In the troposphere the air temperature decreases linearly, while the static pressure and air density follow a decreasing power law.

The flight altitude is measured by the barometric altimeter aboard the aircraft. The instrumentation determines the altitude above sea level through air pressure. This so-called *pressure altitude*  $h$  is calculated from the static pressure  $p$  according to an exponential relationship [US-NOAA ET AL., 2021]:

$$h = 145366.45 \left( 1 - \left( \frac{p [\text{Pa}]}{101325} \right)^{0.190284} \right) \quad [\text{ft}] \quad (8.7)$$

The pilot reads the pressure altitude and adjusts the flight level according to the mission profile. This reading is one of the measurement channels in the DAQ system and is more accurate than the available geodesic (GPS) altitude. In this chapter, when talking about “altitude”, we always intend the pressure altitude. When the mission profile designates the flight level, small static pressure and air density variations can be neglected. At fixed altitude the static pressure and temperature are constant, consequently the air density is also constant. Under this condition the true airspeed, Mach number and square of the dynamic pressure differ only by a scaling factor.

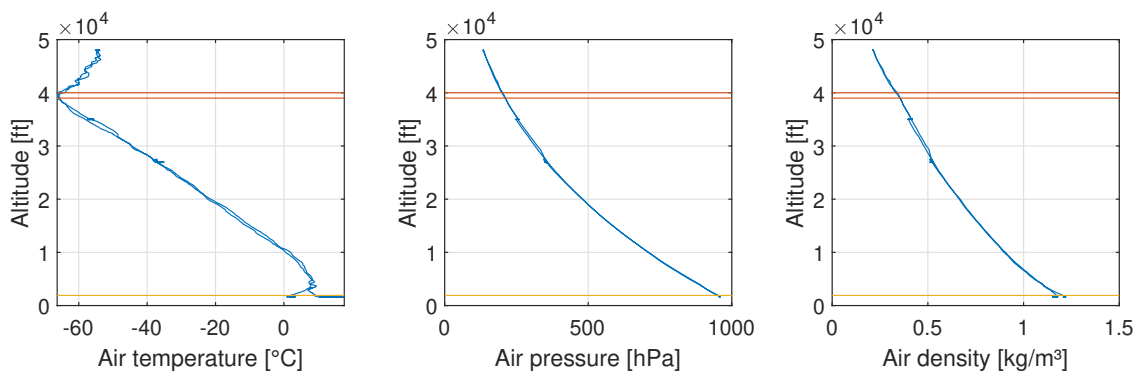


FIGURE 8.13: Measured atmospheric data during one of HALO’s flights as function of the pressure altitude. The temperature varies linearly in a wide range, the air pressure and altitude follow a decaying power law. The horizontal red lines delimit the tropopause. Below them is the troposphere, above them the stratosphere. The yellow line is the ground level. The temperature excursion from early to late morning is recorded in the lower right corner of the temperature plot. See text for discussion.

### 8.2.4 Measurement plan

The HALO flight envelope is reproduced in figure 8.14 as a function of Mach number and pressure altitude with respect to maximal operating conditions and according to certification. The flutter boundary is at a safe distance from the allowed operational range, therefore the steep damping ratio drop of critical wing modes will not be observed. Table 8.1 summarizes the measurement points reported in this chapter. The test campaign defined several stationary measurement points in order to provide a variety of flight conditions and excitation types. The study of the effects of air brakes deployment, rudder kicks, aileron jerks, wake turbulence of a preceding plane and maneuvers on the response are part of the measurement plan and will be elaborated later.

TABLE 8.1: Overview of measurement points (data sets). The first digit of the code denotes the experimental flight, the second digit the specific measurement point.

Code	Pressure altitude	Mach number	Description	Duration
MP11	27000 ft	0.55	Stabilized flight, turbulence excitation	267.4 s
MP12	27000 ft	0.65	Stabilized flight, turbulence excitation	306.3 s
MP13	27000 ft	0.70	Stabilized flight, turbulence excitation	324.4 s
MP14	27000 ft	0.78	Stabilized flight, turbulence excitation	310.3 s
MP15	27000 ft	0.77	Stabilized flight, turbulence excitation, air brakes	304.7 s
MP21	27000 ft	0.70	Stabilized flight, stochastic elevator/aileron excitation	434.5 s
MP40	27000 ft	0.70	Chase flight flying in preceding airplane's wake	375.0 s
MP41	27000 ft	0.53÷0.74	Chase flight as MP40 but with variable speed	2687 s
MP50	<48000 ft	<0.88	Stabilized stochastic elevator/aileron impulses	9650 s
MP51	48000 ft	0.88	Descent maneuver	800 s

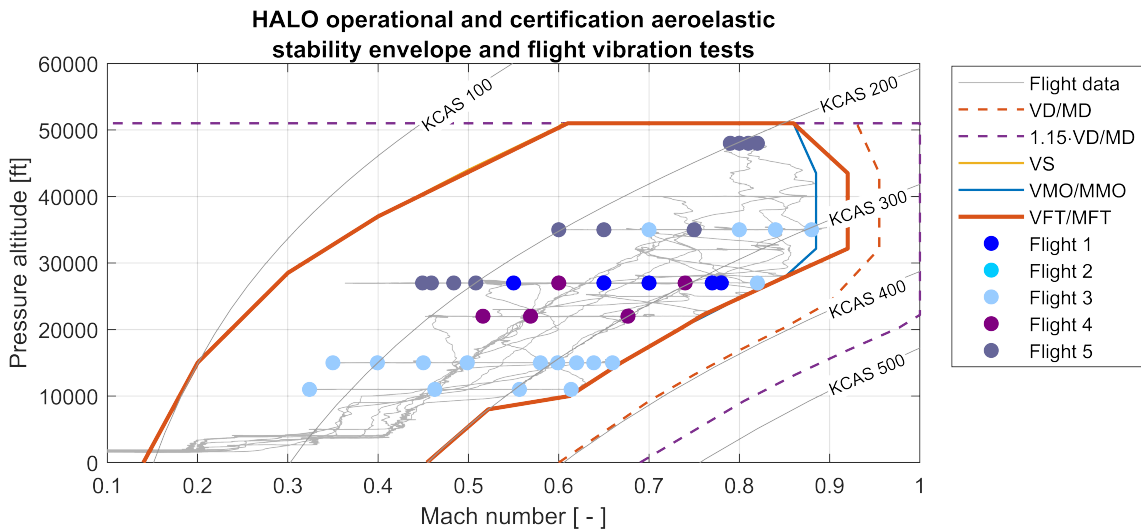


FIGURE 8.14: HALO flight envelope as function of Mach number and pressure altitude. The gray line represents the entire experimental campaign's data. The markers denote stationary measurement points. VD/MD: structural loads design true airspeed/Mach, VS: stall speed, VMO/MMO: maximal operating true airspeed/Mach, VFT/MFT: maximal allowed flight test true airspeed/Mach (according to certification). KCAS: calibrated airspeed in knots. The VS and VMO/MMO are partly or completely covered by the VFT/MFT curve. The flutter boundary is at a safe distance.

### 8.3 Real-time automated modal analysis

The data throughput and the busy schedule during wind tunnel experiments or flight vibration testing require automation. For the task at hand, a real-time automated modal analysis application is deployed to track the evolution of the system's eigenvalues as function of environmental and operational conditions. The purpose of this software is to assist the test engineer during flutter testing. An important factor for success is the ability to process large sensor setups in little time and to produce clear stabilization diagrams. The application developed for automated system identification is called *OnLine Monitoring* (OLM) and meets the following requirements:

- efficient algorithmic implementation: the modal parameters estimates must be refreshed within seconds to provide up-to-date information to the test engineer
- extensive and responsive graphical user interface providing a comprehensive output assisting the test engineer in the interpretation of results
- ability to run continually for indefinite amounts of time and recover autonomously in case of unexpected errors
- ability to track several (possibly closely-spaced) eigenmodes simultaneously

The development of the OLM required a considerable investment in terms of time, therefore it would be a disservice to so much effort not to spend a few words about it. Within the scope of this thesis, many methods have been researched and implemented to perform calculations and analyze time-varying aeroelastic systems. The resulting algorithms have been coupled with a graphical user interface to construct a suite of instruments that can be deployed during experiments. A screenshot of the OLM's graphical user interface is displayed in figure 8.15 as example. The OLM is pictured in action during a wind tunnel test campaign in figure 8.16.

The importance of integration of aeroelastic software development has been recognized early [LOOYE, 1999]. A precursor FVT monitoring application on the HALO is presented in [SCHWOCHOW AND ZÖGER, 2013], where control surface excitation is used in-flight to estimate the damping ratio of critical modes. The first version of the OLM has been deployed in a transonic wind tunnel flutter test to track the damping evolution of critical modes [JELIČIĆ ET AL., 2015]; excitation is provided by air turbulence and shakers. The OLM backbone has been then stress-tested offline using existing FVT data to refine its performance in terms of computational speed and system identification results [JELIČIĆ ET AL., 2016]. The flight vibration test data presented in this chapter were acquired in 2016 by an airworthy OLM version and published in [JELIČIĆ ET AL., 2017]. Since then, the OLM has been deployed to monitor the aeroelastic behavior of a wing with nacelle model in a transonic wind tunnel and to assist the wind tunnel operators while approaching the flutter boundary [BÖSWALD ET AL., 2019; GOVERS ET AL., 2019].



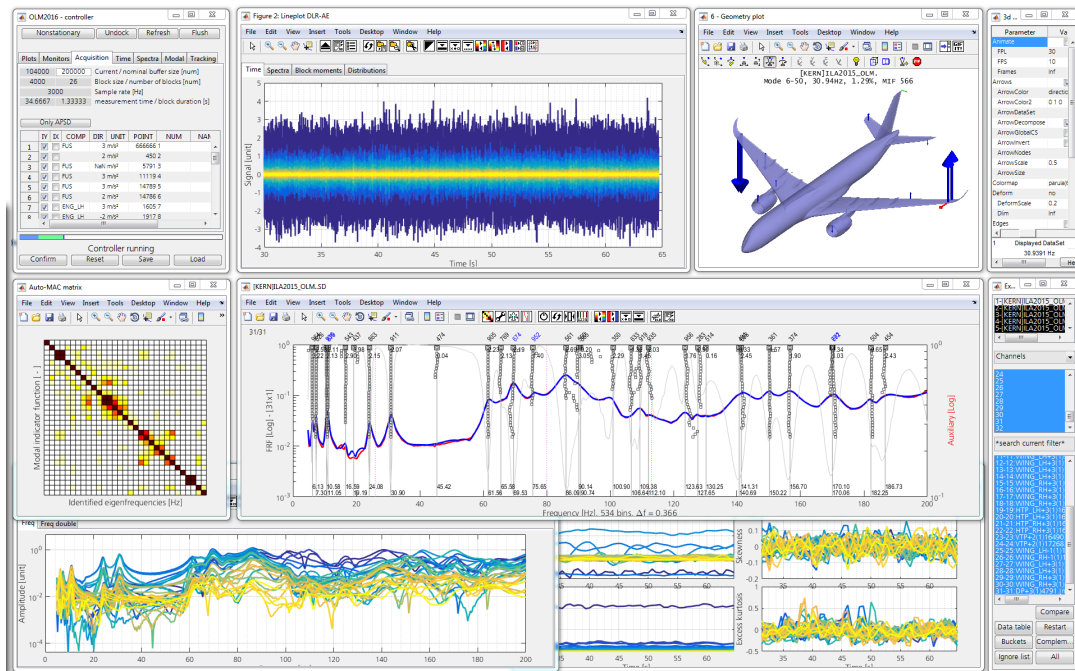


FIGURE 8.15: OLM's graphical user interface. Top row, left to right: window with analysis settings, display of current time data buffer, animated mode shapes plot and options. Middle row: MAC matrix of current modal model, stabilization diagram. Bottom row: spectra of current data buffer, first four principal moments, channel selection window. The user controls which instruments are displayed during experiments.

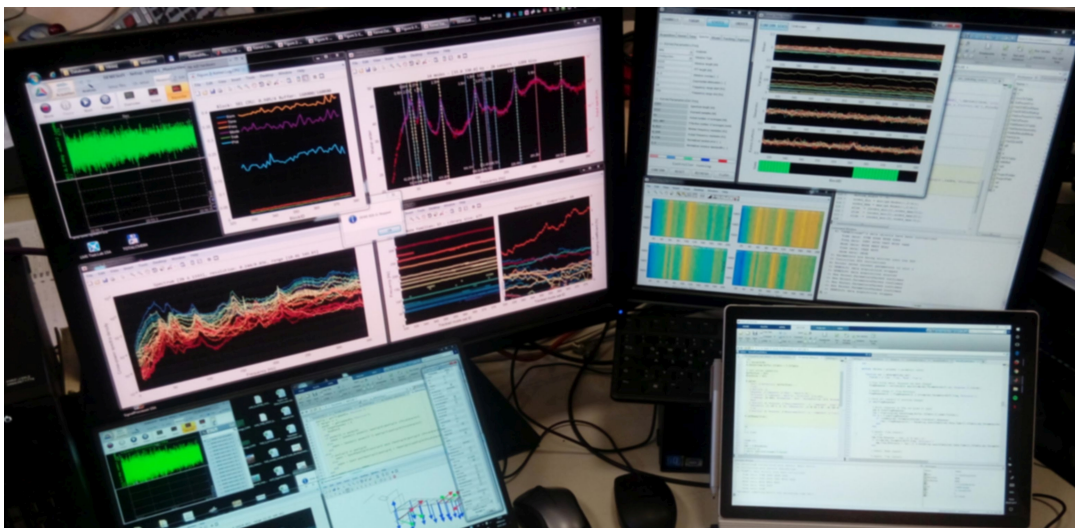


FIGURE 8.16: Computer setup for OLM in a wind tunnel. The two top screens display various instruments and analyses while the experiment is running. A display with estimated spectra, a stabilization diagram, a spectrogram and a tracking can be recognized. The bottom left screen belongs to a computer in a parallel connection that acts as fail-safe. Author's photograph.

### 8.3.1 Design principle

The experience gained with the OLM's precursors made clear that overseeing vibration tests requires considerable internal software development. For example, one requirement is the ability to expand and adapt the suite of instruments according to the test profile.

The core design principle of the OLM is to attain from and contribute to the modal analysis framework used at DLR-AE. This is enforced in order to benefit from the latest scientific developments, from high-quality data visualization meant for publishing and from a larger pool of users for testing and debugging.

The OLM software is written entirely in MATLAB with object-oriented programming. The MATLAB language is well-suited for numeric computing and is widely adopted by the digital signal processing, control engineering and modal analysis communities. Some publicly-available toolboxes and data sets are used as benchmarks. According to experience, fixes and expansions during an experimental campaign are always required, therefore object-oriented programming is much more suitable than "classical" script-based code. The OLM per se acts as a director that manages the hardware data stream, compiles metadata, parses inputs, launches the modal analysis chain, updates the graphical user interface and forwards results to a database. Its algorithmic core is comprised of low-level mathematical functions performing signal processing, system identification and other calculations. Within the scope of this research, several efficient algorithms have been implemented or devised to reach the target performance.

### 8.3.2 Data flow

A general diagram of the OLM data flow is reproduced in figure 8.17:

1. Either a DeweSoft or National Instruments DAQ runs on a dedicated PC ("DAQ computer") that records and broadcasts to a LAN network.
2. Networked PCs ("analysis computers") running a client application forward the acquired data into MATLAB using a DCOM/ActiveX interface. The arrival of new data is detected by the OLM instance.
3. The OLM retrieves a set amount of samples and appends this data block onto a first-in-first-out time data buffer. This event triggers the execution phase, which checks any user inputs or settings, launches the requested analyses and gathers results.
4. The modal analysis output is sent to a database for easy access and browsing.

The OLM is structured as a collection of objects for data acquisition, processing and display, respectively called *Datastream*, *Kernel* and *Monitor* in figure 8.18.

The *Datastream*'s job is to assemble the time data buffer and collect the necessary metadata. This constitutes the data source for all analyses. The buffer typically contains  $10^4 \div 10^5$  samples per channel. Within the course of a measurement campaign several sensor configurations may be tried out, some sensors will have the wrong labels, wiring or direction

and some will fail, consequently a robust channel handling is obligatory. Furthermore, wind tunnel and flight parameters are almost always acquired with a much lower sample rate than accelerometers, therefore at least two data streams with different sampling frequencies must be managed.

The Kernel oversees the analysis parameters and the calculations (see figure 8.19). Input parsing and preprocessing is performed only if there is a change in user input and not at each execution cycle. Low-level but related algorithms are clustered together to ease development and maintenance. Figure 8.20 illustrates the structure of a spectral estimation block as an example.

The Monitor updates the graphical user interface with current results (see figure 8.15). Given the number of instruments and displays, the GUI must be optimized to reduce the CPU time required to refresh the plots.

### 8.3.3 Performance

Computational time complexity is critical because the whole analysis chain must be completed within two refresh events. In particular, spectral analysis and system identification methods are selected by their ability to handle large data sets very efficiently and to produce clear stabilization diagrams. The algorithms are implemented to favor low CPU load over memory efficiency. The OLM must run satisfactorily on a notebook, hence it is important to study the time complexity of its algorithms and to address bottlenecks. Even the cost of data and metadata management is noticeable given the numerous steps in the analysis chain.

The target OLM performance is: a new analysis every two to three seconds. In order to achieve maximum computational speed, said informally, all kinds of optimizations, shortcuts, undocumented features, dirty programming tricks, and hacks have been utilized. Whenever possible, vectorization<sup>6</sup> and lazy copy<sup>7</sup> are exploited. Parallel processing is not employed because set-up time and overhead are a large fraction of the total analysis time, therefore the gain of parallel computation would be eroded according to Amdahl's law at the additional cost of rewriting code. GPU computing is likewise suboptimal because sending and retrieving continually arrays from the GRAM is slow. MATLAB uses automatically multi-threading for matrix division, fast Fourier transform, eigenvalue and singular value decompositions, thus offering a considerable speedup for the most computationally intensive and common operations.

---

<sup>6</sup> Vectorization denotes operations that are performed on whole arrays in one instruction. In MATLAB this is performed, for example, by linear algebra operators. Vectorization improves performance significantly and is thus used whenever possible.

<sup>7</sup> Unlike Python, the MATLAB assignment instruction  $\mathbf{A} = \mathbf{B}$  does not create a pointer/handle  $\mathbf{A}$  to a variable  $\mathbf{B}$ . Instead, it uses lazy copy to create a variable that points to the same memory address (effectively using a pointer/handle!). New memory is allocated *only if* the variable  $\mathbf{A}$  is modified in any way. Performance and code readability can be improved considerably by exploiting lazy copy.

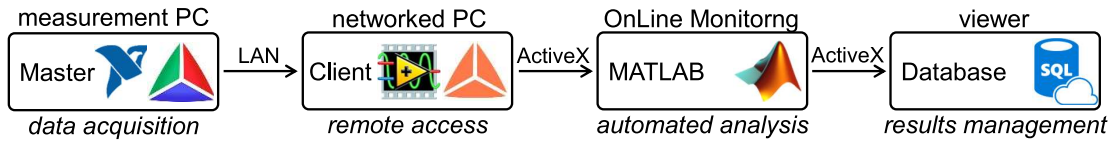


FIGURE 8.17: OnLine Monitoring data flow from acquisition to postprocessing. From left to right: DeweSoft or National Instruments DAQs provide sensor data, networked PCs running a client application retrieve measured data into MATLAB using a DCOM/ActiveX interface, data is processed automatically by the OnLine Monitoring (see figure 8.18). The modal analysis results are organized by an SQL database for easy browsing.

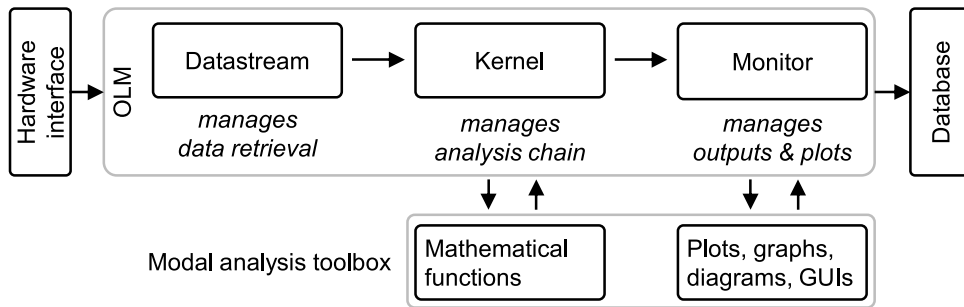


FIGURE 8.18: OnLine Monitoring structure: the Datastream retrieves the latest data and metadata from the hardware interface, appends it to a first-in-first-out buffer and manages all sensor channels. The Kernel then reads any user input or settings, runs the analysis chain and organizes the calculation output (see figure 8.19). The Monitor displays the results and manages the GUIs. Results and metadata are sent to the database.

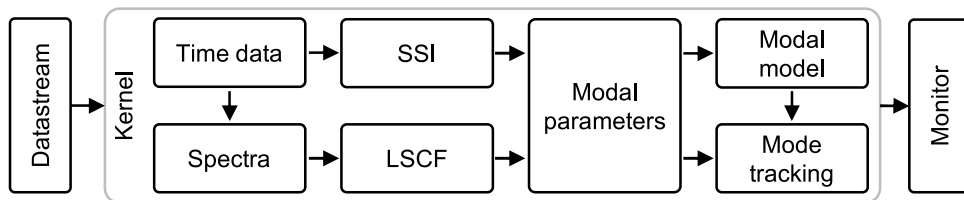


FIGURE 8.19: The OLM Kernel’s modal analysis chain. The “time data” block includes any digital signal processing performed to condition the acquired signals. Spectra are always estimated. Either an SSI or LSCF estimator is used to identify the modal parameters, after which the stabilization diagram is constructed. The tracking diagram is updated when a new data block arrives. Calculations are performed by mathematical functions (see figure 8.20).

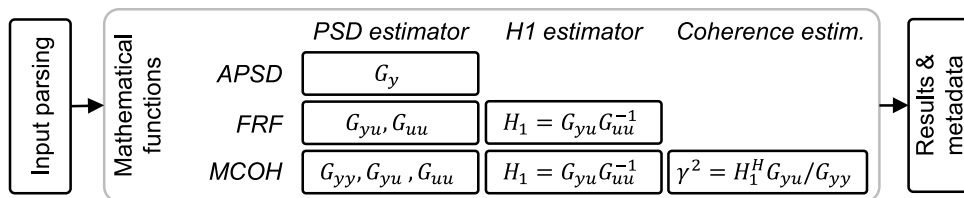


FIGURE 8.20: Mathematical function organization concept. The input parsing is performed separately and only if changes are detected. The algorithmic cores are used by several functions at once to improve speed and maintainability (in this example: APSD: auto-power spectral density, FRF: frequency response function, MCOH: multiple coherence). Results and metadata are collected at the end of the execution phase.

## 8.4 Results

The FVT results are presented in terms of flight parameters, acquired sensor data, estimated spectra, identified modal parameters and tracking diagrams.

The OLM retrieves a block of two to three seconds worth of data (depending on the desired refresh rate) and appends it to a first-in-first-out buffer, which then forms the data source for all calculations. The test engineer tags the data blocks with a code referring to an entry in the measurement matrix and by state (stationary, non-stationary, invalid, maneuver etc...) in order to facilitate offline post-processing.

The time-domain analysis encompasses the measured acceleration response and flight computer data. Vibration data are normally acquired at a higher sample rate than strictly necessary for system identification because of limits imposed by the DAQ, hence the sensor signals are decimated<sup>8</sup> on-line to reduce sample number and frequency range. Accelerometers and flight parameters have different (usually much lower) sample rates, therefore the latter are resampled to match the former.

Spectral analysis includes the estimation of the APSD and spectrogram of the data buffer in order to examine the signals' frequency content, to compare excitation types and to assess data quality. If necessary, digital signal processing is applied at this stage to enhance data quality. The full or positive cross-power spectral density matrix of the responses is estimated only if frequency-domain system identification is performed.

Modal parameters are estimated continually during the course of a test and are displayed in a stabilization diagram, similarity matrix plot, animated mode shapes and tracking diagram. The test engineer can easily follow the eigenvalue evolution of the last hour of flight. Stationary measurement points are evaluated as a whole by dynamically increasing the time data buffer's length until the end of the stationary conditions. The estimated modal parameters are sent to a database to facilitate browsing.

The results in remaining half of the chapter are presented according to the modal analysis chain. Several pages are dedicated to data quality analysis and spectral estimation techniques that guide the experimenter in the search of errors and in the interpretation of system identification results. In the first part of this section we are interested in stationary flight conditions, while the second part treats continuous mode tracking.

*The HALO's eigenfrequencies are adimensionalized because of confidentiality reasons.*

---

<sup>8</sup> Decimation is performed in real-time efficiently by designing an FIR or IIR low-pass filter in advance. The filter has a normalized cut-off frequency of  $0.8/q$ , where  $q$  is the integer decimation factor. The factor 0.8 is set to account for the filter's transition band. Time data is passed through the filter and then every other  $q$  samples are kept.

## 8.5 Stationary system identification

The flight 1 ground track is reproduced on the map in figure 8.21, illustrating a typical mission profile for aeroelastic testing. The experiments during flight 1 take place at three constant altitudes while the Mach number is increased step-wise. The aircraft “flies in circles” because a *temporary reserved airspace* (TRA) is allocated by the air traffic control for every day in the measurement campaign. The maximal duration of a straight flight for each measurement point (see table 8.1) is thus constrained by the size of the TRA. During flight 1 the HALO flew at speeds between 600 and 840 km/h, therefore it can travel straight for 50 to 70 km in 5 minutes before it must turn. The TRA’s size, respectively the duration of a straight flight, imposes a non-negotiable constraint on system identification.

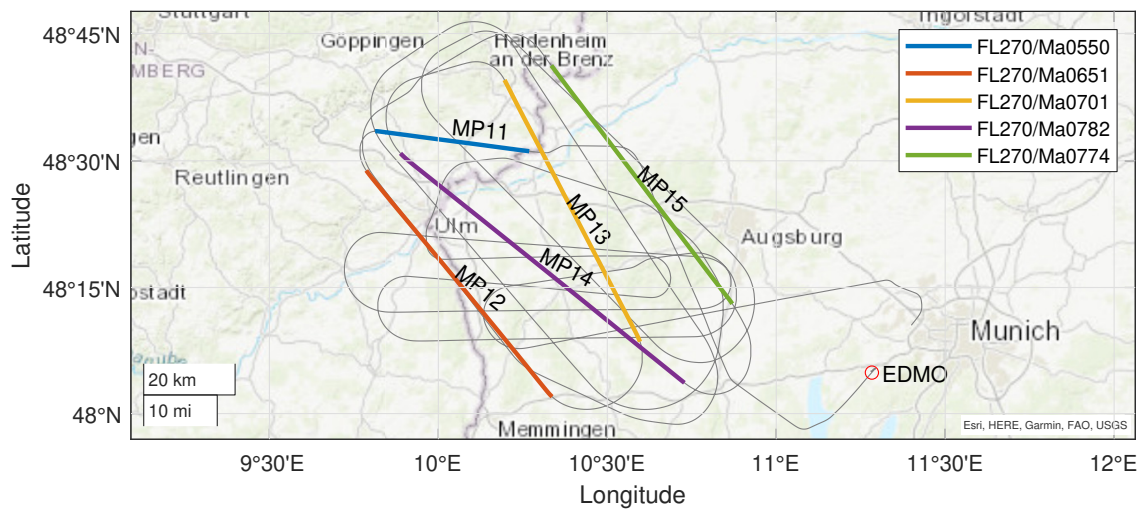


FIGURE 8.21: Flight 1 ground track (gray line). The airfield at DLR-Oberpfaffenhofen near Munich is denoted by its ICAO-code EDMO. The HALO must fly within the temporary reserved airspace (TRA) assigned by traffic control. The measurements points are at altitude 27000 ft, Mach number 0.55, 0.65, 0.70 and 0.78, stabilized flight, with pure turbulence excitation in MP11÷MP14, active air brakes in MP15. The measurement point MP11 is shorter due to an unexpected maneuver.

The flow variables relevant to aeroelasticity are read directly from the BAHAMAS (see instrumentation in section 8.2.1) and plotted in figure 8.22. The air speed is computed using equation (8.1) since the Mach number and static temperature are known. The air density is calculated from the measured static pressure and temperature using the ideal gas law (8.6). It can be noticed that static pressure increases slightly when the aircraft accelerates, whereas the pressure altitude remains constant. As discussed in section 8.2.3, the altitude at which HALO flies is set by the pressure altitude instrument reading and not by the static pressure port measurement. At fixed flight level the air density variation is negligible. Stationary conditions in flight cannot be as precise as those achieved in a wind tunnel, nevertheless within the interval of each measurement point MP11÷MP15 the flow variables do not deviate significantly from the nominal mean (see figure 8.23).

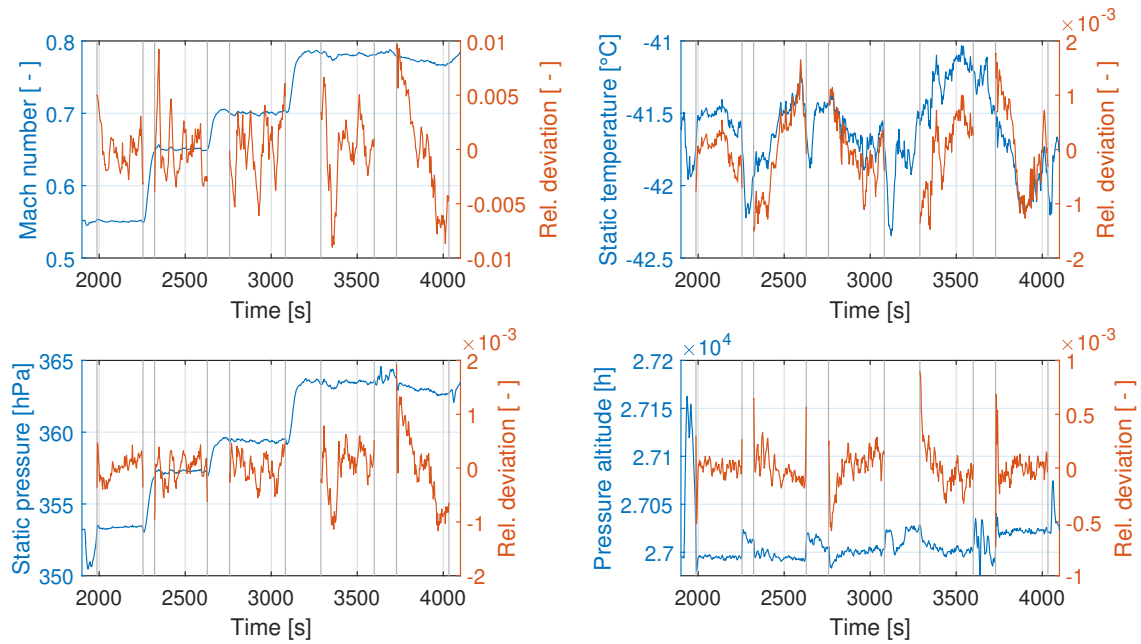


FIGURE 8.22: Flight 1, measurement points MP11÷MP15: measured flow variables (blue lines) and relative deviations from nominal stationary values (orange lines). Each pair of vertical gray lines delimits one measurement point. The Mach number, static pressure, static temperature and pressure altitude are read from the the air data computer (ADC). The temperature, pressure and altitude are constant within 0.2%. Since the temperature is constant, the Mach number and the true airspeed curves have the same shape. The static pressure varies slightly with speed, see text.

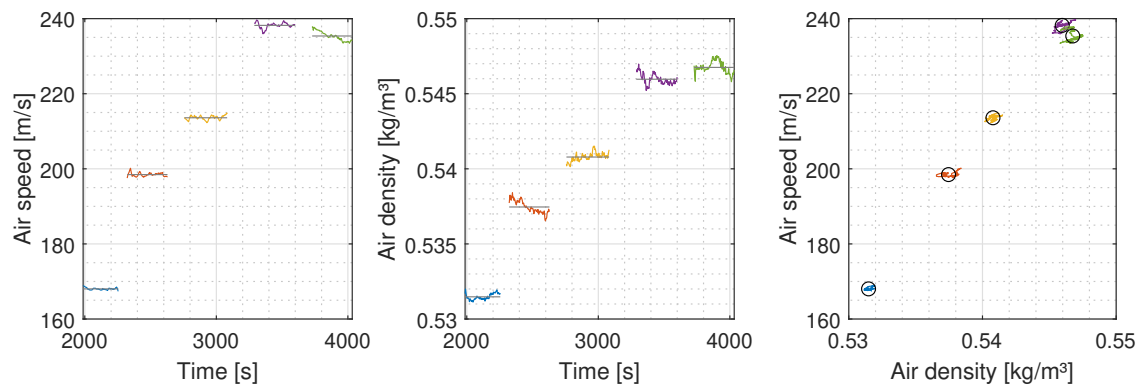


FIGURE 8.23: Flight 1 measurement points MP11÷MP15: aeroelastic quantities. The true airspeed is measured directly, while air density is calculated from the ideal gas law (8.6). The air density varies by less than 0.2 % from the mean value of each measurement point and by less than 3.7 % overall.

### 8.5.1 Time-domain data

Five stationary measurement points have been defined in flight 1 to provide suitable and representative data for the fine-tuning/calibration of the system identification procedure. The signals acquired by all accelerometers during measurement points MP11 to MP15 are displayed in figure 8.24 (straight level flight, see table 8.1). A closer look at the time record reveals that some transients are present, therefore we proceed with statistical analysis. The first four principal moments of the sample data have been calculated in figure 8.25. The appendix A.11 provides more details about their estimation. The mean reveals that some sensors have some drift or very low-frequency components and should be flagged for later analyses. The variance provides an indication of how stationary the excitation level is.

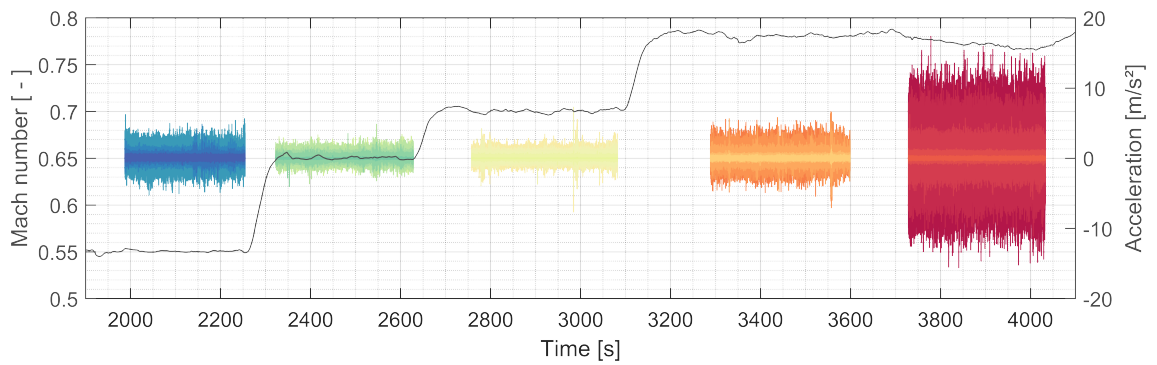


FIGURE 8.24: Flight 1, accelerometer signals during stationary flight conditions. From left to right, MP11÷MP15 are displayed. The black line is the Mach number. The pressure altitude is constant  $h = 27000$  ft. The higher acceleration level at MP15 is due to air brakes deployment.

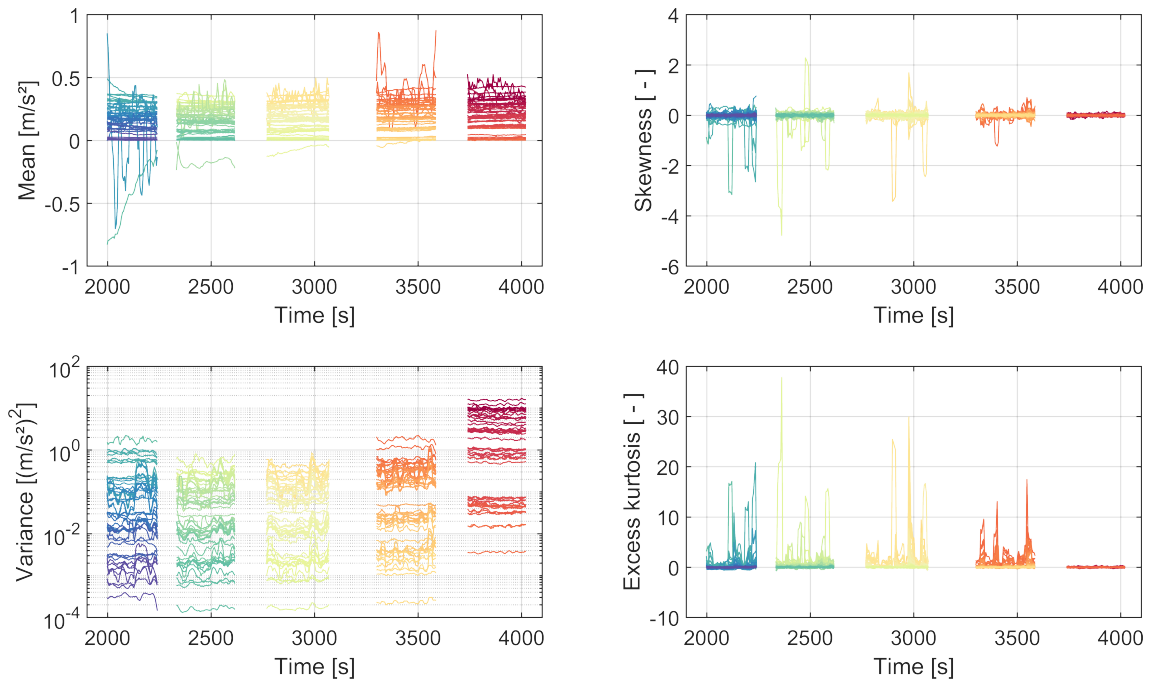


FIGURE 8.25: Flight 1, measurements points MP11÷MP15: first four principal moments of accelerometer signals. The moments have been calculated using the unbiased estimators (see appendix A.11) from 20 s blocks with overlap 0.75. See text for discussion.



The skewness measures the symmetry of a random variable's probability density function. The excess kurtosis quantifies the weight of the tails of a distribution.

Turbulence can be modeled as a normally distributed random variable, therefore, assuming that the aircraft is a linear system, its response must also be a normally distributed random variable. Where the skewness and excess kurtosis are both zero, the response is normally distributed. When nonlinearities are present, the system response can have a different distribution (for example, if a limit cycle is developed, the sample distribution may resemble that of a sine wave). The measured responses have a fairly symmetrical distribution. i.e. there is no preference for one direction or the other. The excess kurtosis plot reveals that the data distribution tends to be leptokurtic (positive excess kurtosis) in MP11 ÷ MP14, which highlights the presence of outliers in the data (the tails of the distribution are heavier). This suggests that in the normal flight regime (without air brakes) the sensors are susceptible to transients, impulsive events, course corrections, gusts or errors. Due to the presence of transient effects, the assumption of ergodicity is violated, but fortunately only locally and temporarily. Nevertheless, ergodicity is a fairly reasonable assumption for steady flight (i.e. the principal moments are independent of time).

Strikingly, when the air brakes are active, the system response is more stationary and normally-distributed. However, air brakes deployment changes the wing's inertial and elastic properties and modifies the flow around it. Raising spoilers impacts the lift in their vicinity by disturbing the attached flow and generating vorticity, which decelerates the aircraft and reduces flight altitude simultaneously. Thus, the measurement points MP14 and MP15 represent effectively two different system configurations. Figure 8.26 illustrates the air brakes deployment.

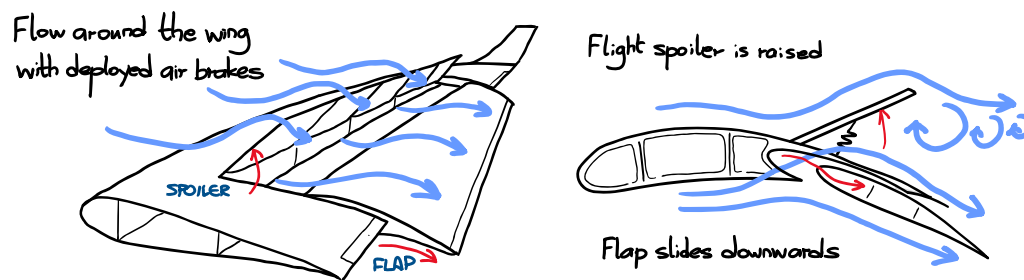


FIGURE 8.26: A schematic representation of airflow around the wing when air brakes are deployed is provided on the left. A wing section is displayed on the right: the flight spoiler is raised to disrupt the suction side flow and the flap slides down to increase lift and drag. The raised spoiler disturbs the attached flow and generates additional vorticity. The flow around the wing and its inertia are thus changed.

### 8.5.2 Frequency-domain data

We recall from chapter 5 that an underlying assumption of OMA is that the magnitude of the input power spectra be constant. Under such condition it is possible to express the output power spectra in modal form 4.21 (weighted sum of simple poles). We also know from section 3.3 that air turbulence has a decaying spectrum, therefore this assumption is not entirely valid, but still helpful for obtaining useful data. In the case of HALO, the three wind spatial components are measured by the five-hole probe positioned at the nose boom. The measured power spectral density in figure 8.27 shows the power-law magnitude decrease with frequency as modeled by the von Kármán spectra (3.35).

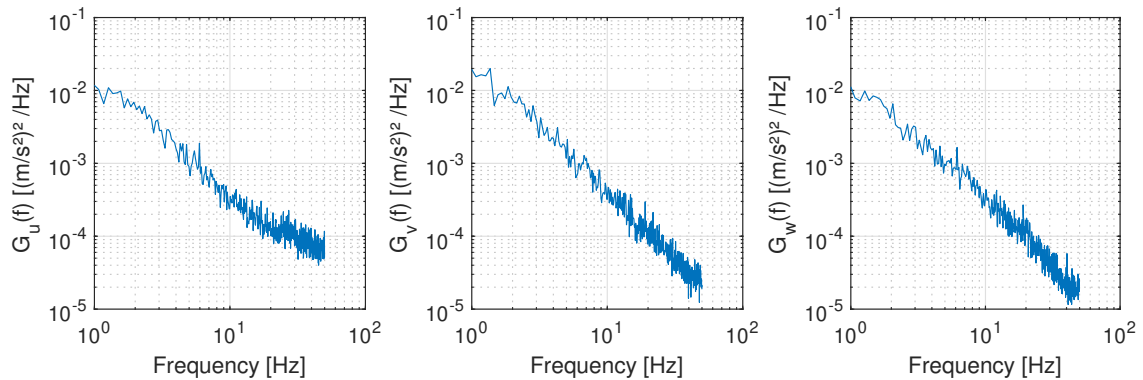


FIGURE 8.27: Auto-power spectral densities of longitudinal  $G_u(f)$ , lateral  $G_v(f)$  and vertical  $G_w(f)$  free-stream velocity components measured by five-hole probe located at HALO's nose boom. The lateral and vertical components are very similar.

The recorded aircraft response is monitored by a spectrogram in order to observe the variation of its frequency content over time. In operational modal analysis, the spectrogram provides vital information about transients, stationarity or harmonic components; the PSD plot alone is not sufficient because it condenses any information about spectral variance. The spectrogram is used to gain precious insight into the acquired data and to set up the system identification, particularly concerning the choice reference channels and frequency range for SSI or LSCF. Figure 8.28 displays the spectrogram of a triaxial sensor (see figures 8.8 and 8.9 for the instrumentation). In this case it highlights the magnitude variance over nominally stationary conditions and the energy distribution over frequency depending on sensor direction. Figure 8.29 displays the power spectral density for all sensors grouped by component and by direction (evaluated over stationary conditions). The sensors of the hanger beam, PMS carrier, wings and winglets are arranged symmetrically on the left and right sides of the aircraft. Each pair has almost identical response spectra. Some sensor/direction combinations have systematically low response levels (for example lateral hanger beam and wings, longitudinal fuselage and under-wing stores). In some channels, the frequency range where the PSD sets on a “noise plateau” and does not have visible antiresonances indicates a low signal-to-noise ratio (for example for the  $y$ -direction sensors on the wing and hanger beam components). Such sensors are excluded from the reference channel selection.

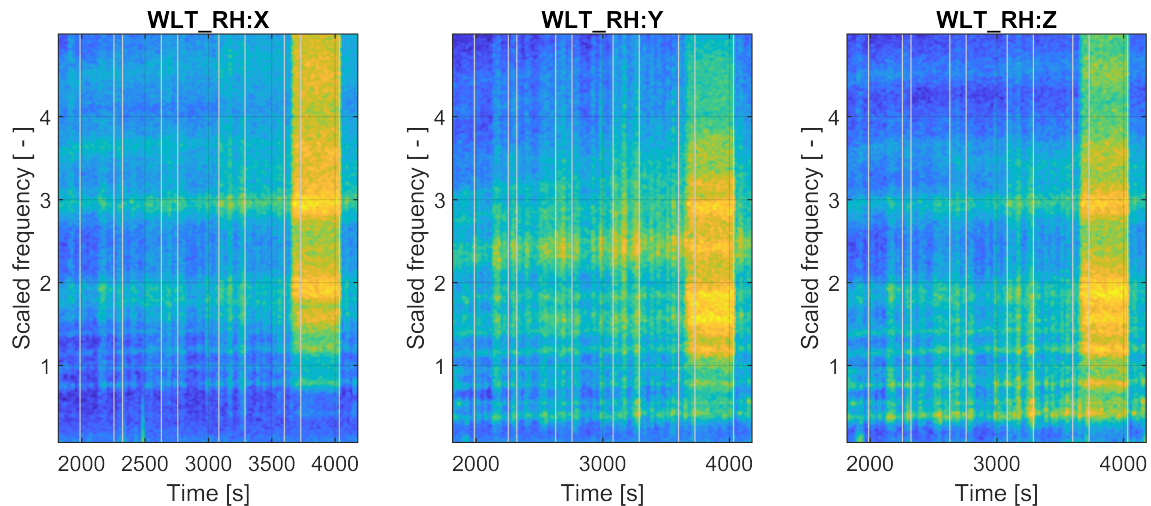


FIGURE 8.28: Flight 1, spectrogram of a triaxial sensor on the right winglet. From left to right, each pair of gray lines delimits MP11÷MP15. The resonance peaks of elastic modes  $f < 2$  are clearly visible. This spectrogram illustrates nicely the broadband effect of air brakes deployment compared to pure air turbulence. The spectrogram is estimated by the segmented multi-taper method (algorithm 3) to produce a better qualitative time-frequency representation of the data.

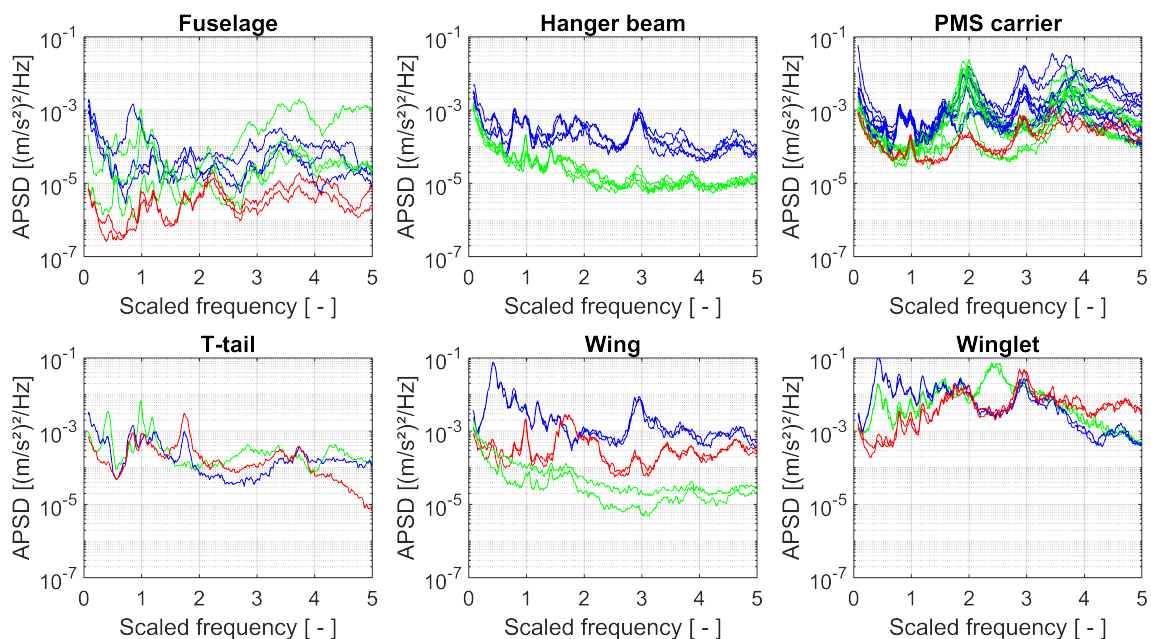


FIGURE 8.29: Flight 1, measurement point MP13: power spectral density of all sensors grouped by component. The colors denote the sensor direction: red:  $x$ -direction (longitudinal), green:  $y$ -direction (lateral), blue:  $z$ -direction (vertical). The PSD of stationary points is here estimated with Welch's modified periodogram; a Hann window with optimal overlap is used and its size is set to obtain at least 50 averages. See text for discussion.

The power spectral density of the vertical winglet sensors during stationary flight is displayed in figure 8.30. It can be noticed that the excitation level grows with airspeed and that air brake deployment injects more energy into the system, in particular in the higher frequency range ( $f \geq 2$ ). The variance of the estimated APSD is typical for the system response during FVT (see for comparison another FVT in [JELIČIĆ ET AL., 2016]).

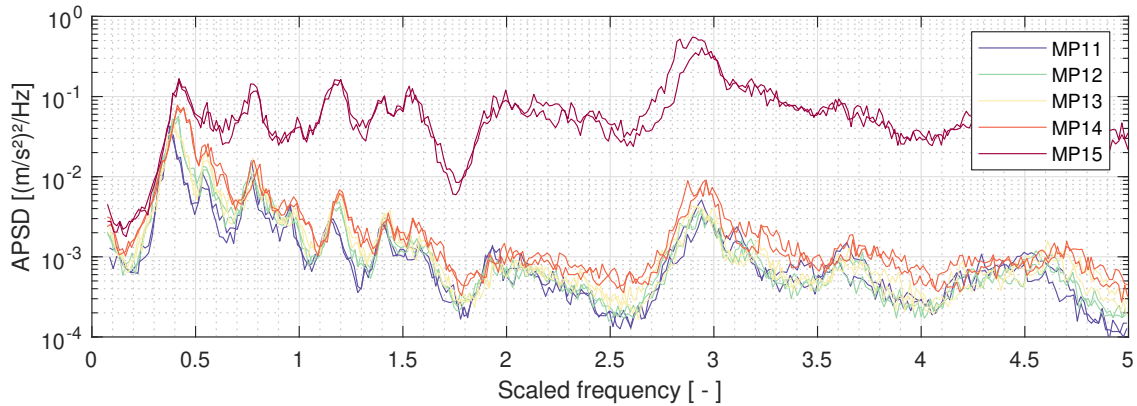


FIGURE 8.30: Auto-power spectral density of the left and right WING+Z sensors for stationary flight level and Mach number MP11÷MP15. The response spectra of the left and right accelerometer are practically identical. The excitation level grows with the Mach number. The turbulence induced by the air brakes clearly injects more energy into higher frequencies. The spectra are estimated using the segmented multi-taper method from about 5 min of data.

Various excitation types have been tested during the measurement campaign in order to assess the capabilities of the system identification methods:

- *Continuous air turbulence* (MP13) is the baseline excitation in terms of magnitude and frequency content encountered during steady level flight. It is representative of the aircraft's design operating condition and does not require any additional excitation devices.
- *Air brakes deployment* (MP15) manifests globally as increased vibration in the higher frequency range. A benefit of this excitation method is that the system response is less susceptible to transients. However, the air brakes alter the aircraft's mass distribution (inertial and elastic properties) and especially the flow around it (aerodynamics), thus deviating from the "nominal" operating condition (see figure 8.26). The flow interaction between the PMS carrier and the extended trailing edge flaps results in a more complex excitation spectrum at its location.
- *Stick raps* (MP21) are random rudder kicks and aileron jerks performed by the pilot. The impulse duration determines the main lobe width in the frequency-domain. The resulting excitation is limited to the lower frequency range and has a modest magnitude increase compared to continuous air turbulence. The physical effort and strain that are required from the pilot restrict this technique. Furthermore, the impulse duration and amplitude are constrained by the aircraft's controls. Control surface excitation for FVT is usually performed by dedicated devices.
- *Wake turbulence* (MP40) was generated by the DLR-Falcon 20-E5 flying ahead at a safe distance. Judging from the response spectra, the spectrum of the wake turbulence appears to have the same shape but different magnitudes compared to the pure continuous air turbulence. However, given that the aircraft tends to be expelled from the wake, the pilot must actively try to fly back inside, which results in an excitation that is hardly stationary.

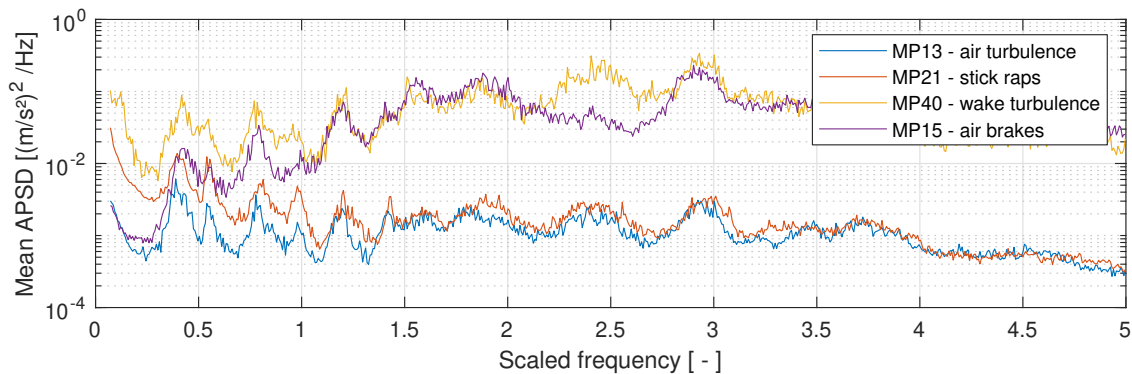


FIGURE 8.31: Comparison of different excitation types. The plot shows the mean APSDs of all channels for  $h = 27000$  ft, Mach number  $Ma = 0.70$  (level flight with constant heading). MP13 is pure air turbulence and noise excitation, MP21 is obtained by stochastic aileron/elevator maneuvers, MP40 is the response spectrum during flight inside the wake of a preceding aircraft. Measurement point MP15 (air brakes,  $h = 27000$  ft,  $Ma = 0.77$ ) is plotted for comparison.

Figure 8.31 compares the power spectral densities acquired for different excitation types for the same altitude and Mach number. The spectra have been estimated at constant altitude and speed and with a long buffer in order to determine an average.

The stationarity of the response can be conveniently visualized by a persistence spectrum in figure 8.32. This is essentially a histogram of the occurrences of a combination of frequency bin and spectrum amplitude that is displayed as an image. It can be also seen as quantifying the percentage of time a given frequency component is present in the signal. The more stationary the data are, the more the persistence spectrum approaches the mean obtained from the whole data buffer.

Furthermore, the presence of transients in frequency-domain can be quantified by the spectral kurtosis  $k(f)$  of each response  $y(t)$ :

$$k(f) = \frac{\langle |\tilde{y}(t, f)|^4 \rangle}{\langle |\tilde{y}(t, f)|^2 \rangle^2} - 2 \quad [\text{adim}] \quad (8.8)$$

where  $\tilde{y}(t, f) = \int_{-\infty}^{+\infty} y(t)w(t - \tau)e^{-2\pi ft}dt$  is the short-time Fourier transform of the signal,  $w(t)$  the window function and  $\langle \cdot \rangle$  is the time-average operator. If the response contains only stationary Gaussian noise, then  $k(f)$  is asymptotically normally distributed with zero mean and variance  $4/N$ , where  $N$  is the number time bins of  $\tilde{y}(t, f)$ . Mode details can be found in [ANTONI, 2006]. Spectral kurtosis can be used as a type of weighting for system identification because frequencies with larger kurtosis (more variance or transients) can be weighted down in the pole estimation. Figure 8.33 displays the spectral kurtosis of a vertical wing sensor for different excitation types.

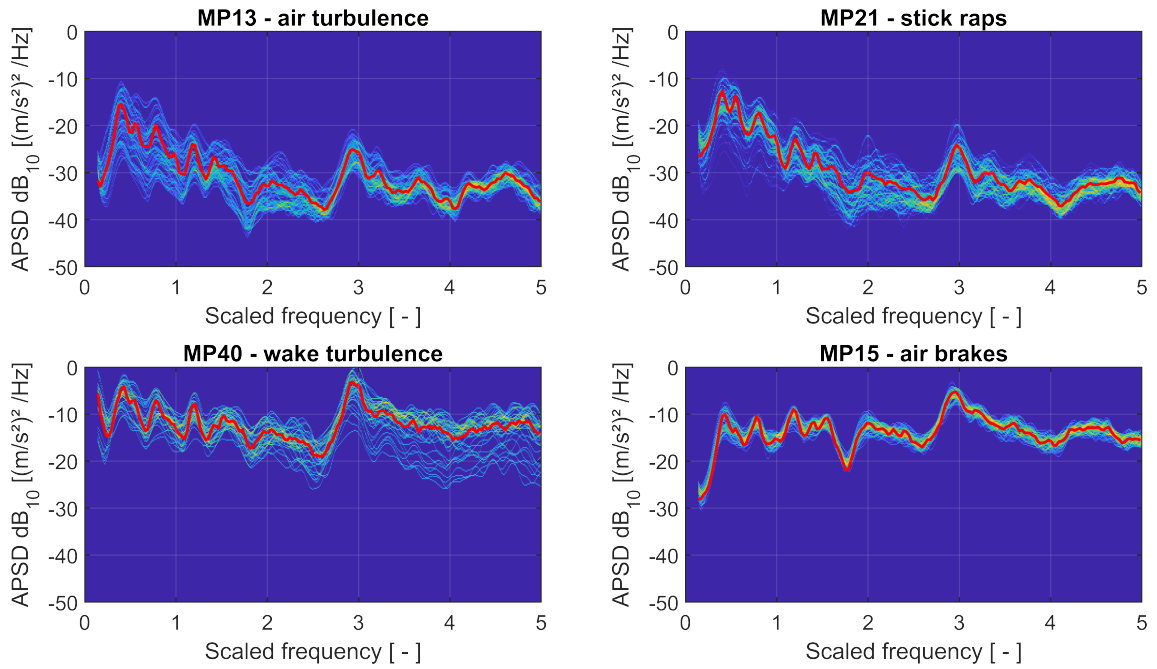


FIGURE 8.32: Persistence spectrum of a vertical wing sensor for various excitation types (same data as in figure 8.31). The red line is the APSD estimated from the whole data buffer. The image is the persistence spectrum estimated from short blocks of 4096 samples, 0.75 overlap and 128 amplitude levels (yellow: high occurrence, blue: no occurrence).

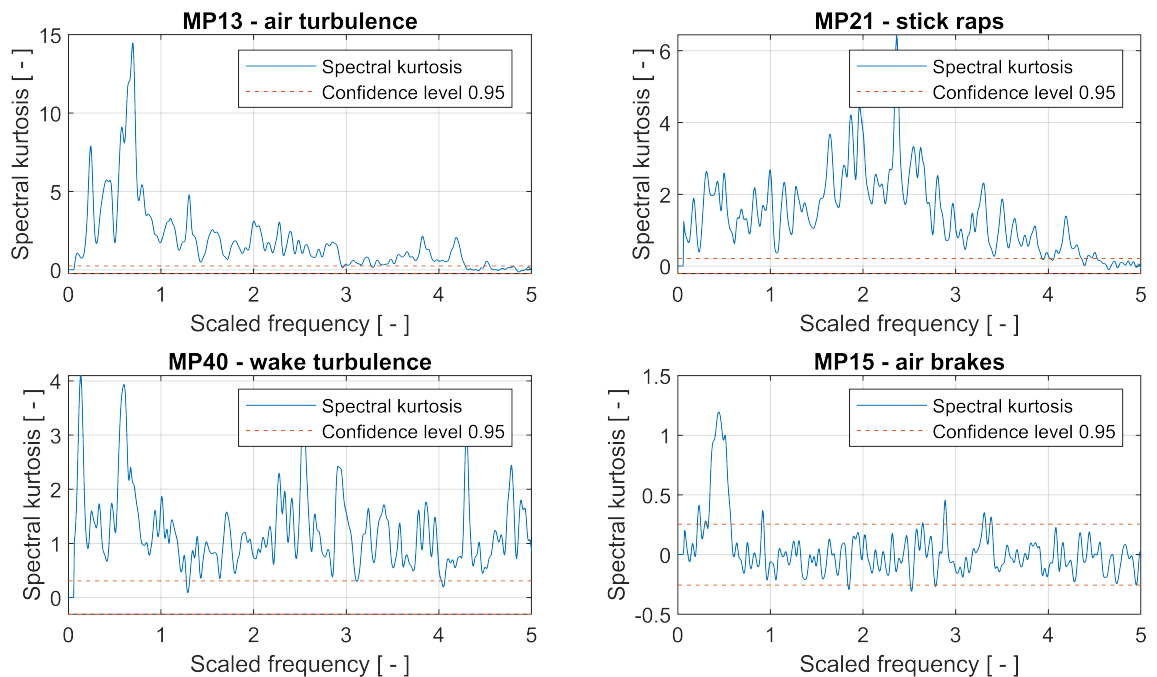


FIGURE 8.33: Spectral kurtosis of a vertical wing sensor for various excitation types (same data as in figure 8.31). The band delimited by dashed red lines contain the area of stationary and normally-distributed signals with a confidence interval of 95%. The larger the amount of spectral lines within this band, the smaller the effect of transients. The data is leptokurtic (more concentrated around the mean and with heavier tails of the distribution).

### 8.5.3 Reference channels

System identification methods such as SSI-ref and LSCF require reference signals chosen among the available responses. In the OMA context the selection of reference channels may not be straightforward because of noise and transients. It is known from experience that the reference channel selection should be balanced according to the modes of interest, i.e. the sensor locations and orientation should be representative of the most important mode shapes. For instance, if we consider HALO's modes 8.12, we see that the wing's participation is significant, therefore vertical wing sensors should be included. A possible and effective criterion is to select the most stationary and normally-distributed outputs as references. It is possible to localize transients in both the time and frequency domains and to select the reference channels accordingly. As already shown in figure 8.25, a fairly simple way of revealing the presence of outliers and errors in the data buffer is the estimation of the principal moments of each data block, specifically when skewness and kurtosis vary unpredictably over time. For example, sensors whose principal moments deviate considerably from the trend of all other sensors during steady flight may be faulty or detached and should be ignored. Since the airplane is constantly performing course corrections, the movement of the control surfaces appears to have a noticeable effect on the measured responses even during steady flight. To this end, the stationary measurement points MP11 to MP15 from flight 1 have been analyzed in detail before flight 2 in order to gain more knowledge about the system.

### 8.5.4 Harmonic components

The presence of extraneous frequency components due to operating rotating machinery – pumps in wind tunnels, engines in aircraft – can disrupt the modal parameter estimation. Engine harmonics appear as well-defined and narrow peaks in the frequency domain. If they are stationary, the identification algorithm will correctly find a damping ratio equal to zero at the right frequency (see, for example, the stabilization diagram 5.1 in chapter 5). However, if they vary within the spectral estimation buffer, they can form a wide peak akin to the example in figure 8.2. Fortunately, for the HALO experimental campaign the frequency range of interest is below the engine's RPM. [BRANDT, 2015] discusses periodic disturbances in machinery.

### 8.5.5 System identification

System identification on stationary data sets is performed by OMA techniques described in chapter 5. The stationary measurement points are held for approximately 300 seconds (see table 8.1), which is appropriate given the low eigenfrequencies of the aircraft. The purpose of these measurements is to provide information for continuous tracking, which will be discussed in the next section. The determination of the damping ratio of the first few elastic modes is important for aeroelastic testing, therefore system identification is tailored towards this goal.

The SSI algorithms require decimation or resampling to reduce bandwidth and computation time because the frequency band of interest  $\Delta f_B$  is very small compared to the sampling rate  $f_s$  (in this case:  $\Delta f_B/f_s < 0.02$ ). Figure 8.34 displays a typical stabilization diagram obtained by the data-driven SSI. The DAQ computer performs the first decimation stage before transmitting the data to the analysis computers in order to increase  $\Delta f_B/f_s$ . In some cases, identification results can be improved by removing the low-frequency components around DC. In principle it is possible to use a low-pass or band-pass filter to reduce the bandwidth at will, but this approach is difficult to realize during FVT because

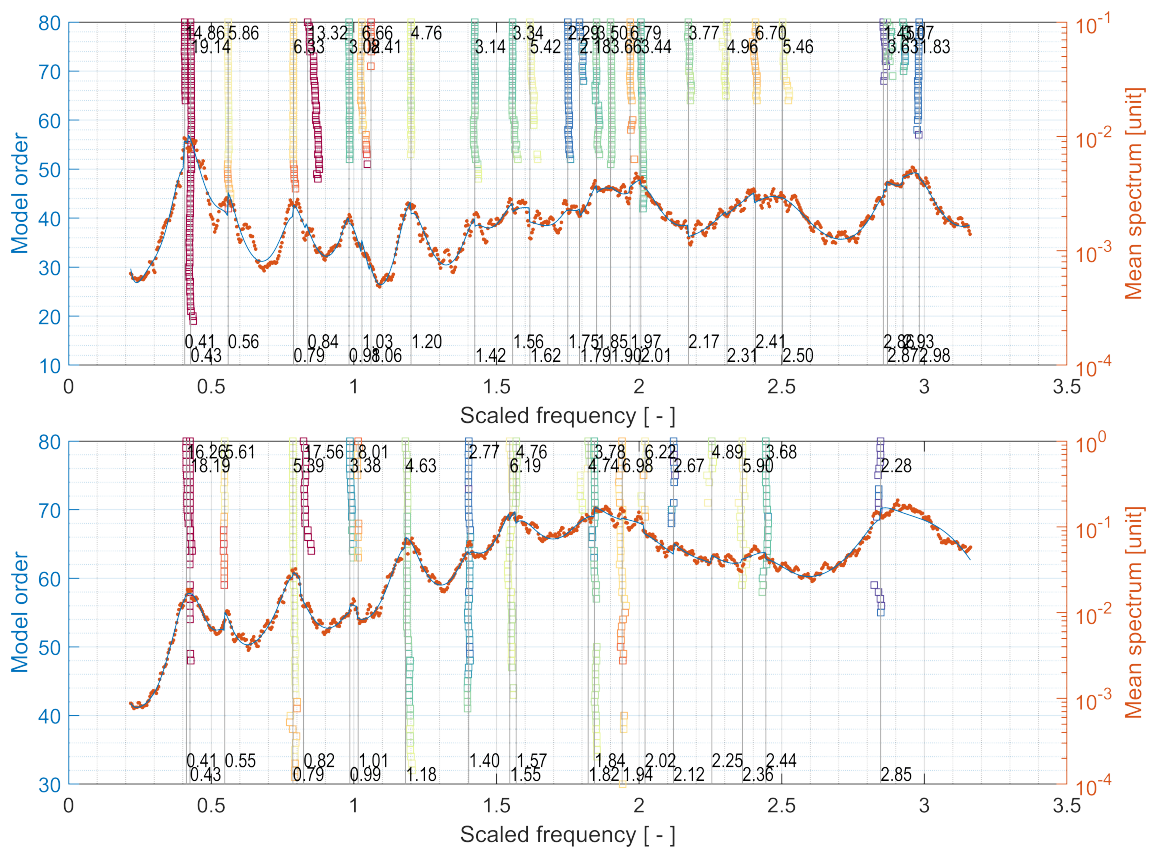


FIGURE 8.34: Stabilization diagram of measurement points MP14 (top) and MP15 (bottom) (flight level 27000 ft,  $Ma = 0.78$  and  $Ma = 0.77$ , without and with air brakes). The eigenvalues have been identified with SSI using a single band  $[0.25, 1.75]$  and  $[1.7, 3.15]$  for orders up to 80, without weighting and without any pole sorting/filtering. The use of two bands reduces the overall model order.



it requires careful filter design (for instance, the requirements on the filter's transition band might be too tight). Instead, another decimation stage followed by a frequency shift is applied as detailed in section 5.4.4. Another possibility is to use mode tracking to remove the spurious poles around DC.

The LSCF algorithm estimates modal parameters either from the full or positive cross-power spectral densities. The former can be computed very efficiently with Welch's modified periodogram or the multi-taper method (see section 4.3). The latter are more computationally expensive, but they can be coupled with exponential windowing to reduce noise and are easier to fit when estimating the mode shapes. Given the amount of sensors on the HALO, the poly-reference pLSCF algorithm has been found to be computationally feasible only when a limited number of reference channels is selected. This may be necessary depending on the data quality. A stabilization diagram obtained with LSCF is displayed in figure 8.35.

The stabilization diagrams in figures 8.34 and 8.35 reveal that the excitation type (air turbulence versus air brakes) affects identified modes, particularly in the range above  $f > 1.5$ . The ambient excitation can be considered white noise colored by some filter whose poles are highly-damped, therefore they can be easily separated from structural poles. Certain excitation types have repercussions on damping identification, i.e. the estimated

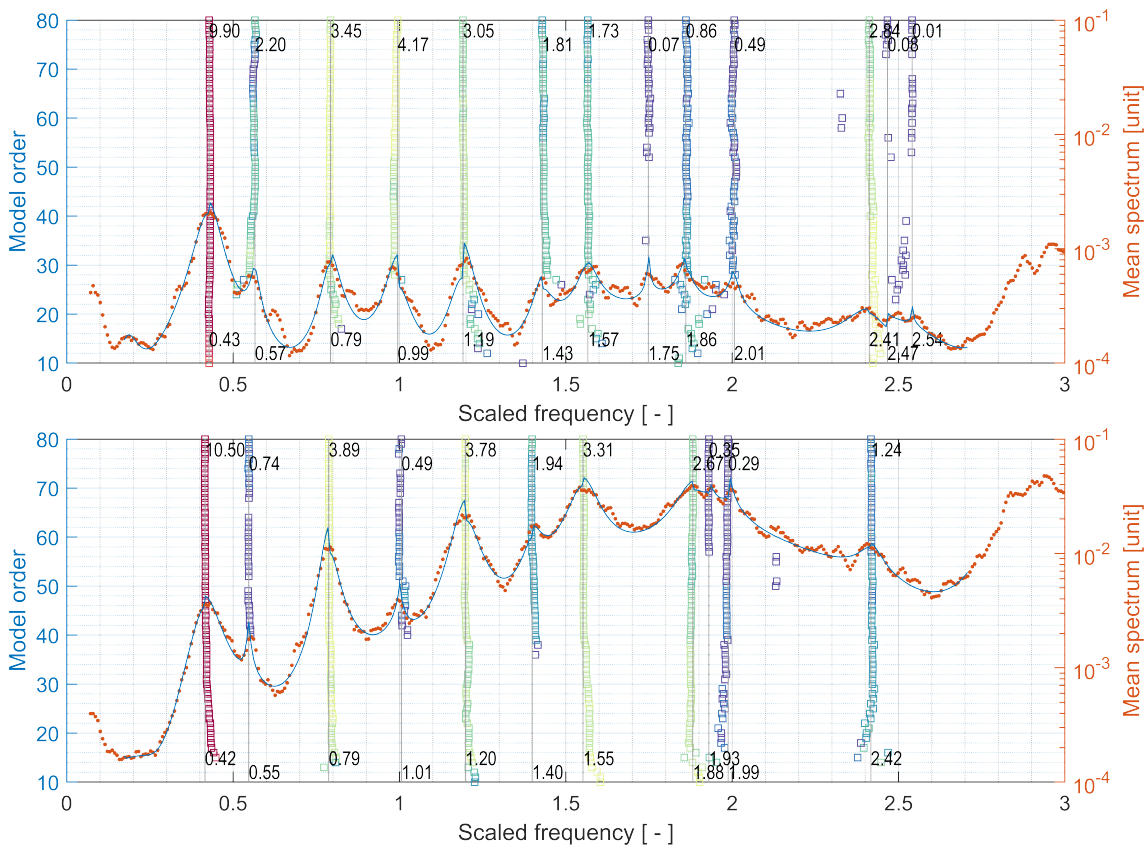


FIGURE 8.35: Same data as for 8.35, frequency-domain system identification. The data source for LSCF is a  $48 \times 38$  output CPSD matrix. The eigenvalues are identified using two bands  $[0.25, 1.75]$  and  $[1.7, 3.15]$  for orders up to 80 without weighting and without any pole sorting/filtering. The resulting stabilization is of clear interpretation.

damping ratio is very low and the corresponding peak fit is not good or the estimate does not converge along a column of the stabilization diagram. For example, in figure 8.35 the second  $f_2 = 0.55$  and fourth  $f_4 = 1.01$  modes are not identified well when air brakes are active. Another tell-tale sign is the complexity of the associated eigenvectors: the mode shapes of aeroelastic systems do become more complex, but with a smooth phase difference between neighboring degrees of freedom compared to badly-identified mode shapes. Complexity due to bad identification can be easily spotted by the test engineer, but can still confuse the tracking algorithm. This happens often to antisymmetric wing modes and will be observed when performing continuous tracking.

The identification algorithms have been studied with numerical data in chapter 7, particularly with regard to damping estimation. In the OMA framework with real data, eigenfrequencies can be estimated well, whereas accurate damping estimation is much more difficult or sensitive to errors. In this regard the tested SSI algorithms tend to provide higher (less conservative) estimates than LSCF in terms of mean values. LSCF always requires the careful selection of reference channels, whereas this is only the case for the reference-based SSI-ref algorithm. On the other hand, LSCF appears to be able to work with smaller buffer lengths and benefits from direct access to various spectral estimation techniques. LSCF usually requires a lower model order (defined as the size of the matrix that must be decomposed to extract the estimated eigenvalues). Table 8.2 condenses a comparison of SSI and LSCF as transpired from their application to the HALO flight vibration data. The two system identification methods will be applied interchangeably, depending on data set at hand.

TABLE 8.2: System identification methods in the OMA framework. This comparison applies to the modal analysis of HALO data.

Method	Advantages	Disadvantages
SSI	<ul style="list-style-type: none"> <li>• Direct time data processing</li> <li>• Fewer identification parameters</li> <li>• Better damping estimate</li> </ul>	<ul style="list-style-type: none"> <li>• Requires data/bandwidth reduction (filtering/resampling/decimation)</li> <li>• High model orders unless multi-band processing is used</li> <li>• Less clean raw stabilization diagram due to spurious modes around DC</li> </ul>
LSCF	<ul style="list-style-type: none"> <li>• Simple multi-band approach</li> <li>• Clean raw stabilization diagram</li> <li>• Works with short data block lengths and low model orders</li> </ul>	<ul style="list-style-type: none"> <li>• Selection of reference channels</li> <li>• Requires spectra with correct parameters (more computation time)</li> <li>• Worse damping estimate if a lot of noise is present</li> </ul>

### 8.5.6 Eigensurface reconstruction

The experimental flutter curves are normally determined by stabilizing at a certain altitude and by performing system identification for all Mach numbers of interest, as illustrated in figure 8.4. The result is a graph of the eigenfrequency and damping variation over true airspeed or Mach number. The flutter diagram reconstructed from part of flight 1 is shown in figure 8.36.

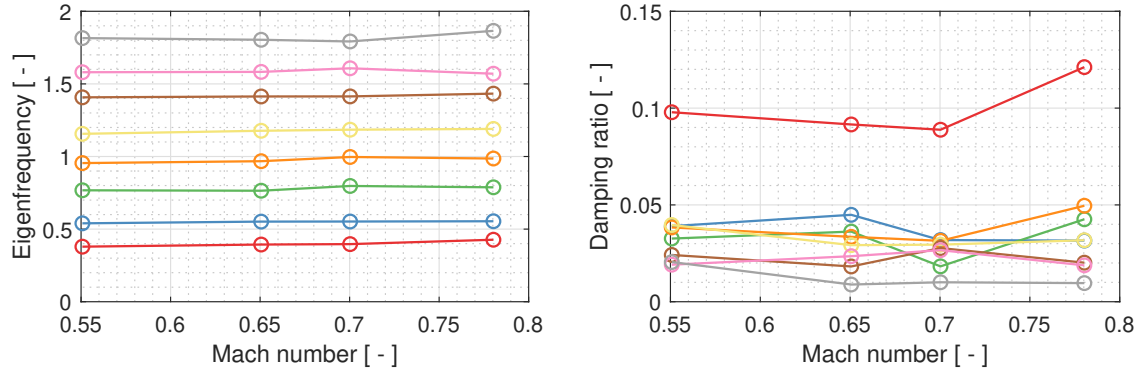


FIGURE 8.36: Flutter diagram reconstructed from MP11–MP14. Measurement point MP15 is excluded because air brakes are deployed. The first eight elastic modes are shown (see figure 8.12). The estimated eigenvalues are denoted by markers and connected by straight lines. Aerodynamic effects on the first symmetric wing bending (mode 1) result in high damping.

The HALO campaign planned several measurement points where the aircraft is stabilized and excited purely by turbulence (not all stationary measurement points have been included in table A.1). This data is used to construct the eigensurface of the first symmetric wing bending, i.e. the eigenfrequency and damping ratio as functions of two aeroelastic variables. Figures 8.37 and 8.38 present the reconstructed eigensurface. The flight parameters do not lie on a regular grid (see flight envelope and test points in figure 8.14) and the identified modal parameters are affected by noise, particularly the damping ratio, therefore the eigensurface is constructed by regression instead of interpolation. We have seen in figure 7.7 in chapter 3 that even analytical eigensurfaces have shapes with sudden bends which may be difficult to describe analytically. No numerical data is available from which to infer an analytical representation, consequently the best fit of a polynomial surface is sought by a robust linear least-squares method with least absolute residuals. The regression results in a third-order function of two variables<sup>9</sup>. Since polynomials tend to overshoot, the fit's domain is only the parameter space enclosed by the convex hull of the available stationary points.

<sup>9</sup> The regression surface has the form

$$f(x, y) = \{1 \quad \hat{x} \quad \hat{x}^2 \quad \hat{x}^3\}^T \begin{bmatrix} p_{0,0} & p_{0,1} & p_{0,2} & p_{0,3} \\ p_{1,0} & p_{1,1} & p_{1,2} & 0 \\ p_{2,0} & p_{2,1} & 0 & 0 \\ p_{3,0} & 0 & 0 & 0 \end{bmatrix} \begin{Bmatrix} 1 \\ \hat{y} \\ \hat{y}^2 \\ \hat{y}^3 \end{Bmatrix} \quad (8.9)$$

where  $\hat{x} \triangleq (x - \mu_x)/\sigma_x$  and  $\hat{y} \triangleq (y - \mu_y)/\sigma_y$  are the centered and scaled independent variables (for example, air speed and air density, or equivalently pressure altitude and Mach number).  $\mu$  and  $\sigma$  are respectively the mean and standard deviation of the independent variables

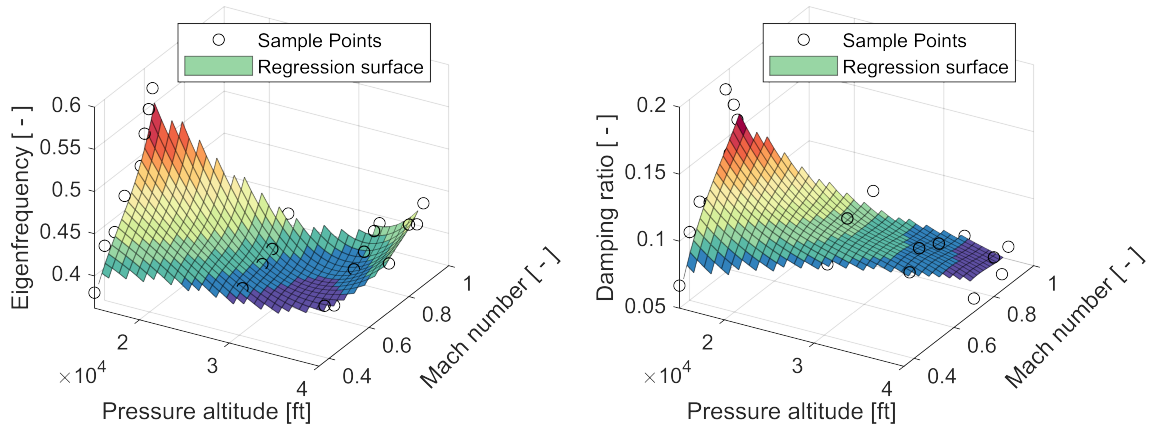


FIGURE 8.37: Eigensurface of the first symmetric wing bending (mode 1) reconstructed from the modal parameters identified at stationary measurements points (denoted by circles in the plots). The eigenfrequency and damping ratio as functions of true airspeed and air density are fitted using a third-degree polynomial surface.

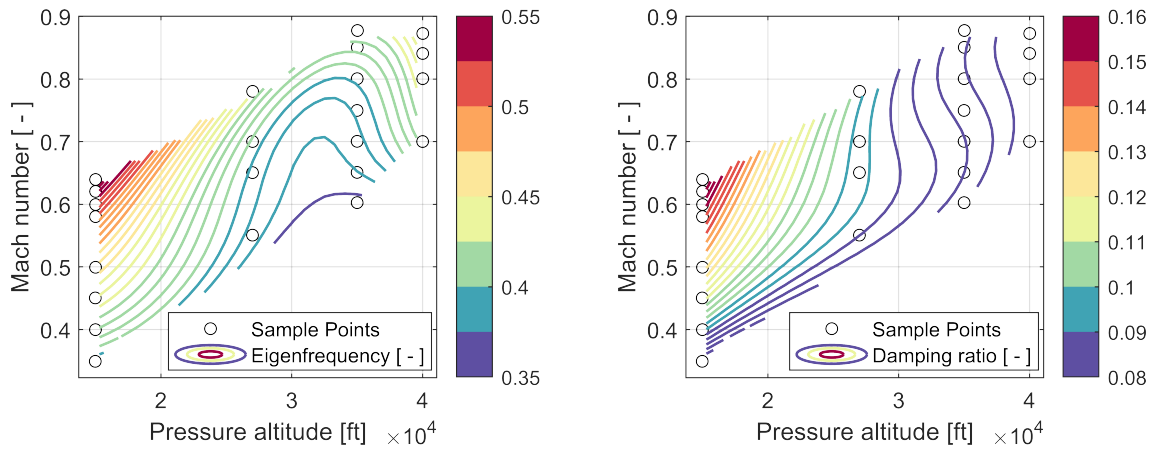


FIGURE 8.38: Contour plot of the eigensurfaces from figure 8.37. The domain of the fitted function is limited to the convex polygon encircling the sample points. The residuals from the resulting approximation are less than 0.01 for the normalized eigenfrequency and less than 0.03 for the damping ratio.

## 8.6 Continuous system identification

The OLM produces permanently new modal analysis results during FVT, therefore mode tracking is carried out to determine the eigenvalues' evolution. As we already know well, the modal parameters' variance is inversely proportional to the buffer duration. In principle the buffer length could be set dynamically depending on flight parameter stationarity, but in practice it is determined through iteration. If the buffer duration is too long, then transient flight parameter variations are averaged out. If the buffer duration is too short, then the modal parameters will be badly identified. The test engineer is thus forced to compromise between responsiveness and accuracy of estimated parameters. The stabilization diagram 8.39 displays a stationary measurement point analyzed first as a single compact data set and then by continuous tracking. The “single” analysis estimates the eigenvalue variance from the whole data set. The “continuous” analysis estimates several mode sets from shorter data blocks. The estimated eigenvalues are clearly scattered, but their centroids are in good accordance with the previous result. In order to be as responsive as possible to aircraft flight parameter variation, continuous tracking attains from a buffer containing only  $40 \div 160$  s of data compared to about 300 s available to stationary measurement points.

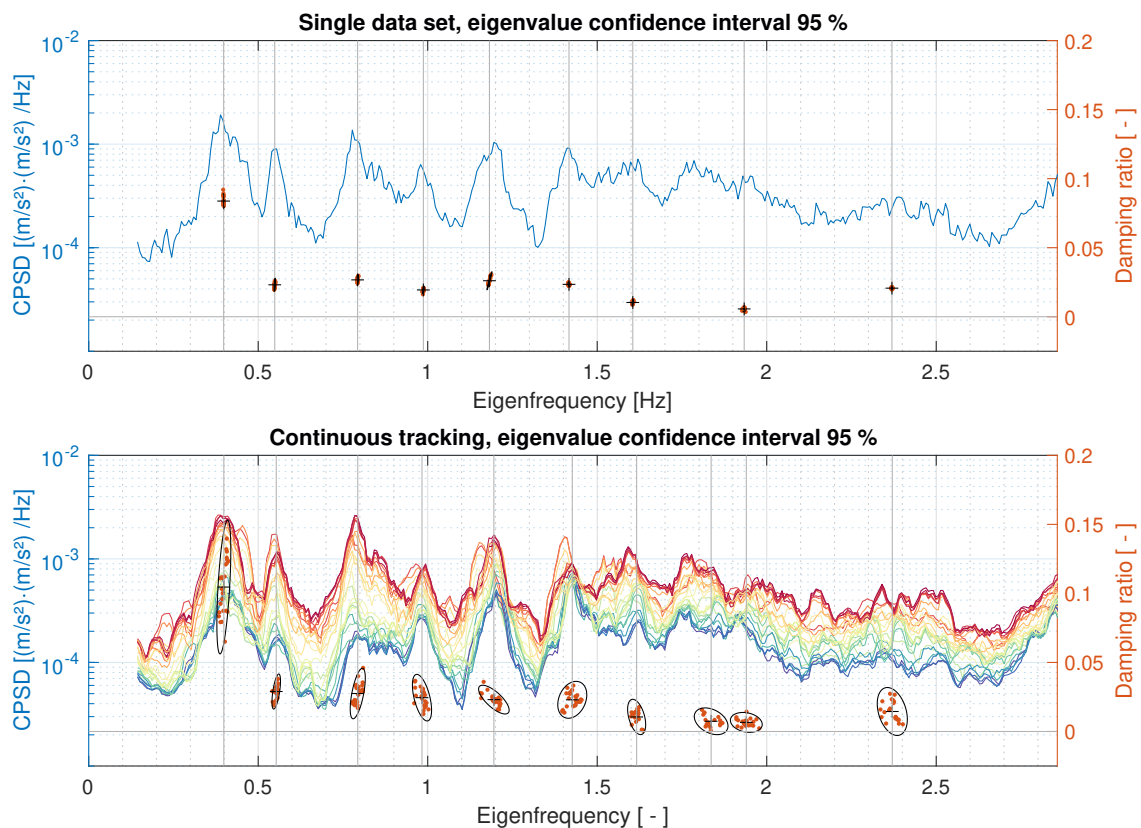


FIGURE 8.39: Modal parameters estimated from measurement point MP14 (steady level flight). The stabilization diagram in the top figure is obtained from the whole dataset ( $T = 300$  s), while in the bottom figure 36 mode sets are estimated from very short overlapping blocks ( $T = 40$  s). The sample covariance of each eigenmode is computed and displayed as an error ellipse. The mean values of eigenfrequency and damping ratio are in good accordance.

The lower limit of 40 s has been found as the minimum duration at which useful results can be produced. This data amount may be too meager for some system identification procedures and leads to a high scatter of damping estimates. Too long a buffer acts as a moving average that “smooths” out the external parameters acting on the system – the maximal duration is thus 160 s for continuous tracking. A new modal analysis is to be completed every two to three seconds, so that the resulting buffer overlap is  $0.925 \div 0.987$ .

### 8.6.1 Chase flight

During the HALO experimental campaign a chase flight was planned together with the DLR-Falcon 20-E5 to create wake turbulence. The purpose was to investigate the effect of wake excitation and of continuous maneuvers on operational modal analysis. The comparison of response spectra for different excitation types has been presented in figures 8.31, 8.32 and 8.33. The illustration 8.40 provides a schematic representation of the chase flight. The Falcon flew about 1 km ahead at constant flight level while the HALO gave chase and carefully approached trying to enter the wake and stay inside. This proved to be not easy because the wake moves and because the aircraft is spontaneously ejected out of it. The pilot must actively maneuver to enter the wake and to keep the aircraft inside it. The maximal turbulence level is experienced when the aircraft is at the wake’s center. In [BURWITZ ET AL., 2017] we provide more information about the chase flight from the perspective of a flight test engineer.

Figure 8.41 displays the flight track of the chase flight. The flight parameters are plotted in figure 8.42. The pressure altitude is kept at 27000 ft, but the static pressure does vary a bit, leading to a 2% variation of air density. The static temperature is constant within 0.4%, therefore the true airspeed and Mach number curves have virtually the same form. The main aeroelastic parameter during the chase flight is the true airspeed.

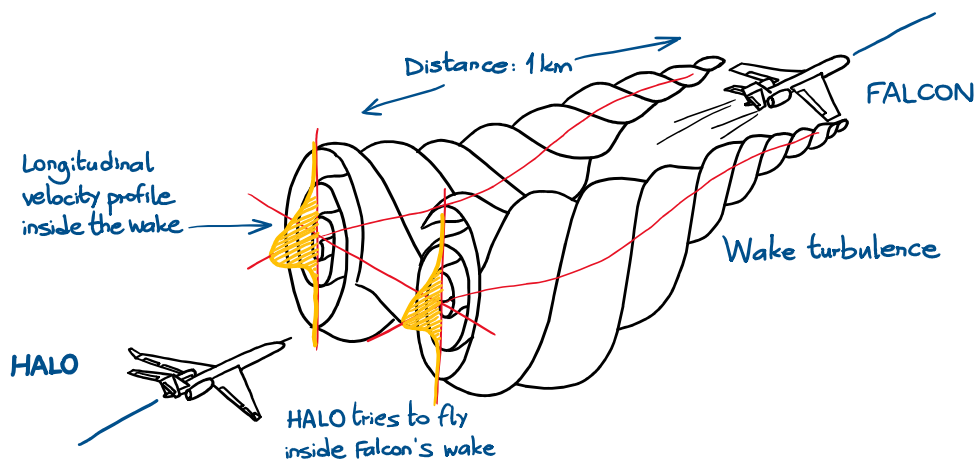


FIGURE 8.40: Schematic representation of the chase flight. The DLR-Falcon 20-E5 aircraft flew 1 km ahead of the HALO. The HALO maneuvered to enter the wake and stay in its central region in order to experience the highest atmospheric turbulence excitation level.

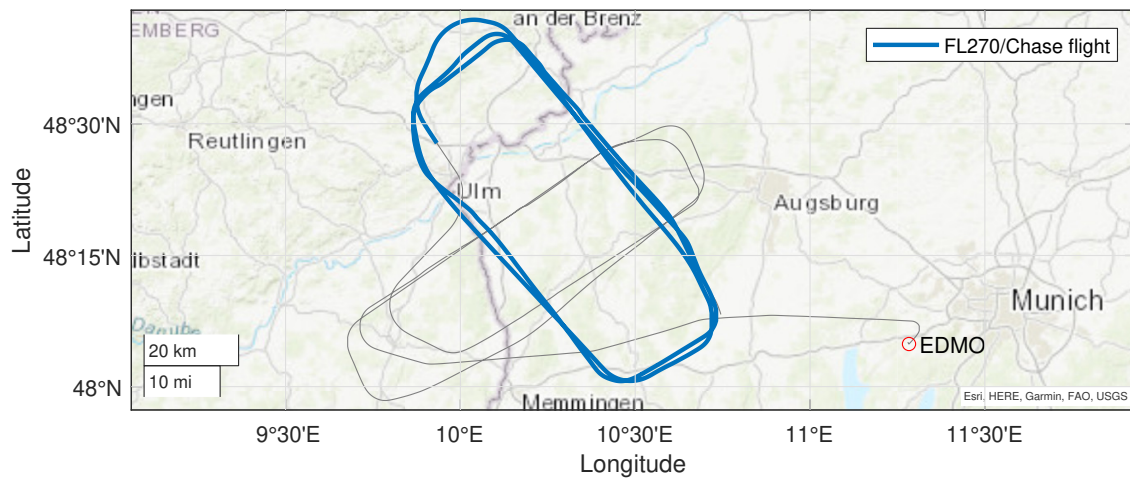


FIGURE 8.41: Flight 4 ground track (gray line), and HALO chase flight at 27000 ft (blue line).

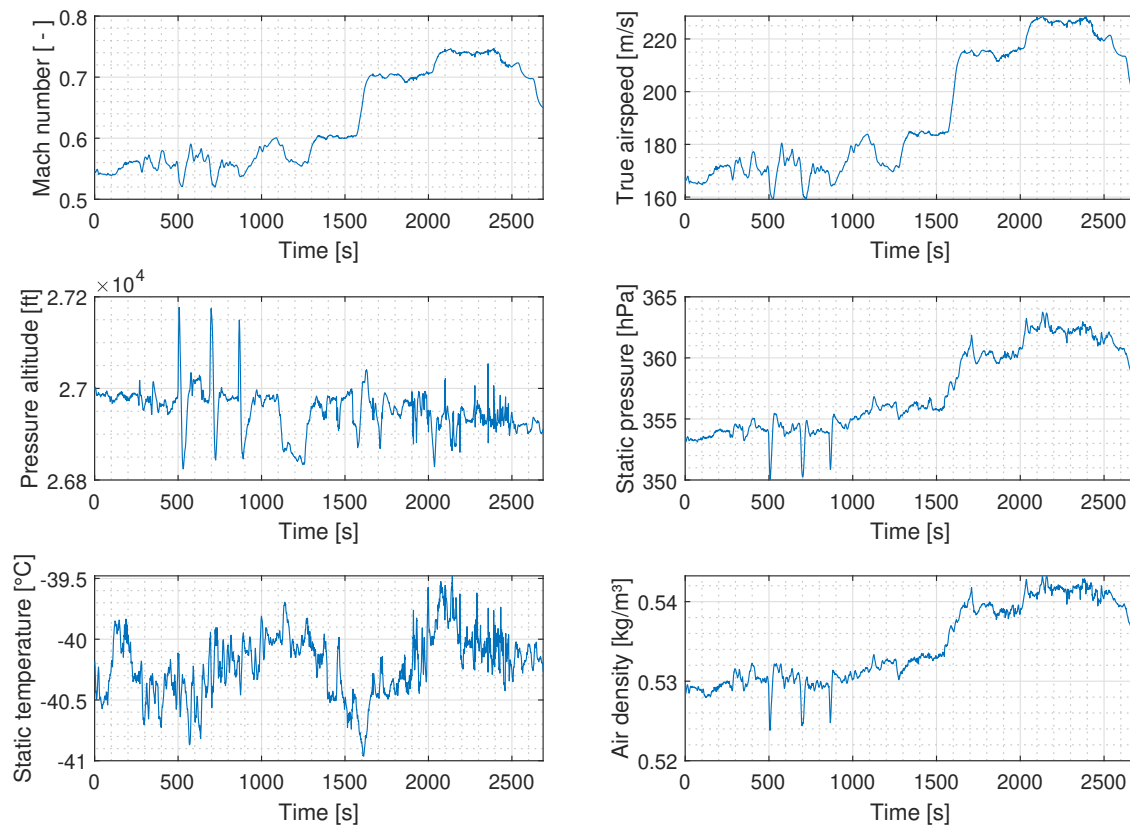


FIGURE 8.42: Flight 4, flow variables during chase flight MP41. The chase flight includes correction maneuvers performed to enter the DLR-Falcon’s wake and bank turns when the edge of the temporary reserved airspace is reached.

### 8.6.2 Time-domain data

The acceleration history of all channels is displayed in the plot 8.43. Various events during the chase flight are labeled in table 8.3 in relation to the flight parameters from figure 8.42. This is not a comprehensive list that can describe every feature seen in the data, but rather a summary of the most important changes in flight attitude.

TABLE 8.3: HALO chase flight MP41 events.

Label	Event	Label	Event
1	Sudden heading change	6	Steep speed increase
2	Impulsive altitude variation	7	Steep speed increase
3	Impulsive altitude variation	8	Sudden heading change
4	Impulsive altitude variation	9	Steep speed increase
5	Sudden heading change	10	Sudden heading change

From the beginning up to section 6, the HALO performs a careful approach of the DLR-Falcon while searching for its wake. In this interval the effect of maneuvering on the aircraft response can be observed. The larger amplitudes in the intervals 6-7, 8-9 and 9-10 correspond to the wake turbulence excitation.

The principal moments of the response sensors are plotted in figure 8.44. Concerning statistics, similar considerations as those expressed for the stationary data points are valid. The maneuvers during chase flight cause a deviation from the normal distribution in the response (recognizable by the larger skewness and kurtosis values). The response RMS clearly increases due to wake turbulence, although it is difficult to maintain a constant excitation level. The variance of the measured accelerations is plotted in figure 8.45 grouped by component and by direction.

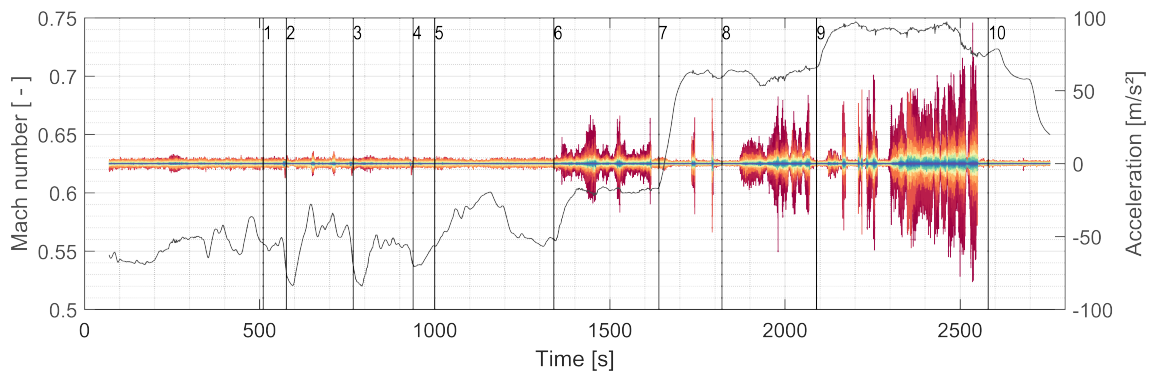


FIGURE 8.43: Measured accelerations during chase flight 1 (MP41). The pressure altitude is constant  $h = 27000$  ft, the black line is the Mach number. The vertical lines mark the events from table 8.3. The HALO is in the wake when the RMS increases significantly. The initial data up to section 6 is the approach phase. Between sections 6-10, little course corrections are sufficient to enter or to exit the wake.



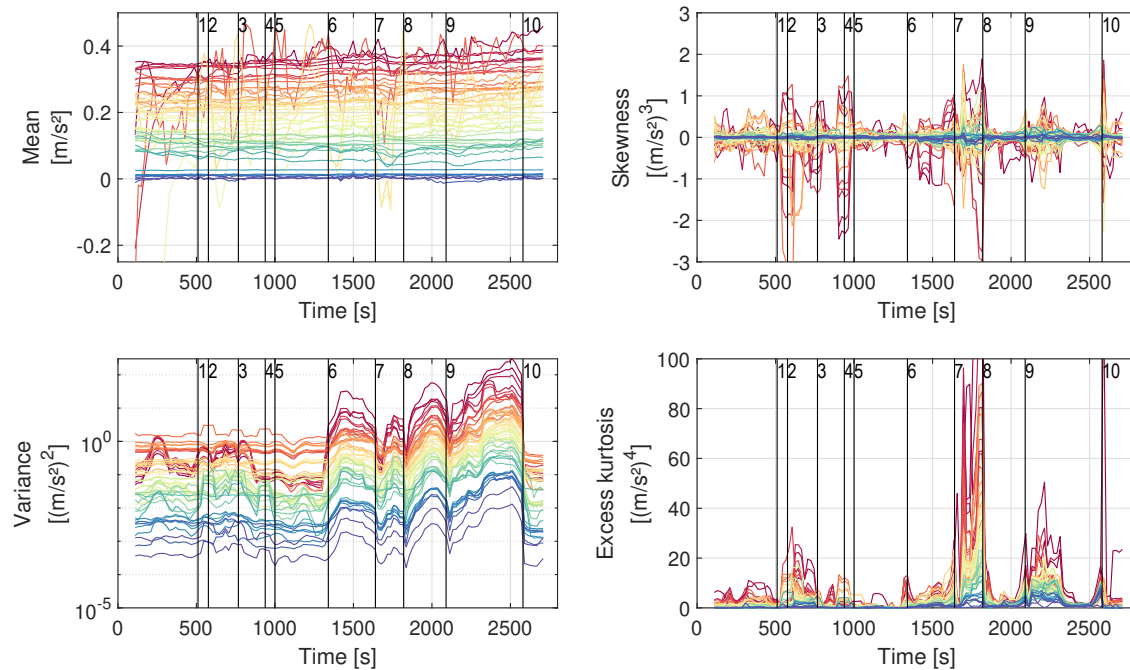


FIGURE 8.44: Chase flight (MP41). The vertical lines mark the events from table 8.3. The skewness suggests that, despite the complicated excitation environment, the signal distribution is symmetrical (there is no preferred direction). The kurtosis increases when with when maneuvers take place (influence of outliers).

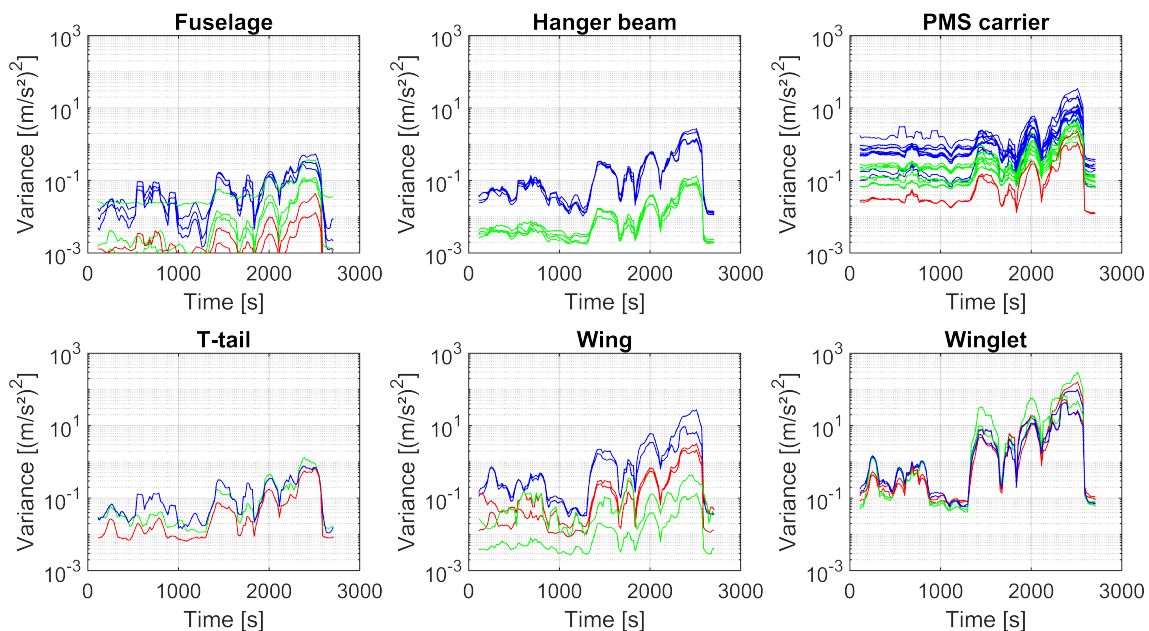


FIGURE 8.45: Response variance during chase flight (MP41) for each sensor component (see 8.9). The colors denote the sensor direction: red:  $x$ -direction (longitudinal), green:  $y$ -direction (lateral), blue:  $z$ -direction (vertical). The winglet and T-tail sensors are have similar load levels for any direction, therefore they are a good choice as references.

### 8.6.3 Frequency-domain data

The time-domain data analysis confirmed the non-stationary behavior of the system response during the chase flight. This is a demanding case for the assumptions of operational modal analysis because the system variation has a complicated profile. We proceed with the analysis of the Mach number because it is the main aeroelastic parameter and is equivalent to the true airspeed in this case. We are interested in its frequency components and their location in time in order to determine if dynamic effects due to parameter variation are expected to appear in the data. We are dealing with a long signal with low frequency content, therefore it is best analyzed by the continuous wavelet transform instead of the spectrogram. To this end, figure 8.46 displays the scalogram of the Mach number for low frequencies (large time scales). Appendix A.12 and especially the books from [WALNUT, 2002] and [MALLAT, 2008] provide more details about this topic. Most of the signal's frequency components are one to two orders of magnitude lower than the aircraft's first eigenfrequency. The signal's duration is  $T = 2687$  s, therefore the scalogram's lower frequency bound is  $\pi/T = 0.0012$  Hz. The upper bound is set at 1 Hz because beyond this point the signal has no significant frequency content. The scalogram reveals that the unsteady flight profile in up to section 5 (where  $Ma \approx 0.55$ ) has negligible components above 0.1 Hz. Furthermore, we know from the data collected from stationary measurement points (see figure 8.36) that a Mach number variation in the range  $Ma = [0.55, 0.78]$  does not cause a large eigenfrequency variation. The high-frequency but small speed changes in the interval 7-10 are thus unimportant. We have seen in chapter 2 that magnitude and frequency must contribute in tandem in order to have appreciable dynamic effects. Rapid and simultaneously large speed changes through maneuvers are constrained by the aircraft's control characteristics or the pilot's judgement. Since the parameter variation is slow compared to the system's eigenfrequencies, we expect only secular variations of

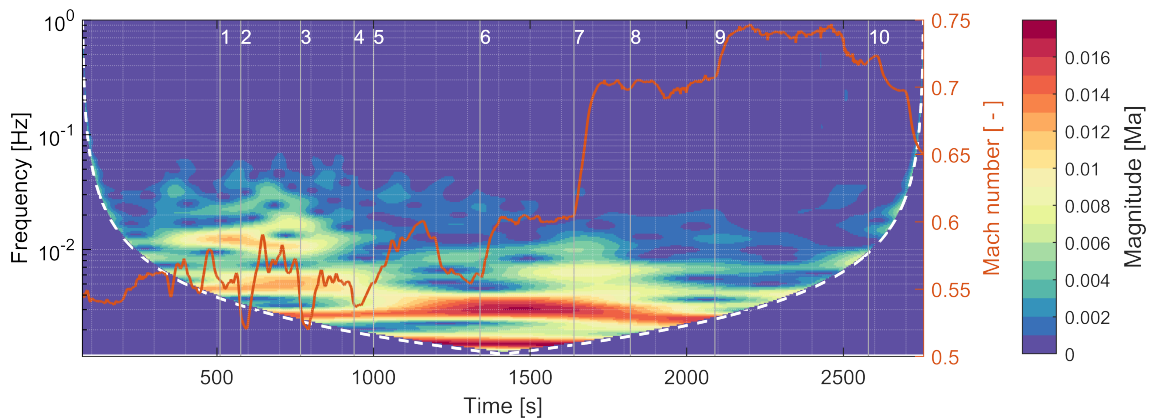


FIGURE 8.46: Mach speed scalogram and superimposed time history. The colormap represents the magnitude of the continuous wavelet transform (using a Morlet wavelet) over the duration of the chase flight and in the frequency range  $[0.001, 1]$  Hz. The white dashed line denotes where edge effects of the continuous wavelet transform occur: the external regions on the left and the right are thus ignored. The vertical white lines denote the chase flight events (refer to table 8.3). See text for discussion.

the eigenvalues, i.e. no observable dynamic peaks and no significant dynamic coupling. Consequently, for the purpose of spectral estimation and modal analysis we may consider the system as slowly-varying.

The spectrogram in figure 8.47 shows the frequency content of one of the sensors during the chase flight. The points in time where the aircraft enters the wake correspond to higher amplitudes, as can be already inferred from the time history. We can assume that the excitation level and its frequency content play a more significant role in the quality of system identification than dynamic effects due to parameter variation. The chase flight data set has already been investigated in terms of persistence spectrum and spectral kurtosis in figures 8.32 and 8.33 respectively.

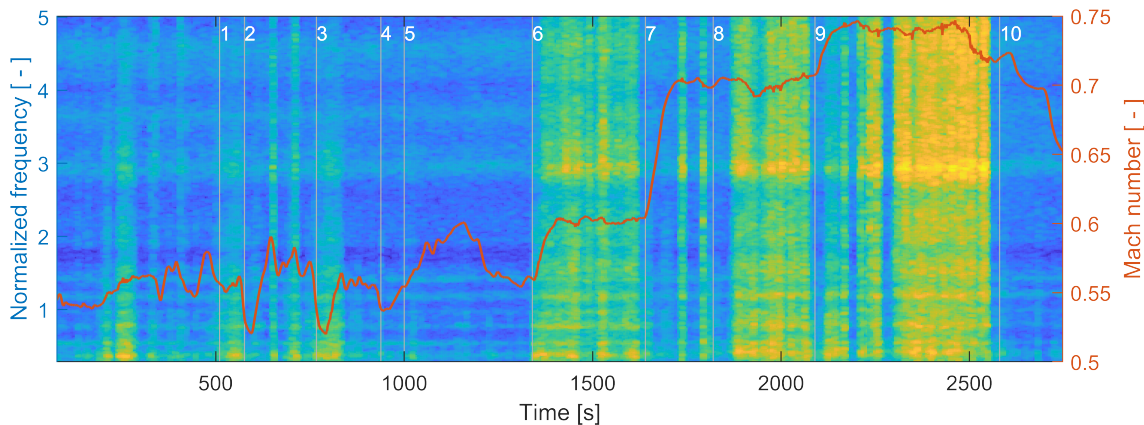


FIGURE 8.47: Flight 4, spectrogram of the vertical right wing sensor (WING\_RH+Z). The white lines mark several events during the chase flight (refer to table 8.3). The time intervals where the amplitude is clearly higher correspond to the wake turbulence. The spectrogram is estimated by the segmented multi-taper method in order to increase the time resolution.

#### 8.6.4 System identification

The test engineer constructs the full stabilization diagram to assess the system identification settings (band, order, weighting etc..). Once these have been fixed, only the highest four model orders are computed in order to save computational resources. The system identification method is selected depending on the application and data quality, but for the purpose of online monitoring the tracking results are an additional evaluation criterion.

The eigenvalues identified using three different identification algorithms are plotted in figure 8.48. For demanding OMA applications such as the chase flight, the system identification parameters for continuous tracking can be determined by iteration over several mode sets as data is acquired until clean tracking diagrams are produced. About ten modes are found in the range of interest  $f = [0.3, 2]$ , therefore a single identification band with modal orders starting at 40 is sufficient. The goal of this analysis is the calibration of each identification algorithm's parameters. The data-driven SSI performs particularly well in the higher frequency range. However, the first symmetric wing bending trace often breaks because several spurious poles are estimated at its location. As a consequence, the tracking algorithm fails to recognize this mode family. The covariance-based SSI-cov delivers better

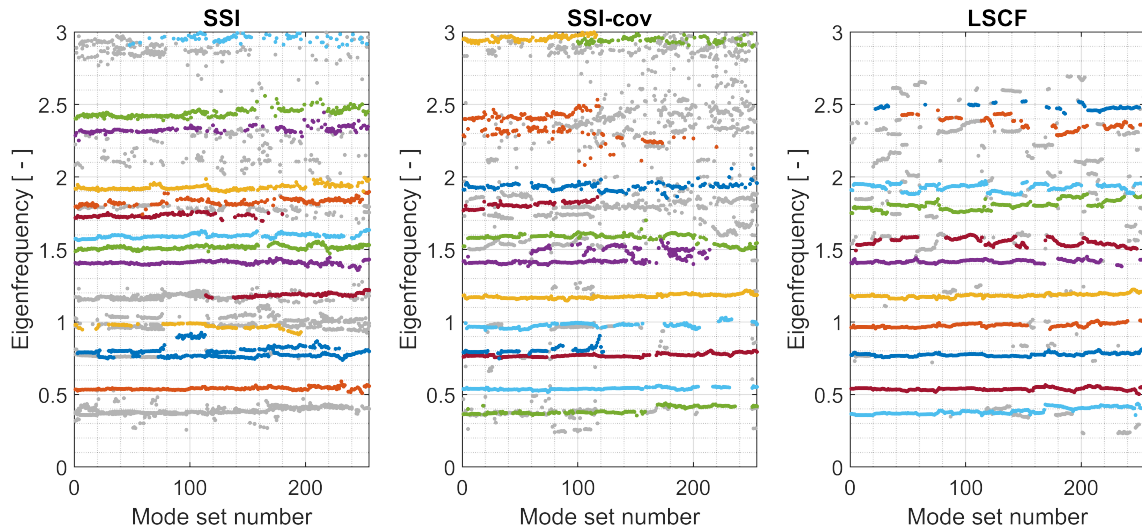


FIGURE 8.48: Chase flight 1 (data set MP41), raw identification results using the data-driven SSI, covariance-based SSI and LSCF. The plots display the mode tracking from 255 modes sets estimated from short overlapping blocks with duration 160 s. The gray dots are spurious modes that have not been associated to any family. The colored dots belong to mode families that have a sufficiently large number of members. See text for discussion.

results because it can track well the first symmetric wing bending. Both SSI methods deliver better identification results when the frequency components around DC are filtered out and the data bandwidth is reduced to about  $f < 2.5$ . On the other hand, the LSCF method leads to a clean tracking diagram, but requires adjustments for spectral estimation. The full or positive cross-power spectral density can serve as data source for LSCF. For the application at hand the estimation of the latter is not feasible unless the acquired response is decimated to remove the influence of out-of-band resonance peaks. Likewise, depending on the number of reference channels, the applicability of the poly-reference pLSCF method may be compromised. Compared to the SSI algorithms, LSCF has the advantage of being able to deliver good tracking results with short data blocks, therefore it is appropriate for the chase flight data set. The next section shall investigate the effect of buffer length on modal parameter estimation.

### 8.6.5 Mode tracking

The continuous evolution of the eigenvalues is reconstructed by tracking the modal models corresponding to each data block. The tracking algorithm identifies and excludes spurious mode families automatically. The modal model is usually formed by picking the eigenvalues corresponding to the highest model order, but if sufficient CPU resources are available, it is composed from the last four model orders of the stabilization diagram by performing a search of the “best” modes as mentioned before. Unexpected interruptions of a mode family chain can occur, for example, due to sudden maneuvers or turbulence. The tracking algorithm can counter with a longer reference memory (reference modes that are further back in time) to “catch” the mode if it is seen again after the disturbance has ended. A sporadic manual correction by the test engineer can be enormously beneficial to the

tracking algorithm. However, it is entirely possible that some modes cannot be tracked reliably. Among the eight HALO eigenmodes displayed in figure 8.12, the six listed in table 8.4 are to be tracked during the chase flight. Mode 5 (aft fuselage torsion plus wing in-plane bending) is weakly excited and difficult to track due to its proximity to mode 4 (first fuselage bending), therefore it is excluded from this list. Mode 8 (first in-plane wing bending) is also excluded in order to display 6 modes in a  $2 \times 3$  grid.

TABLE 8.4: Tracked modes of the HALO chase flight (data set MP41).

Mode number	Mean scaled eigenfrequency	Mode name
1	0.385	first symmetric wing bending
2	0.538	first antisymmetric engine bending
3	0.778	first antisymmetric wing bending
4	0.978	first fuselage bending
6	1.18	second symmetric wing bending
7	1.42	PMS antisymmetric bending

The tracking diagram of the chase flight is displayed in figure 8.49. The flight conditions vary unpredictably, therefore fast/transient variations can be followed more closely by a short buffer, at the expense of modal parameter variance. To this end, a very short data block with  $T = 40$  s is set (the stationary points MP11 ÷ MP15 used about 300 seconds of data). The plot displays the measured (true) Mach number and the moving average corresponding to each data block. The smoothing is indeed noticeable in the interval  $t = [300, 1000]$  s where the Mach number oscillates around  $Ma \approx 0.55$ , but the true value is followed quite closely. System identification is performed by LSCF because the amount of data appears to be too scant for SSI or SSI-cov. The output CPSD matrix is estimated by the segmented multi-taper method (algorithm 3) to increase the number of spectral averages. Figure 8.50 plots the corresponding damping ratio. It displays a large scatter, therefore a simple moving average (FIR filter with equal coefficients) or Savitzky-Golay filter can be applied to facilitate the interpretation of results [SCHAFFER, 2011]. When the system is stationary, the variance of the estimated eigenvalues decreases with buffer duration, but system identification is less responsive. When the system is non-stationary, a long buffer collects the responses produced under disparate flight conditions, impacting the estimated modal parameters. In order to understand the effect of buffer length, the same tracking procedure is repeated with  $T = 40, 80, 160$  s (overlap 0.75) and the results are collected in figure 8.51. The plots suggest that the eigenfrequency trend can be determined even with very short buffer lengths and it appears that sudden speed variations do not severely impact its estimation. A longer buffer leads to a higher damping estimates, while a short buffer corresponds to more conservative values. Continuous tracking during FVT does not compute an interpolating function or a regression of the estimated parameters. Compared to previously published results in [JELIČIĆ ET AL., 2017], the buffer size is reduced by a factor 2 to 8.

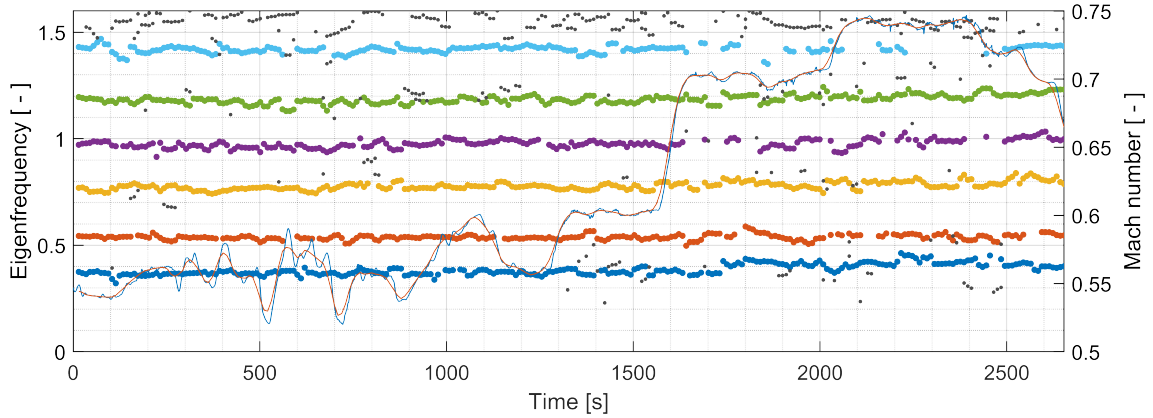


FIGURE 8.49: Fully automated tracking diagram produced during chase flight 1 (MP41). Modes 1, 2, 3, 4, 6, 7 are tracked (see table 8.4). The jagged blue line is the measured Mach number, the smooth red line is its mean value within each data block. The data blocks are only 40 s long with 0.75 overlap. The eigenvalues are identified with LSCF from  $48 \times 38$  CPSDs that are estimated with the multi-taper method. The similarity metric is HDM with 160 s (16 mode sets) of reference memory. See text for discussion.

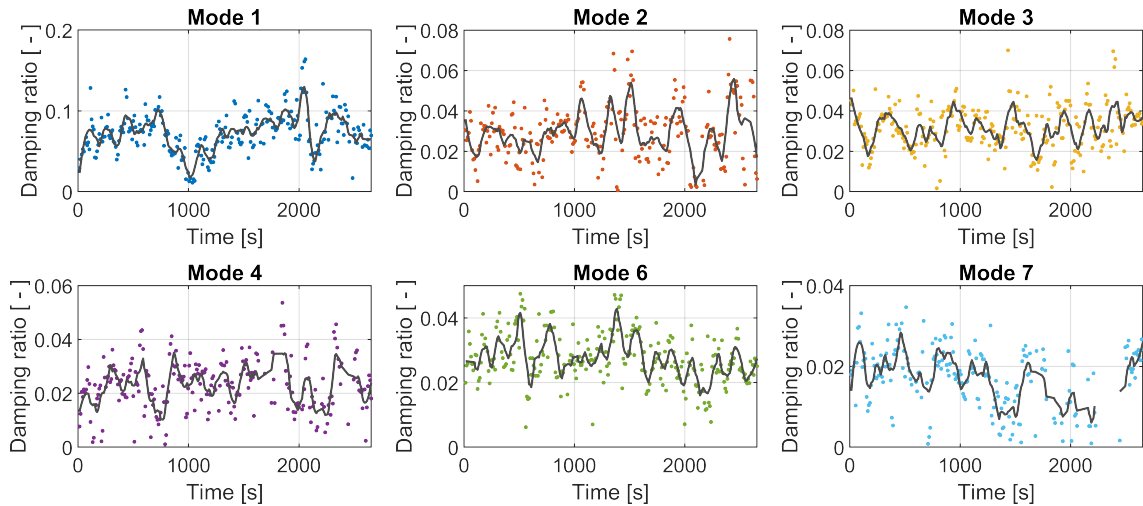
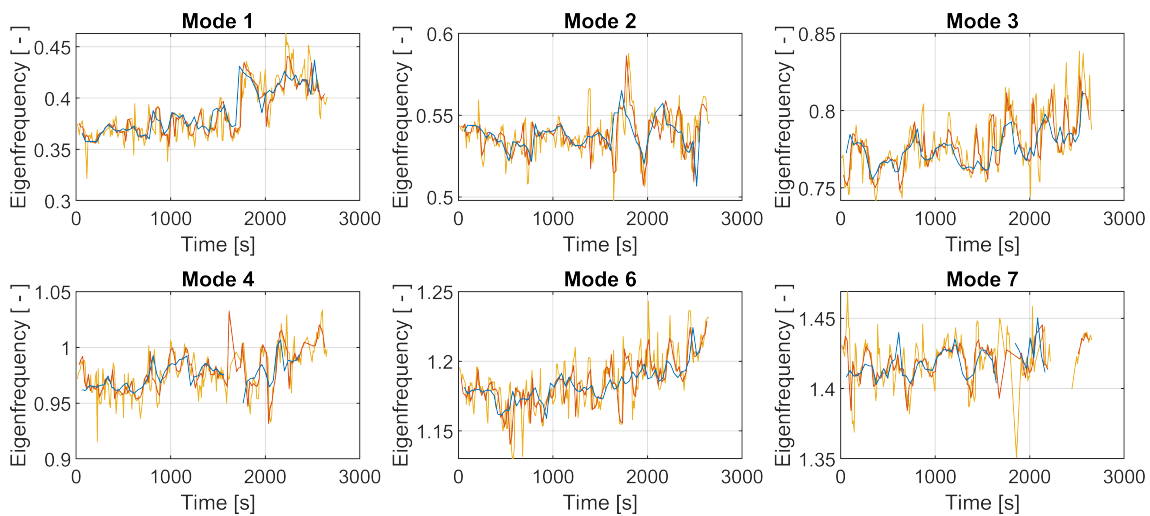


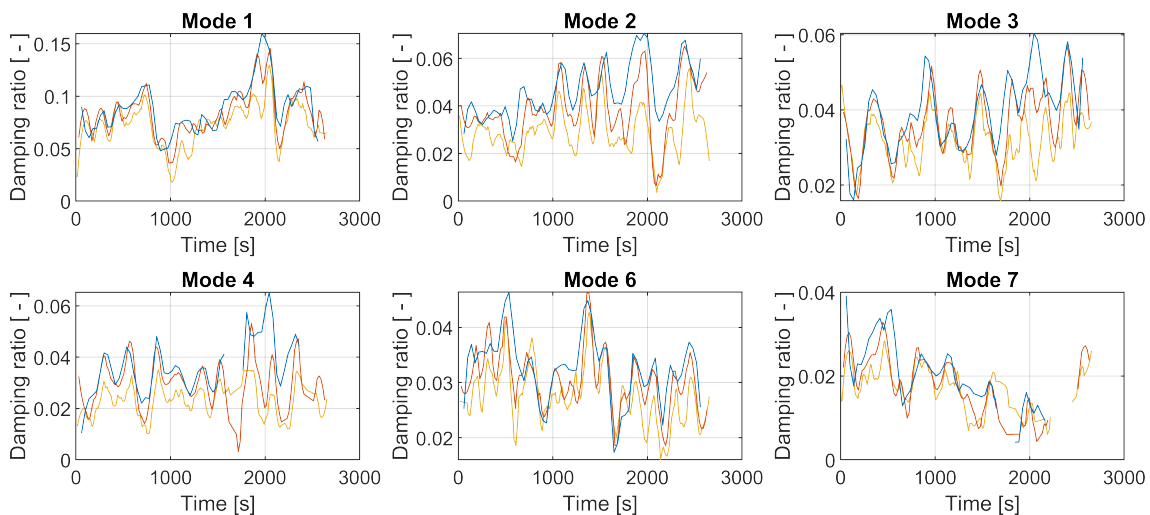
FIGURE 8.50: Estimated damping ratio of the first six eigenmodes from figure 8.49. The black line is the smoothed data obtained with a Savitzky-Golay filter of length 16. See text for discussion.

The aircraft speed in data set MP41 varies unpredictably, therefore it is useful to plot the eigenfrequency and damping ratio of each mode as a function of Mach number. In the ideal case, with equal operational conditions, there would be only one estimated eigenvalue for each Mach number at constant altitude. The system identification results obtained from SSI-cov and LSCF are compared in figure 8.52 using the same block length (buffer duration) and block overlap. The scatter of the estimated parameters at each Mach number is due to the non-stationary flight conditions as the aircraft flies into the wake. This is especially visible in the estimated damping ratio. The system identification results mirror the considerations made for spectral estimation with regard to the effect of maneuvers. The wing's control surfaces alter the airflow around it and the resulting unsteady aerodynamics appear as additional stiffness and damping. The rudder and the vertical stabilizer affect

the T-tail similarly, but to a lesser extent. Furthermore, the control surface actuators may increase energy dissipation and therefore affect the damping ratio of the wing modes. The SSI-cov and LSCF deliver very similar eigenfrequency estimates. SSI-cov identifies generally a higher damping ratio, but in this case it is still comparable with LSCF. In particular, the first symmetric wing bending matches well. However, this mode is not as easy to track because SSI-cov often finds multiple poles around its peak, which somewhat hinders tracking. LSCF has the advantage of producing clear stabilization diagrams and is fast even when factoring in the CPSD computation. If the buffer duration study from



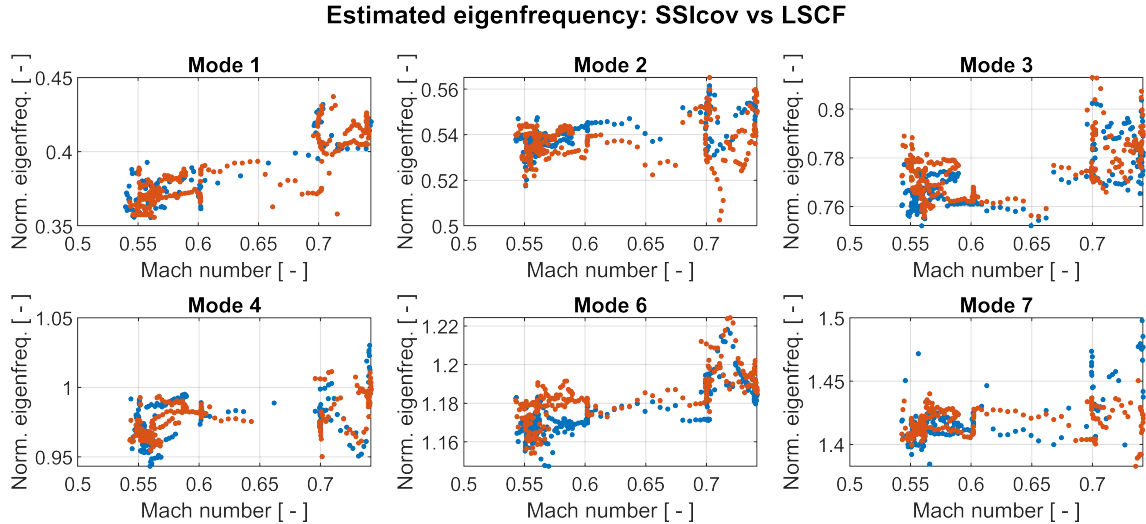
(A) Eigenfrequency estimates using different block lengths



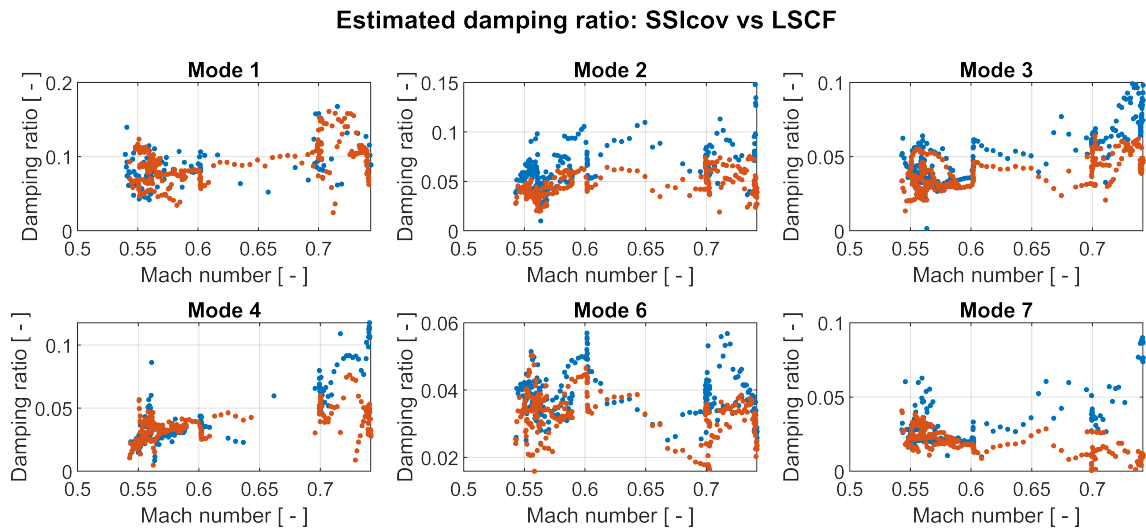
(B) Damping ratio estimates using different block lengths

FIGURE 8.51: Chase flight 1, data set MP41: eigenfrequency and damping ratio estimates with different block lengths (overlap 0.75). Yellow line:  $T = 40$  s, red line:  $T = 80$  s, blue line:  $T = 160$  s. The damping ratio estimates have been smoothed by a Savitzky-Golay filter of length 16, 8 and 4 respectively. The averaging length is inversely proportional to buffer duration so that the smoothed eigenvalue traces are extracted at the same time instants. When a mode family chain has a “jump” longer than the filter length, its edges are not connected by a line. The identification procedure is the same as in figure 8.49. See text for discussion.

figure 8.51 holds under other conditions, then perhaps even a very short buffer duration  $T = 40$  s can be set to accommodate the mission profile. The peaks of the synthesized spectra provide a means to assess the estimates and are always displayed in the stabilization diagram. In particular, mode sets where the damping ratio drops very close to zero can be correlated to bad excitation. Under such conditions both the SSI and LSCF system identification algorithms are affected and produce less reliable results.



(A) Comparison of eigenfrequencies estimated by SSIcov and LSCF



(B) Comparison of damping ratio estimated by SSIcov and LSCF

FIGURE 8.52: Chase flight (data set MP41), comparison of estimated modal parameters using SSIcov (blue) and LSCF (red). The two methods attain from the same data blocks of duration  $T = 80$  s. See text for discussion.



### 8.6.6 Large parameter variation

The previous sections have presented the modal analysis results obtained from continuous mode tracking during the chase flight MP41.

In this section we shall track the modes during the whole Flight 5 (measurement point MP50, see table A.1). This data set features a large parameter variation during a descent maneuver that is of interest to system identification. Some of the events of Flight 5 are reported in table 8.5.

TABLE 8.5: HALO Flight 5 MP50 events.

Label	Event	Label	Event
1	Stochastic aileron/elevon input	4	Beginning of rapid descent
2	Climb into stratosphere	5	End of rapid descent
3	End of climb	6	Beginning descent for landing

Figure 8.53 displays the measured flow variables. The HALO flew just under its operating ceiling at 48000 ft (see flight envelope 8.14). The change of the temperature gradient sign denotes the crossing of the tropopause at  $t = 4000$  s (just after event 2) and at  $t = 6800$  s (just after event 4). Between these two points the HALO is in the stratosphere (see also figure 8.13 in section 8.2.3). The same procedure described for the chase flight in section 8.6 is used to monitor the aircraft response during Flight 5. The HALO's attitude and GPS positioning are not available for this flight.

The spectrogram 8.54 displays the acceleration measured by a wing sensor. The response level varies appreciably between time data blocks (similarly to other data sets). The higher amplitude in interval 1-2 is due to stochastic aileron/elevon excitation. The wandering of the first elastic mode due to the speed increase is already noticeable in the spectrogram.

The tracking diagram 8.55 is constructed from the continuous identification during the whole flight. Higher modes ( $f > 2.2$ ) are difficult to identify at least because of insufficient turbulence excitation levels that lead to a high scatter. Two notable features are the overall eigenfrequency trend due to fuel consumption (mass decrease) and the stronger modal parameter variation during rapid descent (interval 4-5). They will be addressed in the coming sections. The estimated damping ratio is displayed in figure 8.56 along with a moving average using a long window. When viewed over the entire flight, the damping ratio estimate scatters around a secular (slowly-varying) mean value. Such variance has been observed consistently by other authors in flight vibration testing when comparing different estimators and excitation types [PEETERS ET AL., 2006].

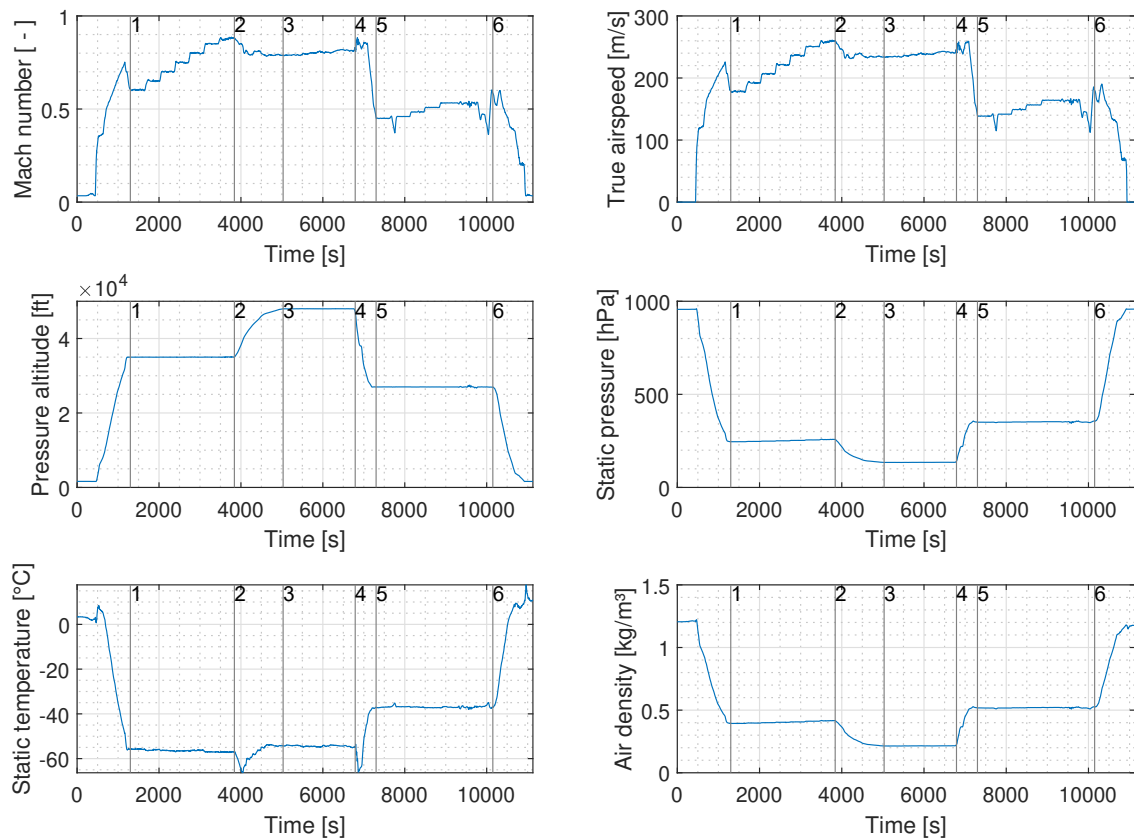


FIGURE 8.53: Flight parameters during HALO Flight 5. The Mach number is increased stepwise in the interval 1-2. Afterwards, in interval 2-3 a slow climb into the stratosphere is performed. The maximum altitude at 48000 ft is maintained in interval 3-4. A rapid descent maneuver takes place in 4-5, followed by various load maneuvers in 5-6.

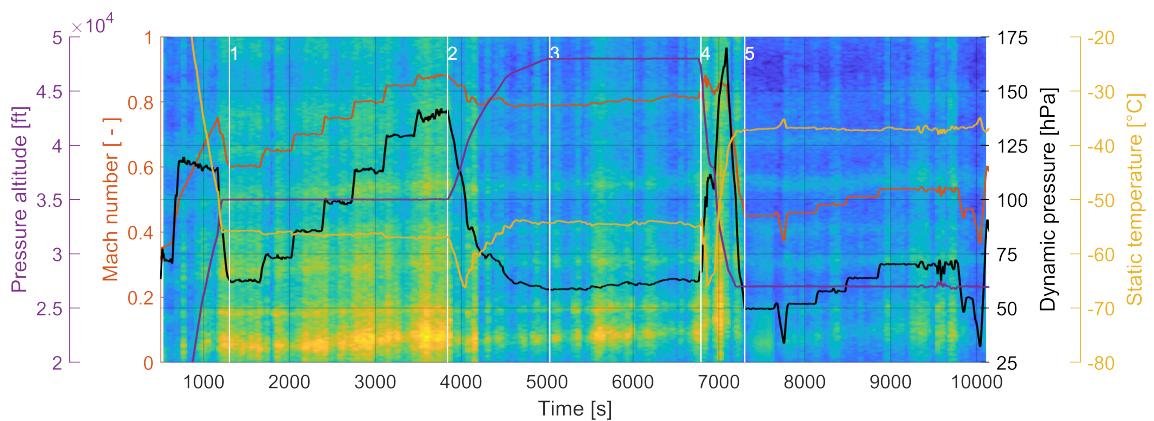


FIGURE 8.54: Spectrogram of a vertical wing sensor during Flight 5 (MP50) with overlaid flight parameters. The higher system response amplitude in interval 1-2 is due to the applied stochastic aileron/elevon inputs. In the middle of 3-4 some light rudder kicks were applied. In 4-5 the flight spoilers are raised during the descent maneuver some periodic flow separation could be observed.

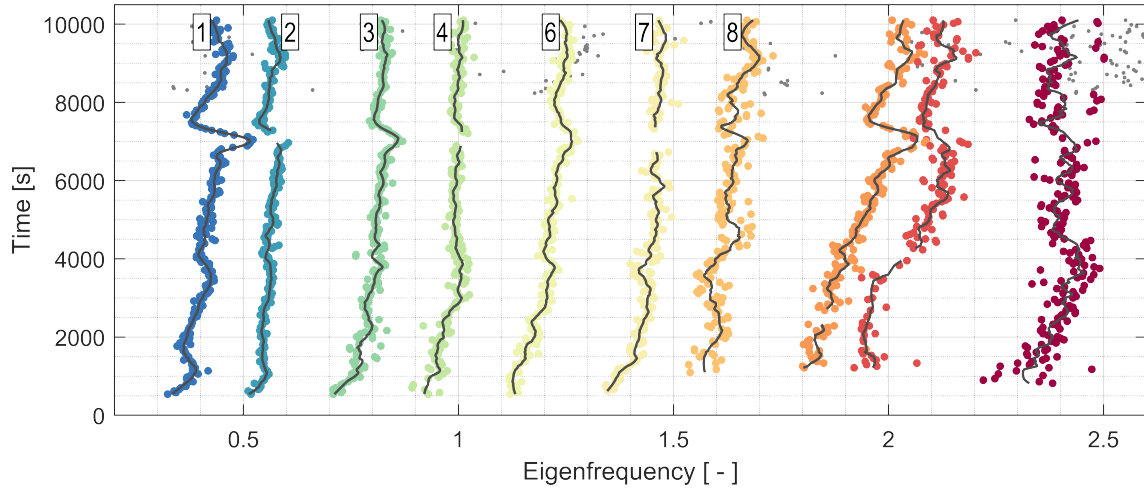


FIGURE 8.55: Mode tracking performed during Flight 5 (measurement point MP50). System identification is performed from data blocks with  $T = 80$  s and overlap 0.5. The black line is a running average of length 4. The corresponding damping is displayed in figure 8.56. The eigenfrequency variation during descent is prominent, particularly for the first symmetric wing bending (mode 1). The overall eigenfrequency trend is due to fuel consumption. Mode 5 cannot be tracked reliably because of its proximity with mode 4.

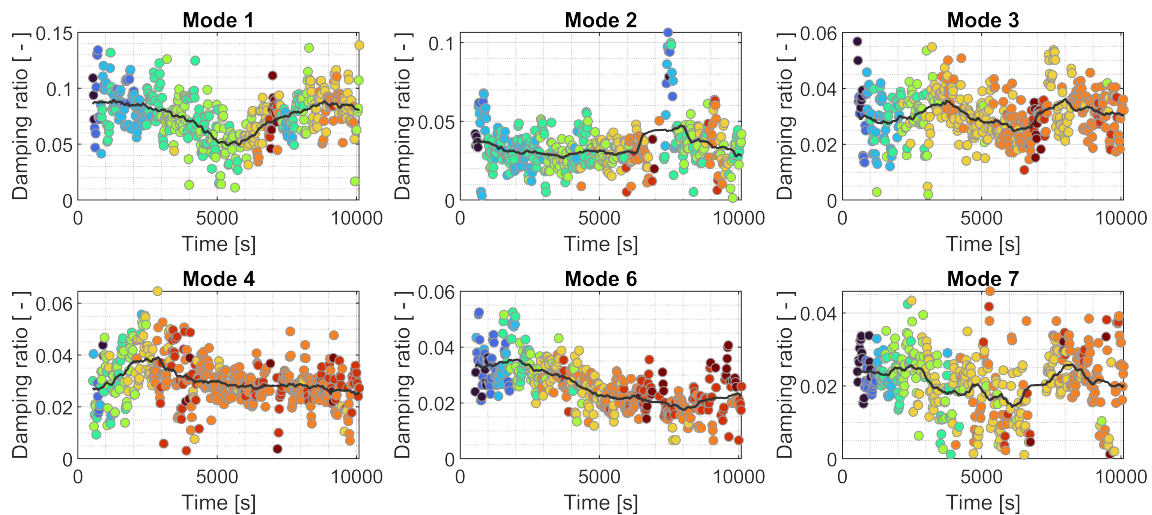


FIGURE 8.56: Mode tracking performed during Flight 5 (MP50). The plots display the damping ratio of the modes shown in figure 8.55. The marker color represents the eigenfrequency (blue: low, red: high). The black line is a moving average with a large window in order to highlight the secular damping ratio variation. See text for discussion.

### 8.6.7 Fuel consumption

The estimated eigenfrequencies display a noticeable trend due to the consumption of fuel over the course of over two hours and a half in figure 8.55. At take-off fuel constitutes about a 27% of HALO's total mass and by the end of Flight 5 the percentage has decreases to about 15%. Fuel is stored mostly in the wing tanks, therefore, as its mass decreases, the eigenfrequency of wing modes is expected to increase. Figure 8.57 displays the reading of the fuel mass during Flight 5; fuel consumption increases with thrust and other factors, but a linear fit still provides a good approximation given the length of the flight.

The effect of fuel consumption is modeled as described in appendix A.13 and the results are presented in figure 8.58. This model takes into account the fuel and dry mass of the wings, the fuel consumption over time and the estimated eigenfrequencies at the beginning of the flight (where aerodynamic effects are low). We are interested in the values towards the end of the mission when aerodynamic effects are not significant. The eigenfrequencies of the modes where the wings participate the most are estimated well. In mode 7 (first PMS antisymmetric bending) the PMS's offset from the elastic axis acts as additional inertia. In mode 8 (first in-plane wing bending) the total wing inertia and stiffness are a combination of the moments around the  $x$  and  $z$  axes, therefore the approximation may be simply too coarse. The simplified model may be used to compare the eigenfrequencies estimated at different times during the flight starting from the values obtained shortly after take-off. The HALO employs a pump to redistribute fuel in-flight over the whole wingspan. The wing spars passing through the tank prevent the fuel from sloshing and thus increasing the energy dissipation. We can see from figure 8.56 that the damping ratio is largely unaffected by fuel consumption.

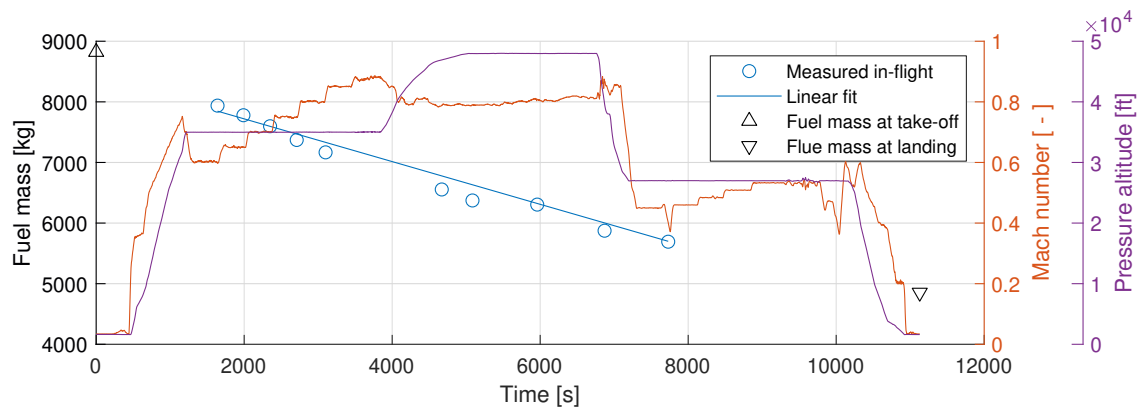


FIGURE 8.57: Measured fuel consumption during Flight 5. The linear fit describing fuel mass over time is used for estimating the eigenfrequency variation of wing modes.

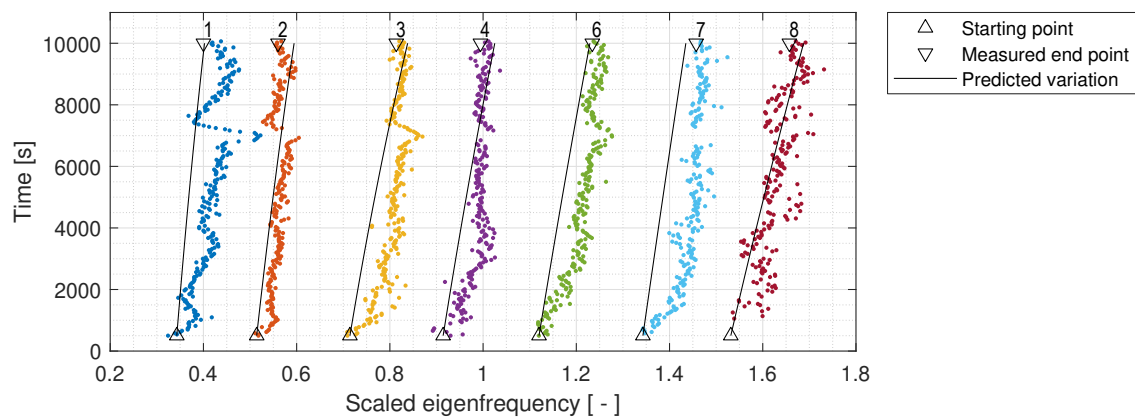


FIGURE 8.58: Model of the eigenfrequency variation due to fuel consumption. The starting values for the eigenfrequency are taken right after take-off. The black lines model the eigenfrequency purely as a function of time (the lines are very slightly curved). This simplified model shows good agreement with experimental data. See text for discussion.

### 8.6.8 Descent maneuver

The HALO climbed slowly and at constant speed up to 48000 ft and then performed a rapid descent maneuver that is interesting for modal analysis. The spectrogram 8.59 of a measured wing response is overlaid with the relevant aerodynamic quantities. During descent, a periodic flow separation could be observed on the wings for a short time and left a trace in the middle of interval 1-2 where the excitation level on the wings is higher. The altitude decreases and the speed is approximately constant in the interval 1-4, therefore dynamic pressure increases. As soon as the speed is also reduced, dynamic pressure decreases as well. The air density increases like the static temperature starting at section 3. We should thus expect that the first wing bending eigenfrequency follows the same trend as the measured dynamic pressure (see section 3.1.5 for the dynamic mass, damping and stiffness).

The evolution of eigenfrequency and damping ratio during the descent is displayed in figure 8.60. It can be noticed already in the tracking diagram of the whole flight 8.55 that during the descent modes 2, 4 and 7 (respectively: first antisymmetric engine bending, first fuselage bending and first antisymmetric PMS bending) cannot be tracked (irrespective of system identification technique). Consequently, we focus on the uninterrupted mode families 1, 3, 6 (first symmetric wing bending, first antisymmetric wing bending and second symmetric wing bending). Due to the swept back wing the frequency of the first symmetric wing bending is increasing with higher dynamic pressure. On the other hand, the aerodynamic damping forces are lower at high altitudes due to the reduced density. That is why there is a maximum in bending frequency in moderate altitudes at high Mach numbers (interval 3-4). The same happens for antisymmetric bending.

Given that the descent maneuver covers a wide parameter space by virtue of the simultaneous Mach number and altitude variation, it would be possible to approximate the eigensurface of a mode shape. Modal parameters can be predicted from past estimates using

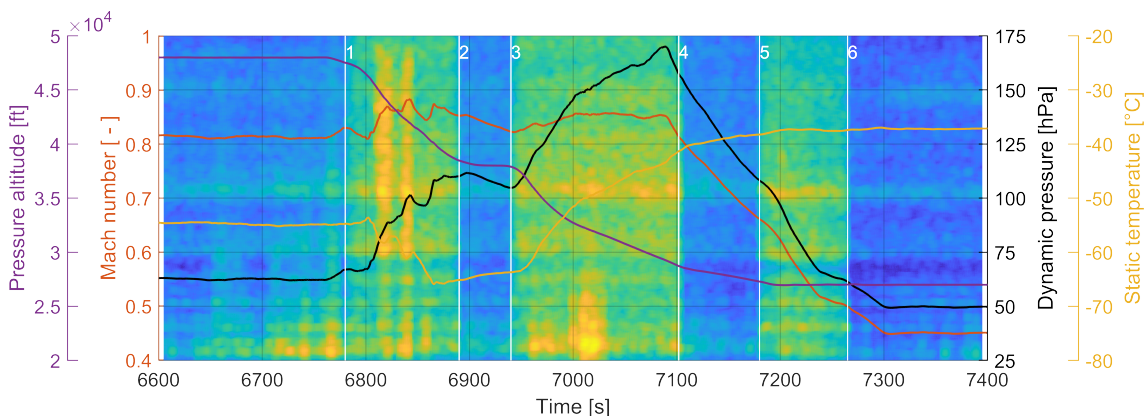


FIGURE 8.59: Spectrogram of a vertical wing sensor in the interval [6600, 7400] s (MP51). The descent maneuver proper begins at section 1 and completes at section 6. Flight spoilers are raised in the intervals 1-2, 3-4 and 5-6. The temperature gradient changes sign as the HALO reenters the troposphere. The dynamic pressure increases while the altitude is decreasing, but as soon as the aircraft starts slowing down, dynamic pressure decreases as well.

a statistical model and a Kalman filter as demonstrated in [SOAL, 2018]. Alternatively, the eigensurface can be then used to extrapolate the modal parameters during other flight conditions. Figure 8.61 provides an example for the first symmetric wing bending mode. The extrapolation works best if the training data is representative of other flight conditions in terms of excitation or maneuvers.

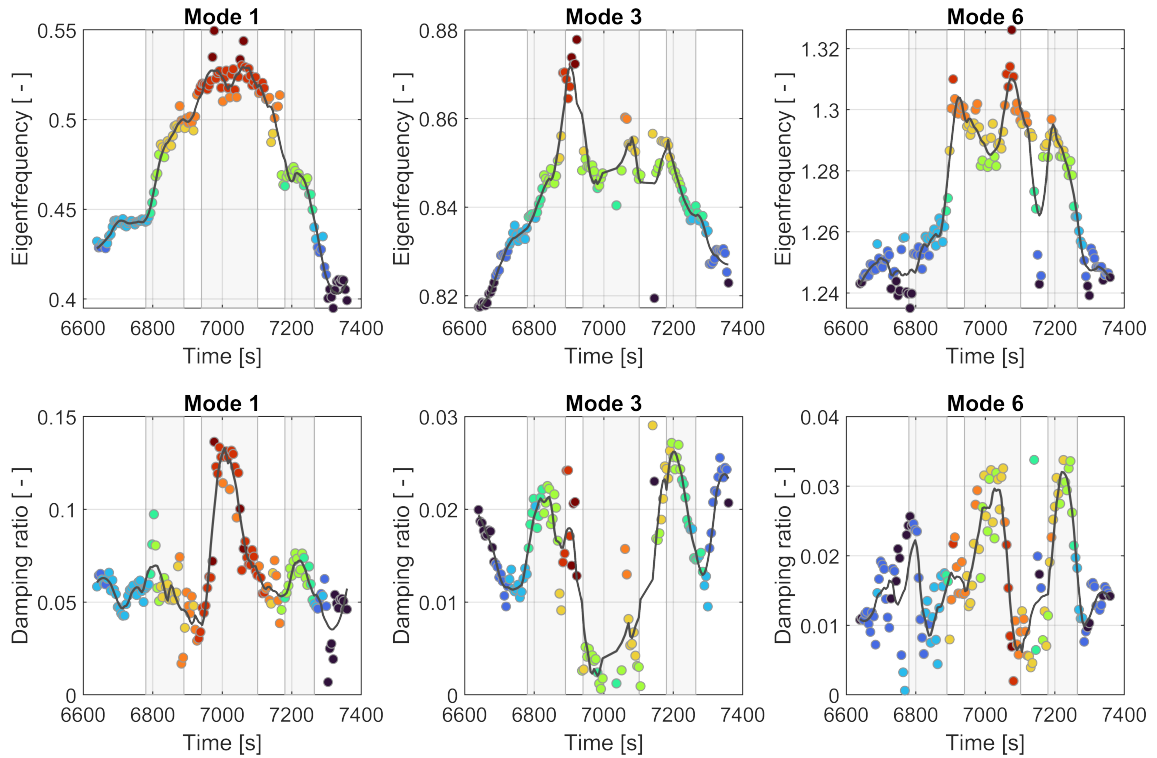


FIGURE 8.60: Eigenfrequency and damping ratio of the first wing bending, first antisymmetric wing bending and second symmetric wing bending (modes 1, 3 and 6) during the descent maneuver. The marker color denotes the eigenfrequency (blue: low, red: high). The black line is a moving average. The gray areas in the background denote, from left to right, the intervals 1-2, 3-4 and 5-6 defined in figure 8.59. See text for discussion.

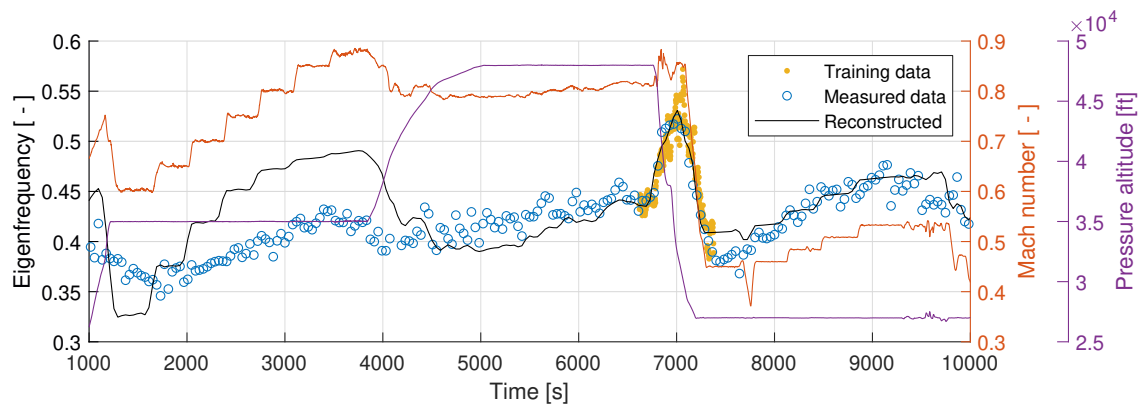


FIGURE 8.61: Eigenfrequency evolution reconstructed using only the descent maneuver compared to data from the whole Flight 5. The Mach number and pressure altitude are overlaid with their axes on the right. The fit before  $t = 4000$  s displays an offset with respect to experimental data due to different excitation conditions (see spectrogram 8.54).

### 8.6.9 Periodic flow separation

Periodic flow separation on the raised spoilers could be observed while descending at  $Ma > 0.86$  during a window of about 40 s. The estimated PSD shows an enlarged resonance peak where the first elastic mode is located. The stabilization diagram 8.62 reveals several poles around the first symmetric wing bending mode  $f_1 = 0.49$ . The first antisymmetric engine and wing bending modes are at  $f_2 = 0.61$  and  $f_3 = 0.84$  respectively. Dynamic poles  $f_1 + k\Delta f$  appear at  $k = -2, -1, +1$ , where  $\Delta f = 0.07$  is the frequency of the induced parameter variation. The mode shapes associated to these poles have  $MAC > 0.9$ . The pole  $f_1 - \Delta f$  has higher damping as would be the case for a periodic parameter variation (see chapter 2). The damping estimate of the dynamic poles  $f_1 - 2\Delta f$  and  $f_1 + \Delta f$  is likely to be biased, given that the duration of available data is very short.

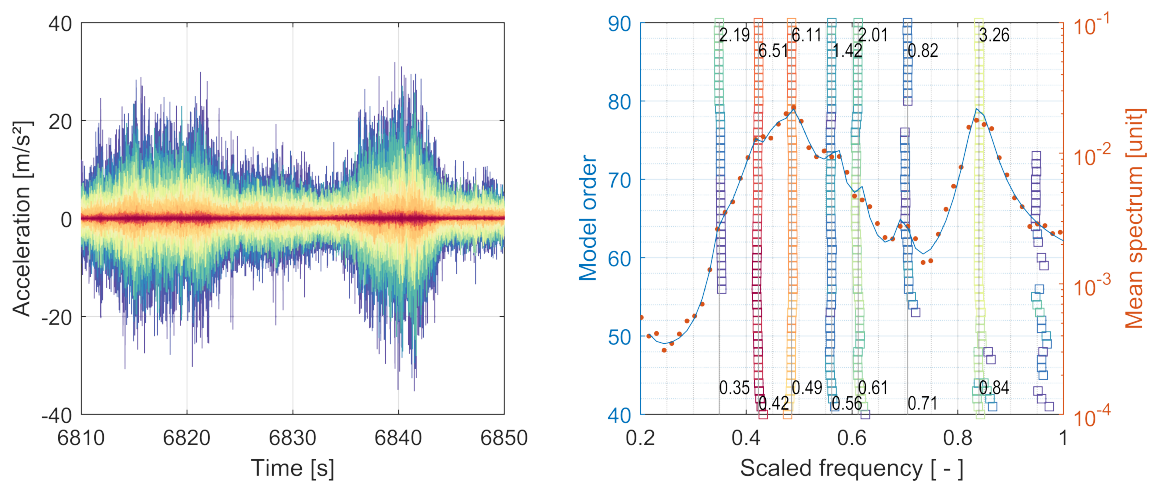


FIGURE 8.62: Aircraft response and corresponding stabilization diagram as periodic flow separation from the raised spoilers is observed. The duration is only 40 s window. The harmonics of the first symmetric wing bending (mode 1) can be observed, with almost identical associated mode shapes. See text for discussion.

## 8.7 Chapter summary

The modal analysis methods and developments detailed in the previous chapters are deployed during flight vibration testing on the DLR-HALO research aircraft. The experimental campaign consists of five flights at different stationary and variable flight conditions. The aircraft is subject to atmospheric turbulence, air brake deployment, stochastic aileron/elevon excitation and the wake of a preceding aircraft.

The modal parameters are permanently estimated and tracked by the online monitoring software developed within the scope of this thesis. The system is identified at stationary measurement points or continually while flight conditions vary. We show that the eigensurfaces can be constructed experimentally by covering several points within the flight envelope. The deployment of air brakes modifies the airflow around the wings and affects accordingly the modal parameters, however the resulting increase in the excitation amplitude and bandwidth leads to a better data quality.

The analysis of data acquired during continuous tracking confirms that it is possible to increase the time resolution of identified modal parameters by decreasing the buffer length, at the cost of increased variance of the estimates. This can be offset by applying an averaging filter on the tracked data, resulting in consistent damping estimates. In continuous tracking with highly variable conditions such as the chase flight, the SSI and LSCF identification algorithms display a similar performance. The influence of fuel consumption on the eigenfrequency of wing modes has been modeled analytically to good agreement with experimental data. The effect of a large parameter variation during rapid descent has been also examined. The modal parameters estimated from this data set can be used to extrapolate the eigenfrequency over the rest of the flight. The results confirm the eigenfrequencies of wing modes are influenced appreciably by changes in the airflow induced by the action of control surfaces. During the rapid descent, periodic flow separation on the wing spoilers took place briefly. Some of the theoretical predictions could be directly observed in the system identification results, for example the appearance of multiple instances of the first wing bending mode due to rapid airflow variation.

In summary: atmospheric turbulence provides sufficient excitation levels for operational modal analysis. The real-time monitoring of the aircraft response proves useful for conducting flight vibration testing by detecting changes in modal parameters with varying flight conditions.





## 9 Conclusions

The conclusions are organized as the three tasks in which the thesis is subdivided:

- Task 1: Develop methods for investigating time-varying systems: linear time-varying systems and aeroelastic systems (chapters 2 and 3).
- Task 2: Implement output-only modal analysis methods: spectral estimation, system identification, mode tracking (chapters 4, 5 and 6)
- Task 3: Demonstrate methods on simulated and experimental test cases: simulation and experimental results (chapters 7 and 8)

**Develop methods for investigating parameter-varying systems:** the relevant linear time-varying systems theory has been reviewed in the first part of the thesis. Based on previous research, we have derived the parametric description of the response in frequency-domain in order to study the dynamic effects on parameter-varying aeroelastic systems.

The main difficulty that we have addressed is that the concepts of transfer function and eigenvalues that are so important in time-invariant case, are in general not well-defined in the time-varying one. Fortunately, periodic systems can be decomposed into equivalent time-invariant ones with periodically-modulated inputs and outputs. The thesis exploits this by computing a periodic representation of a general time-varying system to render it tractable, allowing a parametric description of the response in terms of poles and mode shapes. This theoretical development allows a characterization of the influence of amplitude and rate of parameter variation case-by-case; we proposed a simplified criterion involving frozen-time eigenvalues, while a completely general formulation is not attempted. Furthermore, we introduced a definition of slow, intermediate and fast time-variation regimes. We researched and compared several numerical methods for the solution of time-varying systems. Their application to aeroelasticity appears novel or not as mature as in other fields and some limitations persist. Lastly, we developed a simplified analytical approach by deriving the exact solutions to complex exponential and linear parameter variations.

The theoretical framework focuses on the study of parameter-varying aeroelastic systems. The standard modeling procedure has been researched to improve the generation of aeroelastic models and to understand the role of airflow variables in the onset of flutter. This work's mathematical development introduces the time-dependence of system matrices and criteria for quantifying the dynamic effects of parameter variation. The dynamic mode coupling weakens when the rate of change is lower than the frozen-time eigenfrequencies. Slowly-varying systems can be thus analyzed with good accuracy assuming time-invariance within the estimation window. The parametric representations of LTV systems agree well with nonparametric results obtained by integration of the equations of motion.

**Implement output-only modal analysis methods:** aeroelastic testing is conducted in the operational modal analysis framework because aircraft and wind tunnel models are subject to unknown turbulent excitation. In this task we implemented the analysis chain necessary to perform real-time output-only system identification in order to observe the evolution of modal parameters with varying operating conditions.

Spectral estimation must be performed to monitor the experiments and to provide data to frequency-domain system identification algorithms. The aircraft response is broadband random with many lightly-damped resonances affected by noise and the system's variation is usually slow compared to its dynamics. The theoretical developments have shown that slowly-varying systems can be treated as time-invariant within a sufficiently short time frame. This motivates the use of the short-time Fourier transform over other time-frequency analysis methods because it is computationally fast, produces easy-to-interpret results, does not require any foreknowledge about acquired data and can be coupled with frequency-domain system identification methods. We have combined Welch's modified periodogram and the multi-taper method into the segmented multi-taper estimator to improve spectral estimation when little data is available. This new contribution allows shorter data buffers compared to results we have previously published.

Spectral and modal parameter estimation are performed using sequential or ensemble averaging/identification. The former utilizes a buffer of time data that slides forward as measurements progress and is applicable to slowly-varying systems. The latter can be applied when the system variation is arbitrary, but in turn multiple experiments with the same parameter variation must be conducted. Ensemble averaging is possible in controlled environments such as wind tunnels and simulations but it is not feasible in the case of flight testing. We concluded that modal parameter estimation can be performed by the stochastic subspace identification (SSI) and least-squares complex frequency (LSCF) algorithms. The thesis contributes with a signal processing technique for data reduction and multi-band identification for SSI and with improved stabilization diagrams for LSCF. The interpretation of modal analysis results for time-varying systems is supported by the theoretical development presented before, which provides, for instance, an explanation for the appearance of clustered poles.

The selected system identification techniques are nonparametric with regard to time or parameter variation, therefore we devised a quick mode tracking method based on similarity metrics and mode quality indices to track the identified eigenvalues. The algorithm organizes the estimated modal parameters so that the test engineer is able to observe their evolution over time or as function of airflow variables. The algorithm is capable of processing heterogeneous sets of modal parameters obtained from different model orders, estimators, response channels or arbitrary parameter variations. The tracking output consists of several mode families where all instances of the same mode of vibration are collected together. It is then possible to fit the tracked data to construct a parametric representation of the modal parameter variation.

---

**Demonstrate methods on simulated and experimental test cases:** three-DoF airfoil-rudder system, wind tunnel experiments, flight vibration test.

Time-varying dynamics have been investigated numerically by simulating the response to turbulence of two airfoil-rudder aeroelastic systems. To this end, we have derived an analytical higher-order discretization method for the solution of LTV systems and employed it alongside standard ODE solvers. The objective here is to research the effect of rate of system variation on spectral estimation and modal parameters. We show that damping can be tracked accurately even with a fast parameter variation and short buffers, provided that spectrum variance is reduced by ensemble averaging.

The real-time online monitoring software application developed within the scope of this thesis has been demonstrated in wind tunnel testing at the DNW-TWG, DNW-KKK and DNW-HST facilities and during flight vibration testing on the DLR-HALO research aircraft. We focus on the latter because it operates in the LTV framework. The system is identified in the time-domain by the data-driven or covariance-based SSI. Frequency-domain identification is performed by LSCF from cross-power spectral densities estimated by the segmented multi-taper method. The effect of various excitation types on system identification has been researched. Atmospheric turbulence and acoustic noise at constant speed and altitude constitute the nominal ambient excitation of the aircraft. Outliers in the measured responses due to small course corrections are present. The excitation level can be increased by air brake and spoiler deployment to obtain better data, at the cost of modifying the airflow around the wing and consequently the system's modal parameters. Random impulsive rudder kicks and aileron jerks increase the excitation at the lowest modes, but are straining for the pilot and irregular. High levels of broadband excitation are provided by wake turbulence without the need of any additional control surface deployment, but constant maneuvering and course corrections are necessary to keep the aircraft within the wake. The acceleration responses acquired during stabilized level flight show that some channels have a bad signal-to-noise ratio, measured signals are not normally-distributed, that the excitation is not stationary and that its spectrum is not constant. The evaluation of experimental data shows that the eigenfrequency and damping ratio can be estimated successfully and that the eigensurfaces of the lower modes can be reconstructed from stationary measurement points.

Vibration monitoring has been also performed at constant altitude for varying Mach number while flying in the wake of the DLR-Falcon aircraft. The wavelet analysis of the flight speed profile suggests that dynamic effects due to parameter variation can be neglected. In continuous modal analysis the buffer length is a compromise between the ability to resolve the parameter variation in time-domain and collecting sufficient data for system identification, while the overlap is determined by the desired refresh rate of the analysis (two to three seconds in our case). We show that it is possible to compensate for a short data buffer by averaging the identification results over several time instants. The comparison between LSCF and SSI reveals that the former produces clearer stabilization diagrams and that the latter tends to have less conservative damping estimates. Thanks to

the developments in spectral estimation and system identification presented in this thesis, the modal parameters estimated from the HALO flight vibration test are obtained from shorter buffer lengths than previously published. The analysis confirms that changes in the airflow around the aircraft due to maneuvers or control surface deployment have a marked effect on modal parameters.

Mode tracking over a whole three-hour flight reveals the effect of fuel consumption. While negligible for a stationary measurement point, it is noticeable over timescales in the order of one hour. A simplified analytical model has been devised to predict the eigenfrequency variation of wing modes due solely to aerodynamic effects, showing good agreement with the data. Periodic flow separation could be observed very shortly during a rapid descent maneuver with large air density and air speed variations. System identification confirms that multiple harmonics appear and that the damping ratio assumes the trend predicted by the theory. The change in dynamic pressure has a significant effect on the first symmetric wing bending. We use the tracking data from the rapid descent to extrapolate over the whole flight. It is shown once again that, even at equal flight conditions, the excitation type influences the modal parameter estimation, further motivating the need for real-time online monitoring.

### **9.1 Summary of the conclusions**

The effects of time variation on the system response have been characterized analytically in frequency-domain in order to provide insights about time-varying systems. This theoretical development allows a better characterization of slowly-varying systems and interpretation of identification results. The real-time operational modal analysis of parameter-varying aeroelastic systems has been demonstrated in wind tunnel experiments and during flight vibration testing. The practical aspects and challenges presented by a complex dynamic system have been elaborated. We conclude that the tracking of modal parameters can be performed successfully under a variety of flight and excitation conditions. Online monitoring of vibration tests can enhance security by providing an objective measure of the flutter margin. The continuous identification does not require stationary measurement points within the flight envelope and can provide the flight test engineer with experimental flutter diagrams while the flight vibration test is ongoing. This enables a change in the flight test philosophy and has the potential to reduce testing time.

### **9.2 Take-home message**

The thesis contributes to the theory and solution methods of time-varying systems, to the implementation of a mixed spectral estimation method, to improvements of system identification techniques and to the formulation of an effective mode tracking strategy. These techniques have been implemented into a vibration monitoring software.

The permanent real-time operational modal analysis of parameter-varying aeroelastic systems has been demonstrated experimentally during flight vibration testing.

### 9.3 Further research

There is always room for improvement. This can come from published works, better software or entirely new directions. The section reviews some of the topics.

#### 9.3.1 Parameter-varying aeroelastic systems

Recently, [GOSEA ET AL., 2020] have improved the Loewner framework for the identification of non-proper rational functions in the form of the continuous representation of aerodynamic forces (3.25). It produces a linear state-space model with generalized displacements as inputs and aerodynamic forces as outputs. This can lead to aeroelastic models with fewer lag states compared to Roger's approximation (3.13), with great gain in terms of efficiency. However, some issues concerning pole placement and stability must still be addressed. The Loewner framework (tangential interpolation) has been primarily developed for model order reduction [MAYO AND ANTOULAS, 2007], but it could be adapted to output-only system identification. The main advantage of this technique is the direct construction of implicit state-space models.

Reduced-order aeroelastic models are necessary to simplify calculations. In [KIM, 2019] and the related papers from the same author, the dynamic mode decomposition is applied to parameter-varying systems, resulting in models with a total number of states that is just double the number of structural states. This would be extremely beneficial computationally and from the point of view of mode tracking. This modeling technique can be combined aerodynamic forces identified with the Loewner framework.

The Peano-Baker series (2.14), Magnus expansion (2.15) and MacLaurin series (7.22) of the state transition matrix are extremely cumbersome for a symbolic computing environment. An efficient arbitrary-precision representation using Chebyshev polynomials or exponential basis functions should be employed. This can be implemented by overloading the linear algebra and integration operators to be able to handle series. This could provide precious insight into the frequency-domain structure of the response of linear time-varying systems.

#### 9.3.2 Spectral estimation

In [PRIETO ET AL., 2007] the bias of multi-taper autopower spectral density estimates is reduced by estimating the derivatives of the spectra. This technique could be expanded for estimating full and positive cross-power spectral densities for frequency-domain methods.

Research on various time-frequency distributions [COHEN, 1995] applied to aeroelastic systems could support the estimation of the spectrogram. This investigation falls partly under the future improvements in system identification.

#### 9.3.3 System identification

The implementation of SSI and maximum-likelihood LSCF algorithms for the estimation of the covariance of modal parameters provide more information for the stabilization diagram

and objective measures for assembling the modal model and for mode tracking. It could constitute a criterion for recognizing the poles arising from the fit of transients or time-varying effects, provided enough computing power is available. The eigenvalue covariance estimation in subspace methods is analyzed in [DÖHLER ET AL., 2013b; REYNDERS ET AL., 2008]. The maximum likelihood estimator for operational modal analysis is presented in [GUILLAUME ET AL., 1999].

The time-frequency description of a system can be fitted by a maximum-likelihood LSCF method [ZHOU ET AL., 2014]. This requires ensemble identification, but can be applied to general time-varying systems. By modifying its basis function it may be possible to apply it to different time-frequency distributions.

The Hilbert-Huang transform could provide new insight into the time-frequency structure of nonstationary data and the presence of nonlinearities. While there exist some applications in system identification [BAO ET AL., 2009] and structural health monitoring [CHEN ET AL., 2014], the application to flight vibration testing requires more research.

Recently-developed methods based on the dynamic mode decomposition show promising results in time-varying system identification [ZHANG ET AL., 2017] and compressed sensing [BAI ET AL., 2020]. Their use for aeroelastic testing could be validated with wind tunnel and FVT data collected for this thesis.

#### 9.3.4 Mode tracking

In the future, mode tracking could be performed by more sophisticated techniques. For instance, the linear assignment problem for pairing reference and comparison modes could be solved more quickly using the Jonker-Volgenant algorithm.

The multi-stage automatic mode clustering proposed in [NEU ET AL., 2017] does not require parameters or thresholds from the user, is not tied to a specific identification technique and is consistent with regard to model order.

Some system identification methods estimate the population variance of modal parameters, which can greatly improve mode tracking; when this information is not available, [YAGHOUBI ET AL., 2018] employs a bootstrapping method for assessing the statistical properties of the estimation that could be paired with the current framework.

The automated modal parameter selection using neural networks described in [VOLKMAR ET AL., 2019] is envisaged as a helpful post-processing tool for optimization.

#### 9.3.5 Flight vibration testing

The conventional flight testing procedure relies on stabilizing on a fixed altitude and speed to test for flutter. In the future, operational modal analysis could be conducted while accelerating the aircraft with a constant rate at a fixed altitude. This strategy is supported by numerical investigations [JACQUIER AND AYME, 2018].

Concerning a FVT on the HALO, results could be improved by a more balanced sensor distribution if better access within the airframe were possible. This would help in separating

similar modes with large participation of the wings such as the first antisymmetric engine and wing bending (refer to figure 8.12).

We have shown in [GOVERS ET AL., 2016] that the measured strains can be used to perform system identification. With this method, the estimation of mode shapes requires a transformation from strains to deformations, but the poles of the strain spectra are the same as those estimated using accelerometers or velocimeters. This technology is being developed further for aeroelastic testing [GOVERS ET AL., 2018]. Given the compactness, limited cost and robustness of strain sensors, they should find further modal analysis applications in FVT.

The fusion of modal parameters obtained from different sensor types, spectral estimation and system identification algorithms or settings is conceivable. For instance, higher modes that are known to be sensitive to the change of flight conditions could be estimated from shorter time data buffers (maintaining the same frequency bias error of lower modes). Referring to the previous topic, another possibility is the combination of modal analysis results obtained from strain sensors with those from accelerometers.

## 9.4 Words of wisdom

*The process of doing your second draft, is a process of making it look like you knew what you were doing all along.*

– Neil Gaiman

*Un directeur doit faire un film en accord avec ce qu'il est. Prendre la matière, la déglutir, accoucher à sa façon. Et ça, c'est formidable!*

– Alejandro Jodorowsky

*Vassene 'l tempo e l'uom non se n'avvede.*

– Dante





## Bibliography

- I. Abel. An analytical technique for predicting the characteristics of a flexible wing equipped with an active flutter-suppression system and comparison with wind-tunnel data. Technical Publication, NASA Langley Research Center, Hampton, VA, United States, 1979.
- S. Adhikari. *Damping Models for Structural Vibration*. PhD Thesis, University of Glasgow, Sept. 2000.
- A. H. Al-Mohy and N. J. Higham. A New Scaling and Squaring Algorithm for the Matrix Exponential. *SIAM Journal on Matrix Analysis and Applications*, 31(3):970–989, Jan. 2010. ISSN 0895-4798, 1095-7162. doi: 10.1137/09074721X.
- A. H. Al-Mohy and N. J. Higham. Computing the Action of the Matrix Exponential, with an Application to Exponential Integrators. *SIAM Journal on Scientific Computing*, 33(2):488–511, 2011. doi: 10.1137/100788860. eprint: <https://doi.org/10.1137/100788860>.
- E. Albano and W. P. Rodden. A doublet-lattice method for calculating lift distributions on oscillating surfaces in subsonic flows. *AIAA Journal*, 7(2):279–285, 1969. doi: 10.2514/3.5086. eprint: <https://doi.org/10.2514/3.5086>.
- R. Allemang. The Modal Assurance Criterion (MAC): Twenty Years of Use and Abuse. *Sound and Vibration*, 37, 2003.
- R. J. Allemang and D. L. Brown. A Unified Matrix Polynomial Approach to Modal Identification. *Journal of Sound and Vibration*, 211(3):301–322, 1998. ISSN 0022-460X. doi: <https://doi.org/10.1006/jsvi.1997.1321>.
- M. S. Allen. Frequency-Domain Identification of Linear Time-Periodic Systems Using LTI Techniques. *Journal of Computational and Nonlinear Dynamics*, 4(4), Aug. 2009. ISSN 1555-1415. doi: 10.1115/1.3187151.
- M. S. Allen, M. W. Sracic, S. Chauhan, and M. H. Hansen. Output-only modal analysis of linear time-periodic systems with application to wind turbine simulation data. *Mechanical Systems and Signal Processing*, 25(4):1174–1191, May 2011. ISSN 08883270. doi: 10.1016/j.ymssp.2010.12.018.
- S. Amador, M. El-Kafafy, Á. Cunha, and R. Brincker. A New Maximum Likelihood Estimator Formulated in Pole-Residue Modal Model. *Applied Sciences*, 9(15), 2019. ISSN 2076-3417. doi: 10.3390/app9153120.
- F. Amato, G. Celentano, and F. Garofalo. New sufficient conditions for the stability of slowly varying linear systems. *IEEE Transactions on Automatic Control*, 38(9):1409–1411, 1993. doi: 10.1109/9.237657.

- J. Antoni. The spectral kurtosis: a useful tool for characterising non-stationary signals. *Mechanical Systems and Signal Processing*, 20(2):282–307, 2006. ISSN 0888-3270. doi: <https://doi.org/10.1016/j.ymssp.2004.09.001>.
- J. Antoni and J. Schoukens. A comprehensive study of the bias and variance of frequency-response-function measurements: Optimal window selection and overlapping strategies. *Automatica*, 43(10):1723–1736, 2007. ISSN 0005-1098. doi: <https://doi.org/10.1016/j.automatica.2007.02.020>.
- P. J. Antsaklis and A. N. Michel. *Linear Systems*. Birkhäuser Basel, 1 edition, 2006. ISBN ISBN 978-0-8176-4435-2.
- L. D. Avendaño-Valencia, E. N. Chatzi, and D. Tcherniak. Gaussian process models for mitigation of operational variability in the structural health monitoring of wind turbines. *Mechanical Systems and Signal Processing*, 142:106686, 2020. ISSN 0888-3270. doi: <https://doi.org/10.1016/j.ymssp.2020.106686>.
- M. Baake and U. Schlaegel. The Peano-Baker series, 2012. eprint: 1011.1775.
- B. Babadi and E. N. Brown. A Review of Multitaper Spectral Analysis. *IEEE Transactions on Biomedical Engineering*, 61(5):1555–1564, 2014. doi: 10.1109/TBME.2014.2311996.
- Z. Bai, E. Kaiser, J. L. Proctor, J. N. Kutz, and S. L. Brunton. Dynamic Mode Decomposition for Compressive System Identification. *AIAA Journal*, 58(2):561–574, 2020. doi: 10.2514/1.J057870. eprint: <https://doi.org/10.2514/1.J057870>.
- J. A. Ball, I. Gohberg, and M. A. Kaashoek. A frequency response function for linear, time-varying systems. *Mathematics of Control, Signals and Systems*, 8(4):334–351, Dec. 1995. ISSN 1435-568X. doi: 10.1007/BF01209689.
- C. Bao, H. Hao, Z.-X. Li, and X. Zhu. Time-varying system identification using a newly improved HHT algorithm. *Computers & Structures*, 87(23-24):1611–1623, Dec. 2009. ISSN 00457949. doi: 10.1016/j.compstruc.2009.08.016.
- M. Basseville, A. Benveniste, M. Goursat, and L. Mevel. In-Flight Vibration Monitoring of Aeronautical Structures. *Control Systems, IEEE*, 27:27 – 42, Nov. 2007. doi: 10.1109/MCS.2007.904652.
- C. Beaverstock, M. Friswell, S. Adhikari, T. Richardson, and J. Du Bois. Automatic mode tracking for flight dynamic analysis using a spanning algorithm. *Aerospace Science and Technology*, 47:54–67, Dec. 2015. ISSN 12709638. doi: 10.1016/j.ast.2015.08.013.
- J. S. Bendat and A. G. Piersol. *Random Data: Analysis and Measurement Procedures*. Wiley Series in Probability and Statistics. Wiley, 2010. ISBN 978-0-470-24877-5.
- P. Benner, S. Gugercin, and K. Willcox. A Survey of Projection-Based Model Reduction Methods for Parametric Dynamical Systems. *SIAM Review*, 57(4):483–531, 2015. doi: 10.1137/130932715. eprint: <https://doi.org/10.1137/130932715>.

- A. Benveniste and L. Mevel. Nonstationary Consistency of Subspace Methods. *IEEE Transactions on Automatic Control*, 52(6):974–984, June 2007. ISSN 1558-2523. doi: 10.1109/TAC.2007.898970.
- D. Bernstein. *Matrix Mathematics: Theory, Facts, and Formulas (Second Edition)*. Princeton reference. Princeton University Press, 2009. ISBN 978-0-691-14039-1.
- R. Bisplinghoff, H. Ashley, and R. Halfman. *Aeroelasticity*. Dover Books on Aeronautical Engineering Series. Dover Publications, 1996. ISBN 978-0-486-69189-3.
- S. Blanes, F. Casas, J. Oteo, and J. Ros. The Magnus expansion and some of its applications. *Physics Reports*, 470(5-6):151–238, Jan. 2009. ISSN 0370-1573. doi: 10.1016/j.physrep.2008.11.001. Publisher: Elsevier BV.
- M. Bonnin, F. L. Traversa, and F. Bonani. Efficient spectral domain technique for the frequency locking analysis of nonlinear oscillators. *The European Physical Journal Plus*, 133(7):246, July 2018. ISSN 2190-5444. doi: 10.1140/epjp/i2018-12076-0.
- A. Brandt. *Noise and Vibration Analysis: Signal Analysis and Experimental Procedures*. EBL-Schweitzer. Wiley, 2011. ISBN 978-0-470-97811-5. doi: 10.1002/9780470978160.
- A. Brandt. Comparison and assessment of Methods to treat harmonics in Operational Modal Analysis. In *Paper presented at ICEDyn 2015, International conference on structural engineering dynamics 2015, Lagos, Portugal, June 22-24, 2015* ; Lagos, Portugal, 2015. University of Southern Denmark, Denmark.
- E. J. Breitbach. A Semi-Automatic Modal Survey Test Technique for Complex Aircraft and Spacecraft StructuresB. In *Proceedings of 3rd ESA Testing Symposium*, pages 519–528, Frascati, Italy, 1973.
- M. Brenner, R. Lind, D. Voracek, M. Brenner, R. Lind, and D. Voracek. Overview of recent flight flutter testing research at NASA Dryden. In *38th Structures, Structural Dynamics, and Materials Conference*. 1997. doi: 10.2514/6.1997-1023. eprint: <https://arc.aiaa.org/doi/pdf/10.2514/6.1997-1023>.
- R. Brincker and C. Ventura. *Introduction to Operational Modal Analysis*. John Wiley and Sons Ltd, 2015. ISBN 978-1-118-53514-1. doi: 10.1002/9781118535141.
- R. Brincker, L. Zhang, and P. Andersen. Modal Identification from Ambient Responses using Frequency Domain Decomposition. In *IMAC 18 : Proceedings of the International Modal Analysis Conference (IMAC), San Antonio, Texas, USA, February 7-10, 2000*, pages 625–630, 2000.
- T. Bronez. On the performance advantage of multitaper spectral analysis. *IEEE Transactions on Signal Processing*, 40(12):2941–2946, Dec. 1992. ISSN 1053587X. doi: 10.1109/78.175738.

- R. Burkard, M. Dell'Amico, and S. Martello. *Assignment Problems*. SIAM - Society of Industrial and Applied Mathematics, 1 edition, 2009. ISBN 978-0-89871-663-4.
- S. Burwitz, J. Sinske, G. Jeličić, and V. Handojo. Good vibrations - Surfin' the wake in style: An approach to real-time-in-flight modal and loads analysis. In *SFTE EC Symposium 2017 - 28th European Chapter Symposium*, Sept. 2017.
- E. A. Butcher, M. Sari, E. Bueler, and T. Carlson. Magnus' expansion for time-periodic systems: Parameter-dependent approximations. *Communications in Nonlinear Science and Numerical Simulation*, 14(12):4226–4245, Dec. 2009. ISSN 1007-5704. doi: 10.1016/j.cnsns.2009.02.030. Publisher: Elsevier.
- M. Böswald, D. Göge, U. Füllekrug, and Y. Govers. A Review of Experimental Modal Analysis Methods with respect to their Applicability to Test Data of Large Aircraft Structures. In *ISMA 2006 - International Conference on Noise & Vibration Engineering*, pages 2461–2481, 2006. Journal Abbreviation: Proceedings of the International Seminar of Modal Analysis.
- M. Böswald, Y. Govers, A. Vollan, and M. Basien. Solar Impulse – How to validate the numerical model of a superlight aircraft with A340 dimensions! In *ISMA 2010 - International Conference on Noise & Vibration Engineering*, 2010.
- M. Böswald, J. Schwochow, G. Jeličić, and Y. Govers. New Concepts for Ground and Flight Vibration Testing of Aircraft based on Output-Only Modal Analysis. In T. H. Ingolstadt, editor, *IOMAC 2017 - 7th International Operational Modal Analysis Conference*, pages 15–34. Shaker Verlag, 2017. Journal Abbreviation: Proceedings of the 7th International Operational Modal Analysis Conference (IOMAC).
- M. Böswald, Y. Govers, G. Jeličić, and R. Buchbach. Online monitoring of flutter stability during wind tunnel testing of an elastic wing with pylon and engine nacelle within the HMAE1 project. In *IFASD 2019 - International Forum on Aeroelasticity and Structural Dynamics*, June 2019.
- A. Cabboi, F. Magalhães, C. Gentile, and Á. Cunha. Automated modal identification and tracking: Application to an iron arch bridge. *Structural Control and Health Monitoring*, 24(1):e1854, 2017. doi: <https://doi.org/10.1002/stc.1854>. eprint: <https://onlinelibrary.wiley.com/doi/pdf/10.1002/stc.1854>.
- B. Cauberghe. *Applied Frequency-Domain System Identification in the Field of Experimental and Operational Modal Analysis*. PhD Thesis, Vrije Universiteit Brussel, 2004.
- Y. Chahlaoui and P. Van Dooren. Benchmark Examples for Model Reduction of Linear Time-Invariant Dynamical Systems. 45, Jan. 2005. doi: 10.1007/3-540-27909-1\_24. ISBN: 978-3-540-24545-2.

- B. Chen, S.-l. Zhao, and P.-y. Li. Application of Hilbert-Huang Transform in Structural Health Monitoring: A State-of-the-Art Review. *Mathematical Problems in Engineering*, 2014:317954, June 2014. ISSN 1024-123X. doi: 10.1155/2014/317954. Publisher: Hindawi Publishing Corporation.
- C.-T. Chen. *Linear Systems Theory and Design*. Oxford University Press, 1999. ISBN 978-0-19-511777-6. doi: 10.1002/1099-1239.
- A. Chopra. *Dynamics-of-structures*. Prentice Hall, Dec. 2019. ISBN 978-0-13-455514-0.
- L. Cohen. Time-frequency distributions-a review. *Proceedings of the IEEE*, 77(7):941–981, July 1989. ISSN 1558-2256. doi: 10.1109/5.30749.
- L. Cohen. *Time-frequency Analysis*. Electrical engineering signal processing. Prentice Hall PTR, 1995. ISBN 978-0-13-594532-2.
- M. Collet, M. Ouisse, M. Ruzzene, and M. Ichchou. Floquet–Bloch decomposition for the computation of dispersion of two-dimensional periodic, damped mechanical systems. *International Journal of Solids and Structures*, 48(20):2837–2848, Oct. 2011. ISSN 00207683. doi: 10.1016/j.ijsolstr.2011.06.002.
- S. Corda, F. J. Russel, J. N. Blanton, M. J. Vachon, and J. DeBoer. In-Flight Vibration Environment of the NASA F-15B Flight Test Fixture. Technical Report NASA/TM-2002-210719, Dryden Flight Research Center, 2002.
- J. Covioli and G. Coppotelli. Time-Domain Operational Modal Analysis in Support of Aeroelastic Flight Testing. 2019.
- G. L. Crouse and J. G. Leishman. Transonic aeroelasticity analysis using state-space unsteady aerodynamic modeling. *Journal of Aircraft*, 29(1):153–160, 1992. doi: 10.2514/3.46139. eprint: <https://doi.org/10.2514/3.46139>.
- J. De Caigny, R. Pintelon, J. F. Camino, and J. Swevers. Interpolated Modeling of LPV Systems. *IEEE Transactions on Control Systems Technology*, 22(6):2232–2246, Nov. 2014. ISSN 1558-0865. doi: 10.1109/TCST.2014.2300510.
- K. De Cock, B. Peeters, A. Vecchio, H. Van der Auweraer, and B. De Moor. Subspace system identification for mechanical engineering. In *Proceedings of ISMA 2002: International Conference on Noise and Vibration Engineering, vols 1-5*, pages 1333–1352. KATHOLIEKE UNIV LEUVEN, DEPT WERKTUIGKUNDE, 2002. ISBN 90-73802-79-2. Backup Publisher: Sas, P.
- K. De Cock, G. Mercère, and B. De Moor. Recursive subspace identification for in flight modal analysis of airplanes. In *International Conference on Noise and Vibration Engineering, ISMA 2006*, page CDROM, Leuven, Belgium, Sept. 2006.

- T. De Troyer, R. Zouari, P. Guillaume, and L. Mevel. A new frequency-domain flutter speed prediction algorithm using a simplified linear aeroelastic model. In *Proceedings of the International Conference on Noise and Vibration Engineering ISMA*, Proceedings of the International Conference on Noise and Vibration Engineering ISMA, pages 1197–1206, Sept. 2008.
- R. DeCarlo. *Linear Systems: A State Variable Approach with Numerical Implementation*. Prentice Hall, 1989. ISBN 978-0-13-536814-5.
- J. Den Hartog. *Mechanical Vibrations*. Civil, Mechanical and Other Engineering Series. Dover Publications, 1985. ISBN 978-0-486-64785-2.
- J. D’Errico. Eigenshuffle: Consistently sorted eigenvalue and eigenvector sequences, 2020. <https://www.mathworks.com/matlabcentral/fileexchange/22885-eigenshuffle>.
- DLR.de. G550 DLR-HALO research aircraft technical data, 2021. <https://www.dlr.de/content/en/articles/missions-projects/halo/technical-data.html>.
- DNW. German-Dutch Wind Tunnels, 2021. <https://www.dnw.aero/wind-tunnels/>.
- E. R. Dougherty. *Random Processes for Image Signal Processing*. Wiley-IEEE Press, 1998. ISBN 978-0-7803-3495-3.
- M. Döhler and L. Mevel. Fast Multi-Order Stochastic Subspace Identification. Rapport de recherche 7429, INRIA, Oct. 2010.
- M. Döhler, F. Hille, L. Mevel, and W. Rucker. Estimation of modal parameters and their uncertainty bounds from subspace-based system identification. In M. Klocker, editor, *IRIS Industrial Safety and Life Cycle Engineering - Technologies / Standards / Applications*, pages 91–106. VCE, Aug. 2013a.
- M. Döhler, X.-B. Lam, and L. Mevel. Uncertainty quantification for modal parameters from stochastic subspace identification on multi-setup measurements. *Mechanical Systems and Signal Processing*, 36(2):562–581, 2013b. ISSN 0888-3270. doi: <https://doi.org/10.1016/j.ymsp.2012.11.011>.
- EASA. Certification Specifications for Large Aeroplanes CS-25, Sept. 2007.
- M. El-kafafy, T. D. Troyer, B. Peeters, and P. Guillaume. Fast maximum-likelihood identification of modal parameters with uncertainty intervals: A modal model-based formulation. *Mechanical Systems and Signal Processing*, 37(1):422–439, 2013. ISSN 0888-3270. doi: <https://doi.org/10.1016/j.ymsp.2013.01.013>.
- J. Ertveldt, J. Lataire, R. Pintelon, and S. Vanlanduit. Frequency-domain identification of time-varying systems for analysis and prediction of aeroelastic flutter. *Mechanical Systems and Signal Processing*, 47(1):225–242, 2014. ISSN 0888-3270. doi: <https://doi.org/10.1016/j.ymsp.2013.08.020>.

- M. Eugeni, G. Coppotelli, F. Mastroddi, P. Gaudenzi, S. Muller, and B. Troclet. OMA analysis of a launcher under operational conditions with time-varying properties. *CEAS Space Journal*, 10(3):381–406, Sept. 2018. ISSN 1868-2502, 1868-2510. doi: 10.1007/s12567-018-0209-5.
- FAA. AC 25.629-1B - Aeroelastic Stability Substantiation of Transport Category Airplanes, Oct. 2014.
- Z. Feng, M. Liang, and F. Chu. Recent advances in time–frequency analysis methods for machinery fault diagnosis: A review with application examples. *Mechanical Systems and Signal Processing*, 38(1):165–205, July 2013. ISSN 08883270. doi: 10.1016/j.ymssp.2013.01.017.
- D. Friedewald, R. Thormann, C. Kaiser, and J. Nitzsche. Quasi-steady doublet-lattice correction for aerodynamic gust response prediction in attached and separated transonic flow. *CEAS Aeronautical Journal*, 9(1):53–66, Mar. 2018. ISSN 1869-5582, 1869-5590. doi: 10.1007/s13272-017-0273-0.
- M. Frigo and S. G. Johnson. FFTW: an adaptive software architecture for the FFT. In *Proceedings of the 1998 IEEE International Conference on Acoustics, Speech and Signal Processing, ICASSP '98 (Cat. No.98CH36181)*, volume 3, pages 1381–1384 vol.3, May 1998. doi: 10.1109/ICASSP.1998.681704. ISSN: 1520-6149.
- X. Gao, D. Liberzon, J. Liu, and T. Başar. Unified stability criteria for slowly time-varying and switched linear systems. *Automatica*, 96:110–120, Oct. 2018. ISSN 00051098. doi: 10.1016/j.automatica.2018.06.025.
- W. Geißler. Unsteady Aerodynamic Inputs for Aeroelastic Analyses. Technical Report DFVLR-Mitt. 80-01, Deutsche Forschungs- und Versuchsanstalt für Luft- und Raumfahrt, Institut für Aeroelastik, Göttingen, 1980.
- M. Geuss, H. Panzer, and B. Lohmann. On parametric model order reduction by matrix interpolation. In *2013 European Control Conference (ECC)*, pages 3433–3438, Zurich, July 2013. IEEE. ISBN 978-3-033-03962-9. doi: 10.23919/ECC.2013.6669829.
- S. Giclais, P. Lubrina, and C. Stephan. Aircraft Ground Vibration Testing at ONERA. Dec. 2016.
- A. Giez, M. Zöger, V. Dreiling, and C. Mallaun. Static Source Error Calibration of a Nose Boom Mounted Air Data System on an Atmospheric Research Aircraft Using the Trailing Cone Method. Technical report, Deutsches Zentrum für Luft- und Raumfahrt, 2020.
- J. R. Gilbert, C. Moler, and R. Schreiber. Sparse Matrices In MATLAB: Design And Implementation. *SIAM J. Matrix Anal. Appl.*, 13:333–356, 1992.



- I. Gosea, Q. Zhang, and A. Antoulas. Preserving the DAE structure in the Loewner model reduction and identification framework. *Advances in Computational Mathematics*, 46, Jan. 2020. doi: 10.1007/s10444-020-09752-8.
- M. Goursat, M. Döhler, L. Mevel, and P. Andersen. Crystal Clear SSI for Operational Modal Analysis of Aerospace Vehicles. In *Conference Proceedings of the Society for Experimental Mechanics Series*, volume 3 of *Structural Dynamics*, pages 1421–1430. Springer, 2011. ISBN 978-1-4419-9833-0. [https://doi.org/10.1007/978-1-4419-9834-7\\_125](https://doi.org/10.1007/978-1-4419-9834-7_125).
- Y. Govers. Parameter identification of structural dynamic models by inverse statistical analysis. Technical report, 2012.
- Y. Govers, M. Böswald, P. Lubrina, S. Giclais, C. Stéphan, and N. Botargues. AIRBUS A350XWB Ground Vibration Testing: Efficient techniques for customer oriented on-site modal identification. In *ISMA 2014*, pages 2503–2516, 2014.
- Y. Govers, G. Jelcic, and T. Akbay. The use of strain sensors for modal identification of aeroelastic structures. In *ISMA 2016 - International Conference on Noise and Vibration Engineering*, pages 2207–2216, 2016.
- Y. Govers, J. Sinske, J. Schwochow, G. Jeličić, R. Buchbach, J. Springer, and M. Böswald. Efficient ground vibration testing of aircraft based on output-only modal analysis during taxi. In *AIAA SciTech 2017*, 2017.
- Y. Govers, M. Y. Meddaikar, and K. Sinha. Model validation of an aeroelastically-tailored forward swept wing using fibre-optical strain measurements. In *ISMA 2018 - International Conference on Noise and Vibration Engineering*, pages 1403–1417, 2018.
- Y. Govers, H. Mai, J. Arnold, J. K. S. Dillinger, A. K. A. Pereira, C. B. Jr, E. K. Takara, M. S. Correa, O. A. F. Mello, R. F. A. Marques, E. G. M. Geurts, R. J. C. Creemers, H. S. Timmermans, R. Habing, and K. Kapteijn. Wind tunnel flutter testing on a highly flexible wing for aeroelastic validation in the transonic regime within the HMAE1 project. In *IFASD 2019 – International Forum on Aeroelasticity and Structural Dynamics*, volume IFASD, June 2019. Journal Abbreviation: IFASD 2019 - International Forum on Aeroelasticity and Structural Dynamics.
- W. Gracey. *Measurement of Aircraft Speed and Altitude*. Wiley, 1981. ISBN 978-0-471-08511-9.
- P. Guillaume, L. Hermans, and H. Van der Auweraer. Maximum likelihood identification of modal parameters from operational data. In *IMAC - Proceedings of the 17th International Modal Analysis Conference*, volume 3727, pages 1887–1893. Society of Photo-optical Instrumentation Engineers, 1999. ISBN 0-912053-64-X.

- K. Gupta, M. Brenner, L. Voelker, and D. F. R. Facility. *Development of an Integrated Aeroservoelastic Analysis Program and Correlation with Test Data*. NASA technical paper. National Aeronautics and Space Administration, Office of Management, Scientific and Technical Information Division, 1991.
- K. K. Gupta. Development and Application of an Integrate Multidisciplinary Analysis Capability. *International Journal for Numerical Methods in Engineering*, 40(3):533–550, 1997. doi: [https://doi.org/10.1002/\(SICI\)1097-0207\(19970215\)40:3<533::AID-NME78>3.0.CO;2-W](https://doi.org/10.1002/(SICI)1097-0207(19970215)40:3<533::AID-NME78>3.0.CO;2-W).
- E. Hairer, S. Nørsett, and G. Wanner. *Solving Ordinary Differential Equations I: Nonstiff Problems*. Springer Series in Computational Mathematics. Springer Berlin Heidelberg, 2008. ISBN 978-3-540-56670-0.
- C. L. Haley and M. Anitescu. Optimal Bandwidth for Multitaper Spectrum Estimation. *IEEE Signal Processing Letters*, 24(11):1696–1700, 2017. doi: 10.1109/LSP.2017.2719943.
- HALO.DLR.de. G550 DLR-HALO production aircraft technical data, 2021. <https://www.halo.dlr.de/aircraft/specifications.html>.
- J. Hammond and P. White. The Analysis of Non-Stationary Signals Using Time-Frequency Methods. *Journal of Sound and Vibration*, 190(3):419–447, Feb. 1996. ISSN 0022460X. doi: 10.1006/jsvi.1996.0072.
- K. Hannemann, J. M. Schramm, S. Karl, and S. Laurence. Free Flight Testing of a Scramjet Engine in a Large Scale Shock Tunnel. In *20th AIAA International Space Planes and Hypersonic Systems and Technologies Conference*, Conference Proceedings online, pages 1–15, 2015. Issue: 3608.
- W. Heylen, S. Lammens, and P. Sas. *Modal Analysis Theory and Testing*. Katholieke Universiteit Leuven, Faculty of Engineering, Department of Mechanical Engineering, Division of Production Engineering, Machine Design and Automation, 1998. ISBN 978-90-73802-61-2.
- P. Hill and C. Peterson. *Mechanics and Thermodynamics of Propulsion*. Addison-Wesley, 1992. ISBN 978-0-201-14659-2.
- F. Hoblit. *Gust Loads on Aircraft: Concepts and Applications*. AIAA Education Series. American Institute of Aeronautics & Astronautics, 1988. ISBN 978-0-930403-45-4. doi: 10.2514/4.861888.
- I. Houtzager, J. van Wingerden, and M. Verhaegen. Recursive Predictor-Based Subspace Identification With Application to the Real-Time Closed-Loop Tracking of Flutter. *IEEE Transactions on Control Systems Technology*, 20(4):934–949, 2012. ISSN 1063-6536. Publisher: Institute of Electrical and Electronics Engineers (IEEE).

- C. S. Hsu. On approximating a general linear periodic system. *Journal of Mathematical Analysis and Applications*, 45:234–251, 1974.
- R. Huang and Z. Qiu. Transient aeroelastic responses and flutter analysis of a variable-span wing during the morphing process. *Chinese Journal of Aeronautics*, 26(6):1430–1438, Dec. 2013. ISSN 10009361. doi: 10.1016/j.cja.2013.07.047.
- A. Ilchmann, D. Owens, and D. Prätzel-Wolters. Sufficient conditions for stability of linear time-varying systems. *Systems & Control Letters*, 9(2):157–163, Aug. 1987. ISSN 01676911. doi: 10.1016/0167-6911(87)90022-3.
- M. Iovnovich, T. Nahom, M. Presman, D. Avsaid, T. Braier, and D. E. Raveh. Assessment of Advanced Flutter Flight-Test Techniques and Flutter Boundary Prediction Methods. *Journal of Aircraft*, 55(5):1877–1889, Sept. 2018. ISSN 0021-8669, 1533-3868. doi: 10.2514/1.C034716.
- ISO. International Standard Atmosphere (ISO) 2533:1975. ISO standard ISO/TC 20/SC 6, ISO, 1975.
- B. Jacquier and F. Ayme. On-line tracking of aircraft aeroelastic modes during flutter flight tests. In *28th International Conference on Noise and Vibration engineering (ISMA2018)*, LOUVAIN, Belgium, Sept. 2018.
- G. Jekabsons. Locally Weighted Polynomials toolbox for Matlab/OctaveSymbolic Math Toolbox - ver. 2.2, 2016. <http://www.cs.rtu.lv/jekabsons>.
- G. Jeličić, J. Schwochow, Y. Govers, A. Hebler, and M. Böswald. Real-time assessment of flutter stability based on automated output-only modal analysis. In *ISMA 2014 - International Conference on Noise and Vibration Engineering*, pages 3693–3706, 2014. Journal Abbreviation: International Conference on Noise and Vibration Engineering.
- G. Jeličić, J. Schwochow, Y. Govers, A. Hebler, and M. Böswald. Fast Online Monitoring and System Identification for the Application in the Field of Aeroelasticity. In *ICoEC2015 - International Conference on Engineering Vibration 2015*, 2015.
- G. Jeličić, J. Schwochow, Y. Govers, and M. Böswald. Automatische Schwingungsüberwachung von aeroelastischen Systemen. In V. V. D. Ingenieure, editor, *VDI-Fachtagung Schwingungsanalyse und Identifikation 2016*, volume 2259 of *VDI-Berichte*, pages 211–222. VDI-Verlag, 2016.
- G. Jeličić, J. Schwochow, Y. Govers, J. Sinske, R. Buchbach, and J. Springer. Online Monitoring of Aircraft Modal Parameters during Flight Test based on permanent Output-only Modal Analysis. In *AIAA SciTech 2017*, 2017. Journal Abbreviation: 58th AIAA/ASCE/AHS/ASC Structures, Structural Dynamics, and Materials Conference.

- G. Jeličić, M. Böswald, and A. Brandt. Improved computation in terms of accuracy and speed of LTI system response with arbitrary input. *Mechanical Systems and Signal Processing*, 150:107252, 2021. ISSN 0888-3270. doi: <https://doi.org/10.1016/j.ymssp.2020.107252>.
- A. Jhinaoui, L. Mevel, and J. Morlier. A new SSI algorithm for LPTV systems: Application to a hinged-bladed helicopter. *Mechanical Systems and Signal Processing*, 42(1-2):152–166, Jan. 2014. ISSN 08883270. doi: 10.1016/j.ymssp.2013.08.006.
- D. W. Jordan and P. Smith. *Nonlinear Ordinary Differential Equations*. Oxford University Press, 4th edition, 2007. ISBN 978-0-19-920824-1.
- E. W. Kamen. The poles and zeros of a linear time-varying system. *Linear Algebra and its Applications*, 98:263–289, 1988. ISSN 0024-3795. doi: [https://doi.org/10.1016/0024-3795\(88\)90168-1](https://doi.org/10.1016/0024-3795(88)90168-1).
- M. Karpel. Design for Active and Passive Flutter Suppression and Gust Alleviation. Contractor Report 3482, NASA Langley Research Center, Langley, VA, USA, 1981.
- M. Karpel. Design for Active Flutter Suppression and Gust Alleviation Using State-Space Aeroelastic Modeling. *Journal of Aircraft*, 19(3):221–227, 1982. doi: 10.2514/3.57379. [\\_eprint: https://doi.org/10.2514/3.57379](https://doi.org/10.2514/3.57379).
- J. Katz and A. Plotkin. *Low-Speed Aerodynamics*. Cambridge Aerospace Series. Cambridge University Press, 2 edition, 2001. doi: 10.1017/CBO9780511810329.
- M. Kehoe. *A Historical Overview of Flight Flutter Testing*. NASA technical memorandum. National Aeronautics and Space Administration, Office of Management, Scientific and Technical Information Program, NASA Dryden Flight Research, 1995.
- H. Khalil. *Nonlinear Systems*. Pearson Education. Prentice Hall, 2nd edition, 1996. ISBN 978-0-13-067389-3.
- J. Kierzenka and L. F. Shampine. A BVP Solver Based on Residual Control and the Maltab PSE. *ACM Trans. Math. Softw.*, 27(3):299–316, Sept. 2001. ISSN 0098-3500. doi: 10.1145/502800.502801. Place: New York, NY, USA Publisher: Association for Computing Machinery.
- T. Kim. Flutter prediction methodology based on dynamic eigen decomposition and frequency-domain stability. *Journal of Fluids and Structures*, 86:354–367, Apr. 2019. ISSN 08899746. doi: 10.1016/j.jfluidstructs.2019.01.022.
- G. Kitzhofer, O. Koch, Othmar, G. Pulverer, C. Simon, and E. B. Weinmüller. The New MATLAB Code bypsuite for the Solution of Singular Implicit BVPs. Technical report, 2010.
- W. R. Krüger and T. Klimmek. Definition of a Comprehensive Loads Process in the DLR Project iLOADS. In *Deutscher Luft- und Raumfahrtkongress 2016*, 2016.

- M. H. Kutner, C. J. Nachtsheim, J. Neter, and W. Li. *Applied Linear Statistical Models (5th ed.)*. McGraw-Hill Education, 2008. ISBN 978-0-07-112221-4.
- K. König. Pretension and Reality of Flutter-Relevant Tests. Advanced Aeroservoelastic Testing and Data Analysis AGARD-CP-566, 1995.
- H. G. Küssner. General Airfoil Theory. Technical Report 979, NASA, 1941.
- N. Lang, J. Saak, and T. Stykel. Balanced truncation model reduction for linear time-varying systems. *Mathematical and Computer Modelling of Dynamical Systems*, 22(4): 267–281, 2016. doi: 10.1080/13873954.2016.1198386.
- J. Lanslots, B. Rodiers, and B. Peeters. Automated pole-selection: Proof-of-concept & validation. 2004.
- W. E. Larimore. Canonical variate analysis in identification, filtering, and adaptive control. In *29th IEEE Conference on Decision and Control*, pages 596–604 vol.2, 1990. doi: 10.1109/CDC.1990.203665.
- J. Lataire. *Frequency Domain Measurement and Identification of Linear, Time-Varying Systems*. PhD thesis, Vrije Universiteit Brussel, Brussels, 2011.
- J. Lataire and R. Pintelon. Frequency-domain weighted non-linear least-squares estimation of continuous-time, time-varying systems. *IET Control Theory & Applications*, 5(7): 923–933, 2010. ISSN 1751-8644, 1751-8652. doi: 10.1049/iet-cta.2010.0223.
- A. Lazarus and O. Thomas. A harmonic-based method for computing the stability of periodic solutions of dynamical systems. *Comptes Rendus Mécanique*, 338(9):510–517, Sept. 2010. ISSN 16310721. doi: 10.1016/j.crme.2010.07.020.
- R. Lind. *Robust Flutter Margin Analysis that Incorporates Flight Data*. NASA technical paper. NASA, 1998.
- K. Liu. Identification of Linear Time-Varying Systems. *Journal of Sound and Vibration*, 206(4):487–505, 1997.
- K. Liu. Extension of Modal Analysis to Linear Time-Varying Systems. *Journal of Sound and Vibration*, 226(1):149–167, Sept. 1999. ISSN 0022460X. doi: 10.1006/jsvi.1999.2286.
- E. Livne. Aircraft Active Flutter Suppression: State of the Art and Technology Maturation Needs. *Journal of Aircraft*, 55(1):410–452, Jan. 2018. ISSN 0021-8669, 1533-3868. doi: 10.2514/1.C034442.
- L. Ljung. *System Identification: Theory for the User*. Prentice Hall information and system sciences series. Prentice Hall PTR, 1999. ISBN 978-0-13-656695-3.
- G. Looye. Integrated Flight Mechanics and Aeroelastic Aircraft Modeling using Object-Oriented Modeling Techniques. In *AIAA Modeling and Simulation Technology Conference, AIAA-99-4192*, Sept. 1999.

- T. Luspay, T. Péni, I. Gözse, Z. Szabó, and B. Vanek. Model reduction for LPV systems based on approximate modal decomposition. *International Journal for Numerical Methods in Engineering*, 113(6):891–909, 2018. doi: <https://doi.org/10.1002/nme.5692>.
- K. Lust. Improved Numerical Floquet Multipliers. *International Journal of Bifurcation and Chaos*, 11(09):2389–2410, Sept. 2001. ISSN 0218-1274, 1793-6551. doi: 10.1142/S0218127401003486.
- Z. Ma, L. Liu, S. Zhou, F. Naets, W. Heylen, and W. Desmet. Dynamic Stability Analysis of Linear Time-varying Systems via an Extended Modal Identification Approach. *Chinese Journal of Mechanical Engineering*, 30(2):459–471, Mar. 2017. doi: 10.1007/s10033-017-0075-7.
- M. Majji, J.-N. Juang, and J. L. Junkins. Time-Varying Eigensystem Realization Algorithm. *Journal of Guidance, Control, and Dynamics*, 33(1):13–28, Jan. 2010. ISSN 0731-5090, 1533-3884. doi: 10.2514/1.45722.
- S. Mallat. *A Wavelet Tour of Signal Processing: The Sparse Way*. Elsevier Science, 2008. ISBN 978-0-08-092202-7.
- G. Marrongelli and C. Gentile. Development and Application of automated OMA Algorithms. In *8th International Operational Modal Analysis Conference*, Copenhagen, 2019.
- J. B. Maurice, F. King, W. Fichter, O. Dieterich, and P. Konstanzer. Floquet Convergence Analysis for Periodic Active Rotor Systems Equipped with Trailing Edge Flaps. In *35th European Rotorcraft Forum 2009*, 2009.
- A. J. Mayo and A. C. Antoulas. A framework for the solution of the generalized realization problem. *Linear Algebra and its Applications*, 425(2):634–662, 2007. ISSN 0024-3795. doi: <https://doi.org/10.1016/j.laa.2007.03.008>.
- T. Mckelvey. Subspace methods for frequency domain data. pages 673 – 678 vol.1, 2004. ISBN 0-7803-8335-4. doi: 10.23919/ACC.2004.1383681.
- G. Mercere, M. Lovera, and E. Laroche. Identification of a flexible robot manipulator using a linear parameter-varying descriptor state-space structure. In *IEEE Conference on Decision and Control and European Control Conference*, pages 818–823, Orlando, FL, USA, Dec. 2011. IEEE. ISBN 978-1-61284-801-3 978-1-61284-800-6 978-1-4673-0457-3 978-1-61284-799-3. doi: 10.1109/CDC.2011.6160683.
- L. Mevel, A. Benveniste, M. Basseville, M. Goursat, B. Peeters, H. Van der Auweraer, and A. Vecchio. Input/output versus output-only data processing for structural identification—Application to in-flight data analysis. *Journal of Sound and Vibration*, 295(3-5): 531–552, Aug. 2006. ISSN 0022460X. doi: 10.1016/j.jsv.2006.01.039.

- G. Mogenier, T. Baranger, G. Ferraris, R. Dufour, and L. Durantay. A criterion for mode shape tracking: application to Campbell diagrams. *Journal of Vibration and Control*, pages 1–12, Oct. 2012. doi: 10.1177/1077546312463714. Publisher: SAGE Publications.
- P. Montagnier, R. J. Spiteri, and J. Angeles. The control of linear time-periodic systems using Floquet–Lyapunov theory. *International Journal of Control*, 77(5):472–490, Mar. 2004. ISSN 0020-7179, 1366-5820. doi: 10.1080/00207170410001667477.
- E. A. Morelli and V. Klein. Application of System Identification to Aircraft at NASA Langley Research Center. *Journal of Aircraft*, 42(1):12–25, Jan. 2005. ISSN 0021-8669, 1533-3868. doi: 10.2514/1.3648.
- C. Nam, Y. Kim, and T. A. Weisshaar. *Computational Aids in Aeroservoelastic Analysis Using MATLAB*. 2001.
- E. Neu, F. Janser, A. A. Khatibi, C. Braun, and A. C. Orifici. Operational Modal Analysis of a wing excited by transonic flow. *Aerospace Science and Technology*, 49:73–79, Feb. 2016. ISSN 12709638. doi: 10.1016/j.ast.2015.11.032.
- E. Neu, F. Janser, A. A. Khatibi, and A. C. Orifici. Fully Automated Operational Modal Analysis using multi-stage clustering. *Mechanical Systems and Signal Processing*, 84: 308–323, 2017. ISSN 0888-3270. doi: <https://doi.org/10.1016/j.ymssp.2016.07.031>.
- E. W. Ng and M. Geller. A table of integrals of the Error functions. *Journal of Research of the National Bureau of Standards, Section B: Mathematical Sciences*, 73B(1):1, Jan. 1969. ISSN 0098-8979. doi: 10.6028/jres.073B.001.
- Y. Nureki and S. Murashige. Computation of Floquet Multipliers Using an Iterative Method for Variational Equations. *IEICE Transactions on Fundamentals of Electronics, Communications and Computer Sciences*, E92-A(5):1331–1338, 2009. ISSN 0916-8508, 1745-1337. doi: 10.1587/transfun.E92.A.1331.
- R. O’Brien and P. Iglesias. Poles and zeros for time-varying systems. In *Proceedings of the 1997 American Control Conference (Cat. No.97CH36041)*, pages 2672–2676 vol.5, Albuquerque, NM, USA, 1997. IEEE. ISBN 978-0-7803-3832-6. doi: 10.1109/ACC.1997.611941.
- R. O’Brien and P. Iglesias. On the poles and zeros of linear, time-varying systems. *IEEE Transactions on Circuits and Systems I: Fundamental Theory and Applications*, 48(5): 565–577, May 2001. ISSN 10577122. doi: 10.1109/81.922459.
- A. Oppenheim and R. Schaffer. *Discrete-time Signal Processing*. Prentice-Hall signal processing series. Pearson, 2010. ISBN 978-0-13-198842-2.
- A. V. Oppenheim, A. S. Willsky, and S. H. Nawab. *Signals & Systems (2nd Ed.)*. Prentice-Hall, Inc., USA, 1996. ISBN 0-13-814757-4.

- R. Pappa, K. Elliott, and A. Schenk. A Consistent-Mode Indicator for the Eigensystem Realization Algorithm. In *Journal of Guidance Control and Dynamics - J GUID CONTROL DYNAM*, volume 16, 1993. doi: 10.2514/3.21092.
- R. Pappa, S. Woodard, and J.-N. Juang. The development of autonomous structural modal identification. *S V Sound and Vibration*, 31:18–23, 1997.
- G. Pasinetti and P. Mantegazza. Single Finite States Modeling of Aerodynamic Forces Related to Structural Motions and Gusts. *AIAA Journal*, 37(5):604–612, 1999. doi: 10.2514/2.760. \_eprint: <https://doi.org/10.2514/2.760>.
- B. Peeters and G. de Roeck. Reference-based Stochastic Subspace Identification for Output-only Modal Analysis. *Mechanical Systems and Signal Processing*, 13(6):855–878, 1999. ISSN 0888-3270. doi: <https://doi.org/10.1006/mssp.1999.1249>.
- B. Peeters and H. Van der Auweraer. PolyMax: a revolution in operational modal analysis. *1st International Operational Modal Analysis Conference*, 2005.
- B. Peeters, T. De Troyer, P. Guillaume, and H. Van der Auweraer. In-flight modal analysis—a comparison between sweep and turbulence excitation. In *Proceedings of the 22th International Conference on Noise and Vibration Engineering*, pages 1627–1641, 2006.
- D. B. Percival and A. T. Walden. *Spectral Analysis for Physical Applications*. Cambridge University Press, 1993. doi: 10.1017/CBO9780511622762.
- R. Pintelon and J. Schoukens. *System Identification: A Frequency Domain Approach*. Wiley, 2004. ISBN 978-0-470-64037-1. doi: 10.1002/9781118287422.
- R. Pintelon, P. Guillaume, and J. Schoukens. Uncertainty calculation in (operational) modal analysis. *Mechanical Systems and Signal Processing*, 21(6):2359–2373, 2007. ISSN 0888-3270. doi: <https://doi.org/10.1016/j.ymsp.2006.11.007>.
- A. Poulimenos and S. Fassois. Parametric time-domain methods for non-stationary random vibration modelling and analysis — A critical survey and comparison. *Mechanical Systems and Signal Processing*, 20(4):763–816, May 2006. ISSN 08883270. doi: 10.1016/j.ymsp.2005.10.003.
- G. A. Prieto, R. L. Parker, D. J. Thomson, F. L. Vernon, and R. L. Graham. Reducing the bias of multitaper spectrum estimates. *Geophysical Journal International*, 171(3): 1269–1281, 2007. doi: <https://doi.org/10.1111/j.1365-246X.2007.03592.x>.
- J. G. Proakis and D. K. Manolakis. *Digital Signal Processing: Pearson New International Edition*. Pearson Education Limited, 2013. ISBN 978-1-292-03816-2.
- A. Quarteroni, R. Sacco, and F. Saleri. *Numerical Mathematics (Texts in Applied Mathematics)*. Springer-Verlag, Berlin, Heidelberg, 2006. ISBN 3-540-34658-9.



- D. Quero, P. Vuillemin, and C. Poussot-Vassal. A generalized eigenvalue solution to the flutter stability problem with true damping: The p-L method. *Journal of Fluids and Structures*, 103:103266, May 2021. ISSN 08899746. doi: 10.1016/j.jfluidstructs.2021.103266.
- M. Radeş. Performance of Various Mode Indicator Functions. *Shock and Vibration*, 17: 473–482, Jan. 2010. doi: 10.1155/2010/546802.
- C. Rainieri and G. Fabbrocino. *Operational Modal Analysis of Civil Engineering Structures, An introduction and a guide for applications*. Springer Nature, 2014. ISBN 978-1-4939-0767-0. doi: 10.1007/978-1-4939-0767-0.
- S. S. Rao. *Mechanical Vibrations*. Pearson Education, Incorporated, 6 edition, 2017. ISBN 978-0-13-436130-7.
- D. E. Raveh. Computational-fluid-dynamics-based aeroelastic analysis and structural design optimization—a researcher’s perspective. *Computer Methods in Applied Mechanics and Engineering*, 194(30):3453–3471, 2005. ISSN 0045-7825. doi: <https://doi.org/10.1016/j.cma.2004.12.027>.
- E. Reynders. System Identification Methods for (Operational) Modal Analysis: Review and Comparison. *Archives of Computational Methods in Engineering*, 19(1):51–124, Mar. 2012. ISSN 1886-1784. doi: 10.1007/s11831-012-9069-x.
- E. Reynders, R. Pintelon, and G. D. Roeck. Uncertainty bounds on modal parameters obtained from stochastic subspace identification. *Mechanical Systems and Signal Processing*, 22(4):948–969, 2008. ISSN 0888-3270. doi: <https://doi.org/10.1016/j.ymsp.2007.10.009>.
- E. Reynders, J. Houbrechts, and G. D. Roeck. Fully automated (operational) modal analysis. *Mechanical Systems and Signal Processing*, 29:228–250, 2012. ISSN 0888-3270. doi: <https://doi.org/10.1016/j.ymsp.2012.01.007>.
- J. A. Richards. *Analysis of Periodically Time-Varying Systems*. Communications and Control Engineering Series. Springer, 1983. ISBN 978-3-540-11689-9.
- M. Ripepi and P. Mantegazza. Improved matrix fraction approximation of aerodynamic transfer matrices. *AIAA Journal*, 51(5):1156–1173, 2013.
- M. R. Ritter. *An extended modal approach for nonlinear aeroelastic simulations of highly flexible aircraft structures*. Doctoral Thesis, Technische Universität Berlin, Berlin, 2019.
- W. P. Rodden. *Theoretical and Computational Aeroelasticity*. Crest Publishing, 1st edition, 2011. ISBN 978-0-692-01241-3.
- K. L. Roger. Airplane Math Modeling Methods for Active Control Design. Technical Report AGARD-CP-228, AGARD, 1977.

- A. C. L. M. v. Rooij. *Aeroelastic Limit-Cycle Oscillations resulting from Aerodynamic Non-Linearities*. Doctoral Thesis, TU Delft, DLR Göttingen, Apr. 2017.
- W. J. Rugh. *Linear system theory*. Prentice Hall information and system sciences series. Prentice Hall, Upper Saddle River, N.J, 2nd ed edition, 1996. ISBN 978-0-13-441205-4.
- A. Saxena, M. Prasad, A. Gupta, N. Bharill, O. P. Patel, A. Tiwari, M. J. Er, W. Ding, and C.-T. Lin. A review of clustering techniques and developments. *Neurocomputing*, 267:664–681, 2017. ISSN 0925-2312. doi: <https://doi.org/10.1016/j.neucom.2017.06.053>.
- R. H. Scanlan and R. Rosenbaum. Introduction to the Study of Aircraft Vibration and Flutter. *The Journal of the Royal Aeronautical Society*, 56(493):59–60, 1952. doi: 10.1017/S0368393100123466. Publisher: Cambridge University Press.
- R. Schafer. What Is a Savitzky-Golay Filter? [Lecture Notes]. *IEEE Signal Processing Magazine*, 28(4):111–117, July 2011. ISSN 1053-5888. doi: 10.1109/MSP.2011.941097.
- H. Schmidt. Resolution bias errors in spectral density, frequency response and coherence function measurements, IV: Time delay bias errors. *Journal of Sound and Vibration*, 101(3):405–412, 1985. ISSN 0022-460X. doi: [https://doi.org/10.1016/S0022-460X\(85\)80138-3](https://doi.org/10.1016/S0022-460X(85)80138-3).
- S. Schulze. Numerische Simulation des Flatterverhaltens eines nichtlinearen 2D-Flügel-Ruder-Systems in subsonischer Strömung. Technical report, 1999.
- J. Schwochow. *Die aeroelastische Stabilitätsanalyse - ein praxisnaher Ansatz zur intervalltheoretischen Betrachtung von Modellierungsunsicherheiten am Flugzeug*. Doctoral Thesis, Universität Kassel, DLR Göttingen, 2013.
- J. Schwochow and G. Jeličić. *Automatic Operational Modal Analysis for Aeroelastic Applications*. Proceedings of the 6th International Operational Modal Analysis Conference. Elsevier, 2015. Publication Title: IOMAC 2015.
- J. Schwochow and M. Zöger. Flight Vibration Testing - We Always Did It This Way. In *24th SFTE-EC Symposium*, June 2013.
- W. Sears. Some Aspects of Non-Stationary Airfoil Theory and Its Practical Application. *Journal of the Aeronautical Sciences*, 8:104–108, 1941.
- I. Shafi, J. Ahmad, S. I. Shah, and F. M. Kashif. Techniques to Obtain Good Resolution and Concentrated Time-Frequency Distributions: A Review. *EURASIP Journal on Advances in Signal Processing*, 2009(1):673539, June 2009. ISSN 1687-6180. doi: 10.1155/2009/673539.
- L. Shampine, I. Gladwell, L. Shampine, S. Thompson, and S. Thompson. *Solving ODEs with MATLAB*. Cambridge University Press, 2003. ISBN 978-0-521-53094-1.

- R. E. Sherrill, A. J. Sinclair, S. C. Sinha, and T. A. Lovell. Lyapunov-Floquet control of satellite relative motion in elliptic orbits. *IEEE Transactions on Aerospace and Electronic Systems*, 51(4):2800–2810, Oct. 2015. ISSN 0018-9251. doi: 10.1109/TAES.2015.140281.
- Y. Shmaliy. *Continuous-Time Systems*. Signals and Communication Technology. Springer, Sept. 2007. ISBN ISBN-10: 1402062710. doi: 10.1007/978-3-642-14325-0\_1.
- S. Shokoochi, L. Silverman, and P. Van Dooren. Linear time-variable systems: Balancing and model reduction. *IEEE Transactions on Automatic Control*, 28(8):810–822, Aug. 1983. ISSN 1558-2523. doi: 10.1109/TAC.1983.1103331.
- J. Sinske, Y. Govers, G. Jeličić, V. Handojo, W. R. Krüger, and M. Böswald. HALO flight test with instrumented under-wing stores for aeroelastic and load measurements in the DLR project iLOADS. *CEAS Aeronautical Journal*, 9(1):207–218, Feb. 2018. Publisher: Springer.
- P. F. Skjoldan and M. H. Hansen. On the similarity of the Coleman and Lyapunov-Floquet transformations for modal analysis of bladed rotor structures. *Journal of Sound and Vibration*, 327(3-5):424–439, 2009. ISSN 0022-460X. doi: 10.1016/j.jsv.2009.07.007. Publisher: Elsevier.
- K. I. Soal. *System identification and modal tracking on ship structures*. PhD Thesis, Stellenbosch University, Stellenbosch, 2018.
- V. Solo. On the stability of slowly time-varying linear systems. *Mathematics of Control, Signals, and Systems*, 7(4):331–350, Dec. 1994. ISSN 0932-4194, 1435-568X. doi: 10.1007/BF01211523.
- M. Spiridonakos and S. Fassois. Parametric identification of a time-varying structure based on vector vibration response measurements. *Mechanical Systems and Signal Processing*, 23(6):2029–2048, Aug. 2009. ISSN 08883270. doi: 10.1016/j.ymsp.2008.11.004.
- P. Stoica and R. Moses. *Spectral Analysis of Signals*. Pearson Prentice Hall, 2005. ISBN 978-0-13-113956-5.
- C. Stéphan, T.-P. Vo-Hoang, S. Giclais, Y. Govers, P. Lubrina, M. Böswald, and A. Laporte. State-of-the-Art Techniques to Perform an Industrial Vibration Test Campaign and a Rapid Process to Update Renewed FEM for Clearance of First Flight Test. In *International Forum on Aeroelasticity and Structural Dynamics 2015 (IFASD)*, 2015.
- W. Tang, J. Wu, and Z. Shi. Identification of reduced-order model for an aeroelastic system from flutter test data. *Chinese Journal of Aeronautics*, 30(1):337–347, 2017. ISSN 1000-9361. doi: <https://doi.org/10.1016/j.cja.2016.12.024>.
- D. Tcherniak and M. S. Allen. Experimental Characterization of an Operating Vestas V27 Wind Turbine Using Harmonic Power Spectra And OMA SSI. In *6th International Operational Modal Analysis Conference*, Gijón - Spain, 2015.

- T. Theodorsen. General Theory of Aerodynamic Instability and the Mechanism of Flutter. NACA Technical Report NACA-TR-496, NASA Langley Research Center, Langley Aeronautical Lab. Langley Field, VA, United States, 1935.
- D. J. Thomson. Spectrum estimation and harmonic analysis. *Proceedings of the IEEE*, 70(9):1055–1096, 1982. doi: 10.1109/PROC.1982.12433.
- S. Tiffany and W. J. Adams. Nonlinear programming extensions to rational function approximations of unsteady aerodynamics. Technical Paper 2776, NASA Langley Research Center, Langley Research Center, Hampton. Virginia, 1988.
- F. Traversa and F. Bonani. Frequency-domain evaluation of the adjoint Floquet eigenvectors for oscillator noise characterisation. *IET Circuits, Devices & Systems*, 5(1):46, 2011. ISSN 1751858X. doi: 10.1049/iet-cds.2010.0138.
- P. Trnka and V. Havlena. Subspace identification method incorporating prior information. In *2007 46th IEEE Conference on Decision and Control*, pages 4968–4973, 2007. doi: 10.1109/CDC.2007.4434236.
- T. D. Troyer, P. Guillaume, R. Pintelon, and S. Vanlanduit. Fast calculation of confidence intervals on parameter estimates of least-squares frequency-domain estimators. *Mechanical Systems and Signal Processing*, 23(2):261–273, 2009. ISSN 0888-3270. doi: <https://doi.org/10.1016/j.ymsp.2008.04.009>.
- U.S. Department of Defense. Flying Qualities of Piloted Aircraft. Department of Defense Handbook MIL-HDBK-1797, Department of Defense, United States of America, Dec. 1997.
- US-NOAA, T. Brice, and T. Hall. National Oceanic and Atmospheric Administration - Pressure Altitude Formula, 2021. <https://www.weather.gov/media/epz/wxcalc/pressureAltitude.pdf>.
- İ. Uyanık, M. M. Ankaralı, N. J. Cowan, Ö. Morgül, and U. Saranlı. Identification of a Hybrid Spring Mass Damper via Harmonic Transfer Functions as a Step Towards Data-Driven Models for Legged Locomotion. *CoRR*, abs/1501.05628, 2015. arXiv: 1501.05628.
- İ. Uyanık, U. Saranlı, M. M. Ankaralı, N. J. Cowan, and Ö. Morgül. Frequency-Domain Subspace Identification of Linear Time-Periodic (LTP) Systems. *IEEE Transactions on Automatic Control*, 64(6):2529–2536, June 2019. ISSN 1558-2523. doi: 10.1109/TAC.2018.2867360.
- P. Vacher, B. Jacquier, and A. Bucharles. Extensions of the MAC criterion to complex modes. In *International Conference on Noise and Vibration Engineering 2010 (ISMA 2010)*, Leuven, 2010. Katholieke Universiteit Leuven, Department of Mechanical Engineering. ISBN 978-1-61782-277-3.

- H. Van der Auweraer, W. Leurs, P. Mas, and L. Hermans. Modal parameter estimation from inconsistent data sets. In *Proceedings of SPIE - The International Society for Optical Engineering*, volume 4062, 2000. ISSN: 0277-786X.
- P. Van der Kloet and F. L. Neerhoff. Diagonalization algorithms for linear time-varying dynamic systems. *International Journal of Systems Science*, 31(8):1053–1057, 2000. doi: 10.1080/002077200412195. Publisher: Taylor & Francis eprint: <https://doi.org/10.1080/002077200412195>.
- J. van Nunen, G. Piazzoli, N. A. T. O. A. G. f. A. Research, and D. F. M. Panel. *Aeroelastic Flight Test Techniques and Instrumentation*. AGARD flight test instrumentation series. AGARD, 1979. ISBN 978-92-835-1311-7.
- P. Van Overschee and B. De Moor. Subspace identification for linear systems. Theory, implementation, applications. Incl. 1 disk. In *Springer Science & Business Media*, volume xiv, pages xiv + 254. Springer Science & Business Media, 1996. ISBN 0-7923-9717-7. doi: 10.1007/978-1-4613-0465-4.
- J.-W. van Wingerden, P. Gebraad, and M. Verhaegen. LPV identification of an aeroelastic flutter model. In *49th IEEE Conference on Decision and Control (CDC)*, pages 6839–6844, Atlanta, GA, USA, Dec. 2010. IEEE. ISBN 978-1-4244-7745-6. doi: 10.1109/CDC.2010.5717879.
- P. Verboven. *Frequency-domain System Identification for Modal Analysis*. PhD Thesis, Vrije Universiteit Brussel, 2002.
- P. Verboven, B. Cauberghe, P. Guillaume, S. Vanlanduit, and E. Parloo. Modal parameter estimation and monitoring for on-line flight flutter analysis. *Mechanical Systems and Signal Processing*, 18(3):587–610, 2004. ISSN 0888-3270. doi: [https://doi.org/10.1016/S0888-3270\(03\)00074-8](https://doi.org/10.1016/S0888-3270(03)00074-8).
- M. Verhaegen. Subspace Techniques in System Identification. In J. Baillieul and T. Samad, editors, *Encyclopedia of Systems and Control*, pages 1–13. Springer London, London, 2013. ISBN 978-1-4471-5102-9. doi: 10.1007/978-1-4471-5102-9\_107-1.
- M. Verhaegen and P. Dewilde. Subspace model identification Part 1. The output-error state-space model identification class of algorithms. *International Journal of Control*, 56(5):1187–1210, 1992. doi: 10.1080/00207179208934363.
- M. Verhaegen and V. Verdult. *Filtering and System Identification: A Least Squares Approach*. Cambridge University Press, 2007. doi: 10.1017/CBO9780511618888.
- M. Verhaegen and X. Yu. A class of subspace model identification algorithms to identify periodically and arbitrarily time-varying systems. *Automatica*, 31(2):201–216, Feb. 1995. ISSN 00051098. doi: 10.1016/0005-1098(94)00091-V.

- R. Volkmar, K. I. Soal, L. H. Hughes, Y. Govers, and M. Böswald. Automated optimization of output only modal parameter identification. In *IOMAC 2019 - 8th International Operational Modal Analysis Conference*, 2019. Journal Abbreviation: Proceedings of the 8th International Operational Modal Analysis Conference (IOMAC).
- A. Voß. *Design and Structural Optimization of a Flying Wing of Low Aspect Ratio Based on Flight Loads*. Doctoral Thesis, Technische Universität Berlin, Berlin, 2020a.
- A. Voß. An Implementation of the Vortex Lattice and the Doublet Lattice Method. Technical Report DLR-IB-AE-GO-2020-137, DLR German Aerospace Center, DLR Göttingen, Oct. 2020b.
- D. Walnut. *An Introduction to Wavelet Analysis*. Applied and Numerical Harmonic Analysis. Birkhäuser Boston, 2002. ISBN 978-0-8176-3962-4.
- E. W. Weisstein. "k-Statistic.", 2022. <https://mathworld.wolfram.com/k-Statistic.html>.
- N. Wereley and S. Hall. Frequency response of linear time periodic systems. In *29th IEEE Conference on Decision and Control*, pages 3650–3655 vol.6, Dec. 1990. doi: 10.1109/CDC.1990.203516.
- N. M. Wereley. *Analysis and control of linear periodically time varying systems*. PhD thesis, Massachusetts Institute of Technology, MIT Department of Aeronautics and Astronautics, 1991.
- J. Wright and J. Cooper. *Introduction to Aircraft Aeroelasticity and Loads*. AIAA education series. American Institute of Aeronautics and Astronautics, 2007. ISBN 978-1-56347-722-5.
- M.-Y. Wu. A new concept of eigenvalues and eigenvectors and its applications. *IEEE Transactions on Automatic Control*, 25(4):824–826, Aug. 1980. ISSN 1558-2523. doi: 10.1109/TAC.1980.1102448.
- M.-Y. Wu. On stability of linear time-varying systems. *International Journal of Systems Science*, 15(2):137–150, 1984. doi: 10.1080/00207728408926550. Publisher: Taylor & Francis.
- V. Yaghoubi and T. Abrahamsson. The Modal Observability Correlation as a Modal Correlation Metric. Feb. 2014. ISBN 978-1-4614-6584-3. doi: 10.1007/978-1-4614-6585-0\_47.
- V. Yaghoubi, M. K. Vakilzadeh, and T. J. S. Abrahamsson. Automated modal parameter estimation using correlation analysis and bootstrap sampling. *Mechanical Systems and Signal Processing*, 100:289–310, 2018. ISSN 0888-3270. doi: <https://doi.org/10.1016/j.ymsp.2017.07.004>.
- L. Zadeh. Frequency Analysis of Variable Networks. *Proceedings of the IRE*, 38(3):291–299, Mar. 1950. ISSN 0096-8390. doi: 10.1109/JRPROC.1950.231083.

- L. A. Zadeh. On Stability of Linear Varying-Parameter Systems. *Journal of Applied Physics*, 22(4):402–405, Apr. 1951. ISSN 0021-8979, 1089-7550. doi: 10.1063/1.1699972.
- H. Zhang, C. W. Rowley, E. A. Deem, and L. N. Cattafesta. Online dynamic mode decomposition for time-varying systems, 2017. \_eprint: 1707.02876.
- H. Zhou, K. Yu, Y. Chen, R. Zhao, and Y. Bai. Time-Varying Modal Parameters Identification by Subspace Tracking Algorithm and Its Validation Method. *Shock and Vibration*, 2018:4378793, Mar. 2018. ISSN 1070-9622. doi: 10.1155/2018/4378793. Publisher: Hindawi.
- S.-D. Zhou, W. Heylen, P. Sas, and L. Liu. Maximum likelihood estimator of operational modal analysis for linear time-varying structures in time–frequency domain. *Journal of Sound and Vibration*, 333(11):2339–2358, May 2014. ISSN 0022460X. doi: 10.1016/j.jsv.2014.02.001.
- J. Zhu and C. D. Johnson. New Results in the Reduction of Linear Time-Varying Dynamical Systems. *SIAM Journal on Control and Optimization*, 27(3):476–494, 1989. doi: 10.1137/0327025. \_eprint: <https://doi.org/10.1137/0327025>.

## APPENDIX





# A Appendix

## A.1 Matrix exponential

The matrix exponential is defined as the infinite Taylor series (2.17). This equation converges slowly, therefore the Padé approximant is used instead. MATLAB implements Padé approximants in the function `expm` as described in [AL-MOHY AND HIGHAM, 2010]. For example, for numerator and denominator orders 3 we obtain:

$$\exp \mathbf{M} \approx (120\mathbf{I} - 60\mathbf{M} + 12\mathbf{M}^2 - \mathbf{M}^3)^{-1} (120\mathbf{I} + 60\mathbf{M} + 12\mathbf{M}^2 + \mathbf{M}^3) \quad (\text{A.1})$$

## A.2 Iterative diagonalization of the state matrix

It is possible to diagonalize the state matrix iteratively without computing the state transition matrix [VAN DER KLOET AND NEERHOFF, 2000; WU, 1984]. While of fairly simple formulation, its implementation must compute the mode coupling term  $\Psi(t)^{-1}\dot{\Psi}(t)$ , which requires a solid mode sorting method that can pair together the same eigenvalue at two different time instants (eigenvalues cross each other's path and bifurcations occur).

---

**Algorithm 5:** Iterative diagonalization of LTV systems

---

*The time-dependency such as  $\mathbf{A}(t)$  is dropped for legibility*

Initialize:  $j \leftarrow 0$      $\Lambda_0(t) \leftarrow \mathbf{A}(t)$      $\Psi_0 \leftarrow \mathbf{I}$      $\mathbf{E} = \mathbf{I}$ ;

**while**  $\|\mathbf{E}\|_{Fro} > \varepsilon_{tol}$  **do**

    Compute the instantaneous eigenvectors:

$$\Lambda_{j-1} \stackrel{\text{eig}}{=} \Psi_j \Lambda_j \Psi_j^{-1}$$

    Calculate the dynamic mode coupling term (cost function):

$$\mathbf{E} \leftarrow \Psi_{j-1}^{-1} \dot{\Psi}_{j-1}$$

    Compute the dynamically similar new state matrix:

$$\Lambda_j \leftarrow \Psi_j^{-1} (\Lambda_{j-1} - \mathbf{E}) \Psi_j$$

    Increase loop counter:  $j \leftarrow j + 1$

**end**

**Result:** Diagonalized state matrix and transformation matrix

$$\Lambda(t) = \Lambda_j(t) \quad \mathbf{T}(t) = \prod_{n=0}^j \Psi_n(t)$$

---

### A.3 Linear parameter variation

This section derives the analytical expressions of the solutions in time and frequency domains for the case of linear parameter variation of 1-DoF systems. The homogeneous and inhomogeneous solutions are obtained from equation (2.123):

$$A(t) = a_0 t + \frac{1}{2} a_1 t^2 + c \implies \begin{cases} x_h(t) &= x(0) e^{A(t)} \\ x_i(t) &= e^{A(t)} \int_0^t e^{-A(\tau)} \sum_{q=1}^{N_q} c_q e^{s_q \tau} d\tau \end{cases} \quad (\text{A.2})$$

Time now appears squared in the exponent. This type of integrals is best handled with the error function<sup>1</sup>:

$$\text{erf}(z) \triangleq \frac{2}{\sqrt{\pi}} \int_0^z e^{-u^2} du \quad z \in \mathbb{C} \quad (\text{A.3})$$

The notation in this section is simplified by introducing:

- $\alpha \triangleq \sqrt{-a_1/2}$  is the coefficient of the quadratic term so that it appears squared and with a negative sign in all equations
- $\beta$  is the linear term's coefficient (case-specific)
- $\mu \triangleq \beta/(2\alpha)$  is an adimensional quantity defined case by case (analogous to the mean of the Gaussian distribution)

Under these definitions, the linear and quadratic terms' coefficients in equation (A.2) both have units  $[time^{-1}]$ . With this in mind, the following recurring indefinite integral is solved by completing the square in the exponent:

$$\int e^{-\alpha^2 t^2 \pm \beta t} dt = \int e^{-(\alpha t \mp \frac{\beta}{2\alpha})^2 + (\frac{\beta}{2\alpha})^2} dt = \frac{\sqrt{\pi}}{2\alpha} e^{\mu^2} \text{erf}(\alpha t \mp \mu) + c \quad (\text{A.4})$$

This expression will be helpful in the coming pages. It reduces to the Gaussian integral when the limits of integration are  $]-\infty, +\infty[$ :

$$\int_{-\infty}^{+\infty} e^{-\alpha^2 t^2 - \beta t} dt = \frac{\sqrt{\pi}}{\alpha} \exp\left(\left(\frac{\beta}{2\alpha}\right)^2\right) \quad \Re\{\alpha^2\} > 0 \quad (\text{A.5})$$

The condition for the convergence of this integral is  $\Re\{\alpha^2\} > 0$ , equivalently  $\Re\{a_1\} < 0$  (even if  $\Re\{a_0\} > 0$ ). The underlying time-invariant system may be unstable, but a parameter variation can stabilize the whole system (and vice versa). The  $N$ -point discrete Fourier transform with sampling rate  $f_s = 1/\Delta t$  is calculated analytically:

$$x_h[k] = x(0) \frac{\sqrt{\pi}}{2\alpha} e^{\mu[k]^2} (\text{erf}(\alpha t_1 + \mu[k]) - \text{erf}(\alpha t_2 + \mu[k])) \quad (\text{A.6})$$

<sup>1</sup> If the argument  $z$  is real, then  $\text{erf}(z)$  is a monotonic, odd and bounded real function. Since in this analysis the argument  $z$  is generally complex,  $\text{erf}(z)$  is oscillating, unbounded and complex. Along the real axis, the error function is exactly  $\pm 1$  at  $\pm\infty$ ; along the imaginary axis, it tends to  $\pm i\infty$ .

where the new symbols are:

$$\mu[k] \triangleq \frac{\frac{2\pi i}{N\Delta t}k - a_0}{2\alpha} \quad t_1 = \frac{N - 1/2}{\Delta t} \quad t_2 = -\frac{1/2}{\Delta t} \quad (\text{A.7})$$

The inhomogeneous solution in time-domain (A.2) can be written explicitly by calculating the definite integral of a shifted Gaussian:

$$\begin{aligned} x_i(t) &= e^{a_0t + \frac{1}{2}a_1t^2} \int_0^t e^{-a_0\tau - \frac{1}{2}a_1\tau^2} \sum_{q=1}^{N_q} c_q e^{s_q\tau} d\tau \\ &= e^{-\alpha^2t^2 + a_0t} \sum_{q=1}^{N_q} c_q \int_0^t e^{-(i\alpha)^2\tau^2 - (a_0 - s_q)\tau} d\tau \\ &= e^{-\alpha^2t^2 + a_0t} \sum_{q=1}^{N_q} c_q \left[ \frac{\sqrt{\pi}}{2i\alpha} e^{\left(\frac{a_0 - s_q}{2i\alpha}\right)^2} \operatorname{erf}\left(ia\tau + \frac{a_0 - s_q}{2i\alpha}\right) \right]_{\tau=0}^{\tau=t} \\ &= \frac{\sqrt{\pi}}{2i\alpha} \sum_{q=1}^{N_q} c_q e^{-\alpha^2t^2 + a_0t + \mu_q^2} (\operatorname{erf}(i\alpha t + \mu_q) - \operatorname{erf}(\mu_q)) \end{aligned} \quad (\text{A.8})$$

where the constants are  $\alpha \triangleq \sqrt{-a_1/2}$  and  $\mu_q \triangleq \frac{a_0 - s_q}{2i\alpha}$ . The first addend of equation (A.8) is the forced (steady-state) response, the second addend is the transient response due to the inhomogeneous term. The inhomogeneous solution in frequency domain is:

$$x_i(\omega) = \frac{\sqrt{\pi}}{2i\alpha} \sum_{q=1}^{N_q} c_q e^{\mu_q^2} \mathcal{F} \left\{ e^{-\alpha^2t^2 + a_0t} (\operatorname{erf}(i\alpha t + \mu_q) - \operatorname{erf}(\mu_q)) \right\} \quad (\text{A.9})$$

The first addend is the integral of a shifted Gaussian multiplying the error function, which is not easy to evaluate because of the particular factors of the quadratic terms<sup>2</sup>:

$$I_1(\omega) \triangleq \int_{-\infty}^{+\infty} e^{-\alpha^2t^2 + a_0t} \operatorname{erf}(i\alpha t + \mu_q) e^{-i\omega t} dt \quad (\text{A.11})$$

In order to calculate integral (A.11), the Faddeeva<sup>3</sup> function is introduced:

$$w(z) \triangleq e^{-z^2} \left( 1 + \frac{2i}{\sqrt{\pi}} \int_0^z e^{u^2} du \right) \equiv e^{-z^2} (1 + \operatorname{erf}(iz)) \quad (\text{A.12})$$

<sup>2</sup> The comprehensive tables in reference [NG AND GELLER, 1969] provide the solution for:

$$\int_{-\infty}^{+\infty} e^{-(\alpha x + \beta)^2} \operatorname{erf}(\gamma x + \delta) dx = \frac{\sqrt{\pi}}{\alpha} \operatorname{erf}\left(\frac{\alpha\delta - \beta\gamma}{\sqrt{\alpha^2 + \gamma^2}}\right) \quad \Re\{\alpha^2/\gamma^2\} > 0 \quad (\text{A.10})$$

however, in the case at hand:  $\gamma = i\alpha \implies \Re\{\alpha^2/\gamma^2\} = -1$

<sup>3</sup> The function  $w(z)$  has many names: Faddeeva function, Kramp function, complex error function, probability integral, plasma dispersion function. Specialized algorithms are needed for calculating  $w(z)$  accurately with complex input

Its integral representation is equal to the convolution of a Gaussian with a simple pole, i.e. to the Hilbert transform of a Gaussian:

$$w(z) = \frac{i}{\pi} \int_{-\infty}^{+\infty} \frac{e^{-u^2}}{z-u} du = e^{-z^2} * \frac{i}{\pi z} = i\mathcal{H} \left\{ e^{-z^2} \right\} \quad \Im z > 0 \quad (\text{A.13})$$

This observation allows us to calculate the following Fourier transform<sup>4</sup>:

$$\begin{aligned} \mathcal{F} \left\{ e^{-\alpha^2 t^2} \operatorname{erf}(i\alpha t) \right\} &= \mathcal{F} \left\{ w(\alpha t) - e^{-\alpha^2 t^2} \right\} \\ &= \mathcal{F} \left\{ e^{-\alpha^2 t^2} * \frac{i}{\pi t} - e^{-\alpha^2 t^2} \right\} \\ &= \mathcal{F} \left\{ e^{-\alpha^2 t^2} \right\} \mathcal{F} \left\{ \frac{i}{\pi t} \right\} - \mathcal{F} \left\{ e^{-\alpha^2 t^2} \right\} \\ &= \frac{\sqrt{\pi}}{\alpha} \exp \left( \frac{i\omega}{2\alpha} \right)^2 (\operatorname{sgn}(\omega) - 1) \end{aligned} \quad (\text{A.14})$$

It is now possible to calculate the Fourier transform (A.11) by changing integration variable  $t' \triangleq t + \frac{\mu_q}{i\alpha}$ , then by substituting  $s_q \equiv a_0 - 2i\alpha\mu_q$  in order to isolate the  $e^{-\alpha^2 t'^2} \operatorname{erf}(i\alpha t')$  term in the integrand:

$$\begin{aligned} I_1(\omega) &= \int_{-\infty}^{+\infty} e^{-\alpha^2 t^2 + a_0 t} \operatorname{erf}(i\alpha t + \mu_q) e^{-i\omega t} dt \\ &= \int_{-\infty}^{+\infty} e^{-\alpha^2 (t' - \frac{\mu_q}{i\alpha})^2 + (a_0 - i\omega)(t' - \frac{\mu_q}{i\alpha})} \operatorname{erf}(i\alpha t') dt' \\ &= e^{\mu_q^2 + \frac{\mu_q}{i\alpha}(i\omega - a_0)} \mathcal{F} \left\{ e^{i(-is_q)t'} e^{-\alpha^2 t'^2} \operatorname{erf}(i\alpha t') \right\} \\ &= \frac{\sqrt{\pi}}{\alpha} e^{\left( \frac{i\omega - a_0}{2\alpha} \right)^2} (\operatorname{sgn}(i\omega - s_q) - 1) \end{aligned} \quad (\text{A.15})$$

which takes care of the first addend of equation (A.9). This integral can also be solved by using ‘‘Feynman’s trick’’ to differentiate the constant  $\mu_q$  under the integral sign. For each index  $q$ :

$$\begin{aligned} \frac{\partial I_1}{\partial \mu_q} &= \frac{2}{\sqrt{\pi}} \int_{-\infty}^{+\infty} e^{-\alpha^2 t^2 - (i\omega - a_0)t} \left( e^{-(iat + \mu_q)^2} - e^{-\mu_q^2} \right) dt \\ &= \frac{2}{\sqrt{\pi}} e^{-\mu_q^2} \mathcal{F} \left\{ e^{(a_0 - 2i\alpha\mu_q)t} - e^{-\alpha^2 t^2 + a_0 t} \right\} \\ &= \frac{2}{\sqrt{\pi}} e^{-\mu_q^2} \left( \delta(i\omega - a_0 + 2i\alpha\mu_q) - \frac{\sqrt{\pi}}{\alpha} e^{\left( \frac{i\omega - a_0}{2\alpha} \right)^2} \right) \end{aligned} \quad (\text{A.16})$$

Integrate

$$\begin{aligned} \int_0^{\mu_q} \frac{\partial I_1}{\partial \mu_q} du &= \frac{2}{\sqrt{\pi}} \int_0^{\mu_q} e^{-u^2} \delta(i\omega - a_0 + 2i\alpha\mu_q) - \frac{\sqrt{\pi}}{\alpha} e^{-\left( \frac{i\omega - a_0}{2i\alpha} \right)^2} du \\ &= \frac{\sqrt{\pi}}{i\alpha} e^{\left( \frac{\omega + ia_0}{2i\alpha} \right)^2} (\operatorname{sgn}(i\omega - a_0 + 2i\alpha\mu_q) - 1) \end{aligned} \quad (\text{A.17})$$

<sup>4</sup> The Fourier transform  $\mathcal{F} \left\{ \frac{i}{\pi t} \right\} = \operatorname{sgn}(\omega)$  is obtained by taking the Cauchy principal value of the integral. The signum function is defined as  $\operatorname{sgn}(z) \triangleq z/|z|$  for complex arguments.

This is the same result that was derived with Faddeeva's function in equation (A.16). The second addend is a shifted Gaussian and has an immediate transform:

$$I_2(\omega) \triangleq - \int_{-\infty}^{+\infty} e^{-\alpha^2 t^2 + a_0 t} \operatorname{erf}(\mu_q) e^{-i\omega t} dt = -\frac{\sqrt{\pi}}{\alpha} e^{\left(\frac{i\omega - a_0}{2\alpha}\right)^2} \operatorname{erf}(\mu_q) \quad (\text{A.18})$$

The inhomogeneous solution (A.8) in frequency domain can now be written by substituting  $I_1(\omega)$  and  $I_2(\omega)$  into equation (A.9):

$$x_i(\omega) = \frac{\pi}{2\alpha^2} \sum_{q=1}^{N_q} c_q e^{\mu_q^2} e^{\left(\frac{i\omega - a_0}{2\alpha}\right)^2} (\operatorname{sgn}(i\omega - s_q) - 1 - \operatorname{erf}(\mu_q)) \quad (\text{A.19})$$

The time-varying case with linear parameter variation has now a complete frequency-domain description of the inhomogeneous solution.

#### A.4 Exponential parameter variation

This section denotes summations as  $\sum_{k=1}^{N_k} a_k$ , where  $N_k$  is the size of the set containing elements  $a_k$  with index  $k$ . The goal is deriving the complete solution to equation (2.131) in frequency-domain. The integral of the parameter  $a(t)$  is

$$A(t) \triangleq \int a(\tau) d\tau = a_0 t + \sum_{p=1}^{N_p} a_p e^{s_p t} + c \quad (\text{A.20})$$

where  $a_p \triangleq c_p/s_p$  in order to simplify the notation. The complete solution is given explicitly by the method of variation of constants (2.123):

$$x(t) = c_0 e^{A(t)} + \sum_{q=1}^{N_q} \int_0^t e^{A(t)-A(\tau)} c_q e^{s_q \tau} d\tau \quad (\text{A.21})$$

where the constant  $c_0$  is determined from the initial condition  $x(0)$ :

$$x(0) = c_0 e^{-\sum_{p=1}^{N_p} a_p} \implies c_0 = x(0) e^{\sum_{p=1}^{N_p} a_p} \quad (\text{A.22})$$

Consider the Taylor series expansion of a double exponential:

$$e^x = \sum_{n=0}^{\infty} \frac{1}{n!} x^n \implies \exp(a_p e^{s_p t}) = \sum_{n=0}^{\infty} \frac{a_p^n}{n!} e^{n s_p t} \quad (\text{A.23})$$

Its Fourier transform is an infinite sum of poles with spacing  $|s_p|$  that decay faster than geometrically:

$$\mathcal{F} \{ \exp(a_p e^{s_p t}) \} = 2\pi \sum_{n=0}^{\infty} \frac{a_p^n}{n!} \delta(i\omega - n s_p) \quad (\text{A.24})$$

The exponential of a sum can be reduced to a single infinite sum<sup>5</sup>:

$$e^{P(t)} = \exp \left( \sum_{p=1}^{N_p} a_p e^{s_p t} \right) = \prod_{p=1}^{N_p} \sum_{n=0}^{\infty} \frac{a_p^n}{n!} e^{n s_p t} \triangleq \sum_{k=1}^{\infty} c_k e^{s_k t} \quad (\text{A.26})$$

The last summation is over all elements  $\{c_k, s_k\} \in \mathbb{S}_p$  of the set of complex amplitude and frequency pairs that results from repeatedly applying the Cauchy product. The complex frequencies  $s_k$  have dimensions [rad/s] and in general their spacing is unequal. If  $s_p = i n_p \omega_0$ ,  $n_p \in \mathbb{Z}$ ,  $\omega_0 \in \mathbb{R}$ , then the energy of  $\mathcal{F}\{e^{P(t)}\}$  is concentrated at multiples of the fundamental frequency  $s_k = i k \omega_0$ ,  $k \in \mathbb{Z}$ .

An explicit expression for the inhomogeneous solution in time domain under the assumption (2.131) is sought:

$$x_i(t) = e^{A(t)} \int_0^t e^{-A(\tau)} q(\tau) d\tau \quad (\text{A.27})$$

The term  $e^{-A(t)}$  can be expressed as a series<sup>6</sup> according to equation (A.26):

$$e^{-A(t)} = \exp \left( -a_0 t - \sum_{p=1}^{N_p} a_p e^{s_p t} \right) \triangleq \sum_{k=1}^{\infty} \bar{c}_k e^{(s_k - a_0)t} \quad (\text{A.28})$$

The integrand  $e^{-A(\tau)} q(\tau)$  is therefore a sum of exponentials:

$$\begin{aligned} e^{-A(\tau)} q(\tau) &= \exp \left( -a_0 \tau - \sum_{p=1}^{N_p} a_p e^{s_p \tau} \right) \cdot \sum_{q=1}^{N_q} c_q e^{s_q \tau} \\ &= \left( \sum_{k=1}^{\infty} \bar{c}_k e^{(s_k - a_0)\tau} \right) \cdot \sum_{q=1}^{N_q} c_q e^{s_q \tau} \\ &= \sum_{q=1}^{N_q} \sum_{k=1}^{\infty} \bar{c}_k c_q e^{(s_k + s_q - a_0)\tau} \end{aligned} \quad (\text{A.29})$$

<sup>5</sup> Apply the Cauchy product  $N_p - 1$  times:

$$\left( \sum_{i=0}^{\infty} a_i e^{\alpha_i t} \right) \cdot \left( \sum_{j=0}^{\infty} b_j e^{\beta_j t} \right) = \sum_{k=0}^{\infty} c_k e^{\theta_k t} \quad c_k e^{\theta_k t} = \sum_{l=0}^k a_l b_{k-l} e^{(\alpha_l + \beta_{k-l})t} \quad (\text{A.25})$$

<sup>6</sup> In general,  $\mathcal{F}\{e^{A(t)}\}$  and  $\mathcal{F}\{e^{-A(t)}\}$  are not easily related unless all terms of  $A(t)$  have zero phase.

The inhomogeneous solution  $x_i(t)$  can be now written explicitly by integrating the last equation and then applying the Cauchy product rule:

$$\begin{aligned}
x_i(t) &= e^{A(t)} \int_0^t \sum_{q=1}^{N_q} \sum_{k=1}^{\infty} \bar{c}_k c_q e^{(s_k + s_q - a_0)\tau} d\tau \\
&= e^{a_0 t} \sum_{k=1}^{\infty} c_k e^{s_k t} \cdot \sum_{q=1}^{N_q} \sum_{k=1}^{\infty} \left[ \frac{\bar{c}_k c_q}{s_k + s_q - a_0} e^{(s_k + s_q - a_0)\tau} \right]_{\tau=0}^{\tau=t} \\
&= \sum_{q=1}^{N_q} \left( \sum_{k=1}^{\infty} c_k e^{s_k t} \cdot \sum_{k=1}^{\infty} \frac{\bar{c}_k c_q}{s_k + s_q - a_0} \left( e^{(s_k + s_q)t} - e^{a_0 t} \right) \right) \\
&= \sum_{l=1}^{N_q} \sum_{n=0}^{\infty} \sum_{m=0}^n c_{k,n-m} c_{m,l} \left( e^{(s_{q,l} + s_{k,m} + s_{k,n-m})t} - e^{(a_0 + s_{k,n-m})t} \right)
\end{aligned} \tag{A.30}$$

where the newly introduced constant (dimensions:  $[state]$ ) is:

$$c_{m,l} \triangleq \frac{\bar{c}_{k,l} c_{q,k}}{s_{k,l} + s_{q,k} - a_0} \tag{A.31}$$

This result suggests that equation (A.30) is the sum of a forced (steady-state) part and a transient part: the inhomogeneous term's poles  $s_q$  affect only the forced part and the time-invariant pole  $a_0$  affects only the transient part. The inhomogeneous solution can be expressed as a sum of poles similarly to the homogeneous solution:

$$x_i(\omega) = \sum_{\mathbb{S}_f} \frac{r_f}{i\omega - \lambda_f} + \sum_{\mathbb{S}_t} \frac{r_t}{i\omega - \lambda_t} \tag{A.32}$$

where the sets of residue-eigenvalue pairs  $\{r_f, \lambda_f\} \in \mathbb{S}_f$  and  $\{r_t, \lambda_t\} \in \mathbb{S}_t$  are calculated with equation (A.30). The formulation can be extended to handle combinations of polynomial and exponential functions:

$$\dot{x}(t) = a(t)x(t) + q(t) \quad a(t) = \sum a_p t^p e^{\sigma t} \tag{A.33}$$

$$A_p(t) = \int a_p t^p e^{\sigma_p t} dt = e^{\sigma_p t} \sum_{k=0}^{p-1} c_k t^k \quad c_k \triangleq -a_p \frac{p!}{k!} (-\sigma_p)^{k-p-1} \tag{A.34}$$

$$e^{A_p(t)} = \sum_{n=0}^{\infty} \frac{(c_k t^p e^{\sigma_p})^n}{n!} \tag{A.35}$$

The sums can be worked out until terms in the form  $t^p e^{\sigma t}$ , which are simple poles with multiplicity  $p + 1$ :

$$t^p e^{\sigma t} \quad \circ \bullet \quad \frac{p!}{(s - \sigma)^{p+1}} \tag{A.36}$$



## A.5 Theodorsen's function

The Theodorsen's function original definition is found in [THEODORSEN, 1935, Eq. XI]. A simplified formulation is found in [BISPLINGHOFF ET AL., 1996, Eq. 5-309]:

$$C(k) \triangleq F(k) + iG(k) = \frac{H_1^{(2)}(k)}{H_0^{(2)}(k) + iH_1^{(2)}(k)} = \frac{K_1(ik)}{K_0(ik) + K_1(ik)} \quad (\text{A.37})$$

where  $H_0^{(2)}$  and  $H_1^{(2)}$  are Hankel functions of the second kind,  $K_0$  and  $K_1$  are Bessel's functions of the second kind and  $k$  is the reduced frequency (3.6).

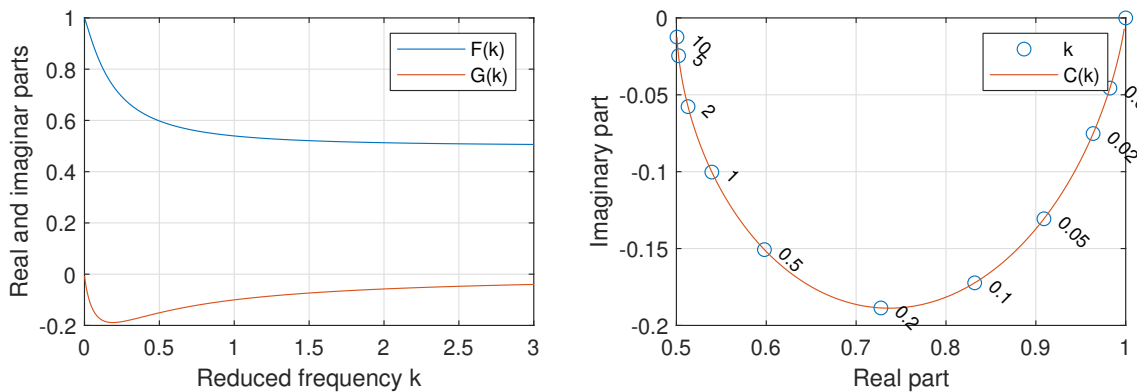


FIGURE A.1: Theodorsen's function  $C(k) = F(k) + iG(k)$ .

## A.6 Wagner's function

Wagner's function is defined as [BISPLINGHOFF ET AL., 1996, eq. 5-368b]:

$$\Phi(\tau) = H(\tau) + \frac{1}{\pi} \int_0^{+\infty} (F(k) - 1) \frac{\sin(k\tau)}{k} + G(k) \frac{\cos(k\tau)}{k} d\tau \quad (\text{A.38})$$

where  $H(\tau)$  is the Heaviside function and  $\tau$  is the adimensional time  $\tau \triangleq tV_\infty/b$  and  $k$  is the reduced frequency. A good approximation of  $\Phi(\tau)$  is [BISPLINGHOFF ET AL., 1996, eq. 5-372]:

$$\Phi(\tau) = \frac{\tau + 2}{\tau + 4} \quad (\text{A.39})$$

Alternatively, a form that has an elementary Laplace transform is [BISPLINGHOFF ET AL., 1996, eq. 5-371]:

$$\Phi(\tau) = 1 - 0.165e^{-0.0455\tau} - 0.335e^{-0.3\tau} \quad (\text{A.40})$$

but is less accurate for large  $\tau$ .

### A.7 Measurement time nomogram

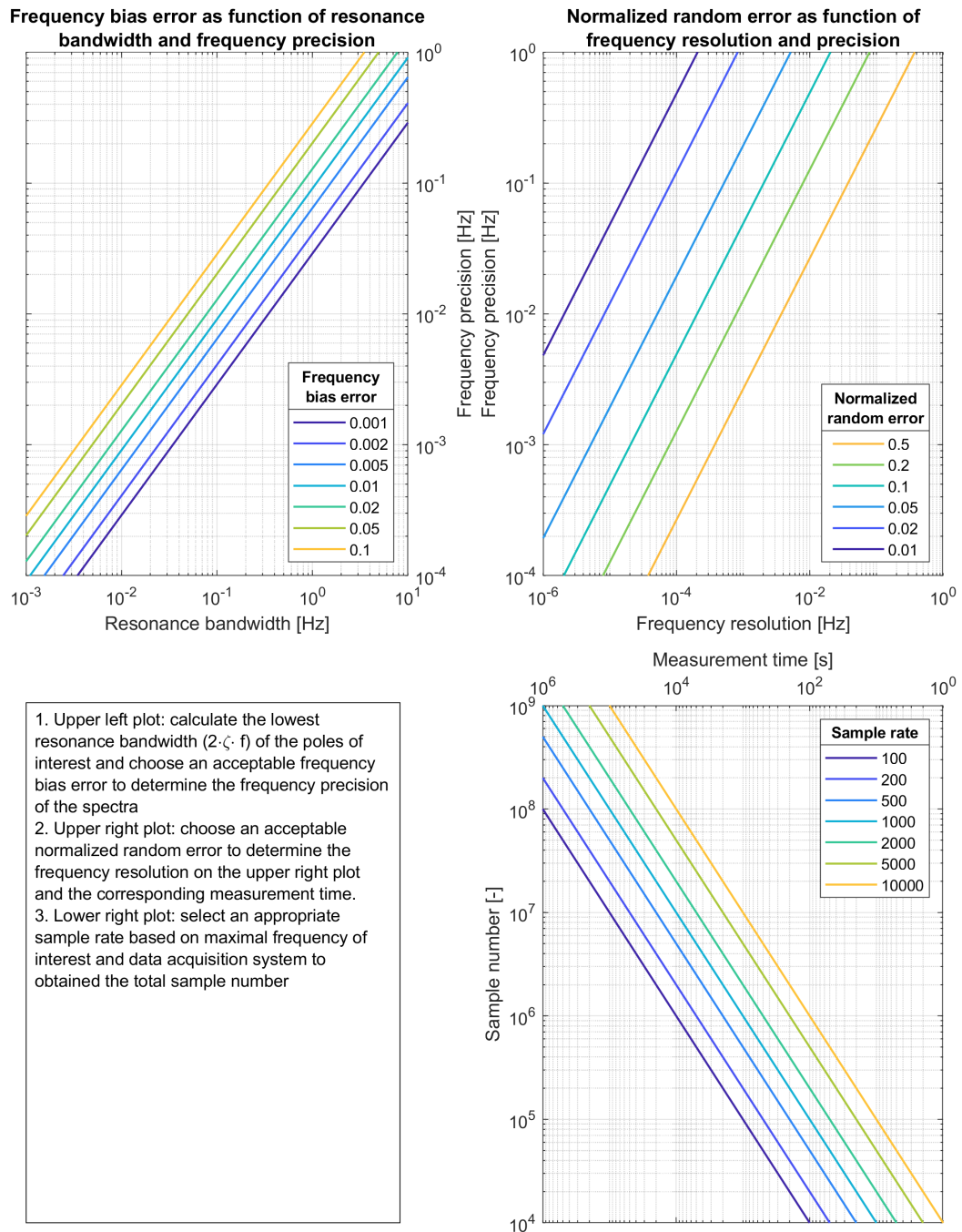


FIGURE A.2: Nomogram for computing the measurement time for reducing the spectral estimation's frequency bias error  $\varepsilon_f$  (4.28) and random error  $\varepsilon_r$  (4.29) below the desired threshold for a given resonance bandwidth  $2\zeta f_n$ .

## A.8 Automated decimation algorithm

---

### Algorithm 6: Automated decimation staging

---

**Data:** Frequency band  $[f_{min}, f_{max}]$ , sample rate  $f_s$ , number of stages  $S$

**Result:** Integer decimation factors for each stage  $\mathbf{q}$

**Run:**

Set maximal decimation factor:  $q_{max} = 13$

Get effective decimation factor:  $q_0 \triangleq f_s/2/(f_{max} - f_{min})$

Get first integer small or equal to decimation factor:  $M = \lfloor M_0 \rfloor$

Get prime factors:  $\mathbf{k} = \text{factors}\{M\}$

Reduce decimation factor until all its factors are smaller than  $q_{max}$ :

**while** *any*( $\mathbf{k} > q_{max}$ ) **do**

$q \leftarrow q - 1$   
     $\mathbf{k} = \text{factors}\{q\}$

**end**

Compute optimal staging ratio:  $k_0 \triangleq q^{1/S}$

Find appropriate divisors of the decimation factor

$n \leftarrow 1$

**while**  $q > 1$  **do**

    Find divisors (exclude 1):

**if**  $q > q_{max}$  **then**

$\mathbf{x} \leftarrow 2 : \min(\lceil q/2 \rceil, q_{max})$

**else**

$\mathbf{x} \leftarrow 2 : q$

**end**

    Find divisor nearest to staging ratio:  $\mathbf{d} \leftarrow \mathbf{x}(\text{rem}(q, \mathbf{x}) \neq 0)$

**if**  $\mathbf{d}[\text{end}] = q$  **then**

$\mathbf{q}[n] \leftarrow \mathbf{d}_{\text{end}}$

**else**

        Get index  $\mathbb{I}$  of minimum  $\min |\mathbf{d} - R|$

$\mathbf{q}[n] \leftarrow \mathbf{d}(\mathbb{I})$

**end**

    Set decimation factor of next stage:  $q \leftarrow q/\mathbf{q}[n]$

    Increase stage count:  $n \leftarrow n + 1$

**end**

Calculate new optimal staging ratio with current number of stages:

**if**  $n \neq S$  **then**

$k_0 \leftarrow q^{1/n}$

**end**

Sort  $\mathbf{q}$  according to deviation from  $R$ :  $\mathbb{I} \leftarrow \text{sort}(|\mathbf{q} - k_0|, \text{descend})$

Let the first stage do the most work:  $\mathbf{q} \leftarrow \mathbf{q}[\mathbb{I}]$

---

## A.9 Ordinary differential equation solvers

The pseudo-code of the ODE solvers used for the state-space representation of time-varying systems in this thesis is displayed in this section. A recommended book on ODE solvers is [QUARTERONI ET AL., 2006].

The Runge-Kutta coefficients are arranged in so-called Butcher's tableaux [HAIRER ET AL., 2008]. For example, if we denote the number of stages as  $s$ , then a Butcher's tableau has the form:

$$\begin{array}{c|cccc}
 0 & & & & \\
 c_2 & a_{21} & & & \\
 c_3 & a_{31} & a_{32} & & \\
 \vdots & \vdots & \vdots & \ddots & \\
 c_s & a_{s1} & a_{s2} & \cdots & a_{s,s-1} \\
 \hline
 & b_1 & b_2 & \cdots & b_{s-1} & b_s
 \end{array}$$

The matrix  $[a_{ij}]$  is the *Runge-Kutta matrix*,  $[b_j]$  are the *weights* and  $[c_i]$  are the *nodes*.

**Note.** In the code the indexing of the Runge-Kutta matrix  $\mathbf{A}^{RK}$  ignores the first row for convenience, therefore  $\mathbf{A}^{RK}[1,1]$  in the algorithm 7 corresponds to “ $a_{21}$ ” in literature.

In literature, the Adams-Bashforth and Adams-Moulton coefficients are arranged so that the first element corresponds to the newest sample. For example, written explicitly, the fifth-order ABM method is:

$$\begin{aligned}
 \mathbf{f}_n &\triangleq \mathbf{A}_n \mathbf{x}_n + \mathbf{B}_n \mathbf{u}_n \\
 \mathbf{x}_{n+4} &= \mathbf{x}_{n+3} + \frac{\Delta t}{24} (55\mathbf{f}_{n+3} - 59\mathbf{f}_{n+2} + 37\mathbf{f}_{n+1} - 9\mathbf{f}_n) \\
 \mathbf{x}_{n+4} &= \mathbf{x}_{n+3} + \frac{\Delta t}{24} (9\mathbf{f}_{n+3} + 19\mathbf{f}_{n+2} - 5\mathbf{f}_{n+1} + 1\mathbf{f}_n)
 \end{aligned} \tag{A.41}$$

**Note.** In the code presented in this section, the order of the coefficients  $b$  is reversed. This change has been made to have the states  $\mathbf{x}$  and outputs  $\mathbf{y}$  with consistent indices across all methods.

**Algorithm 7:** Ad-hoc Runge-Kutta method

**Data:** System matrices  $\mathcal{S}$ , input  $\mathbf{u}_n$ , parameters  $\mathbf{p}_n$ , time step  $\Delta t$ , initial conditions  $\mathbf{x}_0$ , Butcher's tableau, number of steps  $N$

**Result:** System response  $\mathbf{y}$

**Set-up:**

Get coefficients from Butcher's tableau ( $N_s$ : number of stages):

Runge-Kutta matrix:  $\mathbf{A}^{RK}$  ( $a_{ij}$  coefficients of Butcher's tableau)

weights:  $\mathbf{b}^{RK}$

nodes:  $\mathbf{c}^{RK}$

initialize slopes:  $\mathbf{K} \leftarrow \mathbf{0}_{N_x, N_s}$

Construct interpolants:

input:  $\mathbf{f}_p(t_j) = \text{interp}(\mathbf{u}_n, (0 : N - 1)\Delta t, t_j)$

parameters:  $\mathbf{f}_u(t_j) = \text{interp}(\mathbf{p}_n, (0 : N - 1)\Delta t, t_j)$

Set initial conditions  $\mathbf{x}_1 \leftarrow \mathbf{x}_0$

Get system matrices:  $\mathcal{S}_1 \leftarrow \mathcal{S}(0)$  ( $[\mathbf{A}(0), \mathbf{B}(0), \mathbf{C}(0), \mathbf{D}(0)]$ )

**Run-time:**

**for** for every time step  $n = 1 : N$  **do**

**for** for every stage  $j = 1 : N_s$  **do**

        Calculate  $\mathbf{x}(t_j)$ :  $\hat{\mathbf{x}}_j \leftarrow \mathbf{x}_n + \mathbf{K}[:, 1 : j]\mathbf{A}^{RK}[1 : j, j]$

**if**  $\mathbf{c}^{RK}[j] == 0$  (*beginning of n-th step*) **then**

            Retrieve system matrices from previous step:  $\mathcal{S}_j \leftarrow \mathcal{S}_n$

            Retrieve input from previous step:  $\hat{\mathbf{u}}_j \leftarrow \mathbf{u}_n$

**else**

            Get time of current slope:  $t_j \leftarrow (n - 1 + \mathbf{c}^{RK}[j])\Delta t$

            Get input:  $\hat{\mathbf{u}}_j \leftarrow \mathbf{f}_u(t_j)$

            Get parameters:  $\mathbf{p}_j \leftarrow \mathbf{f}_p(t_j)$

**if**  $\|\mathbf{p}_n - \mathbf{p}_j\| > \varepsilon_p \|\mathbf{p}_n\|$  (*no significant parameter variation*) **then**

                Construct system matrices:  $\mathcal{S}_j \leftarrow \mathcal{S}(\mathbf{p}_j)$

**end**

**if**  $\mathbf{c}^{RK}[j] == 1$  (*end of n-th step*) **then**

                Store system matrices for next step:  $\mathcal{S}_n \leftarrow \mathcal{S}_j$

                Store input for next step:  $\mathbf{u}_n \leftarrow \hat{\mathbf{u}}_j$

**end**

            Evaluate integrand  $\mathbf{f}(\mathbf{x}_j, t_j)$ :  $\mathbf{f}_j = \mathbf{A}_j \hat{\mathbf{x}}_j + \mathbf{B}_j \hat{\mathbf{u}}_j$

            Update  $j$ -th slope:  $\mathbf{K}[:, j] \leftarrow \Delta t \mathbf{f}_j$

**end**

        Calculate next state vector:  $\mathbf{x}_{n+1} \leftarrow \mathbf{x}_n + \mathbf{K} \mathbf{b}^{RK}$

**end**

    Calculate output:  $\mathbf{y}_n \leftarrow \mathbf{C}_n \mathbf{x}_n + \mathbf{D}_n \mathbf{u}_n$

**end**

**Algorithm 8:** Ad-hoc Adams-Bashforth-Moulton method

**Data:** System matrices  $\mathcal{S}$ , input  $\mathbf{u}_n$ , parameters  $\mathbf{p}_n$ , time step  $\Delta t$ , initial conditions  $\mathbf{x}_0$ , order  $N_s$ , number of steps  $N$

**Result:** System response  $\mathbf{y}$

**Set-up:**

Get Adam-Bashforth predictor coefficients for order  $N_s$ :  $\mathbf{b}^p$  and  $k^p$

Get Adam-Moulton corrector coefficients for order  $N_s$ :  $\mathbf{b}^c$  and  $k^c$

Calculate first  $N_s$  steps using RK:  $\mathbf{y}_{1:N_s}$  and  $\mathbf{x}_{1:N_s}$

Seed circular array:

```
for  $j = 1 : N_s$  do
  |  $[\mathbf{A}_j, \mathbf{B}_j, \mathbf{C}_j, \mathbf{D}_j] \leftarrow \mathcal{S}(\mathbf{p}_j)$ 
  |  $\mathbf{v}_j \leftarrow \mathbf{B}_j \mathbf{u}_j$ 
end
```

**end**

**Run-time:**

```
for for every time step  $n = N_s : N - 1$  do
```

Get system matrices:

```
if  $|\mathbf{p}_n - \mathbf{p}_{n+1}| > \varepsilon_p |\mathbf{p}_n|$  (no significant parameter variation) then
```

```
  |  $[\mathbf{A}_1, \mathbf{B}_1, \mathbf{C}_1, \mathbf{D}_1] \leftarrow \mathcal{S}(\mathbf{p}_{n+1})$ 
```

```
  |  $\mathbf{A}_{N_s+1} \leftarrow \mathbf{A}_1$ 
```

```
  |  $\mathbf{v}_{N_s+1} \leftarrow \mathbf{B}_1 \mathbf{u}_{n+1}$ 
```

```
else
```

```
  |  $\mathbf{A}_{N_s+1} \leftarrow \mathbf{A}_{N_s}$ 
```

```
  |  $\mathbf{v}_{N_s+1} \leftarrow \mathbf{B}_{N_s} \mathbf{u}_{n+1}$ 
```

```
  |  $\mathbf{C}_1 \leftarrow \mathbf{C}_n$ 
```

```
  |  $\mathbf{D}_1 \leftarrow \mathbf{D}_n$ 
```

```
end
```

Adams-Bashforth predictor:

```
for  $j = 1 : N_s$  do
```

```
  |  $\mathbf{F}[:, j] \leftarrow \mathbf{A}_j \mathbf{x}_{n-N_s+j} + \mathbf{v}_j$ 
```

```
end
```

```
 $\mathbf{x}_{n+1} \leftarrow \mathbf{x}_n + \Delta t / k^p \cdot \mathbf{F} \mathbf{b}^p$ 
```

Adams-Moulton corrector:

```
for  $j = 1 : N_s$  do
```

```
  |  $\mathbf{F}[:, j] \leftarrow \mathbf{A}_{j+1} \mathbf{x}_{n-N_s+j+1} + \mathbf{v}_{j+1}$ 
```

```
end
```

```
 $\mathbf{x}_{n+1} \leftarrow \mathbf{x}_n + \Delta t / k^c \cdot \mathbf{F} \mathbf{b}^c$ 
```

Calculate output:  $\mathbf{y}_n \leftarrow \mathbf{C}_n \mathbf{x}_n + \mathbf{D}_n \mathbf{u}_n$

Perform circular shift of state equation terms:

```
 $\mathbf{A} \leftarrow [\mathbf{A}_{2:N_s+1}, \mathbf{A}_1]$        $\mathbf{v} \leftarrow [\mathbf{v}_{2:N_s+1}, \mathbf{v}_1]$ 
```

Store input and feedthrough matrices for next step:

```
 $\mathbf{C}_n \leftarrow \mathbf{C}_1$        $\mathbf{D}_n \leftarrow \mathbf{D}_1$ 
```

```
end
```

```
Calculate output at last step:  $\mathbf{y}_N \leftarrow \mathbf{C}_n \mathbf{x}_N + \mathbf{D}_n \mathbf{u}_N$ 
```

## A.10 G550 DLR-HALO aircraft data

TABLE A.1: G550 DLR-HALO technical data [DLR.DE, 2021]. These specifications differ somewhat from the production aircraft [HALO.DLR.DE, 2021].

### Aircraft Performance

---

Maximum Range	12,501 km at Mach 0.8
(the actual range is affected by speed, weather, outfitting options etc.)	
Maximum Operating Mach Number	Mach 0.885 (340 KCAS, 1054 km/h)
Maximum Cruise Altitude	15545 m (51000 ft)
Range	> 8000 km

---

### Weights

---

Maximum Takeoff Weight	41277 kg (91000 lb)
Maximum Landing Weight	34156 kg (75300 lb)
Maximum Zero Fuel Weight	22230 kg (49000 lb)
Maximum Payload	2812 kg (6200 lb)
Fuel capacity	18734 kg (4100 lb)

---

### Design Standards

---

Propulsion	2 Rolls-Royce BR710 Engines
Thrust	$2 \times 68.4$ kN

---

### Exterior

---

Length	29.4 m
Height	7.9 m
Wingspan	28.5 m

---

### Interior

---

Cabin Length	11.3 m
Cabin Height	1.88 m
Cabin Width	2.24 m
Cabin Volume	47.3 m <sup>3</sup>
Seating capacity	19 (normally 3 crew and 5 to 8 scientists and engineers)

---

## A.11 Standardized principal moments

Let  $X$  be a random variable. The first four principal moments are:

$$\begin{aligned}
 \text{mean: } \mu &= \mathbb{E}\{X\} & \text{skewness: } \mu_3 &= \mathbb{E}\left\{\left(\frac{X-\mu}{\sigma}\right)^3\right\} \\
 \text{variance: } \sigma^2 &= \mathbb{E}\{(X-\mu)^2\} & \text{kurtosis: } \mu_4 &= \mathbb{E}\left\{\left(\frac{X-\mu}{\sigma}\right)^4\right\}
 \end{aligned} \tag{A.42}$$

where  $\mathbb{E}[X] = \int_{-\infty}^{+\infty} xp(x)dx$  is the expectation operator and  $p(x)$  the probability density function of  $X$ .

The estimation of the principal moments from a sample of finite size is more involved. We take the formulae from [WEISSTEIN, 2022], where many additional references for the  $k$ -statistic are listed. Let us suppose there are  $N$  samples of the random variable  $X$ . We define  $s_p$  as the average of  $X^p$ :

$$s_p \triangleq \frac{1}{N} \sum_{n=1}^N X_n^p \tag{A.43}$$

The first four central moments are then:

$$\begin{aligned}
 m_1 &= s_1 & m_3 &= s_3 - 3s_1s_2 + 2s_1^3 \\
 m_2 &= s_2 - s_1^2 & m_4 &= s_4 - 4s_1s_3 + 6s_1^2s_2 - 3s_1^4
 \end{aligned} \tag{A.44}$$

The biased estimators for the first four principal moments are:

$$\begin{aligned}
 \mu &= m_1 & g_1 &= \frac{m_3}{\frac{m_2^{3/2}}{m_2}} \\
 \sigma^2 &= m_2 & g_2 &= \frac{m_4}{m_2^2}
 \end{aligned} \tag{A.45}$$

The unbiased estimators for the first four principal moments are:

$$\begin{aligned}
 \mu &= m_1 & G_1 &= \frac{\sqrt{N(N-1)}}{N-2}g_1 \\
 s^2 &= \frac{N}{N-1}\sigma^2 & G_2 &= \frac{(N-1)(N+1)}{(N-2)(N-3)}g_2 - \frac{3(N-1)^2}{(N-2)(N-3)} + 3
 \end{aligned} \tag{A.46}$$

The skewness and kurtosis of a Gaussian distribution are 0 and 3 respectively. The *excess kurtosis* is defined as kurtosis minus 3 and is used throughout this thesis. The sample moments are calculated using the unbiased estimators.



## A.12 Continuous wavelet transform

Refer to [MALLAT, 2008; WALNUT, 2002] for more information. The continuous wavelet transform (CWT)  $\tilde{x}_w(a, b)$  of a signal  $x(t)$  is defined as:

$$\tilde{x}_w(a, b) \triangleq \frac{1}{\sqrt{a}} \int_{-\infty}^{+\infty} x(t) \psi^* \left( \frac{t-b}{a} \right) dt \quad \begin{array}{l} a \in \mathbb{R}^+ \\ b \in \mathbb{R} \end{array} \quad (\text{A.47})$$

where  $\psi(t)$  (the “mother wavelet”) is a continuous function in both time and frequency domains,  $a$  the wavelet scales and  $b$  the locations. In the case of a time-domain sequence  $x(t)$ , the CWT returns a time-frequency representation  $\tilde{x}_w(f, t)$  of the signal.

The mother wavelet  $\psi(t)$  is a rapidly decreasing function localized in both time and frequency domains. For example, the Morlet (or Gabor) wavelet is:

$$\psi(t) = c_\sigma e^{-t^2/2} \left( e^{i\sigma t} - e^{\sigma^2/2} \right) \quad \circ \bullet \quad \psi(\omega) = c_\sigma \left( e^{-(\sigma-\omega)^2/2} - e^{-(\sigma^2+\omega^2)/2} \right) \quad (\text{A.48})$$

where a  $\sigma$  is a width parameter and  $c_\sigma \triangleq \pi^{-1/4} \left( 1 + e^{-\sigma^2} - 2e^{-\frac{3}{4}\sigma^2} \right)^{-1/2}$  a normalization parameter. Figure A.3 shows the Morlet (Gabor) wavelet in the time and frequency domains for various values of the parameter  $\sigma$ . The FFT is a special case of CWT where  $\psi(t) = e^{-i2\pi t}$ , which extends over the whole time domain, but is localized to one Dirac delta in frequency domain.

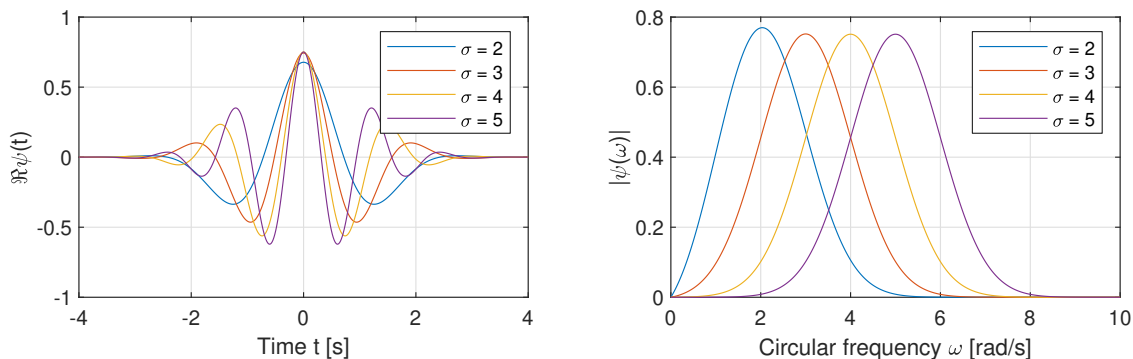


FIGURE A.3: Morlet (Gabor) wavelet in the time and frequency domains.

### A.13 Model of the eigenfrequency variation due to fuel consumption

Our objective is to model the eigenfrequency variation of the wing modes due to fuel consumption during flight. The available data are the geometry and masses of the wing and fuel and the eigenfrequencies of the wing modes estimated with full tank at the start of the flight. We use [DEN HARTOG, 1985] as reference for the structural dynamics of the wing components.

The wing is modeled as illustrated in figure A.4. It consists of three sub-models: a cantilevered beam with mass, a point mass and a spring with mass suspended at the end. The beam has only flexural modes and there is no fuel sloshing.

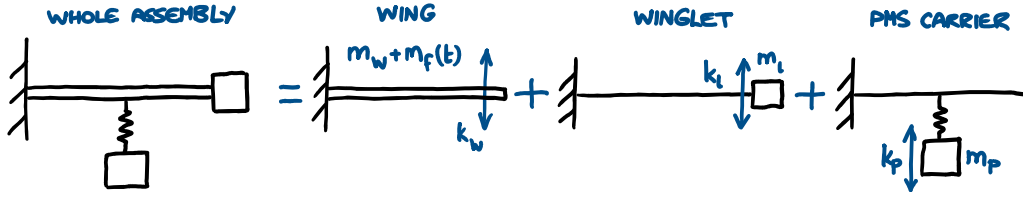


FIGURE A.4: The wing is modeled as a combination of a continuous cantilevered beam (structure and fuel), a point mass (winglet) and a heavy, flexible appendage (PMS carrier).

**Notation.** We adopt the following subscripts for the masses: “w” wing (dry), “f” fuel, “l” winglet, “p” PMS carrier. The numerical subscripts for the fuel mass are 0 for take-off and 1 for landing.

The eigenfrequencies of a continuous cantilevered beam are given by:

$$\omega_w^2 = \alpha_n \frac{EJ}{\rho AL^4} \quad (\text{A.49})$$

where  $E$  is Young’s modulus,  $J$  the area moment of inertia,  $\rho$  the material density,  $A$  the section area,  $L$  the beam’s length and  $\alpha_n$  is the constant pertaining to the  $n$ -th bending mode eigenfrequency of the beam  $\alpha_n = [1.875, 4.694, 7.885, \dots]$ . The eigenfrequency of the beam with a point mass  $\omega_l$  is:

$$\omega_l^2 = \frac{3EJ}{m_l L^3} \quad (\text{A.50})$$

The eigenfrequency of the PMS carrier  $\omega_p$  is unknown at this stage and will be determined later.

We can use Dunkerley’s method to determine the eigenfrequency of the whole assembly from those of the three sub-models:

$$\frac{1}{\omega_n^2} \approx \frac{1}{\omega_w^2} + \frac{1}{\omega_l^2} + \frac{1}{\omega_p^2} \quad (\text{A.51})$$

Equation (A.51) can be then written as:

$$\frac{1}{\omega_n^2(t)} = \frac{1}{k_0} \left( \frac{m_w + m_f(t)}{\alpha_n} + \frac{m_l}{3} \right) + \frac{1}{\omega_p^2} \quad (\text{A.52})$$

where the fuel mass is time-dependent  $m_f(t)$  and where

$$\omega_w^2 = \alpha_n \frac{k_0}{m_w + m_f} \quad \omega_l^2 = 3 \frac{k_0}{m_l} \quad (\text{A.53})$$

since the structural stiffness term  $k_0 = EJ/L^3$  does not change because we consider two instants  $t_0$  and  $t_1$  when the aerodynamic contributions to the overall wing stiffness can be either neglected or are equal.

We can equate this expression for the time instants 0 and  $t$  to remove  $k_0$ :

$$\left( \frac{1}{\omega_n^2(t)} - \frac{1}{\omega_p^2} \right) \left( \frac{m_w + m_f(0)}{\alpha_n} + \frac{m_l}{3} \right) = \left( \frac{1}{\omega_n^2(0)} - \frac{1}{\omega_p^2} \right) \left( \frac{m_w + m_f(t)}{\alpha_n} + \frac{m_l}{3} \right) \quad (\text{A.54})$$

where the unknowns are  $\omega_n(t)$  and  $\omega_p$ . The latter can be determined by a least-squares fit of all known eigenfrequencies  $\omega_n(0)$  or taken from GVT data.

The fuel consumption is determined by thrust, angle of attack, altitude et cetera. Nevertheless, the fuel mass variation  $m_f(t)$  over the duration  $t_1 - t_0$  of an experimental flight (less than 3 hours) can be assumed to be linear:

$$m_f(t) = m_f(t_0) + \frac{m_f(t_1) - m_f(t_0)}{t_1 - t_0} t \quad (\text{A.55})$$

Fuel mass has been recorded in the flight records after every maneuver and is displayed in figure 8.57, showing good agreement with this assumption.

Finally we need to estimate the wing dry mass  $m_f$ . The zero-fuel mass and fuel mass are recorded in the flight sheets after every flight. Most fuel is stored in the wings, but up to 10% is found within the fuselage, so the fuel mass in the wings  $m_f$  is about 45% of the total fuel mass. The wing dry mass can be estimated from the HALO's *Weight and Balance Record* where all relevant items, including paint, are accounted for.

Equation (A.54) can now be solved for  $\omega_n(t)$  to obtain the eigenfrequency variation over time for each eigenmode. The results are plotted in figure 8.58.